WILEY-VCH

Edited by Yuliang Zhao, Zhiyong Zhang,
and Weiyue Feng

Toxicology of Nanomaterials

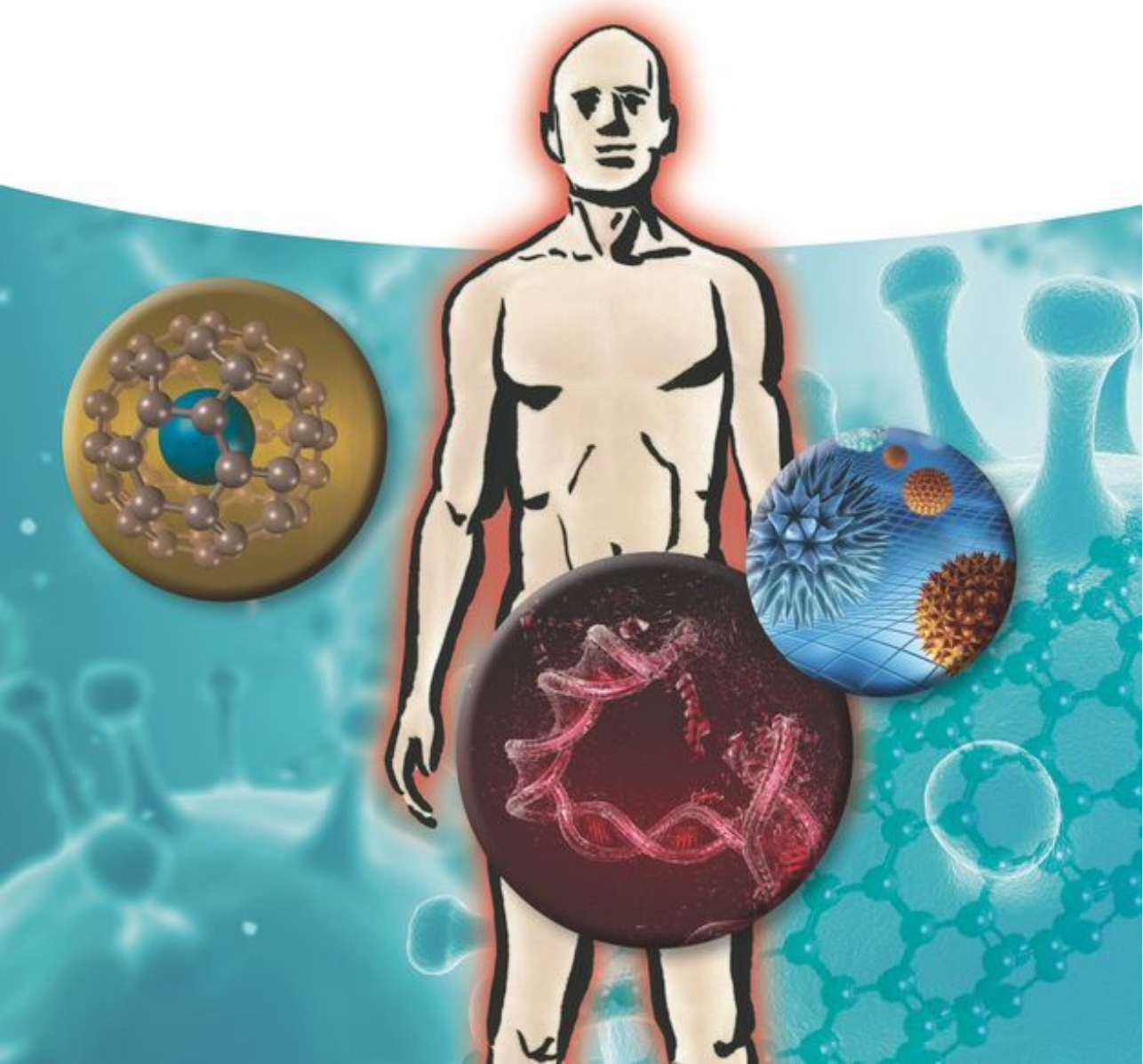

Edited by
Yuliang Zhao, Zhiyong Zhang, and
Weiyue Feng

Toxicology of Nanomaterials

Edited by
Yuliang Zhao, Zhiyong Zhang, and
Weiyue Feng

Toxicology of Nanomaterials

WILEY-VCH
Verlag GmbH & Co. KGaA

Editors

Prof. Yuliang Zhao
Chinese Academy of Sciences
Center for Nanosciences and Technology
19B Yuquan Road
100049 Beijing
China

Prof. Zhiyong Zhang
Chinese Academy of Sciences
Key Laboratory of Biomed Effects of Nanomaterials
19B Yuquan Road
100049 Beijing
China

Prof. Weiyue Feng
Chinese Academy of Sciences
Key Laboratory of Biomed Effects of Nanomaterials
19B Yuquan Road
100049 Beijing
China

Cover
fotolia/MP (background)fotolia/psdesign1 (circle element at the right)istock/Firstsignal (circle element in the middle)

Library of Congress Card No.: applied for

British Library Cataloguing-in-Publication Data
A catalogue record for this book is available from the British Library.

Bibliographic information published by the Deutsche Nationalbibliothek
The Deutsche Nationalbibliothek lists this publication in the Deutsche Nationalbibliografie; detailed bibliographic data are available on the Internet at <http://dnb.d-nb.de>.

Print ISBN: 978-3-527-33797-2
ePDF ISBN: 978-3-527-68913-2
ePub ISBN: 978-3-527-68915-6
Mobi ISBN: 978-3-527-68914-9
oBook ISBN: 978-3-527-68912-5

Cover Design Schulz Grafik-Design, Fußgönheim, Germany
Typesetting SPi Global, Chennai, India
Printing and Binding

Printed on acid-free paper

Contents

List of Contributors

Xueling Chang
Institute of High Energy Physics
CAS Key Laboratory for
Biomedical Effects of
Nanomaterials and Nanosafety
Chinese Academy of Sciences
Beijing 100049
China

Chunying Chen
CAS Key Laboratory for
Biomedical Effects of
Nanomaterials and Nanosafety
National Center for Nanoscience
and Technology
Beijing 100190
China

Weiyue Feng
Institute of High Energy Physics
CAS Key Laboratory for
Biomedical Effects of
Nanomaterials and Nanosafety
Chinese Academy of Sciences
Beijing 100049
China

Yuxi Gao
Institute of High Energy Physics
CAS Key Laboratory for
Biomedical Effects of
Nanomaterials and Nanosafety
Chinese Academy of Sciences
Beijing 100049
China

Zhanjun Gu
Institute of High Energy Physics
CAS Key Laboratory for
Biomedical Effects of
Nanomaterials and Nanosafety
Chinese Academy of Sciences
Beijing 100049
China

Xiao He
Institute of High Energy Physics
CAS Key Laboratory for
Biomedical Effects of
Nanomaterials and Nanosafety
Chinese Academy of Sciences
Beijing 100049
China

Chenchen Li
Shanghai University
Institute of Nanochemistry and
Nanobiology
Shanghai 200444
China

Wei Li
Institute of High Energy Physics
CAS Key Laboratory for
Biomedical Effects of
Nanomaterials and Nanosafety
Chinese Academy of Sciences
Beijing 100049
China

and

Wuhan Institute of Virology
Chinese Academy of Sciences
Wuhan 430071
China

Yu-Feng Li
Institute of High Energy Physics
CAS Key Laboratory for
Biomedical Effects of
Nanomaterials and Nanosafety
Chinese Academy of Sciences
Beijing 100049
China

Xueying Liu
Institute of High Energy Physics
CAS Key Laboratory for
Biomedical Effects of
Nanomaterials and Nanosafety
Chinese Academy of Sciences
Beijing 100049
China

Yuhui Ma
Institute of High Energy Physics
CAS Key Laboratory for
Biomedical Effects of
Nanomaterials and Nanosafety
Chinese Academy of Sciences
Beijing 100049
China

Bing Wang
Institute of High Energy Physics
CAS Key Laboratory for
Biomedical Effects of
Nanomaterials and Nanosafety
Chinese Academy of Sciences
Beijing 100049
China

Liming Wang
Institute of High Energy Physics
CAS Key Laboratory for
Biomedical Effects of
Nanomaterials and Nanosafety
Chinese Academy of Sciences
Beijing 100049
China

Meng Wang
Institute of High Energy Physics
CAS Key Laboratory for
Biomedical Effects of
Nanomaterials and Nanosafety
Chinese Academy of Sciences
Beijing 100049
China

Yanli Wang
Shanghai University
Institute of Nanochemistry and
Nanobiology
Shanghai 200444
China

Liang Yan
Institute of High Energy Physics
CAS Key Laboratory for
Biomedical Effects of
Nanomaterials and Nanosafety
Chinese Academy of Sciences
Beijing 100049
China

Peng Zhang
Institute of High Energy Physics
CAS Key Laboratory for
Biomedical Effects of
Nanomaterials and Nanosafety
Chinese Academy of Sciences
Beijing 100049
China

Zhiyong Zhang
Institute of High Energy Physics
CAS Key Laboratory for
Biomedical Effects of
Nanomaterials and Nanosafety
Chinese Academy of Sciences
Beijing 100049
China

Feng Zhao
Institute of High Energy Physics
CAS Key Laboratory for
Biomedical Effects of
Nanomaterials and Nanosafety
Chinese Academy of Sciences
Beijing 100049
China

Jiating Zhao
Institute of High Energy Physics
CAS Key Laboratory for
Biomedical Effects of
Nanomaterials and Nanosafety
Chinese Academy of Sciences
Beijing 100049
China

Lina Zhao
Institute of High Energy Physics
CAS Key Laboratory for
Biomedical Effects of
Nanomaterials and Nanosafety
Chinese Academy of Sciences
Beijing 100049
China

Yuliang Zhao
Institute of High Energy Physics
CAS Key Laboratory for
Biomedical Effects of
Nanomaterials and Nanosafety
Chinese Academy of Sciences
Beijing 100049
China

Preface

After more than 30 years of basic and applied research, nanotechnology is coming to play a big role in almost all of our lives, ranging from industry, food, and agriculture to biomedicine, and so on. Nanomaterials are known as the most important bases of nanotechnology and possess more novel and unique physicochemical properties than bulk materials. So, the impacts of their unpredictable behaviors on human health and the environment undoubtedly cause public concern. The understanding of the safety and potential hazards of engineered nanomaterials (ENMs), that is, nanotoxicity, has witnessed an explosion in the past decade and become one of key issues in nanotechnology, in particularly, the sustainable development of nanotechnology.

The study of toxicology of nanomaterials, unlike the classic one for those ordinary chemical compounds, should be approached by many ways, as multiparameters associated with the size, shape, chemical composition, crystalline structure, aspect ratio, surface property (chemical modification, surface charge, surface area, biological/chemical activity, etc.), agglomeration, concentration, and so on, likely combine to contribute to the overall toxicity. To obtain the whole picture, the advanced methods with integrated techniques for quantitatively monitoring the biological responses with material-specific or exposure-route-specific are needed. Moreover, it is expected that some new techniques, such as synchrotron-radiation-based analytical techniques, high-throughput "omic" techniques, *in situ*, and *in vivo* image techniques, as well as computational biology are involved for the exploration of exposure, early effect, differentially sensitive targets, and molecular mechanisms of ENMs in biological systems and, furthermore, trigger revolutionary research to understand the complex reactions of nanomaterials occurring at a nano–bio interface of biological or environmental systems.

Toxicology of Nanomaterials focuses on topics describing the current tools and methods that have been developed to study nanomaterial effects on biological and environmental systems, including the following: Characterization of Nanomaterials in Nanotoxicological Analyses (Ma Yuhui); Quantitative Analysis of Metal-Based Nanomaterials in Biological Samples Using inductively coupled plasma–mass spectrometry (ICP-MS) (Wang Meng); Stable Isotopic Tracing of Nanomaterials *In Vivo* (Chang Xueling, Zhao Yuliang); Radiolabeling

of Nanoparticles (Zhang Zhiyong); New Methods for Nanotoxicity Analyses: Synchrotron-Radiation-Based Techniques (Wang Bing, Feng Weiyue); Imaging Techniques in Nanotoxicology Research (Yan Liang, Li Yufeng, Gu Zhanjun); *In Vivo* Nanotoxicity Assays in Animal Models (He Xiao); *In Vitro* Testing Methods for Nanomaterials (Zhao Feng, Liu Xueying); Localizing cellular uptake of nanomaterials (Li wei); Methods and Techniques in Molecular Toxicology of Nanomaterials (Wang Yanli, Li Chenchen, Chen Chunying); Analyses Methods for Nanoparticle Interaction with Biomacromolecules (Wang Liming, Chen Chunying); Omics Techniques in Nanosafety (Feng Weiyue); Nanometallomics: New Approach on Analyzing Biological Effects of Metal-Related Nanomaterials (Li Yufeng, Zhao Jiating, Gao Yuxi, Chen Chunying); Molecular Simulation Methods for safety Analyses of Nanomaterials (Zhao Lina): Ecotoxicity Analyses of Nanomaterials (Zhang Peng). Excepting Yanli Wang, all the other authors are from Chinese Academy of Sciences Key Laboratory for Biomedical Effects of Nanomaterials and Nanosafety. Please note that the book is not possible to describe detailed principles of all the aforementioned analyses methods, but describes how to apply these methods in the study of nanotoxicology.

The outcomes from more than 10 years of nanosafety research have shown that the interactions between nanomaterials and cells, animals, humans, or the environment are remarkably complex. Thus, this book also intends to give the state-of-art information on multidisciplinary techniques from biology, chemistry, and physics that enables the study of nanotoxicology. The book is designed to benefit researchers who plan to investigate nanotoxicology, nanomedicines, nanobiotechnology, and biomedical nanomaterials, nanochemistry, nanobioanalytical sciences, and so on, in particularly, to understand how the physical, chemical, and other properties of nanomaterials influence their biological/environmental behaviors and interactions and thus determine the ultimate impacts on health and the environment, and to design/synthesize/manufacture safer nanomaterials in various applications.

Beijing June, 2016 *Yuliang Zhao, Zhiyong Zhang, and Weiyue Feng*

Abbreviations

2-DGE	two-dimensional gel electrophoresis
ADME	absorption, distribution, metabolism, and excretion
AES	auger electron spectroscopy
AFM	atomic force microscope
AMBER	assisted model building with energy refinement
AMs	alveolar macrophages
AMU	atomic mass unit
ARDRA	amplified ribosomal DNA restriction analysis
BALF	bronchoalveolar lavage fluid
BBB	blood–brain barrier
BFG	bovine fibrinogen
BO	bond order
BSA	bovine serum albumin
C2	molecule of two C atoms
CAT	catalase
CD	circular dichroism
CE	capillary electrophoresis
CE-MS	capillary electrophoresis–mass spectrometry
CHARMM	chemistry Harvard macromolecular mechanics
CMAP	cross-term map
CNS	central nervous system
CTAB	cetyltrimethylammonium bromide
CT-SPECT	computed tomography coregistered with single-photon emission computerized tomography
Cyt c	cytochrome c
DCFH-DA	dichlorodihydrofluorescein diacetate
DCS	differential centrifugal sedimentation
DFT	density function theory
DGGE	denaturing gradient gel electrophoresis
DLS	dynamic light scattering
DMEM	Dulbecco's modified eagle's medium
DOTA	1,4,7,10-tetraazacyclododecane-tetraacetic acid
dsDNA	double-strand DNA

EDX or EDS	energy-dispersive X-ray spectroscopy
EE	electron equilibration
EELS	electron energy-loss spectroscopy
EGP	effective group potentials
ELISA	enzyme-linked immunosorbent assay
ENM	engineered nanomaterial
EPR	electron paramagnetic resonance
ESCA	electron spectroscopy for chemical analysis
ESEM	environmental scanning electronic microscopy
ESI-MS	electrospray ionization – mass spectrometry
EXAFS	extended X-ray absorption fine structure
FBS	fetal bovine serum
FCM	flow cytometry
FFF	field flow fractionation
FISH	fluorescence in situ hybridization
FTIR	Fourier-transform infrared spectroscopy
GC	gas chromatography
GC-MS	gas chromatography – mass spectrometry
GE	gel electrophoresis
GGA	generalized gradient approximation
GHO	generalized hybrid orbital
GO	graphene oxide
GROMOS	Groningen molecular simulation
GPx	glutathione peroxidase
HCS	high-content screening
HDC	hydrodynamic chromatography
HPLC	high-performance liquid chromatography
HPRT	hypoxanthine-guanine phosphoribosyltransferase
HSA	human serum albumin
ICP-MS	inductively coupled plasma – mass spectrometry
ICP-OES	inductively coupled plasma – optical emission spectrometer
Ig	gamma globulin
IgG	immunoglobulin G
IR	infrared spectroscopy
IRMS	isotope ratio mass spectrometry
ITC	isothermal titration calorimetry
LA-ICP-MS	laser ablation – inductively coupled plasma – mass spectrometry
LC-MS	liquid chromatography – mass spectroscopy
LCSM	laser confocal scanning microscopy
LDH	lactate dehydrogenase
LEIS	low-energy ion scattering
LSCF	local self-consistent field
LSDA	local spin density approximation

MALDI-TOF-MS	matrix-assisted laser desorption/ionization time-of-flight mass spectrometry
MD	molecular dynamics
MDA	malondialdehyde
MFM	multiphoton fluorescence microscope
MMP-9	matrix metalloproteinases-9
MN	micronucleus
MRI	magnetic resonance imaging
MTT	3-(4,5-dimethylthiazol-2-yl)-2,5-diphenyltetrazolium bromide
MWCNTs	multiwalled carbon nanotubes
NAA	neutron activation analysis
NADH	nicotinamide adenine dinucleotide
NADPH	nicotinamide adenine dinucleotide phosphate
NanoXRF	SRXRF with the nanosized spatial resolution
NEGF	nonequilibrium Green's function
NM	nanomaterial
NMR	nuclear magnetic resonance
NOM	natural organic matters
NOTA	1,4,7-triazacyclononane-1,4,7-triacetic acid
NP	nanoparticle
OPLS-AA	optimized potentials for liquid simulations-all atom
PAA	poly(acrylic acid)
PC	protein corona
PCR-DGGE	polymerase chain reaction–denaturing gradient gel electrophoresis
PET	positron emission tomography
PLFA	phospholipid fatty acid
PME	particle mesh Ewald
PMF	potential of mean force
PVP	polyvinyl pyrrolidone
QDs	quantum dots
QEq	Q Equilibration
QM/MM	quantum mechanics/molecular mechanics
qPCR	quantitative polymerase chain reaction
REMD	replica-exchange molecular dynamics
RES	reticuloendothelial systems
REST	replica exchange with solvent tempering
rGO	reduced graphene oxide
RMSD	root mean square deviation
RMSF	root mean square fluctuation
ROS	reactive oxygen species
RT-PCR	reverse transcription polymerase chain reaction
SAXS	small-angle X-ray scattering
SBO	sum of π-bond order

SCE	sister chromatid exchange
SCGE	single-cell gel electrophoresis assay
SDS-PAGE	sodium dodecylsulphate–polyacrylamide gel electrophoresis
SEC	size-exclusion chromatography
SEM	scanning electron microscope
SERS	surface-enhanced Raman spectroscopy
SIEMN	inhalation exposure for manufactured nanomaterials
SIMS	secondary ion mass spectroscopy
SOD	superoxide dismutase
SPECT	single-photon emission computerized tomography
sp-ICP-MS	single-particle inductively coupled plasma–mass spectrometry
SPIONs	superparamagnetic iron oxide nanoparticles
SQUID	superconducting quantum interference device
SR	synchrotron radiation
SRXRF	synchrotron radiation X-ray fluorescence
STM	scanning tunneling microscopy
STXM	scanning transmission X-ray microscopy
SWCNTs	single-walled carbon nanotubes
TEM	transmission electron microscope
TETA	1,4,8,11-tetraazacyclotetradecane-*N*,*N*′,*N*″,*N*‴-tetraacetic acid
Tf	transferrin
TOF-SIMS	time-of-flight secondary-ion mass spectrometry
T-RFLP	terminal restriction fragment length polymorphism
UV-Vis	ultraviolet–visible spectrophotometry
XANES	X-ray absorption near-edge structure spectra
XAS	X-ray absorption spectroscopy
XPS	X-ray photoelectron spectroscopy
XRD	X-ray diffraction
XRF	X-ray fluorescence
γ-H2AX IF	γ-H2AX immunofluorescence assay

1
Characterization of Nanomaterials in Nanotoxicological Analyses

Yuhui Ma

1.1
Introduction

In accordance with the European Commission's Recommendation, "Nanomaterial" is defined as a natural, incidental, or manufactured material containing particles, in an unbound state or as an aggregate or as an agglomerate and where, for 50% or more of the particles in the number size distribution, one or more external dimensions are in the size range 1 – 100 nm [1]. Nanomaterials (NMs) have attracted great attention because of their unique physical, chemical, and mechanical properties that differ from those of bulk solids and molecules, which enabled them to be widely used in the fields of electronics, chemical industry, medicine, machinery, energy, and so on. With the widespread applications of NMs, the environmental and health impacts of these materials have caused the attention of scientific community, regulatory agencies, environmentalists, industry representatives, and the public. They all agree that more efforts are required to ensure the responsible and safe development of new nanotechnologies. Characterization of NMs is a key aspect in this effort because physicochemical properties of NMs are important factors determining their biological effects and environmental fate. However, there is no universal agreement upon the minimum set of characteristics, although certain common properties are included in most recommendations. Particle characterization is an essential aspect of any attempt to assess potential biological effects of nanoparticulate systems. The thorough characterization of NMs is a daunting task, especially in the context of a complex biological environment. The characteristics of NMs should be measured under conditions as close to the point of application as possible. For toxicology studies, this should include, if possible, the biological environment. For example, if *in vitro* cell studies are being conducted, the particle size should be measured in cell culture media or at least under the same pH and ionic strength conditions.

Toxicology of Nanomaterials, First Edition. Edited by Yuliang Zhao, Zhiyong Zhang, and Weiyue Feng.

Physicochemical properties are the basis for understanding the biological effects of test materials. In this chapter, we emphasize and illustrate the major characterization parameters, including size and size distribution, shape, agglomeration state, crystal structure, chemical composition, surface area, surface chemistry, and surface charge, which should be investigated before, during, and after administration. In addition, the available analytical techniques, methods, and procedures are evaluated to be capable of detecting and quantifying NMs during *in vivo*/*in vitro* studies. These topics provide a comprehensive review of more adequate characterization techniques, methods, and procedures.

1.2 Size and Morphology of NMs

1.2.1 Transmission Electron Microscopy (TEM)

TEM has become one of the most powerful characterization tools in NM research, which provides direct images and information such as the size, shape, morphology, agglomeration state, and crystalline structure of particles at a spatial resolution down to the level of atomic dimensions (<1 nm) [2]. In the conventional TEM mode, an incident electron beam is transmitted through a very thin foil specimen, during which the incident electrons interacting with specimen are transformed to unscattered electrons, elastically scattered electrons, or inelastically scattered electrons [3]. The magnification of TEM is mainly determined by the ratio of the distance between objective lens and the specimen and the distance between objective lens and its image plane. The scattered or unscattered electrons are focused by a series of electromagnetic lenses and then projected on a screen to generate an electron diffraction (ED), amplitude-contrast image, a phase-contrast image, or a shadow image of varying darkness according to the density of unscattered electrons [3]. In addition to the high spatial resolution of TEM, one should ensure that enough particles are examined to provide statistically valid representation of the full size or shape distribution. This can be very difficult and time-consuming and may require the image analysis of literally thousands of individual particles. There are many commercial automated image analysis systems and computer software packages that are used for this purpose. Although TEM is a useful characterization tool, a wide variety of analytical techniques can be coupled with TEM for different applications; for example, energy-dispersive spectroscopy (EDS), electron diffraction (ED), or electron energy-loss spectroscopy (EELS) may be useful for determining additional characterization parameters such as chemical composition and speciation at the atomic scale.

However, there are certain drawbacks accompanying the advantages of TEM. Since a high vacuum and thin sample section are required for electron-beam penetration in TEM measurement, care should be taken to validate the system used against standardized materials and sample preparation [4]. The

representativeness of the sample depends on their dispersion, so it is necessary to select the appropriate disperse conditions to achieve a uniform dispersion of the particles. It should also be noted that electron microscopy normally provides only two-dimensional images, so care must be taken to avoid bias introduced by orientation effects. High-resolution microscopy is subject to artifacts caused by sample preparation or special analysis conditions.

1.2.2 Scanning Electron Microscopy (SEM)

SEM is a surface imaging method in which the incident electron beam scans across the sample surface and interacts with the sample to generate signals reflecting the topographic detail of the specimen surface [4, 5]. The incident electrons cause emissions of elastic scattering of electrons, referring to backscattered electrons, low-energy secondary electrons, and cathodoluminescence from the atoms on the sample surface or near-surface material. Among these emissions, detection of the secondary electrons is the most common mode in SEM and can achieve resolution smaller than 1 nm [5]. It does not require electron-beam penetration in SEM measurement, so it can be used for bulk samples, except for soft biological tissues, which contain large amounts of water.

The size, size distribution, and shape of NMs can be directly acquired from SEM. For conducting materials, the sample preparation is simple, with the size and weight of samples being required for different SEM sample rooms. While for many biological samples with poor electrical conductivity or even insulator, the surface of specimens should be coated by spraying an ultrathin layer of electrically conducting material, such as gold, silver, or other precious metals [4]. When the size of the particles was below 10 nm, the sample cannot be sprayed by gold, for the size of this coating is about 8 nm. The carbon evaporation coating is an alternative method. In short, the samples for SEM should be dry and conductive, as well as the surface structure should be well preserved without deformation or contamination.

1.2.3 Scanning Tunneling Microscopy (STM)

Scanning probe microscopy (SPM) techniques adapt a generic principle, that is, bringing a susceptible probe in close proximity to the surface of an object measured to monitor the reactions of the probe [6]. As the earliest developed technique in the SPM family, STM uses quantum tunneling current to generate electron density images for conductive or semiconductive surfaces and biomolecules attached on conductive substrates at the atomic scale [7–9]. The essential components of STM include a sharp scanning tip, an xyz piezo scanner controlling the lateral and vertical movements of the tip, a coarse control unit positioning the tip close to the sample within the tunneling range, a vibration isolation stage, and feedback regulation electronics. As the tip-sample separation

is maintained in the range of 4–7 Å, a small voltage applied between the scanning tip and the surface causes tunneling of electrons by which variation of the responding current can be recorded while the tip moves across the sample in the *x-y* plane to generate a map of charge density. Alternatively, keeping the responding current unchanged by adjusting the tip height through the use of feedback electronics can generate an image of tip topography across the sample [10].

STM can provide the information of the sample surface at atomic-scale resolution, with parallel resolution of 0.1 nm and perpendicular resolution of 0.01 nm, by using a very sharp tip [11]. It can directly observe the morphology, defects, adsorption, and reconstruction on the surface of specimen by monitoring the structure of single atomic layer on the surface. Different from the samples being usually embedded into a matrix to preserve their original conformations and detection in vacuum in EM techniques, SPM does not need special sample preparation and can perform under environmental conditions, even in water and other solution, with no damage to the sample. Although the high spatial resolution of STM should benefit the characterization of nanoscale biomaterials such as size, shape, structure, and states of dispersion and aggregation, only few studies using gold or carbon as substrates have been reported [12]. The requirements of the conductive surface of the sample and detection of the surface electronic structure were the main practical obstacles, for most biomaterials are insulating and a simple connection of the sample's surface electronic structure with its surface topography may not necessarily exist. Still, STM is a preferred tool for investigating conductive atomic structures of, for example, carbon nanotubes, fullerenes, and graphene [12].

1.2.4
Atomic Force Microscopy (AFM)

AFM does not require electrically conductive surfaces and is a SPM imaging tool consisting of a micromachined cantilever (typically made of silicon or silicon nitride) with a sharp tip at one end to detect the deflection of the cantilever tip caused by electrostatic and van der Waals repulsion, as well as attraction between atoms at the tip and on the measured surface [13–15]. The oscillating cantilever then scans over the surface of specimen to generate an image. Unlike SEM and TEM techniques, which have only high lateral resolutions, AFM can also be used for investigating the size, shape, structure, sorption, dispersion, and aggregation of NMs with a high vertical resolution of around 0.5 nm [16, 17]. The different scanning modes employed in AFM studies include noncontact mode (also called *static mode*), contact mode, and intermittent sample contact mode (also called *dynamic mode* and *tapping mode*). In addition to probing the sizes and shapes of NMs under physiological conditions, AFM is capable of characterizing dynamics between NMs in biological situations, such as observing the interaction of NMs with supported lipid bilayers in real time, which is not achievable with the current EM techniques [18].

The main strength of AFM is its capability to image a variety of biomaterials at the subnanometer scale in aqueous fluids without causing appreciable damage to

many types of native surfaces [19]. However, a major drawback is that the size of the cantilever tip is generally larger than the dimensions of the NMs examined, leading to incorrect estimation of the lateral dimensions of the samples [16]. On the other hand, AFM lacks the capability of detecting or locating specific molecules. Recently, this disadvantage has been eliminated by the progress in single-molecule force spectroscopy with an AFM cantilever tip carrying a ligand, a cell adhesion molecule, or chemical groups, which can probe or detect single functional molecules on cell surfaces [20, 21].

1.2.5
Dynamic Light Scattering (DLS)

Dynamic light scattering (DLS), one of the most popular light scattering techniques, can determine the size distribution of small particles, molecules, or polymers at the scale from submicron down to 1 nm in solution or suspension using a laser as light source [22, 23]. In a DLS experiment, a laser beam is directed at the nanoparticle dispersion, and fluctuations in the intensity of the scattered light are monitored with a photon detector and related to the size of a hypothetical hard sphere that diffuses in the same fashion as the nanoparticles being measured using the Stokes–Einstein equation [23–25]. Thus, the DLS is unsuited to accurately measuring the sizes of nonspherical NMs because equivalent spherical nature of particles is already assumed in the analysis. The polydispersity index (PDI) can indicate the size distribution of the NP dispersion. The larger the PDI, the broader is the size distribution, and a PDI value from 0.1 to 0.25 implies a narrow size distribution [26]. For physicochemical characterization of NMs, the main strengths of DLS include its noninvasive manner, short experiment duration, accuracy in determining the hydrodynamic size of monodisperse samples, and capabilities of measuring diluted samples, analyzing samples in a wide range of concentrations and detecting small amounts of higher molecular weight species, along with lower apparatus costs and more reproducible measurement than other methods [27, 28].

However, it should be noted that DLS measurements can be performed only for a certain range of nanoparticle concentrations, since it is difficult to correlate size fractions with a particular composition when certain amounts of aggregates are present. Also, the nanoparticle suspensions should be sufficiently stable so that there is no significant sedimentation for the duration of the experiment, and dust particles can interfere in the scattering intensity. In addition, DLS has limited utility for analysis of samples with heterogeneous size distributions and resolving the dimensions of a mixed sample population varying in size less than a factor of 3 [27, 29, 30].

1.2.6
X-ray Diffraction (XRD)

An ideal nanocrystalline sample is composed of highly uniform NMs in size and shape. One technique that characterizes both size and crystallinity of NMs at the

atomic scale is X-ray diffraction (XRD). Nanocrystals diffract X-rays in unique ways. The diffraction of X-ray can be simply described as the reflection of a collimated beam of X-rays incident on the crystalline planes of an examined specimen according to Bragg's law. An XRD pattern does not exist in an amorphous sample. Typically, XRD is a tool for characterizing crystalline size, shape, and lattice distortion by long-range order of a crystalline sample. Sizes will change depending on the chemical composition of the crystal. The following Equation 1.1 can be used to determine the grain size of a nanocrystal:

$$D = \frac{0.89\lambda}{\beta \cos \theta} \tag{1.1}$$

where D is the crystallite size, λ is the X-ray wavelength (1.54 Å for Cu Kα radiation), and θ is the Bragg angle. β is taken as the full width at half max of a sample.

Although XRD can confirm a crystalline product and has frequently been used to determine the material structure at the atomic scale, difficulty in growing crystals and the requirement of the amount of powder sample (about 100 mg) limit the applications of XRD technique [31]. Because nanocrystals have such small grain sizes, a long collection time is needed for the sample of interest. In addition, the measured value is more accurate when the grain size is less than 50 nm than the larger ones. Another disadvantage of XRD is the low intensity of diffracted X-rays, particularly for low atomic number materials, compared with ED. A recent X-ray diffraction study reported a new approach using femtosecond pulses from a hard X-ray free-electron laser for structure determination, which may benefit structure determination of macromolecules that do not yield sufficient crystal size for using conventional radiation sources or are not sensitive to radiation damage [32].

1.2.7 Small-Angle X-ray Scattering (SAXS)

Different from XRD, whose applications are limited to crystalline materials, small-angle X-ray scattering (SAXS) provides information of several characteristics by examining either crystalline or amorphous materials in the range of 1–300 nm [23, 33, 34]. SAXS can be used to analyze inorganic and organic materials from polymers, proteins to nanoparticles, without special sample preparation process. In SAXS, a portion of an incident X-ray beam elastically scattered from the sample forms a scattering pattern on a two-dimensional flat X-ray detector perpendicular to the direction of the incident X-ray beam. By analyzing the intensity of the scattered X-ray collected within the scattering angle, ranging from 0.1° to 3°, SAXS can evaluate the size/size distribution, shape, orientation, and structure of a variety of polymers and NM-bioconjugate systems in solutions [35].

The features of small-angle scattering in SAXS lead to the capability of studying nonrepeating structures; thus, perfect crystallized structures are not required, which simplifies sample preparation and makes SAXS a nondestructive method. On the other hand, SAXS measurements provide holistic information about the structure of large number of samples, which exhibits the averaged

characteristics rather than local probes of individual grains [34]. This feature can be a disadvantage if high resolution is required. Recently, synchrotron radiation as a high-energy X-ray source has greatly enhanced the resolution of SAXS in the analysis of polymers, proteins, aggregates, gel, catalyst, as well as NMs with different dispersions [36]. However, SAXS is not suitable to measure the particles whose shapes are not such spherical or the mixed powder, which are composed of different materials. In addition, it is important to choose the proper angle for measurement, because the interference effects may impact the accuracy of results.

1.2.8 Brunauer–Emmett–Teller (BET)

Specific surface area, the total surface area of the materials per unit mass (m^2/g), is one of the most important physical properties of NMs, which is usually used to evaluate the ability of reactivity, adsorption, and catalysis of them [37, 38]. Some NMs are designed into porous for the catalyst and adsorption agent. The sizes, shape, volume, and size distribution of pores are very important for these materials [39]. Surface area and porosity of NMs are frequently analyzed using the Brunauer–Emmett–Teller (BET) gas absorption/desorption method [40–42].

The method is based on a model of multilayer adsorption, which satisfies several conditions that adsorption occurs on the adsorbing sites and on top of the adsorbed molecules, that the number of adsorbing sites in each layer is constant, that the energy of the first-layer adsorbing sites is uniform, and that molecules in all layers above the first behave as if in a bulk liquid [39]. Given these conditions, the particle diameter can be calculated according to the specific surface area S_ω per unit weight of the powder by the Equation 1.2:

$$D = \frac{k}{\rho S_\omega} \tag{1.2}$$

where D is the average diameter of the particles, ρ is the density, and k is a factor of particle shape, with different values for different shapes and 6 for spherical particles. It should be noted that this method is only applicable for the spherical particles without pores. On the other hand, BET surface area measurements involve heating of the sample in vacuum before the measurement of nitrogen adsorption/desorption. Thus, the obtained surface area value may not necessarily be a relevant measure of available surface area in a liquid medium due to the fact that NMs in liquid may aggregate together.

1.2.9 Raman Scattering (RS)

Raman scattering (RS) is a widely used tool for structural characterization of NMs and nanostructures that provides submicron spatial resolution for light-transparent material without the requirement of sample preparation, making it suitable for *in situ* experiments [43]. The process of RS records frequency

differences between the incident photons and the inelastically scattered photons associated with the characteristics of the molecular vibrational states, during which the inelastically scattered photons emitting frequencies lower than the incident photons refer to the Stokes lines in Raman spectrum and the inelastically scattered photons emitting frequencies higher than the incident photons are named anti-Stokes lines. The principle of RS is to measure the inelastic scattering of photons possessing different frequencies from the incident light after interacting with electric dipoles of the molecule. RS is generally considered to be complementary to IR spectroscopy, since vibrational modes that are Raman active should be IR inactive, and vice versa. Raman transitions result from nuclear motion modulating the polarizability of the molecules, rather than a net change in the dipole moment of the molecules. Raman spectroscopy can be used to investigate conformations and concentrations of tissue constituents, which demonstrates the potential of RS for detecting tissue abnormalities [44]. Also, it can be used to calculate the average particle size of nanocrystalline by the Equation 1.3:

$$d = 2\pi\left(\frac{B}{\Delta\omega}\right)^{1/2} \tag{1.3}$$

where B is a constant, $\Delta\omega$ is the peak shift for the microcrystalline as compared to the amorphous-like samples [45].

RS is suitable for studying biological samples in aqueous solution because water molecules tend to be weak Raman scatterers. However, while the conventional RS technique provides indirect characterization of NMs, such as average size and size distribution through analysis of the spectral line broadening and shift, it lacks the spatial resolution necessary to delineate different domains for application in nanotechnology [43, 46]. Other disadvantages of conventional RS include interference of fluorescence and extremely small cross section, demanding intense laser excitation and a large amount of sample materials to provide sufficient RS signals [47]. In contrast, implementation of surface-enhanced Raman scattering (SERS) can strongly enhance RS signals and increase spatial resolution while the measured biomolecules are adhered to the surface of metallic structures, such as commonly used Au or Ag NP colloid substrates [48–50]. SERS can be used to (i) study surface functionalization of metallic NPs, (ii) monitor the conformational change in proteins conjugated to the metallic NPs, and (iii) track intracellular drug release from the nanoplatform and measurement of the pH in the surrounding medium [51–55].

1.3 Composition and Structure

In addition to size and shape, chemical composition is another important factor in determining toxicity of NMs. Composition of an NM affects its transport, delivery, and biodistribution. For example, cytotoxicity is generally observed in

quantum dots with core metalloid complexes consisting of widely used metals such as cadmium and selenium [56]. Still, quantum dots can be rendered non-toxic, when core and coatings are appropriately designed [57–59]; alternatively, the cytotoxicity of quantum dots was only observed after degradation of their core coating *in vivo* or *in vitro* [60, 61]. There are several studies addressing toxicological concerns about NPs of different compositions [56]. In biomedical applications of NMs, there may be a need to combine two or more types of NMs to forma complex such as a chelate, a conjugant, or a capsule. Consequently, chemical composition analysis of the NM complex is more complicated than that for a single entity [18].

The atomic absorption spectroscopy (AAS), optical emission spectroscopy (OES), mass spectrometry (MS), energy spectrum analysis, nuclear magnetic resonance (NMR), and X-ray absorption fine structure (XAFS) can be used to analyze the chemical composition or structure of NMs. Some of these methods, such as AAS, OES, and inductively coupled plasma–mass spectrometry (ICP-MS), require performing acid digestion of the samples before determination [42]. Other methods, such as X-ray fluorescence and diffraction analysis, called *non-destructive methods*, allow direct measurement of the solid samples.

1.3.1
Absorption and Emission Spectroscopy

Spectroscopy is one of the most common analytical techniques in nanoscience. This characterization technique measures and interprets various areas of the electromagnetic spectra from either the emission or the absorption of energy by different materials. Different types of spectroscopic techniques can be used to characterize engineered NMs. For example, Raman spectroscopy is used to study vibrational, rotational, and other low-frequency modes in a system and can be utilized to determine the type and degree of functionalization on the sidewall of a carbon nanotube. Absorption spectroscopy is used to quantify the amount of photons a substance absorbs and can be utilized to measure the size of gold nanoshells. Fluorescence spectroscopy is used to analyze the different frequencies of light emitted by a substance, which is then used to determine the structure of the vibrational levels of that substance.

1.3.2
Mass Spectrometry (MS)

MS is one of the major analytical techniques used to examine the mass, elemental composition, and chemical structure of a particle or molecule. The basic principle of MS is to distinguish charged particles with different masses based on their mass-to-charge ratios. MS provides a high degree of precision and accuracy for molecular weight determination, as well as high detection sensitivity, which only requires a small amount of sample (10^{-9} to 10^{-21} mol). Several physicochemical characteristics of NMs, including mass, composition, and structure, can be

depicted using various MS procedures, distinguished by their ion sources, separation methods, and detector systems. Among the ionization techniques coupled with MS analyzers, inductively coupled plasma (ICP) ionization is mainly implemented in the analysis of metal-containing NMs [16, 62]. Applications of different MS procedures for NMs include using time of flight (TOF)-MS to determine the size/size distribution of NMs [63], MALDI-TOF-MS to measure the molecular weights of macromolecules, polymers, and dendrimers as well as to illustrate proteins binding to NMs [18, 64], ICP-MS to validate the conjugation reaction of a functionalized NP with a modified contrast agent [65], and secondary ion MS to access the elemental and molecular properties of the top layer of NPs, as well as to examine biomaterial surface properties in physiological conditions [66, 67]. Although these MS techniques have been applied to the analysis of physicochemical properties of various biomolecules, the currently incomplete MS spectral databases still cause difficulties in identifying molecular species, for example, in the analysis of MALDI-TOF-MS outcome measures [68]. Additionally, the applications of MS techniques for NMs to date are constrained in NM-bioconjugate characterization, mainly due to the cost of instrumentation, sample destruction, and necessary instruments generally supplied for other investigations [23].

1.3.3 X-ray Fluorescence Spectrometry (XRF)

X-ray fluorescence spectrometry (XRF) can be used to measure the solid samples, which has great advantages in the analysis of chemical composition of NMs. X-rays are electromagnetic radiation and are manifested in two forms, continuous radiation and characteristic radiation. Continuous radiation is produced when a high-energy electron beam decelerates as it approaches the electron clouds that surround the atomic nucleus. Characteristic radiation is produced following the ejection of an inner orbital electron by high-energy particles and subsequent transition of atomic orbital electrons from states of high to low energy. There is a simple relationship between the emission wavelengths and the atomic number of the excited element. XRF, in which primary X-rays are used to excite characteristic secondary radiation from the specimen being analyzed, is a technique used for qualitative and quantitative elemental analysis [69, 70].

The sample for XRF analysis can be a solid or a solution. Powdered samples of NMs can be pressed into discs or be directly placed in the sample cell and then be measured. Analysis of NM suspensions can be performed by dropping the liquids on the filter paper and drying them. Thin-film samples of NMs can be directly determined. The advantages of composition analyses of NMs using XRF are listed as follows: (i) a wide range of elements, from ^{4}Be to ^{92}U, can be measured; (ii) the spectral lines of X-ray fluorescence are plain with less interference; (iii) the analysis method is simple and noninvasive; and (iv) a wide range of concentrations, from constant to trace, of elements can be analyzed.

1.3.4
Nuclear Magnetic Resonance (NMR)

In contrast to imaging and diffraction techniques affording structural information at long-range order, that is, the crystalline property, NMR is sensitive to the local environment to resolve the structures of amorphous materials, polymers, and biomolecules that lack long-range order. In addition to evaluating the structures and compositions of the species, NMR spectroscopy can be used to investigate dynamic interactions of the species under different conditions [16, 23]. The relaxation, molecular conformation, and molecular mobility can be evaluated through different dynamic measurements using specifically designed RF and/or gradient pulse sequences [71]. NMR spectroscopy has been implemented to determine several physiochemical characteristics of NMs, including structure, purity, and functionality in dendrimers, polymers, and fullerene derivatives, as well as conformational changes occurring in the interactions between ligands and NMs [72–75]. Pulsed field gradient NMR has been implemented to evaluate the diffusivity of NMs, through which the sizes and interactions of species under investigation can be calculated [76].

NMR is a nondestructive technique that requires little sample preparation. However, the low detection sensitivity of NMR, in contrast to optical techniques, requires a relatively large amount of the sample for measurement. It can also be time-consuming if a certain level of signal-to-noise ratio is necessary for spectral analysis.

1.3.5
X-ray Absorption Spectroscopy (XAS)

X-ray absorption spectroscopy (XAS) is an effective method to study the composition and structure of NMs. It includes X-ray absorption near-edge structure spectra (XANES) and extended X-ray absorption fine structure (EXAFS). XANES can yield information about chemical state and symmetries of the absorption site of the specific atom. EXAFS, the oscillatory structure in the X-ray absorption coefficient, contains much of the local structure near an absorbing atom without the requirement of long-range order in the measured species, including quantitative information concerning coordination numbers, near-neighbor distances, and structural and vibrational disorder in bond distances [31, 77]. EXAFS can provide the averaged structural information of a NM, resulting from a local order of samples examined in the manner of inelastic X-ray interaction with the samples. Because of the high energy and broad spectrum of the synchrotron radiation source, EXAFS has become one of the most effective methods to study the structure of the specific atom in the material. It can provide the local structure information near the absorption atom at about 0.002 nm.

XAS has enabled scientists to analyze samples that could not be analyzed using classical techniques such as XRD and proven to be a powerful technique in several fields including biology, and environmental and material sciences. In

addition, it allows for the direct determination of elemental oxidation states and local coordination environments of specific elements, where the use of other methods is time-consuming, is cumbersome, and can lead to false results [78, 79]. Detailed description of XAS and its applications in nanotoxicology studies can also be found in Chapter 5 of this book.

1.4 Surface Properties

The surface properties of NMs are expected to contribute substantially to the mode and extent of their biological effects. Surface composition, energy, charge, and reactivity clearly affect NM interactions with biomolecules and biological systems. It is recommended that an interactive approach to surface characterization be undertaken, since it is often impractical to characterize the full spectrum of surface properties for each NM. It is also suggested that NMs are stored under inert conditions and the surface composition and structure of the "as-received" NMs should be measured at the very minimum. Where possible, measurements should also be performed on the NMs "postexposure."

1.4.1 Surface Area

There has been a good deal of discussion regarding the role of surface area in NM toxicology. Some researchers have argued that surface area plays an important role in the toxicity of NMs and is the measurement metric that best correlates with particle-induced adverse health effects [1, 80, 81]. There is a growing consensus that the potential for adverse health effects is most directly proportional to particle surface area. Since surface area almost always scales with size (at least for nonporous materials), one could equally make the case that size is the best correlation. In fact, if one measures the mass, density, and primary particle size distribution of a material, the approximate surface area can be readily calculated by assuming spherical geometry. Thus, the question is not so much what surface area of material was used to dose an animal or cell culture, but rather whether the dose should be normalized by total surface area concentration rather than mass or number concentrations.

Particle surface area is clearly an important characteristic of an NM and should always be measured. As described previously, the surface area of NMs can be accurately measured using gas adsorption and the BET method. For particles dispersed in water or air, measuring surface area is somewhat more difficult. Aqueous dispersions can be carefully dried and the resulting powders measured by BET. Care must be exercised to ensure that the surface area is not perturbed by drying and that there are no other salts or components of the solution that influence the measurement.

1.4.2 Surface Charge

The surface charge may reflect the native NM surface or the adsorption of ions and biomolecules at their interface, which will influence the dispersion stability of NMs in aqueous solutions. In an ionic solution, the surface of a charged particle is firmly bound to opposite charged ions, forming a thin liquid layer named Stern layer, which is encompassed by an outer diffuse layer consisting of loosely associated ions. These two layers compose the so-called *electrical double layer* [82]. Zeta potential refers to the sign and magnitude of charge at the shear plane, which divides the fluid envelope that associates itself with the particle and the bulk solution phase. It is usually determined by measuring the velocity of the charged species toward the electrode in the presence of an external electric or acoustic field across the sample solution [23, 25].

Zeta potentials of NMs are typically measured by electrophoresis or electroacoustic methods. The light-scattering electrophoresis is the most commonly used technique since commercial fully automatic instruments are widely available in the market [83]. The equipment is designed to measure the movement of the NMs under an applied electrical field by laser Doppler velocimetry (LDV). To obtain reliable results, the material of interest must have a refractive index sufficiently different from that of the dispersing medium and the dispersing medium must be transparent to light. The absolute value of zeta potential greater than 30 mV indicates a stable condition, whereas a low zeta potential value of less than 30 mV indicates a condition toward instability, aggregation, coagulation, or flocculation [23]. Zeta potential can be significantly affected by the concentration of the sample, pH, temperature, and ionic composition of the dispersion medium [82, 84, 85]. When reporting the value, these parameters should be clearly specified. In particular, pH should be measured just before or after in the dispersion in which the zeta potential was measured, but not in the solution used for preparing the dispersion [86]. The particles will adjust their surface charge and zeta potential according to the current solution composition. The choice of sample concentration is particle-specific and is dependent on the particle scattering properties. High concentrations will lead to multiple scattering and significant particle interactions and hence will result in experimental artifacts [82]. On the other hand, a precise, repeatable zeta potential measurement in a diluted solution cannot reflect the true value in a concentrated suspension [84]. In addition, the values of zeta potential will change with the temperature since the viscosity of the dispersing media depends on the temperature, although the effect is not dramatic [87]. Therefore, zeta measurement should be carried out with temperature control and the results should be reported with the temperature. One should also pay attention to the ionic strength and composition of the dispersing medium. Ions have the potential to adsorb on the particle surface and thus affect the surface charge distribution. Surface complexes or coatings can also be formed and lead to a change in zeta potential. Air bubbles introduced to the solution during sample filling should

also be avoided. Any obstacle along the optical path would have an effect on light scattering and result in experimental artifacts or irreproducible data.

1.4.3 Surface Composition

NMs possess a very high surface-area-to-volume ratio, and the molecular composition and structure of the surface will ultimately define their chemistry. However, it is often difficult to directly measure the atomic composition of surfaces because many of these systems are subject to trace surface contaminants that may not be detectable by general chemical analysis. Directly measuring the atomic composition of "as-received" or "as-administered" NMs is very important. Postexposure examination of changes in surface composition and structure will undoubtedly provide priceless clues with respect to their behavior and the fate of these NMs in biological systems. Methods such as X-ray photoelectron spectroscopy (XPS) and secondary ion massspectroscopy (SIMS) have been extensively used for characterizing NMs, as well as correlating biomaterial surface properties to physiological endpoints [67]. Many of the methods used for surface characterization require ultrahigh-vacuum environments ($<10^{-5}$ Pa). Under such conditions, the surface properties and bonding structure of some materials have been shown to change. Therefore, washing and remova1 of biomolecules from the surface of the particles are likely to be a necessary step. Care must be taken to prevent artifacts from this process.

XPS, also known as *electron spectroscopy for chemical analysis* (ESCA), is one of the most widely used techniques for analyzing the surface composition of NMs. The popularity of XPS comes from its ability to identify and quantify the elemental composition of the outer 10 nm or less of any solid surface for all elements from lithium to uranium on the assumption that the element of interest exists at greater than 0.05 atomic%. Each element has a characteristic electronic structure and thus a characteristic XPS spectrum. Since the binding energies of the electron orbitals in atoms are known, the positions of the peaks in the XPS spectrum can be used to identify the atomic surface composition of the sample. XPS not only allows the identification of the elements constituting the sample but also provides information on their oxidation state based on the binding energy or chemical shift. For example, it has been used for the estimation of the concentration of oxygen vacancies in CeO_2 NPs, based on the concentration of Ce^{3+} and Ce^{4+} [88]. However, it should be noted that the use of XPS to estimate the concentration of oxygen vacancy defects on the basis of oxygen concentration or the fitting of the oxygen peak in the XPS could result in erroneous estimates due to the presence of oxygen in any molecules on the surface of the samples.

Auger electron spectroscopy (AES) is another common surface analysis tool for NMs. Both AES and XPS detect electrons emitted from samples with kinetic energies typically below 2000 eV. In AES, the sample is irradiated with electrons instead of X-rays [89]. AES and XPS provide similar information, but AES gives a higher lateral resolution since the electron beam can be focused to a smaller size than

X-rays. However, the electron beam can also impart more damage to the sample surface than X-rays. Other ion-based techniques, such as time-of-flight secondary ion mass spectrometry (TOF-SIMS) and low-energy ion scattering (LEIS), can provide information on surface coatings, functional groups, or contaminants to complement the electron spectroscopic techniques.

1.4.4 Surface Reactivity

Some NMs actively participate in oxidation or reduction reactions when interacting with biological systems. The surface reactivity of NMs can be measured through comparative microcalorimetry, via the use of probe molecules that are monitored for either degradation or changes in oxidative state, or through a number of electrochemical methods. All of these techniques can potentially be used to monitor particle reactivity in biological fluids, although losses in sensitivity and artifacts are likely. The choice of method will depend on the types of molecular transformations that occur at the particle surface. Comparisons between the surface compositions of the "as-received" particles and those exposed to biological systems can provide further insight for selection.

The surface energy and wettability of NMs can be important for understanding NM aggregation, dissolution, and bioaccumulation behavior. The surface energy of NM systems can be measured through heat of immersion microcalorimetry studies or through contact angle measurements with various liquids. Dynamic and static contact angle measurements can be performed to determine directly the particle wettability within biological fluids. Phospholipids, proteins, and other biomolecules are known to adsorb to surfaces in physiological fluids and change their wettability and sometimes biodistribution characteristics [90, 91].

1.5 Interactions between NMs and Biological Environments

With the increasing applications, NMs can be released into the environment intentionally or accidentally. When NMs are introduced into the environment or biological systems, many undesirable effects such as aggregation, coagulation, and nonspecific absorption can occur. These may be due to a variety of intermolecular interactions occurring at the interfaces of NMs with biomolecules and interaction-mediating fluids [92]. The toxic effects will depend not only on the initial properties of NMs, including chemical composition, shape, surface geometry and crystallinity, porosity, heterogeneity, and hydrolytic stability, but also on the physicochemical evolution in the surroundings, such as ionic strength, pH, temperature, and the presence of biological or organic macromolecules, which can characterize the surface charge, dissolution, hydration, size distribution, dispersion stability, agglomeration, and aggregation of NMs in a given medium [93–96]. Thus, it is necessary to assess the physicochemical characteristics of

NMs before use, at the moment of delivery, as well as after exposure to the *in vitro* or *in vivo* test [97]. Techniques for determining the shelf life of NM formulations are essential before considering the manufacture. For example, it is important to guard against degradation of the NMs caused by moisture, oxidation, and/or aggregation. In this respect, different characterization techniques will be useful for quality assurance.

1.6 Conclusions

Given the novelty of physicochemical characteristics at the nanometer scale, NMs have potential to impact interactions in the biological environment from the molecular to the systemic level. The rapid development and production of NMs for use indicate the demand for comprehensive determination of the properties of NMs. Robust techniques for characterization of NMs are fundamental to regulatory guidelines for ensuring safety of NMs in general use and toxicological studies. This chapter introduces different methods that are commonly used for characterizing NMs. Indeed, it is necessary to characterize the NM in both its originally manufactured condition and after introduction into a physiological environment. These issues become quite complex when trying to determine the mechanism of toxicity. Outside of the body, the environmental conditions can be manipulated to promote the dispersion and stability for measuring size and surface chemistry, while in the biological environment, one is restricted to the conditions under which the organism lives. Often, properties can only be measured after NMs are removed or tissues fixed, potentially introducing artifacts into the measurements. Until better techniques for characterization in these environments are developed, researchers must use the tools available to reconstruct the particle properties *in situ* and how they interact with biological systems. The brief description of each technique, together with its strengths and limitations, provides us with a picture for selecting suitable techniques for characterization of NMs.

References

1. EC (2011) Commission Recommendation of 18 October 2011 on the definition of nanomaterial. *Off. J. Eur. Union*, **50**, 38–40.
2. Wang, Z.L. (2000) Transmission electron microscopy of shape-controlled nanocrystals and their assemblies. *The Journal of Physical Chemistry B*, **104** (6), 1153–1175.
3. Williams, D.B. and Carter, C.B. (eds) (2009) *Transmission Electron Microscopy: A Textbook for Materials Science*, Springer.
4. Hall, J.B., Dobrovolskaia, M.A., Patri, A.K., and McNeil, S.E. (2007) Characterization of nanoparticles for therapeutics. *Nanomedicine*, **2**, 789–803.
5. Johal, M.S. (2011) *Understanding Nanomaterials*, CRC Press, Boca Raton, FL.
6. Chi, L. and Röthig, C. (2000) in *Characterization of Nanophase Materials* (ed.

Z.L. Wang), John Wiley & Sons, Inc., pp. 133–163.
7. Albrecht, T., Dovek, M., Lang, C., Grütter, P., Quate, C., Kuan, S., Frank, C., and Pease, R. (1988) Imaging and modification of polymers by scanning tunneling and atomic force microscopy. *J. Appl. Phys.*, **64** (3), 1178–1184.
8. Avouris, P. (1990) Atom-resolved surface chemistry using the scanning tunneling microscope. *J. Phys. Chem.*, **94** (6), 2246–2256.
9. Binnig, G. and Rohrer, H. (1983) Scanning tunneling microscopy. *Surf. Sci.*, **126** (1), 236–244.
10. Bonnell, D. (2001) *Scanning Probe Microscopy and Spectroscopy: Theory, Techniques, and Applications*, Wiley-VCH Verlag GmbH.
11. Koçum, C., Çimen, E.K., and Pişkin, E. (2004) Imaging of poly(NIPA-co-MAH)–HIgG conjugate with scanning tunneling microscopy. *J. Biomater. Sci., Polym. Ed.*, **15** (12), 1513–1520.
12. Wang, H. and Chu, P.K. (2013) in *Characterization of Biomaterials*, Chapter 4 (eds B. Amit and B. Susmita), Academic Press, Oxford, pp. 105–174.
13. Gadegaard, N. (2006) Atomic force microscopy in biology: technology and techniques. *Biotech. Histochem.*, **81** (2-3), 87–97.
14. Hansma, P., Elings, V., Marti, O., and Bracker, C. (1988) Scanning tunneling microscopy and atomic force microscopy: application to biology and technology. *Science*, **242** (4876), 209.
15. Marti, O., Drake, B., Ribi, H., Albrecht, T.R., and Quate, C.F. (1988) Atomic force microscopy of an organic monolayer. *Science*, **239**, 50–52.
16. Tiede, K., Boxall, A.B., Tear, S.P., Lewis, J., David, H., and Hassellöv, M. (2008) Detection and characterization of engineered nanoparticles in food and the environment. *Food Addit. Contam.*, **25** (7), 795–821.
17. Zhu, L., Attard, P., and Neto, C. (2011) Reliable measurements of interfacial slip by colloid probe atomic force microscopy. II. Hydrodynamic force measurements. *Langmuir*, **27** (11), 6712–6719.
18. Patri, A., Dobrovolskaia, M., Stern, S., and McNeil, S. (2007) in *Nanotechnology for Cancer Therapy* (ed. M. Amiji), CRC Press, pp. 105–138.
19. Parot, P., Dufrêne, Y.F., Hinterdorfer, P., Le Grimellec, C., Navajas, D., Pellequer, J.L., and Scheuring, S. (2007) Past, present and future of atomic force microscopy in life sciences and medicine. *J. Mol. Recognit.*, **20** (6), 418–431.
20. Dufrêne, Y.F. and Garcia-Parajo, M.F. (2012) Recent progress in cell surface nanoscopy: light and force in the near-field. *Nano Today*, **7** (5), 390–403.
21. Francius, G., Domenech, O., Mingeot-Leclercq, M.P., and Dufrêne, Y.F. (2008) Direct observation of *Staphylococcus aureus* cell wall digestion by lysostaphin. *J. Bacteriol.*, **190** (24), 7904–7909.
22. Inagaki, S., Ghirlando, R., and Grisshammer, R. (2013) Biophysical characterization of membrane proteins in nanodiscs. *Methods*, **59**, 287–300.
23. Sapsford, K.E., Tyner, K.M., Dair, B.J., Deschamps, J.R., and Medintz, I.L. (2011) Analyzing nanomaterial bioconjugates: a review of current and emerging purification and characterization techniques. *Anal. Chem.*, **83** (12), 4453–4488.
24. Brar, S.K. and Verma, M. (2011) Measurement of nanoparticles by light-scattering techniques. *TrAC, Trends Anal. Chem.*, **30** (1), 4–17.
25. Pons, T., Uyeda, H.T., Medintz, I.L., and Mattoussi, H. (2006) Hydrodynamic dimensions, electrophoretic mobility, and stability of hydrophilic quantum dots. *J. Phys. Chem. B*, **110** (41), 20308–20316.
26. Pitts, N. (2004) Are we ready to move from operative to non-operative/preventive treatment of dental caries in clinical practice? *Caries Res.*, **38** (3), 294–304.
27. Filipe, V., Hawe, A., and Jiskoot, W. (2010) Critical evaluation of Nanoparticle Tracking Analysis (NTA) by Nanosight for the measurement of nanoparticles and protein aggregates. *Pharm. Res.*, **27** (5), 796–810.
28. Lim, J., Yeap, S.P., Che, H.X., and Low, S.C. (2013) Characterization of magnetic

nanoparticle by dynamic light scattering. *Nanoscale Res. Lett.*, **8** (1), 1–14.
29. Bootz, A., Vogel, V., Schubert, D., and Kreuter, J. (2004) Comparison of scanning electron microscopy, dynamic light scattering and analytical ultracentrifugation for the sizing of poly (butyl cyanoacrylate) nanoparticles. *Eur. J. Pharm. Biopharm.*, **57** (2), 369–375.
30. Uskokovic, V. (2012) Dynamic light scattering based microelectrophoresis: main prospects and limitations. *J. Dispersion Sci. Technol.*, **33** (12), 1762–1786.
31. Wang, Z.L. (ed.) (2000) *Characterization of Nanophase Materials*, Wiley-VCH Verlag GmbH, Weinheim, pp. 13–36.
32. Chapman, H.N., Fromme, P., Barty, A., White, T.A., Kirian, R.A., Aquila, A., Hunter, M.S., Schulz, J., DePonte, D.P., and Weierstall, U. (2011) Femtosecond X-ray protein nanocrystallography. *Nature*, **470** (7332), 73–77.
33. Lipfert, J. and Doniach, S. (2007) Small-angle X-ray scattering from RNA, proteins, and protein complexes. *Annu. Rev. Biophys. Biomol. Struct.*, **36**, 307–327.
34. Rao, C. and Biswas, K. (2009) Characterization of nanomaterials by physical methods. *Annu. Rev. Anal. Chem.*, **2**, 435–462.
35. Doniach, S. (2001) Changes in biomolecular conformation seen by small angle X-ray scattering. *Chem. Rev.*, **101** (6), 1763–1778.
36. Petoukhov, M.V. and Svergun, D.I. (2013) Applications of small-angle X-ray scattering to biomacromolecular solutions. *Int. J. Biochem. Cell Biol.*, **45** (2), 429–437.
37. Fubini, B. (1997) Surface reactivity in the pathogenic response to particulates. *Environ. Health Perspect.*, **105** (Suppl. 5), 1013–1020.
38. Lin, W., Huang, Y., Zhou, X., and Ma, Y. (2006) *In vitro* toxicity of silica nanoparticles in human lung cancer cells. *Toxicol. Appl. Pharmacol.*, **217** (3), 252–259.
39. Gelb, L.D. and Gubbins, K. (1998) Characterization of porous glasses: simulation models, adsorption isotherms, and the Brunauer-Emmett-Teller analysis method. *Langmuir*, **14** (8), 2097–2111.
40. Deng, X., Luan, Q., Chen, W., Wang, Y., Wu, M., Zhang, H., and Jiao, Z. (2009) Nanosized zinc oxide particles induce neural stem cell apoptosis. *Nanotechnology*, **20** (11), 115101.
41. Handy, R.D., Von der Kammer, F., Lead, J.R., Hassellöv, M., Owen, R., and Crane, M. (2008) The ecotoxicology and chemistry of manufactured nanoparticles. *Ecotoxicology*, **17** (4), 287–314.
42. Dhawan, A. and Sharma, V. (2010) Toxicity assessment of nanomaterials: methods and challenges. *Anal. Bioanal. Chem.*, **398** (2), 589–605.
43. Popović, Z., Dohčević-Mitrović, Z., Šćepanović, M., Grujić-Brojčin, M., and Aškrabić, S. (2011) Raman scattering on nanomaterials and nanostructures. *Ann. Phys.*, **523** (1-2), 62–74.
44. Kumar, C.S. (ed.) (2012) *Raman Spectroscopy for Nanomaterials Characterization*, Springer Science & Business Media.
45. Wu, X., Siu, G., Tong, S., Liu, X., Yan, F., Jiang, S., Zhang, X., and Feng, D. (1996) Raman scattering of alternating nanocrystalline silicon/amorphous silicon multilayers. *Appl. Phys. Lett.*, **69**, 523.
46. Kumar, C.S. (ed.) (2012) *Raman Spectroscopy for Nanomaterials Characterization*, Springer, pp. 417–444.
47. Kumar, C.S. (eds) (2012) *Raman Spectroscopy for Nanomaterials Characterization*, Springer, pp. 119–135.
48. Lee, H.M., Jin, S.M., Kim, H.M., and Suh, Y.D. (2013) Single-molecule surface-enhanced Raman spectroscopy: a perspective on the current status. *Phys. Chem. Chem. Phys.*, **15** (15), 5276–5287.
49. Lin, X.M., Cui, Y., Xu, Y.H., Ren, B., and Tian, Z.Q. (2009) Surface-enhanced Raman spectroscopy: substrate-related issues. *Anal. Bioanal. Chem.*, **394** (7), 1729–1745.
50. Wilson, A.J. and Willets, K.A. (2013) Surface-enhanced Raman scattering imaging using noble metal nanoparticles. *Wiley Interdiscip. Rev. Nanomed. Nanobiotechnol.*, **5** (2), 180–189.
51. Ando, J., Yano, T.-a., Fujita, K., and Kawata, S. (2013) Metal nanoparticles for nano-imaging and nano-analysis.

Phys. Chem. Chem. Phys., **15** (33), 13713–13722.

52. Huang, J., Zong, C., Shen, H., Cao, Y., Ren, B., and Zhang, Z. (2013) Tracking the intracellular drug release from graphene oxide using surface-enhanced Raman spectroscopy. *Nanoscale*, **5** (21), 10591–10598.
53. Kneipp, J., Kneipp, H., Wittig, B., and Kneipp, K. (2010) Novel optical nanosensors for probing and imaging live cells. *Nanomed. Nanotechnol. Biol. Med.*, **6** (2), 214–226.
54. Mannelli, I. and Marco, M.-P. (2010) Recent advances in analytical and bioanalysis applications of noble metal nanorods. *Anal. Bioanal. Chem.*, **398** (6), 2451–2469.
55. Kumar, J. and Thomas, K.G. (2011) Surface-enhanced Raman spectroscopy: investigations at the nanorod edges and dimer junctions. *J. Phys. Chem. Lett.*, **2** (6), 610–615.
56. Hardman, R. (2006) A toxicologic review of quantum dots: toxicity depends on physicochemical and environmental factors. *Environ. Health Perspect.*, **114**, 165–172.
57. Michalet, X., Pinaud, F., Bentolila, L., Tsay, J., Doose, S., Li, J., Sundaresan, G., Wu, A., Gambhir, S., and Weiss, S. (2005) Quantum dots for live cells, *in vivo* imaging, and diagnostics. *Science*, **307** (5709), 538–544.
58. Chan, W.C., Maxwell, D.J., Gao, X., Bailey, R.E., Han, M., and Nie, S. (2002) Luminescent quantum dots for multiplexed biological detection and imaging. *Curr. Opin. Biotechnol.*, **13** (1), 40–46.
59. Kho, R., Torres-Martinez, C.L., and Mehra, R.K. (2000) A simple colloidal synthesis for gram-quantity production of water-soluble ZnS nanocrystal powders. *J. Colloid Interface Sci.*, **227** (2), 561–566.
60. Buzea, C., Pacheco, I.I., and Robbie, K. (2007) Nanomaterials and nanoparticles: sources and toxicity. *Biointerphases*, **2** (4), MR17–MR71.
61. Derfus, A.M., Chan, W.C., and Bhatia, S.N. (2004) Probing the cytotoxicity of semiconductor quantum dots. *Nano Lett.*, **4** (1), 11–18.
62. Gmoshinski, I., Khotimchenko, S.A., Popov, V., Dzantiev, B., Zherdev, A., Demin, V., and Buzulukov, Y.P. (2013) Nanomaterials and nanotechnologies: methods of analysis and control. *Russ. Chem. Rev.*, **82** (1), 48.
63. Powers, K., Brown, S., Krishna, V., Wasdo, S., Moudgil, B., and Roberts, S. (2006) Research strategies for safety evaluation of nanomaterials, part 6: characterization of nanoscale particles for toxicological evaluation. *Toxicol. Sci.*, **90**, 296–303.
64. Tom, R.T., Samal, A., Sreeprasad, T., and Pradeep, T. (2007) Hemoprotein bioconjugates of gold and silver nanoparticles and gold nanorods: structure-function correlations. *Langmuir*, **23** (3), 1320–1325.
65. Endres, P.J., Paunesku, T., Vogt, S., Meade, T.J., and Woloschak, G.E. (2007) DNA-TiO2 nanoconjugates labeled with magnetic resonance contrast agents. *J. Am. Chem. Soc.*, **129** (51), 15760–15761.
66. Guo, Z., Ganawi, A.A., Liu, Q., and He, L. (2006) Nanomaterials in mass spectrometry ionization and prospects for biological application. *Anal. Bioanal. Chem.*, **384** (3), 584–592.
67. Ratner, B.D., Hoffman, A.S., Schoen, F.J., and Lemons, J.E. (eds) (2004) *Biomaterials Science: an Introduction to Materials in Medicine*, Academic Press.
68. Lavigne, J.-P., Espinal, P., Dunyach-Remy, C., Messad, N., Pantel, A., and Sotto, A. (2013) Mass spectrometry: a revolution in clinical microbiology? *Clin. Chem. Lab. Med.*, **51** (2), 257–270.
69. Cesareo, R. (ed.) (2010) *X-ray Fluorescence Spectrometry*, Wiley Online Library.
70. Jenkins, R. (1984) X-ray fluorescence analysis. *Anal. Chem.*, **56** (9), 1099A–1106A.
71. Wang, L.Q., Exarhos, G.J., and Liu, J. (1999) Nuclear magnetic resonance—characterization of self-assembled nanostructured materials. *Adv. Mater.*, **11** (16), 1331–1341.
72. Lundqvist, M., Stigler, J., Elia, G., Lynch, I., Cedervall, T., and Dawson, K.A. (2008) Nanoparticle size and surface properties determine the protein corona with possible implications for biological

impacts. *Proc. Natl. Acad. Sci. U.S.A.*, **105** (38), 14265–14270.
73. Mullen, D.G., Fang, M., Desai, A., Baker, J.R. Jr.,, Orr, B.G., and Banaszak Holl, M.M. (2010) A quantitative assessment of nanoparticle- ligand distributions: implications for targeted drug and imaging delivery in dendrimer conjugates. *ACS Nano*, **4** (2), 657–670.
74. Pan, B., Cui, D., Gao, F., and He, R. (2006) Growth of multi-amine terminated poly (amidoamine) dendrimers on the surface of carbon nanotubes. *Nanotechnology*, **17** (10), 2483.
75. Tomalia, D., Huang, B., Swanson, D., Brothers, H., and Klimash, J. (2003) Structure control within poly (amidoamine) dendrimers: size, shape and regio-chemical mimicry of globular proteins. *Tetrahedron*, **59** (22), 3799–3813.
76. Valentini, M., Vaccaro, A., Rehor, A., Napoli, A., Hubbell, J.A., and Tirelli, N. (2004) Diffusion NMR spectroscopy for the characterization of the size and interactions of colloidal matter: the case of vesicles and nanoparticles. *J. Am. Chem. Soc.*, **126** (7), 2142–2147.
77. Koningsberger, D. and Prins, R. (1988) *X-ray Absorption: Principles, Applications, Techniques of EXAFS, SEXAFS, and XANES*. John Wiley and Sons, New York, NY.
78. Belyakova, O., Zubavichus, Y., Neretin, I., Golub, A., Novikov, Y.N., Mednikov, E., Vargaftik, M., Moiseev, I., and Slovokhotov, Y.L. (2004) Atomic structure of nanomaterials: combined X-ray diffraction and EXAFS studies. *J. Alloys Compd.*, **382** (1), 46–53.
79. Wu, Z., Guo, L., Li, H., Benfield, R.E., Yang, Q., Grandjean, D., Li, Q., and Zhu, H. (2001) Cerium oxide nanoparticles coated by surfactant sodium bis (2-ethylhexyl) sulphosuccinate (AOT): local atomic structures and x-ray absorption spectroscopic studies. *J. Phys. Condens. Matter*, **13** (22), 5269.
80. Oberdörster, G. (2004) Manufactured nanomaterials (fullerenes, C60) induce oxidative stress in the brain of juvenile largemouth bass. *Environ. Health Perspect.*, **112**, 1058–1062.
81. Oberdörster, G. (2000) Pulmonary effects of inhaled ultrafine particles. *Int. Arch. Occup. Environ. Health*, **74** (1), 1–8.
82. McNeil, S.E. (ed.) (2011) *Characterization of Nanoparticles Intended for Drug Delivery*, Springer, pp. 63–70.
83. Kosmulski, M. (ed.) (2009) *Surface Charging and Points of Zero Charge*, CRC Press.
84. Xu, R. (2008) Progress in nanoparticles characterization: sizing and zeta potential measurement. *Particuology*, **6** (2), 112–115.
85. Weiner, B.B., Tscharnuter, W.W., and Fairhurst, D. (1993) Zeta potential: a new approach. Canadian Mineral Analysts Meeting.
86. Kosmulski, M. (2011) The pH-dependent surface charging and points of zero charge: V. Update. *J. Colloid Interface Sci.*, **353** (1), 1–15.
87. Kosmulski, M. (2003) A literature survey of the differences between the reported isoelectric points and their discussion. *Colloids Surf., A*, **222** (1), 113–118.
88. Korsvik, C., Patil, S., Sealb, S., and Self, W.T. (2007) Superoxide dismutase mimetic properties exhibited by vacancy engineered ceria nanoparticles. *Chem. Commun.*, 1056–1058.
89. Childs, K.D., Carlson, B.A., LaVanier, L., Moulder, J.F., Paul, D.F., Stickle, W.F., and Watson, D.G. (1995) *Handbook of Auger Electron Spectroscopy*, Physical Electronics Inc.
90. Boguslavsky, Y., Fadida, T., Talyosef, Y., and Lellouche, J.-P. (2011) Controlling the wettability properties of polyester fibers using grafted functional nanomaterials. *J. Mater. Chem.*, **21** (28), 10304–10310.
91. Neumann, A.W., David, R., and Zuo, Y. (eds) (2010) *Applied Surface Thermodynamics*, CRC Press.
92. Nel, A., M dler, L., Velegol, D., Xia, T., Hoek, E., Somasundaran, P., Klaessig, F., Castranova, V., and Thompson, M. (2009) Understanding biophysicochemical interactions at the nano–bio interface. *Nat. Mater.*, **8** (7), 543–557.
93. French, R.A., Jacobson, A.R., Kim, B., Isley, S.L., Penn, R.L., and Baveye,

P.C. (2009) Influence of ionic strength, pH, and cation valence on aggregation kinetics of titanium dioxide nanoparticles. *Environ. Sci. Technol.*, **43** (5), 1354–1359.

94. Hull, M. and Bowman, D. (eds) (2014) *Nanotechnology Environmental Health and Safety: Risks, Regulation, and Management*, William Andrew.

95. Schwabe, F., Schulin, R., Rupper, P., Rotzetter, A., Stark, W., and Nowack, B. (2014) Dissolution and transformation of cerium oxide nanoparticles in plant growth media. *J. Nanopart. Res.*, **16** (10), 1–11.

96. Nowack, B., Ranville, J.F., Diamond, S., Gallego-Urrea, J.A., Metcalfe, C., Rose, J., Horne, N., Koelmans, A.A., and Klaine, S.J. (2012) Potential scenarios for nanomaterial release and subsequent alteration in the environment. *Environ. Toxicol. Chem.*, **31** (1), 50–59.

97. Hussain, S.M., Braydich-Stolle, L.K., Schrand, A.M., Murdock, R.C., Yu, K.O., Mattie, D.M., Schlager, J.J., and Terrones, M. (2009) Toxicity evaluation for safe use of nanomaterials: recent achievements and technical challenges. *Adv. Mater.*, **21** (16), 1549–1559.

2
Quantitative Analysis of Metal-Based Nanomaterials in Biological Samples Using ICP-MS

Meng Wang

2.1
Introduction

Metal-based engineered nanomaterials (ENMs) have been widely used in consumer products, mechanical and electrical devices, and drug delivery systems [1]. These ENMs can enter the human body directly from daily intake or via environmental exposure. Currently, a complete understanding of the size, shape, composition, and aggregation-dependent interactions of nanostructures with biological systems is lacking, and thus, it is unclear whether the exposure of humans, animals, and plants to ENMs could produce harmful biological responses [2]. It is crucial to understand the fate and behavior of these nanomaterials in biological systems before they pose a threat to human beings. Thus, a full assessment of the uptake, biokinetics, clearance, and roles of nanomaterials in biological and ecological system is necessary so that their possible undesirable effects can be avoided [3].

Hence, a new interdiscipline between nanoscience and biomedical science called *nanotoxicology* has emerged [4–6]. Nanotoxicology refers to the study of the interactions of nanostructures with biological systems with an emphasis on elucidating the relationship between the physical and chemical properties (e.g., size, shape, surface chemistry, composition, and aggregation) of nanostructures with induction of toxic biological responses [7]. These relationships are crucial to formulate a set of regulations for the design of safe nanomaterials. The increased prevalence of these materials in consumer goods has brought nanotoxicology to the forefront and has called attention to the gap in toxicological information regarding these materials [8]. Although there are large amounts of progresses in nanotoxicology research, there are still a lot of significant challenges. From an analytical chemistry perspective, the emerging discipline poses enormous challenges, which will draw from both material characterization and bioanalytical chemistry expertise within the field [8].

One of challenges for analytical chemists is characterization of ENMs. In comparison with conventional analytes, the metrology of nanomaterials involves

Toxicology of Nanomaterials, First Edition. Edited by Yuliang Zhao, Zhiyong Zhang, and Weiyue Feng.

not only their detection and quantification but also their physicochemical characterization [9]. Besides ENMs' chemical composition, a number of physical properties have to be characterized, including size, shape, surface charge, and surface area. The detailed and comprehensive physicochemical characterizations of ENMs are required before conducting the nanotoxicological research. However, available methods, such as electron microscopy, scanning probe microscopy, and dynamic light scattering, can reveal the size and distribution of ENMs, but usually give little information about aggregation that may occur within the biological environment, adsorption of biomolecules, or degradation of the ENMs because they often change during residence within biological system and thus greatly influence ENM behavior.

The detection limit of an analytical instrument is often another issue, especially when analyzing ENMs in real environmental or biological samples. The detection limit of mass concentration below parts per billion should be achieved in many occasions. Again, many available methods cannot be applied for analyzing the ENMs at a low concentration due to lack of detection sensitivity.

The ideal methods for nanotoxicology research have to be capable of characterizing and quantifying all of the major parts of a nanostructure in tissues and organs. Since many ENMs are constructed of nonnative elements in biological organisms, such as cadmium in quantum dots (QDs) and gold in Au NPs, the fate and behavior of these ENMs can be analyzed by determining the mass or concentration of these elements. Inductively coupled plasma – mass spectrometry (ICP-MS) has many unique advantages in trace element analysis, such as sub-ppb detection limits, high precision, and a wide dynamic range (up to eight orders of magnitude) [10], making it widely applicable to many ENMs in the literature [1, 7]. When coupling to another separation instrument, this kind of hyphenated technique is able to provide more information of ENMs. For example, the coupling of asymmetric flow field-flow fractionation (AF4) and ICP-MS was used for separation and quantitative characterization of Au NPs [11]. On the other hand, an emerging ICP-MS-based method, named single-particle inductively coupled plasma – mass spectrometry (SP-ICP-MS), was developed to detect, characterize, and quantify ENMs in the literature [9].

In this chapter, we first give a brief introduction to ICP-MS. Second, the theory and recent applications of SP-ICP-MS in nanoanalysis are described. Finally, we discuss about various ICP-MS hyphenated techniques and their applications for ENM analysis.

2.2 ICP-MS: A Power Tool for Element Analysis

ICP-MS was introduced in the early 1980s [12] and nowadays has become a powerful technique to determinate trace, minor, and major elements in a

variety of samples and thus has been applied in environmental, geological semiconductor, biomedical, and nuclear research [13]. As the name indicates, the ionization source of the mass spectrometry is inductively coupled plasma (ICP), which is a high-temperature plasma (normally partly ionized argon). Different mass analyzers, including a quadrupole mass filter, a magnetic sector analyzer, and a time-of-flight (TOF) analyzer, have been introduced as the detector in ICP-MS [14]. On the other hand, a variety of sample introduction systems have been combined with ICP-MS, such as high-performance liquid chromatography (HPLC), gas chromatography (GC), capillary electrophoresis (CE), and laser ablation (LA), making ICP-MS-based techniques highly versatile.

In many publications, mass spectrometry is automatically associated with the soft or low-temperature ion source, such as matrix-assisted laser desorption ionization (MALDI) or electrospray ionization (ESI), whereas ICP-MS and its capabilities are not well known. In fact, ICP-MS should also be considered as a valuable technique in many aspects of analytical chemistry, especially in the element and isotope analysis, owing to its outstanding characteristics. In this section, an overview of ICP-MS is briefly given with an emphasis on the unique characterization of ICP-MS and ICP-MS-based hyphenated techniques for element and isotope analysis.

2.2.1
Unique Features of ICP-MS

The commercial ICP-MS system is normally composed of a sample introduction system, a plasma source, an interface, a mass analyzer, a detector, and a vacuum system.

Argon plasma is the most common ionization source in plasma-source mass spectrometry. In contrast to soft-ionization sources, such as ESI and MALDI, the ICP operates at a high temperature between 6000 and 10 000 K [14]; the energy is enough for sample desolvation, vaporization, atomization, and ionization of the atoms formed. The high-temperature plasma mainly consists of electrons and argon ions and thus has a very high ion density. The ionization efficiency of an element is dependent on its ionization potential. Because the first ionization potential of argon is about 15.8 eV, it is high enough to ionize most of elements in the periodic table, the majority of which have the first ionization potentials in the range of 4–12 eV. Chemical bonds in molecules are broken readily, and the isotopes are ionized into ions with a positive charge. Therefore, the response of an element in ICP-MS is independent of its molecular environment; that factor means that the quantitative analysis of an element in a sample can use any species of the element as a calibration standard. For example, it is reported that protein quantification by ICP-MS can achieve high accuracy of 10% or better [15]. Moreover, the atomic mass spectra are more straightforward than the ones from a molecular mass spectrometer because the number of natural isotopes is limited.

All those unique characterizations are propitious for ICP-MS to approach accurate quantification via element determination regardless of the diverse matrixes of samples. The unique characteristics of ICP-MS are summarized as follows: (i) high analytical throughput; (ii) excellent detection limits (pg/g to ng/g) for most elements; (iii) minimal matrix effects; (iv) isotope information; (v) simple spectrum; (vi) low detector background; (vii) wide linear dynamic range (up to eight orders of magnitudes); (viii) and simple coupling to another separation method (e.g., HPLC, GC, LA).

Generally, the majority of elements in the periodic table can be readily ionized and thus have very good detection limits, from picogram per gram to nanogram per gram. Unfortunately, many abundant elements in samples, such as carbon, oxygen, chlorine, and hydrogen, owing to their high first ionization potentials, are difficult to be ionized and thus have poor detection limits.

The ions generated in the plasma are introduced into the mass analyzer, where the ions are separated by their mass-to-charge ratio (m/z). There are mainly three mass analyzers in commercial ICP-MS systems: the quadrupole, double-focusing magnetic sector, and TOF [16]. Quadrupole-based analyzer was first developed in the early 1980s and is now installed in most of ICP-MS. The resolution of a quadrupole mass analyzer is normally maintained at 0.3–1 AMU (atomic mass unit) and can offer a resolving power of about 300 [16], which is enough for most routine applications. However, the resolution is inadequate for many elements that are liable to the spectral interferences derived from argon, solvent, and sample matrixes, such as the interferences of $^{40}Ar^{16}O$ for ^{56}Fe and $^{40}Ar^{35}Cl$ for ^{75}As determination and so forth. The resolving power of a commercial TOF analyzer in ICP-MS is typically in the range of 500–2200 [17], which is also inadequate to solve most polyatomic interferences in ICP-MS. A TOF analyzer, however, is ideally suited for analysis of rapid transient signals, high precision of isotope ratio analysis, and rapid data acquisition because ions to be determined are sampled at the exact same moment. Compared to the quadrupole and TOF analyzers, a magnetic-sector analyzer has the resolving power of up to 10 000 [18]. The great improvement in resolving power allows the aforementioned elements to be analyzed, even in complex sample matrixes. But the application of high-resolution ICP-MS is limited due to its high cost and complex operation.

Based on a quadrupole ICP-MS, another technique termed collision/reaction cell has frequently been used to reduce polyatomic ion interferences [19]. These techniques provide simplicity, efficacy, and low cost in the face of many difficult interference problems. In these methods, ions first enter a radio-frequency-only multipole (e.g., a quadrupole, hexapole, or octupole), where the analytes react with collision/reaction gas, such as oxygen, ammonia, xenon, and methane [20], to remove the polyatomic interference or generate a new analyte ion of less-interfered m/z. The RF-only multipole does not separate ions similarly to a traditional quadrupole, but it has profound influence on collisional focusing of ions, both of the energy and of the spatial distributions. An example of removing

the polyatomic interference is shown as follows, which uses ammonia gas to reduce the $^{40}Ar^+$ interference in the measurement of $^{40}Ca^+$:

$$Ar^+ + NH_3 \rightarrow NH_3^+ + Ar \quad \text{(fast reaction)}$$
$$Ca^+ + NH_3 \rightarrow NH_3^+ + Ca \quad \text{(slow reaction)}$$

Because of the disparity of the reaction rates of the two neutralization reactions, the analyte can be efficiently determined after the introduction of ammonia as a reactive gas into the multipole. There are many excellent reviews about the development and applications of collision/reaction cell in ICP-MS [19]. In order to eliminate the new isobaric interferences produced by secondary reactions, two methods are commonly used in the commercial instrument: the discrimination of kinetic energy or mass filtering [14]. The former mainly utilizes the postcell kinetic energy discrimination (KED) to suppress transport of the producers of the side reactions to the analyte in the hexapole and octupole cell instruments. Whereas in the latter, the quadrupole cell has a capability to reduce the formation of the unwanted side product ions by selecting an appropriate mass bandpass. For details of the KED and bandpass approaches, one can refer to many excellent books and reviews [16, 19].

2.2.2 ICP-MS Hyphenated to Separation Techniques

Using different types of sample introduction systems, ICP-MS can be easily combined with various separation methods, including GC, HPLC, LA, and CE [21]. Recently, on-line coupling of gel electrophoresis (GE) and ICP-MS has also been achieved [22]. Among these methods, the coupling of HPLC to ICP-MS appears to be one of the most common methods because of its ease of sample preparation and the simplicity of the interface. However, the hyphenated techniques possess some problems when liquid chromatography column is coupled to ICP-MS by a conventional nebulizer. The traditional nebulizer (e.g., Meinhard and cross-flow) has a very low nebulization efficiency (usually <3%) and large dead volume and thus deteriorates the detection limits. On the other hand, although RP-HPLC can offer a best separation performance for proteins and peptides, the gradients of organic modifiers may significantly decrease the signal sensitivity of ICP-MS.

To overcome these problems, many kinds of micronebulizers, such as a total-consumption micronebulizer with a low-volume spray chamber [23] and direct-injection high-efficiency nebulizer (DIHEN) [24], have been developed as interfaces of HPLC to ICP-MS. In comparison with the traditional interface, these devices can minimize the dead volume, improve the nebulization efficiency, and allow efficient coupling of HPLC to ICP-MS. Another method that applied for HPLC-ICP-MS is to use postcolumn sheath flow, which ensures that the sensitivity of ICP-MS remains constant during HPLC gradient elution [25].

CE, as a complement to other separation methods, has dramatically increased its application in analytical laboratories. This method is versatile for diverse analytes because of its extraordinary resolution power of up to 500 000 theoretical plates and fast analytical speed. Because the coupling of CE to ICP-MS is introduced in the speciation analysis, especially in the most recent years, several interfaces of CE-ICP-MS have been developed; thus, the approach has been proven to have the potential for protein quantification [26].

Equipped with LA, ICP-MS can have direct access to analytes in solids and on surfaces. For example, protein identification and semiquantification directly from a 1D or 2D gel combined with LA-ICP-MS have become a general interest for life science studies and was used to determine metal distribution in a proteome [27]. Moreover, with the measurement of LA-ICP-MS, an *in situ* element-related image can be obtained in a tissue section [28]. The available ICP-MS-based hyphenated techniques are illustrated in Figure 2.1 [29].

2.3
Single-Particle ICP-MS: Theory and Application

Traditionally, ENMs in biological system can be determined by element-specific detectors, such as inductively coupled plasma–atomic emission spectroscopy (ICP-AES) or ICP-MS. Chithrani and Chan [30] investigated the mechanism by which transferrin-coated Au NPs of different sizes and shapes entered mammalian cells with solution digestion and ICP-OES analysis, finding that

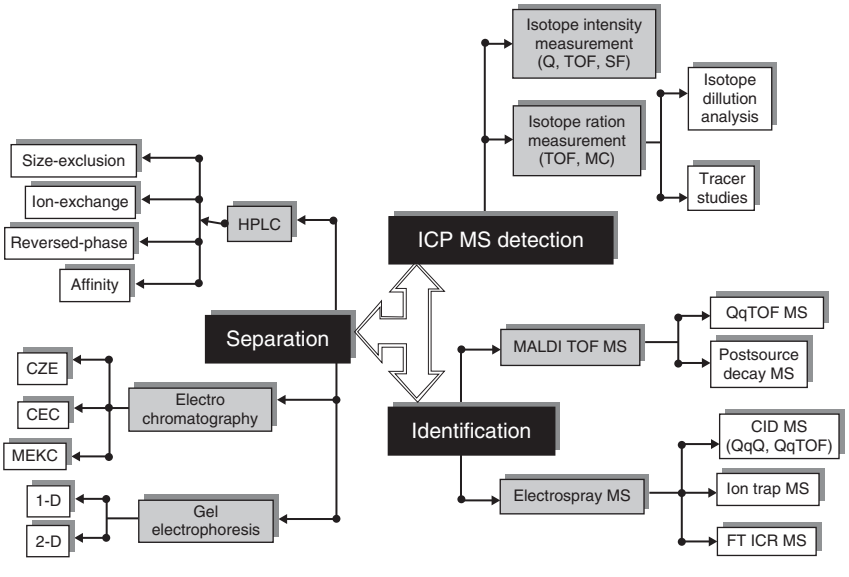

Figure 2.1 ICP-MS-based hyphenated systems [29]. (Reprint with permission from Royal Society of Chemistry.)

transferrin-coated Au NPs entered the cells via clathrin-mediated endocytosis pathway. In another research, Meng *et al.* [31] analyzed Cu contents in mouse kidneys after oral administration of Cu NPs by ICP-MS. They found that high reactivity caused the big toxicological difference between two sizes (23.5 nm and 17 μm). The Cu NPs led to the accumulation of excessive alkalescent substance and heavy metal ions (Cu^{2+} ions) culminating the metabolic alkalosis and Cu^{2+} ion overload.

However, the aforementioned methods for analysis of ENMs are time-consuming and tedious due to the long sample preparation procedure, such as sample homogenization, digestion, and dilution. Degueldre *et al.* [32–34] developed the theory of SP-ICP-MS for direct nanoparticle analysis and showed great potentials in the analysis of ENMs. SP-ICP-MS is a new technique dependent on the extremely sensitive element-specific capability of ICP-MS and can provide information about the elemental composition, number concentration, and size distribution of ENMs. In addition, dissolved forms of ENMs can also be determined under optimal conditions. In the following section, we discuss the basic theory of SP-ICP-MS and its application in biomedical research.

2.3.1
Basic Theory of SP-ICP-MS

The basic assumption about SP-ICP-MS is that each recorded pulse represents a single ENM event, which depends on a short dwell time, a constant flow rate, and a sufficiently low particle number concentration [33]. If this assumption is true, the frequency of the pulses is directly related to the number concentration of ENMs and the intensity of each pulse is proportional to the mass of element, in fact to the number of atoms, in each detected ENM [9]. The basic theory of single-particle analysis by ICP-MS has been discussed in many papers [9, 32, 35]. The SP-ICP-MS concept and its comparison with the traditional ICP-MS analysis are illustrated in Figure 2.2 [36].

Briefly, ENMs are sprayed in sequence into high-temperature plasma where each ENM is desolvated, atomized, and ionized. The resulting ions are then detected by time-resolved ICP-MS. Under optimum conditions, the frequency of the ENM event, F_{np} (number of pulses), is related to a nanoparticle number concentration, N_{np} (particles per ml), using the following equation:

$$N_{np} = \frac{F_{np}}{\varepsilon Q_{sam} t} \tag{2.1}$$

where:

ε is the nebulization efficiency;
Q_{sam} is the sample uptake rate (ml/s);
N_{np} is the nanoparticle number concentration (ml^{-1});
t is the dwell time (s);
F_{np} is the number of nanoparticles detected by ICP-MS.

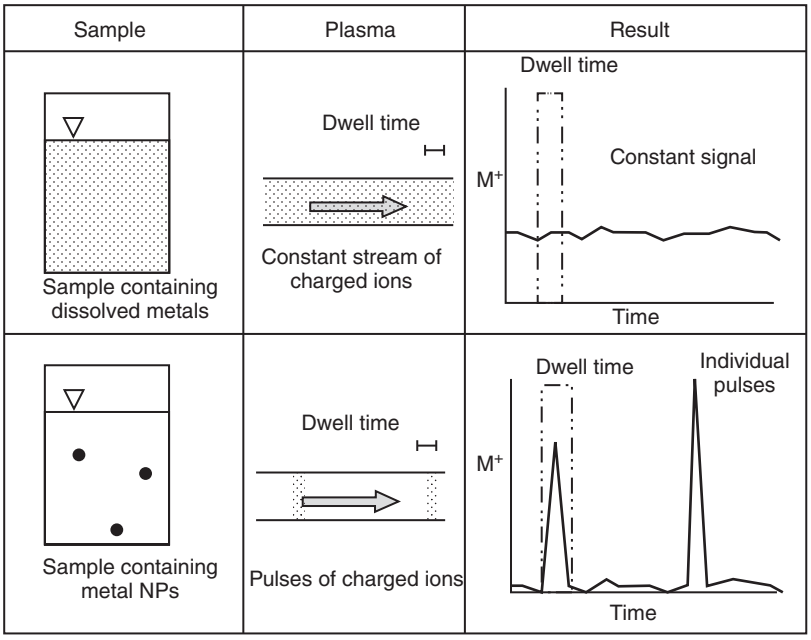

Figure 2.2 Conceptual diagram for the single-particle inductively coupled plasma–mass spectrometry (SP-ICP-MS) method. Samples containing dissolved metals will produce a constant stream of charged ions after passing through the plasma. The detector will then have a relatively constant intensity versus time signal for each dwell time. Conversely, a sample containing inorganic nanoparticles at a sufficiently low concentration will create a pulse of charged ions after passing through the plasma. Here, a resulting spike in intensity versus time will occur for dwell times that contained nanoparticulate metal [36]. (Reprint with permission from John Wiley and Sons.)

If the nebulization efficient ε is known, then Equation 2.1 can be used to determine the nanoparticle number concentration in the analyte.

The pulse signal R (ions counts) can also relate to the mass concentration of a solution of an element M (C_M) in ICP-MS time-resolved mode as shown in the following equation:

$$R = \varepsilon Q_{sam} K_{ICP} K_M C_M t \tag{2.2}$$

where:

ε is the nebulization efficiency;
Q_{sam} is the sample uptake rate (ml/s);
K_{ICP} is the detection efficiency, which represents the ratio of the number of ions detected and the number of atoms introduced into the ICP and involves the processes of ionization, sampling through the IC-PMS interface, as well as transmission through the mass spectrometer.

K_M ($=AN_{Av}/M_M$) includes the contribution from the element measured. A is the atomic abundance of the isotope considered, N_{Av} is the Avogadro number, and M_M is the atomic mass of M.
C_M is the elemental mass concentration of a nanoparticle introduced into ICP-MS;
t is the dwell time.

If ENMs are spherical, solid, and pure, the element mass concentration C_M can be expressed as

$$C_M = \frac{1}{6}\pi\rho d^3 X_{NP} N_{NP} \tag{2.3}$$

where

d is the ENM diameter;
ρ is the density of the ENMs;
X_{NP} is the mass fraction of the element in the ENM (= 1 for a metallic ENM);
N_{NP} is the ENM number concentration.

When measurements are acquired in time-resolved mode, each reading lasts for a period equal to the dwell time (t). If only one nanoparticle is detected during a single reading, $\varepsilon Q_{sam} N_{NP} t = 1$ [9]. Therefore,

$$R = \frac{1}{6}\pi\rho X_{NP} K_{ICP} K_M d^3 \tag{2.4}$$

In summary, ENM number concentration can be calculated using Equation 2.1. The signal intensity of the ENM events is proportional to the mass of each ENM (Equations 2.2 and 2.4). The technique has been applied for environmental, medical, and industrial analysis of ENMs.

However, the technique has some drawbacks. First, if ENMs consist of elements with high natural abundance, separation of the backgrounds from signals is usually a difficult task. Second, simultaneous analysis of different elements in ENMs is still challenging for the most commercial quadrupole ICP-MS, because of limited data acquisition rates. TOF is a promising time-resolved and multielement analyzer for ICP-MS when analyzing ENMs [37].

2.3.2 Applications of SP-ICP-MS

Although SP-ICP-MS is an emerging technique, there are many applications to various research fields in the literature.

The first kind of applications is to characterize ENMs in various matrices, such as in environmental and biological sample. Some applications are focused on spherical nanoparticles in aqueous solution, for example, Au NPs [35, 38–41], Ag NPs [36, 42–44], and CeO_2 NPs [45, 46]. Pace *et al.* [35] Pace *et al.* [35] presented a guide on how to count and size AuNPs and determined transport efficiency, an important parameter in the SP-ICP-MS calculations. Mitrano *et al.* [36] analyzed two wastewater samples using SP-ICP-MS and found the presence of Ag NPs

(100–200 ng/l) and Ag ions (50–500 ng/l). Tuoriniemi *et al.* [43] described the strategies for appropriate choice of dwell time, transport efficiency, and background threshold calculation. Hineman and Stephan [39] showed that a novel instrument using a short dwell time (10 µs or 10^5 Hz data acquisition rate) can benefit from the continuous data acquisition for SP-ICP-MS. Lee *et al.* [47] developed a method to estimate the size detection limit using SP-ICP-MS and applied it to ENMs composed of 40 different elements. The size detection limits range from 10 to 200 nm, depending on the different element compositions of ENMs.

Besides ENMs in aqueous solution, ENMs in biological matrices are analyzed by SP-ICP-MS. Gray *et al.* [48] extracted Au and Ag NPs from biological samples using alkaline digestion for SP-ICP-MS analysis. They suggested minimal shifts in size distribution of ENMs accumulated as compared to the exposure media. Dan *et al.* [49] simultaneously determined Au NP size, size distribution, particle concentration, and dissolved Au concentration in tomato plant using an enzymatic digestion method, followed by SP-ICP-MS analysis.

In combination with labeling techniques, such as nanoparticle labeling on antibodies or DNA probes, SP-ICP-MS has also been successfully applied to detect DNA [50, 51] and proteins [52]. Han *et al.* [50] reported a novel method of one-step homogeneous DNA assay using SP-ICP-MS. As illustrated in Figure 2.3, the hybridization of DNA targets with probes immobilized on the surface of the Au NPs results in the formation of dimers, trimers, or even large aggregates of Au NPs. This polymeric network aggregation leads to decreased concentrations of

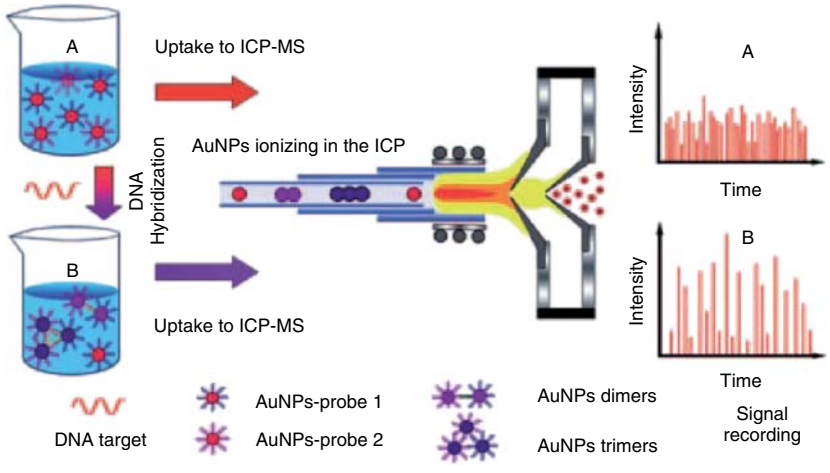

Figure 2.3 DNA hybridization assay with AuNP probes by using SP-ICPMS. The first step was to functionalize citrate-protected AuNPs with two sets of single-stranded DNA, probe 1 and probe 2. Then DNA targets were hybridized with AuNP–probe 1 and AuNP–probe 2 in buffer solution. The solution of AuNP aggregates was introduced into the plasma torch by the nebulizer and then AuNPs underwent desolvation, particle vaporization, atomization, and ionization in the ICP zone at approximately 6000–7000 K. Finally, the frequency and intensity of the 197Au + pulse signals were recorded by the electron multiplier detector [50]. (Reprint with permission from John Wiley and Sons.)

the whole Au NP population and increased individual sizes. These changes can be detected by SP-ICP-MS and DNA concentration can be obtained. The DNA targets can be detected at 1 pM by using Au NP probes, which increase the sensitivity by three orders of magnitude over that of colorimetric methods, without any signal amplification process [50]. Hu *et al.* [52] developed a highly sensitive immunoassay for α-fetoprotein in serum using Au NP tagged α-fetoprotein antibody and SP-ICP-MS analysis. The limit of quantification is 0.016 μg/l with a relative standard deviation of 4.2% for α-fetoprotein.

In addition, the theory and technique of SP-ICP-MS have been applied for single-cell analysis where elements in single cells are analyzed by time-resolved ICP-MS. Similarly to SP-ICP-MS, cells are sprayed in sequence into the high-temperature plasma where each cell is desolvated and its constituents are atomized and ionized. The resulting ions are then detected by mass spectrometry. In the mass spectra, the intensity of each transient signal corresponds to the atomic constituents in a single cell and the frequency of transient signals is directly related to the number of cells. The quadrupole ICP-MS was used to determine intrinsic magnesium [53], uranium [54], mineral elements [55], and metal drugs [56, 57] in single cells. The duration of the ion cloud in the ICP produced from a single cell or single particle event was found to be on the order of 300 μs. In contrast, the stabilization time of quadrupole mass analyzer is typically 50–200 μs [58]. Thus, in the aforementioned applications, only one isotope in a single cell can be determined due to limited data acquisition rate in quadrupole ICP-MS.

Simultaneous multielement detection has been achieved with a TOF mass analyzer. Recently, a new ICP-TOF-MS instrument, named mass cytometry, has been introduced for single-cell analysis [59]. Mass cytometry has essentially the same workflow as conventional flow cytometry (see Figure 2.4), but can address the challenges of polychromatic flow cytometry. Each cell cloud produced in plasma is enough for obtaining 20–30 data points by this ICP-TOF-MS [60]. This "postfluorescence" technology is theoretically capable of simultaneously measuring 70–100 parameters of a single cell and expecting to play an important role in dissecting the complex interactions of cells. Mass cytometry succeeded in measuring 34 parameters simultaneously in single cells of healthy human bone marrow [61]. Such single-cell analysis provides system-wide views of immune signaling in healthy human hematopoiesis, against which drug action and disease can be compared for mechanistic studies and pharmacologic intervention.

In summary, ICP-MS is able to detect ENMs without any optical or electrochemical properties and obtain more information of ENMs. SP-ICP-MS is expected to be further applied for ENM characterization.

2.4
Analysis of Nanoparticles by ICP-MS Hyphenate Techniques

As discussed earlier, ICP-MS has become a very promising analytical technique for ENMs due to its element specificity, excellent resolution, and high sensitivity.

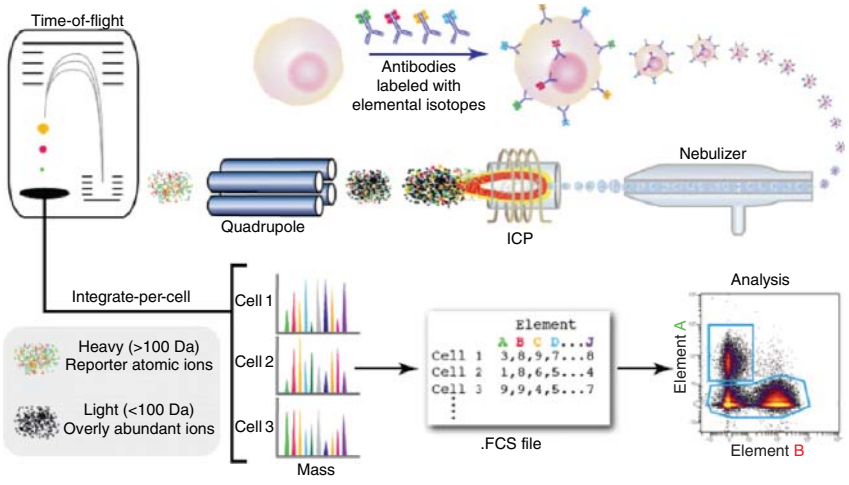

Figure 2.4 Mass cytometry allows single-cell atomic mass spectrometry of heavy elemental (>100 Da) reporters. Schematic of ICP-MS-based analysis of cellular markers. An affinity product (e.g., antibody) tagged with a specific element binds to the cellular epitope. The cell is introduced into the ICP by droplet nebulization. Each cell is atomized, ionized, overly abundant ions removed, and the elemental composition of remaining heavy elements (reporters) is determined. Signals corresponding to each elemental tag are then correlated with the presence of the respective marker and analyzed using conventional cytometry platforms [60]. (Reprint with permission from Elsevier Limited.)

More importantly, ICP-MS can be coupled to a solid sample introduction system (e.g., LA) and various separation methods, such as CE, FFF, and hydrodynamic chromatography (HDC). In this section, we discuss the analysis of ENMs by ICP-MS hyphenated techniques.

2.4.1 Solution-Based ICP-MS Hyphenated Techniques

2.4.1.1 Field Flow Fractionation

FFF can separate particles based on their hydrodynamic size. The separation process is similar to a liquid chromatography, except that the separation is based on physical forces (e.g., diffusion), rather than chemical interactions. FFF consists of a suite of high-resolution sizing techniques, which allow separation and sizing of macromolecules, submicron colloids, and nanoparticles of 1–100 nm, depending on the type of field applied and mode of operation [62]. Several types of FFF are developed and used for various applications: flow FFF, sedimentation FFF, electrical FFF, and thermal FFF. Among them, flow FFF and sedimentation FFF have been widely used for coupling to ICP-MS for ENM analysis. For the detailed theory of FFF, many excellent reviews can be referred [63].

Ranville *et al.* [62] used sedimentation FFF coupled to ICP-MS for simultaneous size separation and elemental analysis of soil colloids. They analyzed two

colloid samples from surface soil horizons and found significant enrichment in iron-containing phases in both smaller and larger colloids relative to intermediate particle size (~0.3 μm). Schmidt *et al.* [11] separated mixtures of three polystyrene (PS) NPs between 20 and 100 nm in diameter and mixtures of three Au NPs between 10 and 60 nm in diameter by FFF. They determined the hydrodynamic diameters of the Au and PS NPs online by multiangle light scattering and dynamic light scattering. The three separated Au NPs were quantified by ICP-MS. The recovery was 50–95% of the injected masses and limit of detection ranged between 0.02 ng Au and 0.4 ng Au.

Tan *et al.* [64] used hollow-fiber flow FFF and minicolumn concentration on-line coupled to multiple detectors (UV, dynamic light scattering, and ICP-MS) for full separation, characterization, and quantification of various Ag(I) species and different-sized Ag NPs. The success of the developed method was also demonstrated by the good recoveries of Ag(I), Ag-Cys, and five species of Ag NPs (1.4, 10, 20, 40, and 60 nm) determined in two spiked surface water samples.

2.4.1.2 **Hydrodynamic Chromatography**

In HDC, particle separation is solely based on particle size and is independent of the particle type or density. The ENMs flow along a column packed with nonporous beads and separated by flow velocity and the velocity gradient across slow-flow regions near the conduit walls. In the narrow conduits, larger particles transported faster than the small ones, thus eluting from the column faster and exhibiting a higher retention time [65]. Similarly to FFF, the elution time of ENMs is related to the apparent particle size. The simultaneous analysis of inorganic ENMs in a single run can be achieved when HDC couples to ICP-MS.

Tiede *et al.* [65] applied the technique of HDC coupled to ICP-MS for separation and detection of metal-based ENMs in environmental samples. The results showed that this methodology has many advantages including rapid analysis time (<10 min), extended sizing range (5–300 nm), and limited sample preparation required, thus expecting to be helpful in investigating the fate of a significant range of nanoparticle types.

For accurate quantification, Lewis [66] modified the HDC-ICP-MS system to facilitate the injection of NIST traceable standards into the postcolumn effluent, allowing quantification of eluting ENMs against the response from postcolumn standards. In this way, particle size, mass concentration, and particle number concentration were obtained in a single run. The approach was validated against reference nanomaterials available, and the robustness of the methodology was successfully proven against real samples.

HDC usually has poor separation resolution and is not able to distinguish ENMs with similar sizes. However, HDC is sufficiently robust and requires little sample preparation. In addition, HDC separates ENMs independent of their density, and one kind of ENM standards (e.g., Au NPs from NIST) can function as universal size calibration standards.

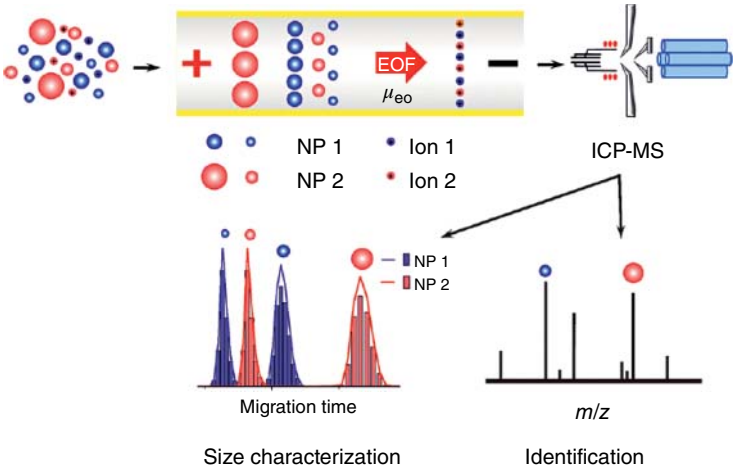

Figure 2.5 Simultaneous identification and size characterization of ENMs in complex media by CE-ICP-MS. EOF = electro-osmotic flow [70]. (Reprint with permission from John Wiley and Sons.)

2.4.1.3 Electrophoresis

CE is a well-developed separation technique and widely used in many applications. Performing electrophoretic separation in capillaries allows the possibility of automated analytical equipment, fast separation, and on-line detection of the separated peaks. In addition, CE has the feature of analyzing different sample types with a high resolution for ions. CE has been used in ICP-MS-based hyphenated technique for elemental speciation analysis [67].

CE methods exhibit great promise for nanoparticle characterization. McCormick [68] achieved good resolving power for silica sols in the range of 5–500 nm using a 190 nm UV. Later, ICP-MS was coupled to CE, providing a more sensitive and specific detector for ENM analysis. Helfrich and Bettmer [69] applied GE coupled to ICP-MS to characterize of Au NPs.

Liu *et al.* [70] developed a new and versatile method based on capillary electrokinetic separation and ICP-MS to provide a reliable platform for the identification and size characterization of ENMs in complex media (see Figure 2.5). The CE-ICP-MS technique can provide multidimensional information of ENMs in complex media, including accurate size-distribution information of ENMs and chemical species of the ENMs as well as related ionic species simultaneously in a single run. Franze and Engelhard [71] also used micellar electrokinetic chromatography coupled to ICP-MS for separation, size characterization, and speciation of Au NPs and Ag NPs.

2.4.1.4 Laser Ablation ICP-MS for ENM Analysis

LA is regarded as a sample introduction system for analyzing solid materials without chemical dissolution or digestion procedure by ICP-MS. The principle behind this approach is the use of a high-powered laser to ablate the surface of a solid and

sweep the sample aerosol into ICP-MS for analysis in the conventional way [72]. At low laser flux, the material is heated by the absorbed laser energy and evaporates or sublimates. At high laser flux, the material is typically converted to plasma. Because of the impressive detection limits (typically better than parts-per-million for most elements), wide dynamic range (up to nine orders of magnitude), and spatial resolution capacity in the micrometer range, LA-ICP-MS has been widely used in many research fields [73]. Unlike solution-based techniques (e.g., mass cytometry), LA-ICP-MS enables *in situ* analysis of microscopic targets, offering new opportunities for analysis of ENMs.

Drescher *et al.* [74] utilized LA-ICP-MS for the spatially resolved bioimaging of the distribution of Ag NPs and Au NPs in individual fibroblast cells [74]. ENMs were visualized with respect to cellular substructures with high spatial resolution and were found to accumulate in the perinuclear region with increasing incubation time. The results provide insight into nanoparticle/cell interactions and have implications for the development of analytical methods in tissue diagnostics and therapeutics. It was demonstrated that high spatial resolution LA-ICP-MS can be utilized in bioimaging to determine the intracellular nanoparticle distribution in cellular substructures of individual cells.

Wang *et al.* [75] developed a new quantitative method for LA-ICP-MS analysis of Au NPs in single cells. Dried residues of picoliter droplets ejected by a commercial inkjet printer were used to simulate matrix-matched calibration standards. The gold mass in single cell exposed to 100 nM NIST Au NPs (reference material 8012, 30 nm) for 4 h showed a log-normal distribution, ranging from 1.7 to 72 fg Au per cell, which approximately corresponds to 9–370 Au NPs per cell. The average result from 70 single cells (15 ± 13 fg Au per cell) was in good agreement with the result from an aqua regia digest solution of 1.2×10^6 cells (18 ± 1 fg Au per cell). The limit of quantification was 1.7 fg Au (see Figure 2.6) This paper demonstrates the great potential of LA-ICP-MS for single-cell analysis and the beneficial study of biological responses to metal drugs or ENMs at the single-cell level.

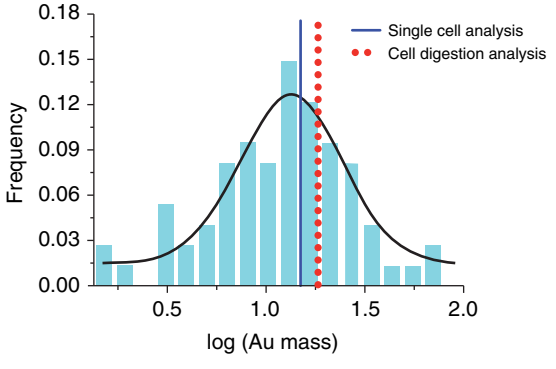

Figure 2.6 Histogram showing the log-normal distribution of Au mass for the ablation of 70 cells. The two averages from single-cell analysis (the blue solid line) and cell digestion analysis (the red dot line) are 15 and 18 fg, respectively [75]. (Reprint with permission from American Chemical Society.)

Yan *et al.* [76] separated and determined Au NPs in aqueous suspensions by coupling thin-layer chromatography (TLC) with laser ablation–inductively coupled plasma–mass spectrometry (LA-ICP-MS). The paper demonstrated that TLC can separate Au NPs from ionic gold and isolate differently sized Au NPs by using the suitable mobile phase. It was found that separations of Au NPs by TLC displayed size-dependent retention behavior with good reproducibility, and the retardation factors (Rf value) increased linearly with decreasing nanoparticle size. The developed thin-layer chromatography–laser ablation–inductively coupled plasma–mass spectrometry (TLC-LA-ICP-MS) method has also been applied to the analysis of spiked Au NPs in lake water, river water, and tap water samples.

2.5 Conclusion and Outlook

The applications of ICP-MS for ENM analysis discussed in the previous sections already show the great analytical potential of ICP-MS. ICP-MS-based techniques benefit from its high sensitivity and precision and give quantitative and qualitative information about the elemental content of ENMs in a single run. In addition, the hyphenated systems, such as coupling of a separation technique or a solid sample introduction system, can provide more information of ENMs, for example, size distribution and particle concentration. ICP-MS-based techniques are expected to become an important tool and be widely used for ENM characterization and analysis in the near future.

References

1. Dykman, L.A. and Khlebtsov, N.G. (2014) Uptake of engineered gold nanoparticles into mammalian cells. *Chem. Rev.*, **114** (2), 1258–1288.
2. Chen, C., Li, Y.-F., Qu, Y. *et al.* (2013) Advanced nuclear analytical and related techniques for the growing challenges in nanotoxicology. *Chem. Soc. Rev.*, **42**, 8266–8303.
3. Krug, H.F. (2014) Nanosafety research-are we on the right track? *Angew. Chem. Int. Ed.*, **53**, 2–18.
4. Nel, A., Xia, T., Meng, H. *et al.* (2013) Nanomaterial toxicity testing in the 21st century: use of a predictive toxicological approach and high-throughput screening. *Acc. Chem. Res.*, **46** (3), 607–621.
5. Zhao, Y., Xing, G., and Chai, Z. (2008) Nanotoxicology: are carbon nanotubes safe? *Nat. Nanotechnol.*, **3**, 191–192.
6. Oberdörster, G., Oberdörster, E., and Oberdörster, J. (2005) Nanotoxicology: an emerging discipline evolving from studies of ultrafine particles. *Environ. Health Perspect.*, **113** (7), 823–839.
7. Fischer, H.C. and Chan, W.C. (2007) Nanotoxicity: the growing need for in vivo study. *Curr. Opin. Biotechnol.*, **18** (2), 565–571.
8. Marquis, B.J., Love, S.A., Braun, K.L., and Haynes, C.L. (2009) Analytical methods to assess nanoparticle toxicity. *Analyst*, **134**, 425–439.
9. Laborda, F., Bolea, E., and Jiménez-Lamana, J. (2014) Single particle inductively coupled plasma mass spectrometry: a powerful tool for nanoanalysis. *Anal. Chem.*, **86** (5), 2270–2278.

10. Wang, M., Feng, W.-Y., Zhao, Y.-L., and Chai, Z.-F. (2010) ICP-MS-based strategies for protein quantification. *Mass Spectrom. Rev.*, **29** (2), 326–348.
11. Schmidt, B., Loeschner, K., Hadrup, N. *et al.* (2011) Quantitative characterization of gold nanoparticles by field-flow fractionation coupled online with light scattering detection and inductively coupled plasma mass spectrometry. *Anal. Chem.*, **83** (7), 2461–2468.
12. Houk, R.S., Fassel, V.A., Flesch, G.D., Svec, H.J., Gray, A.L., and Taylor, C.E. (1980) Inductively coupled argon plasma as an ion source for mass spectrometric determination of trace elements. *Anal. Chem.*, **52** (14), 2283–2289.
13. Beauchemin, D. (2006) Inductively coupled plasma mass spectrometry. *Anal. Chem.*, **78** (12), 4111–4135.
14. Ammann, A.A. (2007) Inductively coupled plasma mass spectrometry (ICP MS): a versatile tool. *J. Mass Spectrom.*, **42**, 419–427.
15. Svantesson, E., Pettersson, J., and Markides, K.E. (2002) The use of inorganic elemental standards in the quantification of proteins and biomolecular compounds by inductively coupled plasma spectrometry. *J. Anal. At. Spectrom.*, **17**, 491–496.
16. Coupled, I., Mass, P., and Handbook, S. (2005) *Inductively Coupled Plasma Mass Spectrometry Handbook*, Blackwell Publishing Ltd, Oxford.
17. Sturgeon, R.E., Lam, J.W.H., and Saint, A. (2000) Analytical characteristics of a commercial ICP orthogonal acceleration time-of-flight mass spectrometer (ICP-TOFMS). *J. Anal. At. Spectrom.*, **15** (6), 607–616.
18. Jakubowski, N., Moens, L., and Vanhaecke, F. (1998) Sector field mass spectrometers in ICP-MS. *Spectrochim. Acta, Part B*, **53**, 1739–1763.
19. Tanner, S.D., Baranov, V.I., and Bandura, D.R. (2002) Reaction cells and collision cells for ICP-MS: a tutorial review. *Spectrochim. Acta, Part B*, **57** (9), 1361–1452.
20. Koppenaal, D.W., Eiden, G.C., and Barinaga, C.J. (2004) Collision and reaction cells in atomic mass spectrometry: development, status, and applications the opinions expressed in the following article are entirely those of the authors and do not necessarily represent the views of the Royal Society of Chemistry. *J. Anal. At. Spectrom.*, **19**, 561.
21. Lobinski, R., Schaumloffel, D., and Szpunar, J. (2006) Mass spectrometry in bioinorganic analytical chemistry. *Mass Spectrom. Rev.*, **25** (2), 255–289.
22. Helfrich, A. and Bettmer, J. (2007) Determination of phosphorylation degrees in caseins by on-line gel electrophoresis coupled to ICP-SFMS. *J. Anal. At. Spectrom.*, **22** (10), 1296.
23. Schaumlöffel, D., Giusti, P., Zoriy, M.V. *et al* (2005) Ultratrace determination of uranium and plutonium by nano-volume flow injection double-focusing sector field inductively coupled plasma mass spectrometry (nFI-ICP-SFMS). *J. Anal. At. Spectrom.*, **20** (1), 17.
24. Wind, M., Eisenmenger, A., and Lehmann, W.D. (2001) Modified direct injection high efficiency nebulizer with minimized dead volume for the analysis of biological samples by micro- and nano-LC-ICP-MS. *J. Anal. At. Spectrom.*, **17**, 21–26.
25. Pereira Navaza, A., Ruiz Encinar, J., and Sanz-Medel, A. (2007) Absolute and accurate quantification of protein phosphorylation by using an elemental phosphorus standard and element mass spectrometry. *Angew. Chem. Int. Ed.*, **46**, 569–571.
26. Prange, A. and Pröfrock, D. (2005) Application of CE-ICP-MS and CE-ESI-MS in metalloproteomics: challenges, developments, and limitations. *Anal. Bioanal. Chem.*, **383**, 372–389.
27. Ma, R., McLeod, C.W., Tomlinson, K., and Poole, R.K. (2004) Speciation of protein-bound trace elements by gel electrophoresis and atomic spectrometry. *Electrophoresis*, **25**, 2469–2477.
28. Becker, J.S., Zoriy, M., Matusch, A. *et al.* (2010) Bioimaging of metals by laser ablation inductively coupled plasma mass spectrometry (LA-ICP-MS). *Mass Spectrom. Rev.*, **29** (1), 156–175.
29. Szpunar, J. (2005) Advances in analytical methodology for bioinorganic speciation analysis: metallomics, metalloproteomics and heteroatom-tagged proteomics

and metabolomics. *Analyst*, **130** (4), 442–465.

30. Chithrani, B.D. and Chan, W.C.W. (2007) Elucidating the mechanism of cellular uptake and removal of protein-coated gold nanoparticles of different sizes and shapes. *Nano Lett.*, **7** (6), 1542–1550.
31. Meng, H., Chen, Z., Xing, G.M. *et al.* (2007) Ultrahigh reactivity provokes nanotoxicity: explanation of oral toxicity of nano-copper particles. *Toxicol. Lett.*, **175** (1-3), 102–110.
32. Degueldre, C. and Favarger, P.Y. (2003) Colloid analysis by single particle inductively coupled plasma-mass spectroscopy: a feasibility study. *Colloids Surf., A*, **217** (1-3), 137–142.
33. Degueldre, C., Favarger, P.-Y., and Wold, S. (2006) Gold colloid analysis by inductively coupled plasma-mass spectrometry in a single particle mode. *Anal. Chim. Acta*, **555**, 263–268.
34. Degueldre, C., Favarger, P.-Y., and Bitea, C. (2004) Zirconia colloid analysis by single particle inductively coupled plasma–mass spectrometry. *Anal. Chim. Acta*, **518**, 137–142.
35. Pace, H.E., Rogers, N.J., Jarolimek, C. *et al.* (2011) Determining transport efficiency for the purpose of counting and sizing nanoparticles via single particle inductively coupled plasma mass spectrometry. *Anal. Chem.*, **83** (24), 9361–9369.
36. Mitrano, D.M., Lesher, E.K., Bednar, A. *et al.* (2012) Detecting nanoparticulate silver using single-particle inductively coupled plasma-mass spectrometry. *Environ. Toxicol. Chem.*, **31** (1), 115–121.
37. Borovinskaya, O., Hattendorf, B., Tanner, M. *et al.* (2013) A prototype of a new inductively coupled plasma time-of-flight mass spectrometer providing temporally resolved, multi-element detection of short signals generated by single particles and droplets. *J. Anal. At. Spectrom.*, **28**, 226–233.
38. Ho, K.-S., Lui, K.-O., Lee, K.-H., and Chan, W.-T. (2013) Considerations of particle vaporization and analyte diffusion in single-particle inductively coupled plasma-mass spectrometry. *Spectrochim. Acta, Part B*, **89**, 30–39.
39. Hineman, A. and Stephan, C. (2014) Effect of dwell time on single particle inductively coupled plasma mass spectrometry data acquisition quality. *J. Anal. At. Spectrom.*, **29** (7), 1252.
40. Cornelis, G. and Hassellöv, M. (2014) A signal deconvolution method to discriminate smaller nanoparticles in single particle ICP-MS. *J. Anal. At. Spectrom.*, **29** (1), 134.
41. Liu, J., Murphy, K.E., MacCuspie, R.I., and Winchester, M.R. (2014) Capabilities of single particle inductively coupled plasma mass spectrometry for the size measurement of nanoparticles: a case study on gold nanoparticles. *Anal. Chem.*, **86** (7), 3405–3414.
42. Laborda, F., Jimenez-Lamana, J., Bolea, E., and Castillo, J.R. (2011) Selective identification, characterization and determination of dissolved silver(I) and silver nanoparticles based on single particle detection by inductively coupled plasma mass spectrometry. *J. Anal. At. Spectrom.*, **26** (7), 1362–1371.
43. Tuoriniemi, J., Cornelis, G., and Hassellöv, M. (2012) Size discrimination and detection capabilities of single-particle ICPMS for environmental analysis of silver nanoparticles. *Anal. Chem.*, **84** (9), 3965–3972.
44. Telgmann, L., Metcalfe, C.D., and Hintelmann, H. (2014) Rapid size characterization of silver nanoparticles by single particle ICP-MS and isotope dilution. *J. Anal. At. Spectrom.*, **29**, 1265–1272.
45. Bi, X.Y., Lee, S., Ranville, J.F. *et al.* (2014) Quantitative resolution of nanoparticle sizes using single particle inductively coupled plasma mass spectrometry with the K-means clustering algorithm. *J. Anal. At. Spectrom.*, **29**, 1630–1639.
46. Montaño, M.D., Badiei, H.R., Bazargan, S., and Ranville, J.F. (2014) Improvements in the detection and characterization of engineered nanoparticles using spICP-MS with microsecond dwell times. *Environ. Sci. Nano*, **1** (4), 338–346.
47. Lee, S., Bi, X., Reed, R.B. *et al.* (2014) Nanoparticle size detection limits by single particle ICP-MS for 40 elements. *Environ. Sci. Technol.*, **48**, 10291–10300.

48. Gray, E.P., Coleman, J.G., Bednar, A.J. *et al.* (2013) Extraction and analysis of silver and gold nanoparticles from biological tissues using single particle inductively coupled plasma mass spectrometry. *Environ. Sci. Technol.*, **47** (24), 14315–14323.
49. Dan, Y., Zhang, W., Xue, R. *et al.* (2015) Characterization of gold nanoparticle uptake by tomato plants using enzymatic extraction followed by single-particle inductively coupled plasma-mass spectrometry analysis. *Environ. Sci. Technol.*, **49** (5), 3007–3014.
50. Han, G., Xing, Z., Dong, Y. *et al.* (2011) One-step homogeneous DNA assay with single-nanoparticle detection. *Angew. Chem. Int. Ed.*, **50** (15), 3462–3465.
51. Zhang, S., Han, G., Xing, Z. *et al.* (2014) Multiplex DNA assay based on nanoparticle probes by single particle inductively coupled plasma mass spectrometry. *Anal. Chem.*, **86** (7), 3541–3547.
52. Hu, S., Liu, R., Zhang, S. *et al.* (2009) A new strategy for highly sensitive immunoassay based on single-particle mode detection by inductively coupled plasma mass spectrometry. *J. Am. Soc. Mass. Spectrom.*, **20** (6), 1096–1103.
53. Ho, K.S. and Chan, W.T. (2010) Time-resolved ICP-MS measurement for single-cell analysis and on-line cytometry. *J. Anal. At. Spectrom.*, **25** (7), 1114–1122.
54. Li, F.M., Armstrong, D.W., and Houk, R.S. (2005) Behavior of bacteria in the inductively coupled plasma: atomization and production of atomic ions for mass spectrometry. *Anal. Chem.*, **77** (5), 1407–1413.
55. Wang, H.-L., Wang, B., Wang, M. *et al.* (2015) Time-resolved ICP-MS analysis of mineral element contents and distribution patterns in single cells. *Analyst*, **140**, 523–531.
56. Tsang, C.N., Ho, K.S., Sun, H., and Chan, W.T. (2011) Tracking bismuth antiulcer drug uptake in single helicobacter pylori cells. *J. Am. Chem. Soc.*, **133** (19), 7355–7357.
57. Zheng, L.-N., Wang, M., Zhao, L.-C. *et al.* (2015) Quantitative analysis of Gd@C82(OH)22 and cisplatin uptake in single cells by inductively coupled plasma mass spectrometry. *Anal. Bioanal. Chem.*, **407**, 2383–2391.
58. Tanner, S.D., Ornatsky, O., Bandura, D.R., and Baranov, V.I. (2007) Multiplex bio-assay with inductively coupled plasma mass spectrometry: towards a massively multivariate single-cell technology. *Spectrochim. Acta, Part B*, **62** (3), 188–195.
59. Bandura, D.R., Baranov, V.I., Ornatsky, O.I. *et al.* (2009) Mass cytometry: technique for real time single cell multitarget immunoassay based on inductively coupled plasma time-of-flight mass spectrometry. *Anal. Chem.*, **81** (16), 6813–6822.
60. Bendall, S.C., Nolan, G.P., Roederer, M., and Chattopadhyay, P.K. (2012) A deep profiler's guide to cytometry. *Trends Immunol.*, **33** (7), 323–332.
61. Bendall, S.C., Simonds, E.F., Qiu, P. *et al.* (2011) Single-cell mass cytometry of differential immune and drug responses across a human hematopoietic continuum. *Science*, **332** (6030), 687–696.
62. Ranville, J.F., Chittleborough, D.J., Shanks, F. *et al.* (1999) Development of sedimentation field-flow fractionation-inductively coupled plasma mass-spectrometry for the characterization of environmental colloids. *Anal. Chim. Acta*, **381**, 315–329.
63. Gigault, J., Pettibone, J.M., Schmitt, C., and Hackley, V.A. (2014) Rational strategy for characterization of nanoscale particles by asymmetric-flow field flow fractionation: a tutorial. *Anal. Chim. Acta*, **809**, 9–24.
64. Tan, Z.-Q., Liu, J.-F., Guo, X.-R. *et al.* (2015) Toward full spectrum speciation of silver nanoparticles and ionic silver by on-line coupling of hollow fiber flow field-flow fractionation and minicolumn concentration with multiple detectors. *Anal. Chem.*, **87** (16), 8441–8447.
65. Tiede, K., Boxall, A.B.A., Tiede, D. *et al.* (2009) A robust size-characterisation methodology for studying nanoparticle behaviour in "real" environmental samples, using hydrodynamic chromatography coupled to ICP-MS. *J. Anal. At. Spectrom.*, **24** (7), 964.

66. Lewis, D.J. (2015) Hydrodynamic chromatography – inductively coupled plasma mass spectrometry, with post-column injection capability for simultaneous determination of nanoparticle size, mass concentration and particle number concentration (HDC-PCi-ICP-MS). *Analyst*, **140** (5), 1624–1628.
67. Kannamkumarath, S.S., Wrobel, K., Wrobel, K. *et al.* (2002) Capillary electrophoresis–inductively coupled plasma-mass spectrometry: an attractive complementary technique for elemental speciation analysis. *J. Chromatogr. A*, **975** (2), 245–266.
68. McCormick, R.M. (1991) Characterization of silica sols using capillary zone electrophoresis. *J. Liq. Chromatogr.*, **14** (5), 939–952.
69. Helfrich, A. and Bettmer, J. (2011) Analysis of gold nanoparticles using ICP-MS-based hyphenated and complementary ESI-MS techniques. *Int. J. Mass Spectrom.*, **307** (1-3), 92–98.
70. Liu, L., He, B., Liu, Q. *et al.* (2014) Identification and accurate size characterization of nanoparticles in complex media. *Angew. Chem. Int. Ed.*, **53** (52), 14476–14479.
71. Franze, B. and Engelhard, C. (2014) Fast separation, characterization, and speciation of gold and silver nanoparticles and their ionic counterparts with micellar electrokinetic chromatography coupled to ICP-MS. *Anal. Chem.*, **86** (12), 5713–5720.
72. Russo, R.E., Mao, X.L., Borisov, O.V., and Liu, H. (2000) Influence of wavelength on fractionation in laser ablation ICP-MS. *J. Anal. At. Spectrom.*, **15** (9), 1115–1120.
73. Konz, I., Fernández, B., Fernández, M.L. *et al.* (2012) Laser ablation ICP-MS for quantitative biomedical applications. *Anal. Bioanal. Chem.*, **403** (8), 2113–2125.
74. Drescher, D., Giesen, C., Traub, H. *et al.* (2012) Quantitative imaging of gold and silver nanoparticles in single eukaryotic cells by laser ablation ICP-MS. *Anal. Chem.*, **84**, 9684–9688.
75. Wang, M., Zheng, L., Wang, B. *et al.* (2014) Quantitative analysis of gold nanoparticles in single cells by laser ablation inductively coupled plasma-mass spectrometry. *Anal. Chem.*, **86** (20), 10252–10256.
76. Yan, N., Zhu, Z., Jin, L. *et al.* (2015) Quantitative characterization of gold nanoparticles by coupling thin layer chromatography with laser ablation inductively coupled plasma mass spectrometry. *Anal. Chem.*, **87** (12), 6079–6087.

3
Stable Isotopic Tracing of Nanomaterials *In Vivo*

Yuliang Zhao and Xueling Chang

3.1
Introduction

With the rapid development of nanotechnology, nanomaterials have been widely used in various fields. However, the increase in the number of products containing these materials has led to growing concerns about the potential adverse effects on human health and on the environment upon exposure to nanomaterials [1–11]. Due to their unique physicochemical properties (such as small size, large specific surface area, high reaction activity, etc.), nanomaterials may exhibit markedly higher toxicity compared with macroscale materials of identical chemical composition [12–16]. The interactions and the underlying mechanisms at the nano–bio interface are rather complicated in nanotoxicology, requiring urgently novel and focused analytical methodology and tools [9–11].

Stable isotopic tracing provides a quantitative, safe, and powerful tool to investigate the behaviors of nanomaterials in environmental and biological systems [17–21]. A stable isotope of the element of interest is incorporated into the molecule or product, and any related transformations can be easily detected by inductively coupled plasma–mass spectrometry (ICP-MS), high-resolution ICP-MS, multicollector ICP-MS, or thermal ionization mass spectrometry (TIMS), and isotope ratio mass spectrometry (IRMS) [22]. The approach avoids the disadvantages of radioactive labeling, such as the strict conditions of radioactivity operation, the generation of radioactive wastes, and the limitation of the shorter half-life of some radioactive elements, which should be a good choice for the very low concentrations and long-term exposure of nanoparticles [23–26]. Moreover, stable isotopic tracers can also easily distinguish the endogenous and exogenous sources of elements of interest in samples and have particular advantages especially for differentiating between carbon nanomaterials (such as carbon nanotubes (CNTs), graphene, and fullerene) and carbon-rich biological samples, which are similar in composition and dimensions [9, 27–30]. Herein, we take ^{13}C tracer as an example to demonstrate how to quantitatively analyze stable-isotope-labeled nanomaterials.

Toxicology of Nanomaterials, First Edition. Edited by Yuliang Zhao, Zhiyong Zhang, and Weiyue Feng.

The stable isotope ratio of an element is the ratio of the quantity of the different stable isotopes of the element in a sample. Carbon has two stable isotopes: ^{12}C and ^{13}C. Carbon stable isotope ratios are normally expressed as an enrichment or depletion of ^{13}C in a sample by the parameter $\delta^{13}C$ defined as

$$ffi^{13}C = \left(\frac{R_S}{R_{STD}} - 1\right) \times 1000‰ \tag{3.1}$$

where R_S and R_{STD} are the $^{13}C/^{12}C$ ratios of the unknown and standard, respectively. $\delta^{13}C$ is the per mille deviation of the sample $^{13}C/^{12}C$ ratio from that of two internationally recognized standard materials, which are generally the primary international PDB standard (*Belemnitella americana Pee Dee Belemnite*) and VPDB standard (*Vienna Pee Dee Belemnite*). R_{STD} ratios of the PDB and VPDB standard were 0.0 112 372 and 0.0 111 802, respectively. Because the PDB standard had been exhausted, International Atomic Energy Agency (IAEA) recommended VPDB as the standard in practical applications. R_{STD}, 0.0 111 802 was used to calculate the $\delta^{13}C$ value in modern IRMS technology.

The δ values can be determined by IRMS and converted into $^{13}C/^{12}C$ ratio (r) following Equation 3.2. Then the percentage of ^{13}C in mass ($\omega^{13}C$) can be obtained following Equation 3.3. Finally, the amount of ^{13}C-labeled material in samples could be calculated from Equation 3.4, where ω_{carbon} from IRMS is the content of carbon in the dry sample; m_{sample} is the weight of sample; m_{dry} and m_{wet} are the weights of sample before and after drying. The value 9.108% is the percentage of ^{13}C in ^{13}C-enriched carbon nanomaterial [29].

$$r = \left(\frac{\delta}{1000} + 1\right) \times \left(\frac{^{13}C}{^{12}C}\right)_{standard} \tag{3.2}$$

$$\omega_{^{13}C} = \frac{r \times 13}{r \times 13 + 12} \times 100\% \tag{3.3}$$

$$m_{^{13}C\text{-fullerene}} = \frac{[\omega_{^{13}C}(\text{sample}) - \omega_{^{13}C}(\text{control})] \times \left(\omega_{carbon} \times m_{sample} \times \frac{m_{dry}}{m_{wet}}\right)}{9.108\%} \tag{3.4}$$

The stable isotope ratio changes and the resulting variations of structures and properties in some molecules or materials can be characterized by IRMS, mass spectrometry (MS), carbon nuclear magnetic resonance (CNMR), and Raman spectroscopy. In view of these stable isotopic effects, stable isotopes, as tracers, are often used to investigate originally the mechanism of some chemical reactions, the formation of molecules or materials, the geological evolution, the source and migration substance or pollution, and forensic identification in diverse disciplines such as archaeology, geology, medicine, biology, chemistry, food authenticity, agriculture, and forensic science for several decades [19–21, 23, 25, 26]. In addition, stable isotopic labeling technology, as a unique quantitative method, has been widely used for quantitative analysis of some biological molecules, drug molecules, and elements *in vitro* or *in vivo* [31–33].

In practical application, there are two main approaches in the use of isotope tracing: one based on naturally occurring differences between stable isotopes and

the other uses the addition of a tracer of the separated isotope. In this chapter, we focus on the investigations and applications of stable isotopes, as a composition or addition in nanomaterials, including light-stable isotope ^{13}C-labeled fullerenes, CNTs, and graphene oxide, heavy-stable isotope ^{68}Zn-labeled ZnO NPs, and ^{65}Cu-labeled CuO NPs, and so on.

3.2 Development of Stable Isotope Labeling in Nanotechnology

Early in 1978, Lyon and Baxter had put forward the particularly relevant significance of stable isotopic tracers in metabolic studies [34, 35]. They reported "natural baseline" of carbon isotope ratios from a wide range of human tissue samples. The mean human tissue values of $\delta^{13}C$ are around −23‰. A final ^{13}C-enrichment of approximately 10‰ is the minimum required for the artificial use of sable isotope tracers in biomedical studies. The use of natural isotope ratios is also significant for the ecological and palaeoecological carbon isotope discrimination in high plant photosynthesis. Subsequently, Tieszen suggested that the $^{13}C/^{12}C$ ratios simply reflected a dietary carbon source. The human diets might derive from C_3 plant $\delta^{13}C$ near −23‰, not from C_4 plant $\delta^{13}C$ near −13‰. He claimed that each tissue and biochemical fraction also had an isotopic "memory." The function of the $\delta^{13}C$ of the carbon in the biochemical synthesis process could be considered reliable for the metabolic studies.

Since 2002, stable isotope labeling with amino acids in cell culture (SILAC) has become increasingly popular for quantitative proteins/peptides [36–38]. SILAC is a powerful approach for high-throughput quantitative proteomics. SILAC uses stable-isotope-labeled amino acids to obtain highly accurate protein quantities through metabolic encoding of whole cell proteomes and then investigates dynamics of posttranslational modifications, protein–protein interactions, and protein turnover [39–45]. Recently, Cai *et al.* [46] utilized SILAC to provide insight into the molecular basis of selectivity in protein binding to CNTs, which led to the formation of protein corona on CNTs.

In 2006, Gulson and Wong [18] suggested for the first time that stable isotopic tracers, as a way forward for nanotechnology, could be used to address some critical issues related to nanomaterials, including in evaluating the confirmatory product, monitoring the workplace and environment, and testing procedures. They used metal oxide nanoparticles (ZnO and TiO_2) as examples to use ^{68}Zn and ^{46}Ti as tracers, which were generally incorporated into the cosmetic products, and monitored their dermal absorption and excretion in humans.

Since 2007, our group has labeled carbon nanomaterials with the stable isotope ^{13}C on skeleton carbon atoms by the arc discharge method, including CNTs, carbon quantum dots, fullerenes, and graphene [27–30, 47, 48]. The ^{13}C-labeling technique does not introduce foreign atoms onto the carbon networks, nor damage the unique intrinsic structure and properties of carbon nanomaterials. The absorption, distribution, metabolism, and excretion (ADME) of these

^{13}C-enriched carbon nanomaterials were investigated quantitatively in mice by IRMS.

Currently, some stable metal isotopes and the light-stable isotopes of hydrogen, carbon, nitrogen, and oxygen, as tracers, have been applied and designed increasingly in nanoparticles (Table 3.1). This stable isotope tracing approach could be used to address potentially many of the current concerns (such as fate and transport of nanoparticles in the environment, pharmacokinetic modeling, and cytotoxicity studies) being raised by scientific bodies and public. Just as ^{13}C-enriched carbon nanomaterials, stable isotopic tracers are very similar with the composition of nanomaterials, which can reflect the pristine properties of nanomaterial in biological systems and can also be potentially used in an analysis of the internal standard substance. The major drawbacks of stable isotopic tracing lie in the difficulties in preparing/purifying sufficient amounts of stable isotopes, in improving the labeled amounts of samples, and the high price. But with the rapid development of the experimental techniques and automatic instruments, their production yields will be increased.

3.3 ^{13}C-Labeled Carbon Nanomaterials

^{13}C atom is only one neutron more than that of ^{12}C. The discrepancy in nuclear mass between ^{13}C and ^{12}C made it feasible for measurable stable isotope ratio changes in biological samples and materials. This inequality also shows a difference in basic thermodynamic properties, such as diffusion coefficients, kinetics of reactions for ^{12}C- and ^{13}C-substituted molecules, equilibrium of reactions, and preferential selections of either the light or the heavy isotope. Hence, the ratio changes of heavy and light isotopes (as ^{13}C/^{12}C) may occur in the aforementioned processes. Generally, stable isotope ^{13}C is incorporated into the skeleton carbon atoms of carbon nanomaterials, hence possessing superstability *in vivo*, without taking into account those influences of the addition of a radioactive tag and covalently or adsorptively linking fluorophores to nanomaterials. Also, the skeleton labeling retains their intrinsic structures, enabling the labels to reflect the real properties of carbon nanomaterials.

3.3.1 Structure and Formation Mechanisms for Fullerene

The stable isotopes ^{13}C were often used as tracers to investigate the isotope effects, structural properties, and the formation mechanism of fullerenes nanomaterials in synthesis process. Several research groups tried to reveal the mysterious formation mechanism of those carbon-caged nanomaterials by ^{13}C-labeling. Meijer and Bethune [49] provided direct evidence that fullerenes can be trapped, stored and accumulated on surface, and then produced in sufficient quantity to make them accessible to separate and analyze. They utilized

Table 3.1 Stable-isotope-labeled nanomaterials and their structure and nanobiological effects.

Stable isotopes	Nanomaterials	Detections/ characteristics	Applications	References
^{13}C	C_{60} C_{60}–OH SWCNT PEG-SWCNT Graphene Graphite oxide	TOF-MS 13C NMR Raman spectroscopy IRMS	Structure or formation mechanism of carbon nanomaterials; quantification, biodistribution, and biotransformation; internal standard; imaging	[27–30] [47, 48] [49–83]
^{68}Zn	ZnO nanoparticles	MC-ICP-MS	Quantification; dermal absorption, bioavailability, and bioaccumulation	[84–97]
^{67}Zn	ZnO nanoparticles/metal nanoparticle	TOF-SIMS		
^{65}Cu	CuO nanoparticles	ICP-MS	Quantification; bioaccumulation and toxicity for ecotoxicological studies	[98, 99]
^{25}Mg	Mg-PMC16	Isotopic mass spectrometer	The pharmacokinetics and pharmacodynamics for the treatment of hypoxic cardiopathies and diabetic neuropathy.	[100–103]
^{109}Ag	Ag nanoparticles	Asymmetric-flow field flow fractionation coupled to optical detection and mass spectrometry	Quantification; bioavailability and toxicity for ecotoxicological studies	[104, 105]
^{57}Fe	Goethite nanorods	ICP-MS	The complex reaction process of sorption, electron transfer, and reductive dissolution and transformation to secondary minerals	[106]
^{18}O	Polystyrene latex nanoparticles; gold nanoparticles	LC-MS and accurate mass and time tag; attenuated total reflectance (ATR) Fourier transform infrared (FT-IR)	Interactions between human blood plasma proteins and nanoparticles; identification of the P═O stretching absorption in catalytic reaction	[107, 108]
^{2}H	$LaFeO_3$ and $BiFeO_3$; Lanthanide-doped upconverting nanoparticles	ESR, IRMS, FT-IR	Examined the applicability of nanocatalysts for heterogeneous Fenton-like reactions; Mediated the luminescence	[109, 110]
^{15}N	Crystalline poly(triazine imide) nanosheets; carbon clusters	NMR, cold-spray ionization mass spectrometry (CSI-MS)	Structure and photoluminescence	[111, 112]

laser deposition of carbon clusters on surface made from different proportions of isotopically enriched amorphous carbon powder (99.9% ^{12}C and 98.1% ^{13}C) and confirmed formation of ^{13}C-labeled C_{60} and C_{70} by time-of-flight mass spectra. The ^{13}C-fullerenes peaks were broadened slightly by the residual ^{12}C. The addition of ^{13}C in fullerene molecules can enhance their sensitivity of nuclear magnetic resonance signal detection. Further, they proved the structure and dynamical behavior of fullerene by magnetic resonance spectroscopy of ^{13}C-enriched fullerenes [50–52]. The authors established molecular symmetry, examined firstly the bond lengths and bonding topology in C_{60} and revealed directly C_{60} molecular rotational dynamics in the solid, and provided useful information about the formation mechanism of fullerenes. Simultaneously, Krätschmer *et al.* [53] prepared carbon dust by evaporating graphite rods. The rods were compressed by ^{13}C isotopically enriched carbon powder. They also observed firstly the ^{13}C isotope shift in the ultraviolet and the infrared spectra of carbon smoke particles and obtained an evidence for the presence of C_{60} molecular. Furthermore, Ebbesen *et al.* [54] clarified the formation mechanism of the initial stage of fullerene through a series of experiments based on $^{12}C/^{13}C$ isotope scrambling measurements. The distribution of ^{13}C among C_{60} molecules exactly followed the Poisson statistics for every ratio of ^{12}C and ^{13}C in a steady-state arc plasma. They thought that fullerenes were formed from atomic carbon vapor. The atomic vapor combined to form small carbon cluster, which in turn combined to form fullerenes. They also studied the isotope effects on superconductivity in ^{13}C-modified Rb_3C_{60} [55]. The superconducting Tc decreased as the ^{13}C content increased. At the same time, Ramirez *et al.* [56] reported the same results in Rb_3C_{60}. Chakravarty *et al.* [57] calculated the isotopic effect in the superconducting doped fullerenes. Hawkins *et al.* [58, 59] quantitatively examined the ^{13}C distribution within enriched C_{60} by ^{13}C NMR. The ^{13}C may be obtained by statistical incorporation of $^{13}C_2$ units into C_{60}. Thereby, they also provided the first definitive proof of the buckminsterfullerene structure and C–C coupling constants and probed the mechanism of C_{60} formation. Chen and Lieber [60] synthesized pure $^{13}C_{60}$ and determined the isotope effect for fullerene superconductors $K_3{}^{13}C_{60}$ versus $K_3{}^{12}C_{60}$. Subsequently, Martin *et al.* [61] investigated the vibrational modes of solid C_{60} in the infrared spectrum. Due to ^{13}C isotope addition in C_{60}, the symmetry of C_{60} molecule was damaged and activated possibly infrared spectroscopy (IR)-silent vibrational modes. Horoyski *et al.* [62] presented high-resolution first-order Raman spectra of isotopically controlled crystalline C_{60}. As ^{13}C substitutions were made in crystalline $^{12}C_{60}$, they found a range of responses that the vibrational modes showed a uniform softening of the lower energy along with a disorder-induced asymmetric line broadening, to the very pronounced splitting of Ag(2) peak. Recently, Dunk *et al.* [63] reported that fullerenes formed bottom-up by ingestion of atomic carbon and small carbon clusters (C_2) through a closed-network growth mechanism. They examined the growth of C_{60} and other higher fullerenes by direct exposure to carbon vapor produced from graphite or ^{13}C-enriched amorphous carbon. Their results showed that ingestion of a ^{13}C atom into the fullerene cage resulted in ^{12}C atom ejection and that atomic carbon simultaneously catalyzed bond rearrangements during

its interaction with the fullerene (Figure 3.1). They conclusively established that C_{60+2n} were formed bottom-up by carbon insertion into C_{60}. These experiments should be important for providing insight into astrophysical processes in the environments of carbon stars or supernovae and be valuable for further deciphering C_{60} formation in extraterrestrial environments.

In our group, ^{13}C-enriched fullerenes (C_{60}, C_{70}, etc.) were synthesized successfully in a large scale from ^{13}C-enriched raw carbon material by the arc discharge method and purified by high-performance liquid chromatography [29, 47]. The stable isotopes ^{13}C were directly incorporated into the skeleton of the fullerene cages without destroying their intrinsic structures. The addition of ^{13}C greatly improved the ^{13}C detection signal in IRMS. The apparent CNMR signal enhancements of fullerenes were observed. The ^{13}C-enriched fullerenes showed significant isotopic effects, such as the strongest peak position shift up and the Poisson distribution of isotopic peaks in the mass spectra and the migration or splitting of infrared and Raman characteristic peaks (Figure 3.2). Their vibration frequencies shift to shorter wavenumbers with increasing ^{13}C content. Our results demonstrated clearly the report about isotope effects of ^{13}C-enriched fullerenes in the literature. Furthermore, in accordance with these findings, we tried to disclose the processes of fullerene formation in arc discharge. Additionally, we prepared water-soluble derivatives of fullerenes and carboxylated and hydroxylated ^{13}C–C_{60} (^{13}C–C_{60}–COOH and ^{13}C–C_{60}–OH). On the basis of theoretical insights combined with the synthesis of IR and NMR structural characterization of ^{13}C-labeled fullerenols, we identified the functional groups and developed and verified a structural model for fullerenols. The functional groups of fullerenol exist as the corresponding conjugate bases or oxidized products, that is, hemiacetals, isolated OH, and epoxides [48]. Hou *et al.* [64] assessed the phototransformations of ^{13}C-enriched nC_{60} that occurred

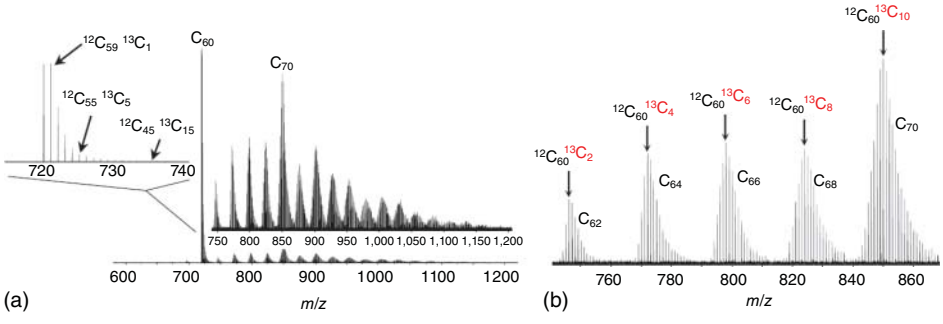

Figure 3.1 Results of exposure of C_{60} to ^{13}C-enriched carbon vapor. (a) Positive ions generated from vaporization of a target comprised of amorphous ^{13}C (99% atom ^{13}C) target mixed with C_{60} under the same conditions, with mass-scale expansion of C_{60} illustrating the occurrence of atom exchange events. (b) C_{62}–C_{70} mass region expanded to show growth of C_{60} to larger fullerenes by successive ^{13}C incorporation events. (Reprinted from the cited paper by permission from Nature Publishing Group [63].)

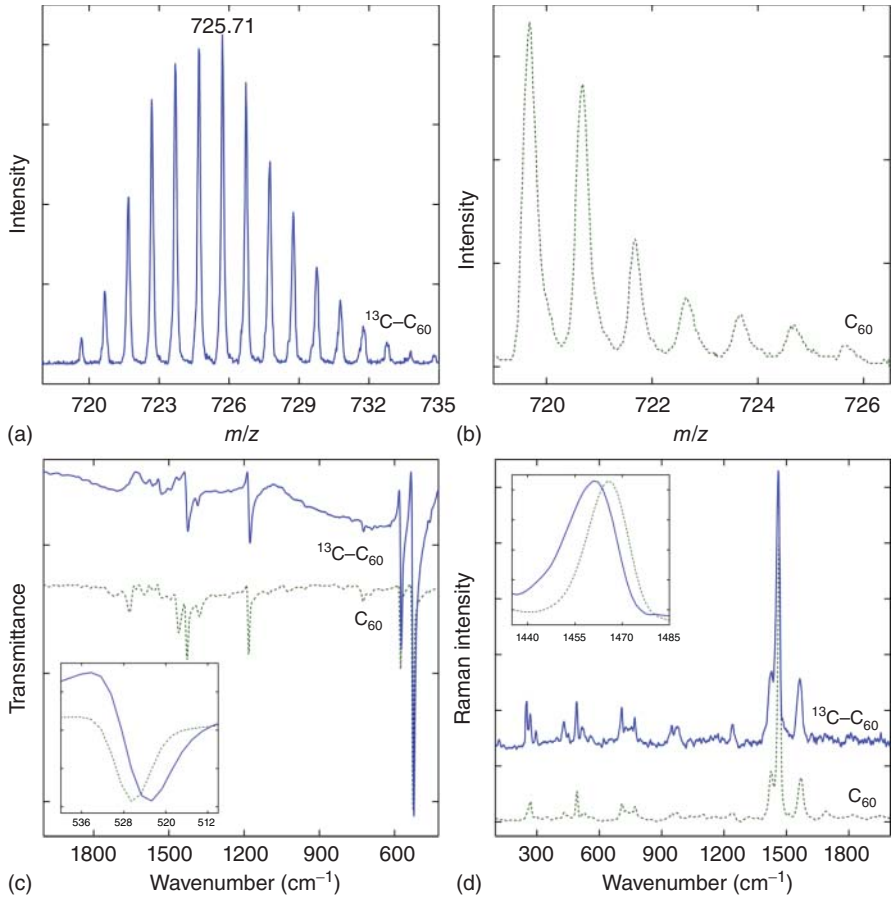

Figure 3.2 Characterization of ^{13}C-enriched C_{60}. (a) MS of ^{13}C-enriched C_{60}; (b) MS of unlabeled C_{60}; (c) IR spectra; and (d) Raman spectra [29].

in the natural sunlight by transmission electron microscopy, mass spectrometry, ^{13}C nuclear magnetic resonance spectroscopy, Fourier transform infrared spectroscopy, and X-ray photoelectron spectroscopy. After 947 h in sunlight, the photoreactivity of nC_{60} produced some water-soluble C_{60} derivatives, which had olefinic carbon atoms as well as a variety of oxygen-containing functional groups, including vinyl ether and carbonyl or carboxyl groups, whose presence destroys the native π-electron system of C_{60} (Figure 3.3).

3.3.2
Trace and Quantification *In Vivo* for Fullerene

Since fullerene C_{60} has a certain structure and the high steady state of ^{13}C skeleton labeling, fullerene nanomaterials could be reliably quantified by IRMS. We first

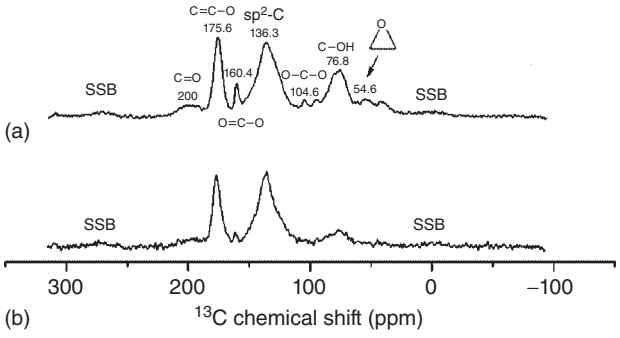

Figure 3.3 ^{13}C NMR spectra of ^{13}C-labeled C_{60} fullerenols; SSB indicates sideband. (a) ^{1}H–^{13}C CP spectra at contact times of 2 ms and (b) ^{13}C MAS NMR spectrum of C_{60} fullerenols [48].

introduced the stable isotope ^{13}C skeleton labeling of carbon cages in the study of fullerenes nanomaterials *in vivo* [29]. The blood clearance and biodistributions of pristine ^{13}C–C_{60} in mice were examined based on the changes in the ^{13}C/^{12}C ratio and were consistent with the previous report on radioactive labeling (Figure 3.4). All of these experimental results strongly indicate that the ^{13}C-labeling technique is a sensitive, reliable, and nondestructive method for tracing carbon nanomaterials *in vivo*. Unlike isotope labeling with iodine, copper, and other conventionally used elements, ^{13}C labeling does not introduce foreign atoms onto the carbon networks. The stable isotopic labeling is proved to be a powerful tool for absolutely quantifying fullerene nanomaterials, and the ^{13}C-labeled nanomaterial can also be potentially used as an internal standard substance. ^{13}C-enriched fullerene nanomaterials, as tracers, could be applied for investigating *in vivo* ADME studies. The present results will be very important for the toxicological effects of the long-term exposure, the consequence of the surface functionalization, and the potential *in vivo* metabolism of fullerene nanomaterials in future. Our results would also largely benefit the ongoing biological/environmental safety studies of carbon nanomaterials by revealing information on the uptake, accumulation level, translocation, and elimination of carbon nanomaterials.

Schreiner *et al.* [65] provided the first evidence of fullerenol biodegradation and utilization. They used ^{13}C-fullerenol to examine the ability of two white rot basidiomycete fungi to metabolize and degrade fullerenol by stable IRMS techniques. After 32 weeks of decay in both fungi, the stable isotope ^{13}C from fullerenol was converted to CO_2 or incorporated into fungal biomass. Recently, Chae *et al.* [66] used ^{13}C–nC$_{60}$ aggregates to incubate with microbial cultures from aged suspensions for 203 days, in which they did not produce significant labeled CO_2. They suggested that these C_{60} nanoparticles had the highly recalcitrant nature and were very difficult to be transformed or degraded into CO_2 through microbes. Isaacson *et al.* [67, 68] used $^{13}C_{60}$ as an internal standard to develop an analytical method of liquid chromatography/electrospray ionization mass

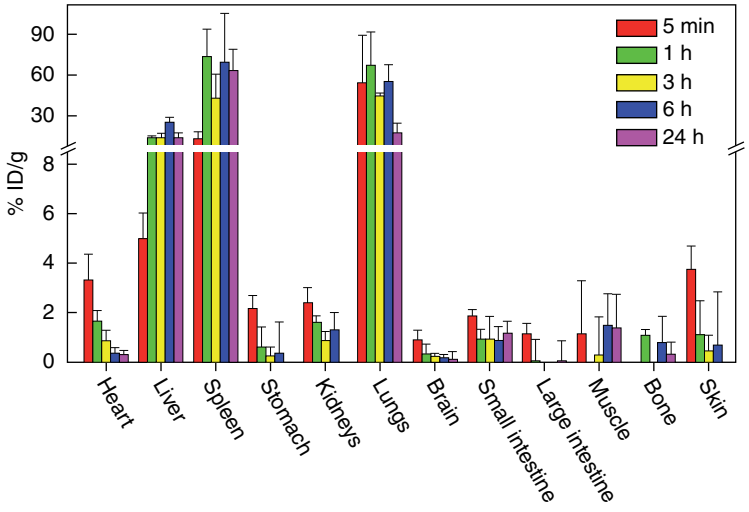

Figure 3.4 Biodistribution of ^{13}C–C_{60} in mice after intravenous(i.v.) administration ($n = 4$) [29].

spectrometry to determine quantitatively a suite of fullerenes from C_{60} to C_{98} in aqueous and biological matrixes. They applied this method to evaluate the toxicological behavior of C_{60} in zebrafish embryos and obtained 130 µg/l lethal concentrations that caused 50% mortality of zebrafish embryo [67].

3.3.3
Quantification and Distribution of ^{13}C-CNT and Carbon Particles

Some research groups used the isotopic ratio and isotopic effects to measure the distribution of ^{13}C-enriched CNTs. Yang *et al.* [28] utilized ^{13}C-enriched amorphous carbon as the precursor to synthesize skeleton ^{13}C-labeled SWCNTs by laser ablation. They took advantage of ^{13}C-SWCNTs to determine isotopic ratio $^{13}C/^{12}C$ through IRMS and traced and quantified the biodistributions of CNTs in mice. The pristine SWCNTs were found to be distributed in the entire body, mainly accumulated in the liver, spleen, and lungs of mice over an extended period of time via a single tail vein injection (Figure 3.5a) [28]. The PEGylated SWCNTs were distributed throughout most organs within 1 h, mainly accumulated in the liver, spleen, and skin of mice after intravenous injection of 7 days (Figure 3.5b). The PEGylated SWCNTs showed higher tumor uptake and a longer blood-circulation time in mice [27]. They exhibited well that the surface chemical modification of CNTs did alter significantly the biological behaviors by stable isotope ^{13}C labeling. Recently, they obtained ^{13}C-enriched carbon nanoparticles by disposing carbon soot in the arc discharge of graphite rods. The ^{13}C-enriched carbon nanoparticles as tracers were investigated for the *in vivo* biodistribution of mice. The distribution profile and time dependencies were largely similar to

those of the pristine CNTs, and the carbon nanoparticles were also captured by reticuloendothelial system (RES) with significant accumulation levels in the spleen, lungs, and liver (Figure 3.5c) [30]. The isotopic effects of carbon nanoparticles in Raman spectra showed a relatively intense D-band and shift compared with ^{12}C carbon nanoparticles [30]. SWCNTs with different ratios of isotopes ^{13}C had been obtained previously and displayed well-shifted Raman G-band peaks to lower wavenumbers with increasing of ^{13}C/^{12}C in SWCNTs [69, 70].

3.3.4
Isotope Effects and Imaging of ^{13}C-CNT

Liu *et al.* [71] synthesized ^{13}C-enriched SWCNTs by chemical vapor deposition (CVD) using ^{12}C- and ^{13}C-pure methane, respectively. They studied the isotope-dependent Raman colors of SWCNTs, which were used for multicolor Raman imaging of live cells (Figure 3.6). Additionally, they established two-color SWCNT Raman-based protein detection method by conjugating different antibodies to pure ^{12}C and ^{13}C SWCNT isotopes as multicolor Raman labels [72]. Plata *et al.* [73] thought that the distinct carbon isotopic signatures in SWCNT might be useful as environmental tracers identifying SWCNTs in natural and artificial samples and allowing assessment of SWCNT sources to the environment. Hanna *et al.* [74] used metal impurities in CNTs and carbon stable isotope ratios as tracers to evaluate CNT biodeposition by mussels, via feces and pseudo feces, as well as accumulation in mussel tissues.

3.3.5
Structure and Formation of ^{13}C-Enriched Graphene Nanomaterials

Cai *et al.* [75] first reported the detailed chemical structure of graphite oxide (GO) by the strong ^{13}C solid-state nuclear magnetic resonance (SSNMR) spectra of approximately 100% ^{13}C-labeled GO. The details of the chemical bonding network in GO included the sp^2 carbon, C–OH, and epoxide of chemical groups and their connections. They also synthesized isotopically modified graphene containing various percentages of ^{13}C by CVD, and investigated the thermal conductivity of the modified graphene [76]. Casabianca *et al.* [77] constructed structural models of noncrystalline graphite-based materials on the basis of 2D ^{13}C double-quantum/single-quantum correlation SSNMR spectrum of ^{13}C-labeled GO. Tian *et al.* [78] prepared bulk quantities of ^{13}C-enriched GO from relatively less expensive precursors (largely amorphous ^{13}C powders) by arc discharge. They presented isotopic effects of ^{13}C-enriched GO by their Raman shift spectra. Kalbac *et al.* [79] prepared bilayer graphene by the subsequent deposition of a ^{13}C single-layer graphene and a ^{12}C single-layer graphene on top of an SiO_2/Si substrate and investigated the single-layer components of bilayer graphene individually. The Raman frequencies of the ^{13}C graphene bands were significantly shifted with respect to those of ^{12}C graphene (Figure 3.7). The bottom layer of the bilayer graphene was significantly doped from the substrate, while the top layer did not exhibit a signature of the doping from

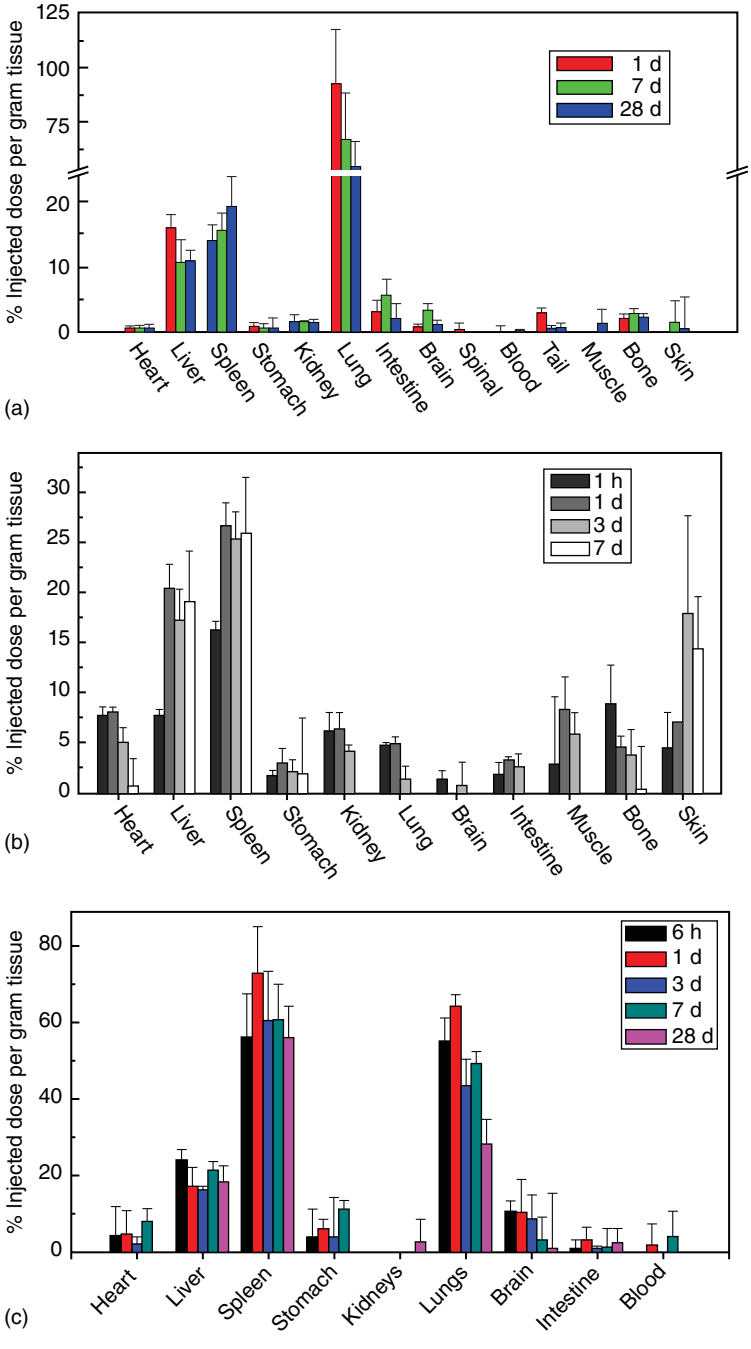

Figure 3.5 (a) The biodistributions of pristine SWNTs (^{13}C-SWNT). (Reprinted with permission from [28], Copyright (2007) American Chemical Society.); (b) the PEGylated SWNTs (^{13}C-SWNT). (Reprinted from the cited paper [27] with permission from Wiley.); (c) ^{13}C-enriched carbon nanoparticles in mice at different time points postexposure via intravenous(i.v.) injection. (Reprinted with permission from [30], Copyright (2014) American Chemical Society.)

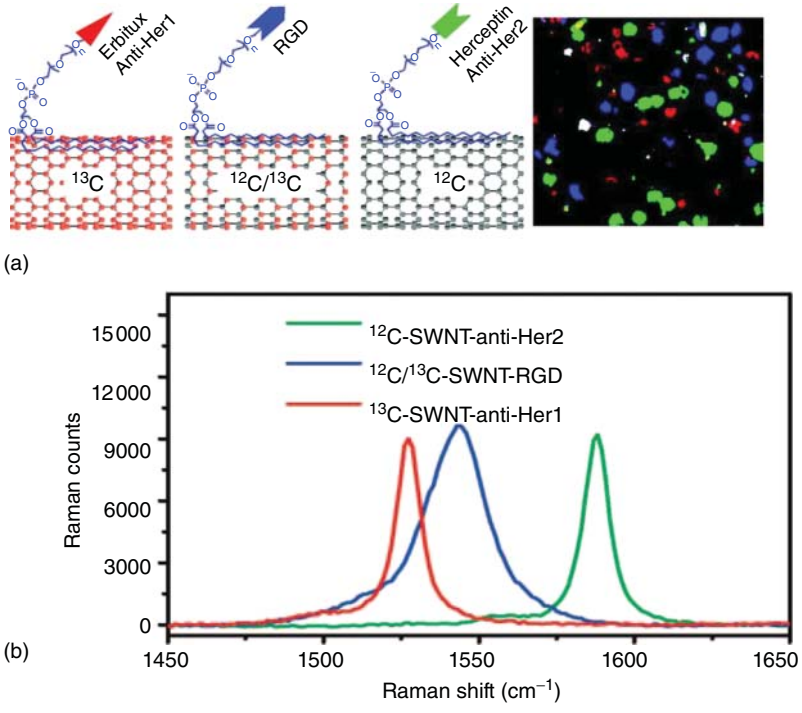

Figure 3.6 SWCNTs with different Raman colors and imaging. (a) Schematic SWNTs with three different isotope compositions (^{13}C-SWNT, ^{12}C/^{13}C-SWNT, ^{12}C-SWNT) conjugated with different targeting ligands and multicolor Raman imaging of live cells. (b) Solution-phase Raman spectra of the three SWNT conjugates under 785 nm laser excitation. (Reprinted with permission from [71], Copyright (2008) American Chemical Society.)

the environment. They also observed an unusual enhancement of the Raman signal of the G mode in the ^{13}C isotopically engineered bilayer graphene on a hexagonal single-crystalline boron nitride substrate and demonstrated the origin of the enhancement effect [80]. Furthermore, they developed an approach to address individual graphene sheets in three-layer graphene (including ^{12}C top, ^{12}C/^{13}C middle, and ^{13}C bottom) by Raman spectroscopy. The doping level was dependent on layer position with respect to the substrate [81]. Based on isotope labeling, Raman spectroscopy was developed to identify rapidly the stacking orientation in chemical-vapor-grown bilayer graphene, which was benefited with the precise control of the stacking orientation, and determined both electronic and vibrational properties of the bilayer graphene system [82]. Recently, they also studied isotope-labeled bilayer graphene during heating cycles from room temperature up to 1173 K by Raman spectroscopy [83]. The isotope labeling was able to follow the heating effect simultaneously and independently in the top and bottom layers.

The aforementioned researchers applied ^{13}C labeling to enhance the detection signal of NMR or Raman spectra for exploring the physical and chemical structure

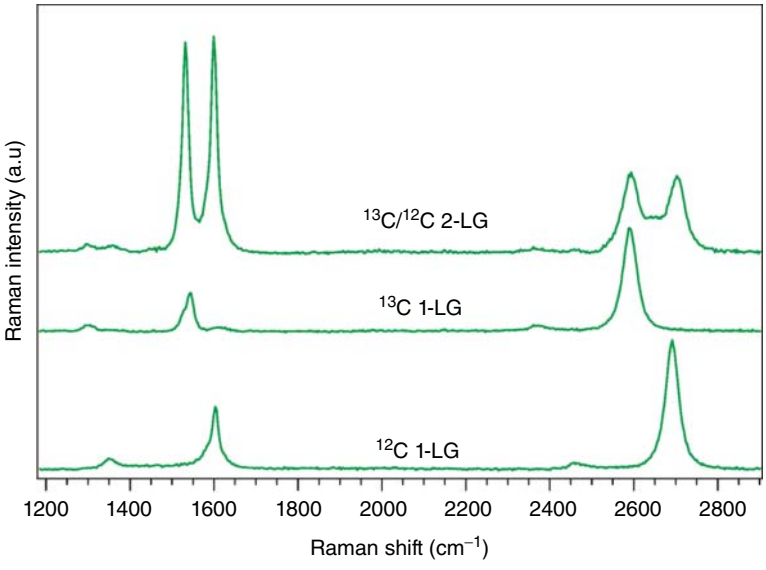

Figure 3.7 Raman spectra of the ^{12}C 1-layer graphene (LG), ^{13}C 1-LG, and ^{13}C/12C 2-LG (^{13}C is on top, ^{12}C at bottom) samples. (Reprinted with permission from [79], Copyright (2011) American Chemical Society.)

of graphene nanomaterials. Unfortunately, applications of ^{13}C-labeled graphene nanomaterials in biological effects and nanosafety have not been reported to this day.

3.4
Metal Stable Isotope Labeled Nanoparticles

3.4.1
Trace and Quantification of ZnO Nanoparticles in Nanotoxicology and Ecotoxicology

UV absorbers TiO_2 and ZnO were often incorporated into commercial sunscreens in amounts of up to 25% v/v, which was a good example for using nanotechnology. However, there was still some controversy surrounding the skin absorption of ZnO. Gulson *et al.* [84–86] first used the stable isotope method to evaluate dermal absorption of ZnO nanoparticles. Nanoparticles (20–30 nm) of an enriched isotope (^{68}Zn 51% enrichment) have been incorporated into a sunscreen formulation for experiments. Using highly sensitive stable ^{68}Zn isotopes as tracers, they found that small amounts of Zn from ZnO particles in sunscreens can pass through the protective layers of the skin and be detected in the blood and urine. However, it was not known whether ^{68}Zn was absorbed as ZnO NPs or soluble Zn or both. Larner *et al.* [87, 88] traced

the bioavailability of ZnO NPs in the aquatic organism of coastal ecosystems using ^{68}Zn labeling by multiple-collector inductively coupled plasma–mass spectrometry (MC-ICP-MS) [87]. They evaluated parallel waterborne exposures of the common mudshrimp *Corophium volutator* to ^{68}ZnO NPs, bulk ^{68}ZnO, and soluble $^{68}ZnCl_2$ in the presence of sediment and found that ionic Zn from ZnO NPs was bioavailable to *C. volutator* (Figure 3.8). Similarly, the limitation of the isotope labeling could not clarify whether the uptake of Zn by organisms occurs as particulate (bulk/nano) ZnO and/or dissolved Zn. Nevertheless, the study provided insights into the bioavailability, fate, and uptake mechanisms of ^{68}ZnO NPs, compared to bulk material and dissolved Zn. Further, they demonstrated that, compared with other four naturally occurring zinc stable isotopes (^{64}Zn, ^{66}Zn, ^{67}Zn, and ^{70}Zn) (Table 3.2.), relatively inexpensive ^{68}Zn for labeling combined with high-precision mass spectrometry might also be able to differentiate between the uptake by organisms of particulate ZnO and Zn^{2+} ions from the dissolution of nanoparticles. ZnO nanoparticles can be reliably detected in natural samples with a Zn background of 100 µg/g at concentrations as low as about 5 ng/g. Recently, Larner *et al.* [89] compared the data in two different laboratories. There is good agreement between the blood δ^{68}Zn values determined independently in the two laboratories for female subjects exposed to nanoparticles and bulk ^{68}ZnO. This demonstrates that stable isotope labeling in conjunction with MC-ICP-MS isotope analysis is a highly sensitive and robust method for the tracing of Zn-rich materials in biological matrices.

Dybowska *et al.* [90] synthesized isotopically enriched (89.6%) with a rare isotope of Zn(^{67}Zn)ZnO NPs and measured the uptake of ^{67}Zn by *Lymnaea stagnalis* exposed to diatoms amended with the particles. They revealed that ^{67}ZnO NPs were bioavailable and toxic for freshwater snails after dietary exposures [91]. They employed ^{67}Zn to trace the fate of ZnO NPs in sediments and effects on two endobenthic species, the clam *Scrobicularia plana* and the ragworm *Hediste diversicolor* [92, 93]. These studies demonstrate that stable isotope technique is sufficiently sensitive to determine the uptake of Zn under a range of environmentally realistic exposure conditions (<15 µg/g), which were much lower than isotopically unmodified ZnO NP detection concentrations (>5000 µg/g). Khan *et al.* [94] took advantage of stable isotope ^{68}Zn to determine uptake and efflux dynamics of ZnO nano- and bulk particles and dissolved Zn in an estuarine snail *Peringia ulvae* by high-precision MC-ICP-MS. The results suggested that the bioavailability and bioaccumulation of Zn from ZnO NPs were primarily dependent upon solubility. The metal stable isotopes Ti (^{46}Ti, ^{47}Ti,^{48}Ti, and/or ^{48}TiH) and Zn (^{64}Zn and/or ^{66}Zn) were analyzed by time-of-flight secondary ion mass spectrometry (TOF-SIMS) combined with X-ray spectroscopy or ICP-MS. Monteiro-Riviere *et al.* [95] carried out safety evaluation of sunscreen formulations containing TiO_2 and ZnO NPs in ultraviolet B-sunburned skin. These nanoparticles were found to penetrate into the dermis layer by TOF-SIMS; no definitive evidence showed them in the perfusate. Recently, Osmond-Mcleod *et al.* [96] also assessed comparatively dermal absorption and short-term biological impact of a traceable form of ^{68}Zn from ^{68}ZnO

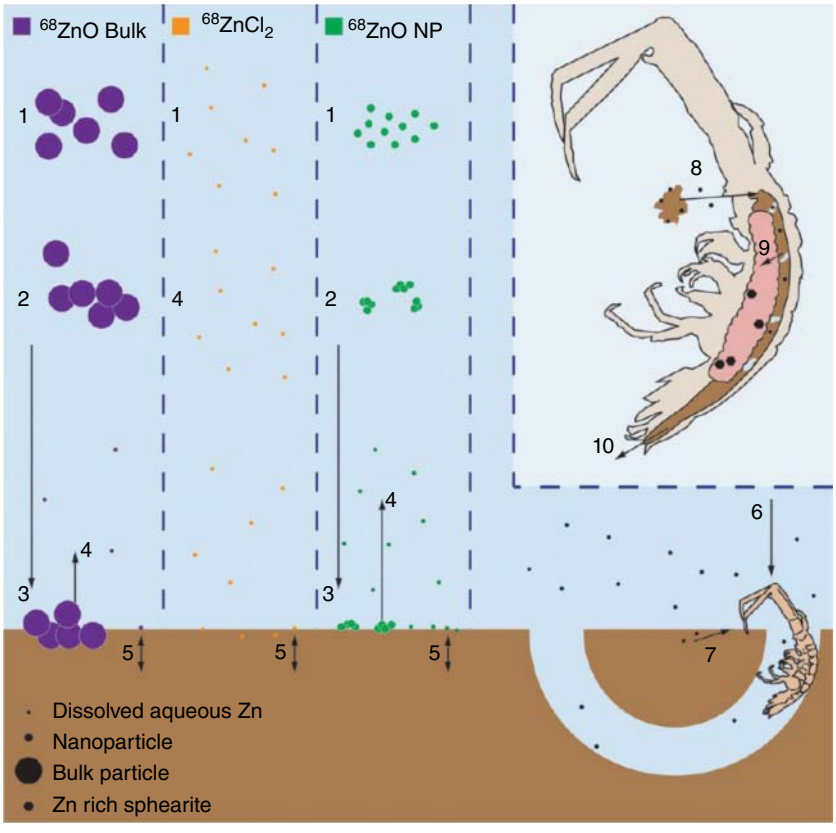

Figure 3.8 Conceptual model. The exposure material is dispersed in artificial seawater (1), which results in the aggregation of the primary bulk and nano ZnO particles (2) and subsequent sedimentation (3). Dissolved aqueous ^{68}Zn is formed by dissolution of oxide precipitates or immediately after dispersion for $^{68}ZnCl_2$ (4) and subsequently sorbed onto sediment particles (5). *Corophium volutator* feed on organic matter on the sediment surface or suspended particles by drawing this food into their U-shaped burrows. Uptake of the ^{68}Zn label from all forms of exposure material occurs via the dissolved state, directly from both the aqueous phase (6) and/or the intake of sediment with adsorbed Zn (7). The inset indicates food intake by *C. volutator* (8) and as the sediment and water pass through the alimentary canal, detoxification of Zn occurs through the formation of Zn-rich sphalerites in the hepatopancreas (9). The *C. volutator* are in a stage of metal accumulation for the duration of the exposure; therefore, defecation (10) does not include ^{68}Zn-rich sphalerites. (Reprinted with permission from [87], Copyright (2012) American Chemical Society.)

nanosized and larger particles of sunscreens in hairless mice. The results showed that the presence of ZnO NPs in sunscreen did not elicit an adverse biological response in the mice following short-term topical applications. Lee *et al.* [97] developed a TOF-SIMS and confocal laser scanning microscopy (CLSM) imaging method for rapid and sensitive cytotoxicity study of ZnO NPs in HaCaT

Table 3.2 Natural Zn isotope abundances and isotopic enrichment and approximate cost of commercially available enriched Zn isotopes [88].

	^{64}Zn	^{66}Zn	^{67}Zn	^{68}Zn	^{70}Zn
Natural isotope abundance (%)[a]	48.26 (21)	27.98 (5)	4.10 (1)	19.02 (8)	0.63(1)
Isotopic enrichment of tracers (%)[b]	99.5	99.0	92.0	99.5	95.0
Price of tracer (in $/mg)[b]	4.50	5.00	35.00	4.00	250.00
Cost of tracer to produce 100 mg of isotopically labeled nanoparticles assuming 10% yield during preparation (in $)	4 500	5 000	35 000	4 000	250 000

[a] The numbers in ( ) denote the 2 SD uncertainty on the least significant digits.
[b] The isotopic enrichment and cost of the single isotopes are approximate average values derived from quotes obtained from Isoflex USA (San Francisco, CA) and Oak Ridge National Laboratory (USA) in October 2009.

cells. The method was confirmed and validated by using stable-isotope-labeled ^{68}ZnO NPs as tracers under the same experimental conditions and yielding similar cytotoxicity effects. Undoubtedly, the stable-isotope-labeled ZnO NPs as tracers are sufficiently sensitive and efficient in evaluating their biological effects and nanosafety in realistic exposure environment and organisms.

3.4.2 Trace and Quantification of CuO Nanoparticles in Nanotoxicology and Ecotoxicology

Croteau's groups of US geological survey used isotopically enriched (99% ^{65}Cu) copper oxide nanoparticles to perform their ecotoxicological studies. The stable isotope labeling enhanced greatly the detection of Cu bioaccumulation in aquatic organisms at exposure concentrations equivalent to background Cu concentrations in freshwater systems (0.2–30 μg/l). ^{65}CuO tracers, independently from background levels, were analyzed by ICP-MS and achieved the high-sensitivity detection (about 10 000-folds) for the uptake of Cu at lower concentration, when compared with the unused stable isotope tracers of the Cu concentrations in the most contaminated water systems (>1 mg/l) [98]. They further characterized the bioaccumulation and toxicity in a freshwater snail after waterborne and dietborne exposures. The dietborne exposures to Cu, in particular CuO NPs, were more likely to cause adverse effects than waterborne exposures [99]. They also tracked metal Cu bioavailability from natural particles and demonstrated that inorganic particulate Cu was bioavailable [113]. The stable isotopic tracing has shown great potential in the environmental contamination and nutrition of nanoparticles for addressing questions involving uptake of an element that naturally has multiple isotopes.

3.4.3 Other Stable Isotopes for Tracing and Quantifying Nanomaterials *In Vivo*

Except for the stable isotopes of carbon, zinc, and copper, other stable isotopes including ^{25}Mg, ^{109}Ag, ^{57}Fe, and ^{18}O as one or more compositions of nanomaterials were also employed to examine their biological effect and properties in the areas of nanotechnology. Amirshahi's groups utilized $^{25}Mg^{2+}$-magnetic isotope effect to explore the pharmacokinetics and pharmacodynamics of ^{25}Mg-PMC_{16} (porphyrin adducts of cyclohexyl fullerene-C_{60}) for the treatment of hypoxic cardiopathies and diabetic neuropathy [100–103]. In order to better evaluate the environmental or biological fate and transformations of Ag NPs, Gigault and Hackley [104] reported a method based on asymmetric-flow field flow fractionation coupled to optical detection and mass spectrometry with the use of stable isotope ^{109}Ag. Croteau *et al.* [105] also assessed the bioavailability and toxicity of isotopically modified ^{109}Ag NPs to a freshwater snail under the typical natural conditions. The concentration-dependent changes in agglomeration and dissolution affected the bioavailability of nanoparticles. Additionally, Zhang *et al.* [107] studied the interactions between human blood plasma proteins and nanoparticles using ^{18}O-labeling and LC-MS-based quantitative proteomics. Quantitative comparison of relative protein abundances was achieved by spiking an ^{18}O-labeled into each individually processed unlabeled sample as an internal standard, enabling simultaneous application of both label-free and isotopic labeling quantification across the entire sample set.

3.4.4 Other Stable Isotopes for the Structure and Reaction of Nanomaterials

Generally, stable isotopes were also used to study the structure, physicochemical properties, and the dynamics of reaction with relative nanomaterials. Handler *et al.* [106] measured the extent and rate of Fe isotope exchange between aqueous Fe(II) and goethite nanorods using a ^{57}Fe isotope tracer approach combined with ICP-MS and understood deeply the complex process of sorption, electron transfer, and reductive dissolution and transformation to secondary minerals in the reaction of aqueous Fe(II) with Fe(III) oxides. Cano *et al.* [108] identified the expected P═O stretching absorption in catalytic studies by ^{18}O-labeled nanoparticles. Rusevova *et al.* [109] examined the applicability of two iron-containing perovskites, $LaFeO_3$ and $BiFeO_3$, as nanocatalysts for heterogeneous Fenton-like reactions using isotopes (^{2}H or ^{13}C) fractionation experiments. Bogdan *et al.* [110] enhanced or deactivated the luminescence of lanthanide-doped upconverting nanoparticles by pH and H/D isotope vibronic control. The structure and photoluminescence of some nanomaterials were investigated using stable isotopes of ^{15}N [111, 112].

3.5 Summary and Outlook

In this chapter, we have shown how to employ stable isotopes to trace and quantify the changes of structure, reaction, and biological and toxicological properties of nanomaterials in complex environmental systems. These were implemented through utilizing the advantages of stable isotope labeling to combine with some highly accurate mass spectrometry. We summarize some advantages and challenges of stable isotope labeling for nanotechnology as follows. (i) Stable isotope labeling has the advantages of high sensitivity, good accuracy, nondestructive and convenient operation, and does not alter intrinsic structure and properties of the marker nanomaterials. (ii) Stable isotope labeling can avoid the disadvantages of radioactive labeling, such as the strict conditions of radioactivity operation, the generation of radioactive wastes, and the limitation of the shorter half-life of some radioactive elements, which is applicable especially for the realistic environmental low concentrations and long-term exposure of nanoparticles. (iii) Stable-isotope-labeled nanomaterials, as tracers or internal standards, can quantify and monitor nanoparticles *in vivo* or *in vitro* for nanotoxicological and ecotoxicological studies. (iv) For metal-containing nanoparticles, multiple metal stable isotopes can be adopted simultaneously. (v) Stable isotope labeling can potentially draw confirmative conclusions for the metabolism, transmission, transformation, and the origin of nanomaterials in complex media or ecological food chain. (vi) Stable isotope tracing can prove valuable for the formation and reactions of nanomaterials especially in "black box" conditions. However, some challenges lie in the following: (i) low natural abundance and high costs of stable isotopes; (ii) high cost of testing for isotopic samples; (iii) availability of suitable isotopically enriched precursor for the synthesis of the material; (iv) difficulty in clarifying whether the uptake of element by organisms occurs as particulate (bulk/nano)/or dissolved atom/ion, or both, such as Zn; (v) identification of nanomaterials generally needs to be combined with high-precision mass spectroscopy or synchrotron radiation analysis technique; and (vi) quantitative detection of the tracer in the animal tissues following short-time exposures at the very low exposure concentrations, such as feces or urine. Most importantly, with the rapid development of detection technology and analysis instrument, we need to develop novel and systematic methods for the evaluations of biological effects and nanosafety of nanomaterials in life environment system.

References

1. Zhao, Y.L., Xing, G.M., and Chai, Z.F. (2008) Nanotoxicology: are carbon nanotubes safe? *Nat. Nanotechnol.*, **3** (4), 191–192.
2. Nel, A.E., Madler, L., Velegol, D. *et al.* (2009) Understanding biophysicochemical interactions at the nano-bio interface. *Nat. Mater.*, **8** (7), 543–557.
3. Hagens, W.I., Oomen, A.G., De Jong, W.H. *et al.* (2007) What do we (need to) know about the kinetic properties

of nanoparticles in the body? *Regul. Toxicol. Pharm.*, **49** (3), 217–229.
4. Klaine, S.J., Alvarez, P.J.J., Batley, G.E. *et al*. (2008) Nanomaterials in the environment: behavior, fate, bioavailability, and effects. *Environ. Toxicol. Chem.*, **27** (9), 1825–1851.
5. Wu, H.C., Chang, X.L., Liu, L. *et al*. (2010) Chemistry of carbon nanotubes in biomedical applications. *J. Mater. Chem.*, **20** (6), 1036–1052.
6. Zhao, F., Zhao, Y., Liu, Y. *et al*. (2011) Cellular uptake, intracellular trafficking and cytotoxicity of nanomaterials. *Small*, **7** (10), 1322–1337.
7. Vedam, H. (2011) Nanosafety policy overview. 2011 International Conference on Nanoscience, Technology and Societal Implications (NSTSI), December 8–10, 2011, pp. 1–6.
8. Yan, L., Zhao, F., Li, S.F. *et al*. (2011) Low-toxic and safe nanomaterials by surface-chemical design, carbon nanotubes, fullerenes, metallofullerenes, and graphenes. *Nanoscale*, **3** (2), 362–382.
9. Wang, H., Yang, S.-T., Cao, A. *et al*. (2012) Quantification of carbon nanomaterials *in vivo*. *Acc. Chem. Res.*, **46** (3), 750–760.
10. He, X., Ma, Y.H., Li, M. *et al*. (2013) Quantifying and imaging engineered Nanomaterials *in vivo*: challenges and techniques. *Small*, **9** (9–10), 1482–1491.
11. Chen, C.Y., Li, Y.F., Qu, Y. *et al*. (2013) Advanced nuclear analytical and related techniques for the growing challenges in nanotoxicology. *Chem. Soc. Rev.*, **42**, 8266–8303.
12. Zhu, M.T., Nie, G., Meng, H. *et al*. (2013) Physicochemical properties determine nanomaterial cellular uptake, transport, and fate. *Acc. Chem. Res.*, **46** (3), 622–631.
13. Wang, B., He, X., Zhang, Z.Y. *et al*. (2013) Metabolism of nanomaterials *in vivo*: blood circulation and organ clearance. *Acc. Chem. Res.*, **46** (3), 761–769.
14. Ma, X.W., Zhao, Y.L., and Liang, X.J. (2011) Theranostic nanoparticles engineered for clinic and pharmaceutics. *Acc. Chem. Res.*, **44** (10), 1114–1122.
15. Liu, Y., Zhao, Y.L., Sun, B.Y. *et al*. (2013) Understanding the toxicity of carbon nanotubes. *Acc. Chem. Res.*, **46** (3), 702–713.
16. Chang, X.-L., Yang, S.-T., and Xing, G. (2014) Molecular toxicity of nanomaterials. *J. Biomed. Nanotechnol.*, **10** (10), 2828–2851.
17. Berezin, A.A. (2009) Stable isotopes in nanotechnology. *Nanotechnol. Percept.*, **5** (1), 27–36.
18. Gulson, B. and Wong, H. (2006) Stable isotopic tracing – A way forward for nanotechnology. *Environ. Health Perspect.*, **114** (10), 1486–1488.
19. Jardine, T.D., Kidd, K.A., and Fisk, A.T. (2006) Applications, considerations, and sources of uncertainty when using stable isotope analysis in ecotoxicology. *Environ. Sci. Technol.*, **40** (24), 7501–7511.
20. Madigan, D.J., Carlisle, A.B., Dewar, H. *et al*. (2012) Stable isotope analysis challenges wasp-waist food web assumptions in an upwelling pelagic ecosystem. *Sci. Rep.*, **2**, 654 (10 pp).
21. Norris, C.E., Quideau, S.A., Landhausser, S.M. *et al*. (2012) Tracking stable isotope enrichment in tree seedlings with solid-state NMR spectroscopy. *Sci. Rep.*, **2**, 719 (5 pp).
22. Muccio, Z. and Jackson, G.P. (2009) Isotope ratio mass spectrometry. *Analyst*, **134** (2), 213–222.
23. Benson, S., Lennard, C., Maynard, P. *et al*. (2006) Forensic applications of isotope ratio mass spectrometry – A review. *Forensic Sci. Int.*, **157** (1), 1–22.
24. Mutlib, A., Espina, R., Atherton, J. *et al*. (2012) Alternate strategies to obtain mass balance without the use of radiolabeled compounds: application of quantitative fluorine (19F) nuclear magnetic resonance (NMR) spectroscopy in metabolism studies. *Chem. Res. Toxicol.*, **25** (3), 572–583.
25. Gregoricka, L.A. (2013) Geographic origins and dietary transitions during the bronze age in the Oman Peninsula. *Am. J. Phys. Anthropol.*, **152** (3), 353–369.
26. Mutlib, A.E. (2008) Application of stable isotope-labeled compounds

in metabolism and in metabolism-mediated toxicity studies. *Chem. Res. Toxicol.*, **21** (9), 1672–1689.

27. Yang, S.T., Fernando, K.A.S., Liu, J.H. *et al*. (2008) Covalently PEGylated carbon nanotubes with stealth character *in vivo*. *Small*, **4** (7), 940–944.
28. Yang, S.T., Guo, W., Lin, Y. *et al*. (2007) Biodistribution of pristine single-walled carbon nanotubes *in vivo*. *J. Phys. Chem. C*, **111** (48), 17761–17764.
29. Chang, X.-L., Ruan, L., Yang, S.-T. *et al*. (2014) Quantification of carbon nanomaterials *in vivo*: direct stable isotope labeling on the skeleton of fullerene C60. *Environ. Sci. Nano*, **1** (1), 64–70.
30. Liu, J.H., Yang, S.T., Wang, X. *et al*. (2014) Carbon nanoparticles trapped *in vivo*-similar to carbon nanotubes in time-dependent biodistribution. *ACS Appl. Mater. Interfaces*, **6** (16), 14672–14678.
31. Allen, D.K., Goldford, J., Gierse, J.K. *et al*. (2014) Quantification of peptide m/z distributions from ^{13}C-labeled cultures with high-resolution mass spectrometry. *Anal. Chem.*, **86** (3), 1894–1901.
32. Li, M., Huang, W.E., Gibson, C.M. *et al*. (2012) Stable isotope probing and Raman spectroscopy for monitoring carbon flow in a food chain and revealing metabolic pathway. *Anal. Chem.*, **85** (3), 1642–1649.
33. Carnielli, V.P., Zimmermann, L.J.I., Hamvas, A. *et al*. (2009) Pulmonary surfactant kinetics of the newborn infant: novel insights from studies with stable isotopes. *J. Perinatol.*, **29** (S2), S29–S37.
34. Tieszen, L.L. (1978) Carbon isotope fractionation in biological material. *Nature*, **276**, 97–98.
35. Lyon, T.D. and Baxter, M.S. (1978) Stable carbon isotopes in human tissues. *Nature*, **273** (5665), 750–751.
36. Mann, M. and Jensen, O.N. (2003) Proteomic analysis of post-translational modifications. *Nat. Biotechnol.*, **21** (3), 255–261.
37. Zhang, H., Li, X.-J., Martin, D.B. *et al*. (2003) Identification and quantification of N-linked glycoproteins using hydrazide chemistry, stable isotope labeling and mass spectrometry. *Nat. Biotechnol.*, **21** (6), 660–666.
38. Peteranderl, R. and Lechene, C. (2004) Measure of carbon and nitrogen stable isotope ratios in cultured cells. *J. Am. Soc. Mass. Spectrom.*, **15** (4), 478–485.
39. Harsha, H.C., Molina, H., and Pandey, A. (2008) Quantitative proteomics using stable isotope labeling with amino acids in cell culture. *Nat. Protoc.*, **3** (3), 505–516.
40. Larance, M., Bailly, A.P., Pourkarimi, E. *et al*. (2011) Stable-isotope labeling with amino acids in nematodes. *Nat. Methods*, **8** (10), 849–851.
41. Chen, C.Y., Chi, L.M., Chi, H.C. *et al*. (2012) Stable isotope labeling with amino acids in cell culture (SILAC)-based quantitative proteomics study of a thyroid hormone-regulated secretome in human hepatoma cells. *Mol. Cell. Proteomics*, **11** (4), M111.011270–19.
42. Aggarwal, P.K., Fuller, M.E., Gurgas, M.M. *et al*. (1997) Use of stable oxygen and carbon isotope analyses for monitoring the pathways and rates of intrinsic and enhanced in situ biodegradation. *Environ. Sci. Technol.*, **31** (2), 590–596.
43. Mutlib, A., Jiang, P., Atherton, J. *et al*. (2006) Identification of potential genomic biomarkers of hepatotoxicity caused by reactive metabolites of N-methylformamide: application of stable isotope labeled compounds in toxicogenomic studies. *Chem. Res. Toxicol.*, **19** (10), 1270–1283.
44. Hegeman, A.D., Schulte, C.F., Cui, Q. *et al*. (2007) Stable isotope assisted assignment of elemental compositions for metabolomics. *Anal. Chem.*, **79** (18), 6912–6921.
45. Jehmlich, N., Schmidt, F., Von Bergen, M. *et al*. (2008) Protein-based stable isotope probing (Protein-SIP) reveals active species within anoxic mixed cultures. *ISME J.*, **2** (11), 1122–1133.
46. Cai, X., Ramalingam, R., Wong, H.S. *et al*. (2013) Characterization of carbon nanotube protein corona by using quantitative proteomics. *Nanomed. Nanotechnol. Biol. Med.*, **9** (5), 583–593.

47. Ruan, L.F., Chang, X.L., Sun, B.Y. *et al*. (2014) Preparation and spectra of ^{13}C-enriched fullerene. *Chin. Sci. Bull.*, **59** (10), 905–912.
48. Wang, Z., Chang, X., Lu, Z. *et al*. (2014) A precision structural model for fullerenols. *Chem. Sci.*, **5** (8), 2940–2948.
49. Meijer, G. and Bethune, D.S. (1990) Laser deposition of carbon clusters on surfaces: a new approach to the study of fullerenes. *J. Chem. Phys.*, **93** (11), 7800–7802.
50. Johnson, R.D., Bethune, D.S., and Yannoni, C.S. (1992) Fullerene structure and dynamics: a magnetic resonance potpourri. *Acc. Chem. Res.*, **25** (3), 169–175.
51. Johnson, R.D., Meijer, G., Salem, J.R. *et al*. (1991) 2D nuclear magnetic resonance study of the structure of the fullerene C_{70}. *J. Am. Chem. Soc.*, **113** (9), 3619–3621.
52. Yannoni, C.S., Bernier, P.P., Bethune, D.S. *et al*. (1991) NMR determination of the bond lengths in C_{60}. *J. Am. Chem. Soc.*, **113** (8), 3190–3192.
53. Krätschmer, W., Fostiropoulos, K., and Huffman, D.R. (1990) The infrared and ultraviolet absorption spectra of laboratory-produced carbon dust: evidence for the presence of the C_{60} molecule. *Chem. Phys. Lett.*, **170** (2–3), 167–170.
54. Ebbesen, T.W., Tabuchi, J., and Tanigaki, K. (1992) The mechanistics of fullerene formation. *Chem. Phys. Lett.*, **191** (3–4), 336–338.
55. Ebbesen, T.W., Tsai, J.S., Tanigaki, K. *et al*. (1992) Isotope effect on superconductivity in Rb_3C_{60}. *Nature*, **355** (6361), 620–622.
56. Ramirez, A.P., Kortan, A.R., Rosseinsky, M.J. *et al*. (1992) Isotope effect in superconducting Rb_3C_{60}. *Phys. Rev. Lett.*, **68** (7), 1058–1060.
57. Chakravarty, S., Kivelson, S.A., Salkola, M.I. *et al*. (1992) Isotope effect in superconducting fullerenes. *Science*, **256** (5061), 1306–1308.
58. Hawkins, J.M. (1992) Osmylation of C_{60}: proof and characterization of the soccer-ball framework. *Acc. Chem. Res.*, **25** (3), 150–156.
59. Hawkins, J.M., Meyer, A., Loren, S. *et al*. (1991) Statistical incorporation of $^{13}C_2$ units into C_{60}. *J. Am. Chem. Soc.*, **113** (24), 9394–9395.
60. Chen, C.C. and Lieber, C.M. (1992) Synthesis of pure $^{13}C_{60}$ and determination of the isotope effect for fullerene superconductors. *J. Am. Chem. Soc.*, **114** (8), 3141–3142.
61. Martin, M.C., Fabian, J., Godard, J. *et al*. (1995) Vibrational study of ^{13}C-enriched C_{60} crystals. *Phys. Rev. B*, **51** (5), 2844–2847.
62. Horoyski, P.J., Thewalt, M.L.W., and Anthony, T.R. (1996) Raman-scattering study of isotopically engineered crystalline C_{60}. *Phys. Rev. B*, **54** (2), 920–929.
63. Dunk, P.W., Kaiser, N.K., Hendrickson, C.L. *et al*. (2012) Closed network growth of fullerenes. *Nat. Commun.*, **3**, 855.
64. Hou, W.-C., Kong, L., Wepasnick, K.A. *et al*. (2010) Photochemistry of aqueous C_{60} clusters: wavelength dependency and product characterization. *Environ. Sci. Technol.*, **44** (21), 8121–8127.
65. Schreiner, K.M., Filley, T.R., Blanchette, R.A. *et al*. (2009) White-rot basidiomycete-mediated decomposition of C_{60} fullerol. *Environ. Sci. Technol.*, **43** (9), 3162–3168.
66. Chae, S.-R., Hunt, D.E., Ikuma, K. *et al*. (2014) Aging of fullerene C_{60} nanoparticle suspensions in the presence of microbes. *Water Res.*, **65**, 282–289.
67. Isaacson, C.W., Usenko, C.Y., Tanguay, R.L. *et al*. (2007) Quantification of fullerenes by LC/ESI-MS and its application to *in vivo* toxicity assays. *Anal. Chem.*, **79** (23), 9091–9097.
68. Isaacson, C.W., Kleber, M., and Field, J.A. (2009) Quantitative analysis of fullerene nanomaterials in environmental systems: a critical review. *Environ. Sci. Technol.*, **43** (17), 6463–6474.
69. Liu, L. and Fan, S. (2001) Isotope labeling of carbon nanotubes and formation of ^{12}C-^{13}C nanotube junctions. *J. Am. Chem. Soc.*, **123** (46), 11502–11503.
70. Rümmeli, M.H., Löffler, M., Kramberger, C. *et al*. (2007) Isotope-engineered single-wall carbon nanotubes: a key material for magnetic

studies. *J. Phys. Chem. C*, **111** (11), 4094–4098.

71. Liu, Z., Li, X., Tabakman, S.M. *et al.* (2008) Multiplexed multicolor Raman imaging of live cells with isotopically modified single walled carbon nanotubes. *J. Am. Chem. Soc.*, **130** (41), 13540–13541.
72. Chen, Z., Tabakman, S.M., Goodwin, A.P. *et al.* (2008) Protein microarrays with carbon nanotubes as multicolor Raman labels. *Nat. Biotechnol.*, **26** (11), 1285–1292.
73. Plata, D.L., Gschwend, P.M., and Reddy, C.M. (2008) Industrially synthesized single-walled carbon nanotubes: compositional data for users, environmental risk assessments, and source apportionment. *Nanotechnology*, **19** (18), 185706 (14 pp).
74. Hanna, S.K., Miller, R.J., and Lenihan, H.S. (2014) Deposition of carbon nanotubes by a marine suspension feeder revealed by chemical and isotopic tracers. *J. Hazard. Mater.*, **279**, 32–37.
75. Cai, W.W., Piner, R.D., Stadermann, F.J. *et al.* (2008) Synthesis and solid-state NMR structural characterization of ^{13}C-labeled graphite oxide. *Science*, **321** (5897), 1815–1817.
76. Chen, S., Wu, Q., Mishra, C. *et al.* (2012) Thermal conductivity of isotopically modified graphene. *Nat. Mater.*, **11** (3), 203–207.
77. Casabianca, L.B., Shaibat, M.A., Cai, W.W. *et al.* (2010) NMR-based structural modeling of graphite oxide using multidimensional^{13}C solid-state NMR and ab initio chemical shift calculations. *J. Am. Chem. Soc.*, **132** (16), 5672–5676.
78. Tian, L.L., Wang, X., Cao, L. *et al.* (2010) Preparation of bulk C-13-enriched graphene materials. *J. Nanomater.*, **2010**, 742167 (5 pp).
79. Kalbac, M., Farhat, H., Kong, J. *et al.* (2011) Raman spectroscopy and in situ Raman spectroelectrochemistry of bilayer^{12}C/^{13}C graphene. *Nano Lett.*, **11** (5), 1957–1963.
80. Kalbac, M., Frank, O., Kong, J. *et al.* (2012) Large variations of the Raman signal in the spectra of twisted bilayer graphene on a BN substrate. *J. Phys. Chem. Lett.*, **3** (6), 796–799.
81. Kalbac, M., Kong, J., and Dresselhaus, M.S. (2012) Raman spectroscopy as a tool to address individual graphene layers in few-layer graphene. *J. Phys. Chem. C*, **116** (35), 19046–19050.
82. Fang, W., Hsu, A.L., Caudillo, R. *et al.* (2013) Rapid identification of stacking orientation in isotopically labeled chemical-vapor grown bilayer graphene by Raman spectroscopy. *Nano Lett.*, **13** (4), 1541–1548.
83. Ek-Weis, J., Costa, S., Frank, O. *et al.* (2014) Heating isotopically labeled bernal stacked graphene: a Raman spectroscopy study. *J. Phys. Chem. Lett.*, **5** (3), 549–554.
84. Gulson, B., Wong, H., Mccall, M. *et al.* (2008) Dermal absorption of ZnO nanoparticles in sunscreen using the stable isotope approach. *Toxicol. Lett.*, **180**, S222.
85. Gulson, B., Mccall, M., Korsch, M. *et al.* (2010) Small amounts of zinc from zinc oxide particles in sunscreens applied outdoors are absorbed through human skin. *Toxicol. Sci.*, **118** (1), 140–149.
86. Gulson, B., Wong, H., Korsch, M. *et al.* (2012) Comparison of dermal absorption of zinc from different sunscreen formulations and differing UV exposure based on stable isotope tracing. *Sci. Total Environ.*, **420**, 313–318.
87. Larner, F., Dogra, Y., Dybowska, A. *et al.* (2012) Tracing bioavailability of ZnO nanoparticles using stable isotope labeling. *Environ. Sci. Technol.*, **46** (21), 12137–12145.
88. Larner, F. and Rehkamper, M. (2012) Evaluation of stable isotope tracing for ZnO nanomaterials-New constraints from high precision isotope analyses and modeling. *Environ. Sci. Technol.*, **46** (7), 4149–4158.
89. Larner, F., Gulson, B., Mccall, M. *et al.* (2014) An inter-laboratory comparison of high precision stable isotope ratio measurements for nanoparticle tracing in biological samples. *J. Anal. At. Spectrom.*, **29** (3), 471–477.

90. Dybowska, A.D., Croteau, M.N., Misra, S.K. *et al*. (2011) Synthesis of isotopically modified ZnO nanoparticles and their potential as nanotoxicity tracers. *Environ. Pollut.*, **159** (1), 266–273.

91. Croteau, M.-N., Dybowska, A.D., Luoma, S.N. *et al*. (2011) A novel approach reveals that zinc oxide nanoparticles are bioavailable and toxic after dietary exposures. *Nanotoxicology*, **5** (1), 79–90.

92. Buffet, P.-E., Amiard-Triquet, C., Dybowska, A. *et al*. (2012) Fate of isotopically labeled zinc oxide nanoparticles in sediment and effects on two endobenthic species, the clam *Scrobicularia plana* and the ragworm *Hediste diversicolor*. *Ecotoxicol. Environ. Saf.*, **84**, 191–198.

93. Mouneyrac, C., Buffet, P.-E., Poirier, L. *et al*. (2014) Fate and effects of metal-based nanoparticles in two marine invertebrates, the bivalve mollusc *Scrobicularia plana* and the annelid polychaete *Hediste diversicolor*. *Environ. Sci. Pollut. Res.*, **21** (13), 7899–7912.

94. Khan, F.R., Laycock, A., Dybowska, A. *et al*. (2013) Stable isotope tracer to determine uptake and efflux dynamics of ZnO nano- and bulk particles and dissolved Zn to an estuarine snail. *Environ. Sci. Technol.*, **47** (15), 8532–8539.

95. Monteiro-Riviere, N.A., Wiench, K., Landsiedel, R. *et al*. (2011) Safety evaluation of sunscreen formulations containing titanium dioxide and zinc oxide nanoparticles in UVB sunburned skin: an *in vitro* and *in vivo* study. *Toxicol. Sci.*, **123** (1), 264–280.

96. Osmond-Mcleod, M.J., Oytam, Y., Kirby, J.K. *et al*. (2014) Dermal absorption and short-term biological impact in hairless mice from sunscreens containing zinc oxide nano- or larger particles. *Nanotoxicology*, **8**, 72–84.

97. Lee, P.-L., Chen, B.-C., Gollavelli, G. *et al*. (2014) Development and validation of TOF-SIMS and CLSM imaging method for cytotoxicity study of ZnO nanoparticles in HaCaT cells. *J. Hazard. Mater.*, **277**, 3–12.

98. Misra, S.K., Dybowska, A., Berhanu, D. *et al*. (2011) Isotopically modified nanoparticles for enhanced detection in bioaccumulation studies. *Environ. Sci. Technol.*, **46** (2), 1216–1222.

99. Croteau, M.-N., Misra, S.K., Luoma, S.N. *et al*. (2014) Bioaccumulation and toxicity of CuO nanoparticles by a freshwater invertebrate after waterborne and dietborne exposures. *Environ. Sci. Technol.*, **48** (18), 10929–10937.

100. Amirshahi, N., Alyautdin, R.N., Sarkar, S. *et al*. (2008) Porphyrin-fullerene nanoparticles for treatment of hypoxic cardiopathies. *Nanotechnol. Russ.*, **3** (9–10), 611–621.

101. Amirshahi, N., Alyautdin, R.N., Sarkar, S. *et al*. (2008) Fullerene-based low toxic nanocationite particles (porphyrin adducts of cyclohexyl fullerene-C_{60}) to treat hypoxia-induced mitochondrial dysfunction in mammalian heart muscle. *Arch. Med. Res.*, **39** (6), 549–559.

102. Rezayat, S.M., Boushehri, S.V.S., Salmanian, B. *et al*. (2009) The porphyrin-fullerene nanoparticles to promote the ATP overproduction in myocardium: $^{25}Mg^{2+}$-magnetic isotope effect. *Eur. J. Med. Chem.*, **44** (4), 1554–1569.

103. Hosseini, A., Sharifzadeh, M., Rezayat, S.M. *et al*. (2010) Benefit of magnesium-25 carrying porphyrin-fullerene nanoparticles in experimental diabetic neuropathy. *Int. J. Nanomed.*, **5**, 517–523.

104. Gigault, J. and Hackley, V.A. (2013) Differentiation and characterization of isotopically modified silver nanoparticles in aqueous media using asymmetric-flow field flow fractionation coupled to optical detection and mass spectrometry. *Anal. Chim. Acta*, **763**, 57–66.

105. Croteau, M.-N., Dybowska, A.D., Luoma, S.N. *et al*. (2014) Isotopically modified silver nanoparticles to assess nanosilver bioavailability and toxicity at environmentally relevant exposures. *Environ. Chem.*, **11** (3), 247–256.

106. Handler, R.M., Beard, B.L., Johnson, C.M. *et al*. (2009) Atom exchange between aqueous Fe(II) and goethite: an Fe isotope tracer study. *Environ. Sci. Technol.*, **43** (4), 1102–1107.

107. Zhang, H., Burnum, K.E., Luna, M.L. *et al*. (2011) Quantitative proteomics analysis of adsorbed plasma proteins classifies nanoparticles with different surface properties and size. *Proteomics*, **11** (23), 4569–4577.

108. Cano, I., Chapman, A.M., Urakawa, A. *et al*. (2014) Air-stable gold nanoparticles ligated by secondary phosphine oxides for the chemoselective hydrogenation of aldehydes: crucial role of the ligand. *J. Am. Chem. Soc.*, **136** (6), 2520–2528.

109. Rusevova, K., Koeferstein, R., Rosell, M. *et al*. (2014) LaFeO3 and BiFeO3 perovskites as nanocatalysts for contaminant degradation in heterogeneous Fenton-like reactions. *Chem. Eng. J.*, **239**, 322–331.

110. Bogdan, N., Vetrone, F., Ozin, G.A. *et al*. (2011) Synthesis of ligand-free colloidally stable water dispersible brightly luminescent lanthanide-doped upconverting nanoparticles. *Nano Lett.*, **11** (2), 835–840.

111. Ito, F. and Yamaguchi, K. (2011) N-15-labeled ionic probe attachment mass spectrometry of carbon clusters. *Org. Biomol. Chem.*, **9** (8), 2674–2679.

112. Schwinghammer, K., Mesch, M.B., Duppel, V. *et al*. (2014) Crystalline carbon nitride nanosheets for improved visible-light hydrogen evolution. *J. Am. Chem. Soc.*, **136** (5), 1730–1733.

113. Croteau, M.-N., Cain, D.J., and Fuller, C.C. (2013) Novel and nontraditional use of stable isotope tracers to study metal bioavailability from natural particles. *Environ. Sci. Technol.*, **47** (7), 3424–3431.

4
Radiolabeling of Nanoparticles

Zhiyong Zhang

4.1
Introduction

Nanotechnology is an emerging field in which medicine and engineering correlate closely with physics and chemistry. The fundamental physical, chemical, and biological properties of materials are remarkably altered as the sizes of their constituent grains decrease to a nanometer scale. These novel materials consisting of nano-sized grains or building blocks offer unique and entirely different electrical, optical, mechanical, and magnetic properties compared with conventional micrometer- and millimeter-sized materials owing to their differences in size, shape, surface chemistry, and topology. Current advances in nanotechnology have led to the development of a new field of nanomedicine, which includes many applications of nanomaterials and nanodevices for diagnostic and therapeutic purposes. The same unique physical and chemical properties that make nanomaterials so attractive may be associated with their potentially adverse effects on cells and tissues [1]. In recent years, a growing number of studies suggest that some engineered nanomaterials can cause toxic effects on animals and cell cultures. These findings have raised a major concern about the potential long-term public health and environmental effects of the increasing use of engineered nanomaterials on consumer products, pharmaceuticals, and industrial materials [2].

In the pharmacology and toxicology studies of nanomaterials, it is essential to know the basic behaviors quantitatively *in vitro* and *in vivo*, that is, cellular uptake, tissue distribution, accumulation, and elimination of these newly designed materials. The detection and quantification of nanomaterials in biological systems are a special challenge to the researchers. Reliable analytical methods are urgently needed in order to overcome some severe experimental difficulties (e.g., the detection and measurement of nanomaterials in small samples of biological media, cells and cell components, and interference) associated with this type of research. In this context, radiotracer techniques are especially well suited to such

Toxicology of Nanomaterials, First Edition. Edited by Yuliang Zhao, Zhiyong Zhang, and Weiyue Feng.

studies and have had the chance to demonstrate their enchantment. In comparison with other analytical methods, radiotracer techniques have many advantages, such as high sensitivity, good accuracy, and time saving. Moreover, this method can easily distinguish the endogenous and exogenous sources of elements of interest in samples [3]. However, the major disadvantage of this method is its low accessibility. The use of radiolabeling techniques requires specialized knowledge and equipments, controlled laboratory space, and careful safety considerations. Only a few laboratories are qualified and permitted to work with radioactive materials.

4.1.1 Radioisotope Production

There are several strategies for producing radioisotopes for research and applications and the two most common ones are via a nuclear reactor or a particle accelerator [4, 5]. Reactor-based radioisotope production relies on the (n, γ) reaction or radiative capture nuclear transformation that occurs when a suitable target material is exposed to the neutron flux in the reactor core. A wide range of isotopes are produced in the reactors, from as light as ^{14}C to as heavy as ^{203}Hg, with irradiations lasting minutes to weeks. For example, ^{99}Mo – the parent of the widely used medical diagnostic radioisotope ^{99m}Tc – is usually produced via neutron-induced fission of targets with ^{235}U using a 4–8 day irradiation time [5]. A variety of β-emitting therapeutic radioisotopes of current interest, such as ^{166}Ho, ^{177}Lu, and ^{186}Re, can be readily produced via the simple radiative neutron capture route (n, γ). Accelerators are used to bombard production targets with beams of charged nuclei impinge on targets to produce a wide range of isotopes. Several positron-emitting, neutron-deficient radioisotopes which are effective for biomedical human imaging via positron emission tomography (PET) can be prepared by accelerators. For example, ^{18}F is produced via the $^{18}O(p,n)^{18}F$ reaction and ^{11}C is produced by $^{14}N(p,\alpha)^{11}C$.

The radioisotopes whose half-lives and energy are appropriate for radiotracer research and their production methods are listed in Table 4.1.

Table 4.1 Suitable isotopes for radiotracer research.

Production methods	Radioisotopes
Nuclear reactors	^{3}H, ^{14}C, ^{32}P, ^{35}S, ^{42}K, ^{45}Ti, ^{45}Ca, ^{47}Ca, ^{51}Cr, ^{55}Fe, ^{59}Fe, ^{58}Co, ^{60}Co, ^{64}Cu, ^{67}Cu, ^{65}Zn, ^{72}Ga, ^{76}As, ^{75}Se, ^{82}Br, ^{85}Kr, ^{86}Rb, ^{90}Y, ^{91}Y, ^{99m}Tc, ^{110m}Ag, ^{111}Ag, ^{113}Sn, ^{125}I, ^{131}I, ^{133}Xe, ^{137}Cs, ^{140}La, ^{141}Ce, ^{153}Sm, ^{153}Gd, ^{165}Dy, ^{166}Ho, ^{175}Yb, ^{177}Lu, ^{182}Ta, ^{186}Re, ^{188}Re, ^{192}Ir, ^{198}Au, ^{203}Hg
Accelerators	^{7}Be, ^{11}C, ^{13}N, ^{18}F, ^{22}Na, ^{45}Ti, ^{48}V, ^{52}Mn, ^{52}Fe, ^{56}Co, ^{57}Co, ^{58}Co, ^{64}Cu, ^{67}Ga, ^{68}Ga, ^{87}Y, ^{111}In, ^{141}Ce

4.1.2 Radiolabeling Methods of Nanoparticles

Radiolabeling of nanoparticles can be achieved by either direct labeling (synthesis of nanoparticles from radioactive precursors, neutron or ion-beam activation, cation exchange or isotopic exchange, physical absorption, and covalent attachment) or indirect labeling (bifunctional chelators, prosthetic groups). Direct labeling is a process in which the nanoparticles remain free of any intended functionalization.

4.1.2.1 Synthesis of Nanoparticles from Radioactive Precursors

Almost all the processes used for the synthesis of nonradioactive NPs such as laser ablation, hydrolysis of organometallic/metal halide compounds, reduction of metal halide compounds, and microemulsion and reverse microemulsion methods can be easily modified for the production of radioactive NPs, provided the compositional elements of the NP contain at least one radioisotope that is suitable for radiolabeling (appropriate half-life, emission energy, and commercially available). Using this method, selected radioisotopes could be well embedded into the crystal lattice of the final nanocrystals, resulting in intrinsically radioactive nanoparticles with high stability [6]. Radioactive ^{110m}Ag [7], $^{141}CeO_2$ [8], ^{198}Au [9], and $^{14}C_{60}$ NPs [10] were synthesized using $^{110m}AgNO_3$, $^{141}Ce(NO_3)_3$, $H^{198}AuCl_4$, and ^{14}C-impregnated graphite electrode as starting materials. Radiolabeled nanoparticles prepared from radioactive precursors share almost the same physical–chemical characteristics of the stable ones.

4.1.2.2 Neutron or Ion-Beam Activation

Under neutron or ion-beam bombardment, some nanomaterials can be radiolabeled via neutron- or ion-beam induced nuclear reactions. The probability of a certain nuclear reaction will take place depending on the effective size of the nucleus for that reaction. It is the probability of the interaction between the target nucleus and the incident particles. Activation of presynthesized "cold" NPs presents an obvious advantage that the exposure to radiation can be reduced, compared with the radiochemical synthesis methods. However, the process of neutron or ion-beam irradiation can potentially modify those NPs, and the irradiation and thermal damages on the nanostructure are almost inevitable. Moreover, neutron-activated atoms may be released from the original crystal lattice by the Szilard–Chalmers effect, so the measured radioactivity might not be from the NPs themselves [11]. If it possible, radiolabeled nanomaterials should be fully characterized after activation. Due care must be taken to ensure that the irradiation conditions are not too harsh to substantially modify their characteristics [4].

Some nanomaterials such as SiO_2, and Al_2O_3 or carbon-based nanomaterials do not offer adequate nuclear reactions producing radionuclides with properties suitable for radiotracing purposes under convenient irradiation conditions can be radiolabeled with ^{7}Be by exposure of dry NP powder mixed with fine-grained LiCl to a proton beam. Labeling occurs in a fraction of the NPs by implantation

of recoiling ^{7}Be atoms produced via the nuclear reaction ^{7}Li(p,n)^{7}Be. It was reported that the process could be controlled in such a way that no alterations of the ^{7}Be-labeled nanoparticles are detectable by dynamic light scattering (DLS), X-ray diffraction (XRD), and transmission electron microscope (TEM) [12].

Pérez-Campaña *et al*. [13] established a novel radiolabeling method for metal oxide NPs using a strategy based on the preparation of ^{18}O-enriched metal oxide NPs. Activation of the NPs via ^{18}O(p,n)^{18}F reaction can then be expected to yield NPs containing the commonly used PET isotope ^{18}F ($T_{1/2} = 1.83$ h, $\beta^{+} = 96.7\%$) in their structure. In addition, another simple and generalized strategy was recently presented from the same group to activate ordinary metal oxide NPs by direct irradiation with protons via the ^{16}O(p,α)^{13}N nuclear reaction. Nitrogen-13 has a 9.98 min half-life and decays purely by positron emission. Despite the short half-life of ^{13}N, the biodistribution of metal oxide NPs can be measured during the first minutes after intravenous administration [14].

4.1.2.3 Isotopic Exchange and Cation Exchange

Isotopic exchange is a process in which two atoms belonging to different isotopes of the same element exchange valency states or locations in the same molecule or different molecules. Isotopic exchange is the preparation method for many radiolabeled compounds, especially for radioiodination. Because the exchange of the radioisotope for the stable atom is proportional to the molar ratio of the substrate and the radioisotope, higher radiochemical yield can be achieved in exchange for lower specificity. This labeling is suitable for many radiotracers for imaging when very high specific activity is not required [15].

Chemical transformations from one solid to another via insertion and exchange of atoms can be used to radiolabel nanoparticles. The labeling processes allow fast creation of radioactive nanosystems, which could not possibly be synthesized using normal techniques at a relatively moderate temperature [6].

4.1.2.4 Physical Absorption

Nanomaterials generally show a high absorptive capacity to molecules and ions in solutions due to their large specific surface area. Radiolabeled nanoparticles can be easily prepared by physical absorption of radioactive ions, but the stability of the radiolabels is questionable.

4.1.2.5 Covalent Attachment

Covalent bonds are known for their rigidity. If the selected radioisotope can be covalently bound to a component element of a certain nanomaterial, a stable radiolabeled nanomaterial can be formed. Carbon-14, fluorine-18, iodine-125, and iodine-131 are commonly used to label nanomaterials via covalent linkage [16].

4.1.2.6 Bifunctional Chelators and Prosthetic Groups

In many cases, direct radiolabeling is impossible or provides only low radiochemical yields, especially for metallic radioisotopes. Consequently, alternative (indirect) labeling strategies via bifunctional chelators and prosthetic groups

have to be considered [17]. Bifunctional chelators are molecules containing two different moieties: a strong metal chelating unit and a reactive functional group [18]. The former then enables the sequestration of the metallic radioisotope while reactive functional group provides the requisite chemistry for covalent attachment to a targeting vector of interest, such as small molecules, proteins, or nanoparticles. The most widely used chelators are 1,4,7,10-tetraazacyclododecane-1,4,7,10-tetraacetic acid (DOTA) and 1,4,7-triazacyclononane-1,4,7-triacetic acid (NOTA) as examples of macrocyclic chelating agents. Further prominent examples are acyclic chelators such as diethylenetriaminepentaacetic acid (DTPA) and deferoxamine (DFO).

Prosthetic groups are bifunctional agents that consist of a suitable site for radioiodination or fluorination and functional groups to allow covalent attachment of a small molecule, protein, or nanoparticle. Radioactive iodine or fluorine is incorporated into prosthetic groups to form radiolabeled reactive precursors. The radiolabels are obtained by the conjugation of the precursors with target materials under mild conditions. The most frequently used precursors for radioiodination are *N*-succinimidyl5-[*I]iodo-3-pyridinecarboxyl ([*I]SIPC) and *N*-succinimidyl-3-[*I]-iodobenzoate ([*I]SIB). The commonly used precursors containing prosthetic groups allowing for the ^{18}F labeling are *N*-[6-(4-[^{18}F]fluorobenzylidene)aminooxyhexyl]maleimide ([^{18}F]FBAM) and *N*-succinimidyl-4-[^{18}F]fluorobenzoate ([^{18}F]SFB).

It should be noted that the aforementioned method needs to functionalize the nanoparticles in the labeling process. Modification of the surface properties of nanoparticles may also affect their behavior in living organisms.

4.1.3
Radioactivity Measurement and Nuclear Imaging

In terms of radiotracer, the most commonly used radioisotopes are β- and γ-emitters. Different techniques have been developed for the quantitative detection of radioactivity, and among them, scintillation counting (liquid and plastic) is applied for the determination of not only β-emitters but also α- and γ-emitters. Liquid scintillator counting is the preferred method for analyzing relatively low-energy emitters such as β-particles. Higher energy γ-ray is measured using solid scintillation counting [19]. Gamma-ray spectrometry is a powerful nondestructive analytical method for the detection of γ-ray. In one single measurement and with little sample preparation, γ-ray spectrometry allows the identification and quantification of several γ-emitting radionuclei in a variety of matrices. There are three types of γ-ray detectors: thallium-doped sodium iodide crystal NaI(Tl) scintillation detector, lithium-drifted crystal of purified germanium detector, and high-purity germanium (HPGe) detector. Among them, HPGe detector is the most sensitive and efficient device, which is widely used in determining the activity of radionuclides from higher order down to 10^{-2}Bq level [20].

Radiotracer techniques provide not only quantitative information on the distribution of radiolabels in biological or environmental samples but also *in vivo*

real-time images. Nuclear imaging techniques include autoradiography, gamma camera, single-photon emission computed tomography (SPECT), and PET. The first autoradiography was obtained accidentally around 1867. This technique laid the foundation for modern nuclear imaging. SPECT and PET are two of today's most important medical imaging methods, providing the spatial distribution and movement of radiolabels in tissues of living subjects. PET is a functional imaging technique that produces a 3D image of functional processes in the body or tissues. The positron-emitting radionuclides such as ^{11}C, ^{13}N, ^{15}O, ^{18}F, and ^{64}Cu used in PET (also called *PET tracer*) can emit positrons without the need for external excitation and then annihilate with electrons up to a few millimeters away [21]. During this process, two gamma photons are emitted in opposite directions and are detected to provide real-time, noninvasive, highly sensitive, and whole-body 3D information about the biodistribution of different drugs. Until now, PET has been approved by the FDA as a clinical molecular imaging technique with a resolution of 1–2 mm. SPECT is similar to PET in its use of radioactive tracers and detection of γ-rays. Unlike PET, the radioisotopes used for SPECT emit only a single γ-ray during decay, such as ^{99m}Tc, ^{123}I, and ^{111}In. The γ radiation emitted from SPECT tracers is measured directly, acquiring multiple 2-D images (also called *projections*). Afterward, a computer is used to apply a tomographic reconstruction algorithm to the multiple projections, obtaining a 3D dataset, which is useful for tumor imaging, infection (leukocyte) imaging, thyroid imaging, or bone scintigraphy.

The most important advantages of SPECT over PET are its lower cost and wider availability. Furthermore, PET tracers generally have a short half-life, necessitating an on-site cyclotron for synthesis. Most of SPECT tracers are readily available and have a relatively long half-life. Several radionuclide generators are available for ready supply of SPECT radionuclides, such as ^{99}Mo-^{99m}Tc and ^{188}W-^{188}Re. On the other hand, PET imaging has a much higher sensitivity and provides images of better resolution compared with SPECT [22].

This chapter reviews the available literature on radiolabeling methods and their applications of a series of nanomaterials—carbon nanomaterials, metal-based nanomaterials, polymeric nanomaterials, and so on. Most of them are among the nanomaterials on the OECD (Organization for Economic Cooperation and Development) list that need immediate toxicological investigations and researches.

4.2 Radiolabeling of Nanomaterials

4.2.1 Radiolabeling of Carbon-Based Nanomaterials

Since all the carbon nanomaterials, fullerene, carbon nanotubes, and graphene are all constructed by the elemental carbon, in the isotope tracing studies, the most

appropriately labeled atom should be isotope of carbon itself. Carbon-14, a β-ray emitter with a half-life of 5715 years is the most often used carbon radioisotope. Carbon-11 is another radioactive isotope of carbon that has a 20.4 min half-life and decays by positron emission. Carbon-11 is often used to radioactive labeling of molecules in PET. Some other radioisotopes generally applied in nuclear medicine, such as ^{125}I, ^{99m}Tc, ^{67}Ga, ^{111}In, and ^{64}Cu, are also used in radiolabeling of carbon nanomaterials. Both direct and indirect labeling methods have been developed.

4.2.1.1 Radiolabeling of Carbon Nanomaterials by Radioactive Carbon

Carbon nanomaterials are among the best-known and most promising products of the nanotechnology movement, and their radiolabeling methods have been extensively studied. Electric arc discharge, laser ablation, and chemical vapor deposition are common approaches for the preparation of fullerenes, carbon nanotubes, and graphene. Using ^{14}C-enriched starting materials, radiolabeled carbon nanomaterials can be synthesized. In 1994, Scrivens *et al*. [10] reported ^{14}C-labeled C_{60} for the first time, the specific activity of the product was 11.2 mCi/mmol, and approximately ^{12}C:^{14}C = 200 : 1. The authors studied the interaction of $^{14}C-C_{60}$ with human keratinocytes and found that $^{14}C-C_{60}$ rapidly became cell-associated in a time-dependent manner. After 6 h of incubation, approximately 50% of the applied radioactivity was taken up by the cells. It was speculated that C_{60} particles might be associated with the cell surface followed by diffusion of molecular C_{60} or small particle sections of the material. Bullard-Dillard *et al*. [23] reported the first study of biodistribution of pristine C_{60} using $^{14}C-C_{60}$ tracer. The $^{14}C-C_{60}$ was rapidly (within 1 min) cleared from the circulation of female Sprague-Dawley rats after intravenous injection and majority of the $^{14}C-C_{60}$ accumulated in the liver (90–95%). The results also suggested that C_{60} was not metabolized by the typical oxidative patterns characteristic of other polycyclic aromatics. Compared to the parent fullerene, the ^{14}C-labeled ammonium-salt-derivatized C_{60} was more widely distributed among various tissues (52.4% in the liver, 28% in the muscle, skin, and lung), likely due to increased hydrophilicity and somewhat slower clearance from the circulation. No radioactivity was detected in rat brain, so the authors concluded that these fullerenes did not cross the blood–brain barrier.

The emergence of ^{14}C skeleton-labeled CNTs is much later than that of $^{14}C-C_{60}$. In 2008, two groups reported the synthesis of ^{14}C-labeled CNTs by chemical vapor deposition with mixtures of ^{14}C-labeled methane and regular methane as feedstock gases (single-walled carbon nanotubes (SWCNTs) and multiwalled carbon nanotubes (MWCNTs)) [24, 25] and the electric arc discharge method with ^{14}C-furfuryl alcohol-doped carbon electrodes (SWCNTs) [26], respectively. The uptake and depuration of ^{14}C CNTs by the earthworm [24, 25] and the effect of sediment-associated CNTs on contaminant uptake from sediments by infaunal deposit feeders were evaluated [26]. Graphene is simply a single layer of graphite, making it only one atom thick. Recently, Guo *et al*. [27] synthesized ^{14}C-labeled graphene by means of graphitization and exfoliation of sandwich-like $FePO_4$/dodecylamine hybrid nanosheets, and ^{14}C

was incorporated in the synthesis in the form of carbon-14 phenol ethanol. The authors investigated the bioaccumulation of ^{14}C-labeled graphene by *Daphnia magna* and found that after exposure to graphene (250 μg/l) for 24 h, the graphene concentration in the organism reached nearly 1% of the organism dry mass.

An alternative labeling method of carbon nanomaterials is the attachment of a labeled carbon fragment to the fullerene moiety or indirect label. Yamago *et al*. [28] synthesized a ^{14}C-labeled water-soluble C_{60}-fullerene using dipolar trimethylenemethane, which underwent cycloaddition to C_{60}-fullerene. The ^{14}C label is placed at the position next to the C_{60} core. When injected intravenously, the labeled fullerene was distributed rapidly to various organs including brain tissue. It was suggested that the high lipophilicity and the rather compact structure of the fullerene must be responsible for the transportation of this large molecule (molecular weight 995) through the blood–brain barrier. Preparation of ^{14}C-labeled water-soluble fullerene derivatives $^{14}C-C_{61}(COOH)_2$ [29] and [^{14}C-taurine]-MWNTs [30] using indirect methods was also reported.

Radioactive-carbon-labeled fullerenes can also be produced by charged-particle, neutron, or high-energy γ-rays irradiation of C_{60}, C_{70}, and their mixture [31, 32]. It was found that a carbon atom of fullerene can be easily exchanged with a radioactive carbon atom produced by a nuclear reaction. The high-performance liquid chromatography (HPLC) method is effective for identification and purification of various labeled fullerene families as chemically stable compounds. The radiochemically interesting aspect of the results is not only the production of ^{11}C- and ^{14}C-labeled fullerenes but also the formation of radioactive higher fullerenes, which can be simultaneously produced with high yield in carrier-free form.

4.2.1.2 Radiolabeling of Carbon Nanomaterials by Radioiodine

Radioiodine is commonly used in nuclear medicine, for both diagnosis (^{123}I, ^{125}I, and ^{131}I) and therapy (^{125}I and^{131}I) of various diseases. Radioiodination is a common procedure and provides excellent sensitivity in many applications. Radioiodination of carbon nanomaterials can be achieved by oxidation of $^*I^-$ to $^*I$ or $^*I^+$ by chloramine-T (*N*-chloro-*p*-toluenesulfonic acid) or Iodogen™ (1,3,4,6-tetrachloro-3,6-diphenyl-glycousil) with subsequent attack of the target material. Iodine-125-labeled carbon nanomaterials such as C_{60} derivatives ^{125}I-$C_{60}(OH)_xO_y$ [33] and ^{125}I-$C_{60}(OH)_x$ [34] and hydroxylated ^{125}I-SWCNTols [35] have been reported. Figure 4.1 shows a synthetic procedure for the preparation of ^{125}I-SWCNTols. The iodine 4d synchrotron radiation X-ray photoelectron spectra (SRXPS) of I-SWCNTols and standard compounds show that the C-I binding on I-SWCNTols is a covalent bond analogous to that in *p*-I-$C_6H_4NO_2$, *m*-I-C_6H_4COOH [36].

Wang *et al*. [35] afforded a quantitative analysis of hydroxylated carbon nanotubes accumulated in animal tissues for the first time using ^{125}I-SWCNTols radiotracer. After intraperitoneal injection, intravenous injection, subcutaneous injection, or stomach intubation, they found that ^{125}I-SWNTols were distributed in measurable levels throughout the entire body quickly, except for the brain, and accumulated readily and retained long in the bone.

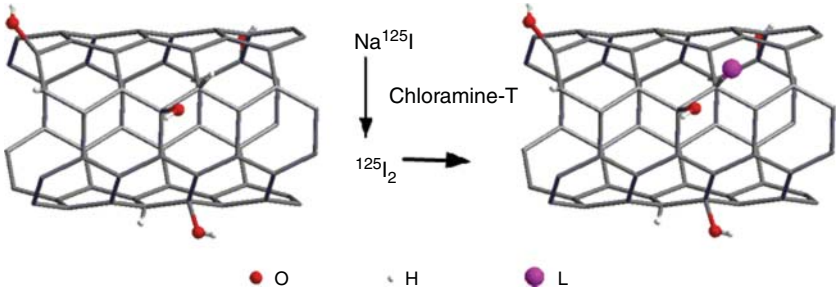

Figure 4.1 Preparation of ^{125}I-SWNTols by chloramine-T method. (Reprinted with permission from [11]. Copyright (2009) Springer.)

Fullerene can also be radioiodinated indirectly. Radioiodination of the C_{60}-PEG (polyethylene-glycol) conjugate has been achieved by chloramine T method following introduction of tyramine [37]. Ran *et al.* [38] developed a procedure for labeling of a fullerene derivative 1-[*N*′,*N*′-bis(2-chloroethyl)-4-aminophenyl]-*N*-methyl-fullereno-C_{60}-[1,9-*c*] pyrrolidine ($C_{60}-C_{13}H_{18}N_2Cl_2$) with ^{125}I. The compound was first iodinated with a large excess of iodine monochloride and then radiolabeled by isotopic exchange with Na^{125}I in a toluene–water two-phase system. The radiolabeling yield of the compound was as high as 94% after heating for 2 h at 130 °C.

4.2.1.3 Radiolabeling of Fullerene Derivates by ^{99m}Tc

Among the radioisotopes used in tracing studies, technetium-99 m ($T_{1/2} = 6.02$ h, $E_\gamma = 141$ keV) is widely used due to the stability of labeled compound and appropriate photo energy for measurement. Li *et al.* [39] reported the synthesis of ^{99m}Tc-$C_{60}(OH)_x(O)_y$. Tc(VII) was first reduced to Tc(V) by $SnCl_2$, then labeled to $C_{60}(OH)_x(O)_y$. The stability of ^{99m}Tc-$C_{60}(OH)_x(O)_y$ is well and the radiochemical purity remains greater than 90% for 25 h. Similar labeling work of ^{99m}Tc-$C_{60}(OH)_x$ was reported by the same group [40].

4.2.1.4 Radiolabeling of Carbon Nanomaterials by ^{66}Ga and ^{67}Ga

Gallium-66 ($T_{1/2} = 9.49$ h) is an intermediate-lived radionuclide that has potential for PET imaging. Gallium-67 ($T_{1/2} = 78.3$ h) is often used as tumor-localizing agent (gallium citrate). Hong *et al.* [41] prepared ^{66}Ga-labeled graphene oxide (GO) using NOTA as the bifunctional chelator. GO sheets with covalently linked, amino-group-terminated six-arm branched polyethylene glycol (PEG; 10 kDa) chains were conjugated to NOTA. ^{66}Ga-NOTA-GO was formed by the reaction of NOTA-GO with ^{66}Ga-acetate. Li *et al.* [42] reported the synthesis of ^{67}Ga-$C_{60}(OH)_x$ by $C_{60}(OH)_x$ and $^{67}GaCl_3$. The radiolabeling yield reached around 90%.

4.2.1.5 Radiolabeling of SWCNTs by ^{111}In

^{111}In is a cyclotron-produced nuclide and decays with a half-life of 2.83 days to stable cadmium. Indium-111-labeled water-soluble SWCNTs can be synthesized

by the following two steps. First, SWCNTs were functionalized with the chelating molecule DTPA, and second, ^{111}In-DTPA-SWCNTs were obtained by cationic exchange from a solution of ^{111}In-citrate or $^{111}InCl_3$ [43, 44].

4.2.1.6 Radiolabeling of SWCNTs and GO by ^{64}Cu

^{64}Cu is an important emerging biomedical radionuclide suitable for labeling a wide range of radiopharmaceuticals for PET imaging, as well as systemic or local radioimmunotherapy of tumors. Liu *et al*. [45] reported the indirect labeling of SWCNTs with ^{64}Cu. SWCNTs were noncovalently functionalized with phospholipid-PEG, and then, macrocyclic chelating agent DOTA was attached to the termini of the PEG chains used to conjugate ^{64}Cu. The ^{64}Cu radiolabels remained intact on SWCNTs after incubation in full mouse serum over 24 h. Using a similar method, Hong *et al*. [46] labeled GO conjugates with ^{64}Cu through NOTA.

4.2.1.7 Synthesis of Radioactive Endohedral Fullerenes

Endohedral fullerenes are a subfamily of fullerenes with potential applications in the field of nuclear medicine, for instance, stable transporter of radioisotopes *in vivo*, because of their resistance to metabolism and their high kinetic stability. Also, radioactive endohedral fullerenes have been used as tracers to monitor the fate of fullerene-based materials *in vivo*.

Kikuchi *et al*. [47] demonstrated the formation of a new fullerene family with a radioactive metal atom encapsulated inside the C_{82} cage, $^{159}Gd@C_{82}$, and $^{161}Tb@C_{82}$ by means of the neutron irradiation in a reactor. $^{140}La@C_{82}$, $^{140}La_2@C_{80}$ [48], $^{166}Ho@C_{82}$, $^{166}Ho_2@C_{82}$, $^{166}Ho_3@C_{82}$ [49], and $^{166}Ho_x@C_{82}(OH)_y$ [50] can be made by the analogous method mentioned earlier. However, this procedure has the drawback that part of the activated nuclide from inside the carbon cage breaks out of the cage by nuclear recoil during activation. Braun and Rusch [51–55] discovered a method for the more efficient production of carrier-free radionuclides containing endohedral fullerenes by using the implantation of atoms from outside the cage into the cage by nuclear recoil after neutron capture. This is the reverse of the aforementioned breakout. The method was also used in synthesis of the noble gas-containing fullerenes by irradiation in a nuclear reactor, followed by dissolving the activated sample in an adequate organic solvent and then removing any free radioactive noble gas from the solution by purging it with inactive argon gas [56–59]. The residual activities in the solution from ^{41}Ar, ^{133g}Xe, ^{135g}Xe, or ^{85m}Kr were attributed to the existence of $^{*}NG@C_{60}$ compounds. HPLC could be adopted for the separation of the formed endohedral radiofullerenes of $^{7}Be@C_{60}$, $^{85m}Kr@C_{60}$, and $^{135}Xe@C_{60}$ [60, 61]. Grushko *et al*. [62] studied the *n,γ-reaction of metallofullerenes* of Tb, Sm, and $Sc_3N@C_{80}$ and found that possibly unfavorable geometry of target/projectile system cannot explain the low yield observed so far.

Another way is to use heavy-ion reactions to prepare radioactive endohedral fullerene by implantation of recoiled isotopes such as ^{24}Na, ^{34m}Cl, ^{65}Zn, ^{69}Ge, ^{71}As, ^{72,73,75}Se, ^{77}Br, ^{79}Kr, ^{81}Rb, ^{83}Sr, ^{86}Zr, and ^{168}Hf into the C_{60} fullerene cage [63].

The endohedral fullerenes produced by implanted recoiled isotopes were subsequently separated by solvent extraction.

4.2.1.8 Production of Radiolabeled Carbon Nanomaterials by Proton Beam Irradiation

Abbas *et al*. [64] carried out a feasibility study regarding the production of radiolabeled carbon nanomaterials by proton beam irradiation. ^{7}Be radioisotope can be produced through the nuclear reactions ^{nat}C(p,x)^{7}Be. The authors demonstrated that sufficient activities of ^{7}Be were produced in carbon black and carbon nanotubes as a tool for their radiotracing biological applications. Further studies should be conducted to assess the stability of the NPs and the binding of the ^{7}Be radiotracer into the NPs.

4.2.1.9 Radiolabeling of Fluorescent Carbon Dots

Fluorescent carbon dots (C-dots) have attracted increasing attention due to their unique optical and biochemical properties. Huang *et al*. [65] synthesized C-dots via laser ablation of a carbon target in the presence of water vapor with argon. Then, diamine-terminated oligomeric poly(ethylene glycol) was used to react with the C-dots for surface passivation. For ^{64}Cu labeling, C-dots were firstly conjugated with DOTA-NHS ester via the amino groups followed by a reaction between the C-dot-DOTA conjugate and $^{64}CuCl_2$.

4.2.1.10 ^{99m}Tc-Technegas

^{99m}Tc-Technegas is a suspension of ^{99m}Tc-labeled, ultrafine carbon particles produced in an atmosphere of high-purity argon [66]. The primary particles composed of Technegas are in the range of 5–20 nm, assuring good peripheral penetration and alveolar deposition. Since its invention and first reported use in 1986 as a diagnostic radioaerosol, Technegas has been recognized as a major contributor to lung ventilation scintigraphy. Commercial Technegas generators are available (Vita Medical Ltd, Sydney, Australia) [67].

4.2.2 Radiolabeling of Metal-Based Nanomaterials

Metal-based nanomaterials are one of the most important classes of nanomaterials and found in a wide range of applications. In the past decade, significant breakthrough has been made toward the development of radiolabeling methods of metal-based nanomaterials, partly because of the rising concerns related to potential toxicological effects these nanoparticles and partly because of their potential applications in the biomedical field [68]. Tremendous efforts have been devoted to the design of various types of multifunctional nanoparticles (e.g., iron oxide nanoparticles, gold nanostructures, and silica nanoparticles), which not only can be used for noninvasive visualization of the tumors with different imaging techniques but also hold the potential for targeted delivery of anticancer drugs [69]. Radiolabeled nanoparticles have proven to be promising tools in the diagnosis

and therapy of malignant processes due to their multivalency and as multimodal agents [70].

4.2.2.1 Aluminum Oxide Nanoparticles (Alumina or Al_2O_3 NPs)

Al_2O_3 NPs have important applications in industrial, domestic, medicinal products, absorbents, biomaterials, and energetic systems [71]. The only Al radioisotope with a half-life longer than 10 min is the long-lived positron emitter ^{26}Al ($T_{1/2} = 7.2 \times 10^5$ a). However, the expense of this radioisotope and the difficulty in attaining sufficiently low determination limits with conventional nuclear analytical techniques have restricted its application.

Pérez-Campaña *et al*. [13] reported a novel and valuable strategy for the activation of ^{18}O-enriched Al_2O_3 NPs by bombardment with protons to yield ^{18}F-labeled NPs via the $^{18}O(p,n)^{18}F$ reaction. Oxygen-18 enriched NPs were prepared using ^{18}O-enriched water (98%). The ^{18}F-labeled NPs were used in biodistribution studies in rats up to 8 h after i.v. administration. It was found that most of the radioactivity accumulated in the liver even at very short times; radioactivity was also detected in the lungs, heart, kidneys, and stomach. In another study, the authors presented a simple method for the direct proton beam activation of ordinary Al_2O_3 NPs via the $^{16}O(p,\alpha)^{13}N$ reaction [14]. The incorporation of radioactive ^{13}N atoms in the Al_2O_3 structure allowed tracing the biodistribution of the NPs in animals after intravenous administration via PET.

4.2.2.2 Cerium Dioxide (Ceria or CeO_2 NPs)

CeO_2 NPs are being used in various engineering and biological applications, such as solid-oxide fuel cells, catalysts for augmenting fossil fuel oxidation, UV-blockers, gas sensors, and potential pharmacological agents [71, 72]. Cerium-141 ($T_{1/2} = 32.5$ days to ^{141}Pr (stable), $E_\beta(\max) = 435$ keV (70%), 580 keV (30%), $E_\gamma = 145$ keV (48.5%)) has been introduced as a radionuclide for therapy, while it can be used in diagnosis as well [73]. Oughton *et al*. [74] first reported the preparation of ^{141}Ce-labeled CeO_2 NPs by bombardment of "cold" CeO_2 NPs with thermal neutrons in a reactor. Using this method, Cohen *et al*. [75] prepared ^{141}Ce-labeled CeO_2 of various primary particle diameter and SiO_2-coated CeO_2 particles and tracked translocation of these particles across alveolar epithelial monolayers *in vitro*. Cerium-141-labeled CeO_2 can also be produced by cyclotron irradiation via (d, p) reaction [76]. The possible damage or structural change of CeO_2 NPs due to the irradiation process was studied and no significant changes of the hydrodynamic size distribution and the surface charge were noticed. Another cerium radioisotope, ^{137m}Ce [$T_{1/2} = 34.4$ h, IT (99.22%), β^+ (0.779%)] can be produced by irradiation of natural lanthanum via $^{nat}La(p,3n)^{137m}Ce$ reaction in a cyclotron. Bakht *et al*. [77] proposed that ^{137m}Ce might be a candidate radionuclide in radiolabeling of CeO_2 NPs for SPECT imaging owing to its appropriate half-life, 99.91% natural abundance of target (La), and its intense gamma line at 254.29 keV.

Activation of presynthesized "cold" CeO_2 is the simplest way for radiolabeling of CeO_2 NPs. But particular care must be taken in choosing the irradiation

conditions, such as temperature, neutron fluxes, or beam currents, energy of the projectile, and irradiation time because these factors directly influence the radiation damage caused by neutron or ion-beam bombardment. Synthesis of radiolabeled CeO_2 NPs using radioactive cerium as precursors provides the best method for the preservation of all parameters that determine the NPs' biological activity. In our laboratory, ^{141}Ce-labeled CeO_2 NPs with different shapes (truncated octahedral, octahedral, nanorod, and nanocube) were synthesized using $^{141}Ce(NO_3)_3$ as a precursor by precipitation or hydrothermal methods. Subsequently, a series of studies on the behavior of CeO_2 NPs in plants [8], animals [78], and the aquatic environment [79] were carried out. Cucumber seedlings were treated with ^{141}Ce-labeled CeO_2 NPs (7 and 25 nm) for 7 days, then two-dimensional distributions of ^{141}Ce in the leaves were obtained by autoradiograph (Figure 4.2). The distribution patterns of 7 and 25 nm CeO_2 NPs are very similar. In young leaves, CeO_2 NPs exclusively accumulated along the leaf margins, while in older leaves, they diffused from the margins to other parts and finally spread all over the leaves. It is notable that CeO_2 NP concentrations in the veins and leaf stalks were much lower than in the other areas of the leaves. In contrast, distribution of cerium (III) ions showed significant accumulation along the veins because of a strong affinity of Ce^{3+} to the carboxyls in xylem. We speculated that once CeO_2 NPs entered into the vascular cylinder, they could move smoothly to the end of the vascular bundle along with water flow [8].

Rojas *et al*. [80] prepared ^{18}F-CeO_2 NPs by reacting *N*-succinimidyl-4-[^{18}F]fluorobenzoate (^{18}F-SFB) on the ω-aminopropyl-functionalized CeO_2 NPs'

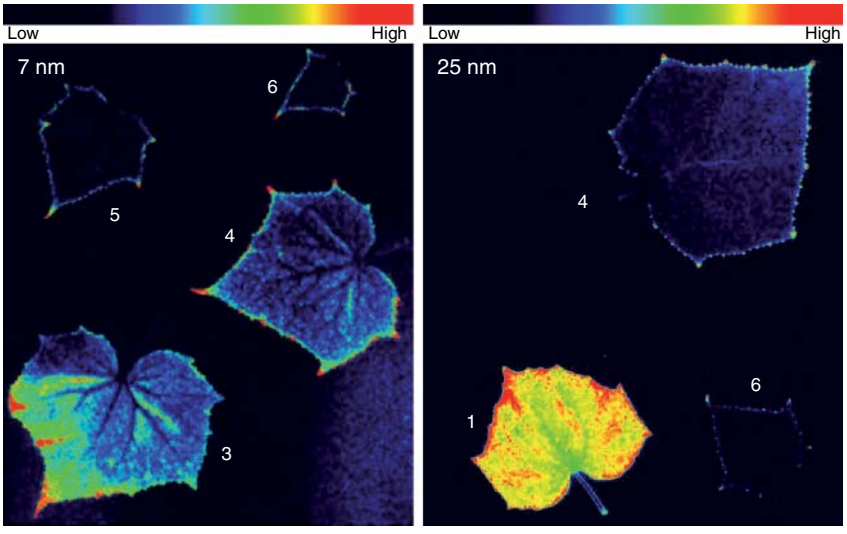

Figure 4.2 Autoradiographs of ceria NPs in cucumber leaves. (a) 7 nm ceria, third, fourth, fifth, and sixth leaves and (b) 25 nm ceria, first, fourth, and sixth leaves. (Reproduced from [8] with permission from The Royal Society of Chemistry.)

surface. The biodistribution study in rats showed that the labeled NPs were retained mainly in the lungs and reticuloendothelial system, probably by size exclusion and phagocytosis, respectively. The metabolic products were finally excreted into urine.

4.2.2.3 Gold Nanoparticles (Au NPs)

Au NPs are enormously used for various different applications such as catalysts, optoelectronic devices, biological sensors, ultrasensitive chemical, separation science, consumer products, biomedical applications such as diagnostics, biomedical imaging, drug delivery, and photothermal therapy [81]. Au-198 ($\beta_{max} = 0.96$ MeV, $\gamma_{max} = 0.412$ MeV, $T_{1/2} = 2.7$ days), a beta emitter, has been widely used in medical therapy and biological research. Since Au-197, the only stable isotope of gold, has a relatively large thermal neutron capture cross section (98.65 b), ^{198}Au with a high specific activity can be easily produced by irradiation of natural gold in a nuclear reactor via (n, γ) reaction.

Researchers from German Research Center for Environmental Health prepared ^{198}Au-radiolabeled NPs by activation of presynthesized "cold" Au NPs with neutrons. They subsequently investigated the relationships between the biodistributions of various ^{198}Au NPs that were intravenously, intratracheally, or intraesophageally administered in rats and their special physicochemical characteristics including sizes and surface charges [82–84]. Cherenkov luminescence imaging based on light emission from the decay of radionuclides has recently drawn great interest in molecular imaging. Xia's group from Georgia Institute of Technology and Emory University reported the Cerenkov luminescence phenomenon of ^{198}Au for the first time [85]. They prepared radioactive ^{198}Au-labeled nanostructures with a similar size but different shapes (nanospheres, nanodisks, nanorods, and cubic nanocages) and then compared their distributions in tumor-bearing mice. At 24 h postinjection, Au nanospheres and nanodisks showed significantly higher tumor accumulation than the Au nanorods and nanocages. Autoradiographic images of thin slices of the tumors indicate that Au nanospheres and nanodisks were only observed on the surfaces of the tumors, whereas the Au nanorods and nanocages could reach the cores of the tumors [86]. Au-195 ($T_{1/2} = 186$ days) is the only isotope of gold that has a half-life of more than a few days. It has several γ energies below 100 keV, allowing investigations of long-term biological processes. Schleh *et al*. [87] irradiated gold electrodes with proton in a cyclotron to produce ^{195}Au. Ultrafine ^{195}Au-radiolabeled Au particles (22 nm count median diameter) were generated by spark discharging. The animal experiments showed that inhaled Au NPs were retained in the mouse lungs and translocated after a short time.

Radiolabeling methods of Au NPs with SPECT and PET isotopes have been extensively studied. Xie *et al*. [88] developed a conjugation procedure to attach Au nanoshells (NSs) with ^{64}Cu. First, a bifunctional chelating agent *p*-NH_2-Bn-DOTA (*S*-2-(4-aminobenzyl)-1,4,7,10-tetraazacyclododecane tetraacetic acid) was conjugated to bifunctional OPSS-PEG2K-NHS (O-pyridyl disulfide–polyethylene glycol 2000–*N*-hydroxysuccinimide ester). Then the

resulting OPSS-PEG-DOTA was combined to the surface of the particles with OPSS group. Finally, NSs were coupled with $^{64}CuCl_2$ through DOTA. Bhatnagar *et al*. [89] radiolabled Au NPs with ^{64}Cu using a similar method, except that they used thioctic acid instead of bifunctional OPSS-PEG2K-NHS. Tian *et al*. [90] labeled hollow gold nanospheres (HAuNSs) with ^{64}Cu in a different sequence. 1,4,7,10-Tetraazacyclododecane-1,4,7-tris(acetic acid)-10-[acetic acid-*N*-(2-(2-(2-aminoethoxy)ethoxy)ethyl)-lipoic acid mono amide] (DOTA-LA) was labeled with ^{64}Cu prior to introduction to HAuNS. ^{64}Cu-DOTA-LA was then mixed with HAuNS to produce ^{64}Cu-HAuNS. In Wang *et al*.'s study, gold nanocages (Au NCs) were first functionalized with amine polyethylene glycol thiol(NH_2-PEG-SH) through an Au-S linkage then conjugated with 1,4,7,10-tetraazacyclododecane-1,4,7,10-tetraacetic acid mono(*N*-hydroxy succinimide ester) (DOTA-NHS-ester), followed by chelating with $^{64}Cu^{2+}$ ions [91].

^{18}F-radiolabeled Au NPs can be quickly synthesized using the silicon-fluoride-acceptor (SIFA) labeling methodology. Maleimide-functionalized PEG grafted to Au NPs were reacted with thiol-substituted silicon–fluorine prosthetic group, resulted in ^{18}F-Au NPs [92]. Shao *et al*. [93–95] reported a novel protocol for the synthesis of ^{125}I-labeled gold nanorods (GNRs) by simply mixing [^{125}I]NaI with GNRs in deionized water at room temperature. It was proven that iodide ions showed high affinity and strong binding to the surface of GNRs. This labeling method can be adapted to ^{123}I, ^{124}I, and ^{131}I for more extensive applications. Iodine labeling of Au nanostructures can also be achieved indirectly. For example, Jang *et al*. [96] functionalized GNRs with (orthopyridyl) disulfide-poly(ethylene glycol)-folate and a short peptide, H2N-Tyr-Asn-Asn-Leu-Ala-Cys-OH through thiol chemistry. Then the tyrosine in the peptide sequence was introduced for radioactive-iodine labeling through an iodine–tyrosine interaction. Stability tests on ^{125}I-GNRs in human serum indicated that 91% of the ^{125}I remained on the GNRs after incubation for 24 h.

4.2.2.4 Iron and Iron Oxide Nanoparticles

4.2.2.4.1 Radiolabeling of Iron-Based NPs for Toxicological and Pharmacokinetic Studies In these studies, ^{59}Fe ($T_{1/2} = 44.5$ days, $E_\gamma = 1099.3$, and 1291.6 keV) is commonly used. Intrinsically radiolabeled iron-based nanoparticles can be easily prepared by using ^{59}Fe as a starting material. Early in 1989, Weissleder *et al*. [97] reported the pharmacokinetic behavior and toxicity of a superparamagnetic iron oxide preparation based on a ^{59}Fe radiotracer study. Postsynthetic techniques, such as neutron activation [98] and isotopic exchange [99], also have been applied for ^{59}Fe labeling. The latter method is thought to be simple, fast, efficient, and widely applicable since it does not need any special equipment and can be downscaled to yield radiolabels with high specific activities within the tolerated doses. It was also demonstrated that the labeled product is stable enough to be used *in vivo*.

Radioiodination of iron oxide NPs can be accomplished via prosthetic groups. de Barros *et al*. [100] surface modified iron oxide NPs with the water-soluble

Bolton–Hunter reagent sulfosuccinimidyl-3-[4-hydroxyphenyl]propionate (SHPP) to enable direct electrophilic aromatic substitution of ^{125}I. The labeled particles showed high stability and long blood circulation.

Ga-67 is a γ-emitting radionuclide with a half-life of 3.26 days. Hosseini-Salekdeh *et al*. [101] synthesized ^{67}Ga-labeled superparamagnetic iron oxide nanoparticles (SPIONs) by incorporation of ^{67}Ga within the nanostructure of iron oxide network under the synthesis procedure. Shanehsazzadeh *et al*. [102] reported an indirect method via cyclic DTPA–dianhydride conjugation. Tissue distribution of the labels in mice was investigated after intravenous injection.

4.2.2.4.2 **Radiolabeling of Iron Oxide NPs for Multimodal Imaging** Iron oxide NPs are superb imaging agents because their physicochemical properties allow the tuning of pharmacokinetics as well as attachment of multiple moieties to their surface. Since PET and SPECT can provide extremely sensitive and high-resolution images, great efforts have been devoted to develop radiolabeled iron oxide NPs. Reported radiolabeling methods of iron oxide NPs for multimodal imaging are summarized in Table 4.2.

4.2.2.5 Silver Nanoparticles (Ag NPs)

Ag NPs are becoming increasingly popular as antibiotic agents in medical devices, wound dressings, textiles, and appliances such as washing machines and refrigerators [123]. Ag-110 m ($T_{1/2} = 250.4$ days, $E_\gamma = 657.7$ keV) labeled Ag NPs have been prepared by direct irradiation of the cold NPs with thermal neutrons via (n, γ) reaction [124], utilization of a radioactive starting material $^{110m}Ag(NO_3)_3$ in the production process [7] or mixing of $^{110m}Ag(NO_3)_3$ with cold Ag NPs via isotopic exchange [7, 125].

In order to track *in vivo* distribution of Ag NPs after systemic administration by SPECT imaging, Chrastina and Schnitzer [126] developed a rapid radioiodination method using Chloramine-T as an oxidant. Poly(*N*-vinyl-2-pyrrolidone)-capped Ag NPs (about 12 nm) were radiolabeled by chemisorption of elemental iodine onto the metal surface with a 80% yield of radiolabeling efficiency. Radiolabeled Ag NPs were intravenously injected in mice, and the distribution pattern of ^{125}I was traced *in vivo* by noninvasive whole-body SPECT imaging, which revealed a strong ^{125}I signal in the abdominal area, particularly, in the liver and spleen. Thyroid uptake was negligible at 0.5 and 4 h postinjection, but it became apparent at 24 h, probably because of catabolism of ^{125}I-Ag NPs and release of free iodine.

4.2.2.6 Titanium Dioxide Nanoparticles (Titania or TiO_2 NPs)

TiO_2 NPs are now massively produced and widely used in many commercial products, including paints, cosmetics, sunscreens, food additives, and photo catalyst [127]. Among radioisotopes of titanium, ^{44}Ti ($T_{1/2} = 60.4$ a, $\varepsilon = 100\%$) and ^{45}Ti ($T_{1/2} = 3.08$ h, $\beta^+ = 84.8\%$) are suitable for radiolabeling. Titanium-45 as a candidate for PET imaging can be produced by proton irradiation of Sc foils using via ^{45}Sc(p,n)^{45}Ti reaction. A recent study carried out by Hildebrand *et al*. [128] presented three different options for radiolabeling of commercial titania NPs. The first method is mixing $^{44,45}TiCl_4$ aqueous solutions with powdered TiO_2

Table 4.2 An overview of radiolabeling of iron oxide NPs for multimodal imaging.

Core	Surface coating	Isotope	Labeling method	Combined imaging modalities	References
Fe_3O_4	$–NH_2$ or –COOH	^{11}C	Methylation with ^{11}C-MeI	PET/MRI	[103]
SPION	Cross-linked dextran	^{18}F	Cu-catalyzed azide–alkyne cycloaddition	PET/CT/MRI	[104]
$MnFe_2O_4$ and Fe_3O_4	$Al(OH)_3$	^{18}F	Chemical sorption	PET/MRI	[105]
SPION	Dextran	^{64}Cu	Dithiocarbamate bisphosphonate (dtcbp)	PET/MRI	[106]
SPION	Dextran sulfate	^{64}Cu	DOTA	PET/MRI	[107]
$MnFe_2O_4$ and Fe_3O_4	$Al(OH)_3$	^{64}Cu	Bifunctional chelate bisphosphonate	PET/MRI	[105]
SPION	PEG	^{64}Cu	Bifunctional chelate NOTA	PET/MRI	[108]
Fe_3O_4	Chitosan	^{64}Cu	Physical sorption	PET/MRI	[109]
Fe_3O_4	HAS	^{64}Cu	DOTA	PET/NIRF/MRI	[110]
SPION	PEGylated phospholipids	^{64}Cu	DOTA	PET/MRI	[111]
SPION-Au	Thiolated PEG	^{64}Cu	Bifunctional chelate NOTA	PET/Optical/MRI	[112]
SPION	Dextran	^{64}Cu	Incorporation during synthesis	PET/MRI	[113]
γ-Fe_2O_3	PLGA-*b*-PEG-COOH	^{68}Ga	Bifunctional chelate NODA	PET/MRI	[114]
SPION	PEG	^{68}Ga	Direct labeling	PET/MRI/Cherenkov luminescence	[115]
SPION	PAA	^{69}Ge	pH-dependent sorption	PET/MRI	[116]
SPION	–	^{99m}Tc	Bifunctional chelate bisphosphonate	SPECT/MRI	[117]
SPION	Dopamine	^{99m}Tc	DTPA	SPECT/MRI	[118]
SPION	Oleylamine	^{99m}Tc	PEG(5)-BP	SPECT/MRI	[119]
SPION	PEG	^{99m}Tc	Physical sorption	SPECT/MRI	[120]
$CoFe_2O_4$	EHO	^{99m}Tc	Physical sorption	SPECT/MRI	[121]
SPION	Carboxy methyl dextran	^{111}In	Carbodiimide coupling reaction	SPECT/MRI	[122]

PAA: water soluble poly(acrylic acid), PLGA-*b*-PEG-COOH: poly(D,L-lactide-*co*-glycolide)-*block*-poly(ethylene glycol) copolymer, PEG: poly-ethylene glycol, NODA: 2,2′-(7-(4-((2-aminoethyl)amino)-1-carboxy-4-oxobutyl)-1,4,7-triazonane-1,4-diyl)diacetic acid, *p*-SCN-Bn-NOTA: 2-*S*-(4-isothiocyanatobenzyl)-1,4,7-triazacyclononane-1,4,7-triaceticacid, *p*-NH2-Bz-DOTA: *S*-2-(4-aminobenzyl)-1,4,7,10-tetraazacyclododecane tetra acetic acid, NIRF: near-infrared fluorescence, HAS: human serum albumin, PEG(5)-BP: polyethylene-glycol polymer conjugate containing a terminal 1,1-bisphosphonate, and EHO: ethyl 12-(hydroxyamino)-12-oxododecanoate.

NPs; $^{44,45}TiO_2$ NPs are obtained via isotopic exchange. The second method is radiolabeling with ^{48}V ($T_{1/2} = 15.97$ days, $\varepsilon = 50.3\%$, $\beta^+ = 49.7\%$) by irradiation of titania with a cyclotron generated proton beam via $^{48}Ti(p,n)^{48}V$ reaction. The last one is exposure of TiO_2 NP powder mixed with fine-grained LiCl to a proton beam; labeling occurs in a fraction of the NPs by implantation of recoiling ^{7}Be atoms produced via $^{7}Li(p,n)^{7}Be$ reaction. The authors indicated that their radiolabeling procedures can ensure the stability and consistency of important particle properties such as size and morphology.

Pérez-Campaña *et al*. [129] demonstrated that direct proton irradiation of ^{18}O-enriched TiO_2 NPs prepared by precipitation in basic aqueous media using ^{18}O-enriched water as solvent allowed sufficient activation through the generation of β^+ emitter ^{18}F via $^{18}O(p,n)$ ^{18}F reaction to perform *in vivo* biodistribution studies in rats using i.v. and oral administration and PET. During activation of TiO_2 NPs, other radionuclides, that is, ^{13}N, ^{47}V, ^{44g}Sc, and ^{48}V were simultaneously generated. The combination of *in vivo* imaging studies using PET to assess the biodistribution of the NPs at short times with relative long-term studies performed by organ removal and determination of the amount of radioactivity using gamma counting can be foreseen.

4.2.2.7 Zinc Oxide Nanoparticles (ZnO NPs)

ZnO NPs are widely used in optoelectronics, cosmetics, catalysts, ceramics, pigments, and so on. Chen *et al*. [130] prepared radioactive ZnO NPs by irradiation of "cold" ZnO NPs with thermal neutrons in a nuclear reactor. A proportion of stable isotopes, ^{64}Zn and ^{68}Zn in the sample, can be converted to radioactive ^{65}Zn (with a half-life of 244 days) and ^{69m}Zn (with half-life of 13.76 h) by (n, γ) reactions. They studied the biodistribution of ^{65}ZnO NPs and further compared the kinetics and tissue distribution of 10 nm ^{65}ZnO NPs, 71 nm ^{65}ZnO NPs, and $^{65}Zn(NO_3)_2$ in mice after intravenous injection [130, 131].

4.2.2.8 Silicon Dioxide Nanoparticles (Silica or SiO_2 NPs)

Silica-based nanoparticles have attracted immense interest in the biomedical field as vehicles for targeted delivery because of their excellent properties such as monodispersity, large surface area, and high drug loading efficiency. Silica NPs are also found in many personal care products and in certain foods [132].

Malfatti *et al*. [132] synthesized amorphous spherical ^{14}C-labeled silica NPs by hydrolyzing tetraethoxysilane with NH_3 as a catalyst in microemulsion media. To introduce the ^{14}C isotope into SiO_2, ^{14}C-acrylic acid was used as a ^{14}C precursor. Carbon-14 was chemically grafted into silane through radical-induced polymerization between the ^{14}C-acrylic acid and allyltrimethoxysilane. The biodistribution and pharmacokinetics profiles of ^{14}C-labeled SiO_2 NPs after intravenous administration were investigated in mice using accelerator mass spectrometry (AMS). The results indicate that silica NPs were rapidly eliminated from the plasma and distributed to tissues of the reticuloendothelial system including the spleen, liver, kidney, lung, and cervical lymph nodes.

Huang *et al*. [133] developed a mesoporous silica nanoparticle–based multifunctional nanoprobe (near-infrared optical, magnetic resonance, and positron emission tomography) for sentinel lymph nodes imaging. Copper-64 labeling was accomplished by incubation of DOTA-labeled particles with $^{64}Cu(OAc)_2$. Then the authors applied the nanoprobe to visualize tumor metastatic sentinel lymph nodes in an animal model. The images obtained from different modalities are consistent and complementary indicating that the imaging probe was highly stable and robust.

4.2.2.9 Dendrimers and Polystyrene Nanoparticles

Polymeric nanomaterials such as dendrimers and polystyrene nanoparticles are of considerable interest in the field of nanomedicine due to their potential for surface modification and biocompatible nature.

Seo *et al*. [134] synthesized a dendritic form of LyP-1 on solid phase using lysine as the core structural element. LyP-1, a cyclic 9-amino acid peptide, recognizes and binds to p32 proteins on activated macrophages. A macrocyclic bifunctional chelating agent, 6-[*p*-(bromoacetamido)benzyl]-1,4,8,11-tetraazacyclotetradecane-*N*,*N*′,*N*″,*N*‴-tetraacetic acid (6-BAT) was attached to the dendrimer via free thiol groups of C-terminal cysteine. ^{64}Cu-labeled LyP-1-dendrimer was obtained by reaction of the functionalized dendrimer with ^{64}Cu.

Polystyrene nanoparticles have been used as models of particulate matters. Chen *et al*. [135] radiolabeled polystyrene nanoparticles with ^{125}I using the thallic method. The results of X-ray photoelectron spectroscopy (XPS) and Fourier transform infrared spectroscopy (FT-IR) confirmed the formation of a stable covalent bond between I and aryl group of the polymer particles. Subsequently, pulmonary and systemic distributions of the labeled nanoparticles in rats after intratracheal instillation were investigated. Palko *et al*. [136] carried out a similar study using ^{64}Cu-labeled polystyrene nanoparticles. Cu-64 was preinserted into a chelator macrocyclic chelating agent *p*-SCN-Bn-DOTA. Cu-64-labeled polystyrene nanoparticles were obtained by the direct conjugate between the amine groups of surfactant-free aliphatic amine polystyrene nanoparticles and an amine-reactive form (isothiocyanate) of DOTA. The deposition and biodistribution of the labeled nanoparticles in mice after intratracheal instillation were determined by PET imaging.

4.3 Summary and Outlook

In the past decade, studies on nano(eco)toxicology and nanomedicine are getting more and more attention. Quantitative determination of engineered nanomaterials in biological and environmental matrices is the main difficulty of these studies and is of paramount importance to understand the behavior of nanoparticles in the environment and organisms. For this purpose, a number of modern

spectroscopic, spectrometric, and spectrophotometric techniques have been used. Radiotracer technique, developed by George de Hevesy about 100 years ago, is considered to be the best answer. It can offer an outstanding approach for the *in vivo* quantification of nanoparticles with high precision and high sensitivity. When combined with nuclear imaging methods such as SPECT and PET, this technique will enable the acquirement of real-time three-dimensional image data of the radiolabeled NPs in the whole body. However, radiotracer technique cannot solve all problems. It is well known that most nanomaterials are chemically reactive and may undergo various transformations in biological and environmental conditions. To fully understand the biological and environmental impacts of engineered nanomaterials, speciation analysis of nanoparticles in samples using X-ray absorption spectroscopy (XAS), scanning transmission X-ray microscopy (STXM), and so on, is generally required.

Other concerns of this technique include the possible modification of the properties of NPs during the labeling processes and stability of the radiolabels *in vivo*. It is can be expected that the technique will become more widely used in the future studies, but the aforementioned issues need to be carefully considered to ensure the validation of the results. Meanwhile, more simple and reliable labeling methods are also needed.

References

1. Kagan, V.E., Bayir, H., and Shvedova, A.A. (2005) Nanomedicine and nanotoxicology: two sides of the same coin. *Nanomedicine*, **1** (4), 313–316.
2. Powell, M.C. and Kanarek, M.S. (2006) Nanomaterial health effects—part 1: background and current knowledge. *Wis. Med. J.*, **105** (2), 16–20.
3. Zhang, Z. *et al.* (2006) Isotopic tracer studies on the metabolism and functional roles of mineral elements in Institute of High Energy Physics, China. *J. Nucl. Sci. Technol.*, **43** (4), 450–454.
4. Gibson, N. *et al.* (2011) Radiolabelling of engineered nanoparticles for in vitro and in vivo tracing applications using cyclotron accelerators. *Arch. Toxicol.*, **85** (7), 751–773.
5. NIDC (2015) Isotope Production Methods, https://www.isotopes.gov/sites/production.html (accessed August 2015).
6. Goel, S. *et al.* (2014) Intrinsically radiolabeled nanoparticles: an emerging paradigm. *Small*, **10** (19), 3825–3830.
7. Zuykov, M., Pelletier, E., and Demers, S. (2011) Colloidal complexed silver and silver nanoparticles in extrapallial fluid of *Mytilus edulis*. *Mar. Environ. Res.*, **71** (1), 17–21.
8. Zhang, Z. *et al.* (2011) Uptake and distribution of ceria nanoparticles in cucumber plants. *Metallomics*, **3** (8), 816–822.
9. Chanda, N. *et al.* (2010) Radioactive gold nanoparticles in cancer therapy: therapeutic efficacy studies of GA-^{198}AuNP nanoconstruct in prostate tumor-bearing mice. *Nanomedicine*, **6** (2), 201–209.
10. Scrivens, W.A., Tour, J.M., Creek, K.E., and Pirisi, L. (1994) Synthesis of ^{14}C-labeled C_{60}, its suspension in water, and its uptake by human keratinocytes. *J. Am. Chem. Soc.*, **116** (10), 4517–4518.
11. Zhang, Z., Zhao, Y., and Chai, Z. (2009) Applications of radiotracer techniques for the pharmacology and toxicology studies of nanomaterials. *Chin. Sci. Bull.*, **54** (2), 173–182.

12. Holzwarth, U. *et al.* (2014) (^{7})Be-recoil radiolabelling of industrially manufactured silica nanoparticles. *J. Nanopart. Res.*, **16** (9), 2574.
13. Pérez-Campaña, C. *et al.* (2012) Tracing nanoparticles in vivo: a new general synthesis of positron emitting metal oxide nanoparticles by proton beam activation. *Analyst*, **137** (21), 4902–4906.
14. Pérez-Campaña, C. *et al.* (2013) Biodistribution of different sized nanoparticles assessed by positron emission tomography: a general strategy for direct activation of metal oxide particles. *ACS Nano*, **7** (4), 3498–3505.
15. Oriuchi, N. and Yang, D. (2001) in *Targeted Molecular Imaging in Oncology* (eds E.E. Kim and D. Yang), Springer, New York, pp. 83–87.
16. Xing, Y. *et al.* (2014) Radiolabeled nanoparticles for multimodality tumor imaging. *Theranostics*, **4** (3), 290–306.
17. Brechbiel, M.W. (2008) Bifunctional chelates for metal nuclides. *Q. J. Nucl. Med. Mol. Imaging*, **52** (2), 166–173.
18. Lattuada, L. *et al.* (2011) The synthesis and application of polyamino polycarboxylic bifunctional chelating agents. *Chem. Soc. Rev.*, **40** (5), 3019–3049.
19. Temple, S. (2006) Scintillation counting, in *Radiotracers in Drug Development* (ed. S.T. Graham Lappin), CRC Press, Boca Raton, FL.
20. Khandaker, M.U., Jojo, P.J., and Kassim, H.A. (2012) Determination of primordial radionuclides in natural samples using HPGe gamma-ray spectrometry. *APCBEE Procedia*, **1**, 187–192.
21. Lu, F.-M. and Yuan, Z. (2015) PET/SPECT molecular imaging in clinical neuroscience: recent advances in the investigation of CNS diseases. *Quant. Imaging Med. Surg.*, **5** (3), 433–447.
22. Alexiou, G.A. *et al.* (2012) Imaging meningiomas with 99mTc-tetrofosmin SPECT. *Neurosurgery*, **70** (4), E1055.
23. Bullard-Dillard, R. *et al.* (1996) Tissue sites of uptake of ^{14}C-labeled C_{60}. *Bioorg. Chem.*, **24** (4), 376–385.
24. Petersen, E.J., Huang, Q., and Weber, W.J. (2008) Ecological uptake and depuration of carbon nanotubes by *Lumbriculus variegatus*. *Environ. Health Perspect.*, **116** (4), 496–500.
25. Petersen, E.J., Huang, Q., and Weber, J.W.J. (2008) Bioaccumulation of radiolabeled carbon nanotubes by *Eisenia foetida*. *Environ. Sci. Technol.*, **42** (8), 3090–3095.
26. Ferguson, P.L. *et al.* (2008) Influence of sediment amendment with single-walled carbon nanotubes and diesel soot on bioaccumulation of hydrophobic organic contaminants by benthic invertebrates. *Environ. Sci. Technol.*, **42** (10), 3879–3885.
27. Guo, X. *et al.* (2013) Biological uptake and depuration of radio-labeled graphene by *Daphnia magna*. *Environ. Sci. Technol.*, **47** (21), 12524–12531.
28. Yamago, S. *et al.* (1995) In vivo biological behavior of a water-miscible fullerene: ^{14}C labeling, absorption, distribution, excretion and acute toxicity. *Chem. Biol.*, **2** (6), 385–389.
29. Foley, S. *et al.* (2002) Cellular localisation of a water-soluble fullerene derivative. *Biochem. Biophys. Res. Commun.*, **294** (1), 116–119.
30. Deng, X. *et al.* (2007) Translocation and fate of multi-walled carbon nanotubes in vivo. *Carbon*, **45** (7), 1419–1424.
31. Ohtsuki, T. *et al.* (1999) Direct preparation of radioactive fullerenes as a tracer for applications. *Biol. Trace Elem. Res.*, **71/72** (1), 489–498.
32. Masumoto, K. *et al.* (1999) Direct synthesis of radioactive carbon labeled fullerenes using nuclear reactions. *J. Radioanal. Nucl. Chem.*, **239** (1), 201–206.
33. Li, Y.G. *et al.* (2001) Radioiodination of C60 derivative C_{60}(OH)xOy. *J. Radioanal. Nucl. Chem.*, **250** (2), 363–364.
34. Ji, Z.Q. *et al.* (2006) Biodistribution and tumor uptake of C_{60}(OH) x in mice. *J. Nanopart. Res.*, **8** (1), 53–63.
35. Wang, H. *et al.* (2004) Biodistribution of carbon single-wall carbon nanotubes in mice. *J. Nanosci. Nanotechnol.*, **4** (8), 1–6.
36. Wang, H.F. *et al.* (2004) XPS study of C-I covalent bond on Single-walled

Carbon Nanotubes (SWNTs). *Acta Phys. Chim. Sin.*, **20** (07), 673–675.
37. Tabata, Y. and Ikada, Y. (1999) Biological functions of fullerene. *Pure Appl. Chem.*, **71**, 2047–2053.
38. Ran, T. *et al.* (2006) Radiolabeling of 1-[N,N'-bis(2-chloroethyl)-4-aminophenyl]-N-methyl-fullereno-C_{60}-[1,9-c]pyrrolidine with ^{125}I. *J. Radioanal. Nucl. Chem.*, **268** (3), 599–603.
39. Li, Q. *et al.* (2001) Biodistribution of fullerene derivative C_{60}(OH)x(O)y. *Chin. Sci. Bull.*, **46** (19), 1615–1617.
40. Li, Q. *et al.* (2002) Preparation of ^{99m}Tc-C_{60}(OH)x and its biodistribution studies. *Nucl. Med. Biol.*, **29** (6), 707–710.
41. Hong, H. *et al.* (2012) In vivo targeting and positron emission tomography imaging of tumor vasculature with ^{66}Ga-labeled nano-graphene. *Biomaterials*, **33** (16), 4147–4156.
42. Li, Y.G. *et al.* (2005) Preparation of ^{67}Ga-C_{60}(OH)x and its biodistribution. *J. Radioanal. Nucl. Chem.*, **265**, 127–131.
43. Kafa, H. *et al.* (2015) The interaction of carbon nanotubes with an in vitro blood-brain barrier model and mouse brain in vivo. *Biomaterials*, **53**, 437–452.
44. Singh, R. *et al.* (2006) Tissue biodistribution and blood clearance rates of intravenously administered carbon nanotube radiotracers. *Proc. Natl. Acad. Sci. U.S.A.*, **103** (9), 3357–3362.
45. Liu, Z. *et al.* (2007) In vivo biodistribution and highly efficient tumour targeting of carbon nanotubes in mice. *Nat. Nanotechnol.*, **2** (1), 47–52.
46. Hong, H. *et al.* (2012) In vivo targeting and imaging of tumor vasculature with radiolabeled, antibody-conjugated nanographene. *ACS Nano*, **6** (3), 2361–2370.
47. Kikuchi, K. *et al.* (1994) Encapsulation of radioactive Gd-159 and Tb-161 atoms in fullerene cages. *J. Am. Chem. Soc.*, **116** (21), 9775–9776.
48. Kobayashi, K. *et al.* (1995) Activation and tracer techniques for study of metallofullerenes. *J. Radioanal. Nucl. Chem. Art.*, **192** (1), 81–89.
49. Cagle, D.W. *et al.* (1996) Synthesis, characterization, and neutron activation of holmium metallofullerenes. *J. Am. Chem. Soc.*, **118** (34), 8043–8047.
50. Cagle, D.W. *et al.* (1999) In vivo studies of fullerene-based materials using endohedral metallofullerene radiotracers. *Proc. Natl. Acad. Sci. U.S.A.*, **96** (9), 5182–5187.
51. Braun, T. and Rausch, H. (1998) Nuclear recoil implosion for producing endohedral radiofullerenes. *Carbon*, **36** (11), 1708–1709.
52. Braun, T. and Rausch, H. (1998) Radioactive endohedral metallofullerenes formed by prompt gamma-generated nuclear recoil implosion. *Chem. Phys. Lett.*, **288** (2-4), 179–182.
53. Braun, T. and Rausch, H. (1998) Chemical effects of nuclear recoil in and on fullerene cages. *Magy. Kem. Foly.*, **104** (6), 232–236.
54. Braun, T. and Rausch, H. (2003) Recoil implosion via nuclear activation for the synthesis of endohedral radiofullerenes. *Indian J. Chem., Sect A*, **42** (12), 2921–2924.
55. Braun, T. and Rausch, H. (2000) Nuclear recoil implosion for generating radioisotopically labeled fullerene endohedrals and cages. *J. Radioanal. Nucl. Chem.*, **243** (1), 27–30.
56. Gadd, G.E. *et al.* (1996) Neutron irradiation of Ar_1C_{60}. *Chem. Phys. Lett.*, **261** (3), 221–227.
57. Gadd, G.E. *et al.* (1997) Endohedral formation from neutron activation of interstitial rare gas C-60 fullerides. *Fullerene Sci. Technol.*, **5** (5), 871–902.
58. Gadd, G.E. *et al.* (1998) Evidence for rare gas endohedral fullerene formation from gamma recoil from HPLC studies. *J. Am. Chem. Soc.*, **120** (40), 10322–10325.
59. Gadd, G.E. *et al.* (1997) Endohedral fullerene formation through prompt gamma recoil. *Chem. Phys. Lett.*, **270** (1-2), 108–114.
60. Ohtsuki, T. *et al.* (1996) Insertion of be atoms in C-60 fullerene cages: Be@C-60. *Phys. Rev. Lett.*, **77** (17), 3522–3524.
61. Ohtsuki, T. *et al.* (1998) Insertion of Xe and Kr atoms into C-60 and C-70

fullerenes and the formation of dimers. *Phys. Rev. Lett.*, **81** (5), 967–970.
62. Grushko, Y.S. *et al.* (2006) Radioactive metallofullerenes: hot atom chemistry aspects. *Fullerenes Nanotubes Carbon Nanostruct.*, **14** (2-3), 249–259.
63. Saha, S.K. *et al.* (2006) Encapsulation of radioactive isotopes into C-60 fullerene cage by recoil implantation technique. *Nucl. Instrum. Methods Phys. Res., Sect. B*, **243** (2), 277–281.
64. Abbas, K. *et al.* (2013) Feasibility study of production of radioactive carbon black or carbon nanotubes in cyclotron facilities for nanobioscience applications. *Appl. Radiat. Isot.*, **73**, 44–48.
65. Huang, X.L. *et al.* (2013) Effect of injection routes on the biodistribution, clearance, and tumor uptake of carbon dots. *ACS Nano*, **7** (7), 5684–5693.
66. James, J.M. and Testa, H.J. (1995) The use of $^{99}Tc^{m}$-technegas in the investigation of patients with pulmonary thromboembolism. *Nucl. Med. Commun.*, **16** (10), 802–810.
67. Senden, T.J. *et al.* (1997) The physical and chemical nature of technegas. *J. Nucl. Med.*, **38** (8), 1327–1333.
68. Llop, J., Gomez-Vallejo, V., and Gibson, N. (2013) Quantitative determination of the biodistribution of nanoparticles: could radiolabeling be the answer? *Nanomedicine (Lond.)*, **8** (7), 1035–1038.
69. Chen, F. *et al.* (2013) In vivo tumor targeting and image-guided drug delivery with antibody-conjugated, radiolabeled mesoporous silica nanoparticles. *ACS Nano*, **7** (10), 9027–9039.
70. Ferro-Flores, G. *et al.* (2014) Multifunctional radiolabeled nanoparticles for targeted therapy. *Curr. Med. Chem.*, **21** (1), 124–138.
71. Srikanth, K. *et al.* (2015) Aluminium oxide nanoparticles induced morphological changes, cytotoxicity and oxidative stress in Chinook salmon (CHSE-214) cells. *J. Appl. Toxicol.*, **35** (10), 1133–1140.
72. Xu, C. and Qu, X. (2014) Cerium oxide nanoparticle: a remarkably versatile rare earth nanomaterial for biological applications. *NPG Asia Mater.*, **6**, e90.
73. Soltani, F. *et al.* (2015) Production of cerium-141 using ceria and nanoceria powder: a potential radioisotope for simultaneous therapeutic and diagnostic applications. *J. Radioanal. Nucl. Chem.*, **303** (1), 385–391.
74. Oughton, D.H. *et al.* (2008) Neutron activation of engineered nanoparticles as a tool for tracing their environmental fate and uptake in organisms. *Environ. Toxicol. Chem.*, **27** (9), 1883–1887.
75. Cohen, J.M. *et al.* (2014) Tracking translocation of industrially relevant engineered nanomaterials (ENMs) across alveolar epithelial monolayers in vitro. *Nanotoxicology*, **8** (Suppl. 1), 216–225.
76. Simonelli, F., Marmorato, P., Abbas, K., Ponti, J., Kozempel, J., Holzwarth, U., Franchini, F., and Rossi, F. (2011) Cyclotron production of radioactive CeO_2 nanoparticles and their application for in vitro uptake studies. *IEEE Trans. Nanobiosci.*, **10** (1), 44–50.
77. Bakht, M., Sadeghi, M., and Tenreiro, C. (2012) A novel technique for simultaneous diagnosis and radioprotection by radioactive cerium oxide nanoparticles: study of cyclotron production of ^{137m}Ce. *J. Radioanal. Nucl. Chem.*, **292** (1), 53–59.
78. Xiao, H. *et al.* (2010) Lung deposition and extrapulmonary translocation of nano-ceria after intratracheal instillation. *Nanotechnology*, **21** (28), 285103.
79. Zhang, P. *et al.* (2012) Distribution and bioavailability of ceria nanoparticles in an aquatic ecosystem model. *Chemosphere*, **89** (5), 530–535.
80. Rojas, S. *et al.* (2012) In vivo biodistribution of amino-functionalized ceria nanoparticles in rats using positron emission tomography. *Mol. Pharmaceutics*, **9** (12), 3543–3550.
81. Yakoh, A. *et al.* (2015) Biomedical probes based on inorganic nanoparticles for electrochemical and optical spectroscopy applications. *Sensors*, **15** (9), 21427.
82. Schleh, C. *et al.* (2012) Size and surface charge of gold nanoparticles determine absorption across intestinal barriers

and accumulation in secondary target organs after oral administration. *Nanotoxicology*, **6** (1), 36–46.

83. Hirn, S. *et al.* (2011) Particle size-dependent and surface charge-dependent biodistribution of gold nanoparticles after intravenous administration. *Eur. J. Pharm. Biopharm.*, **77** (3), 407–416.

84. Lipka, J. *et al.* (2010) Biodistribution of PEG-modified gold nanoparticles following intratracheal instillation and intravenous injection. *Biomaterials*, **31** (25), 6574–6581.

85. Wang, Y. *et al.* (2013) Radioluminescent gold nanocages with controlled radioactivity for real-time in vivo imaging. *Nano Lett.*, **13** (2), 581–585.

86. Black, K.C.L. *et al.* (2014) Radioactive ^{198}Au-doped nanostructures with different shapes for in vivo analyses of their biodistribution, tumor uptake, and intratumoral distribution. *ACS Nano*, **8** (5), 4385–4394.

87. Schleh, C. *et al.* (2013) Biodistribution of inhaled gold nanoparticles in mice and the influence of surfactant protein D. *J. Aerosol Med. Pulm. Drug Deliv.*, **26** (1), 24–30.

88. Xie, H. *et al.* (2010) In vivo PET imaging and biodistribution of radiolabeled gold nanoshells in rats with tumor xenografts. *Int. J. Pharm.*, **395** (1–2), 324–330.

89. Bhatnagar, P. *et al.* (2013) Imaging of genetically engineered T cells by PET using gold nanoparticle complexed to Copper-64. *Integr. Biol.*, **5** (1), 231–238.

90. Tian, M. *et al.* (2013) Tumor uptake of hollow gold nanospheres after intravenous and intra-arterial injection: PET/CT study in a rabbit VX2 liver cancer model. *Mol. Imaging Biol.*, **15** (5), 614–624.

91. Wang, Y. *et al.* (2012) Evaluating the pharmacokinetics and in vivo cancer targeting capability of Au nanocages by Positron emission tomography imaging. *ACS Nano*, **6** (7), 5880–5888.

92. Zhu, J. *et al.* (2014) Rapid ^{18}F-labeling and loading of PEGylated gold nanoparticles for in vivo applications. *Bioconjugate Chem.*, **25** (6), 1143–1150.

93. Agarwal, A. *et al.* (2011) Dual-mode imaging with radiolabeled gold nanorods. *J. Biomed. Opt.*, **16** (5), 051307.

94. Shao, X. *et al.* (2011) ^{125}I-labeled gold nanorods for targeted imaging of inflammation. *ACS Nano*, **5** (11), 8967–8973.

95. Xia, S. *et al.* (2011) Synthesis and bioevaluation of ^{125}I-labeled gold nanorods. *Nanotechnology*, **22** (13), 135102.

96. Jang, B. *et al.* (2012) Gold nanorods for target selective SPECT/CT imaging and photothermal therapy in vivo. *Quant. Imaging Med. Surg.*, **2** (1), 1–11.

97. Weissleder, R., Stark, D.D., Engelstad, B.L., Bacon, B.R., Compton, C.C., White, D.L., Jacobs, P., and Lewis, J. (1989) Superparamagnetic iron oxide: pharmacokinetics and toxicity. *AJR Am J Roentgenol*, **152** (1): 167–173.

98. Zhu, M.T., Feng, W.Y., Wang, Y., Wang, B., Wang, M., Ouyang, H., Zhao, Y.L., and Chai, Z.F. (2009) Particokinetics and extrapulmonary translocation of intratracheally instilled ferric oxide nanoparticles in rats and the potential health risk assessment. *Toxicol Sci*, **107** (2): 342–351.

99. Freund, B., Tromsdorf, U.I., Bruns, O.T., Heine, M., Giemsa, A., Bartelt, A., Salmen, S.C., Raabe, N., Heeren, J., Ittrich, H., Reimer, R., Hohenberg, H., Schumacher, U., Weller, H., and Nielsen, P. (2012) A simple and widely applicable method to 59Fe-radiolabel monodisperse superparamagnetic iron oxide nanoparticles for in vivo quantification studies. *ACS Nano*, **6** (8): 7318–7325.

100. de Barros, A.L.B. *et al.* (2014) Assessment of global cardiac uptake of radiolabeled iron oxide nanoparticles in apolipoprotein E-deficient mice: implications for imaging cardiovascular inflammation. *Mol. Imaging Biol.*, **16** (3), 330–339.

101. Hosseini-Salekdeh, S. *et al.* (2012) Evaluation of radiogallium-labeled, folate-embedded superparamagnetic nanoparticles in fibrosarcoma-bearing mice. *J. Cancer Res. Ther.*, **8** (2), 204–208.

102. Shanehsazzadeh, S. *et al.* (2013) Estimated background doses of ^{67}Ga-DTPA-USPIO in normal Balb/c mice as a potential therapeutic agent for liver and spleen cancers. *Nucl. Med. Commun.*, **34** (9), 915–925.

103. Sharma, R. *et al.* (2013) Carbon-11 radiolabeling of iron-oxide nanoparticles for dual-modality PET/MR imaging. *Nanoscale*, **5** (16), 7476–7483.

104. Devaraj, N.K. *et al.* (2009) ^{18}F labeled nanoparticles for in vivo PET-CT imaging. *Bioconjug. Chem.*, **20** (2), 397–401.

105. Cui, X. *et al.* (2014) Aluminium hydroxide stabilised $MnFe_2O_4$ and Fe_3O_4 nanoparticles as dual-modality contrasts agent for MRI and PET imaging. *Biomaterials*, **35** (22), 5840–5846.

106. de Rosales, R.T.M. *et al.* (2011) Synthesis of Cu-64(II)-bis(dithiocarbamate bisphosphonate) and its conjugation with superparamagnetic iron oxide nanoparticles: in vivo evaluation as dual-modality PET-MRI agent. *Angew. Chem. Int. Ed.*, **50** (24), 5509–5513.

107. Jarrett, B.R. *et al.* (2008) Synthesis of Cu-64-labeled magnetic nanoparticles for multimodal imaging. *Bioconjugate Chem.*, **19** (7), 1496–1504.

108. Yang, X. *et al.* (2011) cRGD-functionalized, DOX-conjugated, and ^{64}Cu-labeled superparamagnetic iron oxide nanoparticles for targeted anticancer drug delivery and PET/MR imaging. *Biomaterials*, **32** (17), 4151–4160.

109. Pala, A. *et al.* (2012) Labelling of granulocytes by phagocytic engulfment with Cu-64-labelled chitosan-coated magnetic nanoparticles. *Mol. Imaging Biol.*, **14** (5), 593–598.

110. Xie, J. *et al.* (2010) PET/NIRF/MRI triple functional iron oxide nanoparticles. *Biomaterials*, **31** (11), 3016–3022.

111. Glaus, C. *et al.* (2010) In vivo evaluation of Cu-64-labeled magnetic nanoparticles as a dual-modality PET/MR imaging agent. *Bioconjugate Chem.*, **21** (4), 715–722.

112. Yang, M. *et al.* (2013) Affibody modified and radiolabeled gold-iron oxide hetero-nanostructures for tumor PET, optical and MR imaging. *Biomaterials*, **34** (11), 2796–2806.

113. Wong, R.M. *et al.* (2012) Rapid size-controlled synthesis of dextran-coated, Cu-64-doped iron oxide nanoparticles. *ACS Nano*, **6** (4), 3461–3467.

114. Locatelli, E. *et al.* (2012) Biocompatible nanocomposite for PET/MRI hybrid imaging. *Int. J. Nanomed.*, **7**, 6021–6033.

115. Madru, R. *et al.* (2014) ^{68}Ga-labeled superparamagnetic iron oxide nanoparticles (SPIONs) for multi-modality PET/MR/Cherenkov luminescence imaging of sentinel lymph nodes. *Am. J. Nucl. Med. Mol. Imaging*, **4** (1), 60–69.

116. Chakravarty, R. *et al.* (2014) Intrinsically germanium-69-labeled iron oxide nanoparticles: synthesis and in-vivo dual-modality PET/MR imaging. *Adv. Mater.*, **26** (30), 5119–5123.

117. de Rosales, R.T.M. *et al.* (2011) Tc-99m-bisphosphonate-iron oxide nanoparticle conjugates for dual-modality biomedical imaging. *Bioconjugate Chem.*, **22** (3), 455–465.

118. Lee, C.M. *et al.* (2009) Superparamagnetic iron oxide nanoparticles as a dual imaging probe for targeting hepatocytes in vivo. *Magn. Reson. Med.*, **62** (6), 1440–1446.

119. Sandiford, L. *et al.* (2013) Bisphosphonate-anchored PEGylation and radiolabeling of superparamagnetic iron oxide: long-circulating nanoparticles for in vivo multimodal (T1 MRI-SPECT) imaging. *ACS Nano*, **7** (1), 500–512.

120. Madru, R. *et al.* (2012) Tc-99m-labeled superparamagnetic iron oxide nanoparticles for multimodality SPECT/MRI of sentinel lymph nodes. *J. Nucl. Med.*, **53** (3), 459–463.

121. Psimadas, D. *et al.* (2012) Preliminary evaluation of a Tc-99m labeled hybrid nanoparticle bearing a cobalt ferrite core: in vivo biodistribution. *J. Biomed. Nanotechnol.*, **8** (4), 575–585.

122. Misri, R. *et al.* (2012) Development and evaluation of a dual-modality (MRI/SPECT) molecular imaging bioprobe. *Nanomedicine*, **8** (6), 1007–1016.

123. Stensberg, M.C. *et al.* (2011) Toxicological studies on silver nanoparticles: challenges and opportunities in assessment, monitoring and imaging. *Nanomedicine*, **6** (5), 879–898.

124. Melnik, E.A. *et al.* (2013) Transfer of silver nanoparticles through the placenta and breast milk during in vivo experiments on rats. *Acta Naturae*, **5** (3), 107–115.

125. Hildebrand, H. and Franke, K. (2012) A new radiolabeling method for commercial Ag^0 nanopowder with ^{110m}Ag for sensitive nanoparticle detection in complex media. *J. Nanopart. Res.*, **14** (10), 1–7.

126. Chrastina, A. and Schnitzer, J.E. (2010) Iodine-125 radiolabeling of silver nanoparticles for in vivo SPECT imaging. *Int. J. Nanomed.*, **5**, 653–659.

127. Wang, J. *et al.* (2008) Potential neurological lesion after nasal instillation of TiO_2 nanoparticles in the anatase and rutile crystal phases. *Toxicol. Lett.*, **183** (1–3), 72–80.

128. Hildebrand, H. *et al.* (2015) Strategies for radiolabeling of commercial TiO_2 nanopowder as a tool for sensitive nanoparticle detection in complex matrices. *J. Nanopart. Res.*, **17** (6), 1–12.

129. Pérez-Campaña, C. *et al.* (2014) Production of ^{18}F-labeled titanium dioxide nanoparticles by proton irradiation for biodistribution and biological fate studies in rats. *Part. Part. Syst. Char.*, **31** (1), 134–142.

130. Chen, J.-K. *et al.* (2010) The use of radioactive zinc oxide nanoparticles in determination of their tissue concentrations following intravenous administration in mice. *Analyst*, **135** (7), 1742–1746.

131. Yeh, T.K. *et al.* (2012) Kinetics and tissue distribution of neutron-activated zinc oxide nanoparticles and zinc nitrate in mice: effects of size and particulate nature. *Nanotechnology*, **23** (8), 085102.

132. Malfatti, M.A. *et al.* (2012) Determining the pharmacokinetics and long-term biodistribution of SiO_2 nanoparticles in vivo using accelerator mass spectrometry. *Nano Lett.*, **12** (11), 5532–5538.

133. Huang, X. *et al.* (2012) Long-term multimodal imaging of tumor draining sentinel lymph nodes using mesoporous silica-based nanoprobes. *Biomaterials*, **33** (17), 4370–4378.

134. Seo, J.W. *et al.* (2014) ^{64}Cu-labeled LyP-1-dendrimer for PET-CT imaging of atherosclerotic plaque. *Bioconjugate Chem.*, **25** (2), 231–239.

135. Chen, J. *et al.* (2006) Quantification of extrapulmonary translocation of intratracheal-instilled particles in vivo in rats: effect of lipopolysaccharide. *Toxicology*, **222** (3), 195–201.

136. Palko, H.A., Fung, J.Y., and Louie, A.Y. (2010) Positron emission tomography: a novel technique for investigating the biodistribution and transport of nanoparticles. *Inhal. Toxicol.*, **22** (8), 657–688.

5
New Methods for Nanotoxicity Analyses: Synchrotron-Radiation-Based Techniques

Bing Wang

5.1
Introduction

It is very necessary to utilize new analytical methods for elucidating the interactions of nanomaterials (NMs) with biological systems, especially the relationship between the physicochemical properties of NMs in biomicroenvironment and their toxicity. Traditional *in vitro* and *in vivo* toxicity test methods have been successfully employed in nanotoxicological studies; however, the mechanisms of nanotoxicity might not be the same as those incurred by molecular toxicants. For instance, most toxicological studies show that NMs present phase transformation, dissolution, oxidation/reduction as well as nano–bio interface reactions in biological milieu, which affect their *in vivo* behavior and biological effects [1]. It has been known that the original form of the NMs will be altered once they enter the complex and dynamic biological systems (with high concentrations of buffered ionic salts, proteinaceous solution, nucleic acids, and so forth) [2]. In addition, it has been known that NMs could interact with biological components (proteins, membranes, phospholipids, endocytic vesicles, organelles, etc.) and the newly formed nanoparticle/biological (nano–bio) interfaces will give them biological identity [3–5]. For instance, the protein adsorption on the surface of NMs, which is well known as protein corona formation, is a key parameter to understand what the cells see and the ways of their interactions [6–8], for example, the signaling events induced by NMs from the cellular surface, intracellular or intercellular systems, and impacts greatly the unique adsorption, distribution, metabolism, and excretion (ADME) profile of NMs *in vivo* [2, 9]. Multiple evidence show that the protein adsorption on surface of NMs appears to be a double-edged sword, underlying both the origin of nanotoxicity and protective role against cell damage induced by naked NMs [10, 11]. In addition, dynamic heterogeneous properties of NMs *in vivo* and dynamically changed nature of nano–bio interface generally accompany the complex small changes of biological components and surface of NMs at the interface. Thus, probing such subtle changes of NMs or biological components

Toxicology of Nanomaterials, First Edition. Edited by Yuliang Zhao, Zhiyong Zhang, and Weiyue Feng.

and the formation of intermediate entity generally requires dedicated analytical methods and tools with high sensitivity and nondestructiveness.

Synchrotron radiation (SR)-based analytical techniques have become extremely valuable tools for probing the speciation transformation and nano–bio interface interactions because of the advantages of high spatial resolution, high sensitivity, excellent accuracy, low matrix effects, and nondestructiveness. With the advent of the third-generation SR sources, which afford enhanced spatial resolution (below a few nanometers) and high penetrating depth (several tens of millimeters), SR-based analytical techniques can resolve 5–10 times smaller object than conventional light microscopy, reveal site-specific interactions on nano–bio interface, and generally require simple sample processing [12]. These advantages are hopeful to probe the speciation transformation of NMs in biomicroenvironment and elucidate the reaction mechanisms at the microscale level.

Some SR-based analytical methods used for the characterization of NMs have been introduced in Chapter 1. In this chapter, we emphatically introduce some new applications of SR-based methods, such as small-angle X-ray scattering (SAXS), X-ray absorption spectroscopy (XAS), circular dichroism (CD), scanning transmission X-ray microscopy (STXM), and X-ray fluorescence (XRF), for the study of speciation transformation of NMs and interactions at nano–bio interface. These SR-based analytical techniques can provide thoughtful insight to understand the interactions of NMs in biological systems.

5.2 Speciation Transformation of NMs in Biological System by SR-Based Techniques

5.2.1 Small-Angle Scattering–Based Techniques for Dissolution and Agglomeration of NMs

The principles of SAXS analysis are based upon the interference of secondary X-ray wave, which was originated from the interaction between the surrounding electrons of an object and incoming X-ray [13]. At small angular range ($1^\circ < 2\theta < 10^\circ$), the interference intensity and pattern ($I(q)$, scattering intensity vs scattering vector) will be associated with spatial fluctuations and inhomogeneities of the electronic density within an object. In general, $I(q)$ is governed by the particle shape and the interparticle interaction, which could be expressed by Equation 5.1:

$$I(q) = I_0 N V_0^2 P(q) S(q) = y_0 P(q) S(q) \tag{5.1}$$

where q is the scattering vector: $q = 4\pi\sin(\theta)/\lambda$, λ is the X-ray wavelength, and θ is half the angle between the scattered beam and the incident beam. P is the shape factor of the particles, S is the structure factor related to the interaction between particles, N is the total number of the particles in an X-ray-irradiated sample, V_0 is the volume of each particle, and I_0 is a proportional coefficient. Thus, based on this equation, it is possible to obtain the NP size, size distribution, and shape information.

Currently, SAXS analytical techniques, including grazing incidence small-angle X-ray scattering (GISAXS), anomalous small-angle X-ray scattering (ASAXS), time-resolved small-angle X-ray scattering (t-SAXS), and ultrasmall-angle X-ray scattering (USAXS, angular range ($0.001° < 2\theta < 1°$)), are useful to deliver the size and structural information (such as the shape, distances of partially ordered materials, and pore sizes) of objects in the size range from approximately 1 nm to several micrometers. SAXS has the unique advantages in studying the structure of NMs, which is able to analyze a wide variety of sample types, including aerosols, colloidal suspensions, powders, and solids; thus, the size and microstructure of NMs in biomicroenvironment can be acquired. In addition, SAXS often requires very little sample preparation time and can provide more statistically reliable estimates of nanoparticle sizes. Particularly, using *in situ* and time-resolved SAXS analysis, the physicochemical behavior and structural evolution of NMs in the biological environment can be acquired as well.

To date, the size distribution and morphology of the various types of NMs (such as gold, Fe_2O_3, TiO_2, SiO_2) in aqueous solution has been investigated by SAXS technique [14–18]. For instance, the stability of TiO_2 NPs (approximately contained 86% anatase and 14% rutile, 21 nm) in complex biologically relevant medium was investigated by SAXS and USAXS techniques [17]. Figure 5.1 shows that three different regimes are observed from left to right, by which the radius of gyration of the primary particles, inner fractal structure containing the

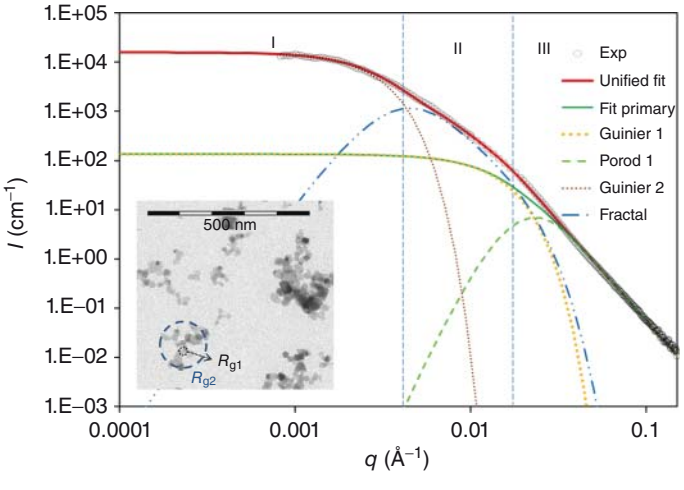

Figure 5.1 Example of SAXS diffractogram (experimental data on NM105 suspension sonicated at pH 2 as circles) illustrating the unified fit (solid red line) and its components, prevailing in each *q*-domain (dashed-dotted lines, see text for details). Insert of transmission electronic micrograph (credit P.-J. de Temmerman and J. Mast, CODA-CERVA) illustrating the gyration radius of primary particles (R_{g1}) and aggregates (R_{g2}) used in the model. (Reprinted with permission from [17]. Copyright (2013) American Chemical Society.)

monodispersed particle and aggregate, and the radius of gyration of the finite size aggregates can be obtained respectively. SAXS diffractograms of TiO_2 NPs in a different medium demonstrated that TiO_2 NPs are directly sonificated in pure water without any addition of salt or adsorbent, the resulting suspension is well dispersed and stable, with intensity-averaged size of 150–160 nm. Once any ion or organic adsorbent such as a protein (e.g., bovine serum albumin, BSA) is added to this suspension, a fast and dramatic aggregation occurs. However, when adjusting the pH (referring to the isoelectric points of BSA and NMs) before the addition of BSA, highly dispersed and stable concentrated stock suspensions of TiO_2 NP with aggregates smaller than 200 nm were observed.

SAXS is a very ideal technique for *in situ* study of NP dissolution because the high X-ray flux yields strong signals suitable for rapid measurements of both NP quantity and size. Using a Teflon disk enclosed by two thin Kapton films as the *in situ* reaction cell, with a circular open window (~20 mm in diameter), the dissolution of ZnS NPs under different pH conditions and coordination agents was investigated by SAXS [19]. SAXS experiments were conducted at the beamline station 1–4, Stanford Synchrotron Radiation Laboratory with an X-ray wavelength of 0.1488 nm. Through fitting of SAXS data, the quantities, including the mean radius, the relative mass, and the dissolution fraction, have been calculated by the following Equations 5.2 and 5.3. The increased diameter of ZnS NPs with the reaction time to 1.4 h during dissolution indicated that preferential dissolution of smaller particles and retainment of bigger particles in the solution, revealing the particle size, play important roles in the dissolution of NPs. Furthermore, the changes in scattering intensity of ZnS NPs over the pH range 9–10 with or without the complexing agent ethylenediaminetetraacetic acid (EDTA) show the lower the pH in the presence of EDTA, the higher the solubility of ZnS NPs.

$$m \approx \left(\frac{4\pi}{3}\right) \times r^3 N \tag{5.2}$$

$$x = 1 - \frac{m}{m_0} \tag{5.3}$$

where m is number-weighted relative mass, r is the average particle radius, N is the total number of particles, x is dissolution fraction, and m_0 represents the mass at reaction time $t = 0$.

The agglomeration process of NMs can be probed by USAXS as well because it can simultaneously measure over the entire nanometer to micrometer size range from a single scattering experiment. For instance, Martin *et al.* [15] used *in situ* USAXS to investigate the complete process between the agglomeration and dissolution of Ag NPs coated with BSA by modeling the agglomerate morphology as packed sphere. Figure 5.2 shows that the changes of diameter of monodispersed BSA-Ag NPs and agglomerates versus time are highly dependent on the HNO_3 concentrations and the integrity of the coated biomolecules. At the lowest nitric acid concentrations (<200 mM), the protein corona protected the particles from dissolution very well with negligible agglomeration, while particles began to dissolve and agglomerate simultaneously at HNO_3 concentrations ranged from

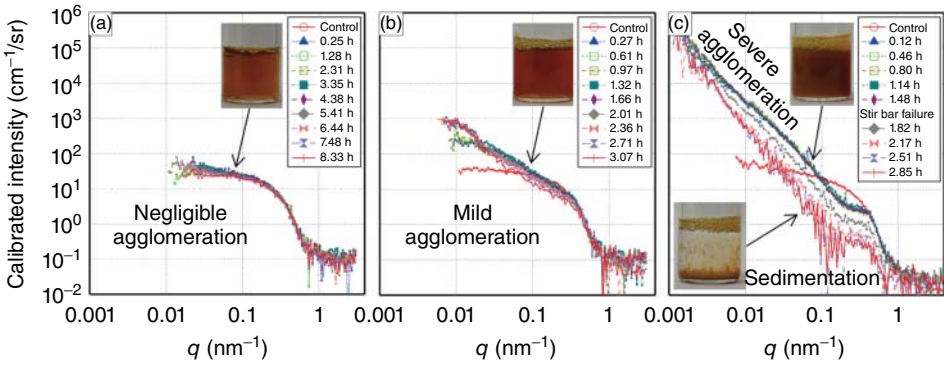

Figure 5.2 Stability regimes of BSA-Ag NPs in HNO_3 measured by absolute-intensity-calibrated USAXS. (a) In 50 mM HNO_3, BSA-Ag NPs slowly dissolve with almost no agglomeration, as evidenced by the relatively flat, low-q scattering curve, and optical clarity of the solution (inset). (b) In 250 mM HNO_3, BSA-Ag NPs simultaneously agglomerate and dissolve while the solution darkens. (c) In 500 mM HNO_3, the BSA coating completely destabilizes, causing rapid clustering of principal particles into agglomerates, as seen in the large scattering intensities at low-q values and the dark turbid suspension. In this case, "steady" dissolution proceeds as long as the particles are stirred; otherwise, they sediment, as detected by an exponential decay in the scattering intensity and by visual inspection. (Reprinted with permission from [15]. Copyright (2014) American Chemical Society.)

200 to 250 mM. At high acid concentrations (>250 mM), the protein corona was destabilized, then Ag NPs dissolved rapidly whatever particles were as individually dispersed or trapped in agglomerates.

5.2.2
XAS for the Oxidation State and Coordination Geometry of NMs in Biological System

SR-based XAS technique is a unique site-selective spectroscopy, which is highly sensitive to the local electronic environment, coordination geometry, and bond distances of absorbed atoms in materials, thus making it a quite precise fingerprint for the local structure determination of NMs [20]. synchrotron radiation–X-ray absorption spectroscopy (SR-XAS) reveals specific information in three different energy regions: the pre-edge region reflects electronic structure and oxidation state; the X-ray absorption near-edge structure (XANES), and the extended X-ray absorption fine structure (EXAFS) provide geometry and coordination information of the local structure. Particularly, the important advantage of XAS is that samples can be operated in gas phase, solution, or condensed matter (i.e., solids).

Oxidation–reduction is one of the important processes for NMs in biological systems because electron transfer reactions can generally occur due to the common presence of various kinds of oxidizing/reducing agents (e.g., cysteine, glutathione, nicotinamide adenine dinucleotide/nicotinamide adenine dinucleotide phosphate (NADH/NADPH), and cytochrome c) in biological

milieu and the highly biochemical reactivity on nanosurface thus mediates the surface speciation transformation of NMs. In a previous work, Fe chemical states on the surface of Fe_2O_3 NPs were detected in biogenic reducing agent (i.e., cysteine and NADPH) containing systems by using the XANES technique [21]. The XANES measurement showed that an *in situ* surface reduction of Fe(III) to Fe(II) had occurred when cysteine and NADPH absorbed on the nanosurface. Similarly, Auffan *et al*. investigated the surface chemical speciation of CeO_2 (7 nm) in abiotic Dulbecco's Modified Eagle medium (DMEM) by XANES and found that about 8.2% of Ce(IV) on NP surface was reduced to Ce(III) [21]. In aqueous solutions, Ag^0 on the surface of citrate- and polyvinylpyrrolidone-coated Ag NPs was observed to be oxidized to Ag(I) by the dissolved O_2 in water [22]. By ultraviolet–visible (UV-Vis) and XANES techniques, a formation of metal-oxide phases (Ag_2O) was found with subsequently high binding capacities within organic or organic ligands of Cl^{-1}, CO_3^{2-}, and cysteine, and so on. In oxygen-dependent living systems, the oxidation reaction and releasing of Ag(I) ions from Ag NPs can be accelerated. These studies indicate that *in situ* oxidation–reduction occurred at the nano–bio interface. Moreover, the reduced or oxidized fractions, such as reduced Fe(II) and oxidized Ag(I) on the surface of NPs, could enhance the reactive oxygen species (ROS) generation in a biological system.

5.2.3 STXM Imaging for the Chemical Transformation of NMs

It is particularly important to obtain the information of spatially resolved chemical fingerprint of NMs, which is a basis for understanding their unique physicochemical and biological properties. Using the intrinsic X-ray absorption properties, soft X-ray STXM with a spatial resolution of a few tens of nanometers may obtain the exquisitely detailed spatial map of the unoccupied density of states (UDOS) from the nanostructure with different compositions, thereby providing a means to obtain directly spatially resolved chemical image (such as chemical components, electronic structure, bond orientation) in a large area sample. Particularly, STXM operate in the "water window" spectral region, which makes it image hydrated specimens with a spatial resolution down to approximately 10 nm. In STXM, the sample is raster-scanned through the X-ray beam, while the total transmitted intensity is recorded at each position, thus yielding a map of the material optical density at the resolution of the X-ray focus size.

STXM has been used to investigate the adsorption of biological components on metal oxide (CeO_2, TiO_2, CuO, Fe_2O_3) NPs by mapping NPs and biological components at nanoscale [23–26]. For instance, the distribution and fate of Cu NPs in a complex natural river biofilm was investigated by STXM at C 1s and Cu 2p edges XANES spectroscopy measurement. The STXM experiment was performed on the spectromicroscopy beamline 10ID-1 at the Canadian Light Source (CLS), Saskatoon, SK, Canada. The biofilms are a complex community of microorganisms, composed of bacteria, cyanobacteria, diatoms, and extracellular polymeric substances. Taking cyanobacteria as an example, a Cu 2p stack was collected from

a region of the cyanobacteria after exposure to Cu NPs for 5 min, 3 or 7 days. Spectral fitting with the Cu NP and Cu acetate spectra was conducted using singular value decomposition (SVD) analysis. The results show that Cu NPs were present in the vicinity of the cyanobacteria via spectral fitting using the Cu NP spectrum (Figure 5.3). The cyanobacterial filament was surrounded by lipids, proteins, and polysaccharides. Further spectral fitting of a C 1s stack from the same

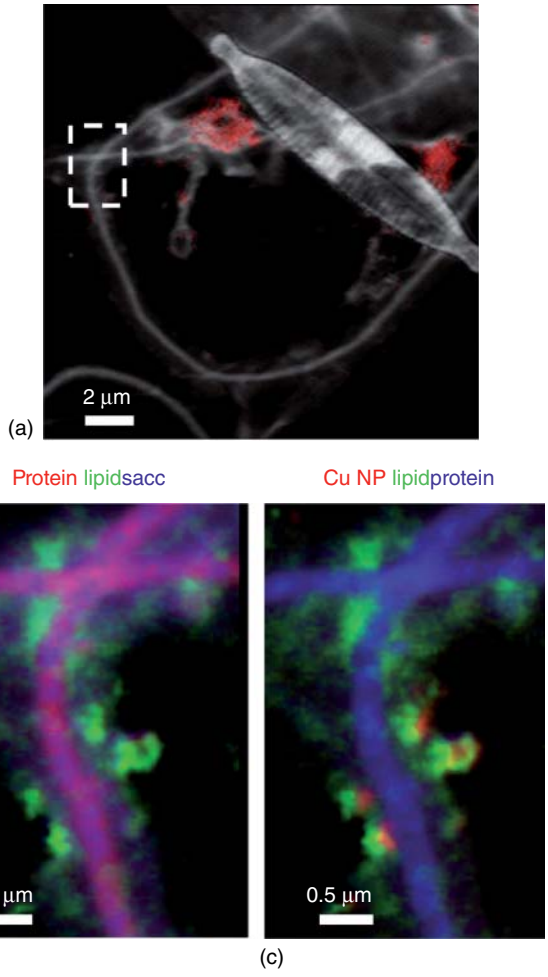

Figure 5.3 River biofilm exposed to 1 mg/l Cu nanoparticles for 5 min. (a) Cu image difference map ($I_{931.3}$ eV−I_{925} eV) (red) overlayed on the gray-scale of the biology image difference map ($I_{288.2}$ eV−I_{280} eV). The white box indicates the area of the detailed study. Detailed study of a cyanobacterial cell. (b) Color-coded composite map of protein (red), lipid (green), and polysaccharides (blue). (c) Overlay of the Cu image difference map from a on the lipid and protein component maps from (b) (red = Cu nanoparticles, green = lipid, blue = protein). (Reprinted from [26] with permission from Elsevier Ltd.)

area of the Cu 2p stack was performed using the biomacromolecule spectra (proteins, polysaccharides, lipids). The Manders' overlap coefficient for the Cu NP with proteins, lipids, and polysaccharides was 0.681, 0.827, and 0.661, respectively, indicating that the adsorption of lipid-rich extracellular substances on Cu NP initially occurred. In addition, a new Cu(II) species, which is considered as dissolved Cu species containing different ligands (e.g., CO_3^{2-}, SO_4^{2-}, SiO_3), was found to be adsorbed on the diatoms [26].

STXM has also been used to investigate the changes of configuration of carbon NMs via mapping their heterogeneities of electronic structure. It has been reported the two-dimensional graphene oxide is generally composed of a variety of configurations, such as corrugation, folding, and rippling in biomicroenvironment, which will appear as a different spectral pattern [27]. Figure 5.4 shows distinct differences in the relative intensities of π^* across the demarcated regions on single-layer graphene (SLG). Based on dipole selection rules, an orbital with perpendicularly symmetric orientation to the basal plane of graphene (P^*) should not be resonant, which is a result of the electric field vector of the incident beam being coincident with the nodal plane, depicted by the blue (perpendicular) and red (tilted) π^* orbitals in Figure 5.4b. Consequently, distinctly different π^* intensities relative to the σ^* can be correlated to electronic corrugations or asperities that are aligned with the electric field vector of the incident radiation, according to angle θ in Figure 5.4b. So, the intensity of π^* directly reflects the topographical state of graphene, such as corrugations, rippling, or folding.

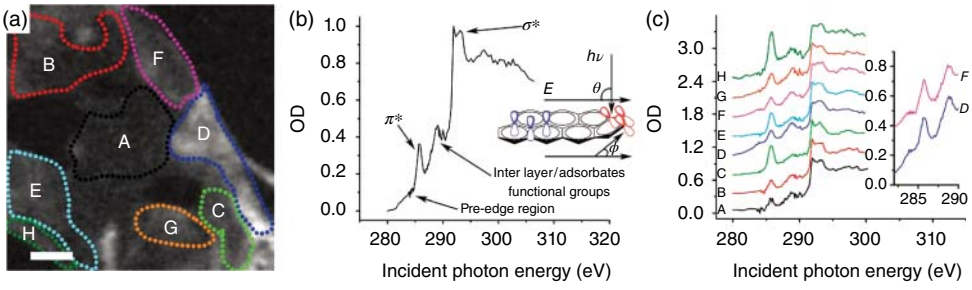

Figure 5.4 STXM mapping of the electronic structure of graphene. STXM images and data of CVD grown SLG on Cu after wet etching in HNO_3 and transfer. (a) Transmission-mode data is converted to OD by I/I_0, where I_0 is measured in an empty scan region; summation of 0.3 eV energy steps is normalized to carbon at 320 eV. Corresponding white intensity describes the thickness and morphology of the graphene sheet. The scale bar is 1 μm and the total distance across the image is 4 μm. (b) Integrated C K-edge spectrum of entire image in (a). The electromagnetic field vector (*E*) and incident X-ray photon energy (*hN*) are at angle (*Q*). The angular difference between the pristine basal plane (blue P orbitals) and the asperity (red P orbitals) represents a degree of corrugation (*F*) of a rippled graphene sheet. (c) Isolated *C* K-edge spectra of each region displayed in (a), where spectra *D* and *F* displayed in the inset have the most prominent pre-edge features. (Reprinted from [27], with permission from the Nature Publishing Group.)

5.3
SR-Based Analytical Techniques for Understanding Nano–Bio Interactions

5.3.1
Synchrotron-Radiation-Based X-ray Microscopy for Visualization of NPs *In Vitro* and *In Vivo*

SR-based X-ray imaging techniques, because of their high spatial resolutions, high sensitivity, and the ability to identify elements, have attracted great attention in life science [28, 29]. The related techniques currently include hard X-ray (>4 keV) and soft X-ray (<1 keV) microscopy imaging methods. For hard X-ray microscopy, with the advances in microfocusing optics for X-ray, such as Kirkpatrick–Baez (KB) mirrors, Fresnel zone plates (FZP), and compound refractive lenses (CRLs), X-ray fluorescence, X-ray diffraction, and X-ray refractive imaging methods have been developed [30]. Hard X-ray fluorescence microprobe (μ-XRF) can identify elements in biological samples with high sensitivity (5×10^{-20} mol/μm^2 (about a few thousand atoms within an irradiated spot)) at a spatial resolution of several micrometers (even below 100 nm) [31–33]. The soft X-ray imaging includes STXM, full-field transmission X-ray microscopy (TXM), and coherent diffraction imaging (CDI). These imaging techniques have been applied in investigating the distribution and translocation of unlabeled NPs (e.g., Au [28], Fe [34], and TiO_2 NPs [35]) in biological samples (from 1 μm to tens of millimeters), covering from cells, large tissue sections to small multicellular organisms.

5.3.1.1 Imaging Techniques for Localizing NPs in Cells and Subcellular Compartments

Cell membrane provides the first interface between cells and NPs, which controls materials entering and leaving cells, and helps cells maintain homeostasis and biofunction. NP adhesion to the cell membrane is a prime example of the interface interactions between NPs and cells and is also the first step in the cellular uptake of NPs. The μ-XRF technique, which can image intact individual cells without the need for ultrathin sectioning, has been used successfully to investigate the particle adhesion on cell membrane, intracellular uptake, and subcellular distribution [36]. For instance, Bussy *et al.* [37] successfully studied carbon nanotube (CNT)–cell interactions within cryofixed murine macrophage cells. The shape of cells was visualized via the phosphorus mapping, which represents a characteristic element of cellular components, and SWCNT aggregate was identified via analysis of the fluorescence signal of catalyst metal particles bound to the CNTs (Figure 5.5a) [37]. In the μ-XRF image of SWCNT-exposed cells, the specific iron-rich zones distinct from cellular endogenous iron indicate that SWCNTs mainly associate with the cell membrane surface (Figure 5.5a) and partly enter intracellular regions (Figure 5.5b). Besides the elemental location, μ-XRF can also reveal physicochemical behavior of CNTs at the nano–bio interface [36]. Figure 5.5c shows an agglomerate of macrophages around a central noncellular area where it is iron-rich but contains nearly no phosphorus, corresponding to an aggregation

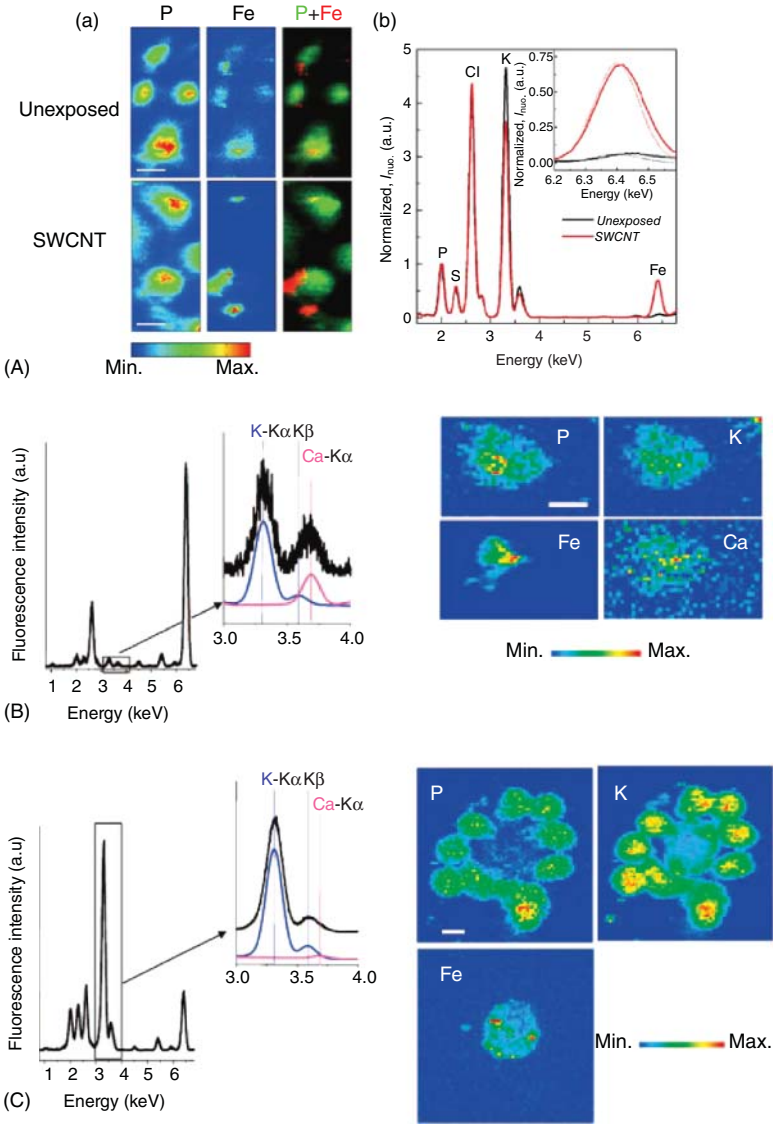

Figure 5.5 (A) Typical μ-XRF maps of P and Fe of macrophages unexposed or exposed to 50 μg/ml SWCNT for 24 h (a) and X-ray fluorescence spectra integrated exclusively over the scanned cells, normalized to the phosphorus signal (b). The inset represents zoomed areas around the positions of the Kα fluorescence peak of iron together with fits of its contribution (dashed lines) [34]. (B) X-ray microfluorescence spectra integrated over the whole murine macrophages exposed for 24 h to MWCNT suspensions at concentrations of 100 μg/ml [34]. (C) X-ray microfluorescence spectra integrated over the whole scanned area of murine macrophages exposed for 24 h to nonpurified SWCNT suspensions at 10 μg/ml [37].

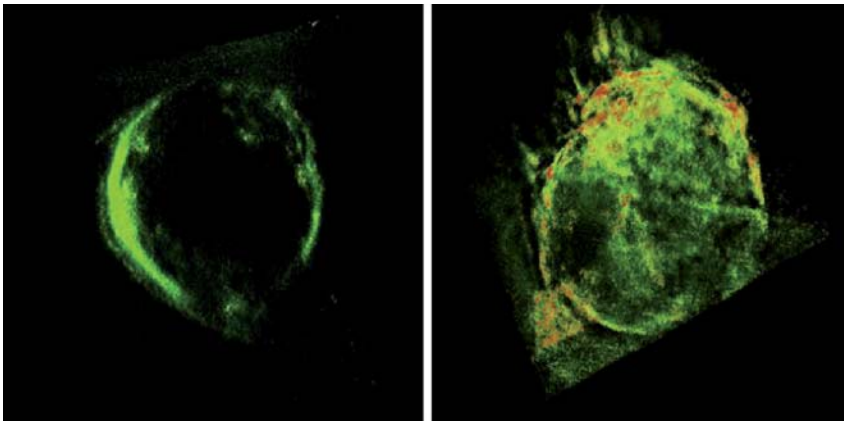

Figure 5.6 The 3 D reconstructed tomography images of Hela cells. (a) Control cells and (b) cells after incubation with TiO_2 NPs for 6 h (red color indicates the TiO_2 NPs. (Reprinted from [35], with permission from Royal Society of Chemistry.)

of nanotubes. A detectable potassium signal on the aggregated nanotube indicated that the K^+ absorption on nanotube aggregate occurred.

The μ-XRF, STXM, and TXM techniques can create three-dimensional (3D) imaging by the reconstruction of the elemental composition as a function of depth, which allows volumetric view of the whole hydrated cells at nanometer scale. The 3D image of intracellular NPs clearly shows whether NPs are intracellular or surface-bounding. Cai *et al.* [35, 38] used TXM tomography to investigate the 3D localization of TiO_2 and Au NPs in human cervical cancer (HeLa) cells. The reconstructed tomography confirmed that TiO_2 NP aggregates were mainly distributed over the cell membrane surface rather than in intracellular space (Figure 5.6) [35]. Furthermore, Wang *et al.* [39] successfully capture the 3D distribution of Ag NPs inside a single human monocyte (THP-1) by synchrotron radiation–transmission X-ray microscopy (SR-TXM). The X-ray absorption ratio and refractive index of Ag are much higher than those of light elements (e.g., C, H, O, N, S, Cl, Na) in cells; thus, Ag and other elements can be distinguished within a cell sample. The SR-TXM images clearly indicated that at 24 h uptake by THP-1 cells, most of Ag NPs were located in the cytoplasm as Ag-containing vesicles sized in the 200–600 nm range (Figure 5.7). During exocytosis, the intracellular concentration of Ag decreased with time, as shown by the decreasing number of red vesicles or spots in cells.

Besides cell membrane, there are a variety of membrane structures in cells, such as nuclear, mitochondrial, endosomal, and lysosomal membranes, which form secondary interface between NPs and organelles. NP translocation across those biological membranes into different subcellular fractions determines their intracellular fate and function, which is particularly important for developing effective and safe nanotechnology-based drug delivery systems. Using STXM

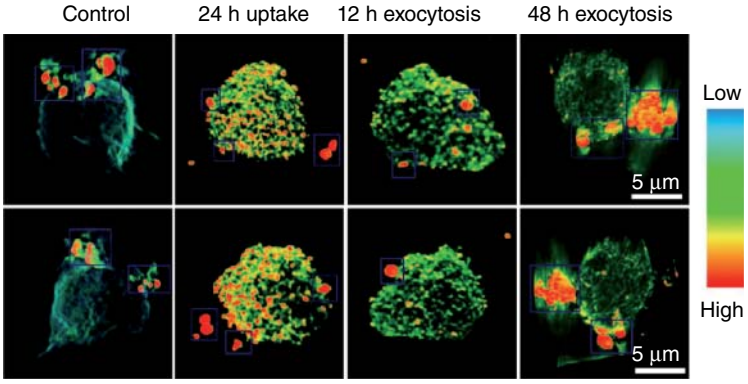

Figure 5.7 Cellular uptake, accumulation, and exocytosis of AgNPs. The spatial distribution of AgNPs in a single cell captured by SR-TXM. Smaller colored spots indicate particles or vesicles on the surface or inside the cells. Green, yellow, and red colors indicate increasing gradients of X-ray absorption intensity by vesicles or aggregated particles. The larger red particles in the square blue frames are gold particles used as a reference for data reconstruction processing. The color bar indicates the related contrast signals from X-ray absorption of silver inside cells. (Reprinted with permission from [39]. Copyright (2015) American Chemical Society.)

method, the intracellular fate of NMs, such as Fe_2O_3 [40], CdTe quantum dots [41], rare earth oxide (REO) NPs [23], and polyhydroxylated metallofullerenols [42] have been investigated. For instance, intracellular uptake of iron oxide and $Gd@C_{82}(OH)_{22}$ NPs were found mainly distributed in cytoplasma of Hela cells [38] and macrophages [42], respectively. In comparison, the CdTe QDs present nonuniform distribution patterns in HEK293 cells, mainly concentrating in the peripheral region of the nuclear membrane [41]. Such uneven distribution of NPs is hypothesized to cause abnormally high local concentrations of Cd^{2+} around the nuclei or certain cellular organelles (such as mitochondria) and enhanced damage to these organelles [41].

5.3.1.2 Imaging NPs in Organic Tissues

The identification and analysis of NPs in organic tissues can provide important information on the capacity of NPs entering into the specific targets. For instance, using μ-XRF technique, the distribution of metal-based NMs, such as Fe_2O_3 [43], TiO_2 [44], and Cu NPs [45], in olfactory bulb tissue section was directly visualized. By analyzing the distribution of Fe in olfactory bulb of mice exposed to 280 nm Fe_2O_3 particles (3W1A, Beijing Synchrotron Radiation Facility), significantly increased Fe content was observed within the olfactory nerve layer of olfactory bulb and other brain regions, including the cerebral cortex, hippocampus, and midbrain regions, indicating that the intranasal exposure of fine Fe_2O_3 particles could be transported into the central nervous system via the sensory nerve endings of olfactory nerve [43] (Figure 5.8). Similarly, by using this method, intranasally

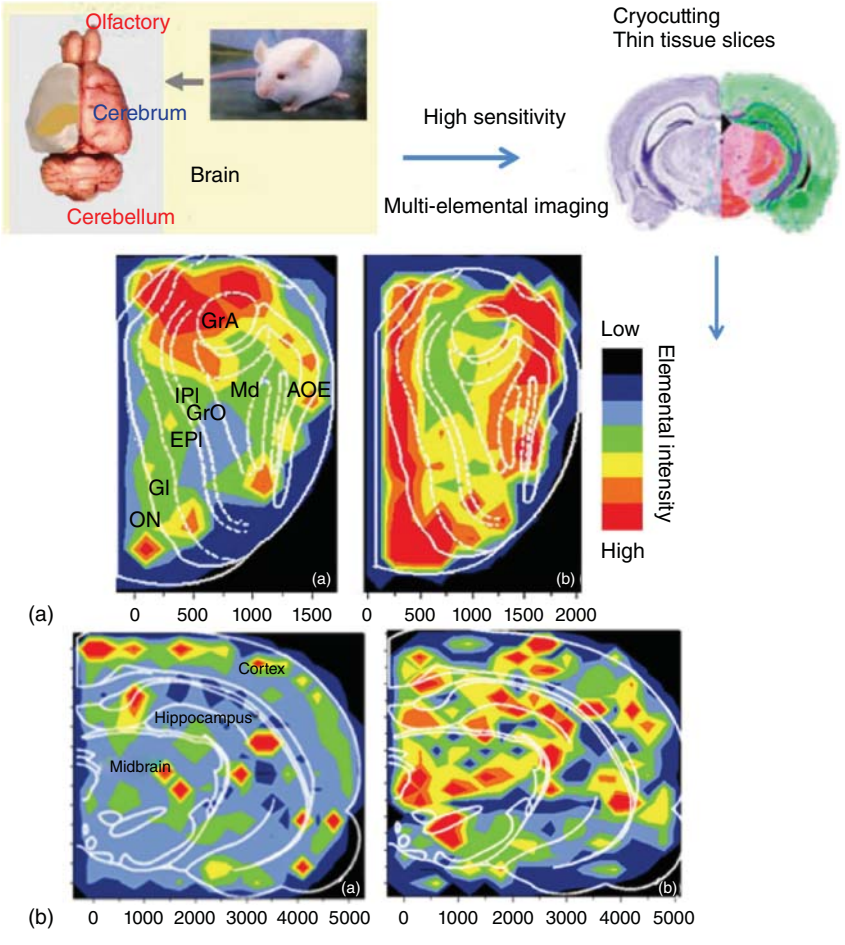

Figure 5.8 Fe distribution in mouse olfactory bulb (A) and brain regions (B) tested by SR-XRF. (a) Control group and (b) Fe_2O_3-NP group. ON: olfactory nerve layer, Gl: glomerular layer, Epl: external plexiform layer, Ipl: internal plexiform layer, GrO: granule cell layer of olfactory bulb, Md: medullary layer, GrA: granule cell layer of accessory olfactory bulb, and AOE: anterior olfactory nucleus external part. (Reprinted from [43] with permission from Elsevier Ireland Ltd.)

exposed TiO_2 (25 nm) and Cu (23.5 nm) NPs were also demonstrated to translocate into olfactory bulb through the olfactory nerve and accumulated in the cerebral cortex, thalamus, and hippocampus of mice [44].

Tumor is a complex tissue that separates the intratumor microenvironment and the surrounding environment. The penetration property of NPs toward tumor tissue is an important index for their therapeutic efficacy. Using μ-XRF technique, the penetration of transferrin-conjugated Au NPs in tumor tissues was identified [46]. The quantitative mapping of Au within the tumor spheroid section (500 μm)

showed that the penetration of Au NPs inside multicellular spheroids was very limited within 48 h [46].

5.3.1.3 Imaging NPs in Model Organisms

To restrict and regulate the exchange of exterior substances (such as H_2O, O_2, drug, etc.) with interior ones, the living organisms create a series of biological barriers, such as blood–brain barrier, air–blood barrier, placenta barrier, intestinal epithelia barrier, mucosal barrier, and so forth, which are made up of specialized cells closely packed and ranged in one or more layers and viewed as an interface

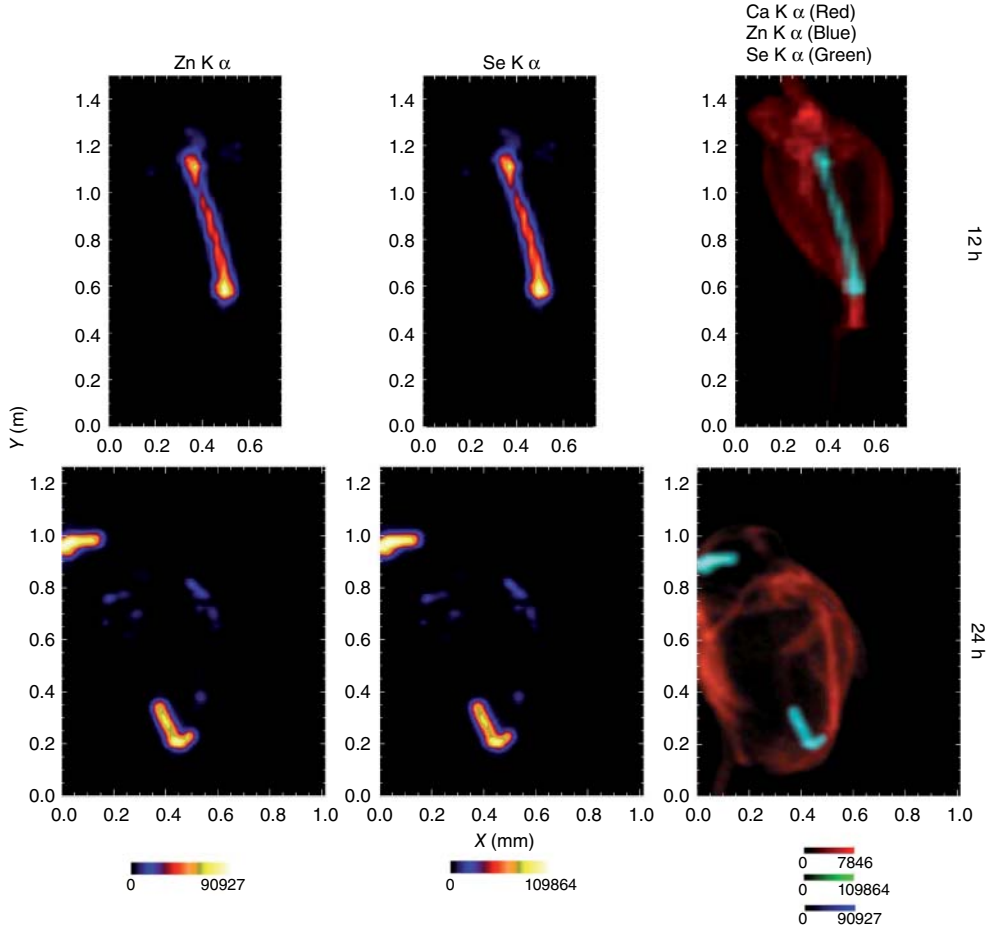

Figure 5.9 Two-dimensional elemental maps for Zn, Se, and Ca, Zn, Se overlay for *D. magna* exposed to red MUA-coated CDSe/ZnS QDs. Vertical columns correspond to Zn, Se, and an overlay of Ca, Zn, and Se, respectively. Horizontal rows correspond to 12 and 24-h exposure time points. (Reprinted from [49] with permission from Springer-Verlag.)

between a central compartment and the surrounding environment. For instance, the intestinal epithelial barrier serves two most important functions: on the one hand, as a filter for selective penetration of needed nutrients from the intestinal lumen into the circulation and the internal milieu; on the other hand, as protector to prevent the penetration of harmful entities including microorganisms, luminal antigens, and luminal proinflammatory factors. Thus, identification of NPs in organisms can explore whether NPs pass across these biological barriers.

The advantages of high penetration depth of hard X-ray and low detection limit for μ-XRF make it possible to monitor *in situ* the distribution of NPs in a tiny organism (such as *Caenorhabditis elegans*, *Daphnia magna*, and *Drosophila*) [47–49]. Jackson *et al.* [49] investigated the biodistribution of CdSe quantum dots (CdSe@ZnS) in living *D. magna* by SR-μ-XRF. The 2D/3Dμ-XRF tomography (Figure 5.9) confirmed that the CdSe QDs accumulated within the digestive tracts of *Daphnia* and, in some cases, adhered to the carapace, antennae, and thoracic appendages. By using *C. elegans* and *Drosophila* as model organisms, some other researchers also found that CdSe@ZnS core/shell QDs were absorbed by the intestinal tract and further transferred to the reproductive system via μ-XRF images of Zn and Se [47, 48]. In combination with μ-XRF and TEM, transportation of oral magnetite NPs from female *Drosophilas* to their embryo was demonstrated [50]. Figure 5.10 shows the iron-containing NPs presented in *Drosophila* embryos and induced the dyshomeostasis of trace elements such as Fe, Ca, and Cu along the anterior–posterior axis of the fertilized eggs, indicating that the female Fe_3O_4 NP exposure could disturb the homeostasis of essential trace elements in their offspring, although the exact mechanism is still unclear [50].

5.3.2
SR-Based Analytical Techniques for the Study of Biophysicochemical Reactions at Nano–Bio Interface

Once NPs enter biological systems, agglomeration/aggregation, protein adsorption, dissolution, metal valence, or coordination changes will occur, which subsequently determine the uptake, bioavailability, translocation, and fate of NPs and finally decide their diagnostic/therapeutic efficiency or toxic effects in biological system. The SR-XAS, because of its unique chemical sensitivity, can render precise fingerprint measurements of NP structure, which sheds light on the molecular mechanism of biophysicochemical interactions, such as adsorption, dissolution, phase transformation, and oxidative–reductive reactions, at the nano–bio interface.

5.3.2.1 Investigation on Intracellular Speciation and Transformation of NPs

So far, speciation transformation of NPs (such as TiO_2, ZnO, Ag, REO, etc.) at cellular or subcellular interface has been probed via SR-XAS. Brun *et al.* [51, 52] analyzed the intracellular environment of titanium atoms by the method of *in situ*

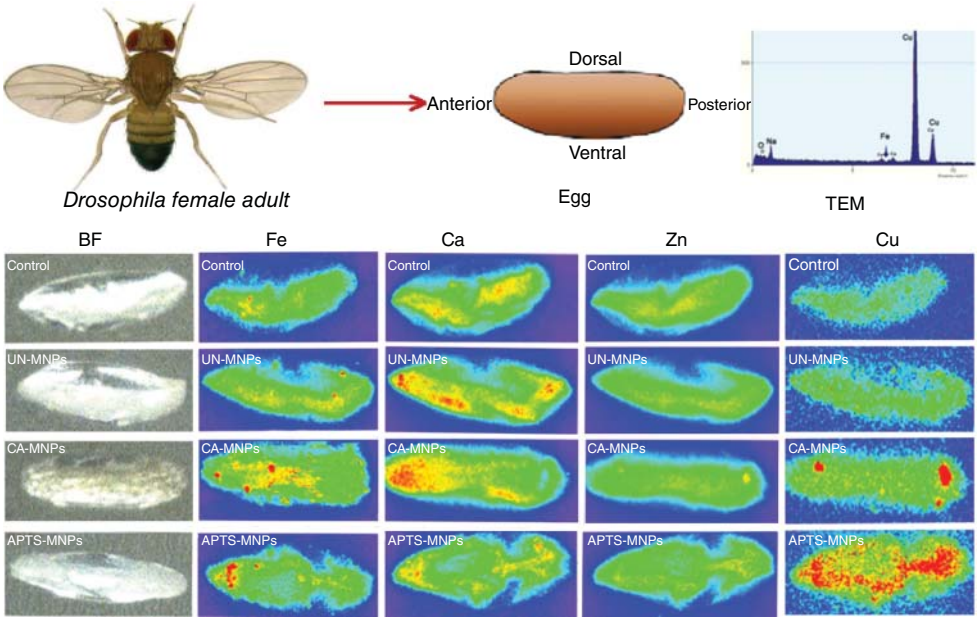

Figure 5.10 The biodistribution of nutritional elements in eggs after parental exposure to MNPs. Synchrotron-radiation-based microbeam X-ray fluorescence (SR-μ-XRF) mappings of Fe, Ca, Zn, and Cu in *Drosophila* eggs of the control and UN-, CA-, and APTS-MNP- (300 μg/g) treated groups. (Reprinted from [50] with permission from Taylor & Francis.)

microbeam X-ray absorbance near-edge structure (μ-XANES); thus, the dissolution and speciation of anatase and rutile TiO_2-NPs in gut cells were assessed. The Ti pre-edge features in XANES are characteristic of the crystalline phase and size of TiO_2 NPs (Figure 5.11). The XANES shows that anatase displays a typical triplet feature (A1, A3, and B peaks), with a weak shoulder (A2) on the low-energy side of the central A3 peak. The intensity of the peak is related to the particle size, that is, the low intensity represents the small size of the particles. The no significant differences among these pre-edge features indicated that the internalized anatase and rutile TiO_2 NPs remained in their original crystalline phase and speciation in cells, and no partial dissolution had occurred. He *et al.* [53], using least-squares linear combination fitting (LC), quantitatively calculated the ion release from REO NPs at particle–cell interface through the fitting of XANES spectra. Their XANES measurement, using Gd_2O_3 as an example, showed that the REO NPs in Gram-negative *Escherichia coli* presented three major rare-earth-bearing phases, REO (53.5%), carboxylates (13.2%), and phosphate (33.3%), implying that great abundance of carboxyl and phosphate groups in cell walls facilitated the dissolution of NPs and the released ions existed as rare-earth carboxylate complex and phosphate complex [53].

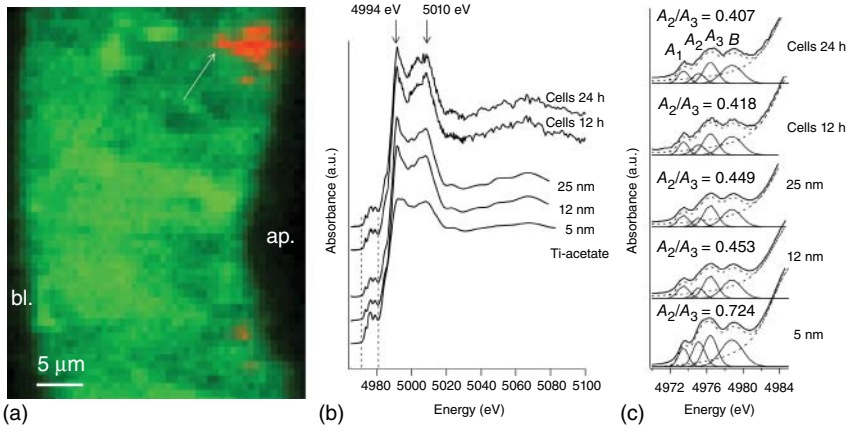

Figure 5.11 *In situ* XAS analysis of intracellular Ti-rich regions. (a) µ-XRF image of a cross section of Caco-2 cells exposed for 24 h, on their apical pole, to 50 µg/ml of TiO_2-NPs. Phosphorus (P) distribution map is depicted in green and titanium (Ti) distribution map is depicted in red. The area pointed out with an arrow was further analyzed by XAS. (b) XAS spectra of reference Ti-acetate and TiO_2-anatase nanopowders (5, 12, and 25 nm) and of Ti-rich regions in Caco-2 cells exposed for 12 h (cells 12 h) or 24 h (cells 24 h) to 50 µg/ml of 12 nm-diameter anatase TiO_2-NPs. (c) Focus on the pre-edge region (4972–4985 eV) and its deconvolution using an arctangent function and four Gaussian peaks (A_1, A_2, A_3, B). Solid line: recorded data; dashed line: fit. Panels indicate A_2/A_3, which is the ratio of intensity of A_2 to intensity of A_3 [52].

Using STXM in combination with XAS, the phytotoxicity and biotransformation of REO, including La_2O_3, Yb_2O_3, and CeO_2 NPs, in the cells of cucumber root were also investigated [23, 54, 55]. After exposure to these REO NPs, there were fine needle-shaped nanoclusters formed in the intercellular regions of the cucumber roots and their chemical species were verified to be $LaPO_4$, $YbPO_4$, and $CePO_4$.

5.3.2.2 Investigation of Dissolution and Microstructural Transformation of NMs *In Vivo*

SR-based XAS can be used to investigate the transformation and structural features of NMs in animal tissues and organs, which provide information on metabolism and degradation of the materials *in vivo*. To reveal the structural transformation of NMs *in vivo*, Wang *et al.* analyzed the chemical speciation of Au in rat liver and spleen by XANES after the rats were subjected to intravenous injection with Au nanorods (Au NRs) [56]. The XANES spectrum showed typical Au L_{III} edge peaks of Au NRs in rat liver and spleen tissue homogenate, demonstrating that Au NRs remained inert for 7 days postinjection and were difficult to degrade completely. In combination with µ-XRF and µ-XANES, Qu *et al.* [48] performed a full assessment of the metabolism and degradation of CdSe QDs (CdSe/ZnS core/shell QDs) in *C. elegans* (Figure 5.12). The Se XANES spectra of the worm intestine showed obvious differences from top to bottom in the retral part, as Figure 5.12 shows that the intensity of peak I in Se K-edge XANES

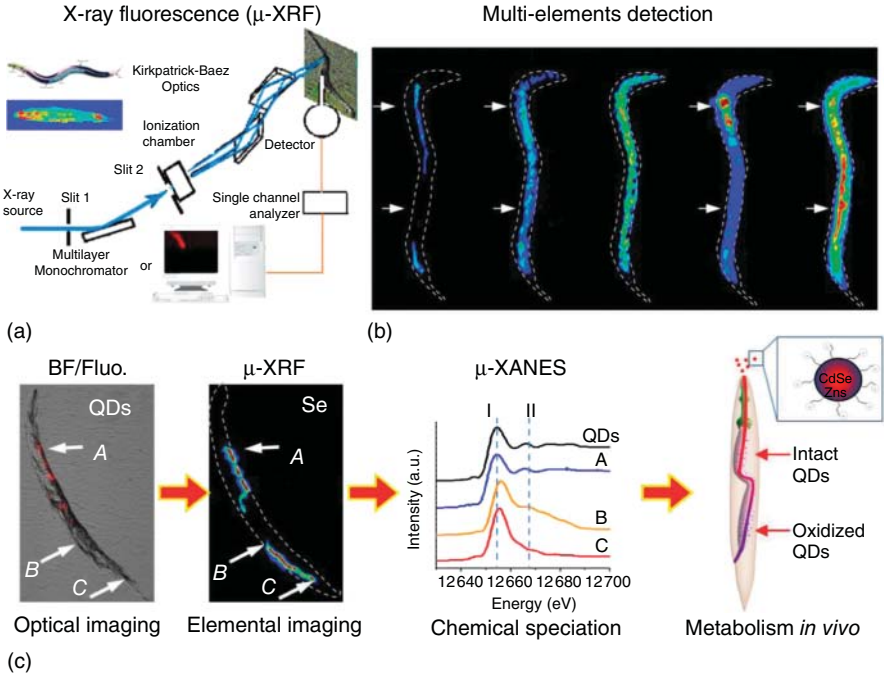

Figure 5.12 *In situ* elemental analysis of the metabolization of QDs in *C. elegans* by XRF and XAS. (a) Scheme of XRF mapping of *C. elegans*; (b) mappings of an intact worm exposed to MEA-CdSe@ZnS for 24 h; and (c) *in situ* Se K edge microbeam X ray absorbance near-edge structure (μ-XANES) spectra of QDs within the digestive tract of *C. elegans* corresponded to points *A*, *B*, and *C* on XRF mappings. The beam size of μ-XRF mappings and μ-XAS spectra was $5 \times 5\ \mu m^2$. (Reprinted with permission from [48]. Copyright (2011) American Chemical Society.)

spectra strongly increases and its position shifts to higher energy by about 2 eV; the intensity of shoulder II gradually decreases and disappears. Collectively, the results suggest that the core/shell structure of CdSe/ZnS collapsed and Se^{2+} in the CdSe core is oxidized to SeO_3^{2-}.

5.3.2.3 Revealing Molecular Mechanism of "Protein Corona" Formation at Nano–Bio Interface

It has been known that once NPs enter biological systems, various proteins can be absorbed on the nanosurface, thus forming a "protein corona," which plays an essential role in mediating cellular uptake and cytotoxicity [57]. However, little has been known about how the corona forms and the interfacial structures between the corona and NPs. By using XANES in combination with least-squares linear fitting, the binding site of BSA corona adsorption on Au NRs has been identified [57]. In the study, cysteine, methionine (Met), and cystine represent three main forms of sulfur-containing proteins in BSA, with sulfur species consisting of R–S–H, R–S–R, and S–S, respectively. In the BSA corona–Au NRs system,

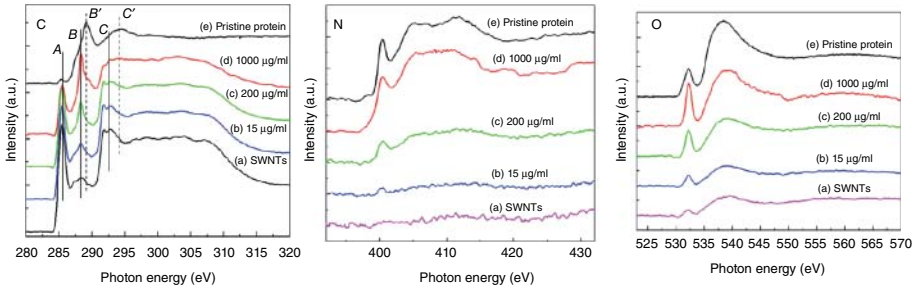

Figure 5.13 Comparison of the C K-edge, N K-edge, and O K-edge XANES spectra of SWCNTs, the pristine streptavidin protein, and SWCNTs treated in streptavidin protein solutions at different concentrations: 15, 200, and 1000 μg/ml. (Reprinted from [58] with permission from Elsevier Ltd.)

the XANES experimental results combined with the theoretical calculation show that the content of disulfides significantly decreased from 82% to 58% by inducing 26% of the sulfur atoms to transform into Au–S, while the content of the R–S form, including Met or cysteine, decreased only slightly, from 18% to 16%, indicating that protein adsorption at the BSA–Au NRs interface was attributed to the transformation from disulfides bonds to Au–S coordination rather than the R–R–S–H and R–S–R ones.

Additionally, by XANES analysis, how the configuration of a protein is affected by the specific region on the surface of NMs has been investigated as well [58]. Figure 5.13 shows the carbon, nitrogen, and oxygen K-edge XANES spectra of SWCNTs after treatment with streptavidin protein solutions [58]. The XANES spectra show that the peptide C═O bonds in proteins were affected by the corresponding aromatic structure of SWCNTs, indicating an effective interaction between SWCNTs and proteins. The experimental data combined with model simulations reveal that the hydrophobic interaction between a hydrophobic pocket (of proteins) and a hydrophobic surface (of SWCNTs) induced the changes of C═O double bond in proteins, subsequently leading to small but relevant structural distortions of the streptavidin protein. These studies demonstrate that XANES is a powerful tool for characterizing the structural details of NMs and proteins of the interactions at nano–bio interface.

5.3.2.4 SR-Based Analytical Techniques for the Study of Microstructural Changes of Biomolecules Bound to NMs

The circular dichroism (CD) spectroscopy is a well-established method in the study of biological chemistry and structural biology that can provide information of protein secondary structure, protein folding dynamics, and protein-folding-associated ligand binding and macromolecular interactions. Particularly, SR-based CD spectroscopy possesses the capacity to obtain the structural information at vacuum ultraviolet wavelength with only small amounts of samples, by which the structural stability and changes of biomolecules bound to NPs can be achieved. The high sensitivity of SRCD enables the accurate detection of low

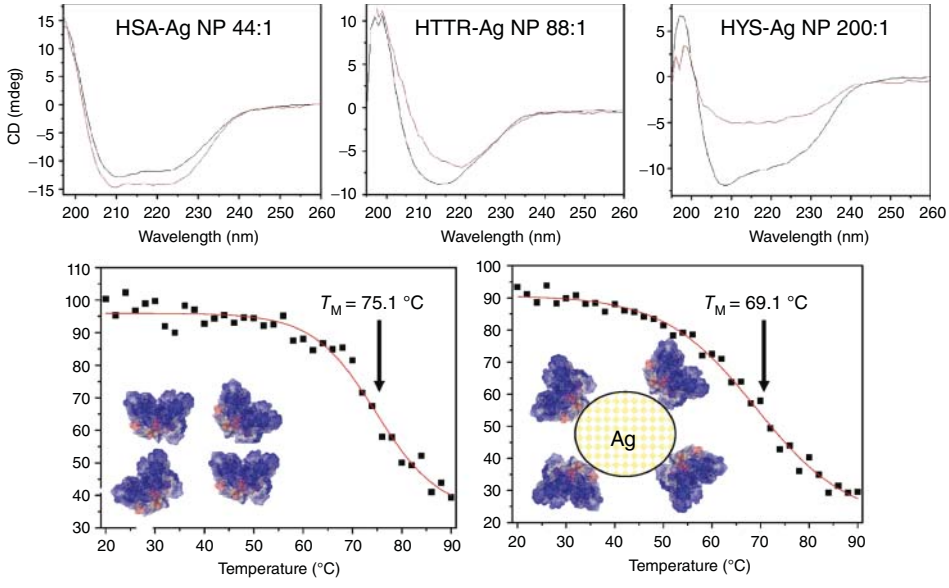

Figure 5.14 Analysis for bio–nano interaction at molecular level. SRCD spectra of protein–Ag NP complex (red) and free protein (black) collected with a low volume capacity 10 cm path length cell. There is a decrease of 6 °C in the thermal unfolding of human serum albumin upon interaction with silver NPs. (Reprinted with permission from [59]. Copyright (2011) American Chemical Society.)

nanomolar concentration of samples and the small conformational changes in the structure of macromolecules; thus, the method is very useful for the analysis of the structural changes of the proteins bound to NPs. Using SRCD, Laera *et al.* [59] analyzed the stability and secondary structure changes in different classes of proteins after interaction with Ag NPs. The studied proteins include human serum albumin (HSA), human transthyretin (hTTR), and lysozyme (LYS). The SR-CD spectra show that HSA retains its overall secondary structure after interaction with 15 nm Ag NPs (Figure 5.14a). In the case of hTTR-Ag NP complex, the content of α-helical in hTTR decreased and the irregular secondary structures increased. For LYS-Ag NP complex, the significant decrease of CD signal intensity suggested that the protein precipitates upon interaction with Ag NPs. The studies of variable-temperature CD spectroscopy show that compared to free HSA, there was a decrease of 6 °C in the thermal unfolding of HSA-AgNP complex, which indicates that the protein bound to NPs initially existed as a flexible and unstable folded structure (Figure 5.14b).

The time-resolved protein-corona profiles can be obtained by probing the dynamic changes of the secondary structure of protein with time using SRCD. For instance, Wang *et al.* studied the dynamic changes in secondary structures of a BSA corona bound to Au NRs [57]. For pristine BSA in a buffer solution, the measured content in α-helix, β-sheet, β-turn, and random coil were 46%,

15%, 8.3%, and 30%, respectively. While, when BSA bound to Au NRs, the corresponding structures of the adsorbed BSA corona changed to 36%, 37.6%, 0%, and 26.4% at 0.5 h; and 32.9%, 41.9%, 1.1%, and 24.2% at 2 h. These rapid changes in the secondary structures of the BSA corona arose from the transformation of disulfide bonds to Au–S coordination [57].

5.4 Conclusion and Prospects

In this chapter, we show that SR-based techniques are very useful in the characterization of NPs' behaviors *in vitro* and *in vivo* in biological systems (Figure 5.15) [60]. The distribution, transformation, and final fate of NPs in biological system can be investigated by XRF, SAXS, and XAS. SR-CD, STXM, XPS, and XAS can be performed to reveal the chemical mechanisms of nanotoxicity. These techniques offer direct evidence of not only the characterization of NMs but also their metabolism and final fate in the biological environment.

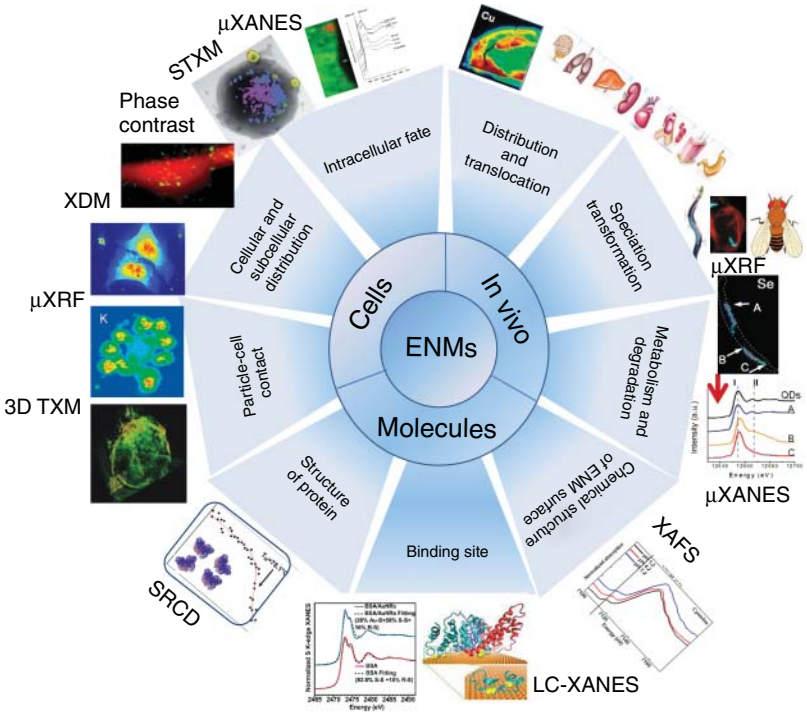

Figure 5.15 Integrated synchrotron radiation analytical techniques for nanotoxicological studies. (Reprinted from [60] with permission from Science China Press and Springer-Verlag, Berlin Heidelberg.)

The design and plans for implementing fourth-generation SR appear achievable and are needed scientifically. The fourth-generation source is known as *free-electron lasers* (FELs) that can generate a source of shorter, femtosecond pulses with the features of brightness, coherence, or pulse duration, particularly at soft and hard X-ray wavelengths. With the performance of the advanced synchrotron light source, the real-time detection of dynamic reaction processes in ultrashort timescale, femtosecond to picosecond; image in very small scale (e.g., nanoscale in cells); and *in situ* and *in operando* measurements in nanotoxicological study can be achieved. The pulse width of SR light is typically tens of picoseconds; therefore, approximately picosecond time-resolved experiments can be carried out by the pump–probe method using femtosecond-pulse lasers [61]. In addition, the developed *in situ* scanning X-ray diffraction method offers the label-free *in situ* and *in operando* measurements on living cells, which provides the possibility to perform *in situ* studies and cell manipulation in a straightforward way [62–64]. Therefore, time-resolved and *in situ* measurements are also possible, which can be applied to monitor the transformation and metabolism of NMs *in vitro* and *in vivo*.

References

1. Wang, B., He, X., Zhang, Z.Y., Zhao, Y.L., and Feng, W.Y. (2013) Metabolism of nanomaterials *in vivo*: blood circulation and organ clearance. *Acc. Chem. Res.*, **46**, 761–769.
2. Wang, B., Feng, W., Zhao, Y., and Chai, Z. (2013) Metallomics insights for *in vivo* studies of metal based nanomaterials. *Metallomics*, **5**, 793–803.
3. Docter, D., Distler, U., Storck, W., Kuharev, J., Wuensch, D., Hahlbrock, A., Knauer, S.K., Tenzer, S., and Stauber, R.H. (2014) Quantitative profiling of the protein coronas that form around nanoparticles. *Nat. Protoc.*, **9**, 2030–2044.
4. Fleischer, C.C. and Payne, C.K. (2014) Cellular binding of charged nanoparticle-protein complexes. *Biophys. J.*, **106**, 623A–624A.
5. Nel, A.E., Mädler, L., Velegol, D., Xia, T., Hoek, E.M.V., Ponisseril, S., Fred, K., Castranova, V., and Thompson, M. (2009) Understanding biophysicochemical interactions at the nano–bio interface. *Nat. Mater.*, **8**, 543–557.
6. Tenzer, S., Docter, D., Kuharev, J., Musyanovych, A., Fetz, V., Hecht, R., Schlenk, F., Fischer, D., Kiouptsi, K., Reinhardt, C., Landfester, K., Schild, H., Maskos, M., Knauer, S.K., and Stauber, R.H. (2013) Rapid formation of plasma protein corona critically affects nanoparticle pathophysiology. *Nat. Nanotechnol.*, **8**, 772–781.
7. Lynch, I., Salvati, A., and Dawson, K.A. (2009) Protein-nanoparticle interactions: what does the cell see? *Nat. Nanotechnol.*, **4**, 546–547.
8. Dobrovolskaia, M.A., Neun, B.W., Man, S., Ye, X., Hansen, M., Patri, A.K., Crist, R.M., and McNeil, S.E. (2014) Protein corona composition does not accurately predict hematocompatibility of colloidal gold nanoparticles. *Nanomedicine*, **10**, 1453–1463.
9. Pozzi, D., Caracciolo, G., Capriotti, A.L., Cavaliere, C., Piovesana, S., Colapicchioni, V., Palchetti, S., Riccioli, A., and Lagana, A. (2014) A proteomics-based methodology to investigate the protein corona effect for targeted drug delivery. *Mol. Biosyst.*, **10**, 2815–2819.
10. Shannahan, J.H., Podila, R., Aldossari, A.A., Emerson, H., Powell, B.A., Ke, P.C., Rao, A.M., and Brown, J.M. (2014) Formation of a protein corona on silver nanoparticles mediates cellular toxicity *via* scavenger receptors. *Toxicol. Sci.*, **10**, 1–11.

11. Ge, C.C., Je, D., Zhao, L.N., Wang, L.M., Liu, Y., Li, D.H., Yang, Y.L., Zhou, R.H., Zhao, Y.L., Chai, Z.F., and Chen, C.Y. (2011) Binding of blood proteins to carbon nanotubes reduces cytotoxicity. *Proc. Natl. Acad. Sci. U.S.A.*, **108**, 16968–16973.
12. Chen, C.Y., Li, Y.F., Qu, Y., Chai, Z.F., and Zhao, Y.L. (2013) Advanced nuclear analytical and related techniques for the growing challenges in nanotoxicology. *Chem. Soc. Rev.*, **42**, 8266–8303.
13. Feigin, L.A. and Svergun, D.I. (1987) *Structure Analysis by Small-Angle X-Ray and Neutron Scattering*, Plenum Publishers.
14. Mehan, S., Chinchalikar, A.J., Kumar, S., Aswal, V.K., and Schweins, R. (2013) Small-angle neutron scattering study of structure and interaction of nanoparticle, protein, and surfactant complexes. *Langmuir*, **29**, 11290–11299.
15. Martin, M.N., Allen, A.J., MacCuspie, R.I., and Hackley, V.A. (2014) Dissolution, agglomerate morphology, and stability limits of protein-coated silver nanoparticles. *Langmuir*, **30**, 11442–11452.
16. Wang, W., Zhang, K., Cai, Q., Mo, G., Xing, X.Q., Cheng, W.D., Chen, Z.J., and Wu, Z.H. (2010) Real-time SAXS and ultraviolet-visible spectral studies on size and shape evolution of gold nanoparticles in aqueous solution. *Eur. Phys. J. B*, **76**, 301–307.
17. Guiot, C. and Spalla, O. (2013) Stabilization of TiO_2 nanoparticles in complex medium through a pH adjustment protocol. *Environ. Sci. Technol.*, **47**, 1057–1064.
18. Siffalovic, P., Majkova, E., Chitu, L., Jergel, M., Luby, S., Satka, A., and Roth, S.V. (2007) Self-assembly of iron oxide nanoparticles studied by time-resolved grazing-incidence small-angle x-ray scattering. *Phys. Rev. B*, **76**, 195432.
19. Zhang, H.Z., Chen, B., and Banfiel, J.F. (2010) Particle size and pH effects on nanoparticle dissolution. *J. Phys. Chem. C*, **114**, 14876–14884.
20. Hummer, A.A. and Rompel, A. (2013) The use of X-ray absorption and synchrotron based micro-X-ray fluorescence spectroscopy to investigate anti-cancer metal compounds *in vivo* and *in vitro*. *Metallomics*, **5**, 597–614.
21. Wang, B., Yin, J.J., Zhou, X.Y., Kurash, I., Chai, Z.F., Zhao, Y.L., and Feng, W.Y. (2013) Physicochemical origin for free radical generation of iron oxide nanoparticles in biomicroenvironment: catalytic activities mediated by surface chemical states. *J. Phys. Chem. C*, **117**, 383–392.
22. Levard, C., Hotze, E.M., Lowry, G.V., and Brown, G.E.J. (2012) Environmental transformations of silver nanoparticles: impact on stability and toxicity. *Environ. Sci. Technol.*, **46**, 6900–6914.
23. Zhang, P., Ma, Y.H., Zhang, Z.Y., He, X., Zhang, J., Guo, Z., Tai, R.Z., Zhao, Y.L., and Chai, Z.F. (2012) Biotransformation of ceria nanoparticles in cucumber plants. *ACS Nano*, **6**, 9943–9950.
24. Ashcroft, J.M., Gu, W., Zhang, T., Hughes, S.M., Hartman, K.B., Hofmann, C., Kanaras, A.G., Kilcoyne, D.A., Le Gros, M., Yin, Y., Alivisatos, A.P., and Larabell, C.A. (2008) TiO_2 nanoparticles as a soft X-ray molecular probe. *Chem. Commun.*, **7**, 2471–2473.
25. Kwon, D., Nho, H.W., and Yoon, T.H. (2014) X-ray and electron microscopy studies on the biodistribution and biomodification of iron oxide nanoparticles in *Daphnia magna*. *Colloids Surf., B*, **122**, 384–389.
26. Lawrence, J.R., Dynes, J.J., Korber, D.R., Swerhone, G.D.W., Leppard, G.G., and Hitchcock, A.P. (2012) Monitoring the fate of copper nanoparticles in river biofilms using scanning transmission X-ray microscopy (STXM). *Chem. Geol.*, **329**, 18–25.
27. Schultz, B.J., Patridge, C.J., Lee, V., Jaye, C., Lysaght, P.S., Smith, C., Barnett, J., Fischer, D.A., Prendergast, D., and Banerjee, S. (2011) Imaging local electronic corrugations and doped regions in graphene. *Nat. Commun.*, **6**, 372.
28. Lewis, D.J., Bruce, C., Bohic, S., Cloetens, P., Hammond, S.P., Arbon, D., Blair-Reid, S., Pikramenou, Z., and Kysela, B. (2010) Intracellular synchrotron nanoimaging and DNA damage/genotoxicity screening of novel lanthanide – coated nanovectors. *Nanomedicine*, **5**, 1547–1557.

29. Barberie, S.R., Iceman, C.R., Cahill, C.F., and Cahill, T.M. (2014) Evaluation of different synchrotron beamline configurations for X-ray fluorescence analysis of environmental samples. *Anal. Chem.*, **86**, 8253–8260.
30. Snigireva, I. and Snigirev, A. (2006) X-ray microanalytical techniques based on synchrotron radiation. *J. Environ. Monit.*, **8**, 33–42.
31. Twining, B.S., Baines, S.B., Fisher, N.S., Maser, J., Vogt, S., Jacobsen, C., Tovar-Sanchez, A., and Saudo-Wilhelmy, S.A. (2003) Quantifying trace elements in individual aquatic protist cells with a synchrotron X-ray fluorescence microprobe. *Anal. Chem.*, **75**, 3806–3816.
32. McRae, R., Bagchi, P., Sumalekshmy, S., and Fahrni, C.J. (2009) In situ imaging of metals in cells and tissues. *Chem. Rev.*, **109**, 4780–4827.
33. Kosior, E., Bohic, S., Suhonen, H., and Cloetens, P. (2013) Absolute zinc quantification at the sub-cellular level by combined use of hard X-ray fluorescence and phase contrast imaging techniques. *J. Phys. Conf. Ser.*, **463**, 12–21.
34. Pascolo, L., Bortot, B., and Severini, G.M. (2014) Detection of PLGA-based nanoparticles at a single-cell level by synchrotron radiation FTIR spectromicroscopy and correlation with X-ray fluorescence microscopy. *Int. J. Nanomed.*, **9**, 2791–2801.
35. Zhang, J.C., Cai, X.Q., Zhang, Y., Li, X.M., Li, W.X., Tian, Y.C., Li, A.G., Yu, X.H., Fan, C.H., and Huang, Q. (2013) Imaging cellular uptake and intracellular distribution of TiO2 nanoparticles. *Anal. Methods*, **5**, 6611–6616.
36. Bussy, C., Cambedouzou, J., Lanone, S., Leccia, E., Heresanu, V., Pinault, M., Mayne-I'Hermite, M., Brun, N., Mory, C., Cotte, M., Doucet, J., Boczkowski, J., and Launoist, P. (2008) Carbon nanotubes in macrophages: imaging and chemical analysis by X-ray fluorescence microscopy. *Nano Lett.*, **8**, 2659–2663.
37. Bussy, C., Paineau, E., Cambedouzou, J., Brun, N., Mory, C., Fayard, B., Salomé, M., Pinault, M., Huard, M., Belade, E., Armand, L., Boczkowski, J., Launois, P., and Lanone, S. (2013) Intracellular fate of carbon nanotubes inside murine macrophages: pH-dependent detachment of iron catalyst nanoparticles. *Part. Fibre Toxicol.*, **10**, 10–24.
38. Cai, X.Q., Chen, H.H., Wang, C.L., Chen, S.T., Lai, S.F., Chien, C.C., Chen, Y.Y., Kempson, I.M., Hwu, Y., and Yang, C.S. (2011) Imaging the cellular uptake of tiopronin-modified gold nanoparticles. *Anal. Bioanal. Chem.*, **401**, 809–816.
39. Wang, L.M., Zhang, T.L., Li, P.Y., Huang, W.X., Tang, J.L., Wang, P.Y., Liu, J., Yuan, Q.X., Bai, R., Li, B., Zhang, K., Zhao, Y.L., and Chen, C.Y. (2015) Use of synchrotron radiation-analytical techniques to reveal chemical origin of silver-nanoparticle cytotoxicity. *ACS Nano*, **9**, 6532–6547.
40. Zhang, X.Z., Xu, Z.J., Tai, R.Z., Zhen, X.J., Wang, Y., and Guo, Z. (2010) Ratio contrast imaging of dual-energy absorption for element mapping with a scanning transmission X-ray microscope. *J. Synchrotron Radiat.*, **17**, 804–809.
41. Chen, N., He, Y., Su, Y.Y., Li, X.M., Huang, Q., and Wang, H.F. (2012) The cytotoxicity of cadmium-based quantum dots. *Biomaterials*, **33**, 1238–1244.
42. Chen, Z., Liu, Y., Sun, B., Li, H., Dong, J., Zhang, L., Wang, L., Wang, P., Zhao, Y., and Chen, C. (2014) Polyhydroxylated metallofullerenols stimulate IL-1beta secretion of macrophage through TLRs/MyD88/NF-kappaB pathway and NLRP(3) inflammasome activation. *Small*, **10**, 2362–2372.
43. Wang, Y., Wang, B., Zhu, M.T., Li, M., Wang, H.J., Wang, M., Ouyang, H., Chai, Z.F., Feng, W.Y., and Zhao, Y.L. (2011) Microglial activation, recruitment and phagocytosis as linked phenomena in ferric oxide nanoparticle exposure. *Toxicol. Lett.*, **205**, 26–37.
44. Wang, J.X., Chen, C.Y., Liu, Y., Jiao, F., Li, W., and Lao, F. (2008) Potential neurological lesion after nasal instillation of TiO2 nanoparticles in the anatase and rutile crystal phases. *Toxicol. Lett.*, **183**, 72–80.
45. Bai, R., Zhang, L., Liu, Y., Li, B., Wanga, L., Wanga, P., Autrup, H., Beer, C., and Chen, C. (2014) Integrated analytical techniques with high sensitivity for studying brain translocation and potential impairment induced by intranasally

instilled copper nanoparticles. *Toxicol. Lett.*, **226**, 70–80.
46. Liu, T.Q., Kempson, I., Jonge, M.D., Howard, D.L., and Thierry, B. (2014) Quantitative synchrotron X-ray fluorescence study of the penetration of transferrin-conjugated gold nanoparticles inside model tumour tissues. *Nanoscale*, **6**, 9774–9782.
47. Liu, H., Wang, B., Wang, Z., Li, M., Bi, X., Yu, X., and Feng, W. (2011) Distribution of CdSe@ZnS QDs in adult *Drosophila* and their stage-1 larva. *Nucl. Technol.*, **34**, 415–418.
48. Qu, Y., Li, W., Zhou, Y.L., Liu, X.F., Zhang, L.L., Wang, L.M., Li, Y.F., Iida, A., Tang, Z.Y., Zhao, Y.L., Chai, Z.F., and Chen, C.Y. (2011) Full assessment of fate and physiological behavior of quantum dots utilizing *Caenorhabditis elegans* as a model organism. *Nano Lett.*, **11**, 3174–3183.
49. Jackson, B.P., Pace, H.E., Lanzirotti, A., Smith, R., and Ranville, J.F. (2009) Synchrotron X-ray 2D and 3D elemental imaging of CdSe/ZnS quantum dot nanoparticles in *Daphnia magna*. *Anal. Bioanal. Chem.*, **394**, 911–917.
50. Chen, H.Q., Wang, B., Feng, W.Y., Du, W., Ouyang, H., Chai, Z.F., and Bi, X.L. (2015) Oral magnetite nanoparticles disturb the development of *Drosophila melanogaster* from oogenesis to adult emergence. *Nanotoxicology*, **9**, 302–312.
51. Brun, E., Jugan, M.L., Herlin-Boime, N., Jaillard, D., Fayard, B., Flank, A.M., Mabondzo, A., and Carrière, M. (2011) Investigation of TiO_2 nanoparticles translocation through a Caco-2 monolayer. *J. Phys. Conf. Ser.*, **304**, 12–48.
52. Brun, E., Barreau, F., Veronesi, G., Fayard, B., Sorieul, S., Chaneac, C., Carapito, C., Rabilloud, T., Mabondzo, A., Herlin-Boime, N., and Carriere, M. (2014) Titanium dioxide nanoparticle impact and translocation through *ex vivo, in vivo* and *in vitro* gut epithelia. *Part. Fibre Toxicol.*, **11**, 1–13.
53. He, X., Pan, Y., Zhang, J., Li, Y., Ma, Y., Zhang, P., Ding, Y., Zhang, J., Wu, Z., Zhao, Y., Chai, Z., and Zhang, Z. (2015) Quantifying the total ionic release from nanoparticles after particle-cell contact. *Environ. Pollut.*, **196**, 194–200.
54. Ma, Y.H., Zhang, P., Zhang, Z.Y., He, X., Li, Y.Y., Zhang, J., Zheng, L.R., Chu, S.Q., Yang, K., Zhao, Y.L., and Chai, Z.F. (2014) Origin of the different phytotoxicity and biotransformation of cerium and lanthanum oxide nanoparticles in cucumber. *Nanotoxicology*, **30**, 1–9.
55. Ma, Y.H., He, X., Zhang, P., Zhang, Z.Y., Guo, Z., Tai, R.Z., Xu, Z.J., Zhang, L.J., Ding, Y.Y., Zhao, Y.L., and Chai, Z.F. (2011) Phytotoxicity and biotransformation of La_2O_3 nanoparticles in a terrestrial plant cucumber (*Cucumis sativus*). *Nanotoxicology*, **5**, 734–753.
56. Wang, L.M., Li, Y.F., Zhou, L.J., Liu, Y., Meng, L., Zhang, K., Wu, X.C., Zhang, L.L., Li, B., and Chen, C.Y. (2010) Characterization of gold nanorods *in vivo* by integrated analytical techniques: their uptake, retention, and chemical forms. *Anal. Bioanal. Chem.*, **396**, 1105–1114.
57. Wang, L., Li, J., Pan, J., Jiang, X., Ji, Y., Li, Y., Qu, Y., Zhao, Y., Wu, X., and Chen, C. (2013) Revealing the binding structure of the protein corona on gold nanorods using synchrotron radiation-based techniques: understanding the reduced damage in cell membranes. *J. Am. Chem. Soc.*, **135**, 17359–17368.
58. Zhong, J., Song, L., Meng, J., Gao, B., Chu, W.S., Xu, H.Y., Luo, Y., Guo, J.H., Marcelli, A., Xie, S.H., and Wu, Z.Y. (2009) Bio-nano interaction of proteins adsorbed on single-walled carbon nanotubes. *Carbon*, **47**, 967–973.
59. Laera, S., Ceccone, G., Rossi, F., Gilliland, D., Hussain, R., Siligardi, G., and Calzolai, L. (2011) Measuring protein structure and stability of protein-nanoparticle systems with synchrotron radiation circular dichroism. *Nano Lett.*, **11**, 4480–4484.
60. Wang, B., Feng, W.Y., Chai, Z.F., and Zhao, Y.L. (2015) Probing the interaction at nano-bio interface using synchrotron radiation-based analytical techniques. *Sci. China Chem.*, **58**, 768–779.
61. Barends, T.R.M., Foucar, L., Botha, S., Doak, R.B., Shoeman, R.L., Nass, K., Koglin, J.E., Williams, G.J., Boutet, S., Messerschmidt, M., and Schlichting, I. (2014) De novo protein crystal structure determination from X-ray free-electron laser data. *Nature*, **505**, 244–247.

62. Weinhausen, B. and Koester, S. (2013) Microfluidic devices for X-ray studies on hydrated cells. *Lab Chip*, **13**, 212–215.
63. Weinhausen, B., Saldanha, O., Wilke, R.N., Dammann, C., Priebe, M., Burghammer, M., Sprung, M., and Koester, S. (2014) Scanning x-ray nanodiffraction on living eukaryotic cells in microfluidic environments. *Phys. Rev. Lett.*, **112**, 102–107.
64. Jones, M.W.M., van Riessen, G.A., Abbey, B., Putkunz, C.T., Junker, M.D., Balaur, E., Vine, D.J., McNulty, I., Chen, B., Arhatari, B.D., Frankland, S., Nugent, K.A., Tilley, L., and Peele, A.G. (2013) Whole-cell phase contrast imaging at the nanoscale using Fresnel coherent diffractive imaging tomography. *Sci. Rep.*, **3**, 1–5.

6
Imaging Techniques in Nanotoxicology Research[1)]

Liang Yan, Yufeng Li, and Zhanjun Gu

6.1
Introduction

The potential toxicity of nanomaterials (NMs) is of great importance for their biomedical applications [1–4]. Thus, the well understanding of the behaviors of NMs in biological systems as well as their toxicology profiles is a critical fundamental question to be addressed in order to use these NMs in various applications in the future. In traditional toxicology, the visualization and assessment of the uptake, translocation, accumulation, and clearance of NMs in living organisms are always the first risk to human health. Therefore, imaging techniques become the powerful tools for the research *in vivo* and *in vitro* to study basic biological and pathological mechanisms and provide important information for the assessment of NMs' toxicity in biological systems. So far, many imaging techniques have been applied for nanotoxicology research. In this chapter, we present a comprehensive overview of various imaging techniques applied to the physicochemical characterization of NMs, structural analysis of bio–nano interactions, visualization of NMs *in vitro*, quantification of biodistribution, bioaccumulation, and transformation of NMs *in vivo*. In particular, the advanced nuclear analytical and related techniques in nanotoxicology research have been highlighted because of their advantages of absolute quantification, high sensitivity, excellent accuracy and precision, low matrix effects, and nondestructiveness compared to traditional imaging techniques.

6.2
Imaging Techniques for *In Vitro* Visualization and Quantification of Nanomaterials

Direct visualization of interactions between the NMs and the cultured cells is always a primary question. Quite a lot of imaging techniques have been applied

1) This chapter is modified from a Review of our laboratory (Chunying Chen, Yufeng Li, Ying Qu, Zhifang Chai, Yuliang Zhao, Chem. Soc. Rev., 2013,42, 8266-8303).

Toxicology of Nanomaterials, First Edition. Edited by Yuliang Zhao, Zhiyong Zhang, and Weiyue Feng.

in the observation of NMs. In general, to get an accurate image of NMs inside cells, certain criteria need to be stressed here, including the ability to accurately quantify NMs, high resolution, high precision, and real time. In addition, in order to view both subcellular and extensive intercellular structures, it is necessary to image them at nanometer scale with sufficient penetration through the sample to obtain a three-dimensional (3D) view. A number of imaging methods that have greatly advanced our understanding of nanoparticles (NPs) in the cellular compartments are illustrated in Figure 6.1.

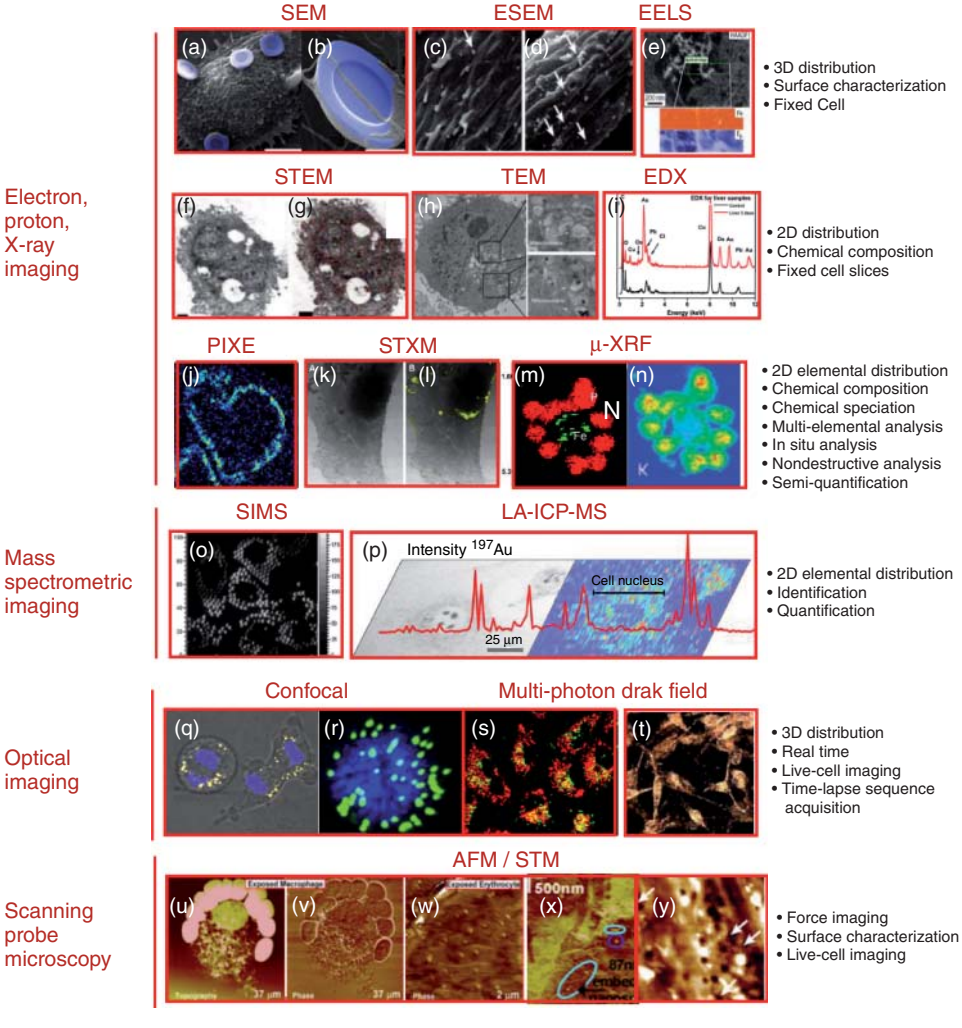

Figure 6.1 Imaging techniques for cellular visualization of nanomaterials. (a,b) SEM [5]; (c,d) ESEM [6]; (e) EELS [7]; (f,g) STEM [8]; (h) TEM [9]; (i) EDX [10]; (j,k) PIXE [11]; (l) STXM; (m,n) μ-XRF[12]; (o) SIMS [13]; (p) LA-ICP-MS [14]; (q,r) confocal [15]; (s) multiphoton luminescence [16]; (t) dark-field microscopy [9]; and (u–y) AFM [6, 17].

6.2.1 Optical Imaging Methods

6.2.1.1 Optical Microscope

As the most classical imaging technique for biologists, optical microscopy has the biggest advantage to visualize the dynamic processes of NMs in living cells using fluorescent labels (Figure 6.1q–t). For example, using a confocal microscope, superparamagnetic iron oxide NPs covered with a photonic ZnO shell are found to be efficiently taken up by dendritic cells, which are important in the initiation and regulation of antigen-specific immune responses, without the need for transfection agents [18]. This is frequently of great advantage in selectively imaging photoluminescence- or fluorescence-labeled NPs and identifiable subcellular components; sometimes multiple fluorophores can be used simultaneously. Optical imaging methods are the most widely used methods for 3D imaging of cells. 3D imaging plays a growing role in the investigation of NMs in biological systems, where it is often important to understand the distribution of NPs in cells where they may also be distributed in depth. Ideally, this is done on a specimen that is minimally modified from its living state. With approaches such as confocal and two-photon confocal microscopy, images of eukaryotic cells have been obtained with a resolution as low as 100 nm in all three dimensions. 3D images can be acquired point-by-point and reconstructed in three dimensions with a computer using the confocal laser scanning microscope (CLSM) and multiphoton fluorescence microscope (MFM) [15]. MFM is a specialized optical microscope that uses pulsed long-wavelength photons to excite fluorophores within the specimen that will then produce an emission wavelength shorter than the excitation wavelength. Recently, the multiphoton luminescence signal of gold nanorods (GNRs) has been investigated in order to image nanorods in biological samples [19–21]. The luminescence signal is superior to fluorescent dye molecules in that it is not prone to bleaching or to blinking [22, 23]. Figure 6.1s shows the colocalization of GNRs and organelles using a near-infrared CLSM [16].

Dark-field microscopy (DFM) is also used extensively in biological and materials research for applications ranging from single NP spectroscopy to label-free live tissue imaging. In NMs research, DFM has become particularly useful because nanoscale objects strongly scatter light at specific wavelengths as a result of optical resonances that depend on the size, shape, and composition of the material [24, 25]. For example, Au NPs can strongly scatter light at their plasmon wavelengths, with the scattering cross sections several times stronger than that of the emission from a fluorescent dye molecule. The frequencies of localized surface plasmon resonances in anisotropic metallic NPs are well known to depend on the particle size and aspect ratio. Au NPs larger than 10 nm in diameter can be readily visualized under dark-field scattering microscopy with a simple optical microscope. In contrast to conventional fluorophores, the light-scattering NPs are indefinitely photostable and do not blink. These features make gold-based NP probes very powerful for bioimaging. For example, Huang *et al.* [26] demonstrated that GNRs scatter strongly in the near-infrared (NIR) region, which is capable of detecting

head and neck cancer cells under excitation at spectral wavelengths where biological tissues exhibit little attenuation.

Another modality in scattering-based imaging is optical coherence tomography (OCT). OCT uses a short coherence light source to provide optical cross-sectional imaging of tissues [27, 28]. It can produce 3D images of a subject with micrometer resolution. Halas and coworkers [29] demonstrated that systematically injected gold nanoshells strongly enhanced OCT image contrast from tumor tissues. Functionalized gold nanospheres, nanorods, and nanocages have also been used for OCT imaging of cancer [30–32]. For example, Chhetri *et al.* [33, 34] demonstrated a strategy by using OCT to depth-resolve diffusion of plasmon-resonant GNRs that were weakly constrained OCT depth-resolves the particle-averaged translational diffusion coefficient of GNRs within each coherence volume, which is separable from the nonequilibrium motile activities of cells based on the unique polarized light-scattering properties of GNRs. Their results have shown how this method enables minimally invasive imaging and monitoring of nanotopological changes in a variety of biological models, including extracellular matrix (ECM) remodeling as relevant to carcinogenesis and dehydration of pulmonary mucus as relevant to cystic fibrosis. Therefore, this method shows the broad potential for sensing changes in diffusion of GNRs in 3D models of mammary ECM and pulmonary mucus.

6.2.1.2 High-Content Screening Method

High-content screening (HCS) is a recent advancement in the integration and automation of quantitative fluorescence microscopy and image analysis, and it has already started to generate impact in pharmaceutical and biotechnology industries. With rapid development of novel NMs, a fast and fairly comprehensive method for screening of biological activity and cytotoxicity of NMs is highly desired. A high-content, high-throughput cytotoxicity assay platform based on HCS technology may meet the future's demand for nanotoxicity studies.

Zhang *et al.* [35] were the first to employ high-content image analysis, in conjunction with high-throughput analysis, to study the cytotoxicity of quantum dots (QDs). HCS analysis was employed in their study for cell counting, quantification of apoptotic and necrotic cell population, and generation of cell cycle profiles. They investigated the cellular and molecular effect of high doses of poly(ethylene glycol) silanized quantum dots (PEG-silane-QDs) in the human lung and skin epithelial cells and reported PEG-silane-QDs induced minimal cytotoxicity even at high dosages. Kotov *et al.* [36] extended the application of HCS technology to the evaluation of cell function, specifically neurite outgrowth, and the development of a multiplexed cytotoxicity assay that may serve as the basis of a standardized nanotoxicity assay and facilitate the formation of a unified nanotoxicology database. They demonstrated the use of various HCS assays to study the cytotoxicity of CdTe QDs and Au NPs in NG108-15 neuroblastoma cells and HepG2 human hepatocellular carcinoma cells. They found the neurite outgrowth assay, which assessed the functionality of differentiated neural cells, to be particularly important and the multiplexed cytotoxicity assay as a sensitive

and informative assessment of toxicological mechanisms. The versatility of the multiplexed cytotoxicity assay was demonstrated across the different NPs tested in this study. The assays were capable of distinguishing the subtle differences in the cytotoxicity generated by TGA-QDs and Gelatin-QDs. Very recently, Chen *et al.* [37] used HCS to evaluate the toxicity of eight different NMs. A set of different endpoints including reactive oxygen species (ROS) production, Ca^{2+} transient, mitochondrial membrane potential, and cellular pH levels were checked in human bronchial epithelial (16HBE) cells after incubating with NMs for 24 h. The advantage of HCS is that it allows for efficient and reliable screening of multiple responses of cells simultaneously within one screen test, which can avoid the problematic interpretation of investigations when carried on a single toxicological endpoint. Therefore, HCS is an effective and powerful method for image-based assessments with a broad set of biological endpoints in toxicity evaluation of NMs.

6.2.2
Electron Microscopes

Electron microscopes (EMs) mainly including transmission electron microscope (TEM) and scanning electron microscope (SEM) have been widely applied to characterize the size and shape of NPs, and they are also widely used in the cellular visualization of NPs. For example, the biocompatibility of mesoporous silicon NPs was observed in vascular endothelial cells by TEM as shown in Figure 6.1a,b [5].

EMs can also be applied to assess the uptake and subcellular localization of various NPs, since NPs composed of heavy elements are marked by a good image contrast (absorbance) from both the electron density of the elements and the thickness of the particles [10, 15, 16, 38]. Cetyltrimethylammonium bromide (CTAB)-coated Au nanorods were found in mitochondria and lysosomes, and cellular inflammatory responses such as the swelling of mitochondria could also be observed from the TEM images (Figure 6.1h) [38]. The capabilities of the EMs can be further extended by additional stages and detectors incorporated into the microscope to allow studies of the interface between NMs and the biological system. Electron cryomicroscope (CryoTEM) has also been employed for visualizing the biosamples, which allows imaging of unstained biomolecules and intercellular structures since it has a specimen holder that is capable of maintaining the specimen at liquid nitrogen or liquid helium temperatures [39, 40].

A TEM can be modified into a scanning transmission electron microscope (STEM) by combining with suitable detectors that raster scans the beam across the sample to form the image. Scanning coils are used to deflect the beam by, for example, an electrostatic shift of the beam; the beam is then collected using a current detector such as a Faraday cup, which acts as a direct electron counter. By correlating the electron count to the position of the scanning beam (known as the *probe*), the transmitted component of the beam may be measured. The nontransmitted components may be obtained either by beam tilting or by the use of annular dark-field detectors. Asharani *et al.* [8] utilized the STEM to analyze

cancer cells treated with 100 μg/ml of Ag NPs. TEM analysis (Figure 6.1f,g) indicated the presence of Ag NPs inside the mitochondria and nucleus, implying their direct involvement in mitochondrial toxicity and DNA damage. Elemental mapping of cell sections using STEM confirmed the distribution of Ag NP within the cell.

For conventional imaging EMs, specimens must be completely dry and electrically conductive to prevent the accumulation of electrostatic charge at the surface in a high-vacuum specimen chamber. Thus, to image biological samples, chemical fixation and dehydration procedure are usually required to preserve and stabilize their structure. However, these procedures may cause the collapse and shrinkage of the sample, which destroys the structure of the biotissues/molecules. In addition, nonconductive biological specimens tend to accumulate charge when they are scanned by the electron beam and cause scanning faults and other image artifacts. Thus, the specimen requires a sputtered coating of electrically conducting material, such as Au or Pt, before it is examined in the EMs, which will obscure the underlying fine detail of the specimen.

New development of EMs such as the environmental scanning electron microscope (ESEM) can produce images of sufficient quality and resolution even when the samples are wet or contained in low vacuum or gas. This greatly facilitates the imaging of biological samples without any pretreatment, such as drying process, which could significantly reduce the destruction of biosamples. An even greater advantage is that the surface coating is unnecessary even for nonconductive samples, which allows the direct observation of surface morphology and *in situ* analysis of chemical composition. As Figure 6.1c,d shows, the specific interaction of functional NPs with an oxidation-damaged cell membrane could be observed by ESEM [6]. The authors found that more spots were observed in oxidation-damaged samples than in the controls. Fullerene aggregations were bound primarily to the cell membrane, and some were observed to be nonspecifically embedded into the membrane.

EMs can be connected to various detectors that give more information of samples about their chemical composition and structure. The combination of energy-dispersive X-ray spectroscopy (EDS or EDX) and electron energy-loss spectroscopy (EELS) with the high-resolution EM provides a very powerful approach to characterizing the composition and chemical states of NMs. EDS relies on the investigation of a sample through interactions between electromagnetic radiation and matter, which analyzes the X-rays emitted by the matter in response to being hit with charged particles. Its characterization capabilities are based on the fundamental principle that each element emits unique X-rays that are characteristic of the atomic structure of an element to be identified. Wang *et al.* [10] utilized TEM integrated with EDX to study the distribution of Au NRs at the intracellular and tissue level in animal organ samples. TEM was used to detect the subcellular localization of Au NRs in mouse liver after treatment by injection with Au NRs. Aggregated NPs were located in lysosomes of lymphocytes in the Kupffer cells in the liver. Meanwhile, chemical analysis

through EDX spectroscopy confirmed that these particles were composed of gold (Figure 6.1i).

EELS is another common spectroscopy technique available on many EMs, which is often complementary to EDX (or EDS) [41]. EELS is capable of measuring atomic composition, chemical bonding, valence and conduction band, electronic properties, surface properties, and element-specific pair distance distribution functions. Compared with EDX, which offers a particular sensitivity for identifying the atomic composition of heavier elements, EELS tends to work best at relatively low atomic numbers and is perhaps the best tool for detecting the elements ranging from carbon through the 3d transition metals. TEM in conjunction with EELS is also called energy-filtered transmission electron microscopy (EFTEM) [42]. Porter *et al.* [43] used EFTEM to image the distribution of C_{60} aggregates within intracellular compartments of human monocyte-derived macrophages (HMMs). They achieved improved contrast between C_{60} and unstained cellular compartments and also between ordered and disordered forms of aggregated C_{60}.

One obvious shortcoming of TEM and SEM is that they prefer to be used for imaging electron-dense materials (such as metallic NPs), but not for soft materials (such as biomolecules) [44]. On the other hand, scanning microscopes such as atomic force microscopy (AFM) and scanning tunnel microscopy (STM) constitute a complementary approach that produces nanometer-scale resolution and accommodates the living cell in its natural environment.

By using AFM, Tetard *et al.* [17] analyzed probe–sample force curves and images of mouse cells with buried NPs to understand the cellular uptake of these NMs. Samples of alveolar macrophages and erythrocytes (red blood cells) were obtained from mice after pharyngeal aspiration exposure to pluronic-coated single-walled carbon nanohorns (SWCNHs) and SiO_2NPs. In the acoustic phase image of the macrophages (Figure 6.2c), the subcellular structures and buried SWCNHs were visualized (Figure 6.2b). A closer view of the erythrocytes (in Figure 6.2d) showed that SWCNHs could be clearly resolved. These observations were further strengthened by Raman spectroscopy. With high-resolution topography and phase images (Figure 6.2e) of buried SiO_2 NPs in macrophages, they resolved individual NPs on the surface of the cell (circled in purple) or within the cell (circled in light blue). Tip–sample excitation forces associated with nanomechanical image formation were further investigated. The results indicated that the natural resonance frequencies of the cantilever probe played an important role in the stability and performance of this new imaging methodology. Images acquired under various operational frequencies and amplitudes are presented (Figure 6.2f). Results showed that MSAFM could provide noninvasive subsurface information on the mechanical properties of materials and might be of tremendous potential for characterizing the properties of nano–bio systems without the limitations of current techniques such as special sample preparation/alteration in the native fluidic environment of many biological systems.

AFM can also be applied in combination with ESEM. Lao *et al.* [6] utilized biological AFM to probe the *in vivo* morphological response of oxidation-damaged

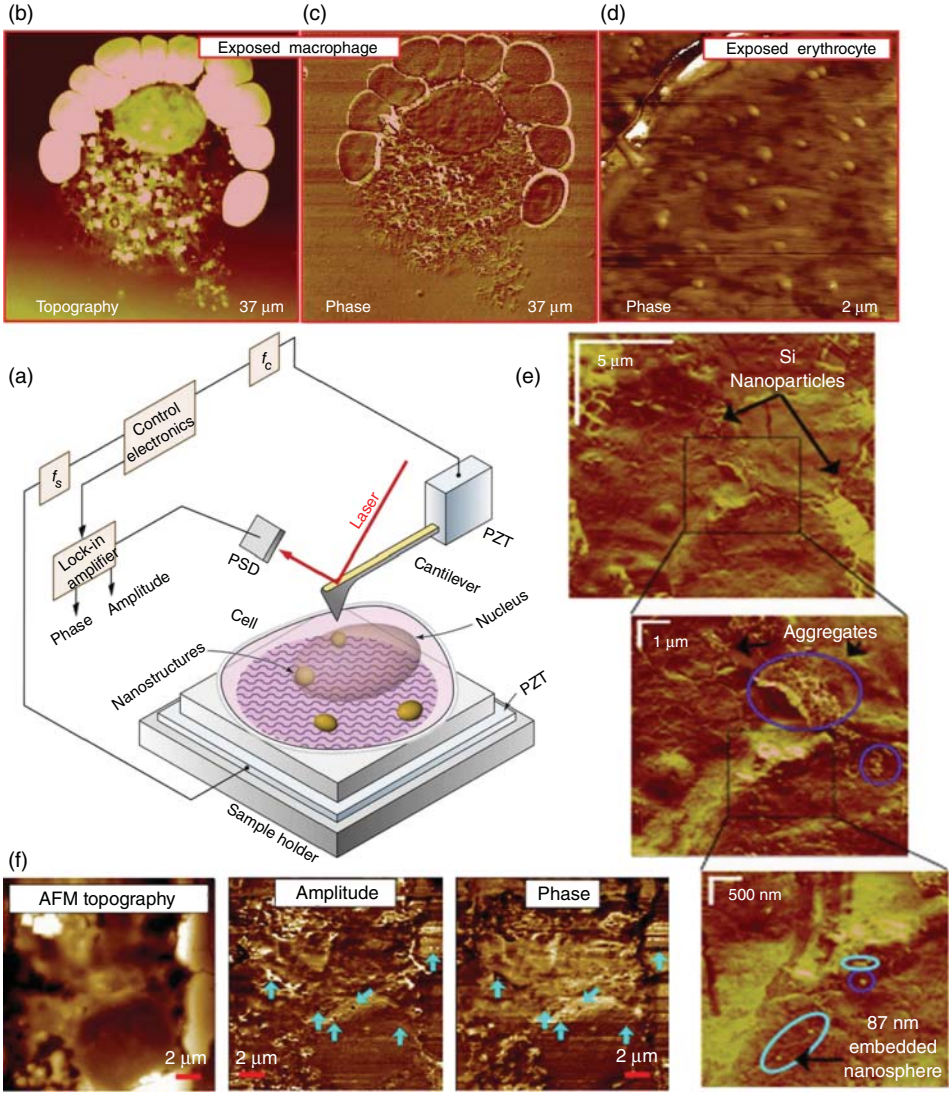

Figure 6.2 Atomic force microscopy of silica NPs and carbon nanohorns in macrophages and red blood cells. (a) Schematic of the experimental set-up; (b) AFM image of macrophages exposed to SWCNH; (c) phase image of macrophages; (d) phase image of erythrocytes; (e) phase images of buried silica NPs in macrophages at different spatial resolution; and (f) influence of the driving frequencies on resulting force curves and phase images [17]. (Adapted from the data of the cited paper by permission from Elsevier.)

cell membranes to NP treatment and confirmed the results by using an ESEM. They found specific interaction of functional NPs with the oxidation-damaged cell membrane. The number of spots on cells that were incubated with fullerene particles alone was lower than that for oxidation-damaged samples, close to that for the controls. By using ESEM, they obtained similar results. More spots were observed in oxidation-damaged samples compared to the controls. Fullerene aggregations were bound primarily to the cell membrane, and some were observed to be nonspecifically embedded into the membrane.

6.2.3
X-ray Imaging

Recent advances in nanotechnology and science have highlighted the need for analytic tools that provide elemental and chemical information with large penetration depths and spatial resolution at the nanoscale. Currently, X-ray analytical imaging techniques such as zone-plate-based microscopy, holography, and "lensless" imaging and combinations such as ptychography are under development [20]. X-rays have better penetration ability compared to electrons. Development of high-brilliance, high-energy X-ray sources, such as synchrotron radiation, coupled with advances in manufacturing technologies of focusing optics, has pushed progress in X-ray microscopy. The resolution of X-ray microscopy is intermediate between the visible light microscope and the EM, which ranks among the most sensitive modalities for detection of elements in biological samples with submicrometer resolution [21]. X-ray imaging methods currently being used to obtain images of biological samples at resolutions less than 100 nm include hard X-ray microanalytical techniques such as X-ray fluorescence (XRF) and soft X-ray imaging such as scanning transmission X-ray microscopy (STXM). Detailed description of hard X-ray microscopy and soft X-ray microscopy and their applications can be found in Chapter 5 of this book.

6.2.4
Proton Microprobes

Proton microprobe methods use a proton beam focused by either electric or magnetic fields to attain elemental distribution maps of samples [21, 45]. The proton microprobe analysis offers both imaging and quantification capability for elemental analysis of NPs. The particle beam size, around 1 μm diameter, and the resulting spatial resolution is compatible with X-ray microanalysis of eukaryotic cells. The most common proton beam method is proton-induced X-ray emission (PIXE) [46, 47]. PIXE is a nondestructive technique based on excitation of the electronic levels of the atoms by means of an ion beam, producing X-ray emission. These X-rays are characteristic and proportional to each element, thus allowing easy identification and quantification of the elemental composition of the measured target (both the NM and its containing matrix). Similarly to XRF, PIXE with a proton microprobe has also been developed to examine elemental distribution in

biological samples. A PIXE spectrum enables the simultaneous detection of multiple elements virtually from Na to U, while lighter elements can be analyzed by particle-induced gamma-ray emission (PIGE), with excellent quantitative precision and analytical sensitivity (1 – 10 μg/g on a dry weight basis). These characteristics are especially important for transition elements, which are the essential trace elements in biological tissues. PIXE is often combined with Rutherford backscattering spectrometry (RBS) and scanning transmission ion microscopy (STIM) for quantitative elemental analyses and identification of structural features within the sample. Proton beams are well suited for acquiring quantitative elemental distribution maps of biological samples including whole cells and tissue sections, in depths up to 100 μm with average beam diameters of 1 μm. PIXE with a tightly focused proton beam (down to 1 μm, micro-PIXE) enables microscopic analysis at the cellular level [48]. Spatial resolutions of 200 – 300 nm are commonly achieved with a proton-induced X-ray emission-Rutherford backscattering spectrometry (PIXE-RBS) setup. 3D micro-PIXE has also been recently developed to perform depth analysis [49].

PIXE offers a number of advantages over electron probe methods, including the ability to simultaneously detect over 20 elements at an enhanced sensitivity up to 100 times than that of electron-based methods with essentially no background contributions and no major sample preparation requirements. Furthermore, PIXE maintains the capacity to obtain fully quantitative elemental distribution maps when combined with RBS and STIM, which makes it particularly attractive for analyzing biological samples at high spatial resolutions [21]. In contrast to EDX, PIXE can be operated under ambient conditions. Through a proper selection of ion beams, energies, and filters, it is possible to precisely quantify the biokinetics or biopersistence of NMs present after *in vivo* or *in vitro* exposure and the elemental composition of the exposed tissues/cells/organs. For nanotoxicological studies, there are some special advantages of PIXE: there is no restriction on NM size, and the sensitivity is in the parts per million range (low background noise when compared to EDX). There is no need for radiolabeling/radioactivation/fluorescence modifications to the NM that could potentially bias the observed response in the biological matrix. There is no need to condition the sample (i.e., digestion), besides obtaining a few droplets (if liquid) or making it a pellet (if solid). Large-volume samples can be measured for statistical significance. Moreover, the proton microprobe is more sensitive than the electron microprobe and the concentration results are fully quantitative.

6.2.5 Mass Spectrometry

Imaging mass spectrometric techniques, such as laser ablation – inductively coupled plasma – mass spectrometry (LA-ICP-MS) and secondary ion mass spectrometry (SIMS), are the most sensitive techniques for chemical element imaging. With them, the distribution and quantities of the NPs' elements may be determined in thin sections of cell samples; they also allow isotopic analysis.

Detailed description of LA-ICP-MS and its applications can be found in Chapter 2 of this book.

SIMS is a well-established technique that permits rapid detection of stable and radioactive nuclides; it offers elemental detection limits ranging from parts per million to parts per billion. It is used to analyze the composition of solid surfaces and thin films by sputtering the surface of the specimen with a focused primary ion beam and collecting and analyzing ejected secondary ions [50, 51]. The mass/charge ratios of these secondary ions are measured with a mass spectrometer to determine the elemental, isotopic, or molecular composition of the surface to a depth of 1–2 nm. The secondary ions emitted by the specimen are analyzed by a sensitive mass spectrometer such as a double-focusing sector field mass spectrometer (SFMS), time-of-flight mass spectrometer (TOF-MS), or quadrupole-based mass spectrometer (QMS). Imaging by SIMS with high spatial resolution is extremely attractive in the investigation of single cells. The primary advantage of SIMS is that the analysis consumes very little sample (essentially nondestructive). Its high sensitivity also means that samples with low concentration levels (down to ppb levels) can be analyzed with SIMS.

Using time-of-flight mass spectrometer–secondary ion mass spectrometry (TOF-SIMS), Shon *et al.* [52] measured the distribution and quantity of Fe_3O_4 NPs inside murine macrophage cells without any labeling. Fe_3O_4 NPs were found mainly in the cytoplasm region of the cells, not in the nucleus, suggesting that the Fe_3O_4 NPs were taken up into the cytoplasm of the cell and not into the nucleus. Quantification signals show that more uptake of Fe_3O_4 NPs took place with higher concentrations of NPs. The image of Fe^+ both brightened and broadened at higher concentrations of Fe_3O_4 NPs.

To facilitate the tracking the Fe_3O_4 NPs within the cell, the main regions of the cell (nucleus, cytoplasm, and cell membrane) were located by characteristic ion signals. The Fe_3O_4 NPs inside the cells were then tracked by obtaining images of Fe^+ (originating from Fe_3O_4, Red), $C_4H_7^+$ (generally originating from the cytoplasm, Green), and CN^- (generally originating from the nucleus, Blue) and overlaying them to produce an RGB image. The image of Fe^+, which indicated the location of Fe_3O_4 NPs, overlaped well with the image of $C_4H_7^+$, which indicated the location of the cytoplasm, but not with the image of CN^-, which indicated the location of the nucleus. Based on these results, it seemed that most of the Fe_3O_4 NPs were taken up into the cytoplasm and not into the nucleus of each cell. In addition, the amount of uptake of NPs into the cells showed a good linear relationship with the concentration of Fe_3O_4 NPs applied to the cells. Ulrich *et al.* [53] studied the microscale mechanisms of agarose-induced disruption of collagen remodeling by TOF-SIMS and SEM. TOF-SIMS can be used to characterize the surface chemistry of protein films because of its chemical selectivity and surface sensitivity, with a sample depth of approximately 1 nm. It was found that the observed differences in glioma cell spreading and bundling of collagen fibers were not attributable to initial differences in exposed collagen as the concentration of agarose was increased.

SIMS can also be applied to 3D analysis of NPs in cells. Hagenhoff *et al.* [13] successfully detected and localized SiO_2 particles with diameters between 2 mm and 150 nm within the cytoplasm of mammalian cells. The particles were selected as model objects for nonluminescent, unlabeled particles that were hard to localize by other experimental approaches. TOF-SIMS analysis proved that particles were taken up into the cell body, provided images of their distribution around the cell nucleus, and indicated that the millimeter-sized particles beneath the cell membranes caused the membranes to undulate. Two ion sources (Cs^+ and O_2^+) were used for sputtering the organic material and exposing the deeper sections of the cells. This study proved that TOF-SIMS was capable of detecting micro- and NPs inside mammalian cells down to a particle diameter of 150 nm. The TOF-SIMS approach allows discrimination between extracellular and intracellular localization of the particles – the key question in many biomedical projects.

The main drawbacks of SIMS are huge matrix effects and high polyatomic ion formation rates, which make the quantification of analytical data extremely difficult [54], because both atomic and molecular species are produced during sputtering of the samples and not all elements in all substrates (matrices) can be analyzed quantitatively. Moreover, the SIMS method only allows analysis under high-vacuum conditions, which has limitations for the study of native cells. Reliable sample preparation for SIMS analysis is a crucial step with respect to maximum preservation of the real information in a biological sample [55].

It is well known that the cellular uptake of the functionalized NPs is mainly dependent on the surface functionality. A different cellular uptake behavior and bioeffects may result if the different surface functionalities are chosen. It is necessary to develop a method for simultaneous imaging of different NPs varying only in surface ligand structure in cells/tissues. Although various approaches have been developed for imaging NPs, simultaneous screening of the cellular uptake of multiple particles with different surface functional groups is still a challenge. Recently, Rotello *et al.* [56] developed laser desorption/ionization mass spectrometry (LDI-MS) in an imaging mode to investigate surface-chemistry-dictated intraorgan distribution of NPs. It tracks NPs by measuring their surface ligand, which could be primary detected because the NPs core absorb the laser energy, and this energy is readily transferred to desorb and ionize the surface ligand. This new LDI-MS imaging method enables multiplexed imaging of NPs with potentially unlimited readouts and without additional labeling of the NPs because this approach uses NP surface-ligand mass as the readout. Using this new "mass barcode" approach, they found that the intraorgan distribution of same-size NPs was directly linked to their surface functionality, which was difficult to obtain using any other techniques.

Together, the aforementioned *in vitro* imaging methods have greatly advanced our understanding of the cellular uptake, location and translocation, and fate of NMs in cells. Among them, the resolution of synchrotron-radiation-based X-ray microscopy is intermediate between the visible light microscope and the EM and has more penetration power than the EM. AFM and STM are complementary approaches to SEM and TEM that produce nanometer-scale resolution and

accommodate the living cell in its natural environment. Mass-spectroscopy-based imaging methods (LA-ICP-MS, LDI-MS, and SIMS) and proton-excited X-ray emission can provide quantitative analysis and elemental distribution of NPs in thin sections of cell samples.

6.3 Distribution and Quantification of Nanomaterials *In Vivo*

6.3.1 Whole-Body Distribution and Quantification of Nanomaterials

6.3.1.1 X-Ray Computed Tomography

X-ray computed tomography (X-ray CT) is a technology that uses computer-processed X-rays to produce tomographic images of specific areas of the scanned object, allowing the user to see inside without cutting [57]. Due to the advantages of rational high-contrast resolution, cost-effectiveness, facile image processing, and unlimited penetration depth, X-ray CT has become one of the most popular diagnostic imaging techniques in medical science, biology, and clinical use [58]. Currently, iodine-containing compounds are the widely used X-ray CT contrast agents with an emphasis on its better cost-effectiveness and safety rather than its performance. However, small iodinated compounds are rapidly excreted via renal elimination, resulting in short circulation times that limit their applications for target-specific imaging and angiography. Therefore, along with the development of nanotechnology, many researchers have focused on the application of various NPs as potential candidates for X-ray CT. In comparison with the conventional iodine-based contrast agents, NPs can be readily functionalized with various biocompatible polymers or biomolecules either for the enhancement of their contrast and blood circulation time or for tissue-specific uptake and multimodal imaging applications, resulting in more dependable diagnostic information [59].

Gold is one of the most well-studied NPs for X-ray CT contrast agents due to the large X-ray absorption coefficients [60, 61]. Al Zaki *et al.* [62] synthesized the gold-loaded polymeric micelles, following intravenous injection of mice. It was found that the prepared polymeric micelles provided blood pool contrast for up to 24 h and improved the delineation of tumor margins via computed tomography (CT). Hayashi *et al.* [63] also used clustered Au NPs – fluorescent SiO_2 core – shell NPs for fluorescence imaging and X-ray CT of tumors. Tumors, specific soft tissues, were inherently low in CT. Liu *et al.* [64] synthesized low-generation poly(amidoamine) dendrimer-stabilized Au nanoparticles (Au DSNPs). The Au DSNPs showed much better performance in CT imaging of the major organs of rats (heart, liver, kidney, spleen, and bladder) *in vivo* than Omnipaque.

Although it is relatively easy to prepare and functionalize Au NPs, the cost of using gold as an X-ray contrast agent is a huge obstacle to its clinical utilization. Alternatively, the sulfide NMs, such as Bi_2S_3 and WS_2, are another strong candidate as CT contrast agents. For example, Cheng *et al.* [65] developed a novel X-ray

CT contrast agent based on PEGylated WS_2 nanosheets, which could be used for CT imaging of tumors upon through i.v. and i.t. injection. Zhao *et al.* [66] also synthesized the Bi_2S_3 nanorods via a facile solvothermal method. The resulting Bi_2S_3 nanorods showed the superior contrast enhancement due to the presence of Bi atoms that have strong X-ray attenuation capability, thus having the capability of CT imaging contrast agents.

In addition, Ba *et al.* [67] reported a facile strategy to synthesize monodispersed X-ray CT contrast agents based on PEGylated lutetium hydroxycarbonate NPs. The nanoparticulate CT contrast agent possessed overall safety and showed promise for further biomedical usages. Liu *et al.* [68] also designed and synthesized PEGylated hybrid Yb_2O_3 NPs as high-performance nanoprobes for X-ray CT imaging both *in vitro* and *in vivo*. The PEG-Yb_2O_3:Gd NPs possessed excellent biocompatibility and revealed overall safety. Tantalum oxide (TaO_x) NPs were recently synthesized as a cost-effective alternative and the distribution of the TaO_x particles was tracked by CT [69]. It was found that once the NPs were injected, the vessels were preferentially enhanced, enabling spatially described, volume-rendered images of the blood pool. The NPs were eventually accumulated in macrophages in the spleen and liver.

Currently, 3D microcomputed tomography with X-ray radiation from a synchrotron source (XMCT) is a relatively new CT technology, which can present better structural information on contrast-enhanced major organs [70]. The high X-ray photon flux, which allows for use of essentially monochromatic photon energy and parallel radiation of the synchrotron X-ray source, provides 3D images of samples with a higher signal-to-noise ratio and higher resolution (~1–5 μm) than conventional micro-CT (~20 μm). This technique allows visualization and examination of the remodeling sites in 3D, providing new insights into the topological changes with treatment. Angiogenesis in mice has been studied using Au NPs as phase-contrast agents by XMCT [71].

6.3.1.2 Magnetic Resonance Imaging

Magnetic resonance imaging (MRI) is a medical imaging technique used in radiology to investigate internal structures of the body in detail in both health and disease. Based on the images formed from the strong magnetic fields and radio waves, it provides good contrast between the different soft tissues of the body, making it especially useful in imaging the brain, muscles, heart, and cancers [72]. Moreover, MRI offers high soft tissue contrast and is capable of deep tissue imaging with high spatial resolution (50 μm). However, its inherent drawback is its low-sensitivity millimolar concentrations of protons are needed, so the technique often requires the use of exogenous contrast agents [73–75].

Bruckman *et al.* [76] reported an NP-based high aspect ratio, molecularly targeted MRI contrast agent for accurate diagnosis of some inflammatory diseases. Specifically, they engineered the plant viral NP platform tobacco mosaic virus (TMV) to target vascular cell adhesion molecule (VCAM)-1, which was highly expressed on activated endothelial cells in atherosclerotic plaques. Liu *et al.* [77] also presented a novel strategy for dynamically imaging the blood–brain

barrier (BBB) damage with PEGylated superparamagnetic iron oxide nanoparticles (SPIONs) as contrast agents. The employment of SPIONs as contrast agents made it possible to dynamically image the BBB permeability alterations and ischemic lesions simultaneously with T_2-weighted MRI, and the monitoring could last up to 24 h with a single administration of PEGylated SPIONs *in vivo*.

The development of rare earth NPs provides another route to design and construct tumor probes suitable for imaging tumors *in vivo*. As a well-investigated probe for T_1 contrast, Gd(III) has been incorporated into various NMs. For example, SiO_2 and perfluorocarbon NPs, carbon nanotubes, nanodiamonds, and metallofullerene NPs all yield high MRI contrast because of a high payload of gadolinium ions and a slow tumbling motion of particles [76, 78–82]. Liu *et al.* [83] reported new approaches for size control synthesis of magnetic/upconversion fluorescent $NaGdF_4$:Yb, ErNPs and in detail investigated their applications for imaging tiny tumors *in vivo*. Owing to their excellent properties, tumors smaller than 2 mm were successfully imaged *in vivo* using the as-made NPs. Hou *et al.* [84] also fabricated $NaGdF_4$-PEG-mAb nanoprobes. The biocompatibility and binding of the nanoprobes were evaluated through *in vitro* experiments. The results revealed that the $NaGdF_4$-based probes possessed satisfying tumor-specific targeting ability and strong MRI contrast enhancement effects.

Recently, smart or responsive contrast agents (SCAs) can have a significant role in MRI. Gunduz *et al.* [85] reported a methodology that enables the preparation of dendrimeric contrast agents sensitive to Ca^{2+} when starting from the monomeric analogue. The *in vivo* MRI studies in the rat cerebral cortex indicate that diffusion properties of dendrimeric contrast agents have great advantages as compared to their monomeric equivalents. Alternatively, chemical exchange saturation transfer (CEST) MRI agents have recently been under intense scrutiny for applications in molecular imaging and in MRI-guided drug delivery. Ferrauto *et al.* [86] reported the LipoCEST/RBC aggregates that could be an innovative blood cell labeling for MRI and provided a route to improve the circulation lifetime of the liposomes, and the CEST procedure allowed assessment of the disassembly of the aggregates and accumulation of the liposomes in the ROI.

6.3.1.3 Nuclear Imaging

Nuclear imaging uses small amounts of radioactive isotopes (radiotracers) and imaging technology to see what is taking place in specific areas of the body. Positron emission tomography (PET) and single-photon emission computed tomography (SPECT) are two major instruments of nuclear imaging, providing images that reveal subtle information about physiological processer in humans and animals. Detailed description of the PET and SPECT and their applications in nanotoxicology can be found in Chapter 4 of this book.

6.3.1.4 Other Complementary Optical Imaging Technologies

6.3.1.4.1 Visible Light, Near-, or Far-Red Infrared Excited Fluorescence Imaging Fluorescence imaging has led to a great leap in biological research owing to the

high sensitivity, synthetic fluorescent molecules, and easy accessibility and has greatly become a powerful imaging technique. In fluorescence imaging, specific probes (such as organic molecules, NPs, carbon nanotubes, and graphene) are illuminated by incident radiation (such as ultraviolet, visible, near-, or far-red infrared), and then emit energy at a lower energy than that needed for exciting them (i.e., down conversion NPs) or at a higher energy than that needed for exciting them (i.e., upconversion NPs, UCNPs). Recently, QDs, organic NPs, UCNPs and carbon-based NPs have been gaining great interest as the newly emerging classes of fluorescent probes for biological and biomedical imaging. However, the greatest limitation of this imaging technique is the lack of the ability to provide anatomical resolution (about 2–3 mm).

Due to the unique optical and electronic properties, including the size- and composition-tunable fluorescence emission, superior photostability, improved brightness, a large absorption coefficients across, and simultaneous excitation of multiple fluorescence colors, multifunctional QDs have been developed for fluorescence imaging in living animals [87, 88]. *In vivo* targeting studies of human prostate cancer growing in nude mice indicate that the QD probes accumulate at tumors both through the enhanced permeability and retention of tumor sites and by antibody binding to cancer-specific cell surface biomarkers. Using both subcutaneous injection of QD-tagged cancer cells and systemic injection of multifunctional QD probes, sensitive and multicolor fluorescence imaging of cancer cells under *in vivo* conditions was achieved.

Unfortunately, fluorescence microscopy using visible light is inherently restricted to biological objects not thicker than a few millimeters. The fluorescence-based detection of NPs in tissues is thus usually performed *in vitro*, after the tissues are collected and sliced. Later, to meet the requirement for deeper penetration depths for most application, fluorescence-based techniques are driven into the near- or far-red infrared region. In the window, either the absorption of water, hemoglobin, and lipids or the antofluorescence and tissue scatter are low, enabling maximum light penetration. Sun *et al.* [89] developed paired gold clusters within apoferritin for intravital kidney imaging using far-red fluorescence microscopy. The phospholipid-PEG-solubilized single-walled carbon nanotubes (SWCNTs) were used to target murine breast tumors in BALB/c mice through NIR emission, which found a selective high accumulation of the functionalized SWCNTs in the tumor region and a correspondingly low uptake in healthy tissues [90]. In the aforementioned cases, however, only the high-level accumulation of NPs in the targeted tissues, that is, tumor, liver, or kidney, could be determined; the relatively lower accumulation in the other sites was below the detection limit. Therefore, these techniques are not suitable for detecting the systemic accumulation of NPs.

Alternatively, due to the high penetration depth, low autofluorescence from biosamples, low phototoxicity, and excellent resistance to photobleaching, UCNPs have been considered as a novel luminescent labels for deep-tissue *in vivo* bioimaging [91–97]. Zhang *et al.* [98] firstly demonstrated the effectiveness of using the PEI-coated $NaYF_4$:Yb/Er NPs for animal imaging *in vivo* and

exhibited the deeper-tissue imaging advantages over QDs. In a later work, Liu *et al.* [99] compared the *in vivo* imaging sensitivity of UCNPs and QDs (QD545 and QD625) side by side and demonstrated that the *in vivo* detection limit of UCNPs was at least one order of magnitude lower than that of QDs. To further increase the penetration depth of upconversion luminescence imaging, tuning the upconversion emission into NIR spectral range (700–1100 nm) and the red light region (600–700 nm) is essential for the deep tissue imaging since the light scatting, absorbance, and autofluorescence of tissue in those range are minimum. Gu *et al.* [100] reported the single-band red-emitting Mn-doped $NaYF_4$:Yb/Er UCNPs for *in vivo* imaging and extended the imaging depth to 15 mm. Besides, Bechet *et al.* [101] provided a new approach for *in vivo* imaging by utilizing NIR-to-NIR $NaYF_4$:Yb/Tm as the probe. High-contrast photoluminescence imaging was performed in mice since both the excitation and emission of the UCNPs used in this work were in the NIR region. From then, NIR-to-NIR upconversion luminescence (UCL) from Yb/Tm codoped UCNPs has been popular as the detection signal and successful UCL imaging of whole-body small animals with light-penetration depth up to 20 mm in mouse has been achieved [102, 103]. Moreover, PAA-$NaLuF_4$:Yb/Tm UCNPs as optical bioprobe has been used in *in vivo* UCL imaging of a normal black mouse and even rabbit with excellent signal-to-noise ratio [104].

6.3.1.4.2 **Photoacoustic Tomography** Photoacoustic (PA) imaging is developed based on the PA effect [105]. When nonionizing laser pulses are delivered into biological tissues, part of the energy can be absorbed and converted into heat, resulting in transient thermoelastic expansion and thus wideband ultrasonic emission. The emitted ultrasonic waves are detected by ultrasonic transducers and then analyzed to produce images. PA imaging is not only a nonionizing imaging modality with deeper penetration compared with other optical methods but also a data-rich, inherently real-time modality suitable for imaging dynamic intestinal processes [106, 107]. Moreover, the corresponding instrumentation costs are low and the systems are small. The NIR light harvesting materials such as the inorganic materials (e.g., carbon nanotubes, graphene oxide, Au NPs, copper sulfide, tungsten disulfide, molybdenum disulfide, bismuth selenide, and bismuth sulfide), organic molecules, and polymers (e.g., porphyrins, indocyanine dyes, squaraine dyes, anthocyanin dyes, semiconducting polymers, and dendrimers) have been used as PAT contrast probes [65, 108–115]. Au NPs allow the localized surface plasmon resonance peaks to be engineered to the NIR region for PAT of tumors for imaging-guided photothermal therapy. Gambhir *et al.* [109] presented a family of novel PA contrast agents that were based on the binding of small optical dyes to single-walled carbon nanotubes (SWCNT-dye). The SWCNT–dye conjugated with cyclic Arg-Gly-Asp peptides to molecularly target the $\alpha v\beta_3$ integrin, which was associated with tumor angiogenesis, for molecularly detection of the tumor angiogenesis. Recently, transition metal sulfides with stable NIR absorption have been used as the contrast agents. Liu's group developed a novel PAT agent based on WS_2 nanosheets for multimodal imaging-guided photothermal ablation of

tumors in a mouse model [65]. Multiple imaging-guided treatment indicated that target specific to tumor was benefit from the intriguing intrinsic merits of thin-band-gap bismuth nanorods. Cai *et al.* [116] constructed highly integrated PA/ultrasonic dual-modality imaging and photothermal therapy platforms using reduced graphene oxide. Zhao *et al.* [66] explored the bismuth sulfide nanorods as the all-in-one system that conveniently integrated a broad range of clinically relevant functions. The bismuth sulfide nanorods served both as the amplifiable multimodality nanoprobes for PAT/CT with high sensitivity for whole-body screening as well as monitor the preferential accumulation in tumors and as the effective photothermal therapy agent. The organic aggregates (supermolecular assemblies), which have the intense NIR absorption, have been exploited as the PAT contrast agents. These aggregates formed from self-assembled molecular monomers and had high light extinction coefficients and unique photothermal and PA properties. Zheng's group has developed porphysomes for sensitive PAT visualization of lymphatic systems and photothermal therapy of tumor. The NIR light-absorbing semiconducting polymer NPs, explored by Rao's group, have been applied as the PA molecular imaging probes *in vivo* for real-time imaging of ROS-vital chemical mediators of many diseases [117].

6.3.1.5 **Multimode Imaging**

Although many imaging techniques have been developed for visualizing NPs *in vivo*, each technique has its own advantages and intrinsic limitations. A current popular method to overcome all of the limitations imposed by a single imaging technique is to combine two or more contrast agents into a single NP-based entity, which has the ability to image the whole body via the multiple techniques [118].

Recently, one of most promising aspects of nanotechnology lies in the ability to design and prepare multifunctional platforms including several contrast agents for multimodal imaging. For example, combination of the anatomical resolution of MRI with the sensitivity of optical imaging is common and has been proved to be a powerful technique for finding and quantifying the size of tumors, especially tumors or metastases that are too small for MRI detection alone. These resulting MR/optical imaging agents have been used to monitor enzyme activity, in brain tumor imaging, or to detect and monitor apoptosis and atherosclerosis [119, 120]. Another example was that Abdukayum *et al.* [121] prepared a novel multimodal nanoprobe via functionalizing PLNPs with the gadolinium complexes functionalized (Gd^{3+}-PLNPs) for *in vivo* MRI and NIR luminescence imaging. The resulting nanoprobe not only exhibited a relatively higher longitudinal relaxivity over the commercial Gd(III)-diethylenetriaminepentaacetic acid complexes but also kept the persistent luminescence. Li *et al.* [122] developed another method to synthesize MRI/NIR nanoprobe via loading the paramagnetic Gd complex on the surface of UCNPs, forming a core–shell NP. The nanoprobe provided highly sensitive signals in both MRI and NIR images. In addition, construction the core–shell structures with Gd-based nanoshell onto the surface of NPs has also been performed to prepare MR/optical dual model probes. For example, by using $NaGdF_4$ nanostructure as the shell, a

series of $NaGdF_4$:Er/Yb(Tm)@$NaGdF_4$[123], $NaYF_4$:Yb/Er@$NaGdF_4$[124], and $NaYbF_4$:Tm@$NaGdF_4$[125] nanocomposites were synthesized, which showed both good UCL emission and high MRI relaxivity.

Alternatively, another important multimodal imaging system is the combination of radioisotope-based imaging techniques with MRI or NIR imaging technique. One example is that linking ^{124}I with tyrosine residues of serum albumin, which was coated on the Fe_3O_4 NPs [126]. The resultant MRI/PET dual-imaging agents provide highly sensitive signals in both MRI and PET images. In an MRI/PET-fused image, the two signals accurately delineated the different types of small sentinel lymph nodes of only a few millimeters in diameter. Because the most host materials for UCNPs are fluorides, ^{18}F can be easily introduced to endow the as-made nanoprobes with both UCL and PET imaging modality. Li's group has doped the ^{18}F into $NaYF_4$:Yb/Tm NPs for dual-modality UCL and PET imaging of whole-body small animals [127, 128]. During the imaging process, the UCNPs could be real-time tracked with high sensitivity *in vivo* from mice to large animals by PET imaging. Other types of multimodal contrast agents are also in development: PET/NIRF used with ICG and QDs, SPECT/fluorescence, PET/MRI, MRI/PAT, TAT/PAT used with SWCNTs, and US/MRI, among others. Probes with three modes of imaging are being considered, for example, MRI/NIRF/PET, PET-CT/MRI/NIRF, and even four modes incorporating MRI/PET/BRET/fluorescence [60, 63, 65, 68, 129–134].

An important concept to consider is that with some multimodal systems, introducing two or more kinds of contrasts into one nanosystem may cause some unwanted side effects, and the enhancement of one modality must not be at the expense of another. For example, because Fe_3O_4 NPs may quench the fluorescent materials, thus concentrations of Fe_3O_4 NPs should usually be lower than those of the agents for fluorescence imaging. However, because of the different sensitivities of the two methods, concentrations of Fe_3O_4 NPs must be higher than those of the agents for fluorescence imaging. Therefore, controlling the ratios of the two types of agents is necessary. Additionally, incorporating more than one modality may cause interferences between the two (e.g., iron-based MRI agents quenching fluorescence agents) or complicate fabrication, resulting in higher production costs or commercial infeasibility. However, multimodal NPs would require only one dose of multiple agents to the patient, hopefully reducing side effects from having to use multiple doses of different agents. This approach is likely to remain an area of interest in the future, but unambiguous data showing enhanced imaging with each technique incorporated in such multimodal NP agents remains to be seen.

6.4 Conclusions

In this chapter, we discussed various imaging techniques, which could be used for the physicochemical characterization of NPs, structural analysis of bio–nano

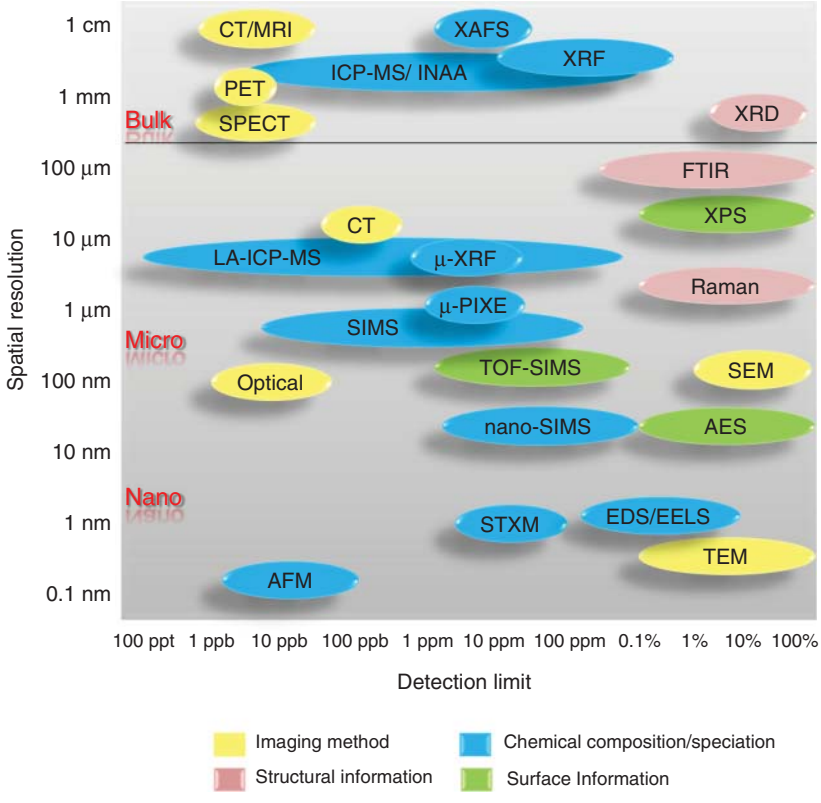

Figure 6.3 Commonly used imaging techniques arranged according to their spatial resolutions and sensitivities.

interactions, visualization of NPs *in vitro*, quantification of biodistribution, bioaccumulation, and transformation of NPs *in vivo*. A summary of the spatial resolution and detection limits of different imaging techniques is illustrated in Figure 6.3.

Imaging techniques that can be used for *in vitro* visualization and quantification of NMs include CLSM, TEM, STXM, and μ-XRF, which can be applied for *in vivo* biodistribution and quantification of NPs in animals, including neutron activation analysis (NAA), isotopic tracing, ICP-MS, ICP-OES, CT, MRI, PET, and SPECT. At the same time, optical imaging methods such as PA-based methods and fluorescence are important complements. In particular, owing to the advantages of high sensitivity, excellent accuracy and accuracy, low matrix effects, and nondestructiveness compared to traditional imaging techniques, the advanced nuclear analytical and related techniques in nanotoxicology research provide new promise to secure enhanced imaging sensitivity and precision for a better understanding of interaction of NPs with biological systems, biodistribution, and transformation.

References

1. Colvin, V.L. (2003) The potential environmental impact of engineered nanomaterials. *Nat. Biotechnol.*, **21**, 1166–1170.
2. Nel, A., Xia, T., Madler, L., and Li, N. (2006) Toxic potential of materials at the nanolevel. *Science*, **311**, 622–627.
3. Oberdorster, G., Oberdorster, E., and Oberdorster, J. (2005) Nanotoxicology: an emerging discipline evolving from studies of ultrafine particles. *Environ. Health Perspect.*, **113**, 823–839.
4. Zhao, Y., Xing, G., and Chai, Z. (2008) Nanotoxicology: are carbon nanotubes safe? *Nat. Nanotechnol.*, **3**, 191–192.
5. Serda, R.E., Ferrati, S., Godin, B., Tasciotti, E., Liu, X.W., and Ferrari, M. (2009) Mitotic trafficking of silicon microparticles. *Nanoscale*, **1**, 250–259.
6. Lao, F., Chen, L., Li, W., Ge, C., Qu, Y., Sun, Q., Zhao, Y., Han, D., and Chen, C. (2009) Fullerene nanoparticles selectively enter oxidation-damaged cerebral microvessel endothelial cells and inhibit JNK-related apoptosis. *ACS Nano*, **3**, 3358–3368.
7. Porter, A.E., Gass, M., Muller, K., Skepper, J.N., Midgley, P.A., and Welland, M. (2007) Direct imaging of single-walled carbon nanotubes in cells. *Nat. Nanotechnol.*, **2**, 713–717.
8. AshaRani, P.V., Mun, G.L.K., Hande, M.P., and Valiyaveettil, S. (2009) Cytotoxicity and genotoxicity of silver nanoparticles in human cells. *ACS Nano*, **3**, 279–290.
9. Qiu, Y., Liu, Y., Wang, L., Xu, L., Bai, R., Ji, Y., Wu, X., Zhao, Y., Li, Y., and Chen, C. (2010) Surface chemistry and aspect ratio mediated cellular uptake of Au nanorods. *Biomaterials*, **31**, 7606–7619.
10. Wang, L., Li, Y.F., Zhou, L., Liu, Y., Meng, L., Zhang, K., Wu, X., Zhang, L., Li, B., and Chen, C. (2010) Characterization of gold nanorods *in vivo* by integrated analytical techniques: their uptake, retention, and chemical forms. *Anal. Bioanal. Chem.*, **396**, 1105–1114.
11. Tkalec, Ž.P., Drobne, D., Vogel-Mikuš, K., Pongrac, P., Regvar, M., Štrus, J., Pelicon, P., Vavpetič, P., Grlj, N., and Remškar, M. (2011) Micro-PIXE study of Ag in digestive glands of a nano-Ag fed arthropod (Porcellio scaber, Isopoda, Crustacea). *Nucl. Instrum. Methods Phys. Res., Sect. B*, **269**, 2286–2291.
12. Bussy, C., Cambedouzou, J., Lanone, S., Leccia, E., Heresanu, V., Pinault, M., Mayne-lhermite, M., Brun, N., Mory, C., Cotte, M., Doucet, J., Boczkowski, J., and Launois, P. (2008) Carbon nanotubes in macrophages: imaging and chemical analysis by X-ray fluorescence microscopy. *Nano Lett.*, **8**, 2659–2663.
13. Hagenhoff, B., Breitenstein, D., Tallarek, E., Möllers, R., Niehuis, E., Sperber, M., Goricnik, B., and Wegener, J. (2012) Detection of micro- and nanoparticles in animal cells by ToF-SIMS 3D analysis. *Surf. Interface Anal.*, **45**, 315–319.
14. Drescher, D., Giesen, C., Traub, H., Panne, U., Kneipp, J., and Jakubowski, N. (2012) Quantitative imaging of gold and silver nanoparticles in single eukaryotic cells by laser ablation ICP-MS. *Anal. Chem.*, **84**, 9684–9688.
15. Liu, Y., Li, W., Lao, F., Liu, Y., Wang, L., Bai, R., Zhao, Y., and Chen, C. (2011) Intracellular dynamics of cationic and anionic polystyrene nanoparticles without direct interaction with mitotic spindle and chromosomes. *Biomaterials*, **32**, 8291–8303.
16. Wang, L.M., Liu, Y., Li, W., Jiang, X.M., Ji, Y.L., Wu, X.C., Xu, L.G., Qiu, Y., Zhao, K., Wei, T.T., Li, Y.F., Zhao, Y.L., and Chen, C.Y. (2011) Selective targeting of gold nanorods at the mitochondria of cancer cells: implications for cancer therapy. *Nano Lett.*, **11**, 772–780.
17. Tetard, L., Passian, A., Farahi, R.H., and Thundat, T. (2010) Atomic force microscopy of silica nanoparticles and carbon nanohorns in macrophages and red blood cells. *Ultramicroscopy*, **110**, 586–591.
18. Cho, N.-H., Cheong, T.-C., Min, J.H., Wu, J.H., Lee, S.J., Kim, D., Yang, J.-S., Kim, S., Kim, Y.K., and Seong, S.-Y. (2011) A multifunctional core-shell

nanoparticle for dendritic cell-based cancer immunotherapy. *Nat. Nanotechnol.*, **6**, 675–682.

19. Sim, R.B. and Wallis, R. (2011) Surface properties: immune attack on nanoparticles. *Nat. Nanotechnol.*, **6**, 80–81.
20. Chao, W., Kim, J., Rekawa, S., Fischer, P., and Anderson, E.H. (2009) Demonstration of 12 nm resolution fresnel zone plate lens based soft X-ray microscopy. *Opt. Express*, **17**, 17669–17677.
21. McRae, R., Bagchi, P., Sumalekshmy, S., and Fahrni, C. (2009) *In situ* imaging of metals in cells and tissues. *J. Am. Chem. Soc.*, **131**, 12497–12515.
22. Farrer, R.A., Butterfield, F.L., Chen, V.W., and Fourkas, J.T. (2005) Highly efficient multiphoton-absorption-induced luminescence from gold nanoparticles. *Nano Lett.*, **5**, 1139–1142.
23. Durr, N.J., Larson, T., Smith, D.K., Korgel, B.A., Sokolov, K., and Ben-Yakar, A. (2007) Two-photon luminescence imaging of cancer cells using molecularly targeted gold nanorods. *Nano Lett.*, **7**, 941–945.
24. Dreaden, E.C., Alkilany, A.M., Huang, X., Murphy, C.J., and El-Sayed, M.A. (2012) The golden age: gold nanoparticles for biomedicine. *Chem. Soc. Rev.*, **41**, 2740–2779.
25. Murphy, C.J., Gole, A.M., Stone, J.W., Sisco, P.N., Alkilany, A.M., Goldsmith, E.C., and Baxter, S.C. (2008) Gold nanoparticles in biology: beyond toxicity to cellular imaging. *Acc. Chem. Res.*, **41**, 1721–1730.
26. Huang, X., El-Sayed, I.H., Qian, W., and El-Sayed, M.A. (2006) Cancer cell imaging and photothermal therapy in the near-infrared region by using gold nanorods. *J. Am. Chem. Soc.*, **128**, 2115–2120.
27. Fujimoto, J.G., Brezinski, M.E., Tearney, G.J., Boppart, S.A., Bouma, B., Hee, M.R., Southern, J.F., and Swanson, E.A. (1995) Optical biopsy and imaging using optical coherence tomography. *Nat. Med.*, **1**, 970–972.
28. Huang, D., Swanson, E., Lin, C., Schuman, J., Stinson, W., Chang, W., Hee, M., Flotte, T., Gregory, K., Puliafito, C. *et al.* (1991) Optical coherence tomography. *Science*, **254**, 1178–1181.
29. Gobin, A.M., Lee, M.H., Halas, N.J., James, W.D., Drezek, R.A., and West, J.L. (2007) Near-infrared resonant nanoshells for combined optical imaging and photothermal cancer therapy. *Nano Lett.*, **7**, 1929–1934.
30. Chen, J., Saeki, F., Wiley, B.J., Cang, H., Cobb, M.J., Li, Z.-Y., Au, L., Zhang, H., Kimmey, M.B., Li, X., and Xia, Y. (2005) Gold nanocages: bioconjugation and their potential use as optical imaging contrast agents. *Nano Lett.*, **5**, 473–477.
31. Oldenburg, A.L., Hansen, M.N., Zweifel, D.A., Wei, A., and Boppart, S.A. (2006) Plasmon-resonant gold nanorods as low backscattering albedo contrast agents for optical coherence tomography. *Opt. Express*, **14**, 6724–6738.
32. Kim, C.S., Wilder-Smith, P., Ahn, Y.-C., Liaw, L.-H.L., Chen, Z., and Kwon, Y.J. (2009) Enhanced detection of early-stage oral cancer *in vivo* by optical coherence tomography using multimodal delivery of gold nanoparticles. *Biomedicine*, **14**, 034008.
33. Chhetri, R.K., Kozek, K.A., Johnston-Peck, A.C., Tracy, J.B., and Oldenburg, A.L. (2011) Imaging three-dimensional rotational diffusion of plasmon resonant gold nanorods using polarization-sensitive optical coherence tomography. *Phys. Rev. E*, **83**, 040903.
34. Chhetri, R.K., Blackmon, R.L., Wu, W.-C., Hill, D.B., Button, B., Casbas-Hernandez, P., Troester, M.A., Tracy, J.B., and Oldenburg, A.L. (2014) Probing biological nanotopology via diffusion of weakly constrained plasmonic nanorods with optical coherence tomography. *Proc. Natl. Acad. Sci. U.S.A.*, **111**, 4289–4297.
35. Zhang, T., Stilwell, J.L., Gerion, D., Ding, L., Elboudwarej, O., Cooke, P.A., Gray, J.W., Alivisatos, A.P., and Chen, F.F. (2006) Cellular effect of high doses of silica-coated quantum dot profiled with high throughput gene expression

analysis and high content cellomics measurements. *Nano Lett.*, **6**, 800–808.
36. Jan, E., Byrne, S.J., Cuddihy, M., Davies, A.M., Volkov, Y., Gun'ko, Y.K., and Kotov, N.A. (2008) High-content screening as a universal tool for fingerprinting of cytotoxicity of nanoparticles. *ACS Nano*, **2**, 928–938.
37. Huo, L., Chen, R., Shi, X., Bai, R., Wang, P., Chang, Y., and Chen, C. (2015) *J. Nanosci. Nanotechnol.*, **15**, 1143–1149.
38. Qu, Y., Li, W., Zhou, Y., Liu, X., Zhang, L., Wang, L., Li, Y.-f., Iida, A., Tang, Z., Zhao, Y., Chai, Z., and Chen, C. (2011) Full assessment of fate and physiological behavior of quantum dots utilizing caenorhabditis elegans as a model organism. *Nano Lett.*, **11**, 3174–3183.
39. Carragher, B. (2004) Rapid routine structure determination of macromolecular assemblies using electron microscopy: current progress and further challenges. *J. Synchrotron Radiat.*, **11**, 83–85.
40. Kaneko, K., Inoke, K., Freitag, B., Hungria, A.B., Midgley, P.A., Hansen, T.W., Zhang, J., Ohara, S., and Adschiri, T. (2007) Structural and morphological characterization of cerium oxide nanocrystals prepared by hydrothermal synthesis. *Nano Lett.*, **7**, 421–425.
41. Sommer, D. and Golla-Schindler, U. (2008) in *EMC 2008 14th European Microscopy Congress 1–5 September 2008, Aachen, Germany*, Chapter 133 (eds S. Richter and A. Schwedt), Springer, Berlin, Heidelberg, pp. 265–266.
42. Thomas, P.J. and Midgley, P.A. (2002) An introduction to energy-filtered transmission electron microscopy. *Top. Catal.*, **21**, 109–138.
43. Porter, A.E., Gass, M., Muller, K., Skepper, J.N., Midgley, P., and Welland, M. (2007) Visualizing the uptake of C_{60} to the cytoplasm and nucleus of human monocyte-derived macrophage cells using energy-filtered transmission electron microscopy and electron tomography. *Environ. Sci. Technol.*, **41**, 3012–3017.
44. Nel, A.E., M dler, L., Velegol, D., Xia, T., Hoek, E.M.V., Somasundaran, P., Klaessig, F., Castranova, V., and Thompson, M. (2009) Understanding biophysicochemical interactions at the nano-bio interface. *Nat. Mater.*, **8**, 543–557.
45. Pinheiro, T., Ynsa, M.D., and Alves, L.C. (2007) Imaging biological structures with proton microprobe. *Mod. Res. Educ. Top. Microsc.*, **3**, 237–244.
46. Bertrand, M., Weber, G., and Schoefs, B. (2003) Metal determination and quantification in biological material using particle-induced X-ray emission. *Trends Anal. Chem.*, **22**, 254–262.
47. Welz, B., Borges, D.L.G. (2009) In: Encyclopedia of Applied Spectroscopy, Andrews, D.L., ed., Wiley-VCH: Weinheim. 421–476.
48. Przybyłowicz, W., Mesjasz-Przybyłowicz, J., Pineda, C., Churms, C., Ryan, C., Prozesky, V., Frei, R., Slabbert, J., Padayachee, J., and Reimold, W. (2001) Elemental mapping using proton induced x-rays. *X-Ray Spectrom.*, **30**, 156–163.
49. Karydas, A.G., Sokaras, D., Zarkadas, C., Grlj, N., Pelicon, P., Žitnik, M., Schütz, R., Malzer, W., and Kanngießer, B. (2007) 3D Micro PIXE-a new technique for depth-resolved elemental analysis. *J. Anal. At. Spectrom.*, **22**, 1260–1265.
50. Wu, B. and Becker, J.S. (2012) Imaging techniques for elements and element species in plant science. *Metallomics*, **4**, 403–416.
51. Adams, F., Van Vaeck, L., and Barrett, R. (2005) Advanced analytical techniques: platform for nano materials science. *Spectrochim. Acta, Part B*, **60**, 13–26.
52. Shon, H.K., Park, J., Choi, I., Park, H.M., Moon, D.W., and Lee, T.G. (2011) Mass imaging of iron oxide nanoparticles inside cells for *in vitro* cytotoxicity. *J. Nanosci. Nanotechnol.*, **11**, 638–641.
53. Ulrich, T.A., Lee, T.G., Shon, H.K., Moon, D.W., and Kumar, S. (2011) Microscale mechanisms of agarose-induced disruption of collagen remodeling. *Biomaterials*, **32**, 5633–5642.
54. Becker, J.S., Zoriy, M., Becker, J.S., Dobrowolska, J., and Matusch, A.

(2007) Laser ablation inductively coupled plasma mass spectrometry (LA-ICP-MS) in elemental imaging of biological tissues and in proteomics. *J. Anal. At. Spectrom.*, **22**, 736–744.

55. Senoner, M. and Unger, W.E.S. (2012) SIMS imaging of the nanoworld: applications in science and technology. *J. Anal. At. Spectrom.*, **27**, 1050–1068.
56. Zhu, Z.-J., Ghosh, P.S., Miranda, O.R., Vachet, R.W., and Rotello, V.M. (2008) Multiplexed screening of cellular uptake of gold nanoparticles using laser desorption/ionization mass spectrometry. *J. Am. Chem. Soc.*, **130**, 14139–14143.
57. Schwenzer, N.F., Springer, F., Schraml, C., Stefan, N., Machann, J., and Schick, F. (2009) Non-invasive assessment and quantification of liver steatosis by ultrasound, computed tomography and magnetic resonance. *J. Hepatol.*, **51**, 433–445.
58. Yu, S.-B. and Watson, A.D. (1999) Metal-based X-ray contrast media. *Chem. Rev.*, **99**, 2353–2378.
59. Pan, D., Williams, T.A., Senpan, A., Allen, J.S., Scott, M.J., Gaffney, P.J., Wickline, S.A., and Lanza, G.M. (2009) Detecting vascular biosignatures with a colloidal, radio-opaque polymeric nanoparticle. *J. Am. Chem. Soc.*, **131**, 15522–15527.
60. Chen, M., Tang, S., Guo, Z., Wang, X., Mo, S., Huang, X., Liu, G., and Zheng, N. (2014) Core–Shell Pd@Au nanoplates as theranostic agents for in-vivo photoacoustic imaging, CT imaging, and photothermal therapy. *Adv. Mater.*, **26**, 8210–8216.
61. Zhang, X.-D., Luo, Z., Chen, J., Shen, X., Song, S., Sun, Y., Fan, S., Fan, F., Leong, D.T., and Xie, J. (2014) Ultrasmall $Au_{10\text{-}12}(SG)_{10\text{-}12}$ nanomolecules for high tumor specificity and cancer radiotherapy. *Adv. Mater.*, **26**, 4565–4568.
62. Al Zaki, A., Joh, D., Cheng, Z., De Barros, A.L.B., Kao, G., Dorsey, J., and Tsourkas, A. (2013) Gold-loaded polymeric micelles for computed tomography-guided radiation therapy treatment and radiosensitization. *ACS Nano*, **8**, 104–112.
63. Hayashi, K., Nakamura, M., Miki, H., Ozaki, S., Abe, M., Matsumoto, T., and Ishimura, K. (2013) Gold nanoparticle cluster-plasmon-enhanced fluorescent silica core-shell nanoparticles for X-ray computed tomography-fluorescence dual-mode imaging of tumors. *Chem. Commun.*, **49**, 5334–5336.
64. Liu, H., Lu, W., Wang, H., Rao, L., Yi, Z., Zeng, S., and Hao, J. (2013) Simultaneous synthesis and amine-functionalization of single-phase $BaYF_5$:Yb/Er nanoprobe for dual-modal *in vivo* upconversion fluorescence and long-lasting X-ray computed tomography imaging. *Nanoscale*, **5**, 6023–6029.
65. Cheng, L., Liu, J., Gu, X., Gong, H., Shi, X., Liu, T., Wang, C., Wang, X., Liu, G., Xing, H., Bu, W., Sun, B., and Liu, Z. (2014) PEGylated WS_2 nanosheets as a multifunctional theranostic agent for *in vivo* dual-modal CT/photoacoustic imaging guided photothermal therapy. *Adv. Mater.*, **26**, 1886–1893.
66. Liu, J., Zheng, X., Yan, L., Zhou, L., Tian, G., Yin, W., Wang, L., Liu, Y., Hu, Z., Gu, Z., Chen, C., and Zhao, Y. (2015) Bismuth sulfide nanorods as a precision nanomedicine for *in vivo* multimodal imaging-guided photothermal therapy of tumor. *ACS Nano*, **9**, 696–707.
67. Ba, Z., Zhang, Y., Wei, J., Han, J., Wang, Z., and Shao, G. (2015) Large-scale synthesis of PEGylated lutetium hydroxycarbonates as nanoparticulate contrast agents for X-ray CT imaging. *New J. Chem.*, **39**, 589–594.
68. Liu, Z., Pu, F., Liu, J., Jiang, L., Yuan, Q., Li, Z., Ren, J., and Qu, X. (2013) PEGylated hybrid ytterbia nanoparticles as high-performance diagnostic probes for *in vivo* magnetic resonance and X-ray computed tomography imaging with low systemic toxicity. *Nanoscale*, **5**, 4252–4261.
69. Oh, M.H., Lee, N., Kim, H., Park, S.P., Piao, Y., Lee, J., Jun, S.W., Moon, W.K., Choi, S.H., and Hyeon, T. (2011) Large-scale synthesis of bioinert tantalum oxide nanoparticles for X-ray computed tomography imaging and bimodal image-guided sentinel lymph

node mapping. *J. Am. Chem. Soc.*, **133**, 5508–5515.

70. Nuzzo, S., Lafage-Proust, M.H., Martin-Badosa, E., Boivin, G., Thomas, T., Alexandre, C., and Peyrin, F. (2002) Synchrotron radiation microtomography allows the analysis of three-dimensional microarchitecture and degree of mineralization of human iliac crest biopsy specimens: effects of etidronate treatment. *J. Bone Miner. Res.*, **17**, 1372–1382.
71. Chien, C.C., Wang, C.H., Wang, C.L., Li, E.R., Lee, K.H., Hwu, Y., Lin, C.Y., Chang, S.J., Yang, C.S., and Petibois, C. (2010) Synchrotron microangiography studies of angiogenesis in mice with microemulsions and gold nanoparticles. *Anal. Bioanal. Chem.*, **397**, 2109–2116.
72. Slichter, C.P. (1996) *Principles of Magnetic Resonance*, vol. **1**, Springer.
73. Na, H.B., Song, I.C., and Hyeon, T. (2009) Inorganic nanoparticles for MRI contrast agents. *Adv. Mater.*, **21**, 2133–2148.
74. Kobayashi, H. and Brechbiel, M.W. (2005) Nano-sized MRI contrast agents with dendrimer cores. *Adv. Drug Delivery Rev.*, **57**, 2271–2286.
75. Liang, X.-J., Meng, H., Wang, Y., He, H., Meng, J., Lu, J., Wang, P.C., Zhao, Y., Gao, X., Sun, B., Chen, C., Xing, G., Shen, D., Gottesman, M.M., Wu, Y., Yin, J.-j., and Jia, L. (2010) Metallofullerene nanoparticles circumvent tumor resistance to cisplatin by reactivating endocytosis. *Proc. Natl. Acad. Sci. U.S.A.*, **107**, 7449–7454.
76. Bruckman, M.A., Jiang, K., Simpson, E.J., Randolph, L.N., Luyt, L.G., Yu, X., and Steinmetz, N.F. (2014) Dual-modal magnetic resonance and fluorescence imaging of atherosclerotic plaques *in vivo* using VCAM-1 targeted tobacco mosaic virus. *Nano Lett.*, **14**, 1551–1558.
77. Liu, D.-F., Qian, C., An, Y.-L., Chang, D., Ju, S.-H., and Teng, G.-J. (2014) Magnetic resonance imaging of post-ischemic blood-brain barrier damage with PEGylated iron oxide nanoparticles. *Nanoscale*, **6**, 15161–15167.
78. Harvey, P., Blamire, A.M., Wilson, J.I., Finney, K.-L.N.A., Funk, A.M., Senanayake, P.K., and Parker, D. (2013) Moving the goal posts: enhancing the sensitivity of PARASHIFT proton magnetic resonance imaging and spectroscopy. *Chem. Sci.*, **4**, 4251–4258.
79. Niu, D., Luo, X., Li, Y., Liu, X., Wang, X., and Shi, J. (2013) Manganese-loaded dual-mesoporous silica spheres for efficient T_1- and T_2-weighted dual mode magnetic resonance imaging. *ACS Appl. Mater. Interfaces*, **5**, 9942–9948.
80. Zhang, B., Li, Q., Yin, P., Rui, Y., Qiu, Y., Wang, Y., and Shi, D. (2012) Ultrasound-triggered BSA/SPION hybrid nanoclusters for liver-specific magnetic resonance imaging. *ACS Appl. Mater. Interfaces*, **4**, 6479–6486.
81. Zhou, S., Wu, Z., Chen, X., Jia, L., and Zhu, W. (2014) PEGylated polyethylenimine as enhanced T_1 contrast agent for efficient magnetic resonance imaging. *ACS Appl. Mater. Interfaces*, **6**, 11459–11469.
82. Zou, P., Chen, H., Paholak, H.J., and Sun, D. (2013) Noninvasive fluorescence resonance energy transfer imaging of *in vivo* premature drug release from polymeric nanoparticles. *Mol. Pharmaceutics*, **10**, 4185–4194.
83. Liu, C., Gao, Z., Zeng, J., Hou, Y., Fang, F., Li, Y., Qiao, R., Shen, L., Lei, H., Yang, W., and Gao, M. (2013) Magnetic/upconversion fluorescent $NaGdF_4$:Yb, Er nanoparticle-based dual-modal molecular probes for imaging tiny tumors *in vivo*. *ACS Nano*, **7**, 7227–7240.
84. Hou, Y., Qiao, R., Fang, F., Wang, X., Dong, C., Liu, K., Liu, C., Liu, Z., Lei, H., Wang, F., and Gao, M. (2012) $NaGdF_4$nanoparticle-based molecular probes for magnetic resonance imaging of intraperitoneal tumor xenografts *in vivo*. *ACS Nano*, **7**, 330–338.
85. Gunduz, S., Nitta, N., Vibhute, S., Shibata, S., Mayer, M.E., Logothetis, N.K., Aoki, I., and Angelovski, G. (2015) Dendrimeric calcium-responsive MRI contrast agents with slow *in vivo* diffusion. *Chem. Commun.*, **51**, 2782–2785.
86. Ferrauto, G., Di Gregorio, E., Baroni, S., and Aime, S. (2014) Frequency-encoded

MRI-CEST agents based on paramagnetic liposomes/RBC aggregates. *Nano Lett.*, **14**, 6857–6862.

87. Alivisatos, A.P. (1996) Semiconductor clusters, nanocrystals, and quantum dots. *Science*, **271**, 933–937.
88. Gao, X., Cui, Y., Levenson, R.M., Chung, L.W.K., and Nie, S. (2004) In vivo cancer targeting and imaging with semiconductor quantum dots. *Nat. Biotechnol.*, **22**, 969–976.
89. Sun, C., Yang, H., Yuan, Y., Tian, X., Wang, L., Guo, Y., Xu, L., Lei, J., Gao, N., Anderson, G.J., Liang, X.-J., Chen, C., Zhao, Y., and Nie, G. (2011) Controlling assembly of paired gold clusters within apoferritin nanoreactor for *in vivo* kidney targeting and biomedical imaging. *J. Am. Chem. Soc.*, **133**, 8617–8624.
90. Robinson, J.T., Hong, G., Liang, Y., Zhang, B., Yaghi, O.K., and Dai, H. (2012) In vivo fluorescence imaging in the second near-infrared window with long circulating carbon nanotubes capable of ultrahigh tumor uptake. *J. Am. Chem. Soc.*, **134**, 10664–10669.
91. Zhou, J., Liu, Z., and Li, F. (2012) Upconversion nanophosphors for small-animal imaging. *Chem. Soc. Rev.*, **41**, 1323–1349.
92. Wang, M., Mi, C.-C., Wang, W.-X., Liu, C.-H., Wu, Y.-F., Xu, Z.-R., Mao, C.-B., and Xu, S.-K. (2009) Immunolabeling and NIR-excited fluorescent imaging of HeLa cells by using $NaYF_4$:Yb,Er upconversion nanoparticles. *ACS Nano*, **3**, 1580–1586.
93. Kumar, R., Nyk, M., Ohulchanskyy, T.Y., Flask, C.A., and Prasad, P.N. (2009) Combined optical and MR bioimaging using rare earth ion doped $NaYF_4$ nanocrystals. *Adv. Funct. Mater.*, **19**, 853–859.
94. Yi, G.S. and Chow, G.M. (2006) Synthesis of hexagonal-phase $NaYF_4$:Yb,Er and $NaYF_4$:Yb,Tm nanocrystals with efficient up-conversion fluorescence. *Adv. Funct. Mater.*, **16**, 2324–2329.
95. Dai, Y., Yang, D., Ma, P., Kang, X., Zhang, X., Li, C., Hou, Z., Cheng, Z., and Lin, J. (2012) Doxorubicin conjugated $NaYF_4$:Yb^{3+}/Tm^{3+} nanoparticles for therapy and sensing of drug delivery by luminescence resonance energy transfer. *Biomaterials*, **33**, 8704–8713.
96. Dai, Y., Zhang, C., Cheng, Z., Ma, P., Li, C., Kang, X., Yang, D., and Lin, J. (2012) pH-responsive drug delivery system based on luminescent CaF_2:Ce^{3+}/Tb^{3+}-poly(acrylic acid) hybrid microspheres. *Biomaterials*, **33**, 2583–2592.
97. Xing, H., Bu, W., Ren, Q., Zheng, X., Li, M., Zhang, S., Qu, H., Wang, Z., Hua, Y., Zhao, K., Zhou, L., Peng, W., and Shi, J. (2012) A $NaYbF_4$:Tm^{3+} nanoprobe for CT and NIR-to-NIR fluorescent bimodal imaging. *Biomaterials*, **33**, 5384–5393.
98. Chatterjee, D.K., Rufaihah, A.J., and Zhang, Y. (2008) Upconversion fluorescence imaging of cells and small animals using lanthanide doped nanocrystals. *Biomaterials*, **29**, 937–943.
99. Cheng, L., Yang, K., Zhang, S., Shao, M., Lee, S., and Liu, Z. (2010) Highly-sensitive multiplexed *in vivo* imaging using pegylated upconversion nanoparticles. *Nano Res.*, **3**, 722–732.
100. Tian, G., Gu, Z., Zhou, L., Yin, W., Liu, X., Yan, L., Jin, S., Ren, W., Xing, G., Li, S., and Zhao, Y. (2012) Mn^{2+}dopant-controlled synthesis of $NaYF_4$:Yb/Er upconversion nanoparticles for *in vivo* imaging and drug delivery. *Adv. Mater.*, **24**, 1226–1231.
101. Bechet, D., Couleaud, P., Frochot, C., Viriot, M.-L., Guillemin, F., and Barberi-Heyob, M. (2008) Nanoparticles as vehicles for delivery of photodynamic therapy agents. *Trends Biotechnol.*, **26**, 612–621.
102. Liu, Q., Sun, Y., Yang, T., Feng, W., Li, C., and Li, F. (2011) Sub-10 nm Hexagonal lanthanide-doped $naLuF_4$ Upconversion nanocrystals for sensitive bioimaging *in vivo*. *J. Am. Chem. Soc.*, **133**, 17122–17125.
103. Pichaandi, J., Boyer, J.-C., Delaney, K.R., and van Veggel, F.C.J.M. (2011) Two-photon upconversion laser (scanning and wide-field) microscopy using Ln^{3+}-doped $NaYF_4$upconverting nanocrystals: a critical evaluation of their performance and potential in

bioimaging. *J. Phys. Chem. C*, **115**, 19054–19064.

104. Yang, T., Sun, Y., Liu, Q., Feng, W., Yang, P., and Li, F. (2012) Cubic sub-20nm $NaLuF_4$-based upconversion nanophosphors for high-contrast bioimaging in different animal species. *Biomaterials*, **33**, 3733–3742.

105. Zhang, H.F., Maslov, K., Stoica, G., and Wang, L.V. (2006) Functional photoacoustic microscopy for high-resolution and noninvasive *in vivo* imaging. *Nat. Biotechnol.*, **24**, 848–851.

106. Kim, C., Favazza, C., and Wang, L.V. (2010) In vivo photoacoustic tomography of chemicals: high-resolution functional and molecular optical imaging at new depths. *Chem. Rev.*, **110**, 2756–2782.

107. Zhang, Y., Jeon, M., Rich, L.J., Hong, H., Geng, J., Zhang, Y., Shi, S., Barnhart, T.E., Alexandridis, P., Huizinga, J.D., Seshadri, M., Cai, W., Kim, C., and Lovell, J.F. (2014) Non-invasive, multimodal functional imaging of the intestine with frozen micellar naphthalocyanines. *Nat. Nanotechnol.*, **9**, 631–638.

108. de la Zerda, A., Bodapati, S., Teed, R., May, S.Y., Tabakman, S.M., Liu, Z., Khuri-Yakub, B.T., Chen, X., Dai, H., and Gambhir, S.S. (2012) Family of enhanced photoacoustic imaging agents for high-sensitivity and multiplexing studies in living mice. *ACS Nano*, **6**, 4694–4701.

109. de la Zerda, A., Liu, Z., Bodapati, S., Teed, R., Vaithilingam, S., Khuri-Yakub, B.T., Chen, X., Dai, H., and Gambhir, S.S. (2010) Ultrahigh sensitivity carbon nanotube agents for photoacoustic molecular imaging in living mice. *Nano Lett.*, **10**, 2168–2172.

110. Gerling, M., Zhao, Y., Nania, S., Norberg, K.J., Verbeke, C.S., Englert, B., Kuiper, R.V., Bergstrom, A., Hassan, M., Neesse, A., Lohr, J.M., and Heuchel, R.L. (2014) Real-time assessment of tissue hypoxia *in vivo* with combined photoacoustics and high-frequency ultrasound. *Theranostics*, **4**, 604–613.

111. Ho, C.J., Balasundaram, G., Driessen, W., McLaren, R., Wong, C.L., Dinish, U.S., Attia, A.B., Ntziachristos, V., and Olivo, M. (2014) Multifunctional photosensitizer-based contrast agents for photoacoustic imaging. *Sci. Rep.*, **4**, 5342.

112. Huang, P., Lin, J., Li, W., Rong, P., Wang, Z., Wang, S., Wang, X., Sun, X., Aronova, M., Niu, G., Leapman, R.D., Nie, Z., and Chen, X. (2013) Biodegradable gold nanovesicles with an ultrastrong plasmonic coupling effect for photoacoustic imaging and photothermal therapy. *Angew. Chem. Int. Ed.*, **52**, 13958–13964.

113. Kircher, M.F., de la Zerda, A., Jokerst, J.V., Zavaleta, C.L., Kempen, P.J., Mittra, E., Pitter, K., Huang, R., Campos, C., Habte, F., Sinclair, R., Brennan, C.W., Mellinghoff, I.K., Holland, E.C., and Gambhir, S.S. (2012) A brain tumor molecular imaging strategy using a new triple-modality MRI-photoacoustic-Raman nanoparticle. *Nat. Med.*, **18**, 829–834.

114. Liu, X., Law, W.C., Jeon, M., Wang, X., Liu, M., Kim, C., Prasad, P.N., and Swihart, M.T. (2013) Cu2-x Se nanocrystals with localized surface plasmon resonance as sensitive contrast agents for *in vivo* photoacoustic imaging: demonstration of sentinel lymph node mapping. *Adv. Healthcare Mater.*, **2**, 952–957.

115. Liu, X., Lee, C., Law, W.C., Zhu, D., Liu, M., Jeon, M., Kim, J., Prasad, P.N., Kim, C., and Swihart, M.T. (2013) Au-Cu(2-x)Se heterodimer nanoparticles with broad localized surface plasmon resonance as contrast agents for deep tissue imaging. *Nano Lett.*, **13**, 4333–4339.

116. Sheng, Z., Song, L., Zheng, J., Hu, D., He, M., Zheng, M., Gao, G., Gong, P., Zhang, P., Ma, Y., and Cai, L. (2013) Protein-assisted fabrication of nano-reduced graphene oxide for combined *in vivo* photoacoustic imaging and photothermal therapy. *Biomaterials*, **34**, 5236–5243.

117. Pu, K., Shuhendler, A.J., Jokerst, J.V., Mei, J., Gambhir, S.S., Bao, Z., and Rao, J. (2014) Semiconducting polymer nanoparticles as photoacoustic molecular imaging probes in living mice. *Nat. Nanotechnol.*, **9**, 233–239.

118. Gu, Z., Yan, L., Tian, G., Li, S., Chai, Z., and Zhao, Y. (2013) Recent advances in design and fabrication of upconversion nanoparticles and their safe theranostic applications. *Adv. Mater.*, **25**, 3758–3779.

119. Lee, J.-H., Jun, Y.-w., Yeon, S.-I., Shin, J.-S., and Cheon, J. (2006) Dual-mode nanoparticle probes for high-performance magnetic resonance and fluorescence imaging of neuroblastoma. *Angew. Chem. Int. Ed.*, **45**, 8160–8162.

120. Josephson, L., Kircher, M.F., Mahmood, U., Tang, Y., and Weissleder, R. (2002) Near-infrared fluorescent nanoparticles as combined MR/optical imaging probes. *Bioconjugate Chem.*, **13**, 554–560.

121. Abdukayum, A., Yang, C.-X., Zhao, Q., Chen, J.-T., Dong, L.-X., and Yan, X.-P. (2014) Gadolinium complexes functionalized persistent luminescent nanoparticles as a multimodal probe for near-infrared luminescence and magnetic resonance imaging *in vivo*. *Anal. Chem.*, **86**, 4096–4101.

122. Li, Z., Zhang, Y., Shuter, B., and Muhammad Idris, N. (2009) Hybrid lanthanide nanoparticles with paramagnetic shell coated on upconversion fluorescent nanocrystals. *Langmuir*, **25**, 12015–12018.

123. Zhao, Z., Han, Y., Lin, C., Hu, D., Wang, F., Chen, X., Chen, Z., and Zheng, N. (2012) Multifunctional core-shell upconverting nanoparticles for imaging and photodynamic therapy of liver cancer cells. *Chem. Asian J.*, **7**, 830–837.

124. Hai, G., Zhengquan, L., Haisheng, Q., Yong, H., and Idris Niagara, M. (2010) Seed-mediated synthesis of $NaYF_4$:Yb,Er/$NaGdF_4$ nanocrystals with improved upconversion fluorescence and MR relaxivity. *Nanotechnology*, **21**, 125602.

125. Chen, G., Ohulchanskyy, T.Y., Law, W.C., Agren, H., and Prasad, P.N. (2011) Monodisperse $NaYbF_4$:Tm^{3+}/$NaGdF_4$ core/shell nanocrystals with near-infrared to near-infrared upconversion photoluminescence and magnetic resonance properties. *Nanoscale*, **3**, 2003–2008.

126. Choi, J.-s., Park, J.C., Nah, H., Woo, S., Oh, J., Kim, K.M., Cheon, G.J., Chang, Y., Yoo, J., and Cheon, J. (2008) A hybrid nanoparticle probe for dual-modality positron emission tomography and magnetic resonance imaging. *Angew. Chem. Int. Ed.*, **47**, 6259–6262.

127. Liu, Q., Sun, Y., Li, C., Zhou, J., Li, C., Yang, T., Zhang, X., Yi, T., Wu, D., and Li, F. (2011) ^{18}F-labeled magnetic-upconversion nanophosphors via rare-earth cation-assisted ligand assembly. *ACS Nano*, **5**, 3146–3157.

128. Sun, Y., Yu, M., Liang, S., Zhang, Y., Li, C., Mou, T., Yang, W., Zhang, X., Li, B., Huang, C., and Li, F. (2011) Fluorine-18 labeled rare-earth nanoparticles for positron emission tomography (PET) imaging of sentinel lymph node. *Biomaterials*, **32**, 2999–3007.

129. Cai, H., Li, K., Shen, M., Wen, S., Luo, Y., Peng, C., Zhang, G., and Shi, X. (2012) Facile assembly of Fe3O4@Au nanocomposite particles for dual mode magnetic resonance and computed tomography imaging applications. *J. Mater. Chem.*, **22**, 15110–15120.

130. Chen, J., Yang, X.-Q., Meng, Y.-Z., Qin, M.-Y., Yan, D.-M., Qian, Y., Xu, G.-Q., Yu, Y., Ma, Z.-Y., and Zhao, Y.-D. (2013) Reverse microemulsion-mediated synthesis of Bi_2S_3-QD@SiO_2-PEG for dual modal CT-fluorescence imaging *in vitro* and *in vivo*. *Chem. Commun.*, **49**, 11800–11802.

131. Yi, Z., Zeng, S., Lu, W., Wang, H., Rao, L., Liu, H., and Hao, J. (2014) Synergistic dual-modality *in vivo* upconversion luminescence/X-ray imaging and tracking of amine-functionalized $NaYbF_4$:Er nanoprobes. *ACS Appl. Mater. Interfaces*, **6**, 3839–3846.

132. Dong, K., Liu, Z., Liu, J., Huang, S., Li, Z., Yuan, Q., Ren, J., and Qu, X. (2014) Biocompatible and high-performance amino acids-capped $MnWO_4$ nanocasting as a novel non-lanthanide contrast

agent for X-ray computed tomography and T1-weighted magnetic resonance imaging. *Nanoscale*, **6**, 2211–2217.

133. Zhang, C., Zhou, Z., Qian, Q., Gao, G., Li, C., Feng, L., Wang, Q., and Cui, D. (2013) Glutathione-capped fluorescent gold nanoclusters for dual-modal fluorescence/X-ray computed tomography imaging. *J. Mater. Chem. B*, **1**, 5045–5053.

134. Miki, K., Inoue, T., Kobayashi, Y., Nakano, K., Matsuoka, H., Yamauchi, F., Yano, T., and Ohe, K. (2015) Near-infrared dye-conjugated amphiphilic hyaluronic acid derivatives as a dual contrast agent for *in vivo* optical and photoacoustic tumor imaging. *Biomacromolecules*, **16**, 219–227.

7
In Vivo Nanotoxicity Assays in Animal Models

Xiao He

7.1
Introduction

Seven young female workers (aged 18–47 years) who worked in the same print plant for 5–13 months were hospitalized due to shortness of breath, pleural effusion, pulmonary fibrosis, and granuloma, and two of them died in 2 years. Clinical and pathological examination showed that the "killer" may be nanoparticles (NPs) [1]! This report published in the *European Respiratory Journal* initiated extensive and deep discussions regarding an emerging discipline: nanotoxicology. The journal *Nature* quickly responded with a report entitled *Nanoparticle Safety in Doubt* [2], to address the debate over the environmental-health effects of nanotechnology. Proponents believed that the pathological damages constrained within the lungs of the patients were similar to those seen in animals exposed to nanoparticles. However, respiratory toxicologist Ken Donaldson, from the University of Edinburgh, UK, doubted whether nanoparticles were actually to blame, as the symptoms described in the article were more typical of chemical exposure. He said, "I don't doubt that nanoparticles were present, but that does not mean they were the main arbiters." Anthony Seaton, an emeritus professor in environmental and occupational medicine at the University of Aberdeen, UK, also agreed that the study does not pin down nanoparticles as the cause of the ill health [2]. The symptoms may result from a combined exposure to various chemicals.

To answer these doubts, basic toxicology research is urgently needed in all the areas including human epidemiological and clinical data, as well as *in vivo* and *in vitro* studies. As an important part of toxicological research, experiments involving laboratory animals are necessary to ensure and enhance human and animal health and protection of the environment. Nowadays, research with experimental animals (in concert with relevant *in vitro* data) is still the most basic, reliable, and meaningful methodology to detect important toxic properties of nanomaterials (NMs), to screen nanodrugs with a great diversity of physicochemical parameters, and to estimate risks to human and environmental health.

Toxicology of Nanomaterials, First Edition. Edited by Yuliang Zhao, Zhiyong Zhang, and Weiyue Feng.

In recent decades, the quest for an alternative to animal testing has gained a new momentum based on respect for animal welfare and ethical considerations. In the context of nanotoxicology, toxicologists have already established a series of *in vitro*, on-chip, and *in silico* methods for toxicological research. These alternative methods are low-cost, quick, high-throughput, suitable for mechanism validation and, therefore, make it easier to link the biological effects of nanomaterials to their physicochemical properties. The great diversity of possible formulations of NMs to be assessed makes these methods and models especially attractive, given the limitations of traditional animal testing. However, it can sometimes be very challenging to extrapolate the results of these alternative researches back to the biology of an entire organism *in vivo*.

Animal models would be particularly useful to study aspects that cannot be mimicked by *in vitro* systems, such as particokinetics (absorption, distribution, metabolism, elimination: ADME). The ADME patterns of NMs *in vivo* are greatly dependent on their physicochemical properties. When in contact with the biological milieu, the surface of NMs is in a dynamic exchange with the surroundings, and thereby, the properties of NMs continually vary during exposure. So, the NM-caused cellular responses *in vivo* tend to be influenced by the exposure mode and the metabolic pathways of NMs, which cannot be simply extrapolated from the experiments *in vitro*. Moreover, the *in vivo* response to NMs also includes the NM-caused intercellular communication, multicellular interactions, and immune regulation, which may be quite difficult to study *in vitro*. Therefore, animal experiments are still indispensable in nanotoxicology.

7.2 Laboratory Animal Models

This section briefly introduces the laboratory animals used in nanotoxicology. The use of "lower vertebrates" and invertebrates is highlighted, as it is in line with the 3Rs principle.

The animals most frequently used in toxicology are mammals, including mice, rats, guinea pigs, rabbits, dogs, pigs, small ruminants, and non-human primates. Rodents (mainly mice and rats) nevertheless constitute the majority of species used in nanotoxicology [3]. Controlled exposure studies are conducted and typically focus on toxicokinetics, LD50 (exposure amount resulting in 50% population death), changes to tissues or organs, or changes in blood cell populations and serum. Various host factors, such as age, gender, preexisting pathology, and genetic defects, can also be taken into the consideration.

Laboratory mice are the most commonly used mammalian research model, popular because of their availability, size, relatively low cost, and ease of handling [4]. They are widely used in pharmacological and toxicological studies of NMs. Laboratory rats have served as an important animal model for research in toxicology, psychology, medicine, and other fields. The historical importance of this species to scientific research is reflected by the amount of literature on it: roughly 50% more than that on laboratory mice [5]. Hamsters have wide cheek

pouches, and their mouth can be opened widely to directly visualize the epiglottis. Therefore, hamsters are commonly used to study the pulmonary clearance and toxicity of NMs after intratracheal instillation. Rabbits are frequently used in animal experimenters because they are mild-tempered and easy to handle (especially for intravenous injection, blood collection, and skin tests), confine, and breed.

Zebrafish (*Danio rerio*), nematode (typically *Caenorhabditis elegans*), and fruit flies (*Drosophila melanogaster*) have already been extensively used as models in nanotoxicology. The advantages provided by these animal models are their small size, short life cycle, high gene homology with superior animals (also human), and availability of a wealth of genetic database (Table 7.1). Hence, they can be used as very effective *in vivo* models to study the toxicity of NMs. Moreover, these species are more commonly permitted from an ethical point of view.

The zebrafish is a tropical freshwater fish belonging to the minnow family (*Cyprinidae*) of the order *Cypriniformes.* It is omnivorous, feeding primarily on zooplankton and insects [7]. *Z*ebrafish has been developed as an important vertebrate model in several fields of biology (notably, developmental biology, oncology, and toxicology).

A number of features make zebrafish a powerful model organism for experimental manipulation. It is a small, robust fish and can be easily bred and housed in large numbers. Generation time is short (for a vertebrate), typically 3–4 months, making it suitable for selection experiments [8]. Zebrafish genome has now been largely sequenced, making it an even more valuable model organism. Mutagenesis screens have now generated many thousands of mutations and have led to the identification of hundreds of genes controlling vertebrate development [8].

The zebrafish embryo assay is commonly to assess both the acute toxic effects and the long-term developmental defects caused by toxicants. Female zebrafish can spawn every 2–3 days and lay 100–200 eggs every week. Not only are the eggs easy to obtain and in large quantities, they are also relatively large in size (0.7 mm in diameter at fertilization) and optically transparent, the yolk being sequestered into a separate cell. Fertilization is external, so live embryos are accessible to manipulation and can be monitored through all developmental stages under a dissecting microscope (Figure 7.1). Development is rapid, with precursors to all major organs developing within 36 h, and larvae display food-seeking and active avoidance behaviors within 5 days after fertilization [8].

Zebrafish embryo assay has now been developed as a high-throughput method for toxicity screening and hazard ranking of NMs. For example, Bai *et al.* [9] assessed the toxicity of ZnO nanoparticles suspension in a 96-h postfertilization embryo-larval test; Lin *et al.* [10] used a bright-field imaging system to detect the morphological abnormalities, interference of hatching, and survival over a 5-day development of embryos. To make the high-throughput investigation fast and automatic, some robotic injection system, computer-aided imaging system, and data processing system have been developed [11–15]. For example, an image recognition system is developed to enable rapid automatic phenotype identification (i.e., hatched, unhatched, and dead) of zebrafish embryos exposed

Table 7.1 Main features of animal models widely used in nanotoxicology.

	Mouse and rat	**Zebrafish**	***C. elegans***	***Drosophila***
Habitat	Terrestrial	Aquatic	Terrestrial	Terrestrial
Cultivation	Expensive	Inexpensive and easy	Inexpensive and easy	Inexpensive and easy
Space	Cages in a dedicated room	Aerated tanks or aquarium system in a dedicated room	Petri dishes or flasks in an incubator	Bottles or cages in a dedicated room
Food	Pelleted feed	Shrimp	Bacteria	Fly food medium
Environmental conditions	18–25 °C; 30–70% humidity	25–31 °C	16–25 °C	18–30 °C
Adult body length	Mouse: 7–10 cm Rat: 15–25 cm	3–5 cm	~1 mm	~2.5 mm
Adult weight	Mouse: 15–35 g Rat: 150–500 g	150–250 mg	~4 μg	200–250 μg
Gender	♀ and ♂	♀ and ♂	Hermaphrodite and ♂ (~0.1%)	♀ and ♂
Life-cycle	2–3 mo	2–3 mo	~3 d	~10 d
Embryogenesis	Mouse:18–21 d Rat: 21–23 d	48–72 h at 28.5 °C	18 h at 20 °C	24 h at 25 °C
Lifespan	2–3 yr	2–3 yr	2–3 wk 20 °C	~30 d
Percentage homology with humans	Up to 99%	70%	60–80%	50–80%
Other features	Ethical restrictions	Transparent embryo	Transparent	Distinct phenotypes
		Developmental phenotypes	Many mutants available Behavioral endpoints	Simple genetic makeup

Adapted with permission from [6]. Copyright (2015) Elsevier.

to NMs without fluorescence-based imaging [14]. In addition, molecular analyses of differential gene expression have also been employed to evaluate toxic effects associated with the exposure to nanomaterials [16, 17].

Adult zebrafish has been exploited for the study of NM fate, transport, biodistribution, and bioaccumulation as well as chronic toxicity. For high-throughput screening on zebrafish larvae, Pardo-Martin [13] established a cellular-resolution imaging system that can automatically load zebrafish from reservoirs or multiwell plates (Figure 7.2) and positions and rotates them for high-speed confocal imaging and laser manipulation of both superficial and deep organs within 19 s without damage. The maintenance of embryonic and larvae/adult zebrafish and the detailed toxicological studies of NMs have been well documented in the literature [9, 17–23].

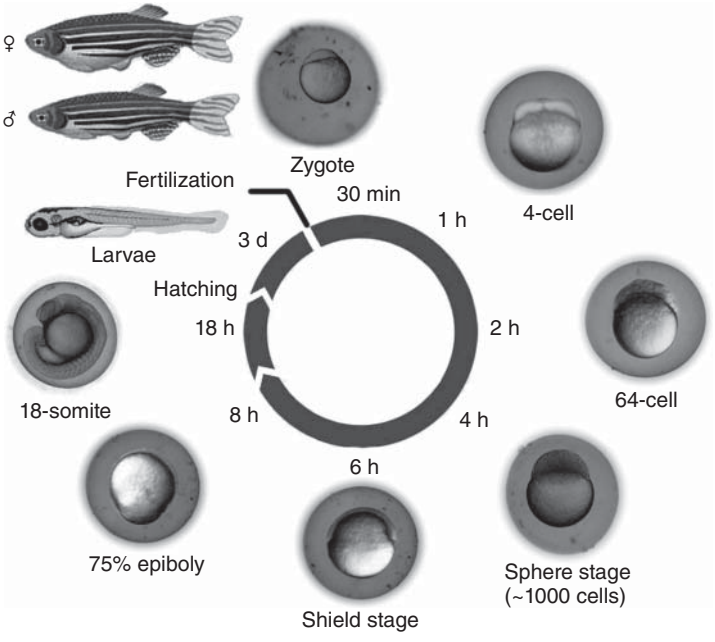

Figure 7.1 Schematic representation of zebrafish life cycle and embryonic development.

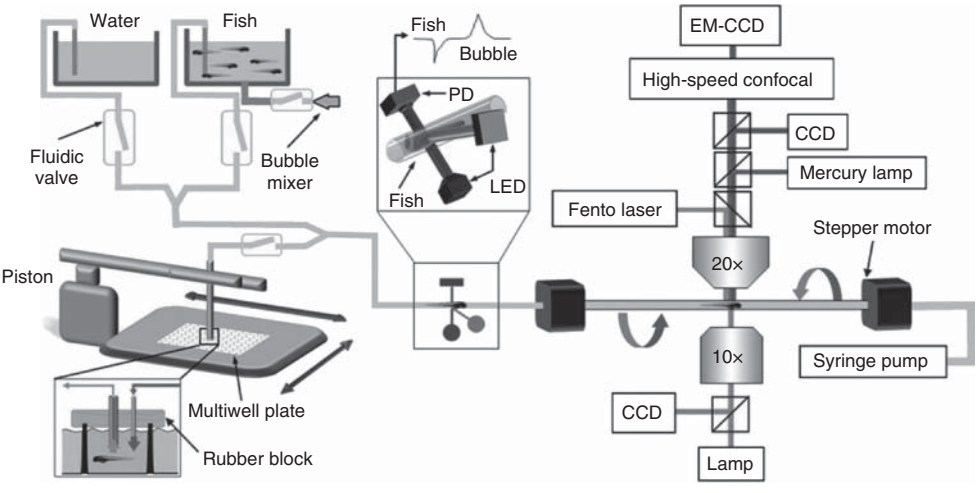

Figure 7.2 Automatic zebrafish manipulation and imaging platform. (Reprinted with permission from [13]. Copyright (2010) Nature Publishing Group.)

C. elegans is a 1 mm long, free-living nematode found worldwide and survives by feeding on bacteria. It exists primarily as a self-fertilizing hermaphrodite, although males arise infrequently (0.1%) [24]. *C. elegans* has a cuticle (a tough outer covering), four main epidermal cords, and a fluid-filled pseudocoelom (body cavity) [25]. *C. elegans* homologs have been identified for 60–80% of human genes [26]. It also has some of the same organ systems as larger animals.

C. elegans is an important model organism for biological research in genomics, neuroscience, and aging. Its small size, transparency, a rapid life cycle (3 days at 20 °C from egg to egg-laying adult, Figure 7.3), a short life span (2–3 weeks at 20 °C), large brood size, compact genome, stereotypical development, low cost of maintenance, and ease of manipulation make *C. elegans* an ideal model. Advances in genetics and molecular biology have allowed the identification of every single somatic cell (959 in the adult hermaphrodite, 1031 in the adult male) and its complete genome, which demonstrated a high conservation of biological mechanisms between the worm and vertebrates [6]. Forward and reverse genetics have led to the molecular identification of many key genes in developmental and cell biological processes.

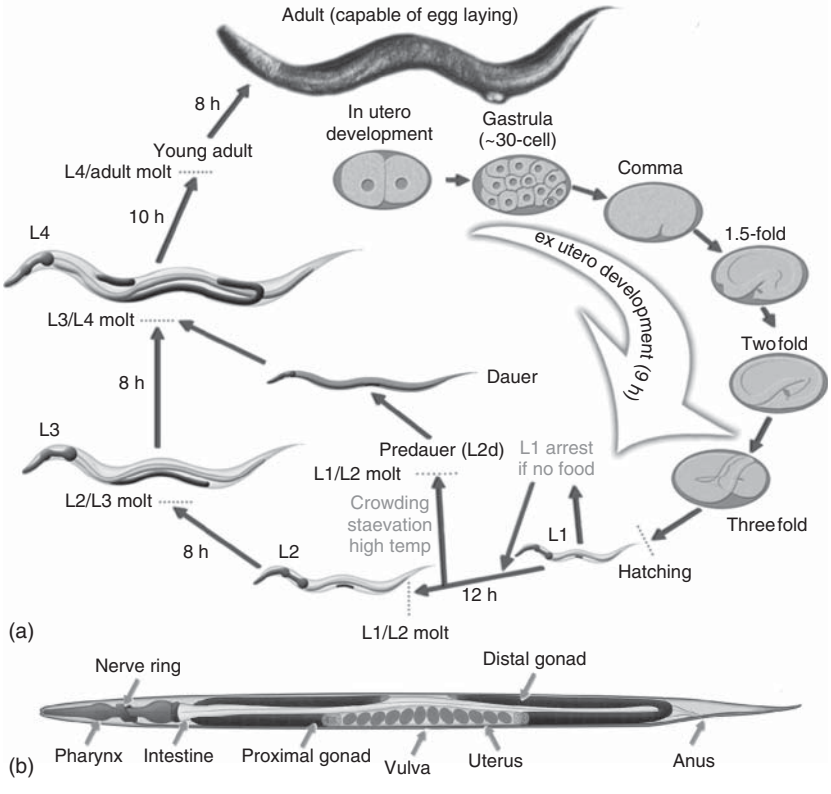

Figure 7.3 (a) Schematic representation of *C. elegans* life cycle and (b) anatomy of an adult hermaphrodite. (Adapted with permission from Wormatlas [24].)

C. elegans model is a multiflexible platform for the *in vivo* toxicological screening of NMs. First of all, the accumulation of oxidative biomarker lipofuscin in *C. elegans* could be easily identified under fluorescence measurement [27, 28], while oxidative stress remains the most appealing paradigm for nanotoxicity [29]. Life span is another indicator of the oxidative stress [30]. The short life cycle of *C. elegans* makes it convenient to perform a whole-life-cycle exposure assessment and makes life span a sensitive parameter for NMs or fine particle exposure [27, 31–35]. There are also some reports showing that exposure to the NMs with antioxidant activity could expand the life span of *C. elegans* [36, 37].

Secondly, *C. elegans* is an ideal model to study the neurotoxicity of NMs. The adult *C. elegans* hermaphrodite has 302 neurons, and the structures of all the neurons have been described in unprecedented detail by electron microscopic reconstruction [38]. These high-resolution images make it possible to identify all the synapses, map all the connections, and work out the entire neuronal circuit (about 6400 chemical synapses, 1500 neuromuscular junctions, and 900 gap junctions) [24]. Despite its compact nervous system, *C. elegans* is capable of several complex behaviors, in addition to the basics such as locomotion, foraging, feeding, defecation, and egg-laying. The endpoints most commonly used to study locomotion behavioral defects include head thrash, body bend frequency, forward turn, backward turn, and Omega/U turn. Previous work demonstrated that these parameters are sensitive enough to reveal the adverse effects of NM exposure at extremely low concentrations [39–41].

Finally, the short life cycle and life span of *C. elegans* make it convenient to study the reproductive, developmental, and multigeneration toxicity of NMs. Previous studies showed that NM exposure could lead to reproductive abnormalities [28, 34, 40–44]. NM exposure would also cause growth inhibition at the larvae and/or adult stage [33, 40, 44, 45]. Zhang *et al.* [46] exposed *C. elegans* to $Gd@C_{82}(OH)_{22}$ (a water-soluble endohedral metallofullerene derivative) up to six generations, and no toxic effects to the nematodes were found.

The basic information of *C. elegans* manipulation as well as the adaptation for nanotoxicology studies could be found in the literature [47, 48].

D. melanogaster, known as *fruit fly*, is a species of fly in the family Drosophilidae. Adult *Drosophila* is yellow-brown, with brick-red eyes and transverse black rings across the abdomen. It has a life span about 30 days and a generation time about 10 days at room temperature (Figure 7.4) [49, 50]. Females are about 2.5 mm in body length; males are slightly smaller with darker backs [51].

Drosophila is certainly the most famous nonmammalian model organism used for biological research in studies of genetics, physiology, microbial pathogenesis, and life history evolution. It is typically used because it is an animal species that is easy to handle, a small animal with a short life cycle, breeds quickly, has four pairs of chromosomes, lays many eggs, and is cheap and easy to keep at large numbers [49]. It provides a relevant model for investigating human health, as counterparts of genes responsible for more than 700 different human genetic diseases are found in *Drosophila*, including neurological, immunological, cardiovascular, auditory, visual, developmental, and metabolic disorders [52].

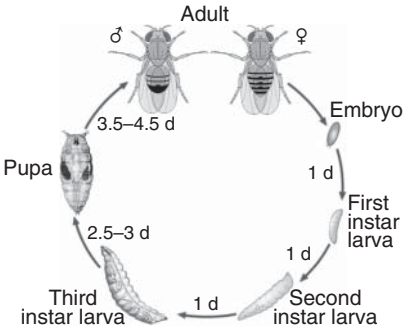

Figure 7.4 Schematic representation of *Drosophila* life cycle.

Genetic manipulability and ease of detecting phenotypes made *Drosophila* the model of choice for mutagenesis screens.

Recent investigations have propagated a number of powerful assay methods with *Drosophila* in developmental, behavioral, and neural toxicology. Measurable endpoints include developmental timing, cell fate determination, organogenesis, hatching, eye and wing phenotypes, behavioral traits (locomotion, circadian rhythm, courtship, mating, olfactory learning and memory, and aggression), defects in nervous system, and cellular phenotypes [53, 54]. Due to its simple genetic makeup, *Drosophila* could also be used to study the genotoxicity of NMs [55–59].

Unlike zebrafish and *C. elegans*, *Drosophila* allows NMs to be administered through various routes including oral ingestion, direct dermal exposure, and respiratory exposure [49]. The respiratory system of *Drosophila* is a branched network of epithelial tubes that ramifies throughout the body for the transport of oxygen and other gases. Considering these physiological similarities of organs between *Drosophila* and humans, *Drosophila* can serve as a suitable model for organ-specific toxicity of NMs after inhalation exposure [60].

The maintenance of *Drosophila* and the detailed toxicological protocols could be found in the literature [53, 54, 61].

To sum up, the most commonly used animal models in nanotoxicology study are mouse, rat, zebrafish, *C. elegans*, and *Drosophila*. Their main features are listed in Table 7.1. Other animal models, such as rabbit, guinea pig, monkey, medaka (*Oryzias latipes*), *Daphnia magna*, snail, and *Xenopus laevis*, have also been employed in the context of nanotoxicology study.

7.3 Administration

NMs can be present in air, water, food, cosmetics, or drugs. It has been demonstrated that the NPs enter the body mainly via inhalation, oral ingestion, dermal penetration, and intravascular injection (Figure 7.5) [62, 63]. In any case, contact will be necessary.

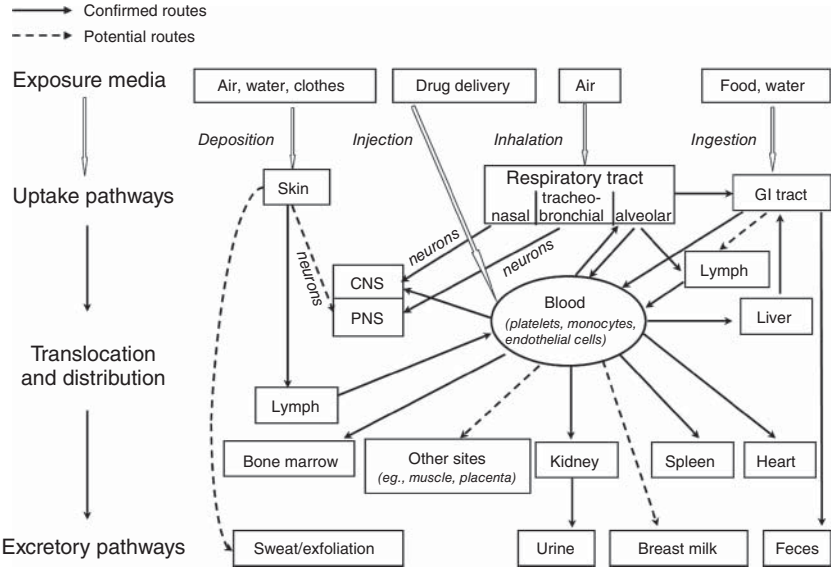

Figure 7.5 Uptake and translocation routes of NMs. (Adapted with permission from Environmental Health Perspectives [62].)

7.3.1 Respiratory Administration

Inhalation is the most common route of exposure to airborne NMs. During breathing, airborne NMs enter the respiratory tract of humans via the mouth or the nose and travel through the pharynx, larynx, and the trachea. The trachea divides into two primary bronchi, then progressively subdivides into a system of bronchi and bronchioles, allowing the passage of particulate matters into the alveoli. These alveoli, where the gas exchange takes place, consist of an epithelial layer and extracellular matrix surrounded by capillaries. The distance from the air in the alveolar lumen to the capillary blood flow is less than 400 nm. The large surface area of the alveoli and the intimate air–blood contact in this region make the alveoli less well protected against inhaled particulate matters as compared to the airways [64].

Our current knowledge and hypotheses regarding the health effects of NMs are mainly derived from decades of research on occupational dusts and ambient fine/ultrafine particles. The present experimental designs for the respiratory exposure of NMs are also mainly derived from these studies. Rodents are the most commonly used animal models for respiratory exposure to NMs. Duration of exposure ranges from a single acute exposure lasting minutes, to repeated and long-term exposure lasting days and months. NMs are delivered to the respiratory system in either the aerosol or suspension state. It is desirable, though not always easy, to limit exposure via dermal, oral, or other nonrespiratory pathway.

Many respiratory exposure techniques have been developed for nanotoxicity studies, including some inhalation methods (whole-body or nose-only exposure, the intratracheal inhalation technique) and instillation methods (intranasal or intratracheal instillation).

Inhalation provides a natural route of entry into the host; however, the facilities for inhalation exposure can be quite complex, consisting of generation and monitoring system, exposure chamber (breathing zone), and cleaning device (remove NMs before discharging the air). NMs are aerosolized in the form of either dry powder (mixed with dry air flow) or a mist (generated with a nebulizer). Under the static inhalation mode, a defined quantity of NMs is introduced into a closed chamber and allowed to mix with the trapped air to form nanoaerosols. This method is efficient in terms of NM usage; however, static inhalation exposure is limited by depletion of oxygen, accumulation of waste, NM settling, and dosimetric inaccuracy [65]. Under the dynamic inhalation exposure, there is a continuous air flow through the chamber to maintain a constant introduction of "fresh" nanoaerosol and removal of waste. Monitoring devices record and control the air flow, aerosol concentration, temperature, humidity, pressure, and so on throughout the duration of the exposure.

7.3.1.1 Whole-Body or Nose-Only Exposure

Animals are exposed to NM aerosol in the breathing zone, via a whole-body mode or nose-only mode (Figure 7.6). The advantages of whole-body inhalation systems include the ability to expose large numbers of animals simultaneously, to accommodate a wide variety of species, and to employ minimal restraint [66]. The major disadvantages include the large quantities of test NMs used and the multiple routes of exposure (e.g., respiratory, dermal, oral, ocular). Nose-only exposure systems could make the usage of test NMs more efficient and avoid or limit confounding exposure routes. Primary disadvantages are that animals are stressed due to restraint, and it is also labor-intensive to manipulate large numbers of animals [67].

Commercial facilities for inhalation exposure are usually quite expensive. Some efforts have been made for low-cost inhalation exposure. Chen *et al.* [68, 69] designed a system of inhalation exposure for manufactured nanomaterials (SIEMNs): five speed-controlled fans are assembled in a sealed columnar Plexiglas™ chamber of diameter 44 cm and height 53 cm, with one bottom fan (12 cm in diameter) and four parietal fans (9 cm in diameter) to ensure an even distribution of nanoaerosol in the compartment; outside the chamber, three crusts are connected to the wall 5 cm below the parietal fans; a detection probe is positioned at the height of naris, and aerosol concentration is measured by a real-time monitor (Model 8520 DustTrak Aerosol Monitor, TSI, USA) (Figure 7.7). Further details about SIEMN could be found in the literature. By using SIEMN, Chen *et al.* [68, 69] exposed Sprague-Dawley rats to SiO_2 nanoparticles for 40 min per day. The online measurement showed that the aerosol concentration of SiO_2 nanoparticles was slowly attenuated from 27.8 mg/m^3 to 21.5 in the chamber,

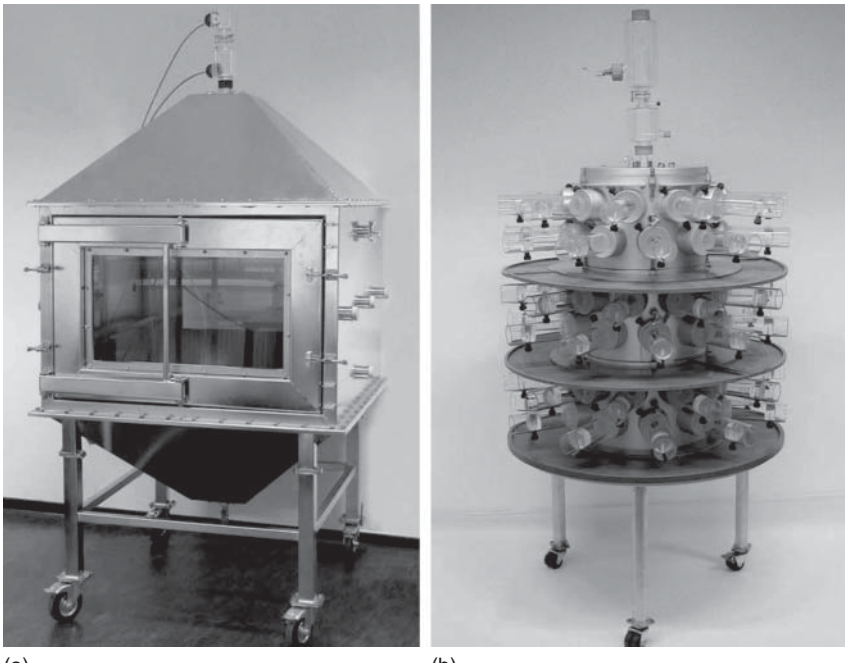

(a) (b)

Figure 7.6 Exposure chamber (breathing zone) for whole-body exposure (a) and nose-only exposure (b). (Reprinted with permission from TSE-Systems.com.)

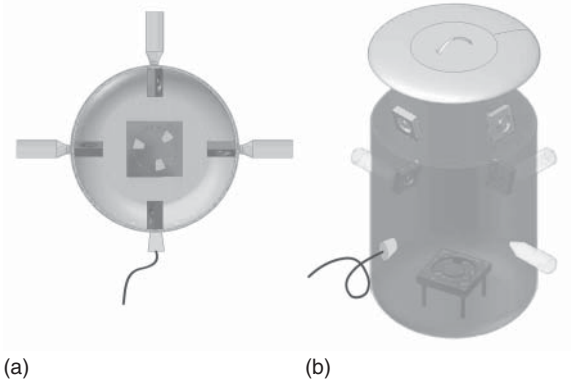

(a) (b)

Figure 7.7 Schematic representation of inhalation exposure system for manufactured nanomaterials. Vertical view (a) and perspective view (b). (Adapted with permission from [68]. Copyright (2008) American Chemical Society.)

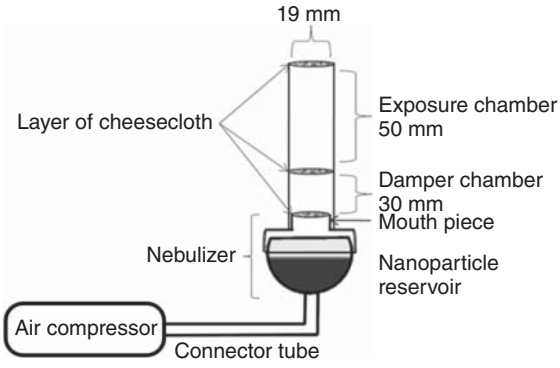

Figure 7.8 Diagram of the nebulizer NM delivery system. (Adapted with permission from [60]. Copyright (2009) Elsevier.)

and the integral average concentration throughout the duration of the exposure is 24.1 mg/m^3.

Posgai *et al.* [60] developed a low-cost method to deliver NMs to the *D. melanogaster* respiratory system, based on a simple nebulizer system. A medical nebulizer is connected to an 8 cm long piece of rubber tubing with a mouthpiece (Figure 7.8); the rubber tubing is subdivided by a single layer of cheesecloth into damper chamber (3 cm) and exposure chamber (5 cm). The damper chamber reduces the air sheer and turbulence before aerosolized nanoparticles enter the exposure chamber containing the flies. By using this system, CdSe/ZnS nanoparticles were successfully delivered to the fly respiratory system at a dose of 4.14×10^{-9} μg/fly.

Determination of dose by inhalation is imprecise due to the difficulty of measuring the amount of air inhaled by the individual animal. As an alternative, Oberdörster and his colleagues [70–72] developed a method of intratracheal inhalation, which could deliver a known amount of test materials directly into the lower respiratory tract. Under intratracheal inhalation, rats were anesthetized and intubated intratracheally with a modified 14-gauge cannula. The open end of the cannula was attached to a port on the inhalation apparatus such that an airtight seal was formed. Then rats were exposed to high aerosol concentrations at a regulated breathing rate and pressure, resulting in high lung particle burdens in a short exposure period. This method allows precise measurement of NM deposition dose, selection of breathing profiles, by passing extrathoracic airways for NM deposition in the lungs, and avoiding unnecessary contamination. However, intratracheal inhalation is technically more difficult and more time-consuming and may cause irritation of the oropharynx and upper trachea [73].

7.3.1.2 **Intranasal Instillation**

Intranasal instillation is one of the most widely used methods for delivery of NMs to the upper and lower respiratory tract. It is inexpensive, noninvasive, and technically less demanding than inhalation exposure. Intranasal instillation should be performed with the animal (usually mouse and rat) anesthetized. The animal is

manually restrained in a horizontal position or a supine position with the head elevated [74]. The end of the micropipette is placed at or in the external nares, and then the suspension of NMs is poured in slowly. The efficiency of intranasal instillation is mainly influenced by the instillation volumes and the types of anesthesia [75]. For mice, the volumes administered range between 4 and 10 μl per naris; for rats, up to 8 doses of 40 μl per naris (4 sprays per naris per dosing session), separated by 1 h, can be performed [76]. But some studies suggested that 35 μl is the optimal instillation volume for the delivery of tracer into the lower respiratory tract of mice [75, 77]. The delivery of NMs to lungs via intranasal instillation is significantly more effective when instillation is performed under anesthesia during the procedure. It was also found that mice anesthetized with isoflurane breathe in a deeper and irregular pattern, facilitating a more efficient delivery to the lower respiratory tract when compared to the instillation after injection anesthesia [75]. Intranasal instillation has its own disadvantages, including the nonphysiological conditions of NM administration, less precise NM dosing because of swallowing, patchy NM distribution when compared to inhalation exposure, less reproducible NM deposition pattern, and nasal irritation.

7.3.1.3 Intratracheal Instillation

Instillation through the oropharynx during anesthesia is the easiest and least invasive method for delivery of NMs to the lungs of animals [78]. Rodents are commonly used for intratracheal instillation, and hamsters are preferred models as their mouth can be opened widely to directly visualize the epiglottis. Intratracheal instillation procedures usually involve positioning of the animal against an angled restraining stand. A cannula or a ball-tipped syringe needle is then inserted through the epiglottis, after which contact with the tracheal rings provides confirmation that the cannula/needle is within the trachea [78, 79]. The detailed protocols could be found in the literature [80, 81]. Intratracheal instillation could also be performed after the trachea is surgically exposed on the ventral side of the neck (also called *transtracheal instillation*). The trachea was isolated by blunt dissection, and then a cannula or needle is inserted through the tracheal wall into the lumen just below the larynx to inject NM suspension [82].

Instillation (either intranasal or intratracheal) is simpler than inhalation exposure procedures and permits the precise introduction of NMs to the lungs within a short time. It can avoid contamination; therefore, it is especially suitable for the respiratory exposure using radiotracer technique [82]. However, the introduction of NMs via instillation is not physiologic, involving invasive delivery, and often stressful for the animal. The injection of NM suspension may lead to less homogenous lung deposition when compared to inhalation exposure [66, 78].

7.3.2 Oral Administration

The gastrointestinal tract is potentially one of the most important entry routes for NMs when the organism ingests foodstuffs or water accidentally or intentionally contaminated with NMs. In addition, inhaled NMs may translocate into

the gastrointestinal tract after they are eliminated from the respiratory tract by mucociliary clearance. Oral exposure may also result from hand-to-mouth contact [83]. Therefore, oral administration is conducted to study the toxicological consequence of ingested NMs *in vivo*.

The two major oral administration methods are oral gavage or NM-supplemented diet feeding. For mice and rats, direct administration by oral gavage is preferred because the intake amount of NMs can be precisely determined. In addition, gavage feeding is possible to give quite large amounts of poor-dispersed, nonsterile NMs. Gavage feeding can also avoid unnecessary contamination when used in a radiotracer experiment [82]. Oral gavage can be performed without anesthesia, but animals need to be restrained appropriately. A ball-tip needle is used to prevent trauma to the oral cavity and ensure that the needle does not enter the trachea. Volumes up to 10 ml/kg in the mouse and 20 ml/kg in the rat may be administered via oral gavage. For those poor-dispersed NMs, thickening agents or stabilizers (e.g., 0.5% carboxymethyl cellulose) are added to prevent NM settling. Sometimes, food additives are also added into the NM suspension to study the synergic effects of NMs and food additives [84]. Detailed procedure for oral gavage could be found in the literature [74]. Although highly effective, gavage occasionally can cause esophageal injury as well as restraint-associated distress, particularly with repeated use [85].

Some laboratory models, for example, *C. elegans* and *Drosophila* fly, are too tiny for oral gavage. For these organisms, NMs are given by mixing the NMs with food or drinking water. In the previous studies, *C. elegans* were cultured on the bacterial lawn or bacterial suspension containing NMs [6, 27]; *Drosophila* were fed with NMs mixed fly food [56]. NM-supplemented diet feeding is a natural route for NM administration; therefore, it is widely used in the *in vivo* studies. It should be understood that the NM-supplemented diet feeding may lead to a mixed exposure to NMs via skin contact and oral ingestion. To calculate the intake amount of NMs, the content of NMs in food or water as well as the daily food and water intake of test animal should be known before the administration. Sometimes, animals are kept in metabolic cages individually to obtain a precise intake amount of NMs by recording the food/water consumption and wastage.

7.3.3 Dermal Exposure

Human skin is the largest organ of the body, and structured in three layers: epidermis, dermis, and hypodermis (Figure 7.9) [86]. However, from a penetration perspective, only the dermis and epidermis are important [87]. They function as the first-line barrier with respect to the external environment. Consequently, it is directly exposed to airborne NMs as well as NMs within personal care products, clothing, toys, and the like. Topically applied NMs can potentially penetrate the skin and access the systemic circulation and exert adverse effects on a systemic scale [88]. Therefore, the penetration of NMs through the skin and the consequent health impact should be studied under dermal exposure.

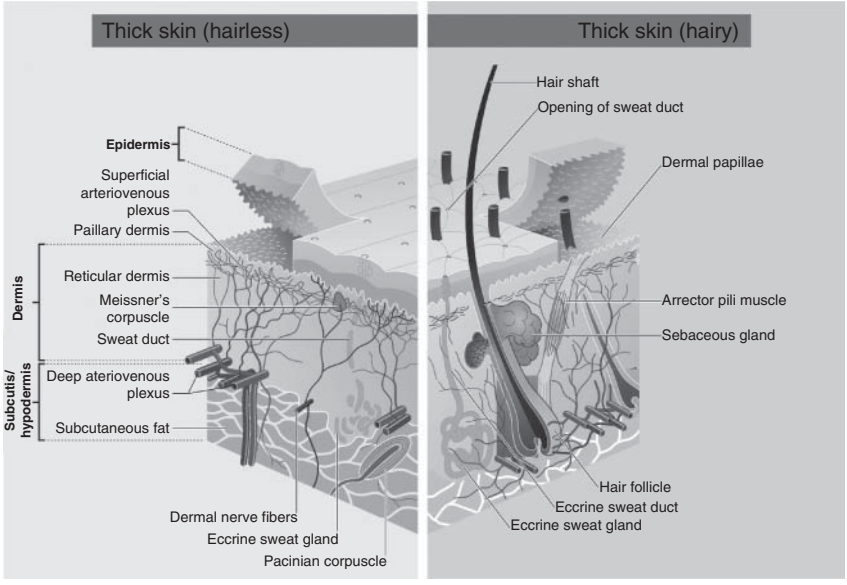

Figure 7.9 Skin layers. (Reprinted with permission from Wikipedia [86].)

Rats are the most common species used for *in vivo* dermal penetration testing. Hairless mice, guinea pigs, rabbits, and pigs are also used. Shaving or chemical depilation should be carried out approximately 24 h before the test when necessary. Care must be taken to avoid abrading the skin, which could alter its permeability. For long-term repeated exposure, repeated shaving is usually needed at approximately weekly intervals.

For skin application, NMs should be moistened sufficiently with water or a suitable vehicle, such as aqueous solutions, creams, or related formulations, to ensure good contact with the skin. For example, Mortensen used glycerol as an application vehicle for carboxyl quantum dots (QDs) (glycerol: 75%; QDs: 25%) [89]; Wu *et al.* [90] mixed 5% TiO_2 NPs with carbopol 940 and triethanolamine in deionized water; Baroli *et al.* [91] dispersed iron oxide NPs in aqueous solutions containing TMAOH (tetramethylammonium hydroxide) or AOT (sodium bis(2-ethylhexyl) sulfosuccinate). When a vehicle is used, the influence of the vehicle on NM penetration should be taken into account. The test NMs must be applied uniformly over the treatment site, and the volume of application should be less than 300 µl. After application, the treated site must be covered with gauze dressing to ensure that the animals cannot ingest the test NMs.

7.3.4
Intravenous and Intraperitoneal Injection

Theranostic NMs with diverse imaging and targeted delivery capabilities have been developed. Their advantageous therapeutic and diagnostic properties

include enhanced permeation and retention in the circulatory system, specific delivery and controlled release of drugs, highly efficient gene transfection, and enhanced medical imaging. For medical application of NMs, injection is the best method of administration for the test animal.

Various routes of injection are useful in NM delivery, for example, intraperitoneal (IP), subcutaneous, intramuscular, and intravenous (IV). The route chosen will depend on the species, volume of sample, and the targeting site of NMs [92]. IV injection is used for the direct delivery of NMs into the systemic circulation. Most of the injected NMs are subject to first-pass metabolism within the liver where they may accumulate or distribute via vasculature to end organs including brain. Therefore, IV injection has a more rapid systemic effect compared to other routes. For mouse and rat, the veins on the lateral aspects of the tail are excellent sites for IV injection. The injection volumes should not exceed 0.2 ml for mouse and 0.5 ml for rat. When the NMs are poorly dispersed, a single IV injection may be insufficient for NM delivery due to the limited injection volume. Sometimes, repeated IV injection, or as an alternative, IV infusion is employed for the IV delivery of a large amount of NMs. Tseng *et al.* [93] surgically inserted 2 PE50 cannulae into bilateral femoral veins of the anesthetized Sprague-Dawley rats, and an infusion pump was connected to the cannulae; the day after cannulation, unanesthetized rats were IV-infused with a citrate-stabilized ceria dispersion at a dose of approximately 85 mg/kg ceria (estimated concentration of 40 mg/ml in water) over 1 h.

IP injection is used to deliver NMs into the peritoneum (body cavity). It is used predominantly in testing for the systemic effects of injected substance. IP injection once provided screening information on effects of fibers, such as asbestos. It is now widely used for NM delivery in the *in vivo* studies due to the ease of administration compared with other parenteral methods. However, validation of this type of experiment will need to be conducted [94]. When performing IP injection on mouse or rat, NMs should be injected in the lower right or left quadrant of abdomen trying to avoid hitting bladder, liver, or other internal organs. The maximum injection volume is 20 ml/kg body weight for mouse and 10 ml/kg for rat.

7.4 Particokinetics

The *in vivo* behaviors of NMs can determine the balance between NM-induced activity and unwanted toxicity. Particokinetics studies the fate of NMs in the body. The corresponding process is described as the pharmacokinetic process, including four simultaneous phases: ADME. The kinetic patterns of NMs combined the bulk properties of solids with the mobility of molecules. Due to their small sizes and surface functionalization, some NMs are allowed to penetrate those barriers *in vivo*. Many qualitative and quantitative methods have been developed to assess the effect of the size, shape, and surface properties of NMs on their *in vivo* behaviors.

7.4.1 ADME

It is now widely accepted that the ADME patterns of NMs can be quite different when administrated via different routes. A systematic and thorough analysis of the ADME patterns of NMs can lead to the following: (i) a better understanding of the nanoproperty-dependent toxicities of NMs *in vivo*, (ii) a better understanding of the possible specific and nonspecific interactions between NMs and tissues and cell types, (iii) assessments of the possible ways to change the basic ADME scenarios to minimize the potential health hazards of NM exposure, and (iv) a more realistic design of high-efficient and less-toxic theranostic NMs.

7.4.1.1 ADME Following Respiratory Administration

Under respiratory exposure, the ADME of NMs mainly refers to the deposition and clearance of NMs in the respiratory tract as well as the possible diffusion to the extrapulmonary tissues and organs. Inhalation exposure may lead to deposition of NMs throughout the entire respiratory tract, from the nasopharyngeal, and down to the alveolar regions. There are three principal mechanisms that determine the deposition patterns: inertial impaction, gravitational sedimentation, and Brownian diffusion.

Mathematical models show that particulate matters with different sizes have different deposition sites, extent, and efficacy in the respiratory tract. Based on the data from the International Commission on Radiological Protection [95], Figure 7.10 shows the fractional deposition of inhaled particles with different sizes in the human respiratory tract [62]. Particles larger than 10 μm are deposited in the nasal cavity and the upper respiratory tract, as a combined result of the changes in airflow direction, the anatomical structure of the upper respiratory tract, and the mucus secretion. The deposition of NMs under natural exposure conditions is dominated by the diffusion, based on the Brownian motion: 80% of NMs with diameter of 1 nm are deposited inside the nasal cavity, the remaining 20% are deposited inside bronchus and can rarely arrive at the alveoli; about 50% of particles with diameter of 10 nm are deposited in the alveoli, and the residue amount in the nasal cavity is relatively small. NMs deposited in the alveoli are between 5 nm and more than 50 nm. Different effects caused by different-sized nanoparticles and diffusion of extrapulmonary organs may be related to differences in the deposition sites.

Airway and alveolar macrophages (AMs) are at the forefront of lung defense. Phagocytic uptake, in concert with mucociliary clearance, is the main mechanism for foreign intruder removal. The phagocytic efficiency of AMs depends largely on the physicochemical parameters of NMs, such as size, morphology, surface charge, stiffness, and surface functionalization [96]. The AMs phagocytize the particles with an optimal size in between 1 and 3 μm. For those micrometer-sized particles deposited in the alveoli, most of them can be phagocytized by AMs within 6 – 12 h. However, *in vivo* studies suggest that AM-mediated clearance of NMs smaller than 100 nm is quite inefficient [82, 97, 98]. Because of the small size, NMs are likely

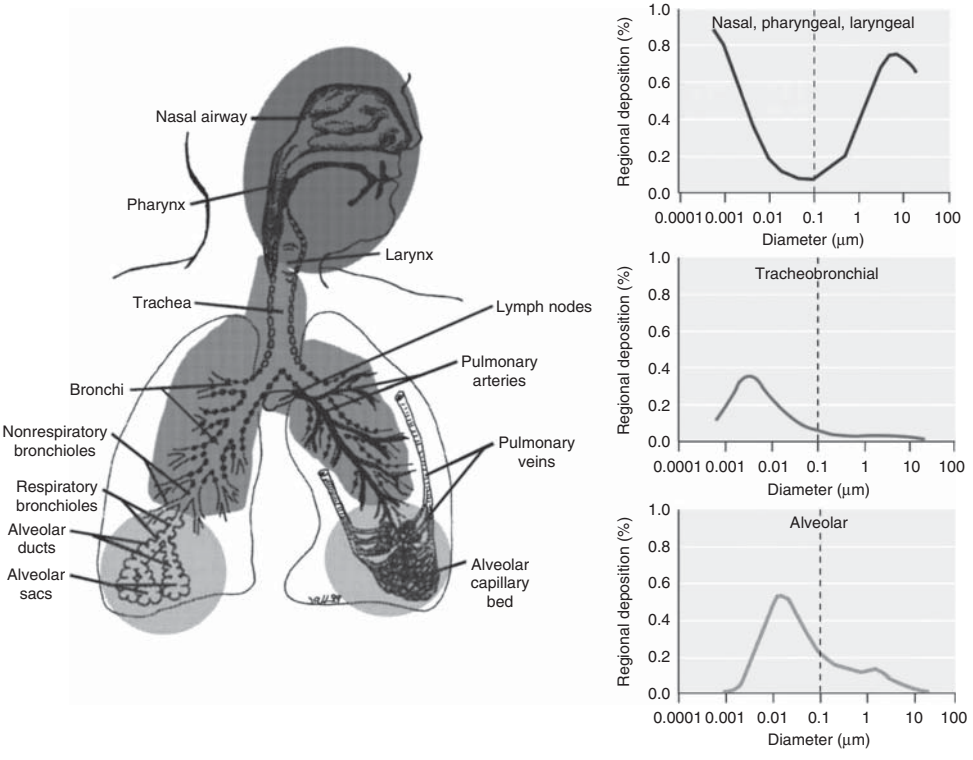

Figure 7.10 Predicted fractional deposition of inhaled particles in the nasopharyngeal, tracheobronchial, and alveolar regions of the human respiratory tract during nasal breathing [62]. (Reprinted with permission from Environmental Health Perspectives.)

to translocate beyond the epithelial barrier, therefore escaping the AM phagocytosis and mucociliary clearance. The inhaled NMs may remain in the lung even up to several years. A portion of those NMs that escaped AM-mediated clearance could penetrate the air–blood barrier and enter the systemic circulation, leading to subsequent accumulation in the secondary organs [96].

Once NMs enter the systemic circulation, they are carried by the blood flow to different organ systems and tissues all over the body. Their further distribution and clearance share some common patterns with the NMs injected intravenously and therefore will be addressed in the section ADME Following Intravenous Injection.

7.4.1.2 **ADME Following Oral Administration**

The gastrointestinal tract is one of the most important portals of entry for NM exposure. The human intestine has a length ranging from 7.5 to 8.5 m. In the small intestine region, the structural adaptations of mucosal folds, villi, and microvilli constitute a total absorptive area of 200–500 m^2. When ingested, most NMs are

rapidly eliminated via the feces; however, some may be taken up by the gut and distributed to the other organs. Exposing by oral administration, mesoporous silica nanoparticles (MSNs) were absorbed into the intestinal tract and persisted in the liver [99]. Most of the ingested ceria nanoparticles were eliminated with feces, only 0.0001% could be found in the liver [82]. When digested, mainly Ag^+, and to a much lesser extent Ag nanoparticles, passed the intestine of rats [100]. Some studies indicate that NMs taken up within the gastrointestinal tract are able to enter the lymphatic and capillary systems and subsequently be transported to other organs.

7.4.1.3 ADME Following Dermal Exposure

Whether NMs could penetrate through the skin has obvious implications to either the toxicological responses/risk assessment of NM or the development of transcutaneous drug carriers. However, there is still very limited information on the *in vivo* dermal penetration of NMs until now. TiO_2 NPs are widely used in commercial sunscreens. Previous work showed that stratum corneum layers blocked all kinds of TiO_2 NPs (cubic or needles, sized 10–15, 20, and 100 nm) [101]; TiO_2 NPs formulated from oil/water emulsion penetrate deeper into the human skin compared to those from an aqueous suspension [102]. Transmission electron microscope/energy-dispersive X-ray spectroscopy (TEM/EDX) assay detected high levels of Ti in the stratum corneum layers and near hair follicle openings after TiO_2 emulsion was applied to mini pigs four times daily, 5 days a week, for a total of 22 days, but found only a few TiO_2 particles in the dermis, which were regarded as contamination [103]. Therefore, no transdermal penetration of insoluble NMs has been found in almost all cases, though there is the presence of NMs in the stratum corneum and epidermis [104]. For those soluble or "soft" (e.g., solid lipid, vesicle-type carriers, biodegradable polymers) NMs, transdermal uptake may be easier. For example, Ag NP absorption through intact skin is low, but a small fraction of the particles was dissolved and diffused through the skin layers as elemental Ag [105]. Leite-Silva *et al.* [106] found that some limited NM penetration might occur into the viable stratum granulosum epidermis adjacent to the furrows after the application of ZnO NPs in sunscreen and cosmetic products for humans *in vivo*, but the extent is not sufficient to affect the redox state of those viable cells. There is evidence that the vehicle formulations, mechanical stress (e.g., flexing) on the skin, and UV radiation may have an effect on NM penetration. There is no clear indication that skin-applied NMs could enter the systemic circulation. However, it has been observed that NPs can be phagocytized by macrophages, Langerhans cells, or other cells [107].

7.4.1.4 ADME Following Intravenous Injection

IV injection is a direct way to deliver NMs into the bloodstream. NMs circulating within the bloodstream can also be a result of the NM absorption process by the various ports of entry or the intertissue redistribution of NMs. The interaction of NMs with blood constituents, such as plasma proteins, coagulation factors, and platelets, can potentially be initiated upon entrance of NMs into blood

circulation. The biophysicochemical interactions will alter the size, aggregation state, and interfacial properties of NMs and therefore influence the biorecognition as well as the tissue uptake of NMs. For example, surface coating of NMs with plasma opsonin (such as IgG, complement factors, and fibrinogen) was found to allow the macrophages within the reticuloendothelial system (RES) to easily recognize and efficiently remove the nanoparticles from the blood [108]. As for the NMs absorbed following respiratory exposure or oral exposure, the biocomponents adsorbed on their surface may be partially from the microenvironment of the administration site and can be quite different from those adsorbed on the NMs injected intravenously. The difference in the biocoating may influence the further distribution, metabolism, and elimination of NMs.

Once NMs enter the blood circulation as a result of either translocation from the site of administration or direct IV injection, the systemic circulation can distribute them to all the organs and tissues in the body. Distribution of NMs to several organs, such as the liver, spleen, heart, and brain, has been shown in different studies [82, 96, 97, 109–111]. So far, the deposition of NMs in the RES organs (i.e., the liver and spleen) has received the most attention. Uptake of NMs in the RES organs is observed as the main destination of the NMs within the bloodstream. Being the site for first-pass metabolism, the liver has consistently been shown to accumulate administered NMs, even long after cessation of exposure. The endothelium of hepatic sinusoid is discontinuous with fenestrations sized approximately 100–200 nm. Thus, NMs smaller than the fenestrations can cross the endothelium into the Disse space [96]. One of the physiologic functions of the liver is to efficiently capture and eliminate viruses or other particles sized 10–20 nm; therefore, NMs within this size range often undergo rapid liver uptake. Phagocytic Kupffer cells are central in the uptake of NMs that cross the epithelial barriers [112]. NMs could also be taken up by hepatocytes. For example, polystyrene NMs (20 nm) were internalized by hepatocytes and were observed within bile canaliculi, indicating a possible elimination via bile.

NMs trapped in the liver may undergo metabolic changes. By using TEM, ferromagnetic resonance and SQUID magnetization measurements, Levy *et al.* [113] evidenced the biotransformation of superparamagnetic maghemite nanoparticles into poorly magnetic iron species probably stored into ferritin proteins over a period of 3 months. Kreyling *et al.* [114] synthesized monodisperse radioactively labeled gold nanoparticles (^{198}Au) and engineered an ^{111}In-labeled polymer shell around them. Quantitative biodistribution analyses performed independently for ^{198}Au and ^{111}In showed a nonparticulate biodistribution of ^{111}In in rats after IV injection, while ^{198}Au accumulated mostly in the liver, suggesting a partial removal of the polymer shell *in vivo*. Further *in vitro* studies suggest that degradation of the polymer shell is caused by proteolytic enzymes in the liver. Graham *et al.* [115] demonstrated that IV-infused ceria nanoparticles (30 nm cubes), after prolonged residence time in the liver (90 days), undergo *in vivo* biotransformation. This transformation includes a particle-size effect toward ultrafines (second-generation ceria, sized 1–3 nm), combined with a measurable valence reduction determined by electron energy-loss spectroscopy (EELS).

Besides EELS, speciation methods based on synchrotron radiation have also been developed to study the biotransformation and biodegradation of NMs *in vivo* [33, 116]. However, there are still very limited information about the metabolic pathways of NMs. Studies on animal models are urgently needed to elucidate the mechanisms and routes involved in the metabolism of NMs *in vivo*.

NMs, upon entering systemic circulation, are destined to be removed from the body via excretion, usually through the kidneys (urine) or in the feces. There are two main sites where the excretion of NMs and their metabolites occurs. The kidney is the most important site, and it is where blood-borne NMs are excreted through urine. The excretion profile of NMs in kidney is fundamental for the toxic assessment and *in vivo* biomedical application of NMs. The basic structural and functional unit of the kidney is the nephron, which consists of a capillary tuft called *glomerulus*, the Bowman's capsule surrounding the glomerulus, and the renal tubule system. Renal clearance is involved in glomerular filtration, secretion from the peritubular capillaries to the tubule, and reabsorption from the proximal tubule back to the peritubular capillaries. The glomerular filtration is the first step for renal clearance of NMs, which allows only the NMs with a hydrodynamic diameter of less than 5–6 nm to be cleared rapidly from the body via urinary excretion. Previous study focusing on the size-dependent renal clearance of QDs showed that a final hydrodynamic diameter less than 5.5 nm resulted in rapid and efficient urinary excretion of QDs from the body [117]. The surface coating group is also an important determinant of the urinary excretion of NMs. Surface functionalization could impact the adsorption of serum protein to NM surface and therefore regulate the hydrodynamic diameter of NMs and further influence renal filterability. Studies evaluating the effect of surface charge on glomerular filtration of NMs with similarly sizes have shown that filtration is the greatest for positively charged NMs due to the fixed negative charges within the glomerular capillary wall. For example, more than 50% of glutathione-coated Au NPs sized 2 nm can be excreted through urine within 24 h after IV injection, while only 0.1% of cysteine-coated Au NPs were able to be excreted in the urine [118].

Hepatic (biliary) route is another excretion pathway that initiates in the liver and passes through to the gut until the NMs are finally excreted along with feces. In a study conducted in male nude mice and male Sprague-Dawley rats exposed to near-infrared fluorescent MSNs, the authors found that MSNs positively charged were quickly excreted from the liver into the gastrointestinal tract, while negatively charged MSNs remain sequestered within the liver [119]. Another study showed that short-rod MSNs have a more rapid biliary excretion than long-rod MSNs. Hirn *et al.* [120] also found that significantly more positively than negatively charged Au NPs were cleared through the biliary excretion, and the clearance of Au NPs showed an inverse linear relationship to their diameter over the size range of 5–200 nm. Therefore, the biliary excretion of NMs is dependent on the size, shape, and surface charge of NMs. However, the excretion pathway and efficiency of NMs remain largely unknown, and it is possible that not all NMs will be removed from the body.

7.4.2 Barrier Crossing

A series of specialized barriers has been identified and characterized in different parts of the body that protect the vital organs and systems of the organism, both physically and biochemically, from exposure to hazardous foreign substances [121]. For example, the skin can prevent the absorption of hazardous chemicals from cosmetics. Many studies have reported that NMs could penetrate the biologic barriers after inhalation or oral or dermal exposure and have used qualitative and quantitative data to elucidate the factors that determine the barrier-crossing behavior of NMs.

7.4.2.1 The Air–Blood Barrier

The air–blood barrier or alveolar–capillary barrier, exists in the gas-exchanging region of the lungs. It is formed by the type 1 pneumocytes of the alveolar wall, the endothelial cells of the capillaries, and the basement membrane between the two cells. To facilitate oxygen diffusion, the barrier is extremely thin, approximately 0.6–2 μm, in some places merely 0.2 μm. Some data are available on the air–blood barrier crossing of NMs, in particular from studies on rodents. For example, Choi *et al.* [122] demonstrated that nanoparticles with hydrodynamic diameter less than ≈34 nm and a noncationic surface charge translocate rapidly from the lung to mediastinal lymph nodes, while nanoparticles of hydrodynamic diameter less than 6 nm can traffic rapidly from the lungs to the lymph nodes and the bloodstream. The air–blood translocation of NMs is greatly dependent on the physicochemical properties (e.g., size) of NMs as well as their interactions with physiologically relevant media and proteins [123, 124].

Once NMs reach the blood circulation, they could be taken up by the vascular endothelial cells or, alternatively, could extravasate the circulation via transcytosis or paracellular pathways [96]. Extravasation of NMs becomes easier where open fenestrations are present in the endothelial walls. For example, the discontinuous endothelium in the liver, spleen, and bone marrow has pores of 50–200 nm in diameter. In addition, when the integrity of the endothelial barrier is perturbed by inflammatory processes or deregulated angiogenesis (e.g., in tumor), nanoparticles can evade systemic circulation. In some delicate organs, NM extravasation is restricted by tight junctions in the capillary endothelium. For example, the brain and the fetus are protected by dedicated protection barriers, that is, the blood–brain barrier (BBB) and the placental barrier.

7.4.2.2 The Placental Barrier

Fetotoxicity of NMs is an important aspect of nanotoxicology, as fetuses are known to be more sensitive to environmental toxins than adults. The human fetus is protected by the placental barrier consisting of a single limiting layer of multinuclear cells as known as *syncytiotrophoblasts* (Figure 7.11). A microvillous brush border membrane, in direct contact with maternal circulation, constitutes the maternal-facing plasma membrane of the syncytium [126]. On the opposite

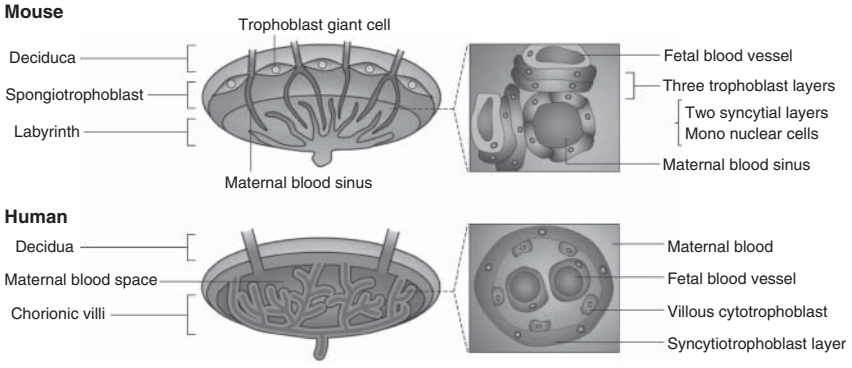

Figure 7.11 Schematic representation of human and mouse placentae. (Reprinted with permission from [125]. Copyright (2011) Nature Publishing Group.)

side, the basal membrane faces the fetal circulation and lacks microvillar projections. Both sides of the syncytium are not only structurally distinct, but also differ in the localization of transporters, enzymes, and hormone receptors. *Ex vivo* perfusion studies using human placentas suggest that NMs sized less than approximately 80 nm could penetrate the placental barrier, while larger NMs were partially or totally excluded [127, 128].

Previous studies have demonstrated the fetotoxicity of NMs using *in vivo* murine models exposed to NMs during pregnancy [129–132]. Therefore, animal experiment is necessary to study the transplacental NM transport qualitatively and quantitatively. The mature placenta in mice is established by embryonic day 10.5 (E10.5) [133], so Yang *et al.* [134] determined the fetal uptake of 13 nm Au NPs following IV administration at different gestation ages between E5.5 and 15.5. The results showed that prior to E11.5, all tested nanoparticles with different surface modifications (ferritin, PEG, and citrate) could be detected in the fetal tissues in significant amounts; however, the transplacental transport of nanoparticles declined dramatically post-E11.5. The fetal accumulation of ferritin- and PEG-modified nanoparticles was considerably greater than that of citrate-capped nanoparticles. The transplacental passage of CdTe/CdS QDs of different sizes and with different surface cappings has also been studied, and the results demonstrated that smaller QDs are more easily transferred than larger QDs [131]. Capping with an inorganic silica shell or organic polyethylene glycol reduces QD transfer but does not eliminate it. Yamashita *et al.* [125] reported that 70 nm silica and 35 nm TiO_2 nanoparticles could be found in the fetal liver and brain, but the particles with diameters of 300 and 900 nm were blocked by the placenta. These results demonstrate that NM translocation from the maternal blood to the fetus occurs during early embryonic development or even when the placental barrier is fully developed. However, it should be kept in mind that mouse, rat, and human placentas differ in their modes of implantation, the relative importance of yolk sac placentation, and the structure (labyrinthine

compared with villous) of the exchange area. Therefore, one has to be cautious to extrapolate the transplacental behaviors of NMs in rodents and humans.

7.4.2.3 The Blood–Brain Barrier

The BBB is a highly selective permeability barrier that separates the circulating blood from the brain extracellular fluid in the central nervous system (CNS). The BBB is composed of specialized endothelial cells connected with each other by tight junctions and surrounded by astrocytes and pericytes. Due to their small size, NMs are able to penetrate the BBB and reach the CNS, which raises concerns regarding their possible unwanted toxic effects on the CNS.

The translocation of NMs through the BBB has been demonstrated in rodents and other vertebrates such as freshwater fish. NMs could enter the CNS with or without disturbing the integrity of the BBB. After IP administration of silica-overcoated magnetic nanoparticles for 4 weeks, Kim *et al.* [135] found that the nanoparticles could reach the neurons of mice without damaging the BBB function. In another study, they demonstrated that their PEGylated nanoparticles have the capacity to diffuse through the BBB after IV administration [136]. The authors suggested that the LDL (Low-Density Lipoprotein) receptor-mediated pathway was involved in the endocytosis mechanism. Polysorbate-80-coated polybutylcyanoacrylate (P80-PBCA) nanoparticles can deliver the peptide "dalargin" into CNS [137], and the barrier crossing appears to result from a dramatically increased BBB permeability [138]. Translocation of NMs through impaired BBB has also been shown by administering silver, aluminum, and copper nanoparticles to rats by various routes and testing the disruption of the BBB using Evans blue or radioiodine [139]. The results show that leakage of Evans blue or radioiodine was found in different parts of the brain depending on the nanoparticle, dose, and route of administration. The disruptive effect on the BBB was most prominent in animals treated with silver and copper nanoparticles sized 50–60 nm when compared to aluminum nanoparticles at equivalent doses [140].

In addition, airborne NMs can arrive at the brain via olfactory neuronal pathway due to their small size. Recent studies support the concept that the CNS may be an important target organ for NM inhalation or intranasal instillation exposure [141–143]. The translocation of NMs via olfactory pathway can bypass the BBB and therefore may cause more severe consequences in the CNS.

7.5 *In Vivo* Toxicity of Nanomaterials

7.5.1 Effects on the Respiratory System

The respiratory system is one of the main conduits of access to the body for NMs. Therefore, it is the primary and probably the most important target of NMs. Large-scale epidemiological studies have demonstrated that exposure to

air pollution particulates contributes to increased respiratory and cardiovascular morbidity and mortality. *In vivo* studies have revealed that pulmonary exposure to NMs produces a greater adverse inflammatory response than their larger counterparts at equivalent mass concentrations.

Carbon nanotubes (CNTs), either single layer (i.e., single-walled carbon nanotubes (SWCNTs)) or multiple layers (i.e., multiwalled carbon nanotubes (MWCNTs)), have received notable attention due to their similarities to asbestos [144]. The type of CNTs (i.e., SWCNT or MWCNT), length, method of processing (i.e., refined or unrefined), presence of residual transition metal catalysts, and functionalization might influence their toxic effects on the respiratory system. In the mice intratracheally instilled with 0, 0.1, or 0.5 mg of CNTs, Lam *et al.* [145] found dose-dependent epithelioid granulomas and, in some cases, interstitial inflammation 7 days after the single treatment. These lesions persisted and were more pronounced 90 days after the exposure; the lungs of some animals revealed peribronchial inflammation and necrosis that had extended into the alveolar septa. Their comparison study also suggests that SWCNTs are much more toxic than carbon black and can be more toxic than quartz, which is considered a serious occupational health hazard in chronic inhalation exposures. Shvedova *et al.* [146] found that pharyngeal aspiration of SWCNT elicited unusual pulmonary effects in C57BL/6 mice that combined a robust but acute inflammation with early onset yet progressive fibrosis and granulomas. Functional respiratory deficiencies and decreased bacterial clearance (*Listeria monocytogenes*) were also found. MWCNT exposure may result in peripheral respiratory disease as a result of combined inflammatory infiltrates and granulomatous/fibrotic parenchymal responses, reflected by a decline in pulmonary function [147]. The *in vivo* experiments indicate that the length of MWCNTs acts as an important factor in macrophage activation and subsequent transforming growth factor (TGF)-β1 secretion: long MWCNTs (20–50 μm), but not short MWCNTs (0.5–2 μm), caused fibrotic responses including granuloma formation, collagen deposition, and fibroblast proliferation; only long MWCNTs can significantly activate macrophages and increase the production of TGF-β1, and then the activation of the TGF-β/Smad2 signaling plays a critical role in the process of the fibroblast-to-myofibroblast transition and the epithelial–mesenchymal transition induced by MWCNTs [148, 149].

There are also many reports focusing on the potential toxic response of metal-based NMs in the respiratory system. Intratracheal instillation of Ag, ZnO, and TiO_2 NPs can all lead to an increase in oxidative injury to the lungs and disorders in regulating the cytokine network [150]. Braakhuis *et al.* [151] found that 15 nm Ag NPs induced more severe pulmonary inflammation after short-term inhalation when compared to the 410 nm particles, and the size dependency is a consequence of both size-related lung deposition and dissolution rate. Zhang *et al.* [152] compared the acute pulmonary inflammation in C57 BL/6 mice induced by oropharyngeal instillation of Co_3O_4, Cr_2O_3, Ni_2O_3, CuO, Mn_2O_3, CoO, Y_2O_3, ZrO_2, CeO_2, HfO_2, In_2O_3, NiO, Fe_2O_3, and Fe_3O_4 NPs and found that both single-parameter cytotoxic as well as multiparameter oxidative

stress assays in cells showed excellent correlation to the generation of acute neutrophilic inflammation and cytokine responses *in vivo*. Therefore, the authors speculated that conduction-band energy levels together with *in vitro* toxicological ranking can be used to predict the *in vivo* pulmonary toxicities of NMs. Exposure to CeO_2 nanoparticles via inhalation or intratracheal instillation could result in pulmonary inflammation in rats, and the level of inflammation by CeO_2 NPs was approximately between NiO and TiO_2 NPs [153]. Amorphous silica coating on CeO_2 NPs could reduce CeO_2-induced inflammation, phospholipidosis, and fibrosis [154].

To sum up, most *in vivo* studies report inflammation, oxidant injury, progressive fibrosis, and granulomas in rodents exposed to NMs via intratracheal installation or pharyngeal aspiration [155]. Various endpoints and indices are used to reflect the effects of NM exposure on the respiratory system, including lung functions [147], cell differentiation in bronchoalveolar ravage fluid (BALF) [79, 152], inflammatory markers in either BALF or tissues (e.g., cytokines, chemokines, protease) [147, 148, 156], immune dysfunctions [157, 158], oxidative stress [159], markers of fibrosis and the relevant signaling pathway [147, 160], hyperplasia, hypertrophy, epithelial–mesenchymal transition [161, 162], and lung histopathology and ultrastructure [156].

7.5.2 Effects on the Cardiovascular System

The cardiovascular system consists of the heart, blood vessels, the cells, and plasma that make up the blood. An increasing body of epidemiological evidence confirms that exposure to environmental particulate matters is associated with multiple adverse cardiovascular effects in both healthy individuals and those with preexisting cardiovascular disease. Although there are no epidemiological data by now addressing the effects of NMs on the cardiovascular system, experimental studies suggest that the pathophysiological changes of cardiovascular system had close association with NM exposure [163].

Duan *et al.* [164] treated newly fertilized zebrafish embryos with SiO_2 NPs at concentrations of 0, 25, 50, 100, and 200 μg/ml during 4–96 h postfertilization and found that the treatment could inhibit the angiogenesis and disturb the heart formation and development. Chen *et al.* [165] examined the cardiovascular effects of TiO_2 NPs in ApoE knockout mice ($ApoE^{-/-}$ mice), an atherosclerosis susceptible model, and found that tracheal instillation of TiO_2 NPs induced considerable systemic inflammation, endothelial dysfunction, and lipid metabolism dysfunction, contributing to the progression of atherosclerosis. Another study in $ApoE^{-/-}$ mice showed no associations between the intratracheal installation of TiO_2 NPs and inflammation or vasodilatory dysfunction, but a modest increase in plaque progression in the aorta [166]. Chen *et al* [68] studied the age-related difference in cardiovascular responses to SiO_2 NP inhalation exposure by analyzing the serum biomarkers, thrombogenesis, heart injury, and pathology in rats. The results showed that the SiO_2 NP inhalation caused severe myocardial

ischemia, elevation of blood viscosity and fibrinogen concentration in old rats, yet less change in young and adult rats. The results indicate that old individuals are more sensitive to nanoparticle exposure than the young and adult rats. Several studies explored the direct interactions between NMs and blood components and showed that NMs could directly cause platelet aggregation and vascular thrombosis [167–170].

Generally, the mechanisms underlying the cardiovascular effects of NMs include the following: (i) pulmonary and/or systemic inflammatory responses leading to endothelial dysfunction and a procoagulatory state, (ii) direct interactions of NMs with endothelium and/or blood constituents promoting thrombogenesis, (iii) dysfunction of the autonomic nervous system mediated by direct reflexes from intrapulmonary receptors and/or by local or systemic inflammatory stimuli, and (iv) cardiac malfunction due to ischemic responses in the myocardium and/or altered ion-channel functions in myocardial cells [171].

The assessments and endpoints commonly used to evaluate the cardiovascular effects of NM exposure include the following: inflammation-related indicators (high-sensitivity C-reactive protein, cytokines, inflammation-related gene expression) [168, 172], markers for oxidative stress [68, 172], heart rate [164], blood pressure [173, 174], vasomotor function [168], blood cell differentials [175], hemorheological changes [68], fibrinogen deposition and blood viscosity [68], platelet aggregation [167, 170], cardiovascular development (angiogenesis and expression of cardiovascular-related proteins) [164], vascular thrombosis and atherosclerosis (e.g., progression of atherosclerotic plaques, expression of adhesion molecules) [166, 167, 176], and cardiovascular histopathologic damage [68, 176].

7.5.3
Effects on the Digestive System

To date, a large number of food products containing NMs have already been used as food supplements and in food packaging: for example, Ag and ZnO NPs as antimicrobial agents, TiO_2 and SiO_2 NPs as food additives, and silicates and aluminosilicates as anticaking and anticlumping agents [177]. This rapid expansion of such applications causes an increase in the population exposure to NMs. According to the existing literature, the adverse effects of NM exposure on the digestive system mainly include intestinal dysfunction and inflammation, disturbances in the gut microflora environment, as well as hepatotoxicity.

The gastrointestinal tract is a complex barrier-exchange system that takes in food substances and expels the remains as waste. The major functions of the intestines are ingestion, digestion, absorption, and defecation. Oral exposure to NMs may cause gastrointestinal dysfunction and inflammation. In an early report, all of the mice exposed to Cu NPs (23.5 nm) appeared obviously symptoms of alimentary canal function disorder, such as loss of appetite, diarrhea, and vomiting, while only a few mice exposed to micro-Cu (17 μm) exhibited symptoms of poising [178]. The gastrointestinal toxicity of Cu NPs belongs to

class 3 (moderately toxic) of Hodge and Sterner Scale. Chickens acutely exposed to carboxylated polystyrene NPs (50 nm in diameter) had a lower iron absorption than unexposed or chronically exposed chickens [179]. Chronic exposure caused remodeling of the intestinal villi, which increased the surface area available for iron absorption. TiO_2 NPs induced inflammatory cytokine production and $CD4^+$ T-cell proliferation in the intestine of male C57BL/6 mice, indicating a Th1-mediated inflammatory response [180]. The exposure also caused hypertrophy and hyperplasia of the mucosal epithelium in the duodenum, jejunum, and ileum of mice. Another study showed that oral exposure to TiO_2 NPs could disturb the gut microflora environment in Wistar rats [181].

As a result of first-pass metabolism, NMs can easily reach and deposit in the liver by the blood circulation, and therefore, the hepatic effects of NMs should be concerned. In a 28 day investigation of the oral exposure to 60 nm Ag NPs, Kim *et al.* [182] found some significant dose-dependent changes in the alkaline phosphatase and cholesterol values in either the male or the female rats, seeming to indicate that exposure to over more than 300 mg of Ag NPs may result in slight liver damage. Bile duct hyperplasia, with eosinophil infiltration of the hepatic lobules and portal tract, was also reported. A subacute oral exposure of ZnO NPs (300 mg/kg) for 14 consecutive days resulted in a significant accumulation of NPs in the liver of mice, and the exposure also induced oxidative stress, which led to DNA damage and subsequent apoptosis in the liver cells [183]. In an experiment conducted in mice fed with a methionine- and choline-deficient (MCD) diet for 4 weeks, the authors found that tail vein injection of 5 mg/kg Au NPs significantly elevated the serum ALT (alanine transaminase) and AST (aspartate aminotransferase) levels [160]. Furthermore, severe hepatic cell damage, acute inflammation, and increased apoptosis and reactive oxygen species (ROS) production were observed in the livers of mice treated with Au NPs; these liver injuries were attenuated in mice fed a normal chow diet. The results suggest that Au NPs display toxicity in a stressed liver environment by stimulating the inflammatory response and accelerating stress-induced apoptosis.

To date, various assays with different endpoints and indices are employed to investigate the effects of NMs on the digestive system, including histopathology and ultrastructure examination [84, 93, 181], hematology test [84], serum and urine metabonomics analysis [181], gastrointestinal function analysis [84, 179], inflammation, oxidative stress and apoptosis evaluation [184–186], quantification of bacterial phyla and relevant genes [187], and digestion-related protein and gene expressions [179, 188, 189]. It should be kept in mind that the state and properties of NMs may be changed during digestion; therefore, new tools should be developed for the *in situ* characterization of NMs within the digestive system.

7.5.4 Effects on the Skin

Skin is the largest organ of the body. It is also a primary route of potential exposure to toxicants, including NMs. Existing studies demonstrate no transdermal

penetration of topically applied NMs in almost all cases, although there is the presence of NMs in the stratum corneum and epidermis [104, 190]. Generally, the NM-induced dermal responses, including dermal irritation and corrosion and skin sensitization, are minimal or negligible when studied *in vivo* [191–195].

7.5.5 Neurotoxicity

The CNS consisting of the brain and spinal cord is responsible for integrating sensory information and responding accordingly. There are a few pathways through witch NMs can reach the CNS and elicit potentially toxic effects. One of the most important portals of entry is the respiratory tract. Inhaled NMs may deposit in the alveolar region, where they readily translocate through the air–blood barrier and reach other target organs, including the CNS, via systemic circulating. In a more direct way, airborne NMs can arrive at the brain via olfactory neuronal pathway due to their small size. Recent studies support the concept that the CNS may be an important target organ for NM inhalation or intranasal instillation exposure [141–143]. The translocation of NMs via olfactory pathway can bypass the BBB, which protects the brain from the toxicants in the peripheral blood and therefore may cause more severe consequences in the CNS.

The term *neurotoxicity* includes anatomical, biochemical, pathological, electrophysiological, or even psychological malfunction of neuronal, glia, axons, and endothelial cells. There are already many reports focusing on the potential neurotoxicity of NMs in animal models under different conditions [196]. Bai *et al.* [197, 198] exposed mice to Cu NPs via intranasal instillation every other day for 20 days, and the exposure significantly increased the Cu content in the brain, altered the homeostasis of metal elements, caused damages in the neurons and astrocytes, and disturbed the neurotransmitter levels in different brain regions. Skalska *et al.* [199] found that oral exposure to Ag NPs over a 2 week period resulted in ultrastructural changes of synapses accompanied by decreased level of synaptic proteins. The evidence that hippocampal synapses are much more strongly affected by the exposure to Ag NPs indicates higher vulnerability of this structure and predicts impairment of cognitive processes. Parveen *et al.* [200] exposed Wistar rats to SiO_2 NPs sized 80 nm up to 90 days (150 μg/50 μl PBS/rat), and the results demonstrated impairment in neurobehavioral indices, as well as the antioxidant defense system and ultrastructures in the corpus striatum (CS) region of rat brain. Furthermore, mitochondrial and endoplasmic reticulum stress-mediated neuronal apoptoses were also found in treated rat brain CS.

Some model organisms, such as *C. elegans*, zebrafish, and *Drosophila*, offer attractive experimental platforms to study the *in vivo* neurotoxic effects of NMs. Hsu *et al.* [34] found that exposure to mercaptosuccinic-acid-capped QDs might cause an egg-laying defect phenotype by disrupting motor neurons during the reproduction process of *C. elegans*, resulting in high embryo mortality and a reduced life span. By using *C. elegans*, Wang and his colleagues studied

the neuromuscular effects of CdTe QDs, graphene oxide, TiO_2, Al_2O_3, ZnO, SiO_2, and Fe_2O_3 NPs [31, 40, 201–205]. They identified the impairments in neurobehavior of *C. elegans* even under exposure to NMs at the environmental relevant concentrations [206, 207], demonstrating *C. elegans* as a very sensitive model organism for the neurotoxicological study of NMs. Xue *et al.* [208] assessed the impact of SiO_2 NPs of different sizes on the rest/wake behavior of zebrafish larvae, and the results showed that the 15 nm NPs have a greater neurotoxic effect than the 50 nm NPs. Exposure to Al_2O_3 NPs could alter the rhythmic activities of local interneurons in the antennal lobe of *Drosophila* [209].

Generally, *in vivo* studies support the epidemiological evidence of neurotoxicity following exposure to airborne NMs, with an important role played by the olfactory tract. In the brain, NMs may induce inflammation, apoptosis, and oxidative stress by releasing various mediators from the microglia and astrocyte. In the existing reports, assays with different endpoints and indices are employed to identify the neurotoxic effects of NMs, including elemental homeostasis [197], inflammation [210], oxidative stress [200], oxidative-stress-related signaling factors [211], cell loss (apoptosis and necrosis, as well as the related protein expressions) [200, 210], histopathological and ultrastructure changes [197, 199], neurotransmitter levels [198, 212, 213], nerve functions (e.g., synaptic plasticity, cognition, learning, and memory) [199, 214], neurobehaviors [40, 200], the development of nerve system [129, 215, 216], and relevant gene expression [217–219].

7.5.6 Reproductive and Developmental Toxicity

It is widely accepted that the fetus may be more sensitive to chemical exposures than the adult organism. While there is a speculation that NMs might pose potential reproductive and developmental harm, toxicological data is, to date, very limited and remains insufficient. For NMs to reach the fetus, they need to first translocate at the portal of entry into the systemic circulation, and then traverse the placental barrier. However, NMs may not need to reach the fetus to affect reproduction and development [220]. Inflammation and oxidative stress induced by NM exposure during pregnancy may result in perturbations that have been shown to have detrimental and long-lasting consequences for fetal development.

The recently published studies do actually indicate that NM exposure may be able to adversely affect both male and female reproductive functions, interfere with fetal development, and have consequences for the offspring later in life. In an experiment conducted in nonpregnant female mice, long-term exposure to TiO_2 NPs (sized 5–6 nm, oral administration) at a concentration of 10 mg/kg was found to cause ovarian dysfunction and alterations in functional gene expression levels. TiO_2 NPs were detected in the ovarian cells of these mice, and the resultant cellular damage led to an imbalance in sex hormones and decreased fertility [221]. The IV injection of TiO_2 and SiO_2 NPs into pregnant mice induced

pregnancy complications [125]. These detrimental effects are linked to structural and functional abnormalities in the placenta on the maternal side and are abolished when the surfaces of the SiO_2 NPs are modified with carboxyl and amine groups. Pubertal Wistar rats were exposed to 0, 0.25, 0.5, 0.75, and 1.0 mg/kg functionalized MWCNTs for 5 days; the spermiogram indicated significant decrease in epididymal sperm number, sperm progressive motility, testicular sperm number, and daily sperm production with elevated sperm abnormalities when compared with the control [222]. The exposure decreased the plasma testosterone level and produced marked morphological changes including decreased germinal epithelium, edema, congestion, reduced spermatogenic cells and focal areas of tubular degeneration in the testes. In another study, intratracheal exposure to carbon black nanoparticles (0.1 mg/mouse for 10 times at weekly intervals) could impair the reproductive function of male ICR mice [223].

NMs may cause damage to embryos after transplacental transport or by altering the signaling pathways in the peripheral blood and tissues. Maternal inhalation of TiO_2 NPs (1 h/day, 42 mg/m^3) from gestational day (GD) 8–18 resulted in the abnormal gene expression related to the retinoic acid signaling pathway in the female offspring of C57BL/6 mice [224]. NPs may also cause altered organogenesis and morphology as well as defects in the reproductive and nervous systems of the offspring. Damage of the genital system, including decreased sperm counts and defects of cranial nerves, was observed in the pups after prenatal exposure to TiO_2 NPs [130].

Zebrafish, *C. elegans,* and *Drosophila* are well-known models for the evaluation of reproductive and developmental toxicities of NMs. Zebrafish embryos are relatively large in size (0.7 mm in diameter at fertilization) and optically transparent and are easy to obtain in large numbers. Fertilization is external, so live embryos are accessible to manipulation and can be monitored through all developmental stages under a dissecting microscope. Development is rapid, with precursors to all major organs developing within 36 h. The embryo model is very convenient for the observation of developmental malformation, mortality, and behavioral changes. The advantages of using *C. elegans* for reproduction development evaluation include small size, transparency, a rapid life cycle (3 days at 20 °C from egg to egg-laying adult), large brood size, stereotypical development, low-cost of maintenance, and ease of manipulation. Genetic manipulability and ease of detecting phenotypes made *Drosophila* the model of choice for mutagenesis screens. By using zebrafish, *C. elegans,* and *Drosophila*, researchers have identified the reproductive and developmental toxicities from various NMs, including fullerene, CNTs, QDs, graphene, TiO_2, SiO_2, Ag, Ni, Cu, ZnO, Al_2O_3, Au, and Pt [9, 28, 34, 44, 225–232].

Assays with different endpoints and indices are employed to identify the reproductive and developmental toxicities of NMs, including elemental homeostasis in reproductive system and offspring [221], reproductive functions (e.g., sperm production and germ cell abnormalities) [222], sex hormone levels (such as estradiol, progesterone, luteinizing hormone, follicle-stimulating hormone, prolactin, and testosterone) [221], histopathologic and ultrastructural evaluation

[125, 222, 223], inflammation, oxidative stress and apoptosis [221, 222, 227], offspring organogenesis and morphology [9, 232], number of offspring [28], and relevant gene expression (related to hormone regulation, immune, inflammatory, oxidative stress, ion transport, offspring development, etc.) [221, 225]. More information about the reproductive and developmental toxicities of NMs could be found in some recent reviews [220, 233–236].

7.5.7 Genotoxicity

A literature search performed by Magdolenova *et al.* showed that NM exposure may result in increased damage to the genetic material both *in vivo* and *in vitro* [237]. For example, Folkmann *et al.* exposed female Fisher 344 rats to pristine C_{60} fullerenes and SWCNT (0.064 or 0.64 mg/kg body weight) suspended in saline solution or corn oil and found that the levels of 8-oxo-7,8-dihydroguanine (8-oxodG, a biomarker for oxidative DNA damage) were elevated in the liver and lung [238]. The increase in 8-oxoG levels was likely to have resulted from a direct genotoxic ability rather than an inhibition of the DNA repair system. Khalil *et al.* found that oral exposure to cobalt-doped and undoped CdSe QDs at doses of 500, 1000, and 2000 mg/kg could induce DNA damage, formation of micronuclei, and generation of DNA adduct in the mice 7 days after the treatment [239].

The *in vivo* genotoxicity of NMs is still a topic of particular interest due to the lack of sufficient toxicity data and mechanistic understanding [240]. It is often not clear if an effect on DNA is particle-specific [237]. Oxidative stress and direct interactions with DNA are considered important in the genotoxicity caused by NM exposure [241]. Oxidative stress has been identified as a major mechanism of toxicity for NMs. Elevated ROS levels in NM-laden cells may trigger indirect oxidative damage to DNA through free-radical attack. Direct DNA interaction could represent a more particle-specific mechanism due to the fact that small nanoparticles may reach the nucleus via transportation through the nuclear pore complexes [241]. Features of NMs such as size, shape, surface properties, composition, solubility, aggregation/agglomeration, and transition metal impurities can influence the mechanisms of genotoxicity.

The methods and endpoints used to estimate the *in vivo* genotoxicity of NMs include comet assay [242–244], micronucleus assay [239, 245], chromosome aberrations [246], 8-oxodG measurement [238, 239], and mRNA expression related to DNA damage or repair [244, 247].

7.6 Recommendations

Keep in mind the 3R principle and conduct animal studies only when necessary.

An appropriate selection of experimental organisms should be considered when performing nanotoxicological studies.

When designing animal studies, it is essential that exposures in animal models should be relevant to human exposures (dose selection, exposure route, exposure duration, vehicle, susceptible models, as well as other conditions).

The tested NMs should be characterized adequately prior to the initiation of toxicological experimentation. In the absence of a careful and complete description of the NMs being evaluated (as well as the experimental conditions being employed), the results of toxicological experiments will have limited significance. It is recommended that the following physicochemical properties should be characterized: composition (including coating and impurity), crystal structure, size distribution, shape, surface area, surface charge, surface chemistry, agglomeration state, and dissolution.

It is recommended that the methods of NM preparation are fully documented, including the selection of appropriate dispersion media, methods of dispersion in the medium, and agglomeration state within the medium.

More sensitive methods should be developed for the quantification of NMs *in vivo*, especially for the studies of particokinetics.

Be cautious when relating the observed responses to the physicochemical properties of NMs, because there may be physicochemical changes in the NMs before and after administration. Therefore, *in situ* characterization of the NMs within organisms is necessary, but this is limited by the current methodological capabilities.

NMs may interact with many biochemical agents, therefore disturbing the assessment outcomes. Sometimes, preliminary experiments should be conducted for biological assays to exclude the interactions between NMs and the test system.

Be cautious when extrapolating the nanotoxicity data from animal studies to humans.

References

1. Song, Y., Li, X., and Du, X. (2009) Exposure to nanoparticles is related to pleural effusion, pulmonary fibrosis and granuloma. *Eur. Respir. J.*, **34** (3), 559–567.
2. Gilbert, N. (2009) Nanoparticle safety in doubt. *Nature*, **460** (7258), 937.
3. Baeza-Squiban, A., Lacroix, G., and Bois, F.Y. (2011) in *Nanoethics and Nanotoxicology* (eds P. Houdy, M. Lahmani, and F. Marano), Springer, Berlin, Heidelberg, pp. 63–86.
4. Wikipedia https://en.wikipedia.org/wiki/Animal_testing_on_rodents (accessed 17 July 2015).
5. Wikipedia https://en.wikipedia.org/wiki/Laboratory_rat (accessed 17 July 2015).
6. Gonzalez-Moragas, L., Roig, A., and Laromaine, A. (2015) *C. elegans* as a tool for in vivo nanoparticle assessment. *Adv. Colloid Interface Sci.*, **219**, 10–26.
7. Wikipedia https://en.wikipedia.org/wiki/Zebrafish (accessed 31 July 2015).
8. Shapiro, L. http://eol.org/data_objects/17763813 (accessed 17 July 2015).
9. Bai, W., Zhang, Z., Tian, W., He, X., Ma, Y., Zhao, Y., and Chai, Z. (2010) Toxicity of zinc oxide nanoparticles to zebrafish embryo: a physicochemical study of toxicity mechanism. *J. Nanopart. Res.*, **12** (5), 1645–1654.
10. Lin, S., Zhao, Y., Xia, T., Meng, H., Ji, Z., Liu, R., George, S., Xiong, S., Wang, X., and Zhang, H. (2011) High content screening in zebrafish speeds

up hazard ranking of transition metal oxide nanoparticles. *ACS Nano*, **5** (9), 7284–7295.

11. Spomer, W., Pfriem, A., Alshut, R., Just, S., and Pylatiuk, C. (2012) High-throughput screening of zebrafish embryos using automated heart detection and imaging. *J. Lab. Autom.*, **17** (6), 435–442.
12. George, S., Xia, T., Rallo, R., Zhao, Y., Ji, Z., Lin, S., Wang, X., Zhang, H., France, B., and Schoenfeld, D. (2011) Use of a high-throughput screening approach coupled with in vivo zebrafish embryo screening to develop hazard ranking for engineered nanomaterials. *ACS Nano*, **5** (3), 1805–1817.
13. Pardo-Martin, C., Chang, T., Koo, B.K., Gilleland, C.L., Wasserman, S.C., and Yanik, M.F. (2010) High-throughput in vivo vertebrate screening. *Nat. Methods*, **7** (8), 634–636.
14. Liu, R., Lin, S., Rallo, R., Zhao, Y., Damoiseaux, R., Xia, T., Lin, S., Nel, A., and Cohen, Y. (2012) Automated phenotype recognition for zebrafish embryo based in vivo high throughput toxicity screening of engineered nanomaterials. *PLoS One*, **7** (4), e35014.
15. Ishaq, O., Negri, J., Bray, M.A., Pacureanu, A., Peterson, R.T., and Wahlby, C. (2013) Automated quantification of Zebrafish tail deformation for high-throughput drug screening. Proceedings of the 10th IEEE International Symposium on Biomedical Imaging, San Francisco, April 7–11, 2013, IEEE.
16. Lin, S., Zhao, Y., Ji, Z., Ear, J., Chang, C.H., Zhang, H., Low-Kam, C., Yamada, K., Meng, H., and Wang, X. (2013) Zebrafish high-throughput screening to study the impact of dissolvable metal oxide nanoparticles on the hatching enzyme, ZHE1. *Small*, **9** (9–10), 1776–1785.
17. Wang, J., Zhu, X., Chen, Y., and Chang, Y. (2012) in *Nanotoxicity: Methods and Protocols* (ed. J. Reineke), Springer, New York, pp. 317–329.
18. Lawrence, C. (2007) The husbandry of zebrafish (*Danio rerio*): a review. *Aquaculture*, **269** (1), 1–20.
19. Usenko, C.Y., Harper, S.L., and Tanguay, R.L. (2007) In vivo evaluation of carbon fullerene toxicity using embryonic zebrafish. *Carbon*, **45** (9), 1891–1898.
20. Ali, S., Champagne, D.L., Spaink, H.P., and Richardson, M.K. (2011) Zebrafish embryos and larvae: a new generation of disease models and drug screens. *Birth Defects Res. C Embryo Today*, **93** (2), 115–133.
21. Lin, S. http://www.cein.ucla.edu/new//file_uploads/Research_Protocols/CEIN_Protocol_Zebrafish_screening_Mar_8_2012.pdf (accessed 15 July 2015).
22. Rizzo, L.Y., Golombek, S.K., Mertens, M.E., Pan, Y., Laaf, D., Broda, J., Jayapaul, J., Möckel, D., Subr, V., and Hennink, W.E. (2013) In vivo nanotoxicity testing using the zebrafish embryo assay. *J. Mater. Chem. B*, **1** (32), 3918–3925.
23. Lin, S., Zhao, Y., Nel, A.E., and Lin, S. (2013) Zebrafish: an in vivo model for nano EHS studies. *Small*, **9** (9–10), 1608–1618.
24. Altun, Z.F. and Hall, D.H. http://www.wormatlas.org/hermaphrodite/hermaphroditehomepage.htm (accessed 23 July 2015).
25. Wikipedia https://en.wikipedia.org/wiki/Caenorhabditis_elegans (accessed 17 July 2015).
26. Kaletta, T. and Hengartner, M.O. (2006) Finding function in novel targets: *C. elegans* as a model organism. *Nat. Rev. Drug Discovery*, **5**, 387–399.
27. Zhang, H., He, X., Zhang, Z., Zhang, P., Li, Y., Ma, Y., Kuang, Y., Zhao, Y., and Chai, Z. (2011) Nano-CeO_2 exhibits adverse effects at environmental relevant concentrations. *Environ. Sci. Technol.*, **45** (8), 3725–3730.
28. Pluskota, A., Horzowski, E., Bossinger, O., and von Mikecz, A. (2009) In *Caenorhabditis elegans* nanoparticle-bio-interactions become transparent: silica-nanoparticles induce reproductive senescence. *PLoS One*, **4** (8), e6622.
29. Stone, V. and Donaldson, K. (2006) Nanotoxicology: signs of stress. *Nat. Nanotechnol.*, **1** (1), 23–24.
30. Honda, Y. and Honda, S. (2002) Oxidative stress and life span determination

in the nematode *Caenorhabditis elegans*. *Ann. N.Y. Acad. Sci.*, **959** (1), 466–474.

31. Wu, Q., Zhao, Y., Zhao, G., and Wang, D. (2014) microRNAs control of in vivo toxicity from graphene oxide in *Caenorhabditis elegans*. *Nanomed. Nanotechnol. Biol. Med.*, **10** (7), 1401–1410.
32. Zhao, Y., Lin, Z., Jia, R., Li, G., Xi, Z., and Wang, D. (2014) Transgenerational effects of traffic-related fine particulate matter ($PM_{2.5}$) on nematode *Caenorhabditis elegans*. *J. Hazard. Mater.*, **274**, 106–114.
33. Qu, Y., Li, W., Zhou, Y., Liu, X., Zhang, L., Wang, L., Li, Y., Iida, A., Tang, Z., Zhao, Y., Chen, C., and Chai, Z. (2011) Full assessment of fate and physiological behavior of quantum dots utilizing *Caenorhabditis elegans* as a model organism. *Nano Lett.*, **11** (8), 3174–3183.
34. Hsu, P.C.L., O'Callaghan, M., Al-Salim, N., and Hurst, M.R. (2012) Quantum dot nanoparticles affect the reproductive system of *Caenorhabditis elegans*. *Environ. Toxicol. Chem.*, **31** (10), 2366–2374.
35. Cha, Y.J., Lee, J., and Choi, S.S. (2012) Apoptosis-mediated in vivo toxicity of hydroxylated fullerene nanoparticles in soil nematode *Caenorhabditis elegans*. *Chemosphere*, **87** (1), 49–54.
36. Kim, J., Shirasawa, T., and Miyamoto, Y. (2010) The effect of TAT conjugated platinum nanoparticles on lifespan in a nematode *Caenorhabditis elegans* model. *Biomaterials*, **31** (22), 5849–5854.
37. Yan, H., Kinjo, T., Tian, H., Hamasaki, T., Teruya, K., Kabayama, S., and Shirahata, S. (2011) Mechanism of the lifespan extension of *Caenorhabditis elegans* by electrolyzed reduced water-participation of PT nanoparticles. *Biosci. Biotechnol., Biochem.*, **75** (7), 1295–1299.
38. White, J., Southgate, E., Thomson, J., and Brenner, S. (1986) The structure of the nervous system of the nematode *Caenorhabditis elegans*: the mind of a worm. *Philos. Trans. R. Soc. London, Ser. B*, **314**, 1–340.
39. Nouara, A., Wu, Q., Li, Y., Tang, M., Wang, H., Zhao, Y., and Wang, D. (2013) Carboxylic acid functionalization prevents the translocation of multiwalled carbon nanotubes at predicted environmentally relevant concentrations into targeted organs of nematode *Caenorhabditis elegans*. *Nanoscale*, **5** (13), 6088–6096.
40. Wu, Q.L., Li, Y.P., Tang, M., and Wang, D.Y. (2012) Evaluation of environmental safety concentrations of DMSA coated Fe_2O_3-NPs using different assay systems in nematode *Caenorhabditis elegans*. *PLoS One*, **7** (8), e43729.
41. Wu, Q., Yin, L., Li, X., Tang, M., Zhang, T., and Wang, D. (2013) Contributions of altered permeability of intestinal barrier and defecation behavior to toxicity formation from graphene oxide in nematode *Caenorhabditis elegans*. *Nanoscale*, **5** (20), 9934–9943.
42. Kim, S.W., Kwak, J.I., and An, Y.-J. (2013) Multigenerational study of gold nanoparticles in *Caenorhabditis elegans*: transgenerational effect of maternal exposure. *Environ. Sci. Technol.*, **47** (10), 5393–5399.
43. Ma, H., Bertsch, P.M., Glenn, T.C., Kabengi, N.J., and Williams, P.L. (2009) Toxicity of manufactured zinc oxide nanoparticles in the nematode *Caenorhabditis elegans*. *Environ. Toxicol. Chem.*, **28** (6), 1324–1330.
44. Wang, H., Wick, R.L., and Xing, B. (2009) Toxicity of nanoparticulate and bulk ZnO, Al_2O_3 and TiO_2 to the nematode *Caenorhabditis elegans*. *Environ. Pollut.*, **157** (4), 1171–1177.
45. Meyer, J.N., Lord, C.A., Yang, X.Y., Turner, E.A., Badireddy, A.R., Marinakos, S.M., Chilkoti, A., Wiesner, M.R., and Auffan, M. (2010) Intracellular uptake and associated toxicity of silver nanoparticles in *Caenorhabditis elegans*. *Aquat. Toxicol.*, **100** (2), 140–150.
46. Zhang, W., Sun, B., Zhang, L., Zhao, B., Nie, G., and Zhao, Y. (2011) Biosafety assessment of $Gd@C_{82}(OH)_{22}$ nanoparticles on *Caenorhabditis elegans*. *Nanoscale*, **3** (6), 2636–2641.

47. Hope, I.A. (ed.) (1999) *C. elegans: A Practical Approach*, Oxford University Press, Oxford.
48. Tyne, W., Lofts, S., Spurgeon, D.J., Jurkschat, K., and Svendsen, C. (2013) A new medium for *Caenorhabditis elegans* toxicology and nanotoxicology studies designed to better reflect natural soil solution conditions. *Environ. Toxicol. Chem.*, **32** (8), 1711–1717.
49. Ong, C., Yung, L.L., Cai, Y., Bay, B., and Baeg, G. (2015) *Drosophila melanogaster* as a model organism to study nanotoxicity. *Nanotoxicology*, **9** (3), 396–403.
50. Vecchio, G. (2015) A fruit fly in the nanoworld: once again Drosophila contributes to environment and human health. *Nanotoxicology*, **9** (2), 135–137.
51. Wikipedia https://en.wikipedia.org/wiki/Drosophila_melanogaster (accessed 28 July 2015).
52. Posgai, R., Cipolla-McCulloch, C.B., Murphy, K.R., Hussain, S.M., Rowe, J.J., and Nielsen, M.G. (2011) Differential toxicity of silver and titanium dioxide nanoparticles on *Drosophila melanogaster* development, reproductive effort, and viability: size, coatings and antioxidants matter. *Chemosphere*, **85** (1), 34–42.
53. Rand, M.D., Montgomery, S.L., Prince, L., and Vorojeikina, D. (2014) Developmental toxicity assays using the Drosophila model. *Curr. Protoc. Toxicol.*, 59:1.12:1.12.1–1.12.20.
54. Rand, M.D. (2010) Drosophotoxicology: the growing potential for *Drosophila* in neurotoxicology. *Neurotoxicol. Teratol.*, **32** (1), 74–83.
55. Demir, E., Vales, G., Kaya, B., Creus, A., and Marcos, R. (2011) Genotoxic analysis of silver nanoparticles in *Drosophila*. *Nanotoxicology*, **5** (3), 417–424.
56. Vecchio, G., Galeone, A., Brunetti, V., Maiorano, G., Rizzello, L., Sabella, S., Cingolani, R., and Pompa, P.P. (2012) Mutagenic effects of gold nanoparticles induce aberrant phenotypes in *Drosophila melanogaster*. *Nanomed. Nanotechnol. Biol. Med.*, **8** (1), 1–7.
57. Vales, G., Demir, E., Kaya, B., Creus, A., and Marcos, R. (2013) Genotoxicity of cobalt nanoparticles and ions in Drosophila. *Nanotoxicology*, **7** (4), 462–468.
58. Demir, E., Turna, F., Vales, G., Kaya, B., Creus, A., and Marcos, R. (2013) In vivo genotoxicity assessment of titanium, zirconium and aluminium nanoparticles, and their microparticulated forms, in *Drosophila*. *Chemosphere*, **93** (10), 2304–2310.
59. Ahamed, M., Posgai, R., Gorey, T.J., Nielsen, M., Hussain, S.M., and Rowe, J.J. (2010) Silver nanoparticles induced heat shock protein 70, oxidative stress and apoptosis in *Drosophila melanogaster*. *Toxicol. Appl. Pharmacol.*, **242** (3), 263–269.
60. Posgai, R., Ahamed, M., Hussain, S.M., Rowe, J.J., and Nielsen, M.G. (2009) Inhalation method for delivery of nanoparticles to the Drosophila respiratory system for toxicity testing. *Sci. Total Environ.*, **408** (2), 439–443.
61. Roberts, D.B. (ed.) (1986) *Drosophila: A Practical Approach*, IRL Press, Oxford.
62. Oberdörster, G., Oberdörster, E., and Oberdörster, J. (2005) Nanotoxicology: an emerging discipline evolving from studies of ultrafine particles. *Environ. Health Perspect.*, **113** (7), 823–839.
63. Oberdörster, G., Maynard, A., Donaldson, K., Castranova, V., Fitzpatrick, J., Ausman, K., Carter, J., Karn, B., Kreyling, W., Lai, D., Olin, S., Monteiro-Riviere, N., Warheit, D., and Yang, H. (2005) Principles for characterizing the potential human health effects from exposure to nanomaterials: elements of a screening strategy. *Part. Fibre Toxicol.*, **2**, 8.
64. Yang, W., Peters, J., and Williams, R. (2008) Inhaled nanoparticles-A current review. *Int. J. Pharm.*, **356** (1-2), 239–247.
65. Witschi, H. and Brain, J.D. (eds) (2012) *Toxicology of Inhaled Materials: General Principles of Inhalation Toxicology*, Springer-Verlag, Berlin, Heidelberg.
66. Dorato, M.A. and Wolff, R.K. (1991) Inhalation exposure technology, dosimetry, and regulatory issues. *Toxicol. Pathol.*, **19** (4, Pt. 1), 373–383.

67. Cheng, Y.S., Bowen, L., Rando, R.J., Postlethwait, E.M., Squadrito, G.L., and Matalon, S. (2010) Exposing animals to oxidant gases: nose only vs. whole body. *Proc. Am. Thorac. Soc.*, **7** (4), 264–268.
68. Chen, Z., Meng, H., Xing, G., Yuan, H., Zhao, F., Liu, R., Chang, X., Gao, X., Wang, T., and Jia, G. (2008) Age-related differences in pulmonary and cardiovascular responses to SiO_2 nanoparticle inhalation: nanotoxicity has susceptible population. *Environ. Sci. Technol.*, **42** (23), 8985–8992.
69. Zhao, Y., Chen, Z., Meng, H., Xing, G., and Yuan, H. (2007) Inhalation exposure system for manufactured nanomaterials. Patent CN 201171714, filed Dec. 4, 2007 and issued Dec. 31, 2008.
70. Osier, M. and Oberdörster, G. (1997) Intratracheal inhalation vs intratracheal instillation: differences in particle effects. *Fundam. Appl. Toxicol.*, **40** (2), 220–227.
71. Oberdörster, G., Cox, C., and Gelein, R. (1997) Intratracheal instillation versus intratracheal inhalation of tracer particles for measuring lung clearance function. *Exp. Lung Res.*, **23** (1), 17–34.
72. Osier, M., Baggs, R., and Oberdörster, G. (1997) Intratracheal instillation versus intratracheal inhalation: influence of cytokines on inflammatory response. *Environ. Health Perspect.*, **105** (Suppl. 5), 1265–1271.
73. Cassee, F.R., Mills, N.L., and Newby, D.E. (eds) (2011) *Cardiovascular Effects of Inhaled Ultrafine and Nano-sized Particles*, John Wiley & Sons, Inc., Hoboken, NJ.
74. Shimizu, S. (2004) in *The Laboratory Mouse* (eds H.J. Hedrich and G. Bullock), Elsevier Science Publishing Co. Inc., San Diego, CA, pp. 527–541.
75. Miller, M.A., Stabenow, J.M., Parvathareddy, J., Wodowski, A.J., Fabrizio, T.P., Bina, X.R., Zalduondo, L., and Bina, J.E. (2012) Visualization of murine intranasal dosing efficiency using luminescent *Francisella tularensis*: effect of instillation volume and form of anesthesia. *PLoS One*, **7** (2), e31359.
76. Charles River Laboratories http://www.criver.com/about-us/news-events/featured-stories/2013/improved-delivery- volumes-in-intranasal-administra (accessed 21 July 2015).
77. Southam, D., Dolovich, M., O'byrne, P., and Inman, M. (2002) Distribution of intranasal instillations in mice: effects of volume, time, body position, and anesthesia. *Am. J. Physiol.-Lung Cell. Mol. Physiol.*, **282** (4), L833–L839.
78. Driscoll, K.E., Costa, D.L., Hatch, G., Henderson, R., Oberdörster, G., Salem, H., and Schlesinger, R.B. (2000) Intratracheal instillation as an exposure technique for the evaluation of respiratory tract toxicity: uses and limitations. *Toxicol. Sci.*, **55** (1), 24–35.
79. Xue, L., He, X., Li, Y., Qu, M., and Zhang, Z. (2013) Pulmonary toxicity of ceria nanoparticles in mice after intratracheal instillation. *J. Nanosci. Nanotechnol.*, **13** (10), 6575–6580.
80. Lizio, R., Westhof, A., Lehr, C.-M., and Klenner, T. (2001) Oral endotracheal intubation of rats for intratracheal instillation and aerosol drug delivery. *Lab. Anim.*, **35** (3), 257–260.
81. Rayamajhi, M., Redente, E.F., Condon, T.V., Gonzalez-Juarrero, M., Riches, D.W., and Lenz, L.L. (2011) Non-surgical intratracheal instillation of mice with analysis of lungs and lung draining lymph nodes by flow cytometry. *J. Vis. Exp.*, **51**, e2702.
82. He, X., Zhang, H., Ma, Y., Bai, W., Zhang, Z., Lu, K., Ding, Y., Zhao, Y., and Chai, Z. (2010) Lung deposition and extrapulmonary translocation of nano-ceria after intratracheal instillation. *Nanotechnology*, **21** (28), 285103.
83. Simonelli, A., Miraglia, N., Basilicata, P., Pieri, M., Loredana, C., Genovese, G., Guadagni, R., Acampora, A., and Sannolo, N. (2007) in *Nanotoxicology* (eds Y. Zhao and H.S. Nalwa), American Scientific Publishers, California, pp. 29–50.
84. Chen, Z., Wang, Y., Zhuo, L., Chen, S., Zhao, L., Chen, T., Li, Y., Zhang, W., Gao, X., Li, P., Wang, H., and Jia, G. (2015) Interaction of titanium dioxide nanoparticles with glucose on young rats after oral administration.

Nanomed. Nanotechnol. Biol. Med., **11** (7), 1633–1642.

85. Atcha, Z., Rourke, C., Neo, A.H., Goh, C.W., Lim, J.S., Aw, C.-C., Browne, E.R., and Pemberton, D.J. (2010) Alternative method of oral dosing for rats. *J. Am. Assoc. Lab. Anim. Sci.*, **49** (3), 335–343.
86. Wikipedia https://en.wikipedia.org/wiki/Skin (accessed 25 November 2015).
87. Baroli, B. (2010) Penetration of nanoparticles and nanomaterials in the skin: fiction or reality? *J. Pharm. Sci.*, **99** (1), 21–50.
88. Yildirimer, L., Thanh, N.T., Loizidou, M., and Seifalian, A.M. (2011) Toxicology and clinical potential of nanoparticles. *Nano Today*, **6** (6), 585–607.
89. Mortensen, L.J., Oberdörster, G., Pentland, A.P., and DeLouise, L.A. (2008) In vivo skin penetration of quantum dot nanoparticles in the murine model: the effect of UVR. *Nano Lett.*, **8** (9), 2779–2787.
90. Wu, J., Liu, W., Xue, C., Zhou, S., Lan, F., Bi, L., Xu, H., Yang, X., and Zeng, F. (2009) Toxicity and penetration of TiO_2 nanoparticles in hairless mice and porcine skin after subchronic dermal exposure. *Toxicol. Lett.*, **191** (1), 1–8.
91. Baroli, B., Ennas, M.G., Loffredo, F., Isola, M., Pinna, R., and López-Quintela, M.A. (2007) Penetration of metallic nanoparticles in human full-thickness skin. *J. Invest. Dermatol.*, **127** (7), 1701–1712.
92. Feng, W., Wang, B., and Zhao, Y. (2009) Nanotoxicity of metal oxide nanoparticles *in vivo*, in *Nanotoxicity: From In Vivo and In Vitro Models to Health Risks* (eds S.C. Sahu and D.A. Casciano), John Wiley & Sons, Ltd., Wiltshire, pp. 247–270.
93. Tseng, M.T., Lu, X., Duan, X., Hardas, S.S., Sultana, R., Wu, P., Unrine, J.M., Graham, U., Butterfield, D.A., and Grulke, E.A. (2012) Alteration of hepatic structure and oxidative stress induced by intravenous nanoceria. *Toxicol. Appl. Pharmacol.*, **260** (2), 173–182.
94. Pleus, R.C. (2012) in *Nanotechnology: Health and Environmental Risks*, 2nd edn (ed. J.A. Shatkin), Raylor & Francis Group, Boca Raton, FL, pp. 79–116.
95. International Commission on Radiological Protection (1994) Human respiratory tract model for radiological protection. ICRP Publication 66. *Ann. ICRP*, **24** (1–3).
96. Wang, B., He, X., Zhang, Z., Zhao, Y., and Feng, W. (2013) Metabolism of nanomaterials *in vivo*: blood circulation and organ clearance. *Acc. Chem. Res.*, **46** (3), 761–769.
97. Zhu, M., Feng, W., Wang, Y., Wang, B., Wang, M., Ouyang, H., Zhao, Y., and Chai, Z. (2009) Particokinetics and extrapulmonary translocation of intratracheally instilled ferric oxide nanoparticles in rats and the potential health risk assessment. *Toxicol. Sci.*, **107** (2), 342–351.
98. Kreyling, W.G., Semmler-Behnke, M., Takenaka, S., and Möller, W. (2013) Differences in the biokinetics of inhaled nano-versus micrometer-sized particles. *Acc. Chem. Res.*, **46** (3), 714–722.
99. Fu, C., Liu, T., Li, L., Liu, H., Chen, D., and Tang, F. (2013) The absorption, distribution, excretion and toxicity of mesoporous silica nanoparticles in mice following different exposure routes. *Biomaterials*, **34** (10), 2565–2575.
100. van der Zande, M., Vandebriel, R.J., Van Doren, E., Kramer, E., Herrera Rivera, Z., Serrano-Rojero, C.S., Gremmer, E.R., Mast, J., Peters, R.J., and Hollman, P.C. (2012) Distribution, elimination, and toxicity of silver nanoparticles and silver ions in rats after 28-day oral exposure. *ACS Nano*, **6** (8), 7427–7442.
101. Schulz, J., Hohenberg, H., Pflücker, F., Gärtner, E., Will, T., Pfeiffer, S., Wepf, R., Wendel, V., Gers-Barlag, H., and Wittern, K.P. (2002) Distribution of sunscreens on skin. *Adv. Drug Delivery Rev.*, **54**, S157–S163.
102. Bennat, C. and Müller-Goymann, C. (2000) Skin penetration and stabilization of formulations containing microfine titanium dioxide as physical UV filter. *Int. J. Cosmet. Sci.*, **22** (4), 271–283.

103. Sadrieh, N., Wokovich, A.M., Gopee, N.V., Zheng, J., Haines, D., Parmiter, D., Siitonen, P.H., Cozart, C.R., Patri, A.K., and McNeil, S.E. (2010) Lack of significant dermal penetration of titanium dioxide from sunscreen formulations containing nano-and submicron-size TiO_2 particles. *Toxicol. Sci.*, **115** (1), 156–166.

104. Nohynek, G.J. and Dufour, E.K. (2012) Nano-sized cosmetic formulations or solid nanoparticles in sunscreens: a risk to human health? *Arch. Toxicol.*, **86** (7), 1063–1075.

105. Monteiro-Riviere, N.A. (2013) in *Nanotechnology in Dermatology* (eds A. Nasir, A. Friedman, and S. Wang), Springer, New York, pp. 51–61.

106. Leite-Silva, V.R., Le Lamer, M., Sanchez, W.Y., Liu, D.C., Sanchez, W.H., Morrow, I., Martin, D., Silva, H.D., Prow, T.W., and Grice, J.E. (2013) The effect of formulation on the penetration of coated and uncoated zinc oxide nanoparticles into the viable epidermis of human skin in vivo. *Eur. J. Pharm. Biopharm.*, **84** (2), 297–308.

107. Liang, X., Chen, C., Zhao, Y., Jia, L., and Wang, P.C. (2008) Biopharmaceutics and therapeutic potential of engineered nanomaterials. *Curr. Drug Metab.*, **9** (8), 697–709.

108. Wang, B., Feng, W., Zhao, Y., and Chai, Z. (2013) Metallomics insights for in vivo studies of metal based nanomaterials. *Metallomics*, **5** (7), 793–803.

109. Gao, F., Cai, P., Yang, W., Xue, J., Gao, L., Liu, R., Wang, Y., Zhao, Y., He, X., and Zhao, L. (2015) Ultrasmall [^{64}Cu] Cu nanoclusters for targeting orthotopic lung tumors using accurate positron emission tomography imaging. *ACS Nano*, **9** (5), 4976–4986.

110. Wang, H.F., Wang, J., Deng, X.Y., Sun, H.F., Shi, Z.J., Gu, Z.N., Liu, Y.F., and Zhao, Y.L. (2004) Biodistribution carbon of single-wall carbon nanotubes in mice. *J. Nanosci. Nanotechnol.*, **4** (8), 1019–1024.

111. Li, Y., Zhou, Y., Wang, H.Y., Perrett, S., Zhao, Y., Tang, Z., and Nie, G. (2011) Chirality of glutathione surface coating affects the cytotoxicity of quantum dots. *Angew. Chem. Int. Ed.*, **50** (26), 5860–5864.

112. Sadauskas, E., Wallin, H., Stoltenberg, M., Vogel, U., Doering, P., Larsen, A., and Danscher, G. (2007) Kupffer cells are central in the removal of nanoparticles from the organism. *Part. Fibre Toxicol.*, **4**, 10.

113. Levy, M., Luciani, N., Alloyeau, D., Elgrabli, D., Deveaux, V., Pechoux, C., Chat, S., Wang, G., Vats, N., and Gendron, F. (2011) Long term in vivo biotransformation of iron oxide nanoparticles. *Biomaterials*, **32** (16), 3988–3999.

114. Kreyling, W.G., Abdelmonem, A.M., Ali, Z., Alves, F., Geiser, M., Haberl, N., Hartmann, R., Hirn, S., de Aberasturi, D.J., and Kantner, K. (2015) *In vivo* integrity of polymer-coated gold nanoparticles. *Nat. Nanotechnol.*, **10** (7), 619–623.

115. Graham, U.M., Tseng, M.T., Jasinski, J.B., Yokel, R.A., Unrine, J.M., Davis, B.H., Dozier, A.K., Hardas, S.S., Sultana, R., and Grulke, E.A. (2014) In vivo processing of ceria nanoparticles inside liver: impact on free-radical scavenging activity and oxidative stress. *ChemPlusChem*, **79** (8), 1083–1088.

116. He, X., Ma, Y., Li, M., Zhang, P., Li, Y., and Zhang, Z. (2013) Quantifying and imaging engineered nanomaterials in vivo: challenges and techniques. *Small*, **9** (9–10), 1482–1491.

117. Choi, H.S., Liu, W., Misra, P., Tanaka, E., Zimmer, J.P., Ipe, B.I., Bawendi, M.G., and Frangioni, J.V. (2007) Renal clearance of quantum dots. *Nat. Biotechnol.*, **25** (10), 1165–1170.

118. Zhou, C., Long, M., Qin, Y., Sun, X., and Zheng, J. (2011) Luminescent gold nanoparticles with efficient renal clearance. *Angew. Chem. Int. Ed.*, **123** (14), 3226–3230.

119. Souris, J.S., Lee, C.-H., Cheng, S.-H., Chen, C.-T., Yang, C.-S., Ja-an, A.H., Mou, C.-Y., and Lo, L.-W. (2010) Surface charge-mediated rapid hepatobiliary excretion of mesoporous silica nanoparticles. *Biomaterials*, **31** (21), 5564–5574.

120. Hirn, S., Semmler-Behnke, M., Schleh, C., Wenk, A., Lipka, J., Schäffler, M.,

Takenaka, S., Möller, W., Schmid, G., and Simon, U. (2011) Particle size-dependent and surface charge-dependent biodistribution of gold nanoparticles after intravenous administration. *Eur. J. Pharm. Biopharm.*, **77** (3), 407–416.

121. Hamidi, M., Azadi, A., Rafiei, P., and Ashrafi, H. (2013) A pharmacokinetic overview of nanotechnology-based drug delivery systems: an ADME-oriented approach. *Crit. Rev. Ther. Drug Carrier Syst.*, **30** (5), 435–467.

122. Choi, H.S., Ashitate, Y., Lee, J.H., Kim, S.H., Matsui, A., Insin, N., Bawendi, M.G., Semmler-Behnke, M., Frangioni, J.V., and Tsuda, A. (2010) Rapid translocation of nanoparticles from the lung airspaces to the body. *Nat. Biotechnol.*, **28** (12), 1300–1303.

123. Kreyling, W.G., Hirn, S., Möller, W., Schleh, C., Wenk, A., Celik, G.l., Lipka, J., Schäffler, M., Haberl, N., and Johnston, B.D. (2013) Air–blood barrier translocation of tracheally instilled gold nanoparticles inversely depends on particle size. *ACS Nano*, **8** (1), 222–233.

124. Thorley, A.J., Ruenraroengsak, P., Potter, T.E., and Tetley, T.D. (2014) Critical determinants of uptake and translocation of nanoparticles by the human pulmonary alveolar epithelium. *ACS Nano*, **8** (11), 11778–11789.

125. Yamashita, K., Yoshioka, Y., Higashisaka, K., Mimura, K., Morishita, Y., Nozaki, M., Yoshida, T., Ogura, T., Nabeshi, H., and Nagano, K. (2011) Silica and titanium dioxide nanoparticles cause pregnancy complications in mice. *Nat. Nanotechnol.*, **6** (5), 321–328.

126. Bode, C.J., Jin, H., Rytting, E., Silverstein, P.S., Young, A.M., and Audus, K.L. (2006) in *Placenta and Trophoblast* (eds M.J. Soares and J.S. Hunt), Humana Press, pp. 225–239.

127. Myllynen, P.K., Loughran, M.J., Howard, C.V., Sormunen, R., Walsh, A.A., and Vahakangas, K.H. (2008) Kinetics of gold nanoparticles in the human placenta. *Reprod. Toxicol.*, **26** (2), 130–137.

128. Wick, P., Malek, A., Manser, P., Meili, D., Maeder-Althaus, X., Diener, L., Diener, P.-A., Zisch, A., Krug, H.F., and von Mandach, U. (2010) Barrier capacity of human placenta for nanosized materials. *Environ. Health Perspect.*, **118** (3), 432–436.

129. Shimizu, M., Tainaka, H., Oba, T., Mizuo, K., Umezawa, M., and Takeda, K. (2009) Maternal exposure to nanoparticulate titanium dioxide during the prenatal period alters gene expression related to brain development in the mouse. *Part. Fibre Toxicol.*, **6**, 20.

130. Takeda, K., Suzuki, K.-I., Ishihara, A., Kubo-Irie, M., Fujimoto, R., Tabata, M., Oshio, S., Nihei, Y., Ihara, T., and Sugamata, M. (2009) Nanoparticles transferred from pregnant mice to their offspring can damage the genital and cranial nerve systems. *J. Health Sci.*, **55** (1), 95–102.

131. Chu, M., Wu, Q., Yang, H., Yuan, R., Hou, S., Yang, Y., Zou, Y., Xu, S., Xu, K., and Ji, A. (2010) Transfer of quantum dots from pregnant mice to pups across the placental barrier. *Small*, **6** (5), 670–678.

132. Hougaard, K.S., Jackson, P., Jensen, K.A., Sloth, J.J., Löschner, K., Larsen, E.H., Birkedal, R.K., Vibenholt, A., Boisen, A.M.Z., and Wallin, H. (2010) Effects of prenatal exposure to surface-coated nanosized titanium dioxide(UV-Titan). A study in mice. *Part. Fibre Toxicol.*, **7**, 16.

133. Solomon, E., Avni, R., Hadas, R., Raz, T., Garbow, J.R., Bendel, P., Frydman, L., and Neeman, M. (2014) Major mouse placental compartments revealed by diffusion-weighted MRI, contrast-enhanced MRI, and fluorescence imaging. *Proc. Natl. Acad. Sci. U.S.A.*, **111** (28), 10353–10358.

134. Yang, H., Sun, C., Fan, Z., Tian, X., Yan, L., Du, L., Liu, Y., Chen, C., Liang, X.-j., and Anderson, G.J. (2012) Effects of gestational age and surface modification on materno-fetal transfer of nanoparticles in murine pregnancy. *Sci. Rep.*, **2**, 847.

135. Kim, J.S., Yoon, T.-J., Yu, K.N., Kim, B.G., Park, S.J., Kim, H.W., Lee, K.H., Park, S.B., Lee, J.-K., and Cho, M.H. (2006) Toxicity and tissue distribution

of magnetic nanoparticles in mice. *Toxicol. Sci.*, **89** (1), 338–347.

136. Kim, H.R., Gil, S., Andrieux, K., Nicolas, V., Appel, M., Chacun, H., Desmaele, D., Taran, F., Georgin, D., and Couvreur, P. (2007) Low-density lipoprotein receptor-mediated endocytosis of PEGylated nanoparticles in rat brain endothelial cells. *Cell. Mol. Life Sci.*, **64** (3), 356–364.

137. Kreuter, J., Alyautdin, R.N., Kharkevich, D.A., and Ivanov, A.A. (1995) Passage of peptides through the blood–brain barrier with colloidal polymer particles (nanoparticles). *Brain Res.*, **674** (1), 171–174.

138. Calvo, P., Gouritin, B., Chacun, H., Desmaële, D., D'Angelo, J., Noel, J.-P., Georgin, D., Fattal, E., Andreux, J.P., and Couvreur, P. (2001) Long-circulating PEGylated polycyanoacrylate nanoparticles as new drug carrier for brain delivery. *Pharm. Res.*, **18** (8), 1157–1166.

139. Zhang, Y., Bai, Y., Jia, J., Gao, N., Li, Y., Zhang, R., Jiang, G., and Yan, B. (2014) Perturbation of physiological systems by nanoparticles. *Chem. Soc. Rev.*, **43** (10), 3762–3809.

140. Sharma, H.S., Hussain, S., Schlager, J., Ali, S.F., and Sharma, A. (2010) in *Brain Edema XIV* (eds Z. Czernicki, A. Baethmann, U. Ito, Y. Katayama, T. Kuroiwa, and A.D. Mendelow), Springer, New York, pp. 359–364.

141. Oberdorster, G., Sharp, Z., Atudorei, V., Elder, A., Gelein, R., Kreyling, W., and Cox, C. (2004) Translocation of inhaled ultrafine particles to the brain. *Inhalation Toxicol.*, **16** (6-7), 437–445.

142. Elder, A., Gelein, R., Silva, V., Feikert, T., Opanashuk, L., Carter, J., Potter, R., Maynard, A., Ito, Y., Finkelstein, J., and Oberdörster, G. (2006) Translocation of inhaled ultrafine manganese oxide particles to the central nervous system. *Environ. Health Perspect.*, **114** (8), 1172–1178.

143. Lucchini, R., Dorman, D., Elder, A., and Veronesi, B. (2012) Neurological impacts from inhalation of pollutants and the nose–brain connection. *Neurotoxicology*, **33** (4), 838–841.

144. Poland, C.A., Duffin, R., Kinloch, I., Maynard, A., Wallace, W.A., Seaton, A., Stone, V., Brown, S., MacNee, W., and Donaldson, K. (2008) Carbon nanotubes introduced into the abdominal cavity of mice show asbestos-like pathogenicity in a pilot study. *Nat. Nanotechnol.*, **3** (7), 423–428.

145. Lam, C.W., James, J.T., McCluskey, R., and Hunter, R.L. (2004) Pulmonary toxicity of single-wall carbon nanotubes in mice 7 and 90 days after intratracheal instillation. *Toxicol. Sci.*, **77**, 126–134.

146. Shvedova, A.A., Kisin, E.R., Mercer, R., Murray, A.R., Johnson, V.J., Potapovich, A.I., Tyurina, Y.Y., Gorelik, O., Arepalli, S., Schwegler-Berry, D., Hubbs, A.F., Antonini, J., Evans, D.E., Ku, B.K., Ramsey, D., Maynard, A., Kagan, V.E., Castranova, V., and Baron, P. (2005) Unusual inflammatory and fibrogenic pulmonary responses to single-walled carbon nanotubes in mice. *Am. J. Physiol. Lung Cell. Mol. Physiol.*, **289** (5), L698–L708.

147. Wang, X., Katwa, P., Podila, R., Chen, P., Ke, P.C., Rao, A.M., Walters, D.M., Wingard, C.J., and Brown, J.M. (2011) Multi-walled carbon nanotube instillation impairs pulmonary function in C57BL/6 mice. *Part. Fibre Toxicol.*, **8**, 24.

148. Wang, P., Nie, X., Wang, Y., Li, Y., Ge, C., Zhang, L., Wang, L., Bai, R., Chen, Z., and Zhao, Y. (2013) Multiwall carbon nanotubes mediate macrophage activation and promote pulmonary fibrosis through TGF-β/Smad signaling pathway. *Small*, **9** (22), 3799–3811.

149. Wang, P., Wang, Y., Nie, X., Braïni, C., Bai, R., and Chen, C. (2015) Multiwall carbon nanotubes directly promote fibroblast–myofibroblast and epithelial–mesenchymal transitions through the activation of the TGF-β/Smad signaling pathway. *Small*, **11** (4), 446–455.

150. Liu, H., Yang, D., Yang, H., Zhang, H., Zhang, W., Fang, Y., Lin, Z., Tian, L., Lin, B., and Yan, J. (2013) Comparative study of respiratory tract immune toxicity induced by three sterilisation nanoparticles: silver, zinc oxide and

titanium dioxide. *J. Hazard. Mater.*, **248**, 478–486.

151. Braakhuis, H.M., Gosens, I., Krystek, P., Boere, J., Cassee, F.R., Fokkens, P., Post, J.A., van Loveren, H., and Park, M. (2014) Particle size dependent deposition and pulmonary inflammation after short-term inhalation of silver nanoparticles. *Part. Fibre Toxicol.*, **11**, 49.
152. Zhang, H., Ji, Z., Xia, T., Meng, H., Low-Kam, C., Liu, R., Pokhrel, S., Lin, S., Wang, X., and Liao, Y.-P. (2012) Use of metal oxide nanoparticle band gap to develop a predictive paradigm for oxidative stress and acute pulmonary inflammation. *ACS Nano*, **6** (5), 4349–4368.
153. Morimoto, Y., Izumi, H., Yoshiura, Y., Tomonaga, T., Oyabu, T., Myojo, T., Shimada, M., Kubo, M., Yamamoto, K., and Kitajima, S. (2015) Pulmonary toxicity of cerium oxide nanoparticle following intratracheal instillation and inhalation of nanoparticles. *Eur. Respir. J.*, **46** (Suppl. 59), PA4118.
154. Ma, J., Mercer, R.R., Barger, M., Schwegler-Berry, D., Cohen, J.M., Demokritou, P., and Castranova, V. (2015) Effects of amorphous silica coating on cerium oxide nanoparticles induced pulmonary responses. *Toxicol. Appl. Pharmacol.*, **288** (1), 63–73.
155. Madl, A.K., Plummer, L.E., Carosino, C., and Pinkerton, K.E. (2014) Nanoparticles, lung injury, and the role of oxidant stress. *Annu. Rev. Physiol.*, **76**, 447.
156. Ge, C., Meng, L., Xu, L., Bai, R., Du, J., Zhang, L., Li, Y., Chang, Y., Zhao, Y., and Chen, C. (2012) Acute pulmonary and moderate cardiovascular responses of spontaneously hypertensive rats after exposure to single-wall carbon nanotubes. *Nanotoxicology*, **6** (5), 526–542.
157. Liu, R., Zhang, X., Pu, Y., Yin, L., Li, Y., Zhang, X., Liang, G., Li, X., and Zhang, J. (2010) Small-sized titanium dioxide nanoparticles mediate immune toxicity in rat pulmonary alveolar macrophages in vivo. *J. Nanosci. Nanotechnol.*, **10** (8), 5161–5169.
158. Mohamud, R., Xiang, S.D., Selomulya, C., Rolland, J.M., O'Hehir, R.E., Hardy, C.L., and Plebanski, M. (2013) The effects of engineered nanoparticles on pulmonary immune homeostasis. *Drug Metab. Rev.*, **46** (2), 176–190.
159. Peng, L., He, X., Zhang, P., Zhang, J., Li, Y., Zhang, J., Ma, Y., Ding, Y., Wu, Z., Chai, Z., and Zhang, Z. (2014) Comparative pulmonary toxicity of two ceria nanoparticles with the same primary size. *Int. J. Mol. Sci.*, **15** (4), 6072–6085.
160. Hwang, J.H., Kim, S.J., Kim, Y.-H., Noh, J.-R., Gang, G.-T., Chung, B.H., Song, N.W., and Lee, C.-H. (2012) Susceptibility to gold nanoparticle-induced hepatotoxicity is enhanced in a mouse model of nonalcoholic steatohepatitis. *Toxicology*, **294** (1), 27–35.
161. Chang, C.-C., Tsai, M.-L., Huang, H.-C., Chen, C.-Y., and Dai, S.-X. (2012) Epithelial-mesenchymal transition contributes to SWCNT-induced pulmonary fibrosis. *Nanotoxicology*, **6** (6), 600–610.
162. Porter, D.W., Hubbs, A.F., Chen, B.T., McKinney, W., Mercer, R.R., Wolfarth, M.G., Battelli, L., Wu, N., Sriram, K., and Leonard, S. (2012) Acute pulmonary dose–responses to inhaled multi-walled carbon nanotubes. *Nanotoxicology*, **7** (7), 1179–1194.
163. Donaldson, K., Duffin, R., Langrish, J.P., Miller, M.R., Mills, N.L., Poland, C.A., Raftis, J., Shah, A., Shaw, C.A., and Newby, D.E. (2013) Nanoparticles and the cardiovascular system: a critical review. *Nanomedicine*, **8** (3), 403–423.
164. Duan, J., Yu, Y., Li, Y., Yu, Y., and Sun, Z. (2013) Cardiovascular toxicity evaluation of silica nanoparticles in endothelial cells and zebrafish model. *Biomaterials*, **34** (23), 5853–5862.
165. Chen, T., Hu, J., Chen, C., Pu, J., Cui, X., and Jia, G. (2013) Cardiovascular effects of pulmonary exposure to titanium dioxide nanoparticles in ApoE knockout mice. *J. Nanosci. Nanotechnol.*, **13** (5), 3214–3222.
166. Mikkelsen, L., Sheykhzade, M., Jensen, K.A., Saber, A.T., Jacobsen, N.R., Vogel, U., Wallin, H., Loft, S., and Moller, P.

(2011) Modest effect on plaque progression and vasodilatory function in atherosclerosis-prone mice exposed to nanosized TiO_2. *Part. Fibre Toxicol.*, **8**, 32.

167. Radomski, A., Jurasz, P., Alonso-Escolano, D., Drews, M., Morandi, M., Malinski, T., and Radomski, M.W. (2005) Nanoparticle-induced platelet aggregation and vascular thrombosis. *Br. J. Pharmacol.*, **146** (6), 882–893.

168. Vesterdal, L.K., Folkmann, J.K., Jacobsen, N.R., Sheykhzade, M., Wallin, H., Loft, S., and Moller, P. (2010) Pulmonary exposure to carbon black nanoparticles and vascular effects. *Part. Fibre Toxicol.*, **7**, 33.

169. Li, Z., Hulderman, T., Salmen, R., Chapman, R., Leonard, S.S., Young, S.-H., Shvedova, A., Luster, M.I., and Simeonova, P.P. (2007) Cardiovascular effects of pulmonary exposure to single-wall carbon nanotubes. *Environ. Health Perspect.*, **115** (3), 377–382.

170. Khandoga, A., Stampfl, A., Takenaka, S., Schulz, H., Radykewicz, R., Kreyling, W., and Krombach, F. (2004) Ultrafine particles exert prothrombotic but not inflammatory effects on the hepatic microcirculation in healthy mice in vivo. *Circulation*, **109** (10), 1320–1325.

171. Schulz, H., Harder, V., Ibald-Mulli, A., Khandoga, A., Koenig, W., Krombach, F., Radykewicz, R., Stampfl, A., Thorand, B., and Peters, A. (2005) Cardiovascular effects of fine and ultrafine particles. *J. Aerosol Med.-Deposition Clearance Eff. Lung*, **18** (1), 1–22.

172. Du, Z., Zhao, D., Jing, L., Cui, G., Jin, M., Li, Y., Liu, X., Liu, Y., Du, H., and Guo, C. (2013) Cardiovascular toxicity of different sizes amorphous silica nanoparticles in rats after intratracheal instillation. *Cardiovasc. Toxicol.*, **13** (3), 194–207.

173. Iversen, N.K., Frische, S., Thomsen, K., Laustsen, C., Pedersen, M., Hansen, P.B., Bie, P., Fresnais, J., Berret, J.-F., and Baatrup, E. (2013) Superparamagnetic iron oxide polyacrylic acid coated γ-Fe2O3 nanoparticles do not affect kidney function but cause acute effect on the cardiovascular function in healthy mice. *Toxicol. Appl. Pharmacol.*, **266** (2), 276–288.

174. Iversen, N.K., Nielsen, A., Wang, T., and Baatrup, E. (2013) Intravascular infusion of PEGylated Au nanoparticles affects cardiovascular function in healthy mice. *Hum. Exp. Toxicol.*, **32** (2), 216–221.

175. Roberts, J.R., McKinney, W., Kan, H., Krajnak, K., Frazer, D.G., Thomas, T.A., Waugh, S., Kenyon, A., MacCuspie, R.I., and Hackley, V.A. (2013) Pulmonary and cardiovascular responses of rats to inhalation of silver nanoparticles. *J. Toxicol. Environ. Health, Part A*, **76** (11), 651–668.

176. Kang, G.S., Gillespie, P.A., Gunnison, A., Moreira, A.L., Tchou-Wong, K.M., and Chen, L.C. (2011) Long-term inhalation exposure to nickel nanoparticles exacerbated atherosclerosis in a susceptible mouse model. *Environ. Health Perspect.*, **119** (2), 176–181.

177. Wang, H., Du, L.-J., Song, Z.-M., and Chen, X.-X. (2013) Progress in the characterization and safety evaluation of engineered inorganic nanomaterials in food. *Nanomedicine*, **8** (12), 2007–2025.

178. Chen, Z., Meng, H., Xing, G., Chen, C., Zhao, Y., Jia, G., Wang, T., Yuan, H., Ye, C., and Zhao, F. (2006) Acute toxicological effects of copper nanoparticles in vivo. *Toxicol. Lett.*, **163** (2), 109–120.

179. Mahler, G.J., Esch, M.B., Tako, E., Southard, T.L., Archer, S.D., Glahn, R.P., and Shuler, M.L. (2012) Oral exposure to polystyrene nanoparticles affects iron absorption. *Nat. Nanotechnol.*, **7** (4), 264–271.

180. Nogueira, C.M., de Azevedo, W.M., Dagli, M.L.Z., Toma, S.H., de Arruda Leite, A.Z., Lordello, M.L., Nishitokukado, I., Ortiz-Agostinho, C.L., Duarte, M.I.S., and Ferreira, M.A. (2012) Titanium dioxide induced inflammation in the small intestine. *World J. Gastroenterol.*, **18** (34), 4729.

181. Bu, Q., Yan, G., Deng, P., Peng, F., Lin, H., Xu, Y., Cao, Z., Zhou, T., Xue, A., and Wang, Y. (2010) NMR-based metabonomic study of the sub-acute

toxicity of titanium dioxide nanoparticles in rats after oral administration. *Nanotechnology*, **21** (12), 125105.

182. Kim, Y.S., Kim, J.S., Cho, H.S., Rha, D.S., Kim, J.M., Park, J.D., Choi, B.S., Lim, R., Chang, H.K., and Chung, Y.H. (2008) Twenty-eight-day oral toxicity, genotoxicity, and gender-related tissue distribution of silver nanoparticles in Sprague-Dawley rats. *Inhalation Toxicol.*, **20** (6), 575–583.

183. Sharma, V., Singh, P., Pandey, A.K., and Dhawan, A. (2012) Induction of oxidative stress, DNA damage and apoptosis in mouse liver after sub-acute oral exposure to zinc oxide nanoparticles. *Mutat. Res./Genet. Toxicol. Environ. Mutagen.*, **745** (1), 84–91.

184. Moller, P., Folkmann, J.K., Danielsen, P.H., Jantzen, K., and Loft, S. (2012) Oxidative stress generated damage to DNA by gastrointestinal exposure to insoluble particles. *Curr. Mol. Med.*, **12** (6), 732–745.

185. Mansouri, E., Khorsandi, L., Orazizadeh, M., and Jozi, Z. (2015) Dose-dependent hepatotoxicity effects of Zinc oxide nanoparticles. *Nanomed. J.*, **2** (4), 273–282.

186. Kermanizadeh, A., Chauché, C., Balharry, D., Brown, D.M., Kanase, N., Boczkowski, J., Lanone, S., and Stone, V. (2014) The role of Kupffer cells in the hepatic response to silver nanoparticles. *Nanotoxicology*, **8** (Suppl. 1), 149–154.

187. Hadrup, N., Loeschner, K., Bergström, A., Wilcks, A., Gao, X., Vogel, U., Frandsen, H.L., Larsen, E.H., Lam, H.R., and Mortensen, A. (2012) Subacute oral toxicity investigation of nanoparticulate and ionic silver in rats. *Arch. Toxicol.*, **86** (4), 543–551.

188. Nagano, T., Higashisaka, K., Kunieda, A., Iwahara, Y., Tanaka, K., Nagano, K., Abe, Y., Kamada, H., Tsunoda, S.-i., and Nabeshi, H. (2013) Liver-specific microRNAs as biomarkers of nanomaterial-induced liver damage. *Nanotechnology*, **24** (40), 405102.

189. Jeon, Y.-M., Park, S.-K., and Lee, M.-Y. (2011) Proteomic analysis of hepatotoxicity induced by titanium nanoparticles in mouse liver. *J. Korean Soc. Appl. Biol. Chem.*, **54** (6), 852–859.

190. Warheit, D.B. and Sayes, C.M. (2015) in *Nanoengineering: Global Approaches to Health and Safety Issues* (ed. P. Dolez), Elsevier B.V., Quebec, pp. 41–54.

191. Fiorito, S., Serafino, A., Andreola, F., Togna, A., and Togna, G. (2006) Toxicity and biocompatibility of carbon nanoparticles. *J. Nanosci. Nanotechnol.*, **6** (3), 591–599.

192. Kim, J.S., Song, K.S., Sung, J.H., Ryu, H.R., Choi, B.G., Cho, H.S., Lee, J.K., and Yu, I.J. (2013) Genotoxicity, acute oral and dermal toxicity, eye and dermal irritation and corrosion and skin sensitisation evaluation of silver nanoparticles. *Nanotoxicology*, **7** (5), 953–960.

193. Ema, M., Matsuda, A., Kobayashi, N., Naya, M., and Nakanishi, J. (2013) Dermal and ocular irritation and skin sensitization studies of fullerene C60 nanoparticles. *Cutaneous Ocul. Toxicol.*, **32** (2), 128–134.

194. Monteiro-Riviere, N.A., Wiench, K., Landsiedel, R., Schulte, S., Inman, A.O., and Riviere, J.E. (2011) Safety evaluation of sunscreen formulations containing titanium dioxide and zinc oxide nanoparticles in UVB sunburned skin: an in vitro and in vivo study. *Toxicol. Sci.*, **123** (1), 264–280.

195. Samberg, M.E., Oldenburg, S.J., and Monteiro-Riviere, N.A. (2010) Evaluation of silver nanoparticle toxicity in skin in vivo and keratinocytes in vitro. *Environ. Health Perspect.*, **118** (3), 407–413.

196. Yokel, R., Grulke, E., and MacPhail, R. (2013) Metal-based nanoparticle interactions with the nervous system: the challenge of brain entry and the risk of retention in the organism. *Wiley Interdiscip. Rev. Nanomed. Nanobiotechnol.*, **5** (4), 346–373.

197. Bai, R., Zhang, L., Liu, Y., Li, B., Wang, L., Wang, P., Autrup, H., Beer, C., and Chen, C. (2014) Integrated analytical techniques with high sensitivity for studying brain translocation and potential impairment induced by intranasally instilled copper nanoparticles. *Toxicol. Lett.*, **226** (1), 70–80.

198. Zhang, L., Bai, R., Liu, Y., Meng, L., Li, B., Wang, L., Xu, L., Le Guyader, L., and Chen, C. (2012) The dose-dependent toxicological effects and potential perturbation on the neurotransmitter secretion in brain following intranasal instillation of copper nanoparticles. *Nanotoxicology*, **6** (5), 562–575.
199. Skalska, J., Frontczak-Baniewicz, M., and Strużyńska, L. (2015) Synaptic degeneration in rat brain after prolonged oral exposure to silver nanoparticles. *Neurotoxicology*, **46**, 145–154.
200. Parveen, A., Rizvi, S.H.M., Mahdi, F., Tripathi, S., Ahmad, I., Shukla, R.K., Khanna, V.K., Singh, R., Patel, D.K., and Mahdi, A.A. (2014) Silica nanoparticles mediated neuronal cell death in corpus striatum of rat brain: implication of mitochondrial, endoplasmic reticulum and oxidative stress. *J. Nanopart. Res.*, **16** (11), 2664.
201. Zhao, Y., Wang, X., Wu, Q., Li, Y., and Wang, D. (2015) Translocation and neurotoxicity of CdTe quantum dots in RMEs motor neurons in nematode *Caenorhabditis elegans*. *J. Hazard. Mater.*, **283**, 480–489.
202. Zhao, Y., Wu, Q., Tang, M., and Wang, D. (2014) The in vivo underlying mechanism for recovery response formation in nano-titanium dioxide exposed *Caenorhabditis elegans* after transfer to the normal condition. *Nanomed. Nanotechnol. Biol. Med.*, **10** (1), 89–98.
203. Li, Y.X., Yu, S.H., Wu, Q.L., Tang, M., Pu, Y.P., and Wang, D.Y. (2012) Chronic Al_2O_3-nanoparticle exposure causes neurotoxic effects on locomotion behaviors by inducing severe ROS production and disruption of ROS defense mechanisms in nematode *Caenorhabditis elegans*. *J. Hazard. Mater.*, **219**, 221–230.
204. Li, Y., Yu, S., Wu, Q., Tang, M., and Wang, D. (2013) Transmissions of serotonin, dopamine, and glutamate are required for the formation of neurotoxicity from Al_2O_3-NPs in nematode *Caenorhabditis elegans*. *Nanotoxicology*, **7** (5), 1004–1013.
205. Wu, S., Lu, J., Rui, Q., Yu, S., Cai, T., and Wang, D. (2011) Aluminum nanoparticle exposure in L1 larvae results in more severe lethality toxicity than in L4 larvae or young adults by strengthening the formation of stress response and intestinal lipofuscin accumulation in nematodes. *Environ. Toxicol. Pharmacol.*, **31** (1), 179–188.
206. Wu, Q., Wang, W., Li, Y., Li, Y., Ye, B., Tang, M., and Wang, D. (2012) Small sizes of TiO_2-NPs exhibit adverse effects at predicted environmental relevant concentrations on nematodes in a modified chronic toxicity assay system. *J. Hazard. Mater.*, **243**, 161–168.
207. Li, Y., Wang, W., Wu, Q., Li, Y., Tang, M., Ye, B., and Wang, D. (2012) Molecular control of TiO_2-NPs toxicity formation at predicted environmental relevant concentrations by Mn-SODs proteins. *PLoS One*, **7** (9), e44688.
208. Xue, J., Li, X., Sun, M., Wang, Y., Wu, M., Zhang, C., Wang, Y., Liu, B., Zhang, Y., and Zhao, X. (2013) An assessment of the impact of SiO_2 nanoparticles of different sizes on the rest/wake behavior and the developmental profile of zebrafish larvae. *Small*, **9** (18), 3161–3168.
209. Huang, N., Yan, Y., Xu, Y., Jin, Y., Lei, J., Zou, X., Ran, D., Zhang, H., Luan, S., and Gu, H. (2013) Alumina nanoparticles alter rhythmic activities of local interneurons in the antennal lobe of Drosophila. *Nanotoxicology*, **7** (2), 212–220.
210. Yuan, Z.-Y., Hu, Y.-L., and Gao, J.-Q. (2015) Brain localization and neurotoxicity evaluation of polysorbate 80-modified chitosan nanoparticles in rats. *PLoS One*, **10** (8), e0134722.
211. Ze, Y., Zheng, L., Zhao, X., Gui, S., Sang, X., Su, J., Guan, N., Zhu, L., Sheng, L., and Hu, R. (2013) Molecular mechanism of titanium dioxide nanoparticles-induced oxidative injury in the brain of mice. *Chemosphere*, **92** (9), 1183–1189.
212. Wu, J., Wang, C., Sun, J., and Xue, Y. (2011) Neurotoxicity of silica nanoparticles: brain localization and dopaminergic neurons damage pathways. *ACS Nano*, **5** (6), 4476–4489.

213. Scharf, A., Gührs, K.-H., and von Mikecz, A. (2016) Anti-amyloid compounds protect from silica nanoparticle-induced neurotoxicity in the nematode C. elegans. *Nanotoxicology*, **10** (4), 426–435.

214. Ze, Y., Sheng, L., Zhao, X., Ze, X., Wang, X., Zhou, Q., Liu, J., Yuan, Y., Gui, S., and Sang, X. (2014) Neurotoxic characteristics of spatial recognition damage of the hippocampus in mice following subchronic peroral exposure to TiO_2 nanoparticles. *J. Hazard. Mater.*, **264** (15), 219–229.

215. Powers, C.M., Slotkin, T.A., Seidler, F.J., Badireddy, A.R., and Padilla, S. (2011) Silver nanoparticles alter zebrafish development and larval behavior: distinct roles for particle size, coating and composition. *Neurotoxicol. Teratol.*, **33** (6), 708–714.

216. Lee, K.J., Nallathamby, P.D., Browning, L.M., Osgood, C.J., and Xu, X.-H.N. (2007) *In vivo* imaging of transport and biocompatibility of single silver nanoparticles in early development of zebrafish embryos. *ACS Nano*, **1** (2), 133–143.

217. Ze, Y., Hu, R., Wang, X., Sang, X., Ze, X., Li, B., Su, J., Wang, Y., Guan, N., and Zhao, X. (2014) Neurotoxicity and gene-expressed profile in brain-injured mice caused by exposure to titanium dioxide nanoparticles. *J. Biomed. Mater. Res. Part A*, **102** (2), 470–478.

218. Rahman, M., Wang, J., Patterson, T., Saini, U., Robinson, B., Newport, G., Murdock, R., Schlager, J., Hussain, S., and Ali, S. (2009) Expression of genes related to oxidative stress in the mouse brain after exposure to silver-25 nanoparticles. *Toxicol. Lett.*, **187** (1), 15–21.

219. Tsyusko, O.V., Unrine, J.M., Spurgeon, D., Blalock, E., Starnes, D., Tseng, M., Joice, G., and Bertsch, P.M. (2012) Toxicogenomic responses of the model organism *Caenorhabditis elegans* to gold nanoparticles. *Environ. Sci. Technol.*, **46** (7), 4115–4124.

220. Hougaard, K.S., Campagnolo, L., Chavatte-Palmer, P., Tarrade, A., Rousseau-Ralliard, D., Valentino, S., Park, M.V., de Jong, W.H., Wolterink, G., and Piersma, A.H. (2015) A perspective on the developmental toxicity of inhaled nanoparticles. *Reprod. Toxicol.*, **56**, 118–140.

221. Gao, G., Ze, Y., Li, B., Zhao, X., Zhang, T., Sheng, L., Hu, R., Gui, S., Sang, X., Sun, Q., Cheng, J., Cheng, Z., Wang, L., Tang, M., and Hong, F. (2012) Ovarian dysfunction and gene-expressed characteristics of female mice caused by long-term exposure to titanium dioxide nanoparticles. *J. Hazard. Mater.*, **243**, 19–27.

222. Farombi, E.O., Adedara, I.A., Forcados, G.E., Anao, O.O., Agbowo, A., and Patlolla, A.K. (2016) Responses of testis, epididymis, and sperm of pubertal rats exposed to functionalized multiwalled carbon nanotubes. *Environ. Toxicol.*, **31** (5), 543–551.

223. Yoshida, S., Hiyoshi, K., Ichinose, T., Takano, H., Oshio, S., Sugawara, I., Takeda, K., and Shibamoto, T. (2009) Effect of nanoparticles on the male reproductive system of mice. *Int. J. Androl.*, **32** (4), 337–342.

224. Jackson, P., Halappanavar, S., Hougaard, K.S., Williams, A., Madsen, A.M., Lamson, J.S., Andersen, O., Yauk, C., Wallin, H., and Vogel, U. (2013) Maternal inhalation of surface-coated nanosized titanium dioxide (UV-Titan) in C57BL/6 mice: effects in prenatally exposed offspring on hepatic DNA damage and gene expression. *Nanotoxicology*, **7** (1), 85–96.

225. Lim, D., Roh, J.y., Eom, H.j., Choi, J.Y., Hyun, J., and Choi, J. (2012) Oxidative stress-related PMK-1 P38 MAPK activation as a mechanism for toxicity of silver nanoparticles to reproduction in the nematode *Caenorhabditis elegans*. *Environ. Toxicol. Chem.*, **31** (3), 585–592.

226. Zhu, X., Zhu, L., Li, Y., Duan, Z., Chen, W., and Alvarez, P.J. (2007) Developmental toxicity in zebrafish (*Danio rerio*) embryos after exposure to manufactured nanomaterials: buckminsterfullerene aggregates (nC60) and fullerol. *Environ. Toxicol. Chem.*, **26** (5), 976–979.

227. Chen, Y., Hu, X., Sun, J., and Zhou, Q. (2016) Specific nanotoxicity of

graphene oxide during zebrafish embryogenesis. *Nanotoxicology*, **10** (1), 42–52.

228. Cheng, J. and Cheng, S.H. (2012) Influence of carbon nanotube length on toxicity to zebrafish embryos. *Int. J. Nanomed.*, **7**, 3731.

229. Seitz, F., Bundschuh, M., Rosenfeldt, R.R., and Schulz, R. (2013) Nanoparticle toxicity in *Daphnia magna* reproduction studies: the importance of test design. *Aquat. Toxicol.*, **126**, 163–168.

230. Ispas, C., Andreescu, D., Patel, A., Goia, D.V., Andreescu, S., and Wallace, K.N. (2009) Toxicity and developmental defects of different sizes and shape nickel nanoparticles in zebrafish. *Environ. Sci. Technol.*, **43** (16), 6349–6356.

231. Wang, J., Zhu, X., Zhang, X., Zhao, Z., Liu, H., George, R., Wilson-Rawls, J., Chang, Y., and Chen, Y. (2011) Disruption of zebrafish (*Danio rerio*) reproduction upon chronic exposure to TiO_2 nanoparticles. *Chemosphere*, **83** (4), 461–467.

232. Asharani, P., Lianwu, Y., Gong, Z., and Valiyaveettil, S. (2011) Comparison of the toxicity of silver, gold and platinum nanoparticles in developing zebrafish embryos. *Nanotoxicology*, **5** (1), 43–54.

233. Ema, M., Hougaard, K.S., Kishimoto, A., and Honda, K. (2016) Reproductive and developmental toxicity of carbon-based nanomaterials: a literature review. *Nanotoxicology*, **10** (4), 391–412.

234. Sun, J., Zhang, Q., Wang, Z., and Yan, B. (2013) Effects of nanotoxicity on female reproductivity and fetal development in animal models. *Int. J. Mol. Sci.*, **14** (5), 9319–9337.

235. Morishita, Y., Yoshioka, Y., Higashisaka, K., and Tsutsumi, Y. (2016) in *Biological Effects of Fibrous and Particulate Substances* (eds T. Otsuki, Y. Yoshioka, and A. Holian), Springer, Tokyo, pp. 77–101.

236. Celá, P., Veselá, B., Matalová, E., Večeřa, Z., and Buchtová, M. (2014) Embryonic toxicity of nanoparticles. *Cells Tissues Organs*, **199** (1), 1–23.

237. Magdolenova, Z., Collins, A., Kumar, A., Dhawan, A., Stone, V., and Dusinska, M. (2014) Mechanisms of genotoxicity. A review of in vitro and in vivo studies with engineered nanoparticles. *Nanotoxicology*, **8** (3), 233–278.

238. Folkmann, J.K., Risom, L., Jacobsen, N.R., Wallin, H., Loft, S., and Moller, P. (2009) Oxidatively damaged DNA in rats exposed by oral gavage to C60 fullerenes and single-walled carbon nanotubes. *Environ. Health Perspect.*, **117** (5), 703–708.

239. Khalil, W., Girgis, E., Emam, A., Mohamed, M., and Rao, K.V. (2011) Genotoxicity evaluation of nanomaterials: DNA damage, micronuclei, and 8-hydroxy-2-deoxyguanosine induced by magnetic doped CdSe quantum dots in male mice. *Chem. Res. Toxicol.*, **24** (5), 640–650.

240. Golbamaki, N., Rasulev, B., Cassano, A., Robinson, R.L.M., Benfenati, E., Leszczynski, J., and Cronin, M.T.D. (2015) Genotoxicity of metal oxide nanomaterials: review of recent data and discussion of possible mechanisms. *Nanoscale*, **7** (6), 2154–2198.

241. Karlsson, H.L., Gliga, A.R., Calleja, F.M.G.R., Goncalves, C.S.A.G., Wallinder, I.O., Vrieling, H., Fadeel, B., and Hendriks, G. (2014) Mechanism-based genotoxicity screening of metal oxide nanoparticles using the ToxTracker panel of reporter cell lines. *Part. Fibre Toxicol.*, **11**, 41.

242. Jacobsen, N.R., Moller, P., Jensen, K.A., Vogel, U., Ladefoged, O., Loft, S., and Wallin, H. (2009) Lung inflammation and genotoxicity following pulmonary exposure to nanoparticles in $ApoE^{-/-}$ mice. *Part. Fibre Toxicol.*, **6**, 2.

243. Ema, M., Tanaka, J., Kobayashi, N., Naya, M., Endoh, S., Maru, J., Hosoi, M., Nagai, M., Nakajima, M., and Hayashi, M. (2012) Genotoxicity evaluation of fullerene C 60 nanoparticles in a comet assay using lung cells of intratracheally instilled rats. *Regul. Toxicol. Pharm.*, **62** (3), 419–424.

244. Wessels, A., Van Berlo, D., Boots, A.W., Gerloff, K., Scherbart, A.M., Cassee, F.R., Gerlofs-Nijland, M.E., Van Schooten, F.-J., Albrecht, C., and Schins, R.P. (2011) Oxidative stress

and DNA damage responses in rat and mouse lung to inhaled carbon nanoparticles. *Nanotoxicology*, **5** (1), 66–78.

245. Shinohara, N., Matsumoto, K., Endoh, S., Maru, J., and Nakanishi, J. (2009) *In vitro* and *in vivo* genotoxicity tests on fullerene C_{60} nanoparticles. *Toxicol. Lett.*, **191** (2), 289–296.

246. Dandekar, P., Dhumal, R., Jain, R., Tiwari, D., Vanage, G., and Patravale, V. (2010) Toxicological evaluation of pH-sensitive nanoparticles of curcumin: acute, sub-acute and genotoxicity studies. *Food Chem. Toxicol.*, **48** (8), 2073–2089.

247. Lee, D.S. and Kim, S. (2012) Gene expression profiles for genotoxic effects of silica-free and silica-coated cobalt ferrite nanoparticles. *J. Nucl. Med.*, **53** (1), 106–112.

8
In Vitro Testing Methods for Nanomaterials

Feng Zhao and Xueying Liu

8.1
Introduction

Nanomaterials are believed to bring great benefits to human beings; however, they are also concerned about inducing potential risk to human health. To date, it has been known that the biological effects of nanomaterials associate not only with their physicochemical properties but also with many extrinsic factors, including dose (presented by mass, specific surface area, particle number), cell/organ specific responsiveness, exposure routes, and animal species [1]. For example, Wang *et al.* found that 120 nm ZnO NPs at doses of 3, 4, and 5 g/kg of body weight caused severe damage in the mouse liver, myocardium, and spleen with a dose-dependent manner [2]. But in mice exposed to 20 nm ZnO NPs, the higher doses produced less pathological damage to the liver, myocardium, and spleen [3]. So the existing database for safety evaluation of chemical compounds, including the effects on health and the environment, is probably no longer valid if extrapolating to the nanomaterials.

Some questions are derived from the knowledge that the life process is based on chemical reactions of biological molecules, and these reactions are largely related to their three-dimensional structure. Do nanomaterials entering the organism cause special biological effects? Are these effects beneficial or harmful to the life process and the human body? Would they cross the blood–brain barrier and enter the brain to affect the brain function? Do the nanomaterials with the character of self-assembly interfere or destroy the natural molecular self-assembly during life process from atoms → amino acids → the proteins or DNA → organelles → cells → organisms? At present, knowledge about the interactions between nanomaterials and biological systems is still lacking. New experimental methodology for nanotoxicological research is demanded.

All the experimental methods in traditionally toxicological sciences can be applied to the toxicological research of nanomaterials, but those are not enough. Firstly, because of the altered physicochemical properties of nanomaterials, many of the conventional techniques need to be modified in some way, such as

Toxicology of Nanomaterials, First Edition. Edited by Yuliang Zhao, Zhiyong Zhang, and Weiyue Feng.

a pretreatment procedure of the test substance, the special characterization for nanoproperties (size for nanoparticles, length and/or diameter for nanotubes, nanowires and nanobelts, particle number, specific surface area, surface properties, and surface labeling, etc.), practicable techniques for a quantitative detection of different nanoparticles *in vivo* or *in vitro.* Secondly, new methods should be developed to investigate the behavior of nanoscale particles. Thirdly, the absence of standardized methodologies and guidelines makes it difficult to compare the data of nanotoxicity from different research groups.

So far, majority of experiments delivered to assess the toxicity of nanomaterials are *in vitro* studies. In this chapter, we attempt to describe some important *in vitro* methods that are used for nanotoxicological studies. Both their advantages and disadvantages are discussed.

8.2 Preparation of Nanoparticle Suspensions

Because of the small size and huge specific surface area, NPs easily aggregate into larger particles or bundles that sometimes can further agglomerate loosely into small clumps. As the first step and one key procedure, we need to develop methods to ensure that the nanomaterials are in a stable and well-dispersive state. For example, in the cell culture experiments, in order to ensure that every cell has equal possibility of exposure, the preparation of NP suspension is one of the key procedures. Some studies are conducted to assess and compare how various suspension media disperse the nanoparticles [4]. Currently, the commonly used available methods of deagglomerating or preventing the agglomeration of nanomaterials are sonication [5–8] and surface modification [4, 9–13].

Sonication is the most preferable and widely used method to disperse nanomaterials in solutions before exposing to cells or animals, which does not have much alteration on the properties of the nanomaterials. Particle aggregation is often broken up by bath sonication of the nanoparticle suspensions [5, 6]. Dickson *et al.* [7] conducted different techniques (vortex, bath sonication, and probe ultrasonication) to disperse bare hematite NPs and found that only probe ultrasonication could efficiently break down the NPs into "nanosize range." However, the method is difficult to standardize (density, dose, power, and local heating) [8].

Surface modification is another important method to prevent the agglomeration of nanomaterials and can homogeneously disperse them in liquid media. One of the reasons is that the chemical modifiers can make nanomaterials more stable and dispersive. For example, the surface coating with humic acids results in negatively charged Fe_3O_4 NPs, which prevents their aggregation in the aqueous environment [11–14]. Sager *et al.* [4] compared dispersion capabilities of various suspension media including phosphate-buffered saline, rat and mouse bronchoalveolar lavage fluid (BALF), PBS containing dipalmitoyl phosphatidylcholine (DPPC), mouse serum albumin or a combination of DPPC and albumin for nanomaterial suspension and found that as an excellent vehicle, BALF could suspend nanomaterials without altering their inflammatory or toxic potentials.

Although surface modification avoids nanomaterial agglomeration, it also raises concerns that should be considered. The first issue is the durability or stability of surface modification of nanomaterials inside biological systems or in the environment. For example, it was revealed that the acidic and oxidative environments of endosomes may cause the decomposition of surface coatings of quantum dot (QD) and subsequently induce the cytotoxicity [15]. The second concern is that the modifiers may alter the surface properties of nanomaterials, thereby shielding or influencing the effects of nanomaterials on biological system, such as the fate, the transport, and the toxicity [16–19]. Alkilany *et al.* [20] evaluated the potential adverse effects of surfactant-capped gold nanorods (GNRs) on blood vessels. The results indicate that thiolated polyethylene-glycol-modified gold nanorods (PEG-GNRs) are superior to polyelectrolyte-modified gold nanorods (PE-GNRs) in terms of biocompatibility with the vascular endothelium in blood vessels. The difference in toxicity and cellular uptake of PE-GNRs versus PEG-GNRs may link to free surfactant molecules and protein adsorption, respectively, which can be prevented by appropriate surface modification.

8.3 Cell Viability Assays

8.3.1 Proliferative Assays

Many methods have been developed to measure cell proliferation, such as tetrazolium salt assay, alamar blue (AB), incorporation of ^{3}H-thymidine into the DNA, and clonogenic assays. These methods to a large degree are based on direct counting of viable cells. Tetrazolium salt assay measures the viability of a cell population relative to control cells and is already widely used [21]. This assay for succinate dehydrogenase was first described by Mosmann [22]. After the treatment of cells with particulates for several times, soluble yellow tetrazolium salts such as MTS (3-(4,5-dimethylthiazol-2-yl)-5-(3-carboxymethoxyphenyl)-2-(4-sulfophenyl)-2*H*-tetrazolium, inner salt) or MTT (3-(4,5-dimethylthiazol-2-yl)-2,5-diphenyltetrazolium bromide) are added to the system and incubate at 37 °C for 2–4 h. Viable cells with active respiratory mitochondrial activity reduce MTS or MTT into insoluble purple formazan crystals by mitochondrial succinic dehydrogenases. These crystals can be solubilized by the addition of dimethyl sulfoxide (DMSO) or isopropanol and subsequently quantified using a visible light spectrophotometer [21]. In contrast with other toxicity assays, this technique has a number of benefits including minimal physical operation requirement of the model cells and quick, reproducible result achievement, and simple optical microscope [23]. However, this assay can be influenced by various conditions and comprises a number of defects. For example, when the test system contains a strong reducing substance, MTT might be reduced to from formazan crystals and thus would show false-positive results [23]. It was reported that the preparations of SWCNTs and MWCNTs were appropriate for the

MTT assay approach; however, the cytotoxicity tests of graphene oxide (GO) or graphene sheets (GSs) could cause false-positive results of cell viability, especially at high GS and GO doses [24]. As a consequence, some modified methods can be chosen instead. For example, the tetrazolium derivative XTT (2,3-bis (2-methoxy-4-nitro-5-sulfophenyl)-5-[(phenylamino) carbonyl]-2*H*-tetrazolium hydroxide) is used, which is soluble in water and forms hydrophilic formazan product [25].

AB is a recent technique to assay the cellular redox potential. The active ingredient resazurin is a blue nonfluorescent dye, which is cell-permeable. When entering the cells, resazurin is reduced to resorufin, which produces very bright red or pink fluorescence. This phenomenon occurs in consequence of accepting electrons from nicotinamide adenine dinucleotide phosphate (reduced form) (NADPH), nicotinamide adenine dinucleotide (reduced form) (NADH), flavin adenine dinucleotide (semiquinone form) (FADH), flavin mononucleotide (semiquinone form) (FMNH), and cytochromes by the enzymes (cytosolic and mitochondrial dehydrogenases in particular). The transformation occurs persistently between resazurin and resorufin, as a result, producing a quantitative measurement of the cytotoxicity [26]. Thus, this conversion is a method that tests the cell viability. The redox indicator is nonpoisonous and hardly destroys cells, users, and the environment.

Incorporation of ^{3}H-thymidine into the DNA can sensitively measure cell proliferation, where thymidine is a kind of deoxy ribonucleic acid. It is more complex than using ^{3}H-thymidine, which is considered to be toxic to living organisms and a money-consuming radioactive material and particular training and facilities are required. In addition, proliferation measured by ^{3}H-thymidine incorporation cannot provide the information where the subsets of cells are actually proliferation by the *in vitro* stimuli [27].

Clonogenic assay is an *in vitro* cell survival assay based on the ability of a single cell to grow into a colony. The method investigates how the particular agents effect on the survival and proliferation of cells. At the beginning of low-density plating, cells are able to cultivate until colonies are observed, then cells can also be preprocessed with particulates according specific interest. Each colony is divided from a single plated cell dyed with crystal violet or nuclear stains if necessary, and the population of colonies can be counted by visual inspection [28].

8.3.2 Apoptosis Assays

Apoptosis, also called *programmed cells death*, has been widely applied to toxicological studies. Various methods constitute the apoptosis assays including DNA laddering, caspase assay, the comet assay, TUNEL assay, and Annexin V assay.

DNA laddering, which is the oldest DNA damage assay technique, characterizes the specific DNA fragmentation from plants or animals exposed to a poisonous substance during cultivating process through isolating and fluorescently labeling DNA from cells. Then the DNA damage can be detected by

gel electrophoresis. It has been investigated that DNA laddering is a kind of biochemical manifestation associated with most generally apoptotic cell death. Therefore, for understanding the floristic molecular mechanisms of apoptosis, it is of significance that the detection of DNA laddering and identification and characterization of the endonucleases are responsible for the DNA fragmentation. However, the mechanism of DNA laddering between diverse species might be different; sometimes the difference exists in various tissues of one organism [29].

Caspase assay builds on the zymogen processing to an active enzyme and proteolytic activity, which is the evaluation standard of this experiment. Once the caspase-3 is motivated, then the cells come into programming death. Measuring the fragmentation of a caspase-3 substrate that is connected to a chromophore or fluorophore, which absorbs or emits light, activated caspase-3 can be efficiently detected [30]. Every organism and every cell use caspases when undergoing apoptotic cell death. These series of proteases hold key position in inflammation and cell death and are also important for initiating and executing apoptosis. Caspase substrates are cleaved at the carboxy-terminal peptide bond of the aspartic acid residue in the peptide motif, leading to damage or gain of the function of target protein, commonly generating the apoptotic signaling pathway in the earlier stage [31].

The comet assay is a simple, versatile, rapid, and sensitive method that is used for quantification and analysis of DNA damage in individual cells, which is named single-cell gel electrophoresis. Cells that were previously exposed to a toxicant are inserted into a thin agarose gel on a microscope slide. The slides are then immersed in a detergent solution that causes the cells to lyse. All cellular proteins are then removed when the DNA is allowed to unwind under the neutral/alkaline pH conditions of the detergent. The DNA is electrophoresed and then stained with a DNA-specific fluorescent dye such as acridine orange, ethidium bromide, propidium iodide (PI), or 4′,6′-diamidino-2-phenylindole (DAPI). The extent of DNA emancipated from the head of the comet is directly proportional to the amount of DNA damage [32].

Terminal deoxynucleotidyl transferase dUTP (deoxy uridine triphosphate) nick end labeling (TUNEL) assay is considered the "gold standard" for measuring apoptosis because it works on 95% of the cells. The method is based on broken double-strand during apoptosis and incorporation of biotinylated nucleotides conjugated to bromodeoxyuridine (BrdU) at the 3′-OH ends of the DNA breakage during apoptosis. In contrast with DNA laddering assay, TUNEL staining can quantify apoptotic cells and detect DNA strand breakage in an individual cell [33].

Annexin V assay is a sensitive, accurate, reproductive, specific, and quantitative method for analyzing apoptotic cells. The method is based on translocation of phosphatidylserine from the inner (cytoplasmic) leaflet of the plasma membrane to the outer (cell surface) leaflet soon after the induction of apoptosis, and the annexin V protein has a strong, specific affinity for phosphatidylserine. The addition of PI to annexin V stained cells allows discrimination between viable cells, early apoptotic, and late apoptotic and necrotic cells [34].

8.3.3
Necrosis Assays

Necrosis assays generally include neutral red uptake assay, trypan blue assay, and Lactate dehydrogenase (LDH) assay.

Neutral red uptake cytotoxicity assay is a cell viability assay, which relies on the ability of viable cells to incorporate neutral red, a weak cationic supravital dye. Neutral red tends to penetrate the cell membranes by passive diffusion and accumulates in the lysosomes by an energy-dependent process [35]. Accordingly, the method measures the cell membrane integrity and the cellular energy status.

The trypan blue assay, which is based on staining of cells, is another test of the cell membrane integrity. In this assay, cells are trypsinized, then stained with trypan blue, a kind of diazo dye. Cells are counted using hemocytometer under the microscope; nonviable cells were stained blue, while viable cells remained unstained. The advantage of this method is that the total amounts of viable cells can be calculated. However, the process of quantification is tedious, excessively wasting time. Moreover, cell counting can cause bias from investigators and sample error [36].

Lactate dehydrogenase (LDH) is an enzyme that helps the process of turning sugar into energy and exists in cell membranes and cytoplasm in all cells. When the cell membranes are damaged, LDH is released from the cells into culture supernatants immediately and can be measured photospectrometrical, for example, via the transformation of the yellow tetrazolium salt into a red formazan [37].

8.4
Oxidative Stress Assay

Oxidative stress refers to an excessive formation and/or removing insufficiently of highly reactive molecules, owing to disturbance of the oxidative balance by stimuli, including reactive oxygen species (ROS) and reactive nitrogen species (RNS). Moreover, ROS contains free radicals and nonfree radicals; among them, free radicals are superoxide ($^{\bullet}O_2^-$), hydroxyl ($^{\bullet}OH$), peroxyl ($^{\bullet}RO_2$), hydroxyperoxyl ($^{\bullet}HRO_2^-$), as well as nonradical species such as hydrogen peroxide (H_2O_2) and hydrochlorous acid (HOCl). RNS contains free radicals such as nitric oxide ($^{\bullet}NO$) and nitrogen dioxide ($^{\bullet}NO_2$) and nonradicals such as peroxynitrite (ONOO−), nitrous oxide (HNO_2) and alkyl peroxynitrates (RONOO). Abnormally high concentrations of ROS and RNS can react with proteins, lipids, or nucleic acids, resulting in disturbed cellular function and toxicological symptoms [28, 38].

Oxidative stress has been identified as the main mechanism of nanotoxicology. Several methods for detection of free radicals generated in test systems have been used for oxidative stress assays, including dichlorodihydrofluorescein diacetate (DCFH-DA) assay, electroparamagnetic resonance (EPR), lipid peroxidation, and plasmid DNA assay.

In DCFH-DA assay, the diacetate precursor is diffused into the cells and is cleaved by cellular esterases to nonfluorescent product DCFH, which is rapidly oxidized to a highly fluorescent product dichlorodihydrofluorescein (DCF) that can be measured by fluorimetry method. Owing to the high sensitivity, DCFH-DA assays are commonly applied to estimate oxidative stress in cells [39].

EPR is the only technique that is capable of providing a direct detection of free radicals. Because the half-life of most free radical species is very short (milliseconds to minutes), not all species can be detected directly. For this reason, compounds that can react with free radical species (spin traps and spin probes) have been used to form stable adducts with radicals.

Lipid peroxidation is considered to be the main molecular mechanisms involved in the oxidative damage to cell membrane structure and function. The measurement of malondialdehyde (MDA), which is one of the most prevalent by-products of lipid peroxidation during oxidative stress, is a convenient and sensitive method for quantitative estimation of lipid peroxide concentration. The MDA levels in samples can be measured via a thiobarbituric acid reactive substances (TBARS) assay.

The plasmid DNA assay is a simple *in vitro* assay, which detects the presence of ROS on the surface of the particulate samples. The initial effect of oxidative damage causes DNA to relax and further become linearized. The undamaged supercoiled DNA, damaged relaxed DNA, and linearized DNA can be separated by electrophoresis. Subsequently, scanning laser densitometry can be used to quantify the proportions of the different forms of DNA. The oxidative capacity, that is, toxicity, is expressed as depletion of the supercoiled DNA band [40].

The oxidative stress is defined as the imbalance between the production of ROS and the antioxidant defenses. Antioxidant enzymes such as superoxide dismutase (SOD), catalase (CAT), and glutathione peroxidase (GPx) are the first line of cellular defense against damage. Changes in antioxidant enzyme activities in cells have been used to document oxidative stress.

8.5 Inflammatory Assay

Enzyme-linked immunosorbent assay (ELISA) is a biochemical method that can determine the presence of an antibody or an antigen in a sample and mainly used in immunology. In ELISA, an unknown amount of antigen is stuck on a surface that is subsequently covered by a specific antibody; consequently, the antibody connects to the antigen. This antibody binds to an enzyme and finally a chromogenic agent is added, so that the enzyme can transform it into specific detectable signal, most generally a color change of the coloration chemical substrate. The most extensive measurements of human and murine inflammatory markers are the chemokine Interleukin-8 (IL-8), TNF-α, IL-6, and so on [41].

Some *in vitro* testing methods for nanotoxicology studies are summarized in Table 8.1.

Table 8.1 *In vitro* methods and in nanotoxicology studies.

Assays	Detection principle	Purpose	Advantages	Used for nanoparticles
Tetrazolium salts (MTT, MTS, XTT, WST)	Mitochondrial activity is determined calorimetrically and by visible light spectrometer	Cell viability/cell growth (cell metabolic activity)	Real-time assay results using low cell numbers Provides a simple method for estimation of live cell number in order to assess rate of cell proliferation and to screen cytotoxic agents Nonradioactive and inexpensive	Ag NPs [42, 43] Carbon nanomaterials [44, 45] SiO_2, ZnO NPs [45]
Neutral red assay	Colorimetric detection of intact lysosomes and detected via fluorescence or absorption measurement	Cell viability (lysosomal activity)	Quantitative estimation of the number of viable cells in a culture One of the most used cytotoxicity tests with many biomedical and environmental applications	24 metal-based NPs [46]
Lactate dehydrogenase (LDH)	Detection of LDH release colorimetrically	Cell viability	Reliable, speed, and simple evaluation	Fullerol [47]
Trypan blue	Detects either colorimetrically or fluorescently	Cell viability/cell growth	Conveys the actual number of viable cells and increases (cell proliferation) or decreases (cytotoxicity) in comparison to control, untreated cells	MWCNTs [48]
Colony formation assay	Detected microscopically or by scanner	Proliferative capacity	Reliable determination of the number of cells required to distinguish between a cluster of cells and a colony Enables rapid and accurate enumeration of colony number and is more suitable for higher-throughput compound assessment than current microscope-based methods Determines colony number through the application of a volume algorithm and permits the differentiation of cytostatic effects	Graphene [49]

Table 8.1 (*Continued*)

Assays	Detection principle	Purpose	Advantages	Used for nanoparticles
Caspase-3 activity	Fluorimetric detection of caspase-3 activity	Apoptosis	Easy, fast, and more convenient Potent, cell-permeable, and nontoxic fluorochrome inhibitor A direct measure of apoptosis expressed as the number of active caspase enzymes present in the cell No need for cell lysis, no membrane permeabilization	ZnO NPs [50]

Adapted and modified from [29].

8.6 Summary and Outlook

In vitro methods with their advantages are preferred and conducted prior to animal experimentation and clinical trials. Assessment of defined toxicity endpoints by *in vitro* methods is more rapid and economical as compared to animal studies. However, the *in vitro* test systems lack the complexity of animal models or the human body, and the metabolic activity of standardized cell lines has often not been comprehensively characterized [51].

As with any other man-made materials, both *in vitro* and *in vivo* studies on biological effects of nanomaterials should be performed. Presently, *in vitro* studies become extremely relevant and important in the absence of any clear guideline(s) by the regulatory agencies on the testing/evaluation of nanomaterials. These *in vitro* model systems could provide a rapid and effective means to access nanomaterials for a number of toxicological endpoints, allow development of mechanism-driven evaluations, and provide refined information on how nanoparticles interact with human cells in many ways.

Due to diverse nature of nanomaterials, there are significant challenges in the interpretation, validation, and correlation of cell and tissue toxicity data collected for nanomaterials. A unique difficulty in nanotoxicity assessments is the lack of appropriate tools to directly observe and interrogate nanomaterials in complex biological systems. Acute versus chronic nanomaterial exposure effects and hazards are, therefore, difficult to monitor. Hence, multiple different measurement techniques must be adapted, carefully assessed for validity, and applied to complex nanomaterial systems.

References

1. Zhao, F., Meng, H., and Yan, L. (2015) Nanosurface chemistry and dose govern the bioaccumulation and toxicity of carbon nanotubes, metal nanomaterials and quantum dots in vivo. *Sci. Bull.*, **60**, 3–20.
2. Wang, B., Feng, W., Wang, M. *et al* (2008) Acute toxicological impact of nano- and submicro-scaled zinc oxide powder on healthy adult mice. *J. Nanopart. Res.*, **10**, 263–276.
3. Wang, B., Feng, W., Wang, T. *et al.* (2006) Acute toxicity of nano and micro-scale zinc powder in healthy adult mice. *Toxicol. Lett.*, **161**, 115–123.
4. Sager, T., Porter, D., Robinson, V. *et al* (2008) Improved method to disperse nanoparticles for in vitro and in vivo investigation of toxicity. *Nanotoxicology*, **1** (2), 118–129.
5. Tian, F., Cui, D., Schwarz, H. *et al* (2006) Cytotoxicity of single-wall carbon nanotubes on human fibroblasts. *Toxicol. In Vitro*, **20** (7), 1202–1212.
6. Dong, L., Joseph, K.L., Witkowski, C.M. *et al* (2008) Cytotoxicity of single-walled carbon nanotubes suspended in various surfactants. *Nanotechnology*, **19** (25), 255702.
7. Dickson, D., Liu, G.L., Li, Z. *et al* (2012) Dispersion and stability of bare hematite nanoparticles: effect of dispersion tools, nanoparticle concentration, humic acid and ionic strength. *Sci. Total Environ.*, **419**, 170–177.
8. Pitt, W.G. and Husseini, G.A. (2008) Ultrasound in drug and gene delivery. *Adv. Drug Delivery Rev.*, **60** (10), 1095–1096.
9. Farah, A.A., Alvarez-Puebla, R.A., and Fenniri, H. (2008) Chemically stable silver nanoparticle-crosslinked polymer microspheres. *J. Colloid Interface Sci.*, **319** (2), 572–576.
10. Skebo, J.E., Grabinski, C.M., Schrand, A.M. *et al* (2007) Assessment of metal nanoparticle agglomeration, uptake, and interaction using high-illuminating system. *Int. J. Toxicol.*, **26** (2), 135–141.
11. Kanel, S.R., Nepal, D., Manning, B. *et al.* (2007) Transport of surface-modified iron nanoparticle in porous media and application to arsenic(III) remediation. *J. Nanopart. Res.*, **9**, 725–735.
12. Yang, G.C.C., Tu, H.-C., and Hung, C.-H. (2007) Stability of nanoiron slurries and their transport in the subsurface environment. *Sep. Purif. Technol.*, **58**, 166–172.
13. Tiraferri, A., Chen, K.L., Sethi, R. *et al.* (2008) Reduced aggregation and sedimentation of zero-valent iron nanoparticles in the presence of guar gum. *J. Colloid Interface Sci.*, **324**, 71–79.
14. Liu, J.F., Zhao, Z.S., and Jiang, G.B. (2008) Coating Fe_3O_4 magnetic nanoparticles with humic acid for high efficient removal of heavy metals in water. *Int. J. Environ. Sci. Technol.*, **42**, 6949–6954.
15. Hoshino, A., Fujioka, K., Oku, T. *et al* (2004) Physicochemical properties and cellular toxicity of nanocrystal quantum dots depend on their surface modification. *Nano Lett.*, **4** (11), 2163–2169.
16. Warheit, D.B. (2008) How meaningful are the results of nanotoxicity studies in the absence of adequate material characterization? *Toxicol. Sci.*, **101** (2), 183–185.
17. Derfus, A.M., Chan, W.C.W., and Bhatia, S.N. (2004) Probing the cytotoxicity of semiconductor quantum dots. *Nano Lett.*, **4** (1), 11–18.
18. Ge, C.C., Du, J.F., Zhao, L.N. *et al* (2011) Binding of blood proteins to carbon nanotubes reduces cytotoxicity. *Proc. Natl. Acad. Sci. U.S.A.*, **108** (41), 16968–16973.
19. Warheit, D.B., Brock, W.J., Lee, K.P. *et al* (2005) Comparative pulmonary toxicity inhalation and instillation studies with different TiO_2 particle formulations: impact of surface treatments on particle toxicity. *Toxicol. Sci.*, **88** (2), 514–524.
20. Alkilany, A.M., Shatanawi, A., Kurtz, T., Caldwell, R.B., and Caldwell, R.W. (2012) Toxicity and cellular uptake of gold nanorods in vascular endothelium and smooth muscles of isolated rat blood vessel: importance of surface modification. *Small*, **8** (8), 1270–1278.
21. Wang, P., Henning, S.M., and Heber, D. (2010) Limitations of MTT and

MTS-based assays for measurement of antiproliferative activity of green tea polyphenols. *PLoS One*, **5** (4), e10202.
22. Mosmann, T. (1983) Rapid colorimetric assay for cellular growth and survival: application to proliferation and cytotoxicity assays. *J Immunol. Methods*, **65** (1–2), 55–63.
23. Wang, S., Yu, H., Wickliffe, J.K. *et al* (2011) Limitation of the MTT and XTT assays for measuring cell viability due to superoxide formation induced by nano-scale TiO_2. *Toxicol. In Vitro*, **25** (8), 2147–2151.
24. Liao, K.H., Lin, Y.S., Macosko, C.W. *et al* (2011) Cytotoxicity of graphene oxide and graphene in human erythrocytes and skin fibroblasts. *ACS Appl. Mater. Interfaces*, **3** (7), 2607–2615.
25. Hatzinger, P.B., Palmer, P., Smith, R.L. *et al* (2003) Applicability of tetrazolium salts for the measurement of respiratory activity and viability of groundwater bacteria. *J. Microbiol. Methods*, **52**, 47–58.
26. Munshi, S., Twining, R.C., and Dahl, R. (2014) Alamar blue reagent interacts with cell-culture media giving different fluorescence over time: potential for false positives. *J. Pharmacol. Toxicol. Methods*, **70**, 195–198.
27. Messele, T., Roos, M.T., Hamann, D. *et al* (2000) Nonradioactive techniques for measurement of in vitro T-cell proliferation: alternatives to the [^{3}H]thymidine incorporation assay. *Clin. Diagn. Lab. Immunol.*, **7**, 687–692.
28. Takhar, P. and Mahant, S. (2011) In vitro methods for nanotoxicity assessment: advantages and applications. *Arch. Appl. Sci. Res.*, **3** (2), 389–403.
29. Jiang, A.L., Cheng, Y., Li, J. *et al* (2008) A zinc-dependent nuclear endonuclease is responsible for DNA laddering during salt-induced programmed cell death in root tip cells of rice. *J. Plant Physiol.*, **165** (11), 1134–1141.
30. Izban, K.F., Wrone-Smith, T., Hsi, E.D. *et al* (1999) Characterization of the interleukin-1β-converting enzyme/Ced-3-family protease, caspase-3/CPP32, in Hodgkin's disease. *Am. J. Pathol.*, **154** (5), 1439–1447.
31. McStay, G.P. and Green, D.R. (2014) Measuring apoptosis: caspase inhibitors and activity assays. *Cold Spring Harb. Protoc.*, **2014** (8), 799–806.
32. Tice, R.R., Agurell, E., Anderson, D. *et al* (2000) Single cell gel/comet assay: guidelines for in vitro and in vivo genetic toxicology testing. *Environ. Mol. Mutagen.*, **35**, 206–221.
33. Haghniaz, R., Umrani, R.D., Paknikar, K.M. (2015) Temperature-dependent and time-dependent effects of hyperthermia mediated by dextran-coated La0.7Sr0.3MnO3: in vitro studies. *Int. J. Nanomedicine*, **10**, 1609–1623.
34. Vermes, I., Haanen, C., Steffens-Nakken, H. *et al* (1995) A novel assay for apoptosis flow cytometric detection of phosphatidylserine expression on early apoptotic cells using fluorescein labelled Annexin V. *J. Immunol. Methods*, **184**, 39–51.
35. Borenfreund, E. and Puerner, J.A. (1985) Toxicity determined in vitro by morphological alterations and neutral red absorption. *Toxicol. Lett.*, **24**, 119–124.
36. Tracy, F. and Uliasz, S.J.H. (2000) A microtiter trypan blue absorbance assay for the quantitative determination of excitotoxic neuronal injury in cell culture. *J. Neurosci. Methods*, **100**, 157–163.
37. Baba, C., Yanagida, K., Kanzaki, T. *et al* (2005) Colorimetric lactate dehydrogenase (LDH) assay for evaluation of antiviral activity against bovine viral diarrhoea virus (BVDV) in vitro. *Antiviral Chem. Chemother.*, **16**, 33–39.
38. Ahamed, M., Akhtar, M.J., Siddiqui, M.A. *et al* (2011) Oxidative stress mediated apoptosis induced by nickel ferrite nanoparticles in cultured A549 cells. *Toxicology*, **283** (2-3), 101–108.
39. Bonini, M.G., Rota, C., Tomasi, A. *et al* (2006) The oxidation of 2',7'-dichlorofluorescin to reactive oxygen species: a self-fulfilling prophesy? *Free Radic. Biol. Med.*, **40** (6), 968–975.
40. Shao, L.Y., Shen, R.R., Wang, J., Wang, Z.S., Tang, U., and Yang, S.S. (2013) A toxicological study of inhalable particulates by plasmid DNA assay: a case study from Macao. *Sci. China: Earth Sci.*, **56**, 1037–1043.

41. Kondo, S., Kono, T., Sauder, D.N. *et al* (1993) IL-8 gene expression and production in human keratinocytes and their modulation by UVB. *J. Invest. Dermatol.*, **101**, 90–94.
42. Flahaut, E., Durrieu, M.C., Remy-Zolghadri, M., Bareille, R., and Baquey, C. (2006) Investigation of the cytotoxicity of CCVD carbon nanotubes towards human umbilical vein endothelial cells. *Carbon*, **44** (6), 1093–1099.
43. Yang, X.L., Fan, C.H., and Zhu, H.S. (2002) Photo-induced cytotoxicity of malonic acid C_{60} fullerene derivatives and its mechanism. *Toxicol. In Vitro*, **16**, 41–46.
44. Davoren, M., Herzog, E., Casey, A., Cottineau, B., Chambers, G., Byrne, H.J., and Lyng, F.M. (2007) *In vitro* toxicity evaluation of single walled carbon nanotubes on human A549 lung cells. *Toxicol. In Vitro*, **21** (3), 438–448.
45. Yang, H., Liu, C., Yang, D., Zhang, H., and Xi, Z. (2009) Comparative study of cytotoxicity, oxidative stress and genotoxicity induced by four typical nanomaterials: the role of particle size, shape and composition. *J. Appl. Toxicol.*, **29** (1), 69–78.
46. Lanone, S., Rogerieux, F., Geys, J., Dupont, A., Maillot-Marechal, E., Boczkowski, J. *et al.* (2009) Comparative toxicity of 24 manufactured nanoparticles in human alveolar epithelial and macrophage cell lines. *Part. Fibre Toxicol.*, **6**, 14.
47. Roberts, J.E., Wielgus, A.R., Boyes, W.K., Andley, U., and Chignell, C.F. (2008) Phototoxicity and cytotoxicity of fullerol in human lens epithelial cells. *Toxicol. Appl. Pharmacol.*, **228** (1), 49–58.
48. Bottini, M., Bruckner, S., Nika, K., Bottini, N., Bellucci, S., Magrini, A., Bergamaschi, A., and Mustelin, T. (2006) Multi-walled carbon nanotubes induce T lymphocyte apoptosis. *Toxicol. Lett.*, **160** (2), 121–126.
49. Chatterjee, N., Yang, J.S., Park, K., Oh, S.M., Park, J., and Choi, J. (2015) Screening of toxic potential of graphene family nanomaterials using *in vitro* and alternative *in vivo* toxicity testing systems. *Environ. Health Toxicol.*, **30**, e2015007.
50. Wang, C., Hu, X., Gao, Y., and Ji, Y. (2015) ZnO nanoparticles treatment induces apoptosis by increasing intracellular ROS levels in LTEP-a-2 cells. *Biomed. Res. Int.*, **2015**, 423287.
51. Dey, S., Mazumder, B., and Pathak, K. (2014) in *Biointeractions of Nanomaterials* (eds V.B. Sutariya and Y. Pathak), CRC Press, pp. 384–424.

9
Localizing the Cellular Uptake of Nanomaterials

Wei Li

9.1
Introduction

The expeditious expansion of nanomaterials in biological and biomedical applications and toxicological assessments calls for the appropriate study of these materials at cellular level. It is known that their small size can allow nanoparticles (NPs) to readily penetrate cells and translocate among different cells, tissues, and organs that are remote from the portal of entry to the body, which ultimately represents a great risk to human health [1–3]. Accordingly, elucidating the underlying mechanism of cellular uptake is an important step toward understanding the biological fate of NPs, both the adverse and favorable aspects [4]. The plasma membrane is a dynamic structure of lipid bilayers and membrane proteins that segregates the cytoplasm from the external medium and regulates the transport of exogenous materials into cells. The processes leading to NPs penetrating the cell membrane directly relate to their cellular uptake [5]. However, we still lack a systematic knowledge of these processes. Take the adverse effect as an example: the toxicity of nanoscale materials in biological systems is a big concern, but results in the published literatures are disparate due to variable methods, the great variety in the types of particles studied, different cell lines, different incubation conditions, surface functionalizations, protein adsorptions, agglomerations and aggregations, different doses used in the experiments, different cell lines, different endpoints of observation, and so on [6–8]. In this chapter, we review the mechanism of cellular uptake of nanomaterials and different detection methods of nanomaterial *in vitro*, especially the works that carried out in our labs. Throughout this best-value review, readers will be possibly concerned with the relationship between different detection methods with different cellular nanomaterials in relevant toxicity effects.

Toxicology of Nanomaterials, First Edition. Edited by Yuliang Zhao, Zhiyong Zhang, and Weiyue Feng.

9.2
Mechanism of Cellular Uptake of Nanomaterials

The uptake of nanomaterials by cells *in vitro* is an important factor to assess nanotoxicity [9]. Cell membranes are the hydrophobic barrier between cytoplasm and external medium, which allows cells to regulate the entry of exogenous molecules [10]. Small molecules, proteins, or peptides can enter the cells through a variety of different mechanisms [11]. Manufactured NPs having either hydrophobic or hydrophilic properties can enter the cells easily [12]. Cellular internalization of NPs may involve active (receptor-mediated) or passive transport across the cell membrane [4, 13]. Cell membranes that separate the cytoplasm from external medium and allow the cell to regulate the entry of exogenous molecules are hydrophobic barriers, although plasma membranes are somewhat permeable and let only smaller molecules to pass through, for instance, water, sugars, ions, and amino acids can traverse the cell membrane through pumps or channels [14]. For a large size substance, for example, macromolecules, however, it is conventionally transported into the cell by active endocytosis, the classic mode of cellular entry for hydrophilic macromolecules [15, 16].

Endocytosis, the conventional mode of cellular entry for hydrophilic macromolecules, occurs by mainly two distinct categories: phagocytosis and pinocytosis (Figure 9.1) [17]. Endocytosis involves the formation, fission, and fusion of vesicles in an energy-dependent manner. Phagocytosis is involved in the uptake of large particles and is usually restricted to phagocytes including macrophages and neutrophiles [18, 19]. Pinocytosis occurs in all cell types and is involved in the uptake of fluids and solutes [16]. Some ultrafine NPs could be transported into cells by diffusion from high concentration areas to cellular low concentration areas [20]. The pinocytosis mainly includes macropinocytosis, clathrin-mediated, and non-clathrin-meditated endocytosis mainly via caveolae [21]. Classically, the route for protein transporting into cells is mainly via clathrin-coated pits,

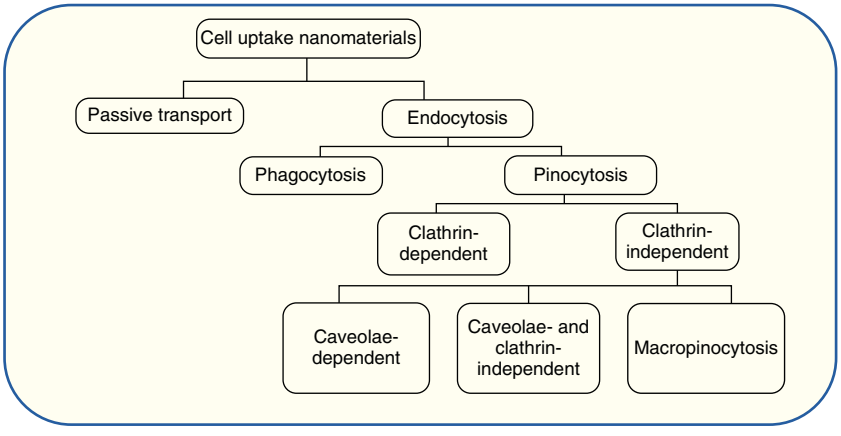

Figure 9.1 Known pathways of cellular uptake of NPs.

which needs protein to bind to a specific receptor on the cell surface and form a ligand–receptor complex cluster, and the latter is then internalized into the cell in an energy-dependent manner by clathrin-coated membrane vesicles [20]. Rejman *et al.* [22] found a size-dependent nature of the endocytosis process. The internalization of microspheres with a diameter less than 200 nm involves the clathrin-coated pits, and the mechanism shifts to a caveolae-mediated process with a size increase. However, the uptake mechanisms for NPs are more likely to occur via vesicular processes (e.g., endocytosis) than uptake on membrane transporters or by diffusion through the cell membrane. All of these described so far are active transport and require an input of energy.

Passive transport differs from active transport in that it does not involve any chemical energy [23]. For example, cellular uptake of Au NPs is involved with diffusion and sedimentation [24, 25]. In addition, passive transport relies on the innate permeability of the cell membrane and its component protein and lipids.

9.3
Methods to Determine Cellular Nanoparticle Uptake *In Vitro*

The cellular uptake of NPs is strongly dependent on the characteristics of NPs themselves. With the development of biophysical techniques [25], cellular NPs can be investigated by flow cytometry (FCM) [26] and several microscopic techniques [27], including atomic force microscope (AFM), scanning electron microscope (SEM), transmission electron microscope (TEM), and laser confocal scanning microscopy (LCSM). Among the most prominent techniques, the capability of multipoint scanner on spinning LCSM could achieve fast real-time cellular endocytosis dynamically [28, 29]. In addition, the intracellular organelle translocation of NPs provides new insight into the roles of cellular NPs.

9.3.1
Flow Cytometry

FCM is a technology that simultaneously measures and analyzes multiple physical characteristics of single cells [30]. As flow in a fluid stream through a beam of light, flow cytometers are mainly used in the clinical laboratory for a variety of analyses including diagnostic immunophenotyping of lymphomas. Flow cytometers may be compared with fluorescence microscopes. With a microscope, the light source is a lamp or laser, the objective lens focuses the image, and the eye is the detector. With a flow cytometer, the light source is a laser, an objective lens focuses the light, and the detector is a photomultiplier tube.

The properties measured include a particle's relative size, relative granularity or internal complexity, and relative fluorescence intensity. These characteristics are determined using an optical-to-electronic coupling system that records how the cell or particle scatters incident laser light and emits fluorescence. FCM has been used and developed in the fields of biochemistry and clinical hematology and has

advantages to analyze thousands of cells in seconds. FCM allows an efficient, fast, and quantitative assessment of cellular fluorescent-labeled NPs or fluorescent NPs [31]. Recently, it was clarified that the side-scattered light of FCM could be used as a guide to measure the uptake potential of NPs [32].

However, FCM is a quantitative method for determination of NPs in a certain number of cells, which could not qualitatively discriminate the cellular location of NPs in a single cell.

9.3.2 Fluorescent Microscopy Techniques

The microscopy imaging technique provides qualitative insight into the subcellular localization of fluorescent-labeled NPs [27]. Consequently, signals from fluorescent nanomaterials located at the surface of cells or colocalization with specific intracellular vesicles or organelles can be detected qualitatively by LCSM [33]. Intracellular localization of particles can be further confirmed using the quenching agent, trypan blue. This dye quenches signals from fluorescent dyes such as fluorescein isothiocyanate. Since trypan blue does not penetrate the membrane, only extracellular signals of free or surface-bound dye molecules are quenched. Alternatively, LCSM provides information on the three-dimensional structure of objects [34, 35]. Fluorescence colocalization studies give insight into intracellular trafficking after fixation of cells or by live-cell imaging.

Meanwhile, imaging dynamic cellular events via nanomaterials could provide new insights into NP uptake via cell membrane receptors and their intracellular transport process. The latter technique relies on spinning disk confocal microscopy and highly photostable fluorophores but avoids artifacts introduced by fixation reagents such as paraformaldehyde.

The spinning disk LCSM could achieve the fast real-time cellular endocytosis dynamically by temporal analytical techniques to track NPs in live cells, which would provide rich information to well understand the biologic properties of NPs at molecular level. Recently, NPs have been developed for real-time imaging and dynamic monitoring in live cells, and the single-NP tracking techniques were being developed to observe the behavior of NPs in live cell. The quality of live cell study will depend on the best match between the optical facility, optical probes, and the cellular system. Various fluorescent microscopy methods have been developed. Especially, the spinning disk LSCM [28] and total internal reflection fluorescent (TIRF) [36] microscopy for live-cell imaging system have shown wide applications in tacking the NPs in live cell. For example, the confocal system (Figure 9.2) with the Nipkow disk technology [29] and a live-cell culture chamber ensures that the system work with high frame rates, long time, and temporal resolution for live-cell imaging [28]. Signal/noise ratio is also good because the spinning disk is achieve at a high speed of about 1000 f/s; even in very short times, many frames are collected and integrated by the camera.

Furthermore, the super-resolution imaging techniques including stimulated emission depletion microscopy (STED)[37], photoactivated localization

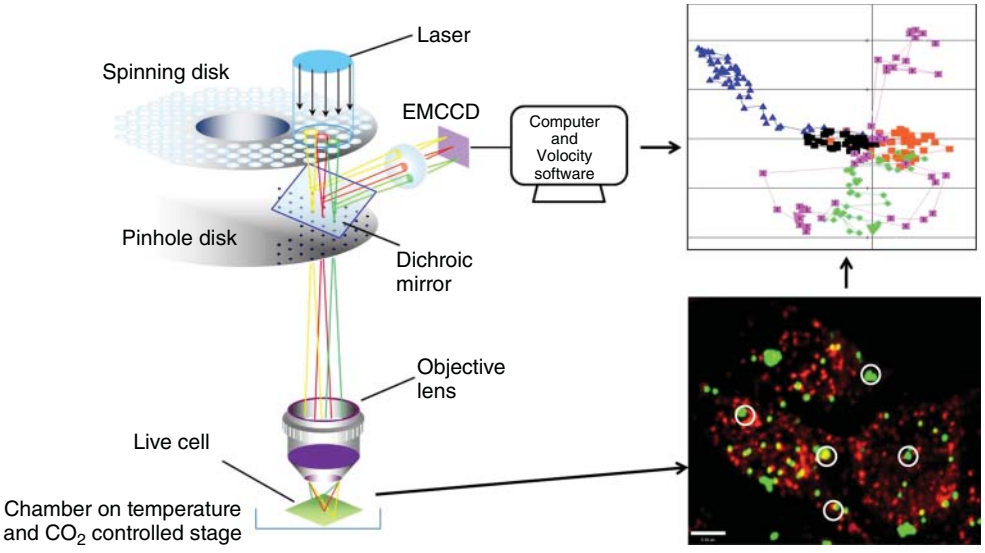

Figure 9.2 The schematic of the spinning disk laser scanning confocal microscopy live-cell imaging system for temporal resolution cell imaging and cellular NP trajectories analysis (left part of picture was afforded by PerkinElmer Inc.). Live cells using a spinning disk laser confocal scanning microscope equipped with a cultivation chamber fitted with a temp control and CO_2-control device. The cellular NPs trajectories were analyzed by professional imaging software Volocity. The circles in the live-cell image of fluorescent dots (right bottom) represent the areas from which the trajectories were generated in the right upper image. (Reprinted from [28] with permission. Copyright (2013) John Wiley & Sons.)

microscopy (PALM) [38], and stochastic optical reconstruction microscopy (STORM) [39] could break the optical diffraction limit and observe single molecule/NP clearly. For example, STED was recently used to image and track vesicle movement with a lateral resolution of 62 nm; this demonstrated the emerging ability of modern fluorescent microscopy to monitor the cellular processes at the nanometer scale.

Unfortunately, although microscopy imaging technique could analyze the cellular fluorescent intensity for semiquantitative determination NPs in a single cell, it is not a typically quantitative method to verify intracellular location in a certain number of cells. In several previous studies, microscopy imaging technique and FCM technique were jointly used for demonstrating the cellular NP internalization and cellular location [40].

9.3.3 TEM Analysis

TEM uses an electron beam to interact with a sample to form an image on a photographic plate or special camera. TEM provides an ideal tool to perform

both qualitative and quantitative analyses and reveals the localization of NPs within tissues and cells with a high resolution [41]. A prerequisite for TEM is that all internalized NPs in cells need fixation, which aims to preserve the specimens as close to the living state as possible. Once a specimen has undergone all fixation and embedding procedures, has maintained its antigenicity, and preserved its ultrastructure, immuno TEM offers some useful applications for NP research: visualization, colocalization, and quantification of NPs and antigens [42]. The purpose of immunogold labeling is to localize pools of proteins and lipids or to identify structures that cannot be clearly identified or cannot be seen at all at high resolution. This gold particle is visible under the TEM due to its electron density. In contrast to light microscopy, this method allows the localization of antigens in association with subcellular structures at the nanometer level.

Despite its wide use in NP research, as previously described, TEM is a sole tool used for the qualitative or quantitative evaluation of the cellular localization of NPs with fixed cells, which could not perform analysis with live-cell dynamics.

9.3.4 Elemental Detection for Cellular NPs

Another quantitative approach is inductively coupled plasma–mass spectrometry (ICP-MS). As a standard technique in elemental analysis, ICP-MS has become one of the most commonly used tools for determination of total concentration of inorganic NP suspensions [43]. ICP-MS is a powerful tool for intracellular quantification of electron-dense materials and is a sensitive method for detecting elements with the exception of H, C, O, N, F, S, and inert gases. However, loading NPs with a heavy metal may make use of ICP-MS possible in such cases, as long as the physicochemical properties of the particles are not changed by the loading procedure. Through direct analysis of an appropriately diluted solution containing NPs, the NPs can be counted. If the NPs consist of just one element, peak height, proportional to the size of the NP, can be used to determine the NP diameter. Although both strategies benefit from the high sensitivity of ICP-MS detection, the single-particle approach limit of particle size detection is actually governed by the signal-to-noise ratio [41], even though this method provides a powerful tool for the characterization of most metal-based NPs in cells, which need special treated with sample. A comparison of different sample preparation procedures was conducted, including microwave-assisted digestion, acidification, and dilution in ultrapure water. In fact, without any further sample preparation, it is very likely that imprecise results and/or instabilities of the measurements occur. Even though for some NP suspensions (e.g., Ag, CeO_2, or Au NPs), acidification was identified as an optimal practice, microwave-assisted digestion can be taken as a universally reliable method.

Detailed description of ICP-MS and its applications can be found in Chapter 2 of this book.

9.4
Representative Cellular Uptake of Nanomaterials and Intracellular Location Determined with Different Methods

9.4.1
Effect of Nanomaterials on Cellular Lipid Membrane for Uptake

Both cytotoxicity and NP uptake are dependent upon direct contact with the cell membrane. Current hypothesized cytotoxicity mechanisms include the following: disruption of intracellular metabolic pathways, oxidative stress, and physical membrane damage. Previous studies indicate that direct contact of nanomaterials such as carbon-based and inorganic engineered NPs with cells resulted in cell inactivation or damage [27]. For example, we used a rat 3T3 L1 fibroblast cell line for analyzing the cellular uptake processes of $[C_{60}(C(COOH)_2)_2]_n$ NPs [27, 44]. AFM images shows the typical "bumpy" surface of the 3T3 L1 fibroblast. After exposure to $[C_{60}(C(COOH)_2)_2]_n$ NPs for 30 min, the shape of invagination appeared obviously in the surface of the cellular membrane. Further, cells were scanned with an environmental scanning electronic microscopy (ESEM) for specific interaction of functional NPs with cell membrane observation [44]. The potent advantage to using ESEM is that it is not necessary to make a nonconductive sample conductive. Cell samples do not need to be coated with gold–palladium such as SEM, and thus, their original characteristics may be preserved for observation.

The phospholipid membrane of cells regulates the transport of molecules into the cells, thereby representing a universal barrier protecting fragile intracellular structures from extracellular materials. Real cell membranes are very complex structures and consist of an asymmetric lipid bilayer comprising several types of lipids with embedded proteins. Production of such complex structures in lab is difficult. Therefore, model biological membranes can be employed for systematic investigations of NP–membrane interactions. Phospholipid vesicles are one of the most commonly and widely studied bilayer model systems. These models will be suited to study the NP–membrane interactions including the man-made phospholipid membrane liposomes such as large unilamellar vesicles (LUVs), small unilamellar vesicles (SUVs), and multilamellar vesicles (MLVs). The assembly of lipids into unilamellar vesicles suspended in an aqueous medium can occur in a variety of ways. This includes the following: sonication of an aqueous dispersion of phospholipids, detergent analysis, and reverse-phase evaporation. Lipids are commonly associated with spherical and nonspherical vesicles, generally by detachment of bilayer fragments. Using these models, we enabled diffused phosphatidylcholine and phosphatidylethanolamine (PC/PE) artificial lipid monolayers to simulate the permeability of fullerene membranes. We then inserted small $C_{60}(C(COOH)_2)_2$ NPs (about 1–10 nm) into PC/PE-containing phospholipid monolayers. Then we investigated how fullerene-mixed bilayer membranes in LUV liposomes influence the leakage of FITC-dextran. Results showed that the fluorescence ratios were much higher than those for liposomes

alone, indicating that man-made fullerene-mixed bilayer membranes decrease membrane permeability to FITC-dextran [33].

9.4.2 Cellular Uptake of Nanomaterials by Endocytosis

All types of cells in the body use the endocytosis process to communicate with the biological environments. This process is an energy-dependent process through which cells internalize ions and biomolecules [45]. The cellular uptake pathways of NPs have direct consequences on its intracellular localization; hence, understanding of the endocytosis mechanisms of NPs will advance our understanding on the biological effects of nanomaterials.

The classically described route for the transportation of proteins into cells is via clathrin-coated pits, where proteins bind to specific receptors on the cell surface, and these ligand–receptor complex clusters are internalized in an energy-dependent manner by clathrin-coated membrane vesicles. The clathrin-mediated endocytic pathway is initiated when clathrin-coated vesicles bud into the cytoplasm, following NP internalization, the clathrin coat disassembles and the vesicle fuses with other newly uncoated vesicles to form early endosome. NPs with a size of 120–150 nm are internalized within clathrin-coated vesicles entering the endosomal/lysosomal trafficking route [46–48]. Then, some ligands are released from their receptors in the acidic early endosome; further fusion with incoming endocytic vesicles is sorted away from soluble ligand in the "sorting endosome." Some receptors interact with a second set of cytosolic proteins and ultimately sort them into domains that invaginate into the central vacuole, creating a multivesicular endosome.

The upper size limit reported for particles entering the cell via this pathway is about 200 nm. Clathrin-mediated endocytosis is either adsorptive or receptor-mediated. Cationic particles or proteins bind nonspecifically to the negatively charged cell surface. This triggers adsorptive clathrin-mediated endocytosis. In addition, the receptor-mediated process is highly selective and specific. Receptor ligands being internalized by this way are low-density lipoprotein (LDL), transferrin, growth factors, and insulin.

Otherwise, vesicles, or phagosomes, mature by several fission and fusion events with late endosomes and lysosomes, resulting in the formation of phagolysosomes. Internalized particles are subsequently degraded, and the receptors are cycled back to the cell surface. The rate of these successive events depends greatly on the ingested particle and typically lasts from 30 min to several hours. Nanomaterials taken up as agglomerate tend to be less easily degraded by the host as they can be detected in macrophages for several months, thus bearing a risk of long-term toxicity [49, 50].

The intracellular vesicles either gradually mature (acidify) to late endosomes through multiple fission and fusion events or are recycled back to the cellular surface as trafficking endosomes. Nanomaterials entrapped in late endosomes are likely to proceed to lysosomes where they are degraded. These compartments

harbor proteases, hydrolases, and other enzymes promoting degradation of NPs. However, some NPs (in particular positively charged, basic NPs) are capable of escaping the endosome. This phenomenon has previously been described as the "proton sponge effect." Other NPs (e.g., certain types of carbon nanotubes) penetrate the vesicle (or cell) membrane directly and enter the cytosol. Once in the cytosol, NPs may induce the production of reactive oxygen species and inflict oxidative stress. Effects that may be harmful for a healthy cell are desired in tumor cells, where an endosomal escape is needed to deliver a specific nanoparticulate drug to its intracellular compartment of action.

In addition, in some NPs such as semiconductor quantum dots (QDs), it was found that NPs aggregate during the uptake process, forming clusters inside cells that are able to enter the cell nucleus [51]. NP uptake is dependent on surface functionalization and can be hindered by increasing the strength of the adhesion force between NPs and the surface. Studying the time-dependent uptake, it was shown that particles are able to exit cells [4]. The electron micrographs revealed a uniform intracellular distribution of Ag NPs both in cytoplasm and in nucleus. Ag NP treated cells exhibited chromosome instability and mitotic arrest in human cells, which have potentially toxic interactions with other cellular organelles, such as mitochondria and the cell nucleus [52].

9.4.2.1 Fullerene and Carbon Nanotubes

Fullerene and its derivatives are typical engineered nanomaterials. Recently, we found that $C_{60}(C(COOH)_2)_2$ NPs entered into cells involving clathrin-dependent endocytosis, and these fullerene NPs were mainly located within the lysosomes (Figure 9.3) [27, 33]. In addition, gadolinium endohedral metallofullerenol $[Gd@C_{82}(OH)_{22}]_n$ NPs possessed strong anticancer effects against the growth of tumor, but without observable toxicity *in vivo* and *in vitro* [53]. Also, these metallofullerenol NPs mainly internalized in cells by endocytosis.

Due to the unique mechanical and chemical properties, carbon nanotubes are used with increasing frequency in application for delivery, antitumor neuroengineering, and ion nanoprobe. Meanwhile, the hazard for health and cytotoxicity of carbon nanotubes exposure are still argued.

The intracellular locations of NPs directly affect their cellular function. The kinetic uptake of COOH-polystyrene sphere (PS) NPs and ssDNA-SWCNTs in SKN-SH cells was investigated by costained with organelle-specific fluorescent probes, namely Lyso Tracker® Red DND-99 and Lyso Sensor® Green DND-189 by LCSM. Our results showed that COOH-PS NPs and ssDNA-SWCNTs aggregates are endocytosed by living cells and mainly located in the lysosomes [54]. The fluorescence of the COOH-PS NPs and ssDNA-SWCNTs was located punctately in the lysosome costained with organelle-specific fluorescent probes in 24 h. Therefore, it is clearly shown that ssDNA-SWCNTs could cross cell membranes by cellular endocytosis and localize in intracellular compartments.

9.4.2.2 Polystyrene Nanoparticles

Polystyrene spheres [55] have been shown to be engulfed and actively transported throughout the cell and provide a reliable way to perform long-term

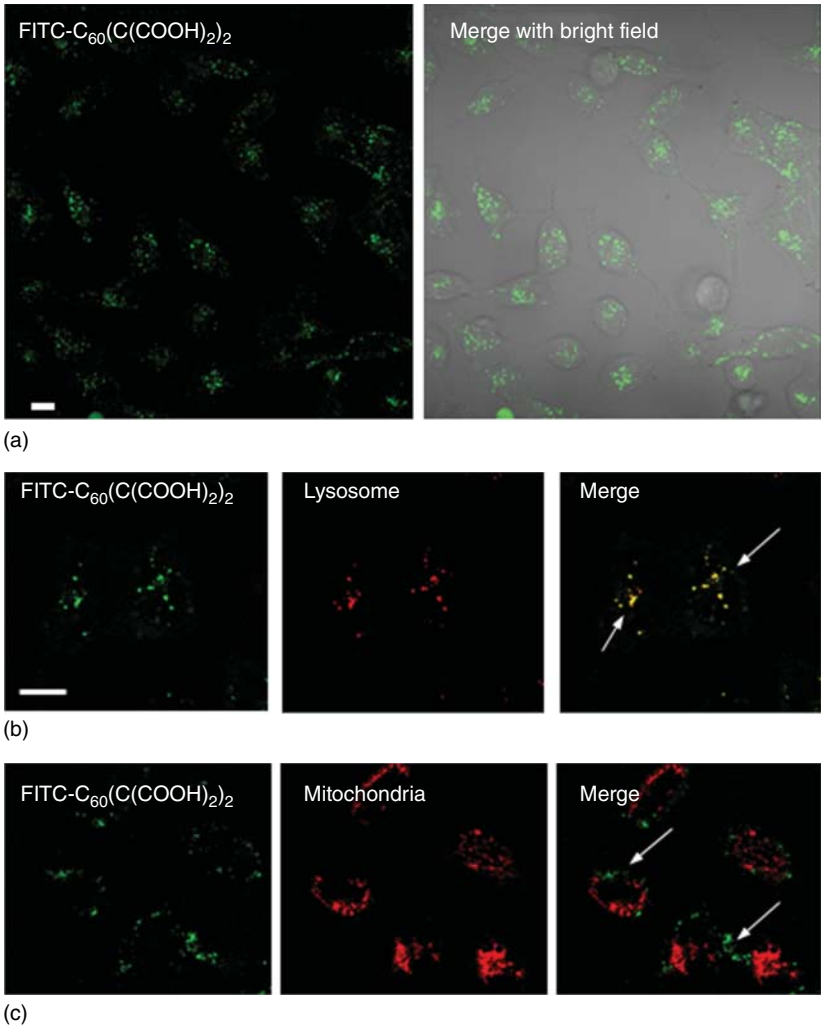

Figure 9.3 Confocal microscopic images show the subcellular localization of FITC-$C_{60}(C(COOH)_2)_2$ mainly in the lysosome. (a). FITC-$C_{60}(C(COOH)_2)_2$ (green fluorescence) were uptake by HeLa cells. (b). Punctate co-localization of FITC-$C_{60}(C(COOH)_2)_2$ with Lyso Tracker Red. (c). $C_{60}(C(COOH)_2)_2$ nanoparticles are not located in mitochondria. Bar: 10 μm. (Reprinted with permission from [33]. Copyright (2011) Elsevier Ltd.)

cell monitoring and imaging such as monitoring of enzymatic activity or drug delivery, and thus, they have been widely used in research on probing, detecting, imaging, and drug delivery system *in vivo* and *in vitro*.

Kim *et al.* [56] studied the accumulation of PS NPs in A549 cells (human lung carcinoma) that cultured with carboxylated polystyrene NPs (PS-COOH) with diameters of 40 nm, fluorescently labeled with a yellow-green dye similar to fluorescein isothiocyanate. NPs were found to enter the cells, and the overlap between

the red fluorescence from lysosomes labeled with LAMP1 antibody and the green fluorescence from the NPs indicates that the NPs accumulated in the lysosomes. We examined the fate of polystyrene NPs of different diameters (50, 100, and 500 nm) modified with carboxyl groups (COOH-PS) or amino groups (NH_2-PS) in dividing cells of normal and cancer cell lines and pointed out for the first time that all the fluorescent PS NPs differing in size and/or charge did not interact with chromosome reorganization and cytoskeleton assembly during the mitotic process in living cells (Figure 9.4) [34].

9.4.2.3 Au Nanomatrials

Gold nanorods (Au NRs) are promising nanomaterials for applications in biomedicine such as photoacoustic imaging [57]. Due to their high electron density, the cellular Au NRs are visible by TEM. In our study, we found that Au NRs entered the A549 cells and located in subcellular structures including the cytoplasm, endosomes/lysosomes, and mitochondria. Consistent with other reports, Au NRs were not detected in the nucleus, thus ruling out the possibility of genotoxicity. The amount of Au NRs internalized and their distribution was time-dependent. Au NRs were first located close to the plasma membrane (at 1.5 h) and then were trafficked to endosomes and lysosomes (at 3 h). During 24 h, more Au NRs entered and filled the endosomes/lysosomes [41].

9.4.2.4 Metallic Oxide NPs

Cellular metallic oxide nanomaterials such as CeO_2, TiO_2, and ZnO could be detected by TEM and ICP-MS [58, 59]. Using TEM, Chen *et al.* [60] found that there were more CeO_2 NPs in the cellular cytoplasm than ZnO when incubating the HUVECs cells. This data agreed with the findings of ICP-MS: the uptake quantity of CeO_2 NPs was about 100 times higher than that of $ZnCl_2$ or ZnO NPs. Furthermore, the number of mitochondria was significantly decreased, which correlated to the decreased activity of the cells, but had more obvious ERs showing a phenomenon of aggregation or swelling in ZnO NP treated cells than for control and CeO_2 NP treated groups. ZnO NPs will decrease the cellular activity and take much more cellular internal damage especially to the ER compared to CeO_2 NPs, although it is not easy to scan the ZnO NPs by TEM.

9.4.2.5 Quantum Dots

QDs are inorganic semiconductor nanocrystals (2–6 nm), whose unique fluorescence properties (strong, sharp, stable, and size-tunable emission) make them attractive biolabels when they are suitably functionalized with biomolecules such as protein and DNA [61, 62]. The surface coating, size, and charge of QD NPs are important parameters in determining how NP uptake occurs in mammalian cells for the cellular toxicity evaluation.

Zhang *et al.* [63] reported a novel optical probe specific to full collapse fusion, capitalizing on the size and superior photoproperties of photoluminescent QDs. QDs with exposed carboxyl groups were readily taken up by synaptic vesicles in an activity-, Ca^{2+}, and clathrin-dependent manner. QD were internalized into early endosomes and then transferred to late endosomes or lysosomes. Electron microscopy imaging showed that QDs were harbored within individual vesicles.

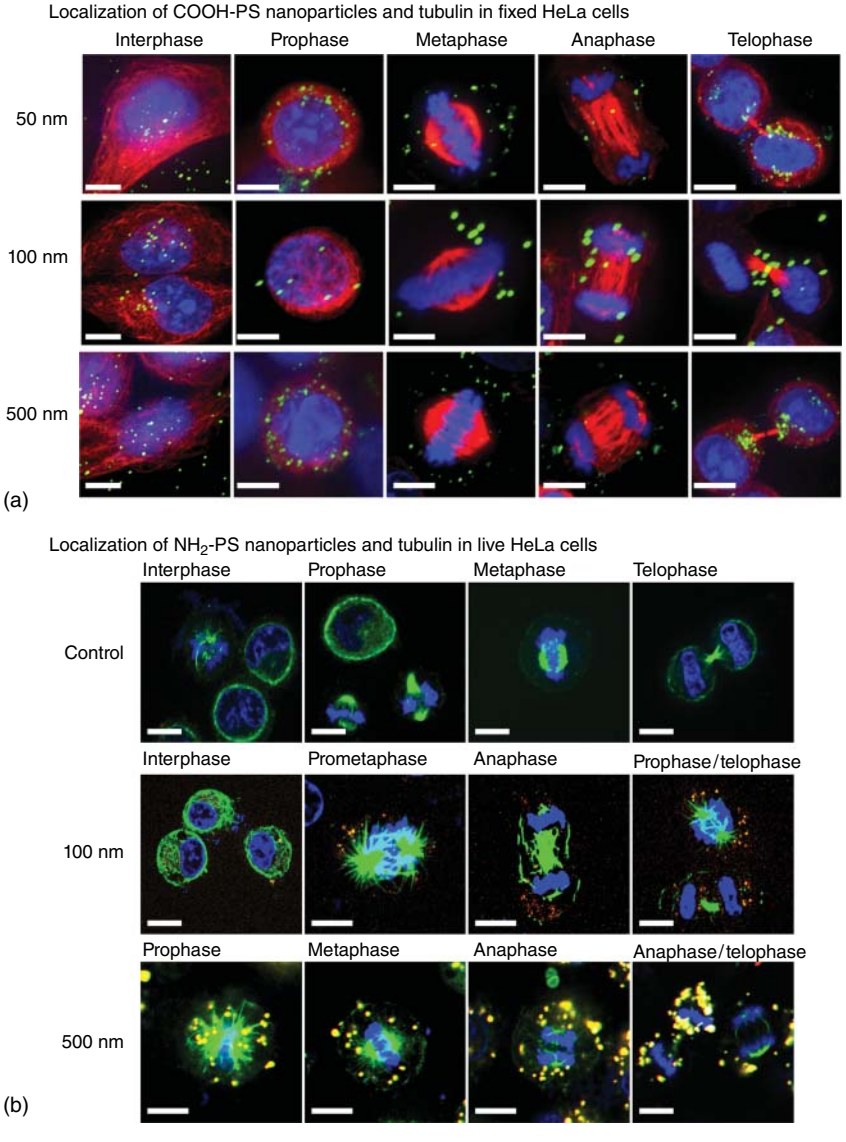

Figure 9.4 Confocal microscopy study of the localization of PS NPs and tubulin in HeLa cells at different phases of mitosis. (a) Colocalization of COOH-PS NPs (green) with tubulin (CY-3-microtubulin antibody, red) after incubation for 24 h in fixed cells. (b) Colocalization of NH2-PS NPs (orange) with tubulin (TubulinTracker Green, Oregon Green 488 Taxol, bis-acetate) in live cells. The nuclei were stained with Hoechst 33342 (blue). Scale bar: 10 μm. (Reprinted with permission from [34]. Copyright (2011) Elsevier Ltd.)

In addition, clathrin-mediated endocytosis is the most important pathway for the intracellular delivery of peptide-conjugated QDs. For example, neuropeptide conjugated with CdSe-ZnS QDs was investigated in the intracellular delivery of the conjugate in living cells such as human epidermoid ovarian carcinoma cells (A431) and mouse embryonic fibroblast cells (3T3). It was found that neuropeptide conjugated with CdSe-ZnS QDs could efficiently deliver QDs in living mammalian cells [64].

9.4.3 Endocytosis Inhibitors for Uptake Study

To study the entry route of specific nanomaterials, physical and pharmacological blockers may be used comprehensively. For example, the internalization of the nanocrystals by HeLa and SW1353 cells is almost completely blocked by the pinocytosis inhibitors filipin, cytochalasin B, and actinomycin D [65]. Using several pharmacological inhibitors, it is demonstrated that the cellular uptake mechanisms of cationic Au NPs in both cancer and normal cells strongly depend on the NP surface monolayer and mostly involve caveolae and dynamin-dependent pathways as well as specific cell surface receptors. Another example, in order to understand whether the differences in cytotoxicity were dependent on amount of Au NRs internalized, the process of NP uptake was quantitatively investigated using ICP-MS [41] (Figure 9.5a).

The three main modes of endocytosis including clathrin-mediated, caveolae/lipid-raft-mediated, and macropinocytosis/phagocytosis would be determined by specific inhibitors. Chlorpromazine and hypertonic challenge with sucrose are specific inhibitors of clathrin-mediated endocytosis, and they strongly constrained endocytosis in three cells by more than 75% and 80%, respectively (Figure 9.5b). It demonstrates that the main pathway is clathrin-mediated. Specific treatment such as cholesterol depletion from membrane structures can also be employed to study lipid-raft-mediated endocytosis. Here, nystatin and methyl-β-cyclodextrin (MβCD) inhibited endocytosis by at least 54% and 48%, showing that lipid-raft-mediated endocytosis is a secondary pathway for internalization of Au NRs. Dynamin, a GTP-dependent enzyme, forms a coil-like structure around the neck of invaginations on the plasma membrane and takes part in the hydrolysis of GTP and the process of pinching of vesicles. Dynasore, a specific inhibitor of dynamin-mediated lipid-raft endocytosis, strongly decreased internalization of Au NRs by 42%, indicating that the dynamin-mediated pathway represents the major mechanism for lipid-raft-dependent endocytosis in both cell types. Therefore, both clathrin- and lipid-raft-dependent (dynamin mediated) endocytosis pathways are involved in the internalization of Au NRs in A549, 16HBE, and MSC cells. The process of removal of Au NRs was quite different for the three types of cells (Figure 9.5c).

The clathrin-mediated endocytosis is sensitive to potassium depletion and hypertonicity, while both clathrin-mediated and caveolae-dependent endocytoses are sensitive to cholesterol depletion. Therefore, the effects of potassium

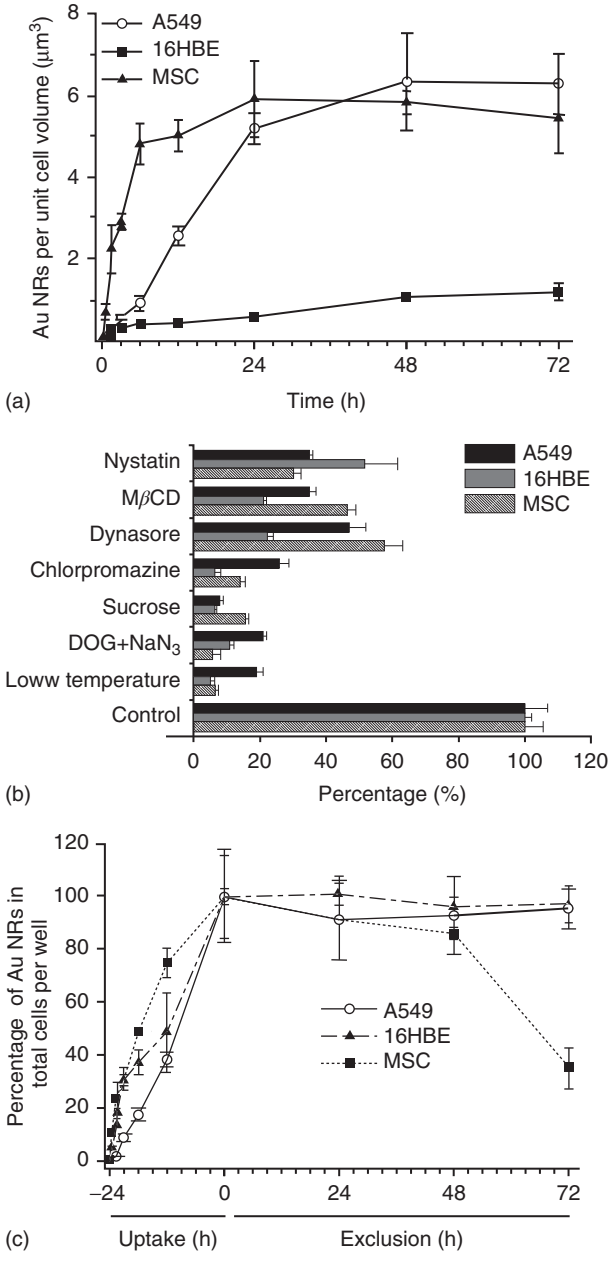

Figure 9.5 Uptake pathways and quantitative process of internalization and removal of Au NRs in A549, 16HBE, and MSC cells by ICP-MS after treated with Au NRs. (a, c) The process of cellular internalization and exclusion of Au NRs, respectively. (b) Uptake pathways for Au NRs in two types of cells using specific endocytosis inhibitors. (Reprinted with permission from [41]. Copyright (2011) American Chemical Society.)

depletion, hypertonicity, and cholesterol depletion on the transportation of NP internalization were investigated by traditional biochemical techniques and confocal imaging techniques [27]. In addition, the caveolae flask-like structures invaginate with the help of dynamin from hydrophobic membrane domains, which are rich in cholesterol and glycosphingolipids in lipid rafts. So, to investigate the relationship of nanomaterials with caveolae, lipid-raft-rich domains were disrupted by depleting cholesterol with MβCD, which is widely used as a lipid-raft-disrupting agent.

Moreover, the actin and microtubule cytoskeleton play an essential role in several of nanomaterial uptake processes [66]. Some actin inhibitors were used as endocytosis blockers such as staurosporine, Latrunculin A, and cytochalasin D. Staurosporine could lead to dephosphorylation and activation of cofilin, so to affect the actin dynamic polymerization, cytochalasin D and Latrunculin A could cause actin filament disassembly by different mechanisms. Nocodazole, a microtubule inhibitor, was found to decrease QD uptake and QD colocalization with EEA1 by confocal imaging. With FCM, nocodazole showed a significant reduction in QD uptake with a dose-dependent inhibitory effect.

Cytochalasin A can disrupt actin filaments (F-actin) polymerization and inhibit the endocytosis of 40 nm particles and 200 nm particles. It was shown that the involvement of actin filaments has an important role in endocytosis of NPs [66]. However, contrary to large particles, small particle size displays less dependency to F-actin related uptake.

Yet, all methods used to induce a physical and pharmacological block of uptake pathways have certain limitations. Most pharmacological inhibitors are not specific and may influence alternative internalization routes and actin cytoskeleton, and some inhibitors are known to induce cytotoxicity at high concentrations [67]. Moreover, compensatory routes of uptake may be activated in target cells upon inhibition of specific transport pathways. Otherwise, it should be taken into account that different cell lines have different uptake strategies.

9.4.4
Actin-Polymerization-Dependent Uptake

F-actin and intermediate filaments are components of the cytoskeleton of the majority of eukaryotic cells. Cytoskeleton is crucial for many cellular functions, such as mitosis, cytokinesis, cell motility, muscle contraction, maintenance of cell shape, endocytosis, intracellular trafficking, and protein secretion. During the past two decades, much attention has been focused on the regulation of membrane traffic by the actin and microtubule cytoskeletal network, including their molecular motor myosin, which moves on actin filaments, dyneins, and kinesins, which use microtubules as tracks [68, 69].

Previously, the actin cytoskeleton and the endocytic machinery were thought to operate independently. However, there is growing evidence that F-actin plays a direct role during endocytic internalization NPs [13]. Actin assembly can create protrusions that encompass extracellular materials. Actin can also support the

processes of invagination of a membrane segment into the cytoplasm, elongation of the invagination, scission of the new vesicle from the plasma membrane, and movement of the vesicle away from the membrane.

As far as cellular uptake and intracellular trafficking are concerned, actin polymerization is a determinant for the formation of phagosomes and macropinosomes, and several myosin isoforms are involved in these processes [16]. As in phagosomes, actin drives the formation of membrane protrusions that collapse onto and fuse with the plasma membrane, forming large endocytotic vesicles called *macropinosomes* for uptake of NPs [20]. In clathrin-mediated endocytosis, actin polymerization and class I myosins generate membrane invagination, coated-pit formation, conscription, and vesicle scission. More recently, it has been suggested that the F-actin network and associated molecular motors such as myosins might be involved in uptake of nanomaterials. Otherwise, receptor ligation is the beginning of a signaling cascade that triggers actin assembly, forming cell surface extensions that zipper up around the particle and engulf it.

Thus, the cytoskeleton plays an important role in multiple cellular events, including endocytosis and trafficking of endocytosis vesicles. Both F-actin and microtubules are essential in most of the uptake mechanism.

9.4.5 Cellular Uptake of NPs by Membrane Penetration (or Passive Fusion)

In addition to intruding cells by active transport, NPs may also enter cells by passive penetration of the cell membrane [70]. Small NPs have a higher probability to be internalized by passive uptake than large ones. Under otherwise identical conditions, small NPs are more likely to cause toxic cellular responses. Passive transport has been understood in the context of Overton's rule, which states that more lipophilic molecules cross membrane lipid bilayers more readily.

In fact, for cells lacking the endocytosis machinery such as red blood cells (RBCs), passive transport is the only option. The impact of NP size on passive cellular internalization and intracellular localization was highlighted. RBCs lack a cell nucleus, most organelles, and, most importantly, the endocytic machinery. Therefore, they have become valuable as a model system to investigate passive NP uptake [25]. In 2005, Geiser *et al.* [71] analyzed the uptake of PS NPs by RBCs and found that less than 200 nm but not 1 μm NPs enter RBCs. Rothen-Rutishauser and coworkers [72] refined the study and exposed RBCs to NPs of different material, size, and surface charge and visualized them inside RBCs using LCSM in combination with digital data restoration, conventional TEM, and energy filtering TEM. A quantitative analysis revealed that only the size determined the uptake efficiency. They confirmed that particles less than 200 nm could enter RBCs. The overall numbers were extremely small, however, with less than 1 particle per cell on average.

9.5 Summary and Outlook

Nanomaterials of different sizes and surface charges enter into cells in different ways *in vitro*, mainly in endocytosis and passive transport diffusion. The fates of most of them are translocated into the endosome and lysosome organelles in the pathway for degrading and releasing after internalized in cells. Few nanomaterials could be located in the mitochondria and the cell nucleus. In these studies, nanomaterials internalized by cells were mainly determined by fluorescent confocal imaging, TEM, and FCM techniques in fixed cells and live cells. However, some issues have to be solved in the future to further understand the relationship of cellular uptake of NPs with the nanocytotoxicity. First, we need much more sensitive methods to detect the cellular nanomaterials in live cells. And a second is how to analyze the internalized nanomaterials transport out of cellular membrane and exocytosis.

However, in the case of nanomaterials, there are only small parts of single particles, which largely exist with aggregated clusters under physiological conditions. Taking the properties of NPs into account, such as the smaller size, larger number of particles, and unique surface nature, the interactions between NPs and biological systems should be different from those between individual molecules. Do NPs traverse the cell membrane through the similar ways that the small molecule and/or macromolecule used to enter the cells or have completely different and unknown ways? These are now generally unclear but of great significance, which need the advanced detection methods to characterize them accurately.

References

1. Wang, Z., Tiruppathi, C., Minshall, R.D. *et al.* (2009) Size and dynamics of caveolae studied using nanoparticles in living endothelial cells. *ACS Nano*, **3**, 4110–4116.
2. Nishikawa, T., Iwakiri, N., Kaneko, Y. *et al.* (2009) Nitric oxide release in human aortic endothelial cells mediated by delivery of amphiphilic polysiloxane nanoparticles to caveolae. *Biomacromolecules*, **10**, 2074–2085.
3. Lai, S.K., Hida, K., Man, S.T. *et al.* (2007) Privileged delivery of polymer nanoparticles to the perinuclear region of live cells via a non-clathrin, non-degradative pathway. *Biomaterials*, **28**, 2876–2884.
4. Kettiger, H., Schipanski, A., Wick, P. *et al.* (2013) Engineered nanomaterial uptake and tissue distribution: from cell to organism. *Int. J. Nanomed.*, **8**, 3255–3269.
5. Yameen, B., Choi, W.I., Vilos, C. *et al.* (2014) Insight into nanoparticle cellular uptake and intracellular targeting. *J. Controlled Release*, **190**, 485–499.
6. Nel, A.E., Madler, L., Velegol, D. *et al.* (2009) Understanding biophysicochemical interactions at the nano-bio interface. *Nat. Mater.*, **8**, 543–557.
7. Soenen, S.J. and De Cuyper, M. (2010) Assessing iron oxide nanoparticle toxicity in vitro: current status and future prospects. *Nanomedicine (London)*, **5**, 1261–1275.
8. Sahay, G., Alakhova, D.Y., and Kabanov, A.V. (2010) Endocytosis of nanomedicines. *J. Controlled Release*, **145**, 182–195.

9. Zhao, Y., Xing, G., and Chai, Z. (2008) Nanotoxicology: are carbon nanotubes safe? *Nat. Nanotechnol.*, **3**, 191–192.
10. Cooper, G.M. (2000) *The Cell: A Molecular Approach*, ASM Press.
11. Alberts, B., Johnson, A., Lewis, J. *et al.* (2002) *Molecular Biology of the Cell*, 4th edn, International Student Edition, Routledge.
12. Zhao, F., Zhao, Y., Liu, Y. *et al.* (2011) Cellular uptake, intracellular trafficking, and cytotoxicity of nanomaterials. *Small*, **7**, 1322–1337.
13. Shang, L., Nienhaus, K., and Nienhaus, G.U. (2014) Engineered nanoparticles interacting with cells: size matters. *J. Nanobiotechnol.*, **12**, 5.
14. Lanyi, J.K. (1997) Mechanism of ion transport across membranes. Bacteriorhodopsin as a prototype for proton pumps. *J. Biol. Chem.*, **272**, 31209–31212.
15. Kumari, S., Mg, S., and Mayor, S. (2010) Endocytosis unplugged: multiple ways to enter the cell. *Cell Res.*, **20**, 256–275.
16. Conner, S.D. and Schmid, S.L. (2003) Regulated portals of entry into the cell. *Nat. Geosci.*, **422**, 37–44.
17. Johannes, L. and Lamaze, C. (2002) Clathrin-dependent or not: is it still the question? *Traffic*, **3**, 443–451.
18. Aderem, A. and Underhill, D.M. (1999) Mechanisms of phagocytosis in macrophages. *Annu. Rev. Immunol.*, **17**, 593–623.
19. Bratosin, D., Mazurier, J., Tissier, J.P. *et al.* (1998) Cellular and molecular mechanisms of senescent erythrocyte phagocytosis by macrophages. A review. *Biochimie*, **80**, 173–195.
20. Panariti, A., Miserocchi, G., and Rivolta, I. (2012) The effect of nanoparticle uptake on cellular behavior: disrupting or enabling functions? *Nanotechnol. Sci. Appl.*, **5**, 87–100.
21. Pelkmans, L. and Helenius, A. (2002) Endocytosis via caveolae. *Traffic*, **3**, 311–320.
22. Rejman, J., Oberle, V., Zuhorn, I.S. *et al.* (2004) Size-dependent internalization of particles via the pathways of clathrin- and caveolae-mediated endocytosis. *Biochem. J.*, **377**, 159–169.
23. Martinez, J.R. (1987) Ion transport and water movement. *J. Dent. Res.*, **66** Spec No:, 638–647.
24. Cho, E.C., Zhang, Q., and Xia, Y. (2011) The effect of sedimentation and diffusion on cellular uptake of gold nanoparticles. *Nat. Nanotechnol.*, **6**, 385–391.
25. Treuel, L., Jiang, X., and Nienhaus, G.U. (2013) New views on cellular uptake and trafficking of manufactured nanoparticles. *J. R. Soc. Interface*, **10**, 20120939.
26. Nuutila, J. and Lilius, E.M. (2005) Flow cytometric quantitative determination of ingestion by phagocytes needs the distinguishing of overlapping populations of binding and ingesting cells. *Cytometry A*, **65**, 93–102.
27. Li, W., Chen, C., Ye, C. *et al.* (2008) The translocation of fullerenic nanoparticles into lysosome via the pathway of clathrin-mediated endocytosis. *Nanotechnology*, **19**, 145102.
28. Li, W., Liu, R., Wang, Y. *et al.* (2013) Temporal techniques: dynamic tracking of nanomaterials in live cells. *Small*, **9**, 1585–1594.
29. Nakano, A. (2002) Spinning-disk confocal microscopy–a cutting-edge tool for imaging of membrane traffic. *Cell Struct. Funct.*, **27**, 349–355.
30. Watson, J.V. (1987) Flow cytometry in biomedical science. *Nat. Geosci.*, **325**, 741–742.
31. Reno, F., Carniato, F., Rizzi, M. *et al.* (2013) Flow cytometry evidence of human granulocytes interaction with polyhedral oligomeric silsesquioxanes: effect of nanoparticle charge. *Nanotechnology*, **24**, 185101.
32. Ibuki, Y. and Toyooka, T. (2012) Nanoparticle uptake measured by flow cytometry. *Methods Mol. Biol.*, **926**, 157–166.
33. Li, W., Zhao, L., Wei, T. *et al.* (2011) The inhibition of death receptor mediated apoptosis through lysosome stabilization following internalization of carboxyfullerene nanoparticles. *Biomaterials*, **32**, 4030–4041.
34. Liu, Y., Li, W., Lao, F. *et al.* (2011) Intracellular dynamics of cationic and anionic polystyrene nanoparticles without direct interaction with mitotic

spindle and chromosomes. *Biomaterials*, **32**, 8291–8303.
35. Torrano, A.A., Blechinger, J., Osseforth, C. *et al.* (2013) A fast analysis method to quantify nanoparticle uptake on a single cell level. *Nanomedicine (London)*, **8**, 1815–1828.
36. Ruthardt, N., Lamb, D.C., and Brauchle, C. (2011) Single-particle tracking as a quantitative microscopy-based approach to unravel cell entry mechanisms of viruses and pharmaceutical nanoparticles. *Mol. Ther.*, **19**, 1199–1211.
37. Hein, B., Willig, K.I., and Hell, S.W. (2008) Stimulated emission depletion (STED) nanoscopy of a fluorescent protein-labeled organelle inside a living cell. *Proc. Natl. Acad. Sci. U.S.A.*, **105**, 14271–14276.
38. Vaziri, A., Tang, J., Shroff, H. *et al.* (2008) Multilayer three-dimensional super resolution imaging of thick biological samples. *Proc. Natl. Acad. Sci. U.S.A.*, **105**, 20221–20226.
39. Jones, S.A., Shim, S.H., He, J. *et al.* (2011) Fast, three-dimensional super-resolution imaging of live cells. *Nat. Methods*, **8**, 499–508.
40. Gottstein, C., Wu, G., Wong, B.J. *et al.* (2013) Precise quantification of nanoparticle internalization. *ACS Nano*, **7**, 4933–4945.
41. Wang, L.M., Liu, Y., Li, W. *et al.* (2011) Selective targeting of gold nanorods at the mitochondria of cancer cells: implications for cancer therapy. *Nano Lett.*, **11**, 772–780.
42. Elsaesser, A., Barnes, C.A., McKerr, G. *et al.* (2011) Quantification of nanoparticle uptake by cells using an unbiased sampling method and electron microscopy. *Nanomedicine (London)*, **6**, 1189–1198.
43. Drescher, D., Giesen, C., Traub, H. *et al.* (2012) Quantitative imaging of gold and silver nanoparticles in single eukaryotic cells by laser ablation ICP-MS. *Anal. Chem.*, **84**, 9684–9688.
44. Lao, F., Chen, L., Li, W. *et al.* (2009) Fullerene nanoparticles selectively enter oxidation-damaged cerebral microvessel endothelial cells and inhibit JNK-related apoptosis. *ACS Nano*, **3**, 3358–3368.
45. Iversen, T.G., Skotland, T., and Sandvig, K. (2011) Endocytosis and intracellular transport of nanoparticles: present knowledge and need for future studies. *Nano Today*, **6**, 176–185.
46. Zhang, S., Li, J., Lykotrafitis, G. *et al.* (2009) Size-dependent endocytosis of nanoparticles. *Adv. Mater.*, **21**, 419–424.
47. Wang, S.H., Lee, C.W., Chiou, A. *et al.* (2010) Size-dependent endocytosis of gold nanoparticles studied by three-dimensional mapping of plasmonic scattering images. *J. Nanobiotechnol.*, **8**, 33.
48. Shan, Y., Ma, S., Nie, L. *et al.* (2011) Size-dependent endocytosis of single gold nanoparticles. *Chem. Commun. (Cambridge)*, **47**, 8091–8093.
49. Zhu, M.T., Feng, W.Y., Wang, Y. *et al.* (2009) Particokinetics and extrapulmonary translocation of intratracheally instilled ferric oxide nanoparticles in rats and the potential health risk assessment. *Toxicol. Sci.*, **107**, 342–351.
50. Wang, X., Xia, T., Ntim, S.A. *et al.* (2011) Dispersal state of multiwalled carbon nanotubes elicits profibrogenic cellular responses that correlate with fibrogenesis biomarkers and fibrosis in the murine lung. *ACS Nano*, **5**, 9772–9787.
51. Alberola, A.P. and Radler, J.O. (2009) The defined presentation of nanoparticles to cells and their surface controlled uptake. *Biomaterials*, **30**, 3766–3770.
52. Rothen-Rutishauser, B., Muhlfeld, C., Blank, F. *et al.* (2007) Translocation of particles and inflammatory responses after exposure to fine particles and nanoparticles in an epithelial airway model. *Part. Fibre Toxicol.*, **4**, 9.
53. Chen, C., Xing, G., Wang, J. *et al.* (2005) Multihydroxylated [Gd@C82(OH)22]n nanoparticles: antineoplastic activity of high efficiency and low toxicity. *Nano Lett.*, **5**, 2050–2057.
54. Wang, J., Liu, R., Su, Y. *et al.* (2014) Embedded carbon nanotubes nanoparticles in plasma membrane induce cellular calcium outflow imbalancing. *J. Nanosci. Nanotechnol.*, **14**, 4058–4065.
55. He, C., Hu, Y., Yin, L. *et al.* (2010) Effects of particle size and surface

charge on cellular uptake and biodistribution of polymeric nanoparticles. *Biomaterials*, **31**, 3657–3666.

56. Kim, J.A., Aberg, C., Salvati, A. *et al.* (2012) Role of cell cycle on the cellular uptake and dilution of nanoparticles in a cell population. *Nat. Nanotechnol.*, **7**, 62–68.
57. Wang, L.M., Jiang, X.M., Ji, Y.L. *et al.* (2013) Surface chemistry of gold nanorods: origin of cell membrane damage and cytotoxicity. *Nanoscale*, **5**, 8384–8391.
58. Johnston, B.D., Scown, T.M., Moger, J. *et al.* (2010) Bioavailability of nanoscale metal oxides TiO(2), CeO(2), and ZnO to fish. *Environ. Sci. Technol.*, **44**, 1144–1151.
59. Zhang, H., He, X., Zhang, Z. *et al.* (2011) Nano-CeO_2 exhibits adverse effects at environmental relevant concentrations. *Environ. Sci. Technol.*, **45**, 3725–3730.
60. Chen, R., Huo, L., Shi, X. *et al.* (2014) Endoplasmic reticulum stress induced by zinc oxide nanoparticles is an earlier biomarker for nanotoxicological evaluation. *ACS Nano*, **8**, 2562–2574.
61. Michalet, X., Pinaud, F.F., Bentolila, L.A. *et al.* (2005) Quantum dots for live cells, *in vivo* imaging, and diagnostics. *Science*, **307**, 538–544.
62. Larson, D.R., Zipfel, W.R., Williams, R.M. *et al.* (2003) Water-soluble quantum dots for multiphoton fluorescence imaging *in vivo*. *Science*, **300**, 1434–1436.
63. Zhang, Q., Cao, Y.Q., and Tsien, R.W. (2007) Quantum dots provide an optical signal specific to full collapse fusion of synaptic vesicles. *Proc. Natl. Acad. Sci. U.S.A.*, **104**, 17843–17848.
64. Anas, A., Okuda, T., Kawashima, N. *et al.* (2009) Clathrin-mediated endocytosis of quantum dot-peptide conjugates in living cells. *ACS Nano*, **3**, 2419–2429.
65. Alsharif, N.H., Berger, C.E.M., Varanasi, S.S. *et al.* (2009) Alkyl-capped silicon nanocrystals lack cytotoxicity and have enhanced intracellular accumulation in malignant cells via cholesterol-dependent endocytosis. *Small*, **5**, 221–228.
66. Kuhn, D.A., Vanhecke, D., Michen, B. *et al.* (2014) Different endocytotic uptake mechanisms for nanoparticles in epithelial cells and macrophages. *Beilstein J. Nanotechnol.*, **5**, 1625–1636.
67. Ivanov, A.I. (2008) Pharmacological inhibition of endocytic pathways: is it specific enough to be useful? *Methods Mol. Biol.*, **440**, 15–33.
68. Geraldo, S., Khanzada, U.K., Parsons, M. *et al.* (2008) Targeting of the F-actin-binding protein drebrin by the microtubule plus-tip protein EB3 is required for neuritogenesis. *Nat. Cell Biol.*, **10**, 1181–1189.
69. Torreano, P.J., Waterman-Storer, C.M., and Cohan, C.S. (2005) The effects of collapsing factors on F-actin content and microtubule distribution of Helisoma growth cones. *Cell Motil. Cytoskeleton*, **60**, 166–179.
70. Wang, T., Bai, J., Jiang, X. *et al.* (2012) Cellular uptake of nanoparticles by membrane penetration: a study combining confocal microscopy with FTIR spectroelectrochemistry. *ACS Nano*, **6**, 1251–1259.
71. Geiser, M., Rothen-Rutishauser, B., Kapp, N. *et al.* (2005) Ultrafine particles cross cellular membranes by nonphagocytic mechanisms in lungs and in cultured cells. *Environ. Health Perspect.*, **113**, 1555–1560.
72. Rothen-Rutishauser, B.M., Schurch, S., Haenni, B. *et al.* (2006) Interaction of fine particles and nanoparticles with red blood cells visualized with advanced microscopic techniques. *Environ. Sci. Technol.*, **40**, 4353–4359.

10
Methods and Techniques in Molecular Toxicology of Nanomaterials

Yanli Wang, Chenchen Li, and Chunying Chen

10.1
Introduction

Nowadays, nanotechnology, life science, and information technology are the mainstream of scientific development [1, 2]. With the prefix of "Nano" becoming widely used in modern science and technology, nanotechnology has invaded into scientific literature and infiltrated into human's life [3–6]. As everyone knows, emerging technologies always bring benefits, but also may cause uncertainties and risks, especially for human health [7–13]. Nanotechnology, similarly to other emerging technologies, has brought both benefits and risks [4, 14–23]. Actually, over the past several years, dozens of studies and reports have suggested that nanomaterials may cause unique risks to organisms from bacteria to mammals [2, 10, 22, 24–34]. So, nanotoxicology emerges as the times require [35]. Recent developments in nanotechnology have provided series of new methods for detecting the toxicity induced by nanomaterials. Molecular toxicology is a discipline that focuses on molecular and cellular biology, in order to understand the functional mechanism of materials, drugs, chemicals and toxins, and so on, at the molecular, cellular, and biochemical levels [36, 37]. In the field of nanotechnology, it is used to study the interactions between the exogenous nanomaterials and organisms at the molecular level [38–40]. In 1983, an article entitled "Toxicology goes molecular" indicated that molecular toxicology had ushered in its vigorous development period [41]. With the development of modern analysis techniques, molecular toxicology has been a research hotspot and been widely used in nanotechnology such as to detect the DNA damage [42–46], chromosome damage [43], and gene expression changes [47, 48]. Recently, various kinds of molecular toxicology analytical techniques are adopted in nanotoxicology studies. In this chapter, we give a short introduction of these techniques in molecular toxicology, which has been widely used in nanotechnology (Figure 10.1).

Toxicology of Nanomaterials, First Edition. Edited by Yuliang Zhao, Zhiyong Zhang, and Weiyue Feng.

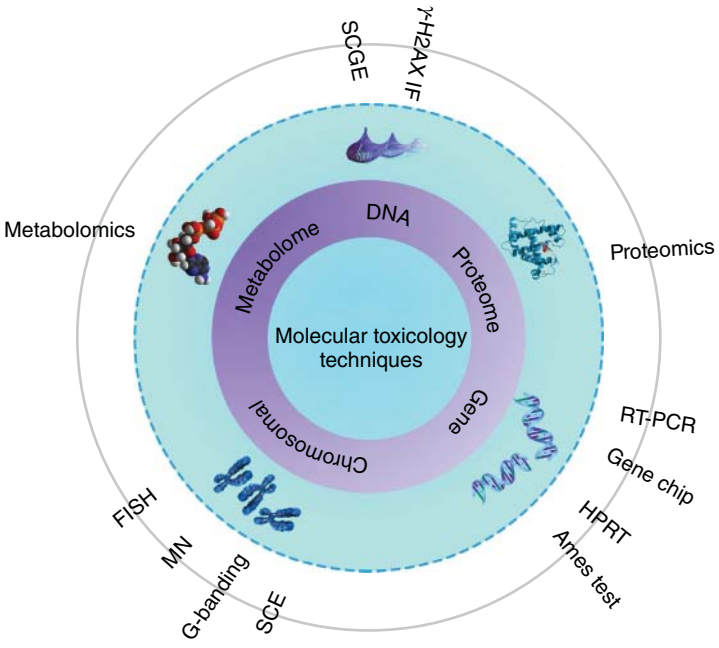

Figure 10.1 Schematic of widely applied techniques in molecular toxicology of nanomaterials.

10.2
Gene Mutation Detection

Gene mutation refers to the permanent variations of the nucleotide base pair composition or sequence [49, 50]. It may occur during any periods of cell growth, usually during DNA replication, namely interphase in cell division. It may be spontaneously or induced by mutagens [51]. In general, it has a tight connection with DNA replication [52–54], DNA damage [55], cancer [56–61], and other various heritable diseases [62–67]. There is extensive biological and toxicological significance for detecting gene mutation.

10.2.1
Ames Test

Ames test, also known as *Salmonella typhimurium* (*S. typhimurium*) reverse mutation assay, was found and described by Ames *et al.* [68–72]. Through protracted and unremitting efforts by researchers, it has been widely employed in many fields around the world [73–78]. It aims to assess the mutagenic potential of chemical compounds and gene mutation of the organism or cell [79].

10.2.1.1 Principle and Procedure

In principle, it is based on the characteristic of spontaneous reverse mutation in the *S. typhimurium*, which carries mutated genes concerned with histidine synthesis. These strains are auxotrophic mutants since they could not produce histidine. Generally, in a medium containing a trace of histidine, most of cells only divide several times, forming some microcolonies, which are only seen under the microscope except for a very few of cells. However, they will reverse mutation spontaneously to be prototroph when treated by mutagen. In addition, the strains also carry the genetic mutation involved in lipopolysaccharide synthesis, which makes the cell wall of the bacteria more permeable [70]. So it could reflect the mutagenic potential of the tested substance by the number and dimensions of the *Salmonella* colonies in a histidine-free medium. Generally, the methods of Ames test include plate incorporation assay and spot test. The completed procedure of plate incorporation assay is shown in Figure 10.2a.

10.2.1.2 Application in Nanotoxicology

Owing to its easy operation, fast, and sensitive, it has been used to evaluate the toxicology of nanomaterials by many researchers. Kumar *et al*. [80] explored the effects of ZnO nanoparticles (NPs) and TiO_2 NPs in *S. typhimurium* and

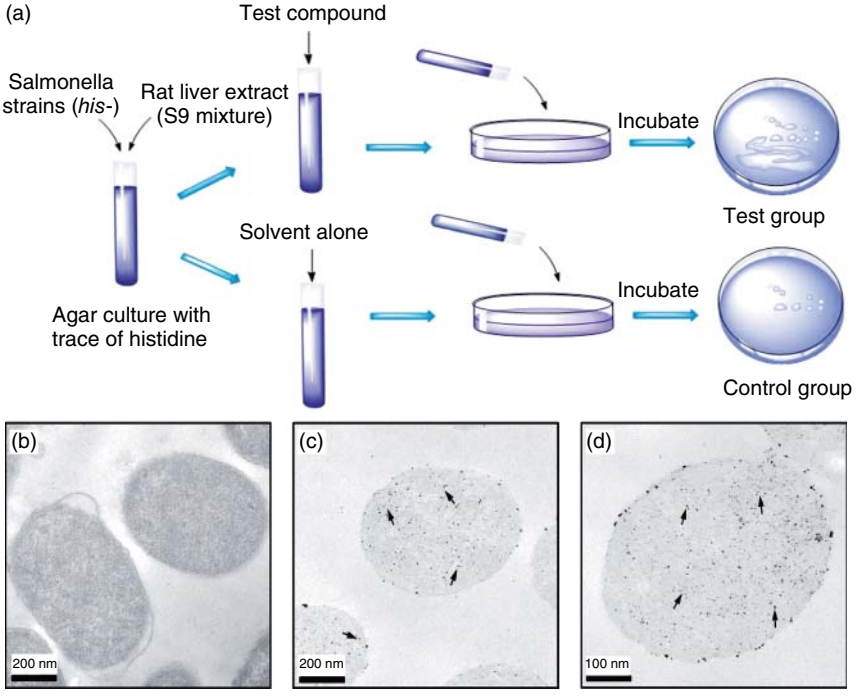

Figure 10.2 (a) Ames test procedure of plate incorporation assay method. (b–d) TEM microphotographs of *Salmonella typhimurium* TA98 showing: (b) control cell, (c) internalization of ZnO NPs, and (d) internalization of TiO_2 NPs [80]. (Copyright © 2011 Elsevier Ltd.)

found that ZnO NPs and TiO_2 NPs were internalized by *S. typhimurium* without agglomeration (Figure 10.2b–d). As the results show, the internalization is achieved in a concentration dependent manner, which is confirmed by flow cytometer. They finally concluded that TiO_2 NPs showed mutagenicity, whether metabolic activation (S9) was present or not. However, ZnO NPs exhibited mutagenic potential in the presence of metabolic activation (S9) only. As the Ames test result show, metal oxide NPs are likely to affect human somatic and germ cells leading to cancer and infertility. Shinohara *et al*. [81] conducted Ames test with *S. typhimurium* TA98, TA100, TA1535, TA1537 strains, and *Escherichia coli* strain with or without metabolic activation to assess the mutagenic potential of C_{60} NPs and found that C_{60} NPs did not show a significant mutagenic response even in the maximum dose of 1000 μg/plate regardless of metabolic activation or irradiation. Additionally, the Ames test is also used to detect the gene toxicity of many other nanomaterials [82], such as FePt [83], Al_2O_3 [82, 84], Fe_3O_4 [79, 82, 85], TiO_2 [80], Ag [86], quantum dots [87], cellulose nanofibrils [88], single-walled carbon nanotubes (SWCNTs) [89], and multiwalled carbon nanotubes (MWCNTs) [90]. However, Ames test also has some limitations. It cannot generalize to eukaryotic cells because *S. typhimurium* is a prokaryote and rat liver S9 fraction cannot replace the human liver cells completely [91].

10.2.2 HPRT Forward Mutation Assays

Hypoxanthine-guanine phosphoribosyltransferase (HPRT) is a transferase that could catalyze the conversion from hypoxanthine to inosine monophosphate and guanine to guanosine monophosphate. HPRT is a cell membrane enzyme encoded by the *hprt* gene on the end of X chromosome [92], called *region q*, so that it could be identified from the cell phenotype when gene mutated [93]. The deficiency or deactivation of this enzyme will result in the overproduction of uric acid leading to gout and nucleic acid metabolic abnormalities leading to genetic diseases [94]. After first coined, it has quickly become a useful target for studying somatic mutations *in vitro* and *in vivo* [95]. Compared to the Ames, there is an important advantage that it can also be applied in human cell types [82].

Currently, the HPRT forward mutation assays have been used to detect the genetoxicity of varieties of nanomaterials. Wang *et al*. [96–98] detected the effect of TiO_2 NPs, ultrafine silica, and ultrafine quartz on WIL2-NS of a human B-cell lymphoblastoid lineage by HPRT forward mutation assays. They found that TiO_2 NPs, ultrafine silica, and ultrafine quartz would lead to a significant increase of the mutation frequency. Huk *et al*. [99] used this method to investigate the mutagenic effect of Ag NPs in V79-4 cells. The results showed that 200 nm Ag NPs are the most mutagenic, regardless

10.3
Gene Expression Analysis

Gene expression refers to the genetic information stored in genes convert into a bioactive functional protein through transcription, translation, and posttranslational modification, and so on [100]. Gene regulation controls the cell over structure and function and is the basis of differentiation, morphogenesis, and versatility. So it is an important part of nanotechnology to measure gene expression.

10.3.1
Gene Chip

Gene chip (also known as *DNA chips*, bio-chips) is a new product of life-scientific development, which developed from southern blotting. It appeared in the mid-1980s and has been a powerful tool for genomic analysis, giving a global view of the genome in a single experiment.

10.3.1.1 Principle and Procedure

The core principle of Gene chip is based on the complementary property of nucleic acid sequences. It is a collection of tens of thousands or even millions of specific fragmented DNA spots (as a gene probe), which attached to a 2 cm^2 solid supporter regularly by micromachining and then probed with known DNA or RNA sequences [101]. Owing to fixing a large number of probes on a supporter, Gene chip can test and analyze a large number of sequences simultaneously [102–104]. So, it has been widely used in many fields, such as gene expression spectrum determination, genomic library mapping and hybridization sequencing, mutation detection, and polymorphism analysis.

Depending on different classification criteria, Gene chip can be divided into the following types,

1. According to different solid supports, there are inorganic and organic chips. The former mainly consist of silicon wafers and slides. The latter primarily include polypropylene membrane and nylon membrane. The probe on them is presynthesized and dropping added to the chip by special micropipette.
2. According to the fabricated technologies of Gene chip, it includes fine-pointed pins, photolithography, electrochemistry, or ink-jet printing.
3. According to different probes, it can be divided into oligonucleotide chip and cDNA chip.
4. According to different synthetic methods of the probe microarrays, there are two main kinds: spotted and *in situ* synthesized arrays. In spotted microarrays, the probe is prior synthesized and then deposited on the array surface in a certain order, "spotted" onto the solid support surface. A common method is to use the fine pin or needles controlled by a mechanical arm. *In situ* synthesized method mainly uses light-directed synthesis. Light-directed synthesis technique is the product of photolithography combined with traditional

solid-phase synthesis technology. The combination provides a fast way for synthesis of high-density probes and arrays.

About the procedure of Gene chip test, it can divided as follows:

1. *Chip Preparation.* At present, the main carrier is glass or silicon. The probes are synthesized through liquid-phase chemical synthesis or polymerase chain reaction (PCR) amplifications and then accurately spotted at the designated location using arraying and replicating device (ARD) or robot controlled by computer.
2. *Sample Preparation.* Biological samples from blood or tissue are often a complex mixture. Generally, except a few special samples, they cannot directly react with chips. So, the samples must be extracted, amplified, and then tagged with fluorescent. Fluorescently labeled target sequences banded to the probe sequence will generate a signal depending on the hybridization conditions.
3. *Molecular Hybridization*. The hybridization conditions should be selected and optimized depending on the kind and length of the probe and the application of the chip. Suitable reaction conditions can produce the reaction between biomolecules in the best situation, reduce the mismatch rate.
4. *Detection and Analysis.* The samples on the chip will emit fluorescence when excited by laser. Hybrid molecules that are strictly matched have high thermodynamic stability and will show strong fluorescence. While the thermodynamic stability of incomplete hybrid molecular is low, and there is no fluorescence emitted. The fluorescence position and the fluorescence intensity of each reaction point on the chip will be converted into data by chip scanner and related software. Then a large quantity of biology information will be obtained.

10.3.1.2 Application in Nanotoxicology

As an oncoming technique, the application of gene chip in nanotechnology is in flourish period. Yu *et al*. [105] explored the mRNA expression profile of MG-63 cells cultured on the TiO_2 nanotubes layers (TiO_2 NTs) by Gene chips to examine the molecular mechanisms of the interactions between nanotubes and osteoblasts. The results indicated that the TiO_2 NTs could enhance osteoblast proliferation and differentiation as well as reduce the adhesion and immunization osteoblast. Li *et al*. [106] examined how TiO_2 NPs affected multiple genes with the microarray analysis. Significant alterations in the expression of 847 genes of lung tissues were induced by exposure to TiO_2 NPs. Husain *et al*. [107] exposed the female C57BL/6 mice to rutile TiO_2 NPs via single intratracheal instillations and analyzed the biological responses in the pulmonary system by DNA microarrays. They found that approximately 3000 genes were altered in all treatment groups, which imply that the retention of TiO_2 NPs may potentially disturb Ca^{2+} homeostasis, and further affect smooth muscle activities. Recently, Sheng *et al*. [108] found TiO_2 NPs altered the expressions of 1041 genes of spleen significantly, which involved in immune/inflammatory responses, apoptosis, oxidative stress, metabolic processes and ion transport, and so on. Lim *et al*. [109] revealed that in addition to stress

genes reactive to reactive oxygen species (ROS), IL-8 increases in early-stage exposure to Ag NPs in macrophage cells through cDNA microarray analysis. Shim *et al*. [110] investigated gene expression with human embryo kidney 293 cells treated with silica-coated magnetic nanoparticles (MNPs@SiO_2) based on the microarray and suggested that overdose of MNPs could cause transcriptomic and metabolic disturbance.

10.3.2 Reverse-Transcription Polymerase Chain Reaction

Reverse-transcription polymerase chain reaction (RT-PCR) is one of PCR variants that appeared in the late 1980s and then developed rapidly. It is a technique that combined RNA reverse transcription and PCR. The RT-PCR has particular advantages of simplicity, specificity, and sensitivity and gradually replaced northern blotting, a traditional method for RNA qualitative and quantitative analysis [111–114]. Now, it is often used in gene expression analysis hereditary disease detection, and so on.

10.3.2.1 Principle and Procedure

In RT-PCR, the total RNA is first extracted from tissues or cells, and then the complementary DNA (cDNA) is synthesized by the reverse transcription of the obtained mRNA template. Subsequently, the cDNA is used as a template to amplify exponentially and synthesize the target fragments by PCR. RT-PCR is currently the most sensitive method of RNA detection available [115].

Depending on the number of tubes used in the procedure, RT-PCR can be divided into a one-step or a two-step reaction (Figure 10.3a). In the one-step approach, the entire reactions are performed in a single tube. Thus, operation procedure and reaction setup are simplified and the likelihood of contamination is reduced. While the two-step reaction needs two separate tubes, which are used for the reverse transcription and PCR amplification, respectively.

In addition, with the development of technology, the quantification of RT-PCR products can be divided into two categories: end-point and real-time [115]. It is preferred to use end-point RT-PCR to measure gene expression changes when the number of samples is small [117]. The use of RT-PCR was to verify the result of array analysis or gene expression changes [117, 118].

10.3.2.2 Applications in Nanotoxicology

The exponential amplification via RT-PCR provides a highly sensitive technique that can detect a very few RNA molecules. Tautzenberger *et al*. [119] examined the differentiation potential of osteogenic, adipogenic, and chondrogenic in mesenchymal stem cells (MSCs) exposed to novel phosphonate-functionalized polystyrene NPs by analyzing representative marker genes using RT-PCR. The results demonstrated that the NP-treated MSCs were undisturbed and maintained their potential for osteogenic, adipogenic, and chondrogenic differentiation. Li *et al*. [116] performed a comparative proteomic analysis, finding

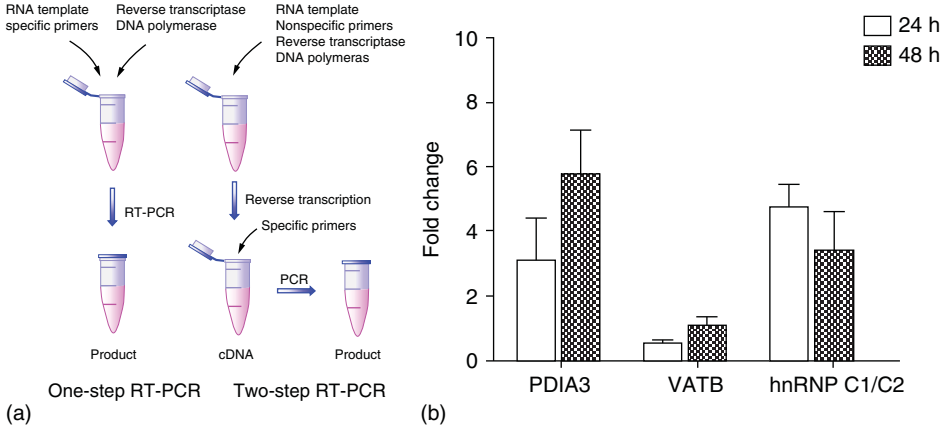

Figure 10.3 (a) The procedure of one-step and two-step RT-PCR. (b) Changes of genes expression from real-time RT-PCR analysis at 24 and 48 h Au NP treatment [116]. (Copyright © 2011 Elsevier Ltd.)

that 16 proteins were differentially expressed in MRC-5 lung fibroblasts exposed to Au NPs. The result was further verified by RT-PCR analysis. As shown in Figure 10.3b, there was a change of trend in the gene expression over time.

Gopinath *et al*. [120] used semiquantitative RT-PCR analysis to study the effects of Ag NPs on cellular apoptotic signaling genes expression and revealed that the apoptotic genes were upregulated, that is, Ag NPs would induce programmed cell death. Lee *et al*. [121] detected the downregulation of mitochondrial DNA-encoded genes, which could maintain the potential of mitochondrial membrane by semiquantitative RT-PCR in human lung cells (WI-26 VA4) exposed to nano-sized polyamidoamine (PAMAM) dendrimers. They confirmed that dendrimers could target the mitochondria and cause the release of cytochrome C. Due to the presence of dendrimers, mitochondrial membrane potential was disrupted and the mitochondria were damaged, resulting in apoptosis.

10.4 DNA Damage Detection

DNA damage is relatively common in the life of a cell, which refers to DNA nucleotide sequence changed permanently during DNA replication. Generally, it includes base changes such as deletions, insertions, fusions, translocations, or aneuploidy and backbone damages, such as DNA double-strand breaks (DSBs), DNA single-strand breaks, and DNA cross-links [122]. It may be generated spontaneously during DNA replication or be induced by environmental agents [123]. According to the damage causes, it could divide into endogenous DNA damage and exogenous DNA damage [124]. No matter what kind of damage, it could cause mutations [125, 126], cellular or organismic death [127–129], cancer

[124, 130–133] and other physical lesions, and so on. Therefore, it is significant for nanotechnology to detect DNA damage.

10.4.1 The Single-Cell Gel Electrophoresis Assay

The single-cell gel electrophoresis assay (SCGE) is a sensitive, simple, and high-speed analysis method for DNA damage detection at individual eukaryotic cell level. The SCGE assay was first developed as a microgel electrophoresis technique by Ostling and Johanson [134] in 1984. Then, through modification by Singh *et al*. [135] in 1988, and Olive *et al*. [136] in 1990, it has been widely applied in molecular toxicology, genotoxicity testing, DNA damage and repair, and so on.

10.4.1.1 Principle and Procedure

Usually, undamaged DNA retains a highly organized structure in the nucleus owing to the high relative molecular mass and supercoiled loops. When damaged, this organization will be disrupted. In SCGE, the cells embedded in gel are lysed by detergents and high salts. As a result, the cell biomembrane system including plasma membrane, nuclear membrane, and other biological membrane is disrupted. The intracellular components (such as RNA, proteins, etc.) flow into the gel and spread into the lysate. Except DNA, it would still remain *in situ* attached to the nuclear skeleton. Then, the slides are immersed in electrophoresis solution, electrolyzing for about 20 min. These slides are then neutralized and stained with a DNA-specific fluorescent stain. Subsequently, they are analyzed by a microscope with an attached CCD (charge-coupled device – essentially a digital camera). In general, the procedure of SCGE mainly includes four parts: (i) encapsulation, (ii) lysis, (iii) electrophoresis, and (iv) analysis. If cells are damaged, DNA chain scission and fragment release from the tight supercoiled structure and leave the nuclear DNA to the anode in gel, appearing as fluorescent tails. The intensity of the SCGE tail relative to the head reflects the number of DNA breaks.

10.4.1.2 Applications in Nanotoxicology

Now, the SCGE assay has been one of the most widely used methods to evaluate the *in vitro* genotoxicity of nanomaterials. To investigate metal NP-induced genotoxic effects and the potential underlying mechanisms, Wan *et al*. [137] studied the DNA damage caused by Co and TiO_2 NPs using SCGE assay with A549 cells. There was a dose–response increase of DNA damage to A549 cells after exposure to Co NPs, while no significant DNA damage was caused by TiO_2 NPs (Figure 10.4a).

Cong *et al*. [139] compared the DNA damage of *Nereis diversicolor* coelomocytes exposed to nano (<100 nm)-, micron (2–3.5 μm)-, and ionic ($AgNO_3$)-Ag by SCGE assay. The results revealed that all types of Ag were able to induce DNA damage in *N. diversicolor* coelomocytes regardless of its forms, and the more the Ag exposure, the more DNA is damaged. Among the three tested Ag forms, Ag NPs had the greatest genotoxicity while Ag^+ ions were the least genotoxic.

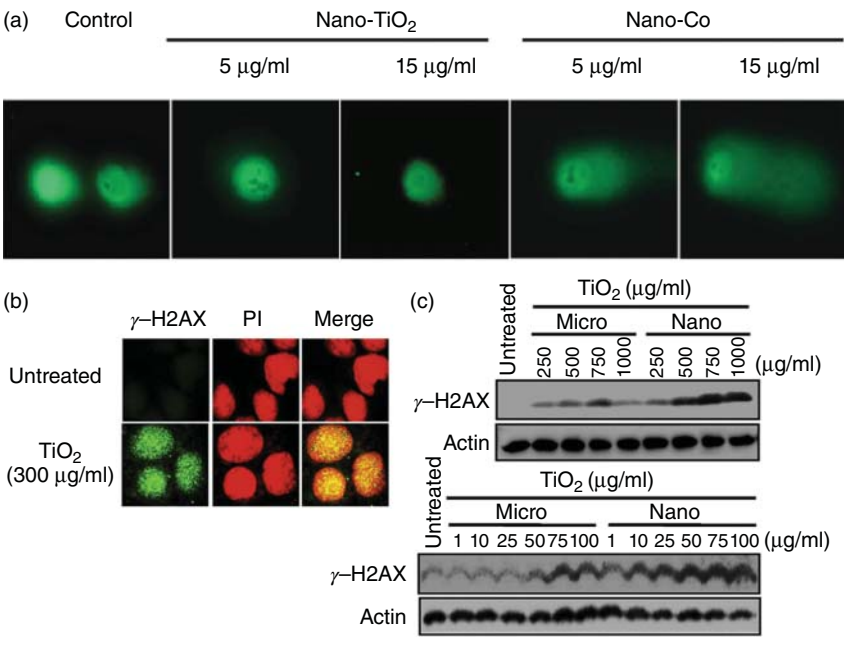

Figure 10.4 (a) Effects of Nano-Co (Co NPs) or Nano-TiO_2 (TiO_2 NPs) exposure on DNA double-strand breaks (DSBs) in A549 cells. (Reprinted with permission from [137], Copyright (2012), American Chemical Society.) (b) Immunofluorescence images of γ-H2AX after treatment with TiO_2 NPs. (c) Comparison of generation of γ-H2AX after treatment with TiO_2 NPs in different size detected by western blotting [138]. (Copyright © 2011, Elsevier B.V.)

Flower *et al*. [140] investigated whether Ag NPs induced DNA damage to peripheral blood cells or not by this assay. In addition, to assess the genotoxicity of Fe_2O_3-30 nm and Fe_2O_3-bulk, Singh *et al*. [141] evaluated their genotoxicity at 6, 24, 48, and 72 h by the SCGE assay in leucocytes. They found that both Fe_2O_3-30 nm and Fe_2O_3-bulk were not genotoxic at the tested doses. Kang *et al*. [142] revealed that lymphocytes treated with TiO_2 NPs showed significant increases in DNA breakage by SCGE assay. Demir *et al*. [143] used the SCGE assay to evaluate the human embryonic kidney (HEK293) and mouse embryonic fibroblast (NIH/3T3) cells exposed to TiO_2 NPs and observed a statistically significant induction of DNA damage at the highest dose tested (1000 μg/ml).

10.4.2
γ-H2AX Immunofluorescence Assay

In eukaryotes, DNA and histone are entwined with each other, forming the nucleosomes. H1, H2A, H2B, H3, H4, and archaebacteria histone are the known six kinds of histones by now, while H2A, H2B, H3, and H4 consist of core histones [144]. H2AX is a variant of the H2A protein family, which accounts for

about 2–10% of total H2A [145]. It has been demonstrated that H2AX will be phosphorylated by phosphatidylinositol 3-kinase (PI-3K) family and then forms "foci" at the locations of DSBs [146]. The phosphorylated H2AX, which is also called gamma-H2AX (γ-H2AX), has a linear relation with DSB grade [145]. So γ-H2AX is considered to be a sensitive specific biomarker for detecting DSBs in cells. Currently, the most used quantitative assay of γ-H2AX is immunofluorescence (IF). It is a technique that is based on the flow cytometry (FCM) and laser scanning confocal microscope (LSCM) and combined with IF labeling technology.

10.4.2.1 Applications in Nanotoxicology

γ-H2AX immunofluorescence (γ-H2AX IF) assay has become a fast and sensitive method to detect the DSBs and widely used in toxicology and molecular toxicology.

Wan *et al*. [137] investigated the effects of Co NPs on expression of γ-H2AX in A549 cells. They found that there was a dose– and time–response increase of γ-H2AX foci in A549 cells when exposed to Co NPs. On the contrary, there was no effect on either the formation of γ-H2AX foci or the expression of γ-H2AX protein in A549 cells incubated with TiO_2 NPs.

Toyooka *et al*. [138] examined the genotoxicity of two different-sized TiO_2 NPs in A549 cells based on the γ-H2AX expression. FCM analysis showed that the generation of γ-H2AX was independent of cell cycle phases. High expression of γ-H2AX was induced after coincubation with high concentration of TiO_2 NPs. As shown in Figure 10.4b,c, both IF images and western blotting can confirm the generation of γ-H2AX distributed within the nucleus after cells were treated with TiO_2 NPs.

To ultimately cure breast cancer, a new formulation based on the incorporation of specific estrogen receptor α (ERα)-targeting siRNAs was developed to improve the down regulation of ERα. Two specific ERα-siRNAs were mixed and incorporated into aqueous-core nanocapsules coupled to PEG (polyethylene glycol). The targeted delivery of ERα-siRNA in breast tumors potentiates the inhibition of E_2-induced proliferative activity by encapsulated antiestrogen (AE) through enhanced antivascular (AV) activity. The surface endocytotic receptor megalin was studied for targeted delivery of anticlusterin siRNAs to these chemo-treated breast cancer cells. Lipid–polyethylenimine hybrid nanocarriers decorated with apolipoprotein E (ApoE) were developed for this purpose. Using immunoblotting, the induction of both megalin and clusterin in MCF-7 cells by previous paclitaxel treatment was demonstrated. The siRNA transfection of these megalin-rich chemo-treated cancer cells was improved by threefold when the siRNAs were delivered by Ap-LPNs (Lipid-polyethylenimine hybrid nanocarriers decorated with apolipoprotein E). This formulation also enhanced clusterin knockdown and improved chemosensitization and paclitaxel treatment (both $p < 0.05$ vs uncoated LPNs). This proof-of-principle study thus validated a "chemoresistance-targeting" strategy for siRNA delivery to the cancer cell subpopulation that began to acquire chemoresistance and was in strong need for chemosensitization.

10.5 Chromosomal Aberration Analysis

10.5.1 Fluorescence *In Situ* Hybridization

Fluorescence *in situ* hybridization (FISH) is a nonradioactive molecular cytogenetic technique developed on the basis of radioactive *in situ* hybridization technique in the early 1980s [147]. It is a new method of *in situ* hybridization that used fluorescent markers rather than isotopic markers to bind the chromosome. It is safe, fast, and highly sensitive. In addition, the probe can be stored for a long time, simultaneously display multiple colors, and show in either metaphase or interphase nuclei. As a result, it is often used to find specific features in DNA for genetic counseling, medicine, and species identification [148].

10.5.1.1 Principle and Procedure

The basic principle of FISH is that the target DNA and nucleic acid probe could form a hybrid by denaturation, annealing, and renaturation if they are homologous complementary. The approximate steps of FISH are outlined as follows:

1. *Preparation of probe*. FISH includes two main components: the DNA (or RNA) probe and the target chromosome or DNA. The probe is often a nucleic acid fragment with particular sequence and length. It can be divided into DNA probe, cDNA probes, RNA probe, and oligonucleotide probe depending the source and nature. Currently, the syntheses of probes are mainly by three ways: the PCR, artificial synthetic, and recombinant plasmid.
2. *Labeling the probe*. There are two main methods to label the probe: indirect labeling and direct labeling. Indirect approach connects a hapten to a nucleic acid molecule to prepare an immunized nucleic acid probe and then detects the target nucleic acid molecule by the labeled-protein, which combines with hapten specifically. The most common hapten has biotin, digoxin, and so on. While in direct labeling, nucleic acid molecule is tagged with a specific enzyme or a fluorescent dye directly and then observes the fluorescent signal by color reaction.
3. *Hybridization of probe*. Before hybridization, the double-stranded DNA probe and the target DNA must be denatured to single-stranded DNA by heat and alkaline treatment. The purpose is to preserve the integrity of organization and achieve the maximum hybridization efficiency. The buffer volume of hybridization carried out is often very small and the salt concentration, pH, and temperature of hybridization depend on the optimal annealed condition of the probe and the target DNA.

10.5.1.2 Applications in Nanotoxicology

Early in 1985, Pinkel *et al*. [149] described the use of FISH to classify chromosomes and detect chromosome aberrations. Recently, it was widely applied in the chromosomal toxicity research of nanomaterials. Gonzalez *et al*. [150] assessed

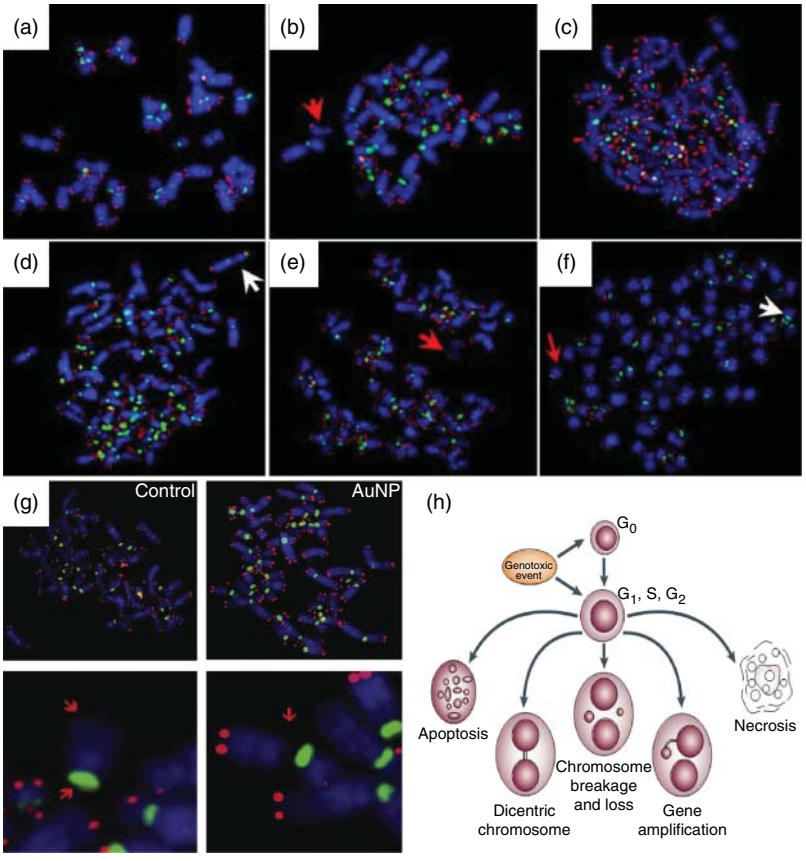

Figure 10.5 (a) Ag NP treated IMR-90 cells show acentric and centric fragments. (b) Arrow indicates acentric fragments. (c) Untreated cancer cells with no aberrations. (d) Ag NP treated U251 cells. White arrow points to a dicentric chromosome. (e) Acentric fragments. (f) Centric fragments. Red arrow points to a chromosome fragment [151]. (g) Fluorescence *in situ* Hybridization (FISH) analysis of control and Au NP treated MRC-5 lung fibroblasts (1 nM concentration and 72 h) [116]. (Copyright © 2011 Elsevier Ltd.) (h) The various possible fates of cultured cytokinesis-blocked cells following exposure to cytotoxic/genotoxic agents [152]. (Copyright © 2007, Nature Publishing Group.)

the potential genotoxicity of A549 lung cancer cells induced by amorphous SiO_2 NPs and proved that there are no significant chromosome breakage and chromosome loss in the cell treated by SiO_2 NPs. While Asharani *et al*. [151] used normal human lung fibroblasts (IMR-90) and human glioblastoma cells (U251) as cell models to study the toxicity of Ag NPs, they found that Ag NPs caused significant chromosomal aberrations in two kinds of cells directly or through activating catabolic enzymes. Cancer cells are more susceptible to damage induced by Ag NPs because of the lack of recovery from the impact (Figure 10.5a–f).

Li *et al*. [116] used the FISH assay to assess DNA damage and chromosomal aberrations of MRC-5 human fetal lung fibroblast cells after coincubation with

Au NPs. The results suggested that Au NPs induce DNA damage and chromosomal breaks. As shown in Figure 10.5g, Au NP treated cells had significant chromosomal aberrations compared to the controls. The main type of aberrations is chromosome breaks, and no chromosomal fusions were found, that is to say, the number of chromosomes has not changed.

To assess the potential adverse health effects of carbon nanomaterials, Kisin *et al*. [153] evaluated DNA damage induced by carbon nanofibers (CNFs), SWCNTs, or asbestos on the Chinese hamster lung fibroblast (V79) cells. They confirmed that CNF could induce genotoxicity and provided powerful evidence to suggest that these particles induce aneugenic and clastogenic events. In addition, Muller *et al*. [154] distinguished the induction mechanisms of breast cancer cell line exposed to MWCNTs and found that the MWCNTs can induce both chromosome break and aneuploid cell generation.

10.5.2 Micronucleus Test

Micronucleus (MN), also called satellite nuclear, is an abnormal structure in eukaryocyte. It is a small nucleus formed by a chromosome or a fragment that does not incorporate into both the daughter nuclei during cell division. Micronucleus was first found in the peripheral of cats and rats by Howell and Jolly and named as Howell–Jolly bodies at that time [155]. In the 1970s, MN test was proposed to detect the chromosomal aberration by the frequency of micronuclei appearance [156]. With the rapid development of molecular biology, Fenech and Morley [157] proposed a new concept in 1985 named as Cytokinesis Block Micronucleus assay (CBMN), which further developed the MN method and promoted its application. Now, the CBMN has become one of the most successful and reliable assays used in toxicological screening [158]. It has been evolved into a comprehensive study method for detecting chromosome breakage and loss, DNA misrepair, nondisjunction, necrosis, apoptosis, and cytostasis (Figure 10.5h).

Because of this, it has more and more applications in nanotechnology. Gurr *et al*. [159] examined the number of micronuclei of human bronchial epithelial BEAS-2B cells with treatment of TiO_2 NPs to detect genetic abnormalities. As their results, the numbers of micronuclei were significantly increased when treated by TiO_2 in anatase phase with diameters of 10 and 200 nm. Treatment by TiO_2 in anatase (>200 nm) and rutile phase (200 nm) did not induce any change in the number of micronuclei. Jaeger *et al*. [160] found that the MN rate of HaCaT keratinocyte cell line (Human adult low-Calcium high-Temperature Keratinocytes) showed significant increase upon exposure to TiO_2 NPs and TiO_2 MPs at the same exposure time. Demir *et al*. [143] performed the MN test to demonstrate the clastogenic/aneugenic potential of TiO_2 NPs and only observed that there are significant increases of the micronucleated binucleates (MNCB) frequency in the two cell lines (HEK293 and NIH/3T3) at the highest tested dose (1000 μg/ml) Shinohara *et al*. [81] performed a bone marrow MN test to detect

chromosomal aberrations in Tween 80 on ICR (Institute of Cancer Research) mice with a stable C_{60} NP suspension and found there are no abnormalities at any dose of C_{60} NPs. That is to say, C_{60} NPs would not cause any *in vivo* cytogenetic damage involved in forming micronuclei in bone marrow cells of mice. Muller *et al*. [154] detected the genotoxicity caused by MWCNTs both *in vitro* and *in vivo*. They assessed the formation of MN induced by MWCNTs *in vivo* in rat type II pneumocytes (AT-II) and found that MWCNTs induced a significant increase in micronucleated AT-II in a dose-dependent manner.

10.5.3
G-Banding Analysis

Giemsa banding, also called *G-banding*, was first established in the 1970s and then improved gradually. It is a member of Chromosome-banding technique, which also includes Q-banding, R-banding, C-banding, T-banding, and N-banding [161, 162]. It is usually used to conduct a visible karyotype analysis by staining chromosomes with Giemsa stain. Then the band of chromosomes is compared and analyzed from their position, bandwidth, and shade [163]. Nowadays, it has been widely used to analyze the chromosomal aberration, including mainly structural abnormality (such as deletions, fracture, translocations, and inversions) and number abnormality.

Luo *et al*. [164] examined the *in vivo anti-Helicobacter pylori* (anti-*Hp*) effect of chitosan nanoparticles (CS NPs) by Giemsa staining using *Hp*-infected mice and found that CS NPs have a bacteriostatic effect on Hp strains. Huang *et al*. [165] found that no structural and number abnormalities were observed in CHL cells exposed to poly(ε-caprolactone)-poly(ethylene glycol)-poly(ε-caprolactone) NPs compared to negative control. Theogaraj *et al*. [166] demonstrated that ultrafine TiO_2 NPs (different forms of uncoated, coated, and doped) would not induce increases in the frequency of chromosome aberrations by G-banding. Honma *et al*. [167] used the CHL/IU (Chinese hamster lung cell line) cells as a model to analyze *in vitro* chromosome aberration test caused by C_{60}. They found that it did not induce structural chromosome aberrations at any concentration. Omid *et al*. [168] monitored the genotoxicity of the reduced graphene oxide nanoplatelets (rGONPs) through monitoring the DNA fragmentations by comet assay and the chromosomal aberrations by Giemsa banding of the cells. They revealed that no significant chromosomal aberration occurred for the rGO sheets. Ema *et al*. [169, 170] also found that both SWCNTs and MWCNTs appeared not to pose a genotoxic risk to Chinese hamster lung fibroblast cell line CHL/IU, while Di Giorgio *et al*. [171] confirmed that CNTs are cyto- and genotoxic to RAW 264.7 mouse macrophages inducing ROS release, necrosis, and chromosomal aberrations as well as ultrastructural damage and apoptosis but did not cause an inflammatory response.

10.5.4
Sister Chromatid Exchange

A sister chromatid refers to two identical chromatids connected by a common centromere, which formed by replication from the same chromosome in mitosis

interphase or meiosis interphase. The two sister chromatids are then separated into two different cells along with centromere division during mitosis and the second division of meiosis. Sister chromatid exchange (SCE), first established in 1938 by McClintock, is the translocation of homologous fragments in the same position of two sister chromatids [172]. The reason of SCE is not very clear now, but it is still one of the useful means for mutation detection. In 1973, Latt first put forward that SCE could be an analytical method to detect chromosomal aberration [173]. It has been proved that the increased rate of SCE may cause pathologies, such as Bloom syndrome and tumors [174, 175].

The principle of SCE is that 5-bromodeoxy-uridine (Brdu), which was added during the cell culture, could replace thymidine to incorporate into the newly synthesized DNA strand. After two-cell replicative cycle, there are obvious differences between two sister chromatids of one chromosome. It shows chromatism between two sister chromatids after being stained and optical treated; one is dark and the other is light.

The SCE technique is very fast and more sensitive than MN assay, so it gains wide application. Kato *et al*. [176] found that MWCNTs significantly enhanced the frequency of SCE in CHO AA8 cells. Mahmoudi *et al*. [177] reported that the frequency of SCE was increased in HepG2 cells exposed to SPIONs. Kuo *et al*. [178] revealed that motorcycle exhaust particles caused an increase in SCEs in a dose-dependent manner. Pierscionek *et al*. [179] confirmed that CeO_2 NPs at experimental dosages did not cause any DNA damage or significant increases in SCEs, suggesting that CeO_2 NPs had no genotoxicity to the eye lens.

10.6 Omics

Omics is a neologism that refers to a biology field ending with -omics, such as genomics, proteomics, or metabolomics. Correspondently, the suffix -ome is used to represent the study of objects of these omics, such as genome, proteome, or metabolome. Proteomics was proposed in 1997 analogized with genomics, and it aims to study the entire proteins proteome in a cell, tissue, or biological fluid [180–182]. In the past decades, proteomics had maintained the momentum of rise steadily along with the evolution of analysis and detection methods. Two-dimensional gel electrophoresis, mass spectrometry, and protein chips are the widely used analysis methods [183–186]. The concept of metabolomics was first proposed formally in 1999 by Nicholson *et al*. based on nuclear magnetic resonance (NMR) [187]. It aims to detect a set of endogenous small-molecule metabolites such as nucleotides, hormones, carbohydrates, phospholipids, amino acids, fatty acids, steroids, and their derivatives and has become another useful tool to reveal the organism activities in the metabolism dynamic process after genomics and proteomics [188, 189].

Currently, proteomics and metabolomics have been widely used in the toxicity studies of nanomaterials, such as SiO_2 NPs [190–192], Ag NPs [193], TiO_2 NPs

[194], Au NPs [116, 195], ultrasmall superparamagnetic particles of iron oxide (USPIO) [196], carbon NPs [197], and Cu NPs [198]. In view of its wide and important applications, omics is introduced in detail in chapter 12.

10.7 Conclusions

Currently, the situations of environmental pollution, food safety, drug abuse, and so on, are more and more serious. The increasing development of nanotechnology also induces a potential menace in human health. However, the traditional toxicology cannot keep pace with the progress and satisfy current needs. While other branches of toxicology are spawned, the molecular toxicology is one of the most novel and important branches. Although the molecular toxicology is in initial stage with many problems unresolved, it can be expected that it will improve itself constantly and promote disease diagnosis continually. There is no doubt that it has a very broad prospect.

References

1. Huang, S., Wang, L., Liu, L. *et al.* (2014) Nanotechnology in agriculture, livestock, and aquaculture in China. A review. *Agron. Sustainable Dev.*, **35** (2), 369–400.
2. Service, R.F. (2004) Nanotoxicology: nanotechnology grows up. *Science*, **304** (5678), 1732–1734.
3. Hingant, B. and Albe, V. (2010) Nanosciences and nanotechnologies learning and teaching in secondary education: a review of literature. *Stud. Sci. Educ.*, **46** (2), 121–152.
4. Erdem, S. (2015) Consumers' preferences for nanotechnology in food packaging: a discrete choice experiment. *J. Agric. Econ.*, **66** (2), 259–279.
5. Invernizzi, N., Foladori, G., Robles-Belmont, E. *et al.* (2015) Nanotechnology for social needs: contributions from Latin American research in the areas of health, energy and water. *J. Nanopart. Res.*, **17** (5).
6. Wang, Y., Yang, S.-T., Wang, Y. *et al.* (2012) Adsorption and desorption of doxorubicin on oxidized carbon nanotubes. *Colloids Surf., B*, **97**, 62–69.
7. Chow, J.C., Watson, J.G., Savage, N. *et al.* (2005) Nanoparticles and the environment. *J. Air Waste Manage. Assoc.*, **55** (10), 1411–1417.
8. Colvin, V.L. (2003) The potential environmental impact of engineered nanomaterials. *Nat. Biotechnol.*, **21** (10), 1166–1170.
9. Owen, R. and Depledge, M. (2005) Nanotechnology and the environment: risks and rewards. *Mar. Pollut. Bull.*, **50** (6), 609–612.
10. Nel, A., Xia, T., Madler, L. *et al.* (2006) Toxic potential of materials at the nanolevel. *Science*, **311** (5761), 622–627.
11. Wang, Y., Yuan, L., Yao, C. *et al.* (2014) A combined toxicity study of zinc oxide nanoparticles and vitamin C in food additives. *Nanoscale*, **6** (24), 15333–15342.
12. Yang, Y.-X., Song, Z.-M., Cheng, B. *et al.* (2014) Evaluation of the toxicity of food additive silica nanoparticles on gastrointestinal cells. *J. Appl. Toxicol.*, **34** (4), 424–435.
13. Anilkumar, P., Lu, F., Cao, L. *et al.* (2011) Fullerenes for applications in biology and medicine. *Curr. Med. Chem.*, **18** (14), 2045–2059.
14. Friedman, S.M. and Egolf, B.P. (2011) A longitudinal study of newspaper

and wire service coverage of nanotechnology risks. *Risk Anal.*, **31** (11), 1701–1717.

15. Williams, R.A., Kulinowski, K.M., White, R. *et al.* (2010) Risk characterization for nanotechnology. *Risk Anal.*, **30** (11), 1671–1679.
16. Wardak, A., Gorman, M.E., Swami, N. *et al.* (2008) Identification of risks in the life cycle of nanotechnology-based products. *J. Ind. Ecol.*, **12** (3), 435–448.
17. Besley, J.C., Kramer, V.L., and Priest, S.H. (2008) Expert opinion on nanotechnology: risks, benefits, and regulation. *J. Nanopart. Res.*, **10** (4), 549–558.
18. Karst, D. and Yang, Y.Q. (2006) Potential advantages and risks of nanotechnology for textiles. *AATCC Rev.*, **6** (3), 44–48.
19. Nicolosi, D., Cupri, S., Genovese, C. *et al.* (2015) Nanotechnology approaches for antibacterial drug delivery: preparation and microbiological evaluation of fusogenic liposomes carrying fusidic acid. *Int. J. Antimicrob. Agents*, **45** (6), 622–626.
20. Yue, C.Y., Zhao, S.L., and Kuzma, J. (2015) Heterogeneous consumer preferences for nanotechnology and genetic-modification technology in food products. *J. Agric. Econ.*, **66** (2), 308–328.
21. Herrmann, I.K. (2015) How nanotechnology-enabled concepts could contribute to the prevention, diagnosis and therapy of bacterial infections. *Crit. Care*, **19**, 239.
22. Wang, Y., Anilkumar, P., Cao, L. *et al.* (2011) Carbon dots of different composition and surface functionalization: cytotoxicity issues relevant to fluorescence cell imaging. *Exp. Biol. Med.*, **236** (11), 1231–1238.
23. Wang, Y., Sui, K., Fang, J. *et al.* (2013) Cytotoxicity evaluation and subcellular location of titanium dioxide nanotubes. *Appl. Biochem. Biotechnol.*, **171** (7), 1568–1577.
24. Chou, L.Y. and Chan, W.C. (2012) Nanotoxicology. No signs of illness. *Nat. Nanotechnol.*, **7** (7), 416–417.
25. Keelan, J.A. (2011) Nanotoxicology: nanoparticles versus the placenta. *Nat. Nanotechnol.*, **6** (5), 263–264.
26. Donaldson, K. and Poland, C.A. (2009) Nanotoxicology: new insights into nanotubes. *Nat. Nanotechnol.*, **4** (11), 708–710.
27. Zhao, Y., Xing, G., and Chai, Z. (2008) Nanotoxicology: are carbon nanotubes safe? *Nat. Nanotechnol.*, **3** (4), 191–192.
28. Kodali, V., Littke, M.H., Tilton, S.C. *et al.* (2013) Dysregulation of macrophage activation profiles by engineered nanoparticles. *ACS Nano*, **7** (8), 6997–7010.
29. Gilbert, B., Fakra, S.C., Xia, T. *et al.* (2012) The fate of ZnO nanoparticles administered to human bronchial epithelial cells. *ACS Nano*, **6** (6), 4921–4930.
30. Deng, X.Y., Xiong, D.M., Wang, Y.L. *et al.* (2010) Water soluble multi-walled carbon nanotubes enhance peritoneal macrophage activity in vivo. *J. Nanosci. Nanotechnol.*, **10** (12), 8663–8669.
31. Wang, L., Wang, Y., Xu, T. *et al.* (2014) Gram-scale synthesis of single-crystalline graphene quantum dots with superior optical properties. *Nat. Commun.*, **5**, 5357.
32. Wang, Y., Yuan, L., Yao, C. *et al.* (2014) Caseinophosphopeptides cytoprotect human gastric epithelium cells against the injury induced by zinc oxide nanoparticles. *RSC Adv.*, **4** (79), 42168–42174.
33. Deng, X., Luan, Q., Chen, W. *et al.* (2009) Nanosized zinc oxide particles induce neural stem cell apoptosis. *Nanotechnology*, **20** (11), 115101.
34. Dong, E.Y., Wang, Y.L., Yang, S.T. *et al.* (2011) Toxicity of nano gamma alumina to neural stem cells. *J. Nanosci. Nanotechnol.*, **11** (9), 7848–7856.
35. Oberdörster, G., Oberdörster, E., and Oberdörster, J. (2005) Nanotoxicology: an emerging discipline evolving from studies of ultrafine particles. *Environ. Health Perspect.*, **113** (7), 823–839.
36. d'Yvoire, M.B., Bremer, S., Casati, S. *et al.* (2012) in *New Technologies for Toxicity Testing* (eds M. Balls, R.D. Combes, and N. Bhogal), pp. 154–180.

37. Park, B.K., Kitteringham, N.R., Powell, H. *et al.* (2000) Advances in molecular toxicology-towards understanding idiosyncratic drug toxicity. *Toxicology*, **153** (1–3), 39–60.
38. Yanamala, N., Kagan, V.E., and Shvedova, A.A. (2013) Molecular modeling in structural nano-toxicology: interactions of nano-particles with nano-machinery of cells. *Adv. Drug Delivery Rev.*, **65** (15), 2070–2077.
39. Zhang, B., Zhai, W.X., Liu, R.T. *et al.* (2015) Evaluation on the toxic effects of nanoAg to catalase. *J. Nanosci. Nanotechnol.*, **15** (2), 1473–1479.
40. Stone, V., Johnston, H., and Clift, M.J.D. (2007) Air pollution, ultrafine and nanoparticle toxicology: cellular and molecular interactions. *IEEE Trans. Nanobiosci.*, **6** (4), 331–340.
41. Marshall, E. (1993) Toxicology goes molecular. *Science*, **259** (5100), 1394–1398.
42. Zhao, X., Wang, S., Wu, Y. *et al.* (2013) Acute ZnO nanoparticles exposure induces developmental toxicity, oxidative stress and DNA damage in embryo-larval zebrafish. *Aquat. Toxicol.*, **136–137**, 49–59.
43. Zheng, D., Wang, N., Wang, X. *et al.* (2012) Effects of the interaction of TiO_2 nanoparticles with bisphenol A on their physicochemical properties and *in vitro* toxicity. *J. Hazard. Mater.*, **199–200**, 426–432.
44. Gao, F., Yuan, Q., Gao, L. *et al.* (2014) Cytotoxicity and therapeutic effect of irinotecan combined with selenium nanoparticles. *Biomaterials*, **35** (31), 8854–8866.
45. Cronholm, P., Karlsson, H.L., Hedberg, J. *et al.* (2013) Intracellular uptake and toxicity of Ag and CuO nanoparticles: a comparison between nanoparticles and their corresponding metal ions. *Small*, **9** (7), 970–982.
46. Kumar, C.S., Raja, M.D., Sundar, D.S. *et al.* (2015) Hyaluronic acid co-functionalized gold nanoparticle complex for the targeted delivery of metformin in the treatment of liver cancer (HepG2 cells). *Carbohydr. Polym.*, **128**, 63–74.
47. Ma, L., Zhao, J., Wang, J. *et al.* (2009) The acute liver injury in mice caused by nano-anatase TiO_2. *Nanoscale Res. Lett.*, **4** (11), 1275–1285.
48. Alaraby, M., Annangi, B., Hernandez, A. *et al.* (2015) A comprehensive study of the harmful effects of ZnO nanoparticles using Drosophila melanogaster as an in vivo model. *J. Hazard. Mater.*, **296**, 166–174.
49. Bertram, J.S. (2001) The molecular biology of cancer. *Mol. Aspects Med.*, **21**, 167–223.
50. Aminetzach, Y.T., Macpherson, J.M., and Petrov, D.A. (2005) Pesticide resistance via transposition-mediated adaptive gene truncation in Drosophila. *Science*, **309** (5735), 764–767.
51. Loeb, L.A. (1989) Endogenous carcinogenesis: molecular oncology into the twenty-first century presidential address. *Cancer Res.*, **49**, 5489–5496.
52. Jiang, C.Y., Hwang, Y.T., Randell, J.C.W. *et al.* (2007) Mutations that decrease DNA binding of the processivity factor of the herpes simplex virus DNA polymerase reduce viral yield, alter the kinetics of viral DNA replication, and decrease the fidelity of DNA replication. *J. Virol.*, **81** (7), 3495–3502.
53. Ulanowska, K., Sikora, A., Węgrzyn, G. *et al.* (2003) Role of the cgtA gene function in DNA replication of extrachromosomal elements in *Escherichia coli*. *Plasmid*, **50** (1), 45–52.
54. Lana, E., Megarbane, A., Tourriere, H. *et al.* (2012) DNA replication is altered in immunodeficiency centromeric instability facial anomalies (ICF) cells carrying DNMT3B mutations. *Eur. J. Hum. Genet.*, **20** (10), 1044–1050.
55. Boreyko, A.V. and Krasavin, E.A. (2011) Mutagenic effect of accelerated heavy ions on bacterial cells. *Phys. Part. Nucl.*, **42** (6), 998–1024.
56. Tian, Q.S., Frierson, H.F., Krystal, G.W. *et al.* (1999) Activating c-kit gene mutations in human germ cell tumors. *Am. J. Pathol.*, **154** (6), 1643–1647.
57. Moreno-Bueno, G., Gamallo, C., Perez-Gallego, L. *et al.* (2001) Beta-catenin expression pattern, beta-catenin gene mutations, and microsatellite

instability in endometrioid ovarian carcinomas and synchronous endometrial carcinomas. *Diagn. Mol. Pathol.*, **10** (2), 116–122.

58. Konopka, B., Paszko, Z., Janiec-Jankowska, A. *et al.* (2002) Assessment of the quality and frequency of mutations occurrence in PTEN gene in endometrial carcinomas and hyperplasias. *Cancer Lett.*, **178** (1), 43–51.
59. Skasko, E., Kluska, A., Niwinska, A. *et al.* (2009) Age at onset of bilateral breast cancer, the presence of hereditary BRCA1, BRCA2, CHEK2 gene mutations and positive family history of cancer. *Onkologie*, **32** (4), 182–188.
60. Tung, N., Battelli, C., Allen, B. *et al.* (2015) Frequency of mutations in individuals with breast cancer referred for BRCA1 and BRCA2 testing using next-generation sequencing with a 25-gene panel. *Cancer*, **121** (1), 25–33.
61. Komminoth, P., Kunz, E.K., Matias-Guiu, X. *et al.* (1995) Analysis of RET protooncogene point mutations distinguishes heritable from nonheritable medullary thyroid carcinomas. *Cancer*, **76** (3), 479–489.
62. Niimura, H., Bachinski, L.L., Sangwatanaroj, S. *et al.* (1998) Mutations in the gene for cardiac myosin-binding protein C and late-onset familial hypertrophic cardiomyopathy. *N. Engl. J. Med.*, **338** (18), 1248–1257.
63. Tu, Z.D., Wang, L., Xu, M. *et al.* (2006) Further understanding human disease genes by comparing with housekeeping genes and other genes. *BMC Genomics*, **7**, 31.
64. Uitto, J. (2009) Progress in heritable skin diseases: translational implications of mutation analysis and prospects of molecular therapies. *Acta Derm. Venereol.*, **89** (3), 228–235.
65. Dickerson, J.E. and Robertson, D.L. (2012) On the origins of Mendelian disease genes in man: the impact of gene duplication. *Mol. Biol. Evol.*, **29** (1), 61–69.
66. Gao, J., Gentzler, R.D., Timms, A.E. *et al.* (2014) Heritable GATA2 mutations associated with familial AML-MDS: a case report and review of literature. *J. Hematol. Oncol.*, **7**, 36.
67. Simons, C., Griffin, L.B., Helman, G. *et al.* (2015) Loss-of-function alanyl-tRNA synthetase mutations cause an autosomal-recessive early-onset epileptic encephalopathy with persistent myelination defect. *Am. J. Hum. Genet.*, **96** (4), 675–681.
68. Ames, B.N., Gurney, E.G., Miller, J.A. *et al.* (1972) Carcinogens as frameshift mutagens: metabolites and derivatives of 2-acetylaminofluorene and other aromatic amine carcinogens. *Proc. Natl. Acad. Sci. U.S.A.*, **69** (11), 3128–3132.
69. Ames, B.N., Durston, W.E., Yamasaki, E. *et al.* (1973) Carcinogens are mutagens: a simple test system combining liver homogenates for activation and bacteria for detection. *Proc. Natl. Acad. Sci. U.S.A.*, **70** (8), 2281–2285.
70. Ames, B.N., Lee, F.D., and Durston, W.E. (1973) An improved bacterial test system for the detection and classification of mutagens and carcinogens. *Proc. Natl. Acad. Sci. U.S.A.*, **70** (3), 782–786.
71. McCann, J., Spingarn, N.E., Kobori, J. *et al.* (1975) Detection of carcinogens as mutagens: bacterial tester strains with R factor plasmids. *Proc. Natl. Acad. Sci. U.S.A.*, **72** (3), 979–983.
72. Ames, B.N., McCann, J., and Yamasaki, E. (1975) Methods for detecting carcinogens and mutagens with the Salmonella/mammalian-microsome mutagenicity test. *Mutat. Res.*, **31** (6), 347–364.
73. Reifferscheid, G. and Hell, J. (1996) Validation of the SOS/umu test using test results of 486 chemicals and comparison with the Ames test and carcinogenicity data. *Mutat. Res. Genet. Toxicol.*, **369** (3–4), 129–145.
74. Kirkland, D., Reeve, L., Gatehouse, D. *et al.* (2011) A core *in vitro* genotoxicity battery comprising the Ames test plus the *in vitro* micronucleus test is sufficient to detect rodent carcinogens and in vivo genotoxins. *Mutat. Res. Genet. Toxicol. Environ. Mutagen.*, **721** (1), 27–73.
75. Harding, A.P., Popelier, P.L., Harvey, J. *et al.* (2015) Evaluation of aromatic

amines with different purities and different solvent vehicles in the Ames test. *Regul. Toxicol. Pharm.*, **71** (2), 244–250.

76. Konuk, M., Baris, A., Liman, R. *et al.* (2008) A study on the mutagenicity of different types of pesticides by using the Ames/Salmonella/Microsome test system. *Fresenius Environ. Bull.*, **17** (4), 463–466.

77. Banerjee, S., Singh, S., Policegoudra, R. *et al.* (2013) Evaluation of the mutagenic potential of a combinational prophylactic transdermal patch by Ames test. *Immuno-Anal. Biol. Spec.*, **28** (5-6), 322–326.

78. Yilmaz, E. (2014) Mutagenecity of enniatin A1 and B1 mycotoxins in Ames Salmonella microsome test. *Kafkas Univ. Vet. Fak. Derg.*, **20** (6), 893–896.

79. Mortelmans, K. and Zeiger, E. (2000) The Ames Salmonella/microsome mutagenicity assay. *Mutat. Res. Fundam. Mol. Mech. Mutagen.*, **455** (1-2), 29–60.

80. Kumar, A., Pandey, A.K., Singh, S.S. *et al.* (2011) Cellular uptake and mutagenic potential of metal oxide nanoparticles in bacterial cells. *Chemosphere*, **83** (8), 1124–1132.

81. Shinohara, N., Matsumoto, K., Endoh, S. *et al.* (2009) *In vitro* and *in vivo* genotoxicity tests on fullerene C60 nanoparticles. *Toxicol. Lett.*, **191** (2–3), 289–296.

82. Doak, S.H., Manshian, B., Jenkins, G.J. *et al.* (2012) *In vitro* genotoxicity testing strategy for nanomaterials and the adaptation of current OECD guidelines. *Mutat. Res.*, **745** (1–2), 104–111.

83. Maenosono, S., Suzuki, T., and Saita, S. (2007) Mutagenicity of water-soluble FePt nanoparticles in Ames test. *J. Toxicol. Sci.*, **32** (5), 575–579.

84. Balasubramanyam, A., Sailaja, N., Mahboob, M. *et al.* (2009) Evaluation of genotoxic effects of oral exposure to aluminum oxide nanomaterials in rat bone marrow. *Mutat. Res.*, **676** (1–2), 41–47.

85. Liu, Y., Xia, Q., Liu, Y. *et al.* (2014) Genotoxicity assessment of magnetic iron oxide nanoparticles with different particle sizes and surface coatings. *Nanotechnology*, **25** (42), 425101.

86. Kim, H.R., Kim, M.J., Lee, S.Y. *et al.* (2011) Genotoxic effects of silver nanoparticles stimulated by oxidative stress in human normal bronchial epithelial (BEAS-2B) cells. *Mutat. Res.*, **726** (2), 129–135.

87. Lopes, I., Ribeiro, R., Antunes, F.E. *et al.* (2012) Toxicity and genotoxicity of organic and inorganic nanoparticles to the bacteria *Vibrio fischeri* and *Salmonella typhimurium*. *Ecotoxicology*, **21** (3), 637–648.

88. Pitkänen, M., Kangas, H., Laitinen, O. *et al.* (2014) Characteristics and safety of nano-sized cellulose fibrils. *Cellulose*, **21** (6), 3871–3886.

89. Kisin, E.R., Murray, A.R., Keane, M.J. *et al.* (2007) Single-walled carbon nanotubes: geno- and cytotoxic effects in lung fibroblast V79 cells. *J. Toxicol. Environ. Health A*, **70** (24), 2071–2079.

90. Wirnitzer, U., Herbold, B., Voetz, M. *et al.* (2009) Studies on the *in vitro* genotoxicity of baytubes, agglomerates of engineered multi-walled carbon-nanotubes (MWCNT). *Toxicol. Lett.*, **186** (3), 160–165.

91. Hakura, A., Suzuki, S., and Satoh, T. (1999) Advantage of the use of human liver S9 in the Ames test. *Mutat. Res. Genet. Toxicol. Environ. Mutagen.*, **438** (1), 29–36.

92. Finette, B.A., Kendall, H., and Vacek, P.M. (2002) Mutational spectral analysis at the HPRT locus in healthy children. *Mutat. Res. Fundam. Mol. Mech. Mutagen.*, **505** (1-2), 27–41.

93. Stoll, U., Schmidt, A., Schneider, E. *et al.* (1995) Killing and mutation of Chinese hamster V79 cells exposed to accelerated oxygen and neon ions. *Radiat. Res.*, **142** (3), 288–294.

94. Sculley, D.G., Dawson, P.A., Emmerson, B.T. *et al.* (1992) A review of the molecular basis of hypoxanthine-guanine phosphoribosyltransferase (HPRT) deficiency. *Hum. Genet.*, **90** (3), 195–207.

95. Albertini, R.J. (2001) HPRT mutations in humans: biomarkers for mechanistic

studies. *Mutat. Res. Rev. Mutat. Res.*, **489** (1), 1–16.

96. Wang, J.J., Sanderson, B.J., and Wang, H. (2007) Cyto- and genotoxicity of ultrafine TiO_2 particles in cultured human lymphoblastoid cells. *Mutat. Res.*, **628** (2), 99–106.
97. Wang, J.J., Sanderson, B.J., and Wang, H. (2007) Cytotoxicity and genotoxicity of ultrafine crystalline SiO_2 particulate in cultured human lymphoblastoid cells. *Environ. Mol. Mutagen.*, **48** (2), 151–157.
98. Wang, J.J., Wang, H., and Sanderson, B.J.S. (2007) Ultrafine quartz-induced damage in human lymphoblastoid cells *in vitro* using three genetic damage end-points. *Toxicol. Mech. Methods*, **17** (4), 223–232.
99. Huk, A., Izak-Nau, E., Reidy, B. *et al.* (2014) Is the toxic potential of nanosilver dependent on its size? *Part. Fibre Toxicol.*, **11**, 65.
100. Pergament, E. and Fiddler, M. (1998) The expression of genes in human preimplantation embryos. *Prenat. Diagn.*, **18** (13), 1366–1373.
101. Maskos, U. and Southern, E.M. (1992) Oligonucleotide hybridizations on glass supports: a novel linker for oligonucleotide synthesis and hybridization properties of oligonucleotides synthesised in situ. *Nucleic Acids Res.*, **20** (7), 1679–1684.
102. Stuart, J.M., Segal, E., Koller, D. *et al.* (2003) A gene-coexpression network for global discovery of conserved genetic modules. *Science*, **302** (5643), 249–255.
103. Feng, C., Araki, M., Kunimoto, R. *et al.* (2009) GEM-TREND: a web tool for gene expression data mining toward relevant network discovery. *BMC Genomics*, **10**, 411.
104. Zhang, M., Zhang, Y., Liu, L. *et al.* (2010) Gene expression browser: large-scale and cross-experiment microarray data integration, management, search & visualization. *BMC Bioinf.*, **11**, 433.
105. Yu, W., Zhang, Y., Xu, L. *et al.* (2012) Microarray-based bioinformatics analysis of osteoblasts on TiO_2 nanotube layers. *Colloids Surf., B*, **93**, 135–142.
106. Li, B., Ze, Y., Sun, Q. *et al.* (2013) Molecular mechanisms of nanosized titanium dioxide-induced pulmonary injury in mice. *PLoS One*, **8** (2), e55563.
107. Husain, M., Saber, A.T., Guo, C. *et al.* (2013) Pulmonary instillation of low doses of titanium dioxide nanoparticles in mice leads to particle retention and gene expression changes in the absence of inflammation. *Toxicol. Appl. Pharmacol.*, **269** (3), 250–262.
108. Sheng, L., Wang, L., Sang, X. *et al.* (2014) Nano-sized titanium dioxide-induced splenic toxicity: a biological pathway explored using microarray technology. *J. Hazard. Mater.*, **278**, 180–188.
109. Lim, D.H., Jang, J., Kim, S. *et al.* (2012) The effects of sub-lethal concentrations of silver nanoparticles on inflammatory and stress genes in human macrophages using cDNA microarray analysis. *Biomaterials*, **33** (18), 4690–4699.
110. Shim, W., Paik, M.J., Duc-Toan, N. *et al.* (2012) Analysis of changes in gene expression and metabolic profiles induced by silica-coated magnetic nanoparticles. *ACS Nano*, **6** (9), 7665–7680.
111. Alwine, J.C., Kemp, D.J., and Stark, G.R. (1977) Method for detection of specific RNAs in agarose gels by transfer to diazobenzyloxymethyl-paper and hybridization with DNA probes. *Proc. Natl. Acad. Sci. U.S.A.*, **74** (12), 5350–5354.
112. Streit, S., Michalski, C.W., Erkan, M. *et al.* (2009) Northern blot analysis for detection and quantification of RNA in pancreatic cancer cells and tissues. *Nat. Protoc.*, **4** (1), 37–43.
113. McMaster, G.K. and Carmichael, G.G. (1977) Analysis of single- and double-stranded nucleic acids on polyacrylamide and agarose gels by using glyoxal and acridine orange. *Proc. Natl. Acad. Sci. U.S.A.*, **74** (11), 4835–4838.
114. Bustin, S.A. (2000) Absolute quantification of mRNA using real-time reverse transcription polymerase chain reaction assays. *J. Mol. Endocrinol.*, **25** (2), 169–193.
115. Schmittgen, T.D., Zakrajsek, B.A., Mills, A.G. *et al.* (2000) Quantitative reverse transcription-polymerase chain reaction

to study mRNA decay: comparison of endpoint and real-time methods. *Anal. Biochem.*, **285** (2), 194–204.

116. Li, J.J., Lo, S.L., Ng, C.T. *et al.* (2011) Genomic instability of gold nanoparticle treated human lung fibroblast cells. *Biomaterials*, **32** (23), 5515–5523.

117. Schmittgen, T.D. and Livak, K.J. (2008) Analyzing real-time PCR data by the comparative CT method. *Nat. Protoc.*, **3** (6), 1101–1108.

118. Rajeevan, M.S., Vernon, S.D., Taysavang, N. *et al.* (2001) Validation of array-based gene expression profiles by real-time (kinetic) RT-PCR. *J. Mol. Diagn.*, **3** (1), 26–31.

119. Tautzenberger, A., Lorenz, S., Kreja, L. *et al.* (2010) Effect of functionalised fluorescence-labelled nanoparticles on mesenchymal stem cell differentiation. *Biomaterials*, **31** (8), 2064–2071.

120. Gopinath, P., Gogoi, S.K., Sanpui, P. *et al.* (2010) Signaling gene cascade in silver nanoparticle induced apoptosis. *Colloids Surf., B*, **77** (2), 240–245.

121. Lee, J.H., Cha, K.E., Kim, M.S. *et al.* (2009) Nanosized polyamidoamine (PAMAM) dendrimer-induced apoptosis mediated by mitochondrial dysfunction. *Toxicol. Lett.*, **190** (2), 202–207.

122. Sancar, A., Lindsey-Boltz, L.A., Unsal-Kacmaz, K. *et al.* (2004) Molecular mechanisms of mammalian DNA repair and the DNA damage checkpoints. *Annu. Rev. Biochem.*, **73**, 39–85.

123. Ciccia, A. and Elledge, S.J. (2010) The DNA damage response: making it safe to play with knives. *Mol. Cell*, **40** (2), 179–204.

124. Dizdaroglu, M. (2012) Oxidatively induced DNA damage: mechanisms, repair and disease. *Cancer Lett.*, **327** (1–2), 26–47.

125. Jackson, A.L. and Loeb, L.A. (2001) The contribution of endogenous sources of DNA damage to the multiple mutations in cancer. *Mutat. Res. Fundam. Mol. Mech. Mutagen.*, **477** (1–2), 7–21.

126. Muller, A.K., Farombi, E.O., Moller, P. *et al.* (2004) DNA damage in lung after oral exposure to diesel exhaust particles in Big Blue (R) rats. *Mutat. Res. Fundam. Mol. Mech. Mutagen.*, **550** (1–2), 123–132.

127. Park, D.S., Morris, E.J., Stefanis, L. *et al.* (1998) Multiple pathways of neuronal death induced by DNA-damaging agents, NGF deprivation, and oxidative stress. *J. Neurosci.*, **18** (3), 830–840.

128. Hur, G.M., Kim, Y.-S., Won, M. *et al.* (2006) The death domain kinase RIP has an important role in DNA damage-induced, p53-independent cell death. *J. Biol. Chem.*, **281** (35), 25011–25017.

129. Calderon-Montano, J.M., Burgos-Moron, E., Orta, M.L. *et al.* (2012) Guanidine-reactive agent phenylglyoxal induces DNA damage and cancer cell death. *Pharmacol. Rep.*, **64** (6), 1515–1525.

130. Loft, S. and Poulsen, H.E. (1996) Cancer risk and oxidative DNA damage in man. *J. Mol. Med.*, **74** (6), 297–312.

131. Lee, S.C. and Chan, J.C.N. (2015) Evidence for DNA damage as a biological link between diabetes and cancer. *Chin. Med. J.*, **128** (11), 1543–1548.

132. Smith, T.R., Miller, M.S., Lohman, K.K. *et al.* (2003) DNA damage and breast cancer risk. *Carcinogenesis*, **24** (5), 883–889.

133. Zhou, B.B.S. and Elledge, S.J. (2000) The DNA damage response: putting checkpoints in perspective. *Nat. Geosci.*, **408** (6811), 433–439.

134. Ostling, O. and Johanson, K.J. (1984) Microelectrophoretic study of radiation-induced DNA damages in individual mammalian cells. *Biochem. Biophys. Res. Commun.*, **123** (1), 291–298.

135. Singh, N.P., McCoy, M.T., Tice, R.R. *et al.* (1988) A simple technique for quantitation of low levels of DNA damage in individual cells. *Exp. Cell. Res.*, **175** (1), 184–191.

136. Olive, P.L., Banath, J.P., and Durand, R.E. (1990) Heterogeneity in radiation-induced DNA damage and repair in tumor and normal cells measured using the "comet" assay. *Radiat. Res.*, **122** (1), 86–94.

137. Wan, R., Mo, Y., Feng, L. *et al.* (2012) DNA damage caused by metal nanoparticles: involvement of oxidative stress

and activation of ATM. *Chem. Res. Toxicol.*, **25** (7), 1402–1411.

138. Toyooka, T., Amano, T., and Ibuki, Y. (2012) Titanium dioxide particles phosphorylate histone H2AX independent of ROS production. *Mutat. Res.*, **742** (1–2), 84–91.

139. Cong, Y., Banta, G.T., Selck, H. *et al.* (2011) Toxic effects and bioaccumulation of nano-, micron- and ionic-Ag in the polychaete, *Nereis diversicolor*. *Aquat. Toxicol.*, **105** (3–4), 403–411.

140. Flower, N.A., Brabu, B., Revathy, M. *et al.* (2012) Characterization of synthesized silver nanoparticles and assessment of its genotoxicity potentials using the alkaline comet assay. *Mutat. Res.*, **742** (1–2), 61–65.

141. Singh, S.P., Rahman, M.F., Murty, U.S.N. *et al.* (2013) Comparative study of genotoxicity and tissue distribution of nano and micron sized iron oxide in rats after acute oral treatment. *Toxicol. Appl. Pharmacol.*, **266** (1), 56–66.

142. Kang, S.J., Kim, B.M., Lee, Y.J. *et al.* (2008) Titanium dioxide nanoparticles trigger p53-mediated damage response in peripheral blood lymphocytes. *Environ. Mol. Mutagen.*, **49** (5), 399–405.

143. Demir, E., Akca, H., Turna, F. *et al.* (2015) Genotoxic and cell-transforming effects of titanium dioxide nanoparticles. *Environ. Res.*, **136**, 300–308.

144. Sedelnikova, O.A., Pilch, D.R., Redon, C. *et al.* (2003) Histone H2AX in DNA damage and repair. *Cancer Biol. Ther.*, **2** (3), 233–235.

145. Redon, C., Pilch, D., Rogakou, E. *et al.* (2002) Histone H2A variants H2AX and H2AZ. *Curr. Opin. Genet. Dev.*, **12** (2), 162–169.

146. Mah, L.J., El-Osta, A., and Karagiannis, T.C. (2010) gamma H2AX: a sensitive molecular marker of DNA damage and repair. *Leukemia*, **24** (4), 679–686.

147. Langer-Safer, P.R., Levine, M., and Ward, D.C. (1982) Immunological method for mapping genes on Drosophila polytene chromosomes. *Proc. Natl. Acad. Sci. U.S.A.*, **79** (14), 4381–4385.

148. Amann, R. and Fuchs, B.M. (2008) Single-cell identification in microbial communities by improved fluorescence in situ hybridization techniques. *Nat. Rev. Microbiol.*, **6** (5), 339–348.

149. Pinkel, D., Straume, T., and Gray, J.W. (1986) Cytogenetic analysis using quantitative, high-sensitivity, fluorescence hybridization. *Proc. Natl. Acad. Sci. U.S.A.*, **83** (9), 2934–2938.

150. Gonzalez, L., Thomassen, L.C.J., Plas, G. *et al.* (2010) Exploring the aneugenic and clastogenic potential in the nanosize range: A549 human lung carcinoma cells and amorphous monodisperse silica nanoparticles as models. *Nanotoxicology*, **4** (4), 382–395.

151. Asharani, P.V., Hande, M.P., and Valiyaveettil, S. (2009) Anti-proliferative activity of silver nanoparticles. *BMC Cell Biol.*, **10**, 65.

152. Fenech, M. (2007) Cytokinesis-block micronucleus cytome assay. *Nat. Protoc.*, **2** (5), 1084–1104.

153. Kisin, E.R., Murray, A.R., Sargent, L. *et al.* (2011) Genotoxicity of carbon nanofibers: are they potentially more or less dangerous than carbon nanotubes or asbestos? *Toxicol. Appl. Pharmacol.*, **252** (1), 1–10.

154. Muller, J., Decordier, I., Hoet, P.H. *et al.* (2008) Clastogenic and aneugenic effects of multi-wall carbon nanotubes in epithelial cells. *Carcinogenesis*, **29** (2), 427–433.

155. Howell, W.H. (1890) The life-history of the formed elements of the blood, especially the red blood corpuscles. *J. Morphol.*, **4** (1), 57–116.

156. Schmid, W. (1975) The micronucleus test. *Mutat. Res.*, **31** (1), 9–15.

157. Fenech, M. and Morley, A.A. (1985) Measurement of micronuclei in lymphocytes. *Mutat. Res.*, **147** (1–2), 29–36.

158. Landsiedel, R., Kapp, M.D., Schulz, M. *et al.* (2009) Genotoxicity investigations on nanomaterials: methods, preparation and characterization of test material, potential artifacts and limitations–many questions, some answers. *Mutat. Res.*, **681** (2–3), 241–258.

159. Gurr, J.R., Wang, A.S., Chen, C.H. *et al.* (2005) Ultrafine titanium dioxide particles in the absence of photoactivation can induce oxidative damage to human bronchial epithelial cells. *Toxicology*, **213** (1–2), 66–73.
160. Jaeger, A., Weiss, D.G., Jonas, L. *et al.* (2012) Oxidative stress-induced cytotoxic and genotoxic effects of nano-sized titanium dioxide particles in human HaCaT keratinocytes. *Toxicology*, **296** (1–3), 27–36.
161. Schreck, R.R. and Disteche, C.M. (2001) Chromosome banding techniques. *Curr. Protoc. Hum. Genet., editorial board, Jonathan L. Haines et al*. **Chapter 4**, Unit4.2.
162. Bayani, J. and Squire, J.A. (2004) Traditional banding of chromosomes for cytogenetic analysis. *Curr. Protoc. Hum. Genet., editorial board, Juan S. Bonifacino et al*. **Chapter 22**, Unit 22.23.
163. Speicher, M.R. and Carter, N.P. (2005) The new cytogenetics: blurring the boundaries with molecular biology. *Nat. Rev. Genet.*, **6** (10), 782–792.
164. Luo, D., Guo, J., Wang, F. *et al.* (2009) Preparation and evaluation of anti-Helicobacter pylori efficacy of chitosan nanoparticles *in vitro* and *in vivo*. *J. Biomater. Sci., Polym. Ed.*, **20** (11), 1587–1596.
165. Huang, Y., Gao, H., Gou, M. *et al.* (2010) Acute toxicity and genotoxicity studies on poly(epsilon-caprolactone)-poly(ethylene glycol)-poly(epsilon-caprolactone) nanomaterials. *Mutat. Res.*, **696** (2), 101–106.
166. Theogaraj, E., Riley, S., Hughes, L. *et al.* (2007) An investigation of the photo-clastogenic potential of ultrafine titanium dioxide particles. *Mutat. Res.*, **634** (1–2), 205–219.
167. Honma, M., Takahashi, T., Asada, S. *et al.* (2012) *In vitro* clastogenicity and phototoxicity of fullerene (C(60)) nanomaterials in mammalian cells. *Mutat. Res.*, **749** (1–2), 97–100.
168. Omid, A., Elham, G., and Alireza, A. (2012) Size-dependent genotoxicity of graphene nanoplatelets in human stem cells. *Biomaterials*, **33** (32), 8017–8025.
169. Ema, M., Imamura, T., Suzuki, H. *et al.* (2013) Genotoxicity evaluation for single-walled carbon nanotubes in a battery of *in vitro* and *in vivo* assays. *J. Appl. Toxicol.*, **33** (9), 933–939.
170. Ema, M., Imamura, T., Suzuki, H. *et al.* (2012) Evaluation of genotoxicity of multi-walled carbon nanotubes in a battery of *in vitro* and *in vivo* assays. *Regul. Toxicol. Pharm.*, **63** (2), 188–195.
171. Di Giorgio, M.L., Di Bucchianico, S., Ragnelli, A.M. *et al.* (2011) Effects of single and multi walled carbon nanotubes on macrophages: cyto and genotoxicity and electron microscopy. *Mutat. Res.*, **722** (1), 20–31.
172. McClintock, B. (1938) The production of homozygous deficient tissues with mutant characteristics by means of the aberrant mitotic behavior of ring-shaped chromosomes. *Genetics*, **23** (4), 315–376.
173. Latt, S.A. (1973) Microfluorometric detection of deoxyribonucleic acid replication in human metaphase chromosomes. *Proc. Natl. Acad. Sci. U.S.A.*, **70** (12), 3395–3399.
174. Kusunoki, Y., Hayashi, T., Hirai, Y. *et al.* (1994) Increased rate of spontaneous mitotic recombination in T lymphocytes from a Bloom's syndrome patient using a flow-cytometric assay at HLA-A locus. *Jpn. J. Cancer Res.*, **85** (6), 610–618.
175. Langlois, R.G., Bigbee, W.L., Jensen, R.H. *et al.* (1989) Evidence for increased in vivo mutation and somatic recombination in Bloom's syndrome. *Proc. Natl. Acad. Sci. U.S.A.*, **86** (2), 670–674.
176. Kato, T., Totsuka, Y., Ishino, K. *et al.* (2013) Genotoxicity of multi-walled carbon nanotubes in both *in vitro* and *in vivo* assay systems. *Nanotoxicology*, **7** (4), 452–461.
177. Mahmoudi, M., Laurent, S., Shokrgozar, M.A. *et al.* (2011) Toxicity evaluations of superparamagnetic iron oxide nanoparticles: cell "vision" versus physicochemical properties of nanoparticles. *ACS Nano*, **5** (9), 7263–7276.
178. Kuo, M.L., Jee, S.H., Chou, M.H. *et al.* (1998) Involvement of oxidative stress

in motorcycle exhaust particle-induced DNA damage and inhibition of intercellular communication. *Mutat. Res. Genet. Toxicol. Environ. Mutagen.*, **413** (2), 143–150.

179. Pierscionek, B.K., Li, Y., Yasseen, A.A. *et al.* (2010) Nanoceria have no genotoxic effect on human lens epithelial cells. *Nanotechnology*, **21** (3), 035102.

180. Wilkins, M. (2009) Proteomics data mining. *Expert Rev. Proteomics*, **6** (6), 599–603.

181. James, P. (1997) Protein identification in the post-genome era: the rapid rise of proteomics. *Q. Rev. Biophys.*, **30** (4), 279–331.

182. Goh, W.W., Lee, Y.H., Ramdzan, Z.M. *et al.* (2012) Proteomics signature profiling (PSP): a novel contextualization approach for cancer proteomics. *J. Proteome Res.*, **11** (3), 1571–1581.

183. Tonge, R., Shaw, J., Middleton, B. *et al.* (2001) Validation and development of fluorescence two-dimensional differential gel electrophoresis proteomics technology. *Proteomics*, **1** (3), 377–396.

184. Aebersold, R. and Mann, M. (2003) Mass spectrometry-based proteomics. *Nat. Geosci.*, **422** (6928), 198–207.

185. Ho, Y., Gruhler, A., Heilbut, A. *et al.* (2002) Systematic identification of protein complexes in *Saccharomyces cerevisiae* by mass spectrometry. *Nat. Geosci.*, **415** (6868), 180–183.

186. MacBeath, G. (2002) Protein microarrays and proteomics. *Nat. Genet.*, **32**, 526–532.

187. Nicholson, J.K., Lindon, J.C., and Holmes, E. (1999) 'Metabonomics': understanding the metabolic responses of living systems to pathophysiological stimuli via multivariate statistical analysis of biological NMR spectroscopic data. *Xenobiotica*, **29** (11), 1181–1189.

188. Lindon, J.C. and Nicholson, J.K. (2008) Spectroscopic and statistical techniques for information recovery in metabonomics and metabolomics. *Annu. Rev. Anal. Chem.*, **1**, 45–69.

189. Nicholson, J.K. and Lindon, J.C. (2008) Systems biology: metabonomics. *Nat. Geosci.*, **445** (7216), 1054–1056.

190. Tenzer, S., Docter, D., Rosfa, S. *et al.* (2011) Nanoparticle size is a critical physicochemical determinant of the human blood plasma corona: a comprehensive quantitative proteomic analysis. *ACS Nano*, **5** (9), 7155–7167.

191. Lu, X., Tian, Y., Zhao, Q. *et al.* (2011) Integrated metabonomics analysis of the size-response relationship of silica nanoparticles-induced toxicity in mice. *Nanotechnology*, **22** (5), 055101.

192. Feng, J., Li, J., Wu, H. *et al.* (2013) Metabolic responses of HeLa cells to silica nanoparticles by NMR-based metabolomic analyses. *Metabolomics*, **9** (4), 874–886.

193. Mirzajani, F., Askari, H., Hamzelou, S. *et al.* (2014) Proteomics study of silver nanoparticles toxicity on *Oryza sativa* L. *Ecotoxicol. Environ. Saf.*, **108**, 335–339.

194. Sund, J., Palomaki, J., Ahonen, N. *et al.* (2014) Phagocytosis of nano-sized titanium dioxide triggers changes in protein acetylation. *J. Proteomics*, **108**, 469–483.

195. Zhang, L., Wang, L., Hu, Y. *et al.* (2013) Selective metabolic effects of gold nanorods on normal and cancer cells and their application in anticancer drug screening. *Biomaterials*, **34** (29), 7117–7126.

196. Feng, J., Zhao, J., Hao, F. *et al.* (2010) NMR-based metabonomic analyses of the effects of ultrasmall superparamagnetic particles of iron oxide (USPIO) on macrophage metabolism. *J. Nanopart. Res.*, **13** (5), 2049–2062.

197. Zanin, H., Hollanda, L.M., Ceragioli, H.J. *et al.* (2014) Carbon nanoparticles for gene transfection in eukaryotic cell lines. *Mater. Sci. Eng. C, Mater. Biol. Appl.*, **39**, 359–370.

198. Lei, R., Wu, C., Yang, B. *et al.* (2008) Integrated metabolomic analysis of the nano-sized copper particle-induced hepatotoxicity and nephrotoxicity in rats: a rapid in vivo screening method for nanotoxicity. *Toxicol. Appl. Pharmacol.*, **232** (2), 292–301.

11
Analyses Methods for Nanoparticle Interaction with Biomacromolecules

Liming Wang and Chunying Chen

11.1
Introduction

Unique physicochemical properties of nanosized materials have attracted much attention from industry and health care, and the employed nanotechnology brings boom times to these fields. Safety concerns also increase with a wide range of uses of nanomaterials in manufacture places (information technology, mechanical and electrical devices, building materials, catalysts, etc.), consumer products (food, cosmetics, clothing, etc.), and biomedical products (drug delivery, antibacterial agents, etc.), as well as the exhausted air pollutants from industry and motor vehicles [1–3]. To better understand and predict the environmental and health effects caused by nanomaterials, scientists have established systematic methods to study nanotoxicity and revealed correlated mechanisms.

Nanotoxicology is a complex research field that refers to various interactions between nanoparticles (NPs) and biological entities at different levels including biomolecules, cells, animals, or human beings. To evaluate toxic potentials of NPs *in vivo* and *in vitro*, it is crucial to study the dynamic processes that initiate from exposure, circulation, distribution, transformation, and metabolism, to biological responses. These processes closely correlate to the microenvironment where NPs stay, which can be influenced by the local temperature, pressure, ionic strength, viscosity, biological components, osmotic pressure, pH value, hydrodynamic shear, and so on [4]. Furthermore, for biomedical application of NPs as drug delivery and imaging carriers, intravenously administrated NPs will enter into the physiological fluids that are filled with several thousand kinds of proteins [5–8].

In the past decade, most researches have focused on the protein adsorption on NPs. It is known that NPs keep in contact with biomacromolecules before and during their interaction with cells, tissue, organs, and animal individuals [9]. In particular, thousands of proteins are ubiquitous in biological fluids including blood, urine, gastric juice, and lymphatic fluid *in vivo*. Proteins are also widely distributed in the biological membranes, the cellular contents, and the extracellular matrix components to serve as building materials for cells, microenvironment,

Toxicology of Nanomaterials, First Edition. Edited by Yuliang Zhao, Zhiyong Zhang, and Weiyue Feng.

and organs. In addition, proteins serve as functional signal molecules and enzymes to modulate the biochemical reaction in the physiological and pathological conditions. Besides, polysaccharides and nucleic acids are considered the other two types of macromolecules that play important biological functions in the life activities [10].

NPs have a larger surface-to-volume ratio than bulk materials, and they have a larger curvature than a flat surface [11]. With an increase in the size, both the ratio of surface-to-bulk atoms and surface curvature of NPs decrease, which means that the surface of NPs have higher free energy compared with bulk materials [4]. When NPs come into contact with biomolecules, these biomolecules will progressively and selectively adsorb on to the NP surface to reduce the surface energy [12]. Due to the multiple components in the biological media, the interaction process of NPs and the macromolecules is quite complicated. Taking protein adsorption as an example, the abundant proteins such as albumin, fibrinogen, and immune globulins immediately bind on NPs to form "soft" corona by nonspecific adsorption [13–15]. These proteins are then replaced by other less abundant proteins with much higher affinity to NPs as "hard corona" [8, 12, 16, 17]. The "hard corona" indicates the long-lived equilibrium state for protein adsorption, representing a proteins signature of NPs in a certain environment, and the NP size and surface hydrophobicity correlate with the types of adsorbed proteins [18]. Meanwhile, the free proteins in biological medium can also exchange with the adsorbed proteins on the surface [16]. Both the characteristics of NPs and the microenvironment determine the adsorption of biomacromolecules on NPs [16]. The adsorption of biomolecules correlates to the intrinsic properties of NPs including size, shape, chemical composition, surface chemistry (charges, coatings, and functional groups), hydrophobicity, crystallinity and crystal face, electronic states, and surface structures (topology, curvature, and roughness) in the biological medium [19–22]. The interactions between biomacromolecules and NPs thus refer to these kinetic and thermodynamic processes, which generally determine the biological responses of the biomacromolecule–NP complexes.

11.2 Biological Effects due to Nanoparticle–Biomolecule Interactions

The interactions between NPs and macrobiomolecules play crucial roles in mediating biomedical events including biological responses and biomedical applications. For example, the protein adsorption on NPs modulates multiple physiological and pathological effects of NPs such as cellular uptake of NPs [23–29], immunological responses [30–34], change in the integrity of the cell membrane or inner membranes [27, 35–38], membrane-receptor-associated signaling pathway [39, 40], oxidation stress and energy generation [41, 42], and the induction of amyloid-associated and other diseases [43]. It is also significant to know how the protein corona on NPs affects the payload and release of drugs [44], target delivery, and therapy of functional nanocarriers *in vivo* in biomedicine [45–47]. The

understanding of the correlation of biomacromolecule–NP interactions with biological effects will benefit the rational design of the safe and efficient nanomaterials used in biomedicine [48–50].

Tailoring the size and surface chemistry of NPs can provide an opportunity to tune the physicochemical properties of the NP surface that enables cellular delivery and other NP-mediated cellular effects. Before the internalization of NPs by cells, the complex of protein–NPs forms in the physiological fluids and their surface characteristics are hidden behind the protein layers [12]. Adsorbed proteins can provide a biological identity to NPs, which influences the ligand–receptor interaction-associated events such as cellular uptake, signaling pathways, target recognition, and immune responses to NPs.

11.2.1
Influences of Protein–NP Interactions on Cellular Uptake and Targeted Recognition

As is known, the cellular uptake of NPs is largely dependent on the size and shape, ligand density, surface charge of NPs, and the expression levels of cell membrane receptors [32], in which the protein corona plays a crucial role. Transferrin (Tf) is a kind of ubiquitous protein distributed in the blood, and many cells express the receptors for transferrin to regulate its endocytosis, trafficking, and exocytosis of the cells. Ligand molecules such as Tf can adsorb on Au NPs. Then, the Tf-Au NP complex binds the surface Tf receptors, induces the cell membrane wrapping, and results in the internalization and exocytosis of NPs. A competition between thermodynamic driving force for the cell membrane wrapping and the receptor diffusion kinetics determines the total uptake of NPs [24]. In contrast, Figure 11.1 shows that the presence of serum protein on NP surfaces reduces the cellular uptake of NPs. Zhu *et al*. [51] prepared five types of Au NPs that feature a core size (about 2 nm) and positive charge but different hydrophobicities. When these Au NPs were incubated with cell culture media with bovine serum, sodium dodecyl sulphate–polyacrylamide gel electrophoresis (SDS-PAGE) results show that bovine serum albumin (BSA), IgG, and Tf are the most abundant proteins adsorbed on Au NPs. Among these three proteins, the adsorption of BSA played a major role in suppressing the interactions of NPs with human cervical carcinoma cells (HeLa) and reducing the internalized amount of Au NPs by cells.

Adsorbed proteins on NPs are capable of not only reducing the aggregate size of TiO_2 NPs in cell culture medium but also increasing the consequent accumulation of NPs, compared with those in the nonserum media. Vitronectin, an abundant glycoprotein in serum and the extracellular matrix, was found to be present on the surface of TiO_2 NPs, and its adsorption determines the endocytosis pathway in clathrin-dependent mode [52]. In serum-free and serum-containing conditions, NPs exhibit different outcomes for cellular uptake [23, 53]. SiO_2 NPs in serum-free media showed a higher degree of adhesion on the cell membrane that contributed to higher uptake efficiency. In contrast, serum protein corona prevents the bare surface of NPs in contacting the cell membrane directly. As a result, SiO_2 NPs in this condition avoid acute cytotoxicity due to the bare NP surface–cell membrane

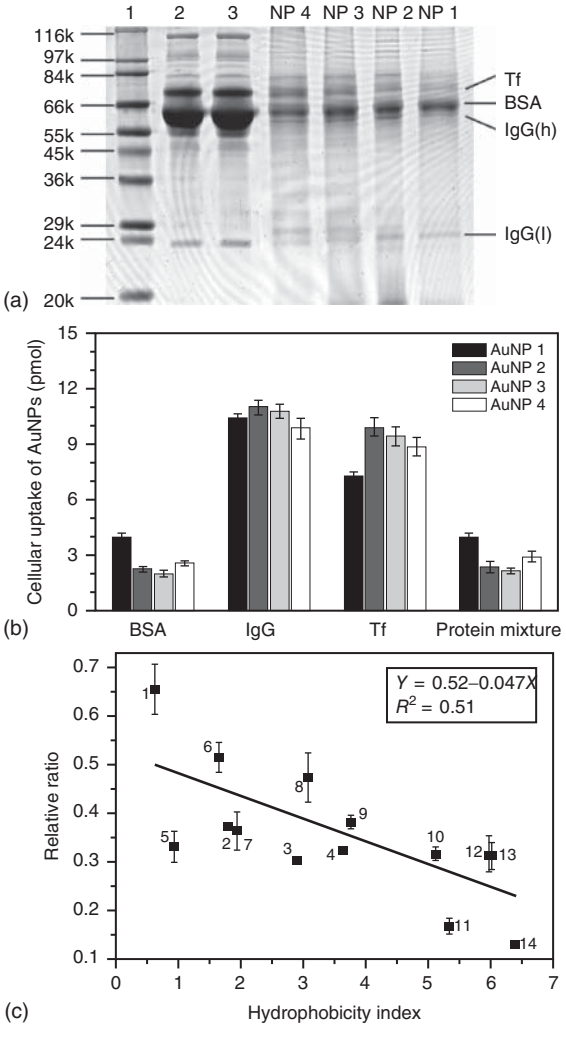

Figure 11.1 Surface hydrophobicity of Au NPs influencing the adsorption of serum proteins that determines the cellular uptake of NPs. (a) SDS-PAGE of serum proteins adsorbed on Au NPs. The lanes labeled with NP 4, NP 3, NP 2, and NP 1 correspond to the proteins adsorbed to the corresponding Au NPs that are incubated with 50% FBS for 6 h. The hydrophobicity index is shown as LogP square values, representing the hydrophobicity of the head groups. The values for four NPs are 0.63, 1.8, 2.9, and 3.65, respectively. (b) Uptake of four Au NPs inside HeLa cells within culture media containing three kinds of serum proteins (BSA, IgG, and Tf). The contents of three proteins are 25 mg/ml (BSA), 5 mg/ml (IgG), and 2 mg/ml (Tf). The protein mixture refers to a medium containing a mixture of all three proteins used at the same concentrations. (c) The relationship between Au NP surface hydrophobicity (LogP square values) and the amount of cellular uptake. HeLa cells that were exposed to Au NPs in the media supplemented with 10% FBS. (Reprinted with permission from [51]. © 2012 John Wiley & Sons, Ltd.)

interaction [23]. However, it is difficult to provide a conclusion whether protein adsorption encourages or inhibits cellular uptake of NPs. The reason may be that the structures of cells and protein–NP complex are complicated [32]. For different types of cells, the expression level and the distribution density of receptors in the cell membrane are quite distinct. Moreover, cells can internalize NPs via different pathways such as micropinocytosis, phagocytosis, and pinocytosis that largely depend on the cell types and the size of the formed engulfed vesicles [54].

Nonspecific adsorption of serum proteins on NPs also influences the target recognition of NPs by the disease cells that overexpress receptors. An ideal strategy for target therapy allows NPs to selectively accumulate in diseased tissues with high sensitivity for diagnosis. To attain this object, the surface of NPs can be simultaneously modified by the antifouling polymer polyethylene glycol (PEG) [55] and target ligands including peptides [56], aptamers [57], and antibodies [58]. However, the formation of serum protein corona may mask the surface ligands of targeted NPs to interact with cell receptors, thereby resulting in a loss of targeting specificity [46]. A recent work has indicated that the proper backfill PEG modified on NPs is necessary to make the targeting of NPs more specific [59]. The designed chain length of the backfilled PEG should be less than that of the ligand linker in order to not prevent the binding of the biorecognition molecule to its target receptor. The ligand chain was composed of OPSS-PEG-Herceptin-AF647, which is composed of Herceptin and the conjugated fluorescent dye Alexa Fluor 647, together with orthopyridyldisulfidepolyethyleneglycol-*N*-hydroxysuccinimideester (OPSS-PEG-NHSester) (Figure 11.2a). The backfilled methoxy-polyethylene glycol (mPEG) has four kinds of chain lengths: 1, 2, 5, and 10 kDa by thiol coordination. In serum-containing medium, Herceptin-conjugated Au NPs were incubated with SKBR3 (overexpression of ErbB2-receptor) and MCF7 cells (low expression of receptor), respectively. Flow cytometry data showed that binding of Au NPs to cells is dependent on the chain length of backfilled PEG molecules (Figure 11.2b,c). Without backfilling or backfilling by long PEG chain, serum proteins will bind to the surface to sterically block the binding of the biorecognition molecule to the receptor. With a short chain length of mPEG, PEG backfilling reduces the amount of serum proteins bound on Au NPs so significantly that it prevents these proteins from sterically blocking the binding of the biorecognition molecule to the receptor target. This work improves our understanding of the binding specificity of the NP conjugates to targeted diseased cells in a serum-rich physiological environment.

11.2.2
Influences of Protein–NP Interactions on Cell Signaling Pathways

When protein–NPs interact with cells, NPs may contact two types of membranes: the cell membrane and the endosomal/lysosomal membrane [4]. The wide distribution of receptor molecules on the cell membrane involves in important cell signaling pathways. The contact of NPs with receptors during the cellular

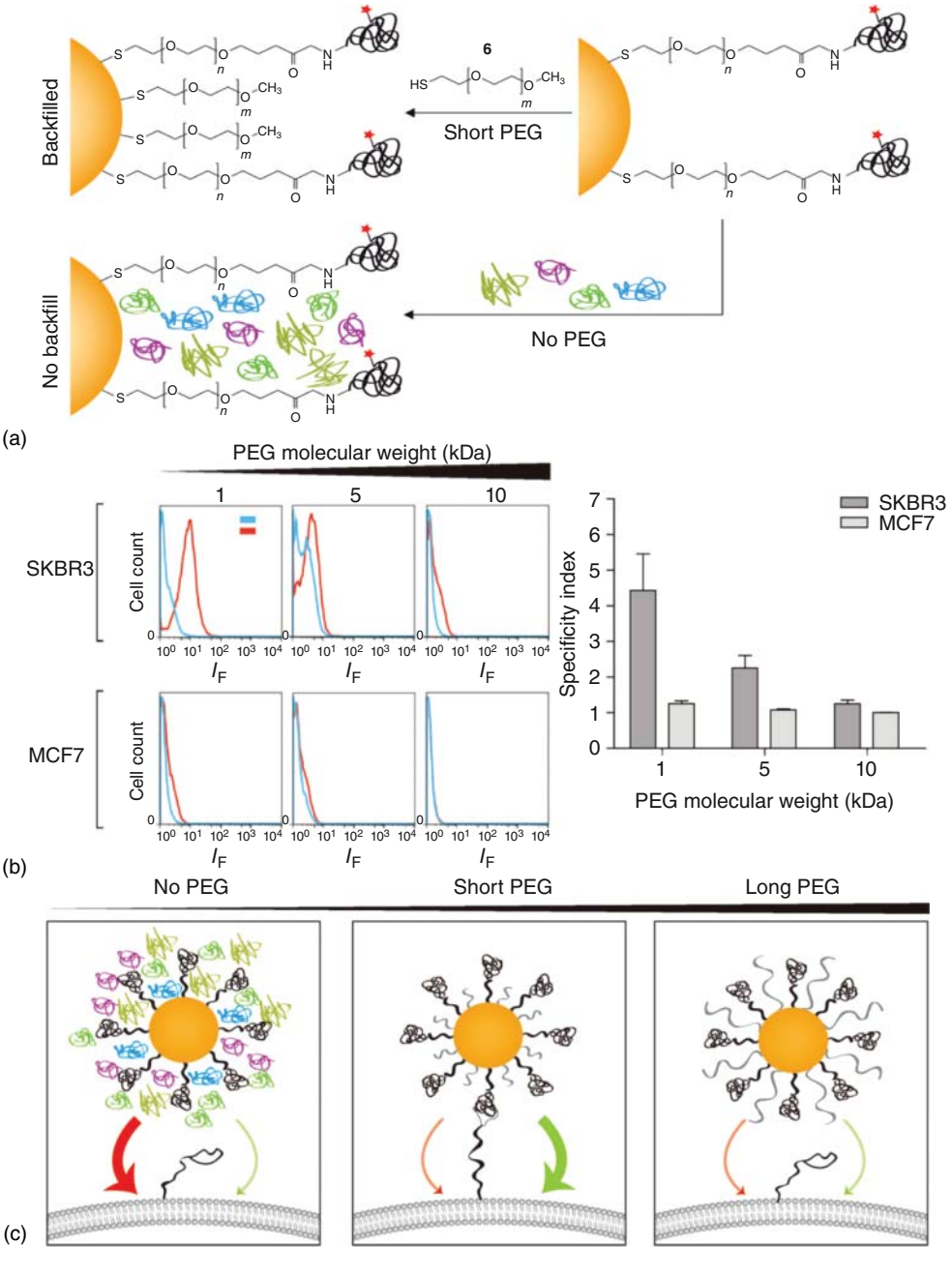
Backfilled
No backfill
6
Short PEG
No PEG
(a)
PEG molecular weight (kDa)
1
5
10
SKBR3
MCF7
Cell count
I_F
Specificity index
SKBR3
MCF7
PEG molecular weight (kDa)
(b)
No PEG
Short PEG
Long PEG
(c)

uptake may affect receptor-associated cell signaling pathways. Once NPs are engulfed in the vesicles, NPs will be transferred to organelles such as endosomes and lysosomes with more acidic pH values. In these vesicles, protein masks on NPs may be dissociated from the surface and NPs will expose the pristine surface to contact the membrane structures of these organelles. For the two cases, protein corona regulates cell signaling pathways that are related to redox [41, 42], inflammation [30, 33], apoptosis and necrosis [27, 36–38, 60], cell proliferation and differentiation [61–63], energy generation, and cell migration [41, 64, 65]. In detail, MAP (mitogen-activated protein) kinase cascades such as ERK (extracellular signal-regulated kinases), p38 mitogen-activated protein kinase, and JNK (c-Jun N-terminal kinases), as well as redox-sensitive transcription factors such as NF-kB and Nrf-2 were closely associated signaling pathways. The modulation of signaling pathways by NPs can help illustrate molecular mechanism about their cytotoxicity.

The interaction of NPs with proteins can trigger inflammation-related signaling pathways and provoke inflammation responses. A recent work has reported that poly(acrylic acid)-coated gold nanoparticles (PAA-GNPs) bound to proteins can result in unfolding of fibrinogen, which promotes interaction with the integrin receptor, Mac-1. It serves as an alternative mechanism for inflammatory response induced by NPs. They used SDS-PAGE and two-dimensional gel electrophoresis (2-DGE) to study human plasma proteins bound to PAA-GNPs. They found that fibrinogen is the major human plasma protein bound by PAA-GNPs and their interaction induced the changes in the secondary structure of fibrinogen. Consequently, the fibrinogen/PAA–GNP complexes selectively bind to Mac-1 receptors of monocytes to activate NF-κB pathway and to induce the expression and release of cytokines. However, neither fibrinogen nor PAA-GNPs alone can activate the Mac-1 receptor pathway and induce more cytokine release [30]. Another work shows that serum albumin protein, BSA-dispersed multiwalled carbon nanotubes (MWCNTs) have different immunological stimulus to monocytes compared to the pluronic PF-108 surfactant-dispersed MWCNTs. The reason is that BSA on the surface undergoes conformational change and detaches from MWCNTs in acidic pH 4.5 of the lysosomes. These MWCNTs can expose the pristine surface and contact the lysosomal membrane directly, activating the TGF-β1 pathway and the associated inflammation such as the lung profibrogenic effect. However, for PF-108-dispersed MWCNTs, the polymer PF-108 attachment remains intact in

←

Figure 11.2 PEG backfilling preventing non-specific adsorption of serum proteins on NPs that improves binding specificity of NPs to targeted cells. (a) Scheme of the backfilling strategy for mPEG docking with different chain lengths on OPSS-PEG-Herceptin-AF647-modifed Au NPs. (b) The specific binding efficiency of Herceptin-conjugated Au NPs to cells in media containing human serum. Two kinds of cells have high-level (SKBR3) or low-level (MCF7) expression of Herceptin-associated receptor, ErbB2-receptor. IF shows fluorescence intensity, and cell count means normalized cell number included in all events counted. Red and blue lines represent cells treated with or without competitive Herceptin molecules, respectively. (c) The binding specificity of NPs to targeted cells is dependent on serum-protein adsorption and the chain length of PEG for backfilling. (Reprinted with permission from [59]. © 2014 John Wiley & Sons, Ltd.)

the lysosomal conditions, possibly due to the terminal PEO (polyethylene oxide) hydroxyl groups bound to protons providing electrostatic repulsion. Therefore, pluronic coating not only exhibits good dispersion but also reduces the adsorption of the protein in physiological fluids on the surface that may cause profibrogenic effects of these tubes *in vitro* and in intact animal lungs [33].

Furthermore, nanomaterials can interact with proteins or receptors to modulate cell differentiation. For example, an interesting work by Yan *et al.* [62] has indicated that carboxylated MWCNTs are able to bind to bone morphogenetic protein (BMP) receptors to form NP corona that is able to promote differentiation of mouse myoblast cells into myocytes and to inhibit cell apoptosis under the myogenic conditions. The authors found that BMP pathway is one of the most affected pathways among the modulated 400 genes by CNTs [66]. The electrostatic, hydrophobic, and pi–pi stacking interactions may involve the formation of CNT–protein specific adsorption. The binding of CNTs to BMP receptor 2 attenuates BMP receptor signaling activity that prevents the phosphorylation of BMP receptor 1. Then, CNTs decreased the expression of id genes on mRNA and protein levels but activated the myogenin-dependent pathways (HEB-MyoD), which triggers the initiation of differentiation into muscles. Additional effect of CNTs on the myocytes is the suppressed apoptosis that was contributed by the upregulated p21 expression after HEB-MyoD (Myogenic Differentiation Antigen D protein) binds to p21 promoter. Finally, CNTs modulate cell differentiation and apoptosis by binding to membrane receptors. Another work also showed that nanocrystalline diamond (NCD) can bind BMP-2 molecules by means of physisorption. To show the interaction details between BMP-2 and NCD, the authors employed highly sensitive analytical methods such as X-ray photoelectron spectroscopy (XPS), X-ray diffraction (XRD), electron energy-loss spectroscopy (EELS), and matrix-assisted laser desorption/ionization time-of-flight mass spectrometry (MALDI-TOF-MS) to understand the surface properties, affinity of binding, binding sites, and the amount of adsorbed proteins, and so on. By combining experiment results with computer simulation, they found that BMP-2 firmly binds H- or O-terminated on the surface of NCD-coated titanium NCD via van der Waals interactions and H bonding. The bound BMP-2 on NCD possessed the physiological functions to bind BMP receptor and to induce the expression of alkaline phosphatase [67]. Therefore, protein corona plays important roles in mediating cell signaling pathways to influence physiological functions for cells or individuals.

11.2.3
Influences of Protein Corona on Oxidative Stress and Catalytic Activity

During the interaction of NPs with cells, many NPs are found to trigger oxidative stress and produce catalytic activity, which induce nanotoxicity [4]. Studies showed that protein corona takes part in these chemical processes. The catalytic nanomaterials can generate electron–hole pairs to transfer electrons on the interfaces, which may impair covalent bonds via SH domain or other bonds in proteins

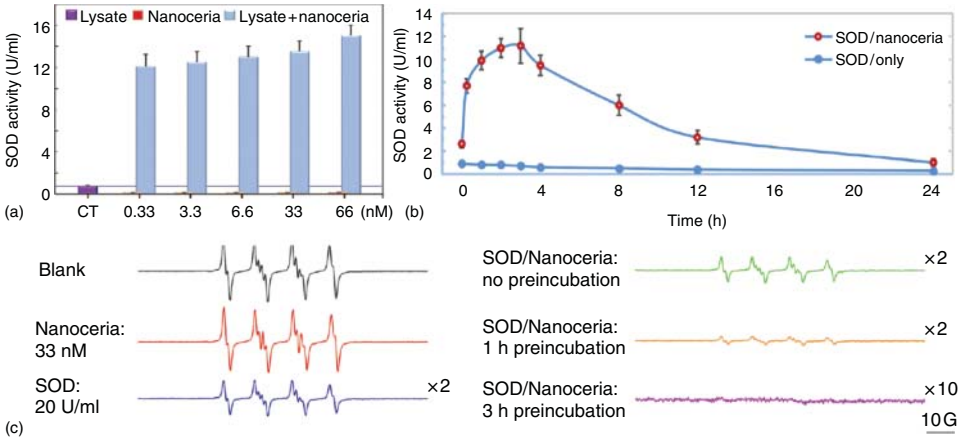

Figure 11.3 Superoxide-scavenging abilities in the CeO_2 NPs (nanoceria). (a) The antioxidant role of CeO_2 NPs mixed with the lysates of human bronchial epithelial cells, (b) the SOD mimetic activity of the CeO_2 NPs after the mixing of CuZn-SOD (final concentration of 1 U/ml) with CeO_2 NPs (0.033 nM) within 24 h, and (c) SOD mimetic activity for CeO_2 NPs. Effect of SOD/CeO_2 NPs on superoxide anions from KO_2 was determined by ESR measurement. (Reprinted with permission from [70]. © 2015 John Wiley & Sons, Ltd.)

and change the structure and conformation of proteins [68, 69]. Furthermore, the catalytic NPs such as iron oxide, CeO_2 NPs, and graphene can decrease cytotoxicity because they can be bound to intracellular proteins with antioxidative capacity [70]. The understanding of NPs and proteins is thus helpful to know the chemical origins of biomedical effects of NPs due to catalysis and redox.

CeO_2 NPs are known as a *superoxide scavenger* and can provide protective effects in physiological environments. A recent work has shown that the incubation of CeO_2 NPs with the cellular lysates can elevate superoxide dismutase (SOD) activity (Figure 11.3a). The catalytic activity is due to the interaction between CuZn-SOD and CeO_2 NPs (Figure 11.3b,c). The active CuZn-SOD can induce the reduction of Ce^{4+} into Ce^{3+} on the surface of CeO_2 NPs [71–73]; however, CeO_2 NPs have plenty of electrons and can regenerate the reactive sites for superoxide scavenging. The CeO_2 NPs can thus present persistent catalytic activity and show antioxidant effects on human bronchial epithelial (16HBE) cells during exposure [70].

Furthermore, graphene oxide (GO) nanosheets possess electron-transfer activity. Besides CuZn-SOD, the electron transfer or redox-associated enzymes may interact with GO, which may affect the activity and functions of enzymes and lead to oxidative stress and perturbation in the physiological behavior of cells. When cells or model animals such as *Caenorhabditis elegans* are exposed to GO, limited hydrogen peroxide can be catalyzed to hydroxyl radicals under normal conditions. However, some external stimuli may induce stress and lead to the released mitochondrial cytochrome c (Cyt c) into the cytoplasm. Cyt c is a heme-containing metalloprotein that can actively react with H_2O_2. The interaction of

Cyt c facilitates the electron transfer in the Cyt c/H_2O_2 system and promotes the catalytic production of active oxidant intermediates (hydroxyl radicals and/or $O{=}Fe^{4+}Cytc^{\bullet+}$) [42]. Therefore, the metalloproteins such as Cyt c can play a cascade amplification role that significantly increases the production of more active free radicals and induces strong nanotoxicity. We found that the intracellular GO can interact with iron–sulfur centers in mitochondrial electron-transfer chain complexes (I–V) and suppresses the reduction of Fe(III) ions to Fe(II) by disrupting electron transfer, resulting in the inhibition of their enzyme activity. Thus, both the ATP synthesis and the activity of succinate dehydrogenase were suppressed in graphene-treated cells. As we know, succinate dehydrogenase participates in both the citric acid cycle and the respiratory electron transfer chain. As a result, suppression in ATP synthesis prevented actin assembly, which attenuated the migration and invasion of cancer cells after graphene treatment [41].

11.2.4 Influences of Protein Corona on NP Surface and the Associated Cytotoxicity

Proteins adsorb on NPs forming protein–NP complexes that change the surface properties of NPs. Besides as the biological identity of protein–NP complex, the adsorbed proteins act as a protective shield to prevent the surface of NPs from directly interacting with the membrane systems of cells.

Cell membrane is a natural barrier to protect cells from the extracellular matters. Damage in the membrane may reduce its integrity and cause acute cytotoxicity such as necrosis. Carbon nanomaterials such as carbon nanotubes and graphene have hydrophobic surface. When they are directly adsorbed on the cell membrane, the hydrophobic forces may abstract the lipid molecules from the membrane and cause defects in the membrane structure. In a physiological environment, the serum proteins are adsorbed on the hydrophobic surface to form a protective shell that effectively prevents the direct contact with carbon surface and reduces damage in the membrane [13, 35]. Furthermore, NPs modified with a bilayer of surfactant molecules have the potential to destroy the cell membrane [37]. For example, the prepared gold nanorods (Au NRs) have cetyltrimethylammonium bromide (CTAB) bilayer on the surface. CTAB bilayer can be dissolved into the lipid and Au NRs can penetrate into the cell membrane to damage its structure. However, proteins can adsorb on the surface of Au NRs and form an organic barrier to cover the toxic CTAB bilayer, resulting in a decreased acute cytoxicity [36]. Of course, the protein corona will detach from NP surface after they are translocated to the digestive endosomes or lysosomes [27]. The re-exposed toxic surface of NPs may also rupture the endosomal/lysosomal membrane to trigger inflammatory responses [74] or apoptosis [38].

In conclusion, it is important to study the interaction of NPs with proteins because the protein–NP complex takes part in various biological process of NPs, influences physiological functions, and may induce pathological changes. Thus, it is necessary to use proper approaches to reveal the detailed information about

the interaction at qualitative and quantitative levels. In the next section, we focus on the methods to understand the interplay between NPs and proteins.

11.3 Basic Methods to Understand NPs and Protein Interactions

With respect to medical applications and biological effects of nanomaterials, the proteins bound to the NP surface to provide biological identity [12]. The dynamic process of protein adsorption and dissociation, the corona composition, the morphology and size, and the structure of corona interface are important to know how NPs have their biological identity. Protein type, local environment, and NP characteristics including surface properties, size, shape, topological structure, and crystal face on NPs play crucial roles in influencing the formation of corona and its properties [75]. For example, composition of protein corona can directly realize the biological identity of corona at the levels of structures and functions. In addition, the interfacial structure of hard/soft corona shows the binding sites, binding forces, and stability of corona.

To know more details on protein adsorption, it is important to study the dynamic process of adsorption and dissociation, the composition of protein corona, the amount of adsorbed proteins, the stability of complex, and the forces and the binding sites for protein–NP interaction. Based on the knowledge, we can reveal the structure or configuration of protein–NP complex that helps understand the structure–activity relationship of NP-induced biological effects. Therefore, it is important to use powerful techniques to improve our knowledge about NP and protein interaction from the aspects of structure, composition, and dynamical and kinetic process. Further, we introduce some conventional methods for characterizing protein–NP interaction.

11.3.1 Methods to Determine Corona Composition

The composition of biomolecules directly links the biological identity of corona; thus, it is important to reveal detailed information on the composition, organization, and dynamics of these biomolecules. It is necessary to identify the protein types and qualify the adsorbed protein components and the dynamic exchange process, which influences the strengths of ligand–receptor interaction, biochemical activity as well as possible biological responses. Proper methods are used to isolate and separate protein corona, and sensitive techniques are useful to identify corona composition before further characterization.

11.3.1.1 Protein Isolation

To study protein–NP interaction, it is necessary to incubate NPs with physiological fluids containing proteins for different time intervals and then isolate the complex from other proteins. The protein components in physiological

fluids such as blood are quite complex. Proper techniques are thus crucial to isolate protein–NP complex from the unbound proteins in the environment to characterize the NP–protein interaction. Differential centrifugal sedimentation (DCS) and size exclusion chromatography (SEC) have been widely used to differentiate the size and density of unbound proteins on the NPs [75].

With respect to DCS, the larger and denser particle can be centrifuged to be pellets at low centrifugal forces. Hard corona bound on NPs can be directly isolated from the rest of proteins by centrifugation, while the soft corona via weak adsorption may be disturbed during the separation process. It is simple to collect firmly adsorbed proteins on NPs, but the loosely adsorbed proteins will be lost due to high-speed centrifugation and repeated washing steps for protein–NP pellets. In addition, the sedimentation of high-molecular-weight proteins or agglomerates at the tube bottom is collected with corona NPs that will mislead the protein identification. The combination of DCS and SEC or magnetic separation and microfiltration can exclude false positives [76].

SEC gel filtration can also measure the rates of exchange with proteins. This method is less perturbing of protein–NP complex than DCS. SEC is capable of revealing quantitative information on protein–NP interactions. Cedervall *et al.* [22] used a chromatographic resin (with a separation range $<5\times10^5$ to $>10^8$ kDa) to differentiate proteins and NPs, rather than different proteins. This method can differentiate the affinity and dissociation rate of proteins bound to the surface of NPs. When human serum albumin (HSA) was incubated with *N*-isopropylacrylamide (NIPAM): *N-tert*-butylacrylamide (BAM) copolymer NPs (NIPAM/BAM NP), the mixture had a quite different elution profile compared to HSA. The hydrophobicity or hydrophilicity of NPs can be tuned by changing the composition of NIPAM and BAM. HSA preferred to bind to hydrophilic NPs so firmly that the mixture of HSA and NPs eluted earlier than the free HSA. When the hydrophobic NPs were mixed with human plasma, the proteins with less hydrophilicity than HSA may a high affinity or low dissociation rate to these hydrophobic NPs. The mixture of proteins and NPs eluted as double peaks with elution time equivalent to the free protein and earlier than HSA on the same particles. Therefore, SEC gel filtration together with SDS/PAGE and isothermal titration calorimetry (ITC) are powerful to assess affinity of protein binding [22].

11.3.1.2 **Protein Identification**

After isolating protein–NP from the mixture, protein separation, quantification, and identification are necessary to study detailed information about individual proteins within the corona. To separate the proteins from NPs, the protein–NP complex is usually treated with high temperature, high salt concentrations, reducing agents (DTT (DL-dithiothreitol) or beta-mercaptoethanol), detergents, and enzymes. The following step is to separate proteins from the mixture. Electrophoresis can be used as a conventional method to separate and analyze multiple proteins in the protein mixtures because molecules with different charges have variant migration rates under electric field. Different proteins can be separated by poly(acrylamide) gel electrophoresis (PAGE) based on

their electrophoretic mobility, which is a function of the length, conformation, and charge of protein molecules. Sodium dodecyl sulfate (SDS) can bind to polypeptide chain to produce an even distribution of charge per unit mass to linearize proteins. According to SDS-PAGE, proteins of different sizes show clear and gradient bands during electrophoresis. It helps in determining the possible proteins bound on NPs by comparing the detached proteins with protein marker references. This method can detect several nanogram proteins, and it is convenient to separate proteins and identify corona due to low cost and good repeatability. SDS-PAGE is quite useful to confirm the possible adsorption of abundant proteins in physiological fluids [14, 30, 76, 77]. Accurate identification of protein should utilize SDS-PAGE together with 2-DGE or liquid chromatography and liquid chromatography–mass spectrometry (LC-MS) [78].

Proteins can be firstly separated according to their charges by isoelectric focusing and then separated by 2-DGE. 2-DGE is widely used to separate proteins with different sizes and molecule weights. Coomassie blue staining, ammoniac silver staining, and cyanine fluorophore dyes (Cy dyes) are common approaches to screen specific protein spots. The migration of most plasma proteins on 2-D gels has their specific characteristics that can be well characterized as 2-D reference protein map in various databases. Therefore, the interested gel spots can be identified by comparing 2-D gel data with the database. Alternatively, proteins at the gel spots can be further analyzed by mass spectrometry to identify protein types. Deng *et al.* [78] used 1-D SDS-PAGE and 2-DGE to study the adsorbed plasma proteins on metal oxide NPs. They studied the binding of human plasma proteins to three metal oxide NPs: TiO_2, SiO_2, and ZnO. 1-DGE together with mass spectrometry can directly identify the profiles of adsorbed proteins. They showed that apolipoprotein A1, albumin, immunoglobulins, and fibrinogen are adsorbed onto three types of NPs. These NPs had specific adsorbed proteins on the surface. 2-DGE had also been used to confirm the adsorbed proteins. Based on the plasma protein database of ExPASy, 2-D maps of gel spots clearly show the similarity and difference in adsorbed proteins on NPs. This method is efficient to study how NP size, surface, shape, and NPs themselves influenced plasma protein adsorption [78]. For example, three NPs had the similar capability of adsorbing immunoglobulins, lipoproteins, acute-phase proteins, and proteins involved in complement pathways and coagulation, suggesting the important biological functions of corona on the biological effects of NPs.

LC-MS combines the physical separation capabilities of liquid chromatography (or high-performance liquid chromatography (HPLC)) with the mass analysis capabilities of mass spectrometry (MS), which is a powerful technique for protein corona study with high selectivity and sensitivity. MS provides qualitative and quantitative information of protein samples. Before the protein identification by LC-MS, the protein corona mixture derived from the cut bands of SDS-PAGE or 2-DGE spots requires protease digestion and denaturation. Considering the complex of peptide mixture, peptides can be separated by 2D-HPLC chromatography and then are resolved by a high-resolution mass spectrometer to provide a peptide mass fingerprinting. 2-DGE together with MS analysis is quite attractive to

separate thousands of plasma proteins within a large concentration range. Thus, proteins with different abundance can be simultaneously detected by LC-MS. LC-MS is appropriate to identify plasma and serum protein corona on NPs and compare how the properties affect the type of adsorbed proteins [7, 8, 14]. In addition, LC-MS together with other techniques can also provide more sensitive and rapid analysis for corona identification [8].

Monopoli *et al.* [7] used SDS-PAGE, dynamic light scattering (DLS), and electrospray LC-MS to analyze the plasma corona components on 200 nm SiO_2 NPs and sulfonated polystyrene ($PSOSO_3$) NPs. According to the band intensity of 1-D PAGE, a semiquantitative description of the variations in the corona composition can be provided. Then, the interested band can be further processed and measured with MS to identify the components. They also used the method of spectral counting (SpC) to perform a semiquantitative assessment of the protein amounts. SpC usually indicates the total number of MS/MS spectra for all peptides attributed to a given protein. For each protein identity, SpC can be normalized to the protein mass and expressed as the relative protein quantity to be NSpC. By calculating the NSpC of proteins at different MW (molecular weight) ranges, LC-MS results provided the information about which proteins contribute most to the overall protein corona. DCS results *in situ* supported the same trend.

Tenzer *et al.* [8] developed a strategy to rapidly separate as well as recover NPs–corona complex by centrifuging the samples through a sucrose cushion. It is powerful to study plasma corona evolution for different time periods even within 0.5 min. Therefore, the time-resolved corona separation technique can combine with LC-MS to quickly identify and quantify protein components. Surprisingly, there are 166 plasma corona proteins on polystyrene nanoparticles (PS NPs) or SiO_2 NPs can be detected and quantified at 0.5 min. Compared to the previous study, this strategy revealed that the composition of plasma corona on NPs is more complex. To understand how the properties of NPs influence the protein component and the time evolution process, they collected the corona samples for a series of time periods after interacting with NPs of different surface coatings, charges, or sizes. They also used time-of-flight instrument combined with a data-independent ion-mobility-enhanced data acquisition workflow to quantify corona proteins for large sample size. Finally, the quantitative proteomic data can drop a hint about the physiological or pathological correlation with the formation of corona on NPs.

11.3.2 Methods to Characterize the Properties of Corona NPs

The adsorbed proteins not only contribute to the corona composition, but also form physical layers around NPs with chemical structures and physiological functions. It is thus crucial to characterize the physical situation of the corona on NPs including the thickness, surface charge, shape, assembly structure, and kinetics of protein adsorption.

11.3.2.1 Methods to Study Surface Properties, Shape, and Size

11.3.2.1.1 Transmission Electron Microscope and Dynamic Light Scattering Transmission electron microscope (TEM) and DLS can measure the thickness of protein corona on NPs in dried samples and in the aqueous solution, respectively. Because protein corona is mainly composed of light elements such as C, H, O, and N, it is difficult to observe the organic layer on metallic NPs under high-resolution TEM. The alternative way is to stain the protein corona with heavy metal ions such as phosphotungstic acid or uranyl acetate solution [36, 38]. When the protein–NP complex is separated from the protein solution and dropped to a copper mesh, the complex is stained by metal ions, washed, and dried in air. High-resolution TEM can capture a layer of structure with good contrast compared to NPs. This layer is regarded as hard corona due to the fact that the soft corona is lost during the separation process. TEM images can reveal the information of corona thickness [38], the aggregation of corona–NP complex [68], and even which kind of proteins based on the equipped energy-dispersive X-ray (EDX) spectroscopy. For example, when some selenium-rich proteins are firmly bound to NPs, TEM image shows the complex shape and the thickness of corona, while EDX can perform total spectra analysis for multiple elements. X-ray fluorescence (XRF) signal of selenium in the spectra means that the selenium-rich protein contributes to corona composition. Based on XRF intensity, step-by-step mapping of selenium on NPs will show the distribution of corona around NPs. However, TEM cannot capture the corona structure either in dynamic process or in a solution environment; thus, TEM together with other methods for wet samples can be more convincible for characterization.

Wavelength (nm) Furthermore, DLS can measure the mean size of sphere-shaped particles in the solution based on the light scattering signals. DLS can also show the monodispersity, stability, and uniformity of the NP colloidal system. Compared to uncoated NPs, NPs coated by proteins increase the hydrodynamic size. The increased thickness indicates the adsorbed corona layer. DLS is suitable for studying both the dynamic process of protein adsorption on NPs and how the physicochemical properties of NPs and the environmental factors such as temperatures, ion concentrations, and pH influence the formation of corona (Figure 11.4a) [7, 14, 79]. Surface charge of NPs is usually determined by zeta potential that fluctuates with the changed surface properties due to protein adsorption and the changed environment [77, 79, 80]. Compared to DLS, change in surface charge of NPs shows the corona formation on NPs more indirectly. For polyelectrolyte-modified Au NRs, the positive charge on NPs will change into negative after the adsorption of serum protein (Figure 11.4c).

11.3.2.1.2 UV–Visible–Near-Infrared (UV-vis-NIR) Spectra For Au or Ag NPs, UV-vis-NIR spectra can detect significant shifts in the peak position of the surface plasmon resonance of NPs when these NPs are incubated with protein. The protein adsorption may broaden the absorption spectra and decrease the

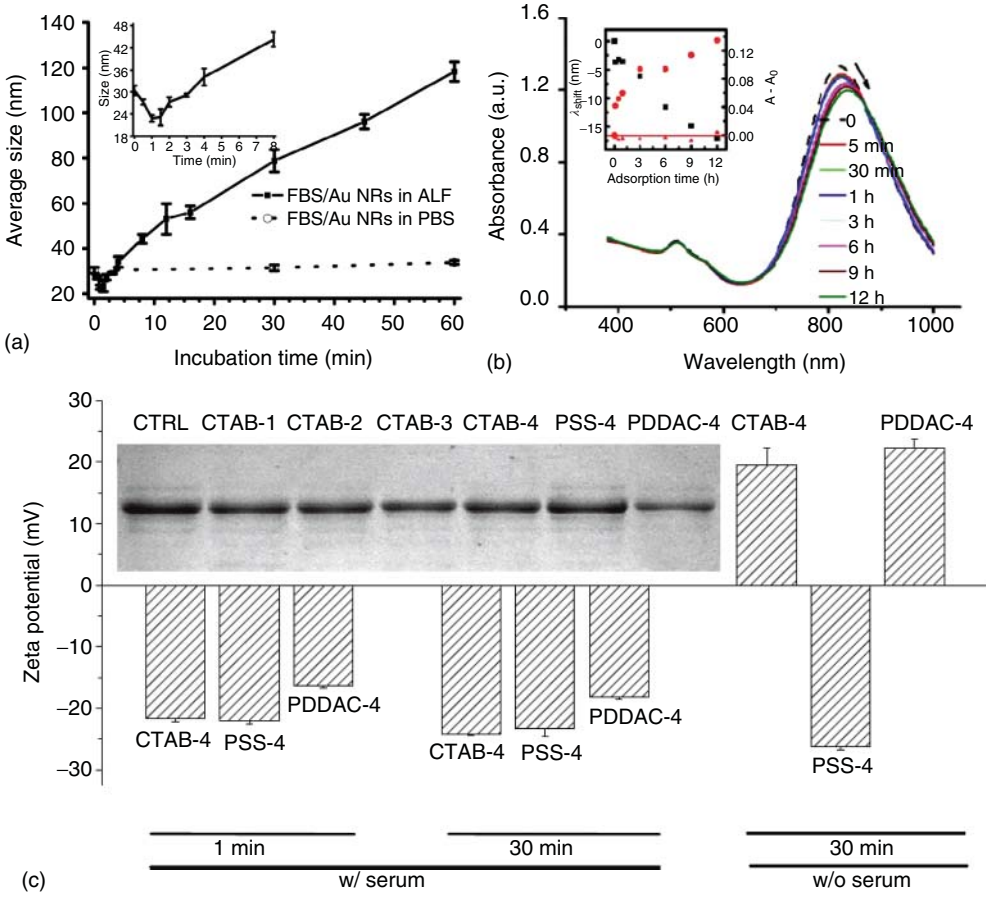

Figure 11.4 The characterization of protein corona on NPs in different physiological media. (a) Mean dynamic sizes of 50 μM FBS-coated Au NRs determined by DLS when incubated in PBS (pH at 7.2) and in artificial lysosomal fluid (ALF, pH at 4.5) during 60 min, respectively. (b) The visible and NIR absorption spectra of Au NRs before and after incubation with 10% fetal bovine serum (FBS) in PBS (Phosphate buffer solution) at different time intervals at 37 °C. (Reprinted with permission from [38]. Copyright © 2011 American Chemical Society.) (c) Zeta potentials of Au NRs dispersed in aqueous solution after being incubated with medium with (w/) or without (w/o) serum at 37 °C for 1 or 30 min and centrifuged. The inset shows reducing band intensity in SDS-PAGE for serum proteins recognized as serum albumin mainly in the supernatant separated from Au NRs and serum mixture after 2 h incubation. CTRL (control) represents the serum proteins without incubation with Au NRs [77]. (Copyright © 2010 Elsevier Ltd.)

absorption intensity, which is a rapid and simple method to characterize the dynamic process of NP–protein interaction. When proteins at a series concentrations interact with Au NRs, the SPR (Surface plasmon resonance) peak intensity of Au NRs has a slight increase, along with 2–4 nm red shift of the SPR peak (Figure 11.4b) [38, 80].

11.3.2.1.3 **Atomic Force Microscope** Atomic force microscope (AFM) is one of the scanning probe microscopies used to image surface profiles of nanomaterials. The resolution is approximately 0.2 nm at horizontal direction and close to 0.01 nm at vertical direction that is superior to those of scanning electron microscope (SEM) and TEM. AFM is used to measure topography and surface forces on the nanoscale [81]. It is powerful to characterize the corona structure and shape on the nanomaterial surface. Ge *et al.* [13] employed AFM to characterize plasma and serum protein absorbed on single-walled carbon nanotubes (SWCNTs). AFM images showed that bovine fibrinogen (BFG) is bound to SWCNTs nonuniformly at the beginning and then interwinds and forms aggregations onto the surfaces of SWCNTs. Gamma globulin (Ig) also binds to the SWCNT surface in nonuniform form in the beginning and then converts to thermodynamically stable and closely packed aggregates on the surface. Transferrin (Tf) adsorbed onto SWCNT surface can form a complex aggregate such as nodes, which are nearly uniformly bound to the surface. BSA) can uniformly bind to the SWCNT surface and continue to stack onto the absorbed BSA and accumulate layer by layer on the SWCNT surface. Based on these AFM results, they found that the adsorption models of SWCNT for different proteins were different and greatly depended on their protein structures. Combining with fluorescence spectroscopy and SDS-PAGE with AFM, they showed competitive adsorption among all the blood proteins, with a competitive order BFG > Ig > Tf > BSA. Finally, the binding stability and structure influence the cytotoxicity of SWCNTs. High resolution is one advantage for AFM imaging to observe the surface information after the binding of corona to NPs. However, it is a challenge to characterize protein–NP complex in the aqueous solution because AFM is appropriate to measure a fixed sample rather than those dispersed in the solution.

11.3.2.1.4 **Small-Angle X-ray Scattering** Based on the X-ray scattered intensity in a small angular range from 0.1° to 3°, small-angle X-ray scattering (SAXS) is an important method to characterize the NP size below 100 nm or the electron density of NPs 100 nm. The electron density and the form factor are basic determinants for the signal intensity of SAXS. In addition, high-energy X-ray source such as a synchrotron radiation X-ray can provide a good resolution for SAXS measurement. SAXS has been widely employed to evaluate the particle size, shape, orientation, and size distribution in aqueous solutions for the biomolecules, polymers, and amorphous and crystalline materials [81]. It can also characterize the inhomogeneity within amorphous materials and the pore sizes in porous materials. For nanocrystals or in polymeric materials, SAXS is useful to evaluate the assembly structure such as long-range ordering structure or interparticle distances [82]. Compared to DLS, SAXS can provide more information about the size and geometry of NPs and protein–NP complexes in solution.

Wang *et al.* [83] employed SAXS to study the interaction of NPs with proteins. SAXS results showed that the interaction of Subtilisin Carlsberg (SC) protein with 11 nm SiO_2 NPs is weak, while that of BSA with SiO_2 NPs is stronger. They firstly

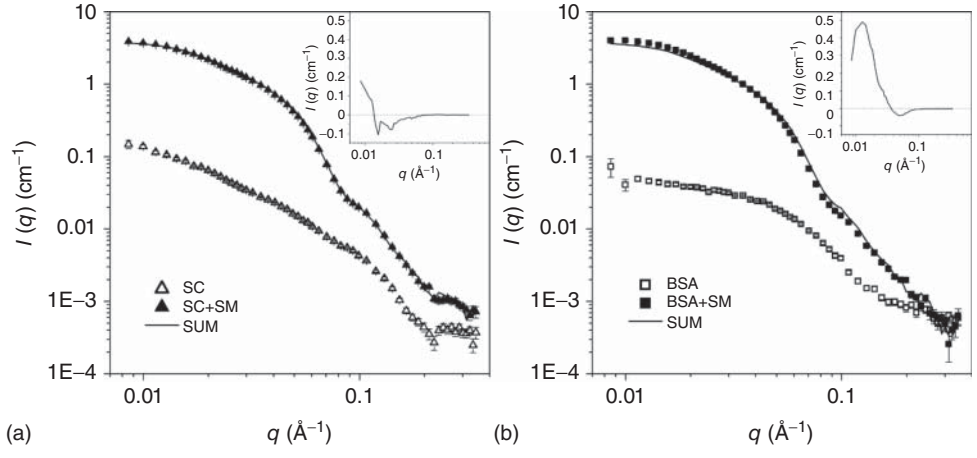

Figure 11.5 The application of SAXS into the study of nano–protein interactions. SAXS data (scattering intensity $I(q)$ versus length of scattering vector q) for, respectively, 1.0 mg/ml SC (open triangles) and 1.2 mg/ml SM particles (the silica NPs) and 1.0 mg/ml SC (closed triangles). The line is the sum of the SC and the SM scattering. (b) SAXS data for, respectively, 1.0 mg/ml BSA (open squares) and 1.2 mg/ml SM particles and 1.0 mg/ml BSA (closed squares). The line is the sum of the BSA and the SM scattering. Insets in both graphs show the residuals between the scattering intensities from the samples with SM + protein and the sum of the SM and protein scattering. (Reprinted with permission from [83]. Copyright © 2011 American Chemical Society.)

used centrifugation to separate free proteins from protein–NP complex. However, proteins bound to the surface via weak interaction are removed by the shear forces during centrifugation. SAXS can characterize *in situ* interaction of the weakly adsorbed proteins with NPs in the aqueous solution. After incubation of NPs with proteins, scattering from particles will change upon protein adsorption. SAXS data (scattering intensity $I(q)$) versus length of scattering vector (q) can directly show the scattering signals of NPs and proteins in the suspension; thus, it provides information on the structure of the particles. The scattering of NPs and SC mixture is simply a coexistence of the results of the individual samples of NPs and SC, which means a weak interaction. Compared to SC, the scattering of NP and BSA mixture is not a coexistence of those of NPs and BSA. This result suggested different modes for two proteins to bind to NPs (Figure 11.5).

11.3.2.2 Method to Characterize the Secondary Structures of Corona

Circular dichroism (CD) spectra are suitable to determine secondary structure of adsorbed proteins on NPs in aqueous solution. Secondary structures of proteins have the characteristic CD in the ultraviolet (UV) region. In the "near-UV" spectral region (250–350 nm), CD spectra of a protein are sensitive to specific tertiary structures. Signals from the region of 250–270 nm are contributed by phenylalanine residues, signals between 270 and 290 nm are from tyrosine, and those from 280 to 300 nm are derived from tryptophan. Disulfide bonds also have broad weak

signals in the near-UV spectrum. In the "far-UV" spectral region (250 nm and below), the different types of regular secondary structure in proteins such as helix, sheet, and turns give rise to characteristic CD spectra. The α-helix has a positive peak at 192 nm and two negative peaks at 208 and 222 nm as the characteristics, while the β-sheet has a negative band at 218 nm. Therefore, CD measurements in the far UV can provide quantitative estimates of the secondary structure composition (% helix, sheet, turns, etc.) in the proteins.

Ge *et al.* [13] employed CD to investigate SWCNTs and protein interaction and correlate the CD results with AFM results about the corona shape after adsorption. The nonuniform adsorption of gamma globulin and BFG on SWCNTs induced irreversible change in protein secondary structures. For example, after incubating SWCNTs with Ig or BFG for 10 min, the content of α-helix significantly reduced and that of β-sheets increased. Compared to these two proteins, transferrin and BSA have more uniform adsorption that cause less and/or reversible changes in protein secondary structures.

CD can also perform studies of time series about the change in protein structure in a mixture that is suitable for dynamic process study. We found that BSA is bound to the surface of Au NRs via Au–S bonds in a time-dependent mode such that the binding changes the secondary structures of BSA supported by CD results [36]. Laera *et al.* [84] used synchrotron radiation CD to measure the critical parameters on protein–NP interactions such as protein secondary structure and binding stability. CD equipped with synchrotron-radiation light source can sensitively detect the secondary structure of proteins with a few hundred nanograms and reduce radiation damage during repeated scans due to the long sample cell. CD spectra showed that HSA retains its overall secondary structure upon interaction with 15 nm Ag NPs. The interaction of human transthyretin (hTTR) with Ag NPs reduces α-helical content and increases the irregular structures. In addition, CD can measure the thermal stability of proteins in the presence of Au NPs and Ag NPs by following changes in the spectra with increasing temperature. The thermal unfolding of HSA on NPs can be described by the "folded" starting spectrum containing the α-helical structure as well as the "unfolded" spectrum containing some residual irregular structure. Compared to free HSA, the interaction of HSA with Au NPs does not alter its thermal stability, while interaction of HSA with Ag NPs reduces its thermal stability with a decreased melting temperature of 6 °C.

11.3.2.3 **Methods to Characterize the Binding Structures of Corona**

11.3.2.3.1 **Nuclear Magnetic Resonance Spectroscopy** Nuclear magnetic resonance (NMR) spectroscopy is a powerful technique to exploit the magnetic properties of certain atomic nuclei. NMR spectroscopy can be employed to investigate the structure properties and dynamics of proteins and nucleic acids. The chemical shift provides information about the structure of proteins and the shape and area of peaks can also indicate chemical structure. Especially, this method can reveal the binding site information at amino acid scale. Calzolai *et al.* [85] employed NMR spectroscopy to investigate ubiquitin and gold interaction in

solution. Chemical shift perturbation analysis is a well-established technique to monitor the interfacial interactions including protein–protein, protein–ligand, and protein–surface interactions. Two-dimensional ^{1}H-^{15}N NMR experiments were used to detect the changes in the chemical environment of all coupled protein H and N atoms after the formation of protein–NP complexes. Human ubiquitin (hUbq) contains 76 amino acids and has a small molecule weight. UV-vis spectrum showed that the surface plasmon resonance band will have a red shift of 5 nm after the adsorption of hUbq. Before and after adding Au NPs, the peaks of hUbq [^{15}N-^{1}H]-HSQC NMR spectra showed the changes in chemical shift that is sensitive to the chemical environment. When Au NPs were incubated with hUbq, only some peaks changed their position, while the majority remained unchanged that suggested specific hUbq-NP interact sites. Combining with three-dimensional structure of hUbq, the NMR spectra showed that Au NPs interact with the domain formed by peptide fragments Gln2-Ile3 and Leu15-Glu18 on the protein surface. However, one drawback for NMR method is the limit for the size of measured proteins with a molecular weight up to 50 kDa as quite standard measurement.

11.3.2.3.2 **X-ray-Based Techniques** X-ray crystallographic techniques can provide structure information with a high resolution to identify and model the probable binding sites of proteins to NPs. Usually, proteins or the fragment in proteins can be produced, purified, and crystallized for X-ray crystallographic analysis. It is a challenge to purify and crystallize the samples of protein–NP complex. Rather than resolving the binding structure directly, crystal structure analysis according to X-ray crystallography together with computer simulation can show binding sites based on putative models. Braden *et al.* [86] used this method to investigate the structure of fullerene antibody Fab fragment and revealed how the fragment binds to the fullerene NPs based on calculation.

XRD can identify the composites and observe their crystallinity before and after protein adsorption onto NPs. Prakasham *et al.* [87] studied diastase enzyme-impregnated (EI) nickel-impregnated silica paramagnetic particles (NSP) using Fourier-transform infrared spectroscopy (FTIR) and XRD. XRD showed the change from amorphous to crystalline nature in the presence of nickel. After enzyme immobilization, the XRD peak intensities of nickel oxide on NSP were observed, which indicated its crystalline nature upon enzyme immobilization. However, no peaks were observed in the presence of SiO_2 within enzyme-impregnated nickel-impregnated silica paramagnetic particles (EI-NSP). It suggested that SiO_2 may lose its crystalline nature after the binding of enzyme. For binding details, FTIR was used to investigate the composites of NSP and EI-NSP. After enzyme binding, an intense OH stretching band between 3410 and 3446 cm^{-1} was evidenced from the spectra, depicting the presence of enzyme on the surface of EI-NSP [87].

X-ray absorption near-edge structures (XANES) can sensitively detect the composition of chemical species of a given element that has advantages in characterizing the interaction mode of the protein corona on NPs via chemical adsorption.

Zhong *et al.* [88] used XANES spectroscopy to investigate the adsorption of proteins onto SWCNTs. After protein adsorption, C K-edge XANES spectra of SWCNTs changed with additional features of C═O bonds. XANES results combined with first-principle calculation reveal the mechanism for interface interaction. We employed sulfur K-edge XANES to study the chemical adsorption of BSA on Au NRs to form a hard corona (Figure 11.6) [36]. TEM images clearly showed that BSA forms corona on the surface of Au NRs (Figure 11.6a) and molecular dynamic simulation revealed the binding interfaces plane S (Figure 11.6b). Sulfur K-edge XANES is sensitive to oxidation states, and its chemical species can be observed from the peak of the first derivative of XANES, the inflection point energy (IPE). There are three major forms of sulfur before and after the interaction of Au NRs with BSA: thiol (R–S–H, R–S–R thiol), disulfide (S–S), and Au–thiol coordination (Au–S) (Figure 11.6c). Least-squares fitting of XANES showed that there are at least 12 Au–S bonds formed upon the adsorption of disulfide to the surface of gold (Figure 11.6d). It was supported by fitting sulfur XANES data that the content of disulfides decreased from 82% to 58% and there was an increase in the composition of Au–S forms. Assisted by sulfur XANES and CD spectra, molecular dynamic simulation results indicate that BSA is adsorbed on Au NRs in a "side-on" orientation, via the binding of plane S consisting of eight disulfide bonds, which can serve as the candidate binding interface with Au NRs. The stable BSA corona on Au NRs via Au–S bonds can be observed after cellular uptake according to XRF imaging-based elemental mapping (Figure 11.6e). As a result, BSA corona can protect cells from acute toxicity of CTAB-coated Au NRs (Figure 11.6f, g). With respect to the degradable NPs, both NPs and the metallic ions can interact with proteins. After the internalization and translocation to the acidic endo/lysosomes, Ag NPs will be degraded into ionic silver forms that further coordinate with sulfur-containing molecules such as cysteine, glutathione, and metallothionein to form Ag–S bonds. We also used XANES to characterize the chemical speciation of degraded silver during Ag NPs and ionic silver interaction in the intracellular environment to interact with proteins [89]. These studies are excellent examples that XANES is a powerful tool capable of characterizing the interface structures such as the binding sites of proteins to nanomaterials.

11.3.2.3.3 **Fourier-Transform Infrared Spectroscopy and Raman Spectroscopy** FTIR spectroscopy and Raman spectroscopy can detect chemical bonds among the measured fingerprints for the protein–NP complexes. The bound proteins have featured groups to bind to the surface of NPs. Both spectroscopic methods can confirm the proteins bound to NPs through determining the alteration of some specific chemical groups and bonds in the spectra compared with NPs and proteins. Goy-López *et al.* [90] used FTIR spectroscopy to detect the interaction of HSA with Au NPs. The second-derivative FTIR spectra provided detailed information about the conformational changes after the adsorption of proteins. Compared with free protein, the HSA-bound citrate Au NPs showed changed derivative spectra of amide I band, depending on the size of Au NPs. Confirmed by Raman spectra of HSA in the absence and the presence of Au NPs, the amide

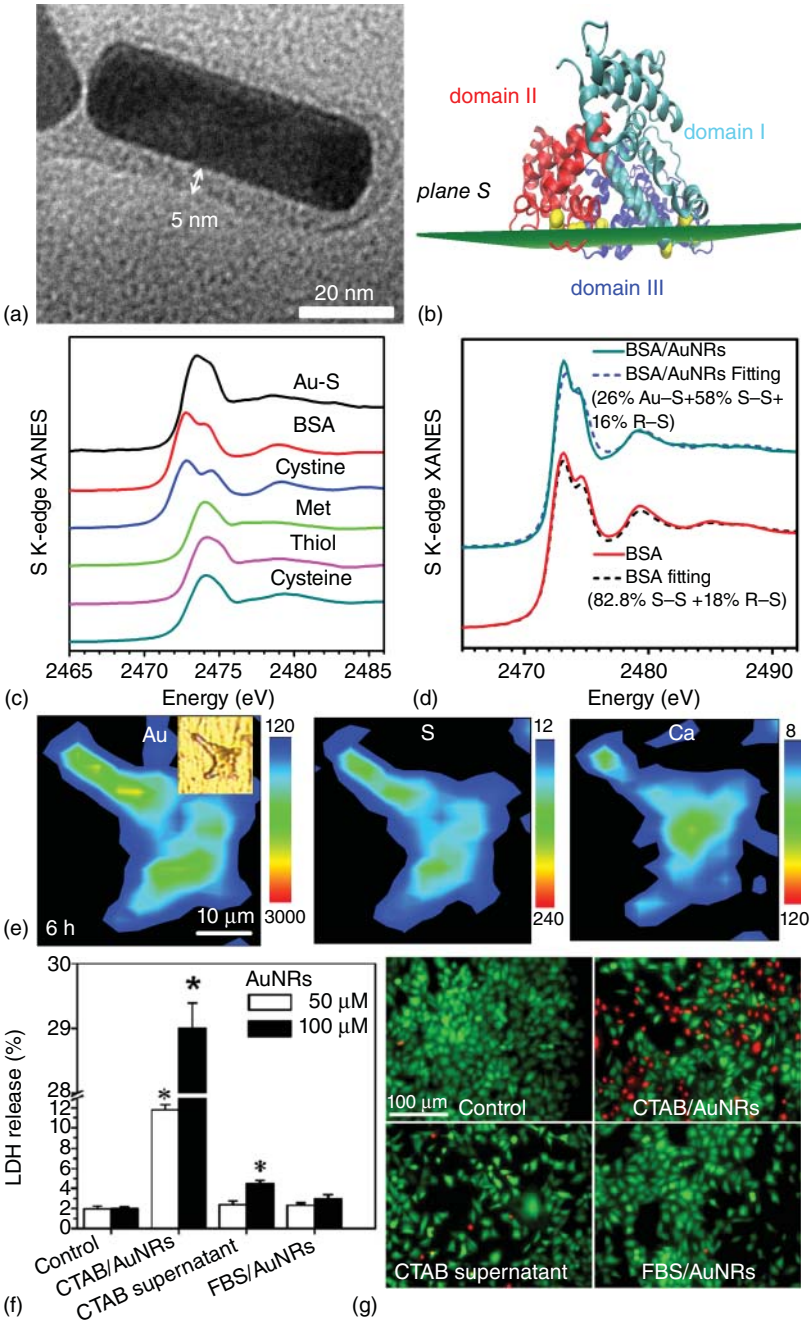
5 nm
20 nm
(a)
domain II
domain I
plane S
domain III
(b)
S K-edge XANES
Au-S
BSA
Cystine
Met
Thiol
Cysteine
2465 2470 2475 2480 2485
Energy (eV)
(c)
BSA/AuNRs
BSA/AuNRs Fitting
(26% Au–S+58% S–S+
16% R–S)
BSA
BSA fitting
(82.8% S–S +18% R–S)
2470 2480 2490
Energy (eV)
(d)
Au
120
3000
10 μm
6 h
(e)
S
12
240
Ca
8
120
LDH release (%)
AuNRs
50 μM
100 μM
Control
CTAB/AuNRs
CTAB supernatant
FBS/AuNRs
(f)
100 μm
Control
CTAB/AuNRs
CTAB supernatant
FBS/AuNRs
(g)

band of the peptide group, amide I, centered at 1700 to 1600 cm^{-1}, proves to be the most sensitive group. For example, the predominant band centered at about 1652 cm^{-1} denotes the significant α-helix content of HSA. The slightly decreased intensity at 1652 cm^{-1} suggests change in secondary structures of HSA after incubating with NPs [90]. Fu *et al.* [91] also used FTIR and Raman spectroscopy to determine the changes in the secondary structure of HSA due to the S–Au interaction. When 40 nm Au NPs were incubated with HSA, the inverted second-derivative amide I FTIR spectra of HSA showed that the intensities of bands assigned to α-helix (1658 and 1665 cm^{-1}) decreased. The contents of β-sheet (at 1630 and 1640 cm^{-1}), β-turn (at 1683 and 1689 cm^{-1}), and random coil (1649 cm^{-1}) increased with the incubation times. Raman spectroscopy can be used to characterize the S–Au interaction with a band at 292 cm^{-1}. With greater incubation time, the S–Au stretch mode at 292 cm^{-1} increased the signal intensity, suggesting the interaction of gold with cystine residues is a time-dependent process. Based on surface-enhanced Raman spectroscopy (SERS) and UV-vis-NIR spectra, Zhang *et al.* [68] also revealed the detailed information about the binding sites of lysozyme at the surface of Au NPs. The spectra changes showed that the content of α-helix structure decreases and random coil conformation increases after protein adsorption and the breakage of the disulfide bonds to form Au–S.

11.3.2.3.4 **Isothermal Titration Calorimetry** ITC is widely used to determine the thermodynamic parameters such as binding affinity, enthalpy changes, and binding stoichiometry in solutions. When proteins are titrated to the suspension of NPs in the sample cell, the difference in heat is monitored when heat is added to the sample in order to maintain the reference and sample cells at the same temperature. The change in the temperature is measured to calculate the Gibbs energy and entropy changes. In addition, the heat changes can be fitted to isothermal functions to provide thermodynamic parameters. Cedervall *et al.* [22] employed ITC to study the interaction of HSA with copolymer NPs (NIPAM and BAM NPs) to determine the stoichiometry, affinity, and enthalpy. The equilibrium association constant can be provided and the number of bound

Figure 11.6 The binding of BSA protein to the surface of Au NRs and its influence on cytotoxicity. (a) TEM images of BSA-adsorbed Au NRs. (b) The interfaces for BSA (*plane S*) via disulfides (yellow) to bind the Au (111) surface of Au NRs. (c) Various sulfur species in reference samples: Au–S, R–S (cysteine, thiol, Met), and R–S–S–R′ (cystine), shown as normalized S K-edge XANES spectra. (d) Chemical species of sulfur in cysteine, Met, and cystine after incubation with Au NRs. (e) Elemental mappings of Au, S, and Ca using μ-XRF to analyze internalized FBS/Au NRs in cells at different time intervals. The insets are cell images under a bright field. (f) LDH release from cells exposed to Au NRs and FBS-coated Au NRs for 24 h, which indicated the changed permeation of cell membrane after treatment. (g) Cytotoxicity was evaluated by alive–dead assay for cells exposed to CTAB/Au NRs and FBS/Au NRs after exposure for 12 and 24 h.(Reprinted with permission from [36]. Copyright © 2013 American Chemical Society.)

protein molecules (stoichiometry) on NPs increases with the particle hydrophobicity. Fleischer and Payne [29] combined CD spectra, ITC, and fluorescence spectroscopy to study how the surface properties of NPs influence the adsorption of BSA on NPs that mediates the BSA–receptor interaction and cellular uptake. The solution of BSA was titrated into solutions containing 60 nm carboxylate-modified NPs and 58 nm amine-modified NPs, respectively. The enthalpy of BSA binding to two types of NPs was identical (about -1.4×10^4 kJ/mol). Unexpectedly, the carboxylate-modified NPs had a significant greater capability of adsorbing BSA compared to amine-modified NPs. The coverage of BSA on the carboxylate-modified NPs ($230 \pm 6\%$) was much higher than that on the other NPs ($8 \pm 2\%$).

11.4 Summary and Outlook

In this chapter, we have listed conventional methods to characterize the interactions of NPs with proteins. These methods include the separation and identification of adsorbed molecules, the characterization of physiochemical properties, and the binding structures for protein corona NPs. They are also suitable for characterization of interactions of NPs with other macromolecules. The understanding of nano–bio interaction is crucial for revealing the mechanism of biological effects and for screening safe and efficient nanomaterials for biomedical applications. These methods will be significant to advance current knowledge about what happens to NPs at the surface and how NP–biological molecule complex determines the biomedical effects and biological responses.

The study of bio–nano interaction is a cutting-edge field. Many scientific questions are needed to be answered and powerful techniques to investigate the interaction process and biological outcome are urgently required. One challenge is how to observe the real-time interaction of macromolecules with NPs inside a single cell and even *in vivo*. The detailed and *in situ* information will greatly benefit the current study in the fields of nanobiology and nanotoxicology. For example, the updated method will help reveal the process of the macromolecule–NP complex forms and changes during the cellular uptake, trafficking, and removal or the induced toxicity of NPs that is important for rational design of nanomaterials. The second challenge is how to finely tune the composition, the structures and functions of adsorbed molecules, and how to link the properties of biological corona to their biomedical effects. The third challenge is to reveal the interfacial structure or binding sites of macromolecules bound to NPs in the physiological environment. Furthermore, high-throughput and rapid analytical methods are highly required to characterize the composite of complex macromolecules on NPs. The rapid progress in physical and chemical methods will indefinitely promote our understanding of the scientific events at nano–bio interfaces.

References

1. Colvin, V.L. (2003) The potential environmental impact of engineered nanomaterials. *Nat. Biotechnol.*, **21** (10), 1166–1170.
2. Oberdorster, G., Oberdorster, E., and Oberdorster, J. (2005) Nanotoxicology: an emerging discipline evolving from studies of ultrafine particles. *Environ. Health Perspect.*, **113** (7), 823–839.
3. Zhao, Y.L., Xing, G.M., and Chai, Z.F. (2008) Nanotoxicology: are carbon nanotubes safe? *Nat. Nanotechnol.*, **3** (4), 191–192.
4. Nel, A.E., Madler, L., Velegol, D., Xia, T., Hoek, E.M.V., Somasundaran, P., Klaessig, F., Castranova, V., and Thompson, M. (2009) Understanding biophysicochemical interactions at the nano-bio interface. *Nat. Mater.*, **8** (7), 543–557.
5. Walczyk, D., Bombelli, F.B., Monopoli, M.P., Lynch, I., and Dawson, K.A. (2010) What the cell "sees" in bionanoscience. *J. Am. Chem. Soc.*, **132** (16), 5761–5768.
6. Mu, Q.X., Jiang, G.B., Chen, L.X., Zhou, H.Y., Fourches, D., Tropsha, A., and Yan, B. (2014) Chemical basis of interactions between engineered nanoparticles and biological systems. *Chem. Rev.*, **114** (15), 7740–7781.
7. Monopoli, M.P., Walczyk, D., Campbell, A., Elia, G., Lynch, I., Baldelli Bombelli, F., and Dawson, K.A. (2011) Physical–chemical aspects of protein corona: relevance to *in vitro* and *in vivo* biological impacts of nanoparticles. *J. Am. Chem. Soc.*, **133** (8), 2525–2534.
8. Tenzer, S., Docter, D., Kuharev, J., Musyanovych, A., Fetz, V., Hecht, R., Schlenk, F., Fischer, D., Kiouptsi, K., and Reinhardt, C. (2013) Rapid formation of plasma protein corona critically affects nanoparticle pathophysiology. *Nat. Nanotechnol.*, **8** (10), 772–781.
9. Lacerda, S.H.D.P., Park, J.J., Meuse, C., Pristinski, D., Becker, M.L., Karim, A., and Douglas, J.F. (2009) Interaction of gold nanoparticles with common human blood proteins. *ACS Nano*, **4** (1), 365–379.
10. Vert, M., Doi, Y., Hellwich, K.H., Hess, M., Hodge, P., Kubisa, P., Rinaudo, M., and Schue, F. (2012) Terminology for biorelated polymers and applications (IUPAC Recommendations 2012). *Pure Appl. Chem.*, **84** (2), 377–408.
11. Klein, J. (2007) Probing the interactions of proteins and nanoparticles. *Proc. Natl. Acad. Sci. U.S.A.*, **104** (7), 2029–2030.
12. Monopoli, M.P., Aberg, C., Salvati, A., and Dawson, K.A. (2012) Biomolecular coronas provide the biological identity of nanosized materials. *Nat. Nanotechnol.*, **7** (12), 779–786.
13. Ge, C.C., Du, J.F., Zhao, L., Wang, L.M., Liu, Y., Li, D.H., Yang, Y.L., Zhou, R.H., Zhao, Y.L., Chai, Z.F., and Chen, C.Y. (2011) Binding of blood proteins to carbon nanotubes reduces cytotoxicity. *Proc. Natl. Acad. Sci. U.S.A.*, **108** (41), 16968–16973.
14. Walkey, C.D., Olsen, J.B., Guo, H.B., Emili, A., and Chan, W.C.W. (2012) Nanoparticle size and surface chemistry determine serum protein adsorption and macrophage uptake. *J. Am. Chem. Soc.*, **134** (4), 2139–2147.
15. Du, J.F., Ge, C.C., Lu, Y., Bai, R., Li, D.H., Yang, Y.L., Liao, L.F., and Chen, C.Y. (2011) The interaction of serum proteins with carbon nanotubes depend on the physicochemical properties of nanotubes. *J. Nanosci. Nanotechnol.*, **11** (11), 10102–10110.
16. Lynch, I. and Dawson, K.A. (2008) Protein-nanoparticle interactions. *Nano Today*, **3** (1-2), 40–47.
17. Tenzer, S., Docter, D., Rosfa, S., Wlodarski, A., Kuharev, J., Rekik, A., Knauer, S.K., Bantz, C., Nawroth, T., Bier, C., Sirirattanapan, J., Mann, W., Treuel, L., Zellner, R., Maskos, M., Schild, H., and Stauber, R.H. (2011) Nanoparticle size is a critical physicochemical determinant of the human blood plasma corona: a comprehensive quantitative proteomic analysis. *ACS Nano*, **5** (9), 7155–7167.
18. Lundqvist, M., Stigler, J., Elia, G., Lynch, I., Cedervall, T., and Dawson, K.A.

(2008) Nanoparticle size and surface properties determine the protein corona with possible implications for biological impacts. *Proc. Natl. Acad. Sci. U.S.A.*, **105** (38), 14265–14270.

19. Mahmoudi, M., Lynch, I., Ejtehadi, M.R., Monopoli, M.P., Bombelli, F.B., and Laurent, S. (2011) Protein-nanoparticle interactions: opportunities and challenges. *Chem. Rev.*, **111** (9), 5610–5637.
20. Paula, A.J., Silveira, C.P., Martinez, D.S.T., Souza, A.G., Romero, F.V., Fonseca, L.C., Tasic, L., Alves, O.L., and Duran, N. (2014) Topography-driven bionano-interactions on colloidal silica nanoparticles. *ACS Appl. Mater. Interfaces*, **6** (5), 3437–3447.
21. Kurylowicz, M., Paulin, H., Mogyoros, J., Giuliani, M., and Dutcher, J.R. (2014) The effect of nanoscale surface curvature on the oligomerization of surface-bound proteins. *J. R. Soc. Interface*, **11**, 20130818.
22. Cedervall, T., Lynch, I., Lindman, S., Berggard, T., Thulin, E., Nilsson, H., Dawson, K.A., and Linse, S. (2007) Understanding the nanoparticle-protein corona using methods to quantify exchange rates and affinities of proteins for nanoparticles. *Proc. Natl. Acad. Sci. U.S.A.*, **104** (7), 2050–2055.
23. Lesniak, A., Fenaroli, F., Monopoli, M.P., Åberg, C., Dawson, K.A., and Salvati, A. (2012) Effects of the presence or absence of a protein corona on silica nanoparticle uptake and impact on cells. *ACS Nano*, **6** (7), 5845–5857.
24. Chithrani, B.D. and Chan, W.C.W. (2007) Elucidating the mechanism of cellular uptake and removal of protein-coated gold nanoparticles of different sizes and shapes. *Nano Lett.*, **7** (6), 1542–1550.
25. Lesniak, A., Campbell, A., Monopoli, M.P., Lynch, I., Salvati, A., and Dawson, K.A. (2010) Serum heat inactivation affects protein corona composition and nanoparticle uptake. *Biomaterials*, **31** (36), 9511–9518.
26. Lunov, O., Syrovets, T., Röcker, C., Tron, K., Ulrich Nienhaus, G., Rasche, V., Mailänder, V., Landfester, K., and Simmet, T. (2010) Lysosomal degradation of the carboxydextran shell of coated superparamagnetic iron oxide nanoparticles and the fate of professional phagocytes. *Biomaterials*, **31** (34), 9015–9022.
27. Wang, F.J., Yu, L., Monopoli, M.P., Sandin, P., Mahon, E., Salvati, A., and Dawson, K.A. (2013) The biomolecular corona is retained during nanoparticle uptake and protects the cells from the damage induced by cationic nanoparticles until degraded in the lysosomes. *Nanomedicine*, **9** (8), 1159–1168.
28. Yan, Y., Gause, K.T., Kamphuis, M.M.J., Ang, C.S., O'Brien-Simpson, N.M., Lenzo, J.C., Reynolds, E.C., Nice, E.C., and Caruso, F. (2013) Differential roles of the protein corona in the cellular uptake of nanoporous polymer particles by monocyte and macrophage cell lines. *ACS Nano*, **7** (12), 10960–10970.
29. Fleischer, C.C. and Payne, C.K. (2014) Nanoparticle-cell interactions: molecular structure of the protein corona and cellular outcomes. *Acc. Chem. Res.*, **47** (8), 2651–2659.
30. Deng, Z.J., Liang, M., Monteiro, M., Toth, I., and Minchin, R.F. (2011) Nanoparticle-induced unfolding of fibrinogen promotes mac-1 receptor activation and inflammation. *Nat. Nanotechnol.*, **6** (1), 39–44.
31. Morishige, T., Yoshioka, Y., Inakura, H., Tanabe, A., Narimatsu, S., Yao, X.L., Monobe, Y., Imazawa, T., Tsunoda, S., Tsutsumi, Y., Mukai, Y., Okada, N., and Nakagawa, S. (2012) Suppression of nanosilica particle-induced inflammation by surface modification of the particles. *Arch. Toxicol.*, **86** (8), 1297–1307.
32. Albanese, A., Tang, P.S., and Chan, W.C.W. (2012) The effect of nanoparticle size, shape, and surface chemistry on biological systems. *Annu. Rev. Biomed. Eng.*, **14**, 1–16.
33. Wang, X., Xia, T., Duch, M.C., Ji, Z., Zhang, H., Li, R., Sun, B., Lin, S., Meng, H., Liao, Y.P., Wang, M., Song, T.B., Yang, Y., Hersam, M.C., and Nel, A.E. (2012) Pluronic f108 coating decreases the lung fibrosis potential of multiwall carbon nanotubes by reducing lysosomal injury. *Nano Lett.*, **12** (6), 3050–3061.
34. Wan, S., Kelly, P.M., Mahon, E., Stöckmann, H., Rudd, P.M., Caruso, F., Dawson, K.A., Yan, Y., and Monopoli,

M.P. (2015) The "sweet" side of the protein corona: effects of glycosylation on nanoparticle–cell interactions. *ACS Nano*, **9** (2), 2157–2166.

35. Hu, W.B., Peng, C., Lv, M., Li, X.M., Zhang, Y.J., Chen, N., Fan, C.H., and Huang, Q. (2011) Protein corona-mediated mitigation of cytotoxicity of graphene oxide. *ACS Nano*, **5** (5), 3693–3700.
36. Wang, L.M., Li, J.Y., Pan, J., Jiang, X.M., Ji, Y.L., Li, Y.F., Qu, Y., Zhao, Y.L., Wu, X.C., and Chen, C.Y. (2013) Revealing the binding structure of the protein corona on gold nanorods using synchrotron radiation-based techniques: understanding the reduced damage in cell membranes. *J. Am. Chem. Soc.*, **135** (46), 17359–17368.
37. Wang, L.M., Jiang, X.M., Ji, Y.L., Bai, R., Zhao, Y.L., Wu, X.C., and Chen, C.Y. (2013) Surface chemistry of gold nanorods: origin of cell membrane damage and cytotoxicity. *Nanoscale*, **5** (18), 8384–8391.
38. Wang, L.M., Liu, Y., Li, W., Jiang, X.M., Ji, Y.L., Wu, X.C., Xu, L.G., Qiu, Y., Zhao, K., Wei, T.T., Li, Y.F., Zhao, Y.L., and Chen, C.Y. (2011) Selective targeting of gold nanorods at the mitochondria of cancer cells: implications for cancer therapy. *Nano Lett.*, **11** (2), 772–780.
39. Monopoli, M.P., Bombelli, F.B., and Dawson, K.A. (2011) Nanotechnology: nanoparticle coronas take shape. *Nat. Nanotechnol.*, **6** (1), 11–12.
40. Jiang, W., Kim, B.Y.S., Rutka, J.T., and Chan, W.C.W. (2008) Nanoparticle-mediated cellular response is size-dependent. *Nat. Nanotechnol.*, **3** (3), 145–150.
41. Zhou, H., Zhang, B., Zheng, J., Yu, M., Zhou, T., Zhao, K., Jia, Y., Gao, X., Chen, C., and Wei, T. (2014) The inhibition of migration and invasion of cancer cells by graphene *via* the impairment of mitochondrial respiration. *Biomaterials*, **35** (5), 1597–1607.
42. Zhang, W.D., Wang, C., Li, Z.J., Lu, Z.Z., Li, Y., Yin, J.J., Zhou, Y.T., Gao, X.F., Fang, Y., Nie, G.J., and Zhao, Y.L. (2012) Unraveling stress-induced toxicity properties of graphene oxide and the underlying mechanism. *Adv. Mater.*, **24** (39), 5391–5397.
43. Linse, S., Cabaleiro-Lago, C., Xue, W.F., Lynch, I., Lindman, S., Thulin, E., Radford, S.E., and Dawson, K.A. (2007) Nucleation of protein fibrillation by nanoparticles. *Proc. Natl. Acad. Sci. U.S.A.*, **104** (21), 8691–8696.
44. Cifuentes-Rius, A., de Puig, H., Kah, J.C.Y., Borros, S., and Hamad-Schifferli, K. (2013) Optimizing the properties of the protein corona surrounding nanoparticles for tuning payload release. *ACS Nano*, **7** (11), 10066–10074.
45. Sun, C.J., Yang, H., Yuan, Y., Tian, X., Wang, L.M., Guo, Y., Xu, L., Lei, J.L., Gao, N., Anderson, G.J., Liang, X.J., Chen, C.Y., Zhao, Y.L., and Nie, G.J. (2011) Controlling assembly of paired gold clusters within apoferritin nanoreactor for *in vivo* kidney targeting and biomedical imaging. *J. Am. Chem. Soc.*, **133** (22), 8617–8624.
46. Salvati, A., Pitek, A.S., Monopoli, M.P., Prapainop, K., Bombelli, F.B., Hristov, D.R., Kelly, P.M., Aberg, C., Mahon, E., and Dawson, K.A. (2013) Transferrin-functionalized nanoparticles lose their targeting capabilities when a biomolecule corona adsorbs on the surface. *Nat. Nanotechnol.*, **8** (2), 137–143.
47. Larson, T.A., Joshi, P.P., and Sokolov, K. (2012) Preventing protein adsorption and macrophage uptake of gold nanoparticles *via* a hydrophobic shield. *ACS Nano*, **6** (10), 9182–9190.
48. Prapainop, K., Witter, D.P., and Wentworth, P. (2012) A chemical approach for cell-specific targeting of nanomaterials: small-molecule-initiated misfolding of nanoparticle corona proteins. *J. Am. Chem. Soc.*, **134** (9), 4100–4103.
49. Welsher, K., McManus, S.A., Hsia, C.-H., Yin, S., and Yang, H. (2015) Discovery of protein- and DNA-imperceptible nanoparticle hard coating using gel-based reaction tuning. *J. Am. Chem. Soc.*, **137** (2), 580–583.
50. Kang, S.G., Zhou, G.Q., Yang, P., Liu, Y., Sun, B.Y., Huynh, T., Meng, H., Zhao, L.N., Xing, G.M., Chen, C.Y., Zhao, Y.L., and Zhou, R.H. (2012) Molecular

mechanism of pancreatic tumor metastasis inhibition by $Gd@C_{82}(OH)_{22}$ and its implication for de novo design of nanomedicine. *Proc. Natl. Acad. Sci. U.S.A.*, **109** (38), 15431–15436.

51. Zhu, Z.J., Posati, T., Moyano, D.F., Tang, R., Yan, B., Vachet, R.W., and Rotello, V.M. (2012) The interplay of monolayer structure and serum protein interactions on the cellular uptake of gold nanoparticles. *Small*, **8** (17), 2659–2663.
52. Tedja, R., Lim, M., Amal, R., and Marquis, C. (2012) Effects of serum adsorption on cellular uptake profile and consequent impact of titanium dioxide nanoparticles on human lung cell lines. *ACS Nano*, **6** (5), 4083–4093.
53. Zhu, Y., Li, W., Li, Q., Li, Y., Li, Y., Zhang, X., and Huang, Q. (2009) Effects of serum proteins on intracellular uptake and cytotoxicity of carbon nanoparticles. *Carbon*, **47** (5), 1351–1358.
54. Doherty, G.J. and McMahon, H.T. (2009) Mechanisms of endocytosis. *Annu. Rev. Biochem.*, **78**, 857–902.
55. Knop, K., Hoogenboom, R., Fischer, D., and Schubert, U.S. (2010) Poly(ethylene glycol) in drug delivery: pros and cons as well as potential alternatives. *Angew. Chem. Int. Ed.*, **49** (36), 6288–6308.
56. Hood, J.D., Bednarski, M., Frausto, R., Guccione, S., Reisfeld, R.A., Xiang, R., and Cheresh, D.A. (2002) Tumor regression by targeted gene delivery to the neovasculature. *Science*, **296** (5577), 2404–2407.
57. Bagalkot, V., Zhang, L., Levy-Nissenbaum, E., Jon, S., Kantoff, P.W., Langer, R., and Farokhzad, O.C. (2007) Quantum dot-aptamer conjugates for synchronous cancer imaging, therapy, and sensing of drug delivery based on bi-fluorescence resonance energy transfer. *Nano Lett.*, **7** (10), 3065–3070.
58. Kirpotin, D.B., Drummond, D.C., Shao, Y., Shalaby, M.R., Hong, K., Nielsen, U.B., Marks, J.D., Benz, C.C., and Park, J.W. (2006) Antibody targeting of long-circulating lipidic nanoparticles does not increase tumor localization but does increase internalization in animal models. *Cancer Res.*, **66** (13), 6732–6740.
59. Dai, Q., Walkey, C., and Chan, W.C.W. (2014) Polyethylene glycol backfilling mitigates the negative impact of the protein corona on nanoparticle cell targeting. *Angew. Chem. Int. Ed.*, **53** (20), 5093–5096.
60. Li, Y., Liu, Y., Fu, Y., Wei, T.T., Guyader, L.L., Gao, G., Liu, R.S., Chang, Y.Z., and Chen, C.Y. (2011) The triggering of apoptosis in macrophages by pristine graphene through the mapk and tgf-beta signaling pathways. *Biomaterials*, **33** (2), 402–411.
61. Rauch, J., Kolch, W., Laurent, S., and Mahmoudi, M. (2013) Big signals from small particles: regulation of cell signaling pathways by nanoparticles. *Chem. Rev.*, **113** (5), 3391–3406.
62. Zhang, Y., Mu, Q., Zhou, H., Vrijens, K., Roussel, M.F., Jiang, G., and Yan, B. (2012) Binding of carbon nanotube to BMP receptor 2 enhances cell differentiation and inhibits apoptosis via regulating bHLH transcription factors. *Cell Death Dis.*, **3**, e308.
63. Meng, L., Chen, R., Jiang, A.H., Wang, L.M., Wang, P., Li, C.Z., Bai, R., Zhao, Y.L., Autrup, H., and Chen, C.Y. (2013) Short multiwall carbon nanotubes promote neuronal differentiation of PC12 cells via up-regulation of the neurotrophin signaling pathway. *Small*, **9** (9-10), 1786–1798.
64. Zhou, T., Zhang, B., Wei, P., Du, Y.P., Zhou, H.J., Yu, M.F., Yan, L., Zhang, W.D., Nie, G.J., Chen, C.Y., Tu, Y.P., and Wei, T.T. (2014) Energy metabolism analysis reveals the mechanism of inhibition of breast cancer cell metastasis by PEG-modified graphene oxide nanosheets. *Biomaterials*, **35** (37), 9833–9843.
65. Zhou, T., Yu, M.F., Zhang, B., Wang, L.M., Wu, X.C., Zhou, H.J., Du, Y.P., Hao, J.F., Tu, Y.P., Chen, C.Y., and Wei, T.T. (2014) Inhibition of cancer cell migration by gold nanorods: molecular mechanisms and implications for cancer therapy. *Adv. Funct. Mater.*, **24** (44), 6922–6932.
66. Mu, Q.X., Du, G.Q., Chen, T.S., Zhang, B., and Yan, B. (2009) Suppression of human bone morphogenetic protein signaling by carboxylated single-walled carbon nanotubes. *ACS Nano*, **3** (5), 1139–1144.

67. Steinmuller-Nethl, D., Kloss, F.R., Najam-U-Haq, M., Rainer, M., Larsson, K., Linsmeier, C., Koehler, G., Fehrer, C., Lepperdinger, G., Liu, X., Memmel, N., Bertel, E., Huck, C.W., Gassner, R., and Bonn, G. (2006) Strong binding of bioactive BMP-2 to nanocrystalline diamond by physisorption. *Biomaterials*, **27** (26), 4547–4556.
68. Zhang, D.M., Neumann, O., Wang, H., Yuwono, V.M., Barhoumi, A., Perham, M., Hartgerink, J.D., Wittung-Stafshede, P., and Halas, N.J. (2009) Gold nanoparticles can induce the formation of protein-based aggregates at physiological pH. *Nano Lett.*, **9** (2), 666–671.
69. Vertegel, A.A., Siegel, R.W., and Dordick, J.S. (2004) Silica nanoparticle size influences the structure and enzymatic activity of adsorbed lysozyme. *Langmuir*, **20** (16), 6800–6807.
70. Li, Y.Y., He, X., Yin, J.J., Ma, Y.H., Zhang, P., Li, J.Y., Ding, Y.Y., Zhang, J., Zhao, Y.L., Chai, Z.F., and Zhang, Z.Y. (2015) Acquired superoxide-scavenging ability of ceria nanoparticles. *Angew. Chem. Int. Ed.*, **54** (6), 1832–1835.
71. Pirmohamed, T., Dowding, J.M., Singh, S., Wasserman, B., Heckert, E., Karakoti, A.S., King, J.E.S., Seal, S., and Self, W.T. (2010) Nanoceria exhibit redox state-dependent catalase mimetic activity. *Chem. Commun.*, **46** (16), 2736–2738.
72. Lee, S.S., Song, W.S., Cho, M.J., Puppala, H.L., Nguyen, P., Zhu, H.G., Segatori, L., and Colvin, V.L. (2013) Antioxidant properties of cerium oxide nanocrystals as a function of nanocrystal diameter and surface coating. *ACS Nano*, **7** (11), 9693–9703.
73. Karakoti, A.S., Singh, S., Kumar, A., Malinska, M., Kuchibhatla, S.V.N.T., Wozniak, K., Self, W.T., and Seal, S. (2009) Pegylated nanoceria as radical scavenger with tunable redox chemistry. *J. Am. Chem. Soc.*, **131** (40), 14144–14145.
74. Wang, X., Duch, M.C., Mansukhani, N., Ji, Z., Liao, Y.P., Wang, M., Zhang, H., Sun, B., Chang, C.H., Li, R., Lin, S., Meng, H., Xia, T., Hersam, M.C., and Nel, A.E. (2015) Use of a pro-fibrogenic mechanism-based predictive toxicological approach for tiered testing and decision analysis of carbonaceous nanomaterials. *ACS Nano*, **9** (3), 3032–3043.
75. Walkey, C.D. and Chan, W.C.W. (2012) Understanding and controlling the interaction of nanomaterials with proteins in a physiological environment. *Chem. Soc. Rev.*, **41** (7), 2780–2799.
76. Cedervall, T., Lynch, I., Foy, M., Berggad, T., Donnelly, S.C., Cagney, G., Linse, S., and Dawson, K.A. (2007) Detailed identification of plasma proteins adsorbed on copolymer nanoparticles. *Angew. Chem. Int. Ed.*, **46** (30), 5754–5756.
77. Qiu, Y., Liu, Y., Wang, L.M., Xu, L.G., Bai, R., Ji, Y.L., Wu, X.C., Zhao, Y.L., Li, Y.F., and Chen, C.Y. (2010) Surface chemistry and aspect ratio mediated cellular uptake of au nanorods. *Biomaterials*, **31** (30), 7606–7619.
78. Deng, Z.J., Mortimer, G., Schiller, T., Musumeci, A., Martin, D., and Minchin, R.F. (2009) Differential plasma protein binding to metal oxide nanoparticles. *Nanotechnology*, **20** (45), 455101.
79. Devi, L.B., Das, S.K., and Mandal, A.B. (2014) Impact of surface functionalization of AgNPs on binding and conformational change of hemoglobin (Hb) and hemolytic behavior. *J. Phys. Chem. C*, **118** (51), 29739–29749.
80. Wang, L.M., Li, Y.F., Zhou, L.J., Liu, Y., Meng, L., Zhang, K., Wu, X.C., Zhang, L.L., Li, B., and Chen, C.Y. (2010) Characterization of gold nanorods *in vivo* by integrated analytical techniques: their uptake, retention, and chemical forms. *Anal. Bioanal. Chem.*, **396** (3), 1105–1114.
81. Rao, C.N. and Biswas, K. (2009) Characterization of nanomaterials by physical methods. *Annu. Rev. Anal. Chem.*, **2**, 435–462.
82. Murray, C.B., Kagan, C.R., and Bawendi, M.G. (2000) Synthesis and characterization of monodisperse nanocrystals and close-packed nanocrystal assembly. *Annu. Rev. Mater. Sci.*, **30** (1), 545–610.
83. Wang, J., Jensen, U.B., Jensen, G.V., Shipovskov, S., Balakrishnan, V.S., Otzen, D., Pedersen, J.S., Besenbacher, F., and Sutherland, D.S. (2011) Soft interactions at nanoparticles alter protein function and conformation in a size dependent manner. *Nano Lett.*, **11** (11), 4985–4991.

84. Laera, S., Ceccone, G., Rossi, F., Gilliland, D., Hussain, R., Siligardi, G., and Calzolai, L. (2011) Measuring protein structure and stability of protein–nanoparticle systems with synchrotron radiation circular dichroism. *Nano Lett.*, **11** (10), 4480–4484.
85. Calzolai, L., Franchini, F., Gilliland, D., and Rossi, F.O. (2010) Protein–nanoparticle interaction: identification of the ubiquitin–gold nanoparticle interaction site. *Nano Lett.*, **10** (8), 3101–3105.
86. Braden, B.C., Goldbaum, F.A., Chen, B.X., Kirschner, A.N., Wilson, S.R., and Erlanger, B.F. (2000) X-ray crystal structure of an anti-buckminsterfullerene antibody fab fragment: biomolecular recognition of C_{60}. *Proc. Natl. Acad. Sci. U.S.A.*, **97** (22), 12193–12197.
87. Prakasham, R.S., Devi, G.S., Rao, C.S., Sivakumar, V.S.S., Sathish, T., and Sarma, P.N. (2010) Nickel-impregnated silica nanoparticle synthesis and their evaluation for biocatalyst immobilization. *Appl. Biochem. Biotechnol.*, **160** (7), 1888–1895.
88. Zhong, J., Song, L., Meng, J., Gao, B., Chu, W.S., Xu, H.Y., Luo, Y., Guo, J.H., Marcelli, A., Xie, S.S., and Wu, Z.Y. (2009) Bio-nano interaction of proteins adsorbed on single-walled carbon nanotubes. *Carbon*, **47** (4), 967–973.
89. Wang, L.M., Zhang, T.L., Li, P.Y., Huang, W.X., Tang, J.L., Wang, P.Y., Liu, J., Yuan, Q.X., Bai, R., Li, B., Zhang, K., Zhao, Y.L., and Chen, C.Y. (2015) Use of synchrotron radiation-analytical techniques to reveal chemical origin of silver-nanoparticle cytotoxicity. *ACS Nano*, **9** (6), 6532–6547.
90. Goy-López, S., Juarez, J., Alatorre-Meda, M., Casals, E., Puntes, V.F., Taboada, P., and Mosquera, V. (2012) Physicochemical characteristics of protein-NP bioconjugates: the role of particle curvature and solution conditions on human serum albumin conformation and fibrillogenesis inhibition. *Langmuir*, **28** (24), 9113–9126.
91. Fu, C., Yang, H., Wang, M., Xiong, H., and Yu, S. (2015) Serum albumin adsorbed on au nanoparticles: structural changes over time induced by S-Au interaction. *Chem. Commun.*, **51** (17), 3634–3636.

12
"Omic" Techniques for Nanosafety

Weiyue Feng

12.1
Introduction

Nanotoxicology, unlike the classic toxicology study for ordinary chemicals, should be approached from many ways, as multiparameters association with the size, shape, chemical composition, crystalline structure, aspect ratio, surface property (chemical modification, surface charge, surface area, biological/chemical activity, etc.), agglomeration, and concentration of nanomaterials, and, in addition, the interactions of their nanomaterial components with multiple cellular molecules and the interference of cellular functions. It is difficult to determine with conventional assay for changes and adverse effects that may occur and biochemical and/or functional changes with material-specific or exposure-route specific. To obtain the whole picture, the advanced high-throughput screening methods to predict and entirely view the biological responses are needed. Moreover, it is expected that "molecular signatures" will become useful biomarkers of exposure, early effect, and differential susceptibility and reveal sensitive targets for engineered nanomaterials (ENMs).

The high-throughput "omic" techniques make it possible to determine the biological events that involve the nano–bio interactions. "Omics" aim at the entire identification and quantification of pools of biological molecules that translate into the structure, function, and dynamics in cells or organisms [1]. Advances in genomics as well as other newer "omics" techniques have triggered revolutionary research to understand the complex biological systems.

Genomics study has made efforts to determine the entire DNA sequence of organisms and to fine-scale genetic mapping [2–4]. Proteomics is considered the next step after genomics in the study of biological systems. The proteome is the entire set of proteins, produced or modified by an organism or system. Proteomics study is considered beneficial because proteins are the actual functional molecules in the cell and represent actual conditions, which are vital parts of living organisms. However, the proteome is much more complex than its corresponding genome because proteins can be chemically modified, such as

Toxicology of Nanomaterials, First Edition. Edited by Yuliang Zhao, Zhiyong Zhang, and Weiyue Feng.

phosphorylated, carbohydrate, acetylated, and methylated, in different ways after synthesis. Additionally, the proteome is also dynamic that the proteome varies in different cell type, and different developmental stage, physiological condition, or bioenvironmental conditions that a cell or organism undergoes. Proteomics studies in the field of toxicology have focused mainly on exploring biomarkers and identifying molecular mechanisms of toxicity [2, 4–6].

Besides proteomics, other newer "omic" techniques, such as metabolomics, metagenomics, and transcriptomics, have been developed that allow researchers to obtain entire molecular profiling of the changes that occur with time and distinct requirements or stresses that a cell or organism undergoes and thus to reveal information about the biological pathways with these changes [4]. Transcriptomics is the study of the complete set of RNAs (transcriptome), including mRNA, rRNA, tRNA, and other noncoding RNA (transcribed mRNA) that are produced by the genome, providing information about which genes are turned on and off, under specific circumstances or in a specific cell [7]. For the study of toxicity, transcriptomics can rapidly respond to chemical exposure, providing a sensitive endpoint for toxicity.

Metabolomics describes the physiological state of the cell. It is a sum of chemical reactions occurring during metabolism in the cell, and as such, they provide a functional readout of cellular state. In metabolomics, the metabolites and molecules that are intermediate or final products in metabolic processes in a cell, tissue, organ, or organism are identified [8]. With this information, what the cell is doing/has done, what energy sources it is using/has used, what toxins it is processing/has processed, and what damage it is repairing/has repaired have all been known [9]. Metabolic profiling can give an instantaneous snapshot of the physiology of that cell, and therefore, metabolites are easier to correlate with phenotype, which becomes a powerful approach to the clinical diagnostics.

Generating "omics" data is usually by high-throughput experiments. Genomics analysis bases on high-throughput DNA sequencing techniques. Transcriptomics technologies use both sequencing and microarray-based methods [10]. Proteomics study usually bases on mass spectrometry measurement (MS) and bioinformatics analysis. The development of instrument of mass spectrometry makes it possible to determine the quantity of a protein in a sample, identify the protein, its primary structure, and posttranslational modifications (PTMs). For metabolomics, the MS and nuclear magnetic resonance (NMR) spectroscopy are the most widely used techniques for the identification and quantification of metabolites. Besides, other methods include ion-mobility spectrometry, electrochemical detection (coupled to high-performance liquid chromatography (HPLC)), and radiolabeling technique (combined with thin-layer chromatography) are also used. The recent innovations in instrumentation, bioinformatic tools, and modern screening technologies speed up the discovery process and enable the integrative analysis and therefore comprehensive understanding of the biochemical events under various physiological states, for example, the exposure to harmful agents, such as chemical substances, environmental pollutants, and radiation.

So far, the utilization of "omics" techniques, including genomics, transcriptomics proteomics, and metabolomics for the study of nanotoxicity, though still

in the early stage, has been approached to predict and comprehensively estimate the safety of ENM applications for human health [5, 10–30]. For instance, high-throughput genomics and transcriptomics measurements have been applied to study the biological interaction of graphene nanomaterials, in regard to the differential surface functionalization, that is, oxidation state of (graphene oxide (GO) and reduced graphene oxide (rGO)), with HepG2 cells [23]. Proteomics has been performed to study the effects of Au nanoparticles (NPs) with Balb/3T3 mouse fibroblast cell line. The alteration of cellular processes and biochemical pathways caused by Au-NP exposure was investigated [5]. Metabolomics is applied to measure a comprehensive range of metabolites to understand the cellular toxicity of SiO_2 NPs to MRC-5 lung fibroblasts [30].

For the study of nanosafety, "Omics" technologies provide integrated testing strategies to reveal the interactions of ENMs with biological systems that affect cell function, communication, and adaptation to bioenvironmental changes in association with the physiochemical properties of ENMs and, finally, to reveal the biomarker and "signatures" of toxicity. Although the challenge of methods for the study of nanotoxicity still exists, the comprehensive screening studies can help to improve the prediction of hazard and the assessment of the toxicity of ENMs and bring a significant advance in applications in biomedicine, industry, agriculture, environment, and so forth.

12.2 Materials and Biological Models

12.2.1 Material Characterization

The prerequisite for ENM safety assessment is the intensive and extensive characterization of its physicochemical properties, including size, shape, crystal structure, aggregation/agglomeration (e.g., in water or in cultured medium), surface charge, surface area, chemical modification, solubility, and impurity. The methods of measurements include transmission electron microscope (TEM), scanning electron microscope (SEM), atomic force microscope (AFM), infrared spectroscopy (IR), ultraviolet–visible spectrophotometry (UV-Vis), Raman spectroscopy, dynamic light scattering (DLS), inductively coupled plasma–mass spectrometry (ICP-MS), inductively coupled plasma–optical emission spectrometer (ICP-OES), matrix-assisted laser desorption/ionization time-of-flight mass spectrometry (MALDI-TOF/MS), electrospray ionization–mass spectrometry (ESI-MS), and various synchrotron-radiation-based analytical methods. The detailed description of the methods can be referenced in Chapters 1, 2, and 5 of this book.

Usually, ENMs differ from each other in their physiochemical properties, which will decide their potential toxicity. Additionally, impurities such as catalyst residues and deficiencies in crystal structure and morphology may exist and are often the main cause of toxicity. By and large, ENMs are enormously

heterogeneous materials, and the scientific community has emphasized the importance of assessing safety of each ENM individually and avoiding group-wide generalization.

12.2.2 Exposure Models

The *in vivo* and *in vitro* studies can all be used for evaluation of genotoxicity of ENMs. *In vitro* assays can be performed with cell lines and primary cells. Genotoxicity screening of ENMs is easily conducted with cells, utilizing robust methods, such as micronucleus, chromosome aberration assays, and single-cell gel electrophoresis (SCGE or Comet). The disadvantages of cell lines are that they are usually derived from tumors and have adapted to growth in culture, do not always function normally, many processes are completely shut down or continuously activated, and genotypic and phenotypic might drift; therefore, the response to ENMs exposure might not reflect the true state of cells in the intact animal. However, although primary cell reactions reflect the real-life situation to stimuli, they are difficult to acquire and handle and are expensive to culture [31]. To accurately obtain molecular phenotypes of the function to be investigated, the cell lines and primary cells should all be used.

For "omics" studies, the *in vivo* studies have used some genetically tractable models, such as *Caenorhabditis elegans* (*C. elegans*), *Drosophila melanogaster* (*D. melanogaster*), and *Danio rerio* (Zebrafish). These tiny organisms can provide critical information about genetic and cellular process underlying certain diseases or environmental exposures in a rapid and cost-effective manner compared with the traditional rodent-based studies. Significantly, approximately 75% of human disease genes have homologs in *D. melanogaster*; *C. elegans* has approximately 65%; while Zebrafish, being a vertebrate, have most human genes homologs, and the functional domains of many key proteins can be nearly 100% identical between homologs [32]. Additionally, the genes in the model organisms have been precisely mapped and well studied; thus, various genetic tools are available for genetic manipulation in the study of nanosafety [33–38].

12.3 Genomics Study for Nanosafety

12.3.1 Genomics Workflow

12.3.1.1 Microarray and Global Gene Expression Analysis

For nanosafety study, the main purpose of genomics analysis is to identify the whole differentially expressed genes, the so-called toxicogenomics study. The workflow for ENM genomics follows the ordinary genome analysis. The cells are exposed to appropriate dose of ENMs (e.g., EC_{20} dose), and then total RNA is

extracted from exposed and control cells separately. The quality and quantity of RNA are determined. Next, RNA samples were hybridized (e.g., using Gene Chip). The hybridization design is a reference design (reference sample is a mixture of equal aliquots from control and exposed samples). After hybridization, the reference sample is labeled with Cy5 and the exposed samples are labeled with Cy3. Three biological replicates are measured for every condition, and samples from different conditions are analyzed in a randomized manner. Arrays are washed with wash buffer and acetonitrile and finally submersed in stabilization and drying solution. Slides are subsequently scanned by using a GeneChip Array scanner.

12.3.1.2 **Data Analysis**

Microarray analysis begins once the slides have been scanned. The performed steps are as follows:

Image analysis. There are many different analysis software and multiple techniques used to carry out the analysis for spot identification and for quantification of the fluorescent signal intensities.

Normalization. Normalization can be carried out within GeneSpring and also from various freeware packages such as ArrayNorm (Bioinformatics Institute Graz).

Quality control of data. There are various quality control methods used to sift out genes with poor intensity values. For example, GeneSpring allows flagged genes from ImaGene to be identified. Other methods can be achieved through filtering on intensity.

Filtering. With toxicogenomics, the crucial aim is to select genes that are in the category of present (core) and absent or highly divergent (variable). Various types of cut-off selection procedures can be used [39]. Generally, only the probes with a detection $p < 0.01$ in more than 50% of arrays are included for further analyses.

Clustering. The aim of clustering is to group strains according to their genomic contents. The comparison uses only absent or highly divergent genes. Clustering backed up with background information about the strains along with evolutionary data can lead to important hypothesis being deduced or confirmed. Many clustering tools exist, such as Bayesian statistics [40].

Gene expression. The web-based tool, such as DAVID (the Database for Annotation, Visualization, and Integrated Discovery) can be used to perform the biological interpretation of differentially expressed genes.

Annotation. Functional annotation of genes extracted from DAVID database are performed based on Gene Ontology, classified into three ontologies: biological process, molecular function, and cellular component.

12.3.1.3 **Pathway Analysis**

Pathway analysis is performed by two approaches: one is with gene set enrichment analysis (GSEA) software using the complete set of gene expression data from the microarray experiments, and the Kyoto Encyclopedia of Genes and Genomes

(KEGG) pathway exploiting the DAVID database using a list of more than 1.5-fold DGE. The network analysis can be carried out by pathway studio (Pathway Studio v 9.0 program, Ariadne Genomics, Inc.).

12.3.2 Genomics in the Study of Nanosafety

The nanosafety study utilizing genomics is still in its early stage. So far, the emerging toxicogenomics approach has been used in assessing specific mechanisms at the molecular level for Ag-, SiO_2-, dendrimer-NPs, (single-walled carbon nanotubes) SWCNTs, (multiwalled carbon nanotubes) MWCNTs, fullerenes, graphene, and so on [15, 20, 23, 38, 41–43]. Toxicogenomics deals with the collection, interpretation, and storage of information about gene and protein activity within the cell or tissue of an organism in response to toxic substances [44]. It combines toxicology with genomics, transcriptomics, proteomics, and metabolomics molecular profiling technologies, to identify patterns of cellular perturbations in specific pathways through identification and quantification of global shifts in gene expression in organism, elucidates molecular mechanisms evolved in the expression of toxicity, and derives molecular expression patterns (i.e., molecular biomarkers) that predict toxicity or the genetic susceptibility to exogenous agents, for example, ENMs [45].

For example, the whole-genome microarray analysis showed that the cell apoptosis induced by SWCNTs was characterized by upregulation expression of apoptosis-associated genes, for example, p16, bax, hrk, bak1, p5, FGFR2, TGF beta receptor 1, and TNFAIP2 genes, and downregulation expression of cell-cycle-associated genes , for example, cyclin D1, cdk2, cdk4, and cdk6, compared to normal cells [41]. It is hypothesized that the size of NP is associated with a comprehensive set of biological responses. Whole-genome microarray analysis of the early gene expression changes induced by 10- and 500-nm unopsonized amorphous silica particles showed that the magnitude of change for the majority of genes affected correlated more tightly with particle surface area than either particle mass or number; however, the overall biological processes represented by all gene expression changes were nearly identical [42]. The comparison of the cell processes represented in the 10- and 500-nm particle gene sets using GSEA revealed that among 1009 total biological processes, none were statistically enriched in one particle size group over the other (Figure 12.1). The results suggested that on an equivalent nominal surface area basis, common biological modes of action were expected for nano- and supranano-sized silica particles [42].

Chatterjee *et al.* [23] investigated the biological interaction of graphene nanomaterials in regard to its oxidation state (GO and rGO) by using toxicogenomics analysis in HepG2 cells. The global gene expression and pathway analysis displayed that TGFb1-mediated signaling played the central role in GO-induced biological/toxicological effects, whereas rGO elicited host–pathogen (viral) interaction and innate immune responses through TLR4eNFkB pathway (Figure 12.2).

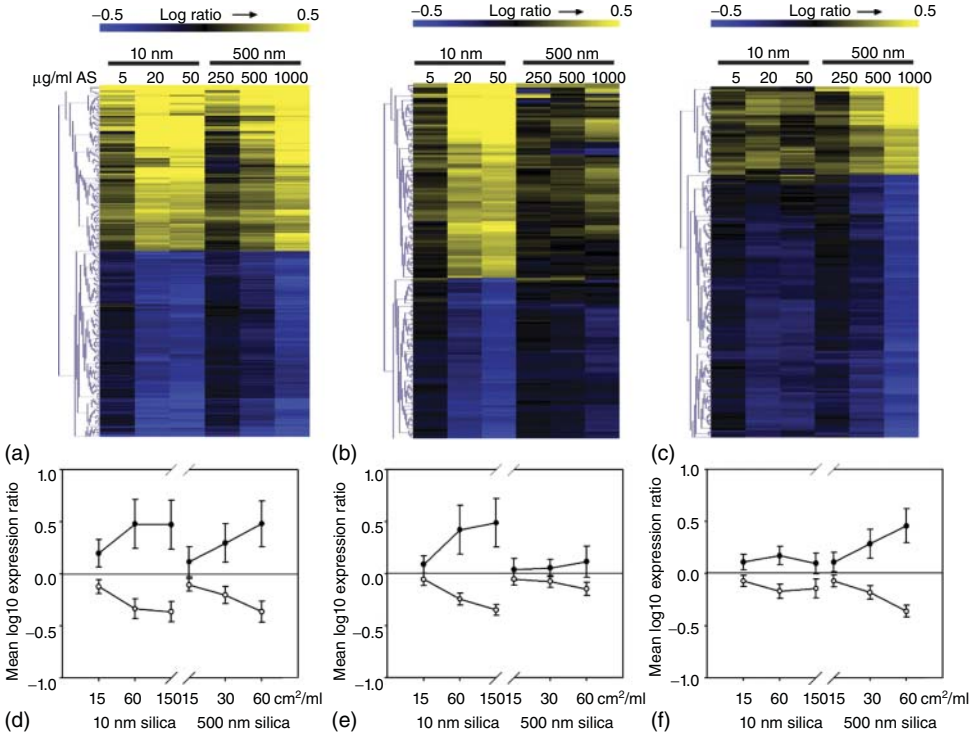

Figure 12.1 Major dose–response profiles for gene expression changes induced by 10 and 500 nm amorphous silica particles. Heat map profiles for the three major dose–response patterns of gene expression (2 h) identified by supervised hierarchical clustering are shown in (a–c). The centroid plots in (d–f) represent the corresponding overall average patterns of expression at three different doses of each particle for pattern a (d), pattern b (e), and pattern c (f). (Reprinted with permission from [42], Copyright (2009) Oxford University Press.)

The toxicogenomics data demonstrate that the physiochemical property of the differential surface oxidation state of GO and rGO mainly determined their distinct biological and molecular mechanisms in cells.

Ma *et al.* [20] investigated the molecular mechanisms of interaction between Ag NPs and human dermal fibroblasts-fetal (HDF-f) at the level of gene expression. After HDF-f was treated with Ag NPs for 1, 4, and 8 h, Global gene expression profiles were examined using Illumina Human-6V3 Expression BeadChip Array, and the results were verified by quantitative real-time polymerase chain reaction (RT-PCR). The obtained differential expressed genes were analyzed by the integration of clustering, gene ontology, and biological pathway analysis. Their results suggest that Ag NPs may cause disruption of cytoskeleton and cellular membrane, disturbance of energy metabolism and gene expression associated pathways, and DNA damage accompanied by cell cycle arrest. It is noteworthy that when Au NPs compared with Ag NPs simultaneously treated with cells,

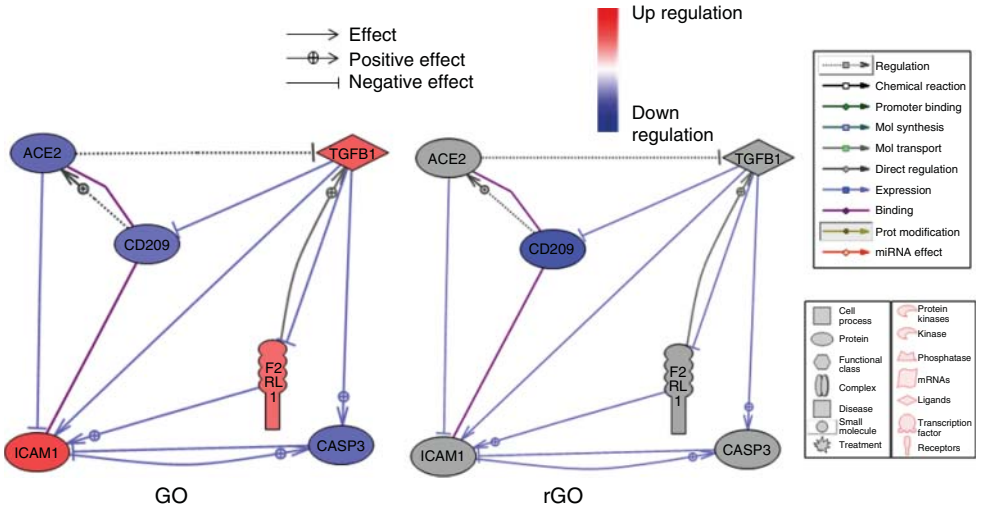

Figure 12.2 Comparison of network analysis between GO and rGO by Pathway Studio. (Reprinted with permission from [23], Copyright (2014) Elsevier.)

both the similarities and differences underlying biological processes and gene regulations were found. The research suggests that the genomics research can provide a convenient and efficient approach to the understanding of cytotoxic mechanisms of nanomaterials [20].

Lan *et al.* [43] reported a comparative and mechanistic toxicogenomics assessment of four ENMs (TiO_2 NPs, carbon black, SWCNTs, and fullerene) across three species, including *Escherichia coli*, yeast, and human cells, with the aim to reveal the distinct potential genotoxicity mechanisms among the different ENMs and their association with physiochemical features (Figure 12.3). The results show that the proposed molecular endpoints derived from the toxicogenomics assays, namely TELI (Transcriptional Effect Level Index) and PELI (Protein Effect Level Index), correlated well with the phenotypic DNA damage endpoints from comet tests. The altered gene and protein expression profiles revealed various potential DNA damage types and relevant genotoxic mechanisms induced by the tested ENMs. The carbon nanomaterials, carbon black, SWCNTs, and fullerene, exhibited distinct, species- and ENM-property-dependent DNA damage mechanisms. The study shows the differences in cellular structure and defense systems among prokaryotic and eukaryotic species leading to distinct susceptibility and mechanisms for ENM uptake and, thus, varying DNA damages and repair responses. The observation suggests that eukaryotes, especially mammalian cells, are likely more susceptible to genotoxicity than prokaryotes in the ecosystem when exposed to these ENMs [43] (Figures 12.4 and 12.5).

The global genome analysis is very useful for the *in vivo* mechanism exploration by using tiny organisms. By using *C. elegans* as a toxicological animal model, Chen *et al.* [38] evaluate the potential *in vivo* genotoxic mechanism via

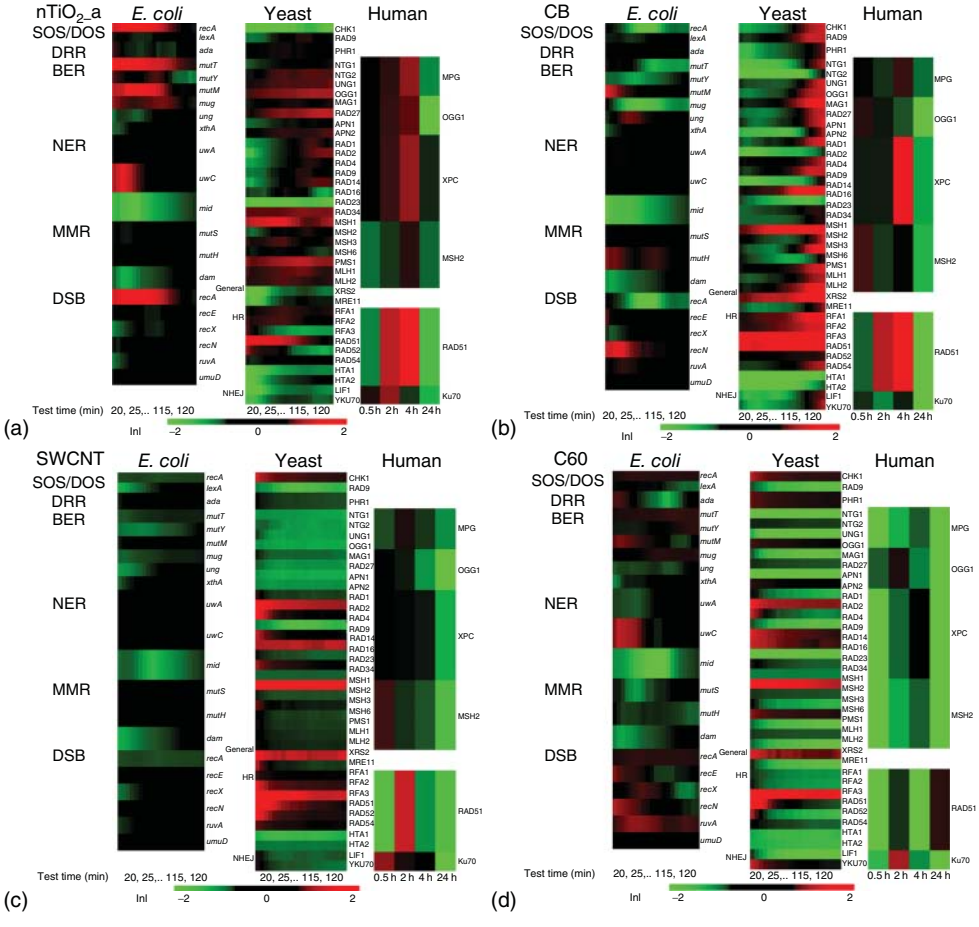

Figure 12.3 Gene/protein expression profiles of biomarkers indicate difference of DNA damage repair pathways upon exposure to four types of ENMs ((a) TiO_2-NPs, 50 μg/ml, (b) carbon black (CB), 5, 50 μg/ml for human cells), (c) single-walled carbon nanotube (SWCNT, 8 μg/ml for *E. coli*, 10 μg/ml/l for yeast and human cells), and (d) purified fullerene (C60, 50 μg/ml) across three species. The mean natural log of induction factor (ln *I*) indicates the magnitude of altered gene/protein expression (represented by a green-black-red color scale at bottom). Red spectrum colors indicate upregulation, green spectrum colors indicate downregulation. Values beyond ±2 are shown as ±2). *X*-axis bottom: for *E. coli* and yeast: testing time in minutes, the first data point shown is at 20 min after exposure due to data smoothing with moving average of every five data points; for human cells: testing time in hours. *Y*-axis left: clusters of genes/proteins by DNA damage repair pathways. *Y*-axis right for each species [43].

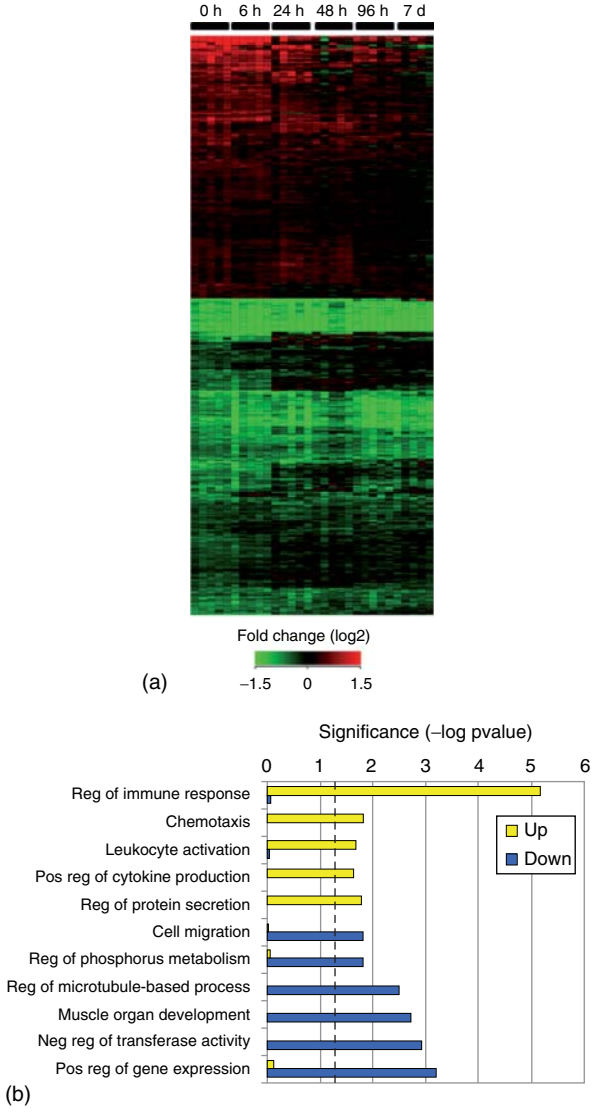

Figure 12.4 Transcriptomic analysis of gene regulation by SPIONPs. (a) Hierarchical clustering of significantly effected (compared to time matched controls) transcripts shows a higher preponderance of downregulation (green) by SPIONP exposures. Upregulation (red) was more prominent during earlier time points where the most highly induced mRNAs encoded inflammatory cytokines. (b) Highest ranking biological processes associated with transcripts upregulated by *in vivo* exposure to SPIO NPs. Cellular processes associated with inflammation and clearance of foreign bodies (cytokine production, cell migration, chemotaxis) were significantly upregulated [24].

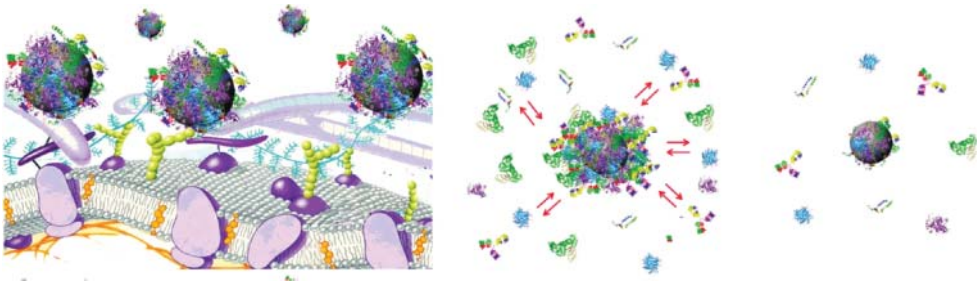

Figure 12.5 (a) Cartoon representation of the possible exchange/interaction scenarios at the bio–nano interface at the cellular level. (b) Schematic drawing of the structure of NP–protein complexes in plasma: the "core" nanoparticle is surrounded by the protein corona composed of an outer weakly interacting layer of protein (left, full red arrows) rapidly exchanging with a collection of free proteins and a "hard" slowly exchanging corona of proteins (right). Diagram is not to scale in representing the proportions of the different objects. (Reprinted with permission from [46], Copyright (2010) American Chemical Society.)

genome-wide gene expression analysis. For microarray analysis, the synchronized worms were exposed to SWCNTs (500 mg/ml) for 48 h (Figure 12.6). The total RNA was extracted from the untreated and SWCNT-treated worms. Purified total RNA products (15 mg each) from three replicates were pooled together and used for reverse and *in vitro* transcription followed by the application to a *C. elegans* Genome GeneChip (Affymetrix), which contains 22 500 probe sets against 22 150 unique *C. elegans* transcripts. The microarray expression data set was submitted to the Gene Expression Omnibus (GEO) database in National Center for Biotechnology Information (NCBI) (accession number GSE41486). Their functional genomic analysis and molecular biology validation suggest that defective endocytosis, the decreased activity of the citrate cycle, and the reduced nuclear translocation of DAF-16 transcription factor play key roles in inducing the observed SWCNT toxicity in worms [38].

12.4
Transcriptomics Study for the Biological Effects of ENMs

Transcriptomics can be applied to the total set of transcripts encoded by the genome in a given organism or to the specific subset of transcripts present in a particular cell type at a specific time or under a specific set of conditions. The use of transcriptomics as an early and specific marker for cellular responses resulting from various diseases and as a marker for exposure to chemicals and therapeutic agents has been increasing over recent years [48]. Transcriptomic markers can provide a linkage to mechanisms of cell injury, cell death, or carcinogenic transformation. Transcriptomics analysis is now being utilized more frequently and is gaining more acceptance as a useful tool in risk and safety assessments.

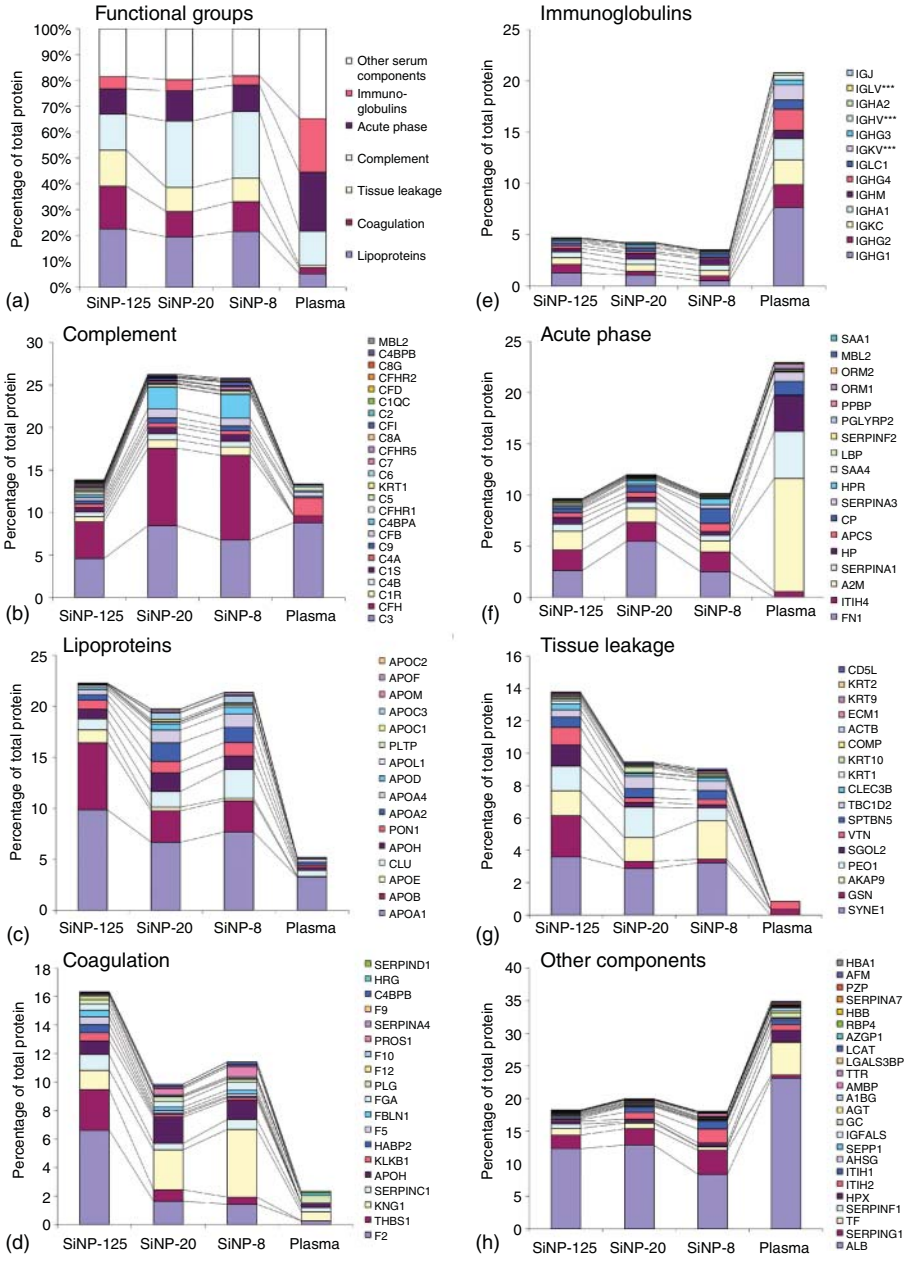

Figure 12.6 Bioinformatic classification of identified corona proteins according to their functions. Employing bioinformatics tools, proteins identified in the respective SiNPs corona were classified according to biological processes of the blood system (a). The relative percentages of the proteins compared to crude plasma are shown. A significant enrichment of plasma proteins involved in complement activation (b), lipoproteins (c), coagulation (d) as well as proteins grouped as "tissue leakage" (g) was evident in the corona. Although immunoglobulins (e), acute-phase response proteins (f), and serum albumin (h) were present in high amounts in the plasma, these proteins displayed a lower affinity for the SiNPs. (Reprinted with permission from [47]. Copyright (2011) American Chemical Society.)

In systems toxicology, sequencing of the genome, annotation of genes, and transcriptomic analysis have been the starting point for elucidation of toxic effects [48].

Different approaches and gene expression technologies have been reported in transcriptomics study. The often used method is high-throughput techniques based on DNA microarray technology. The use of next-generation sequencing technology to study the transcriptome at the nucleotide level is known as RNA sequencing (RNA-Seq) [49]. Currently, the development of microfluidics technologies opens the doors to the study of single-cell transcriptome analysis, which change the analysis of complex samples by definition and quantification populations of single cells [49].

12.4.1 Transcriptomics Workflow

The study of transcriptomics often uses high-throughput techniques based on DNA microarray technology. The main methods for the study of transcriptomics are as follows [48, 50, 51]:

1. Hybridization-based approaches: cDNA-based and oligonucleotide-based microarray systems
2. Sequence-based approaches: serial analysis of gene expression (SAGE); Sanger sequencing of cDNA or EST libraries; cap analysis of gene expression (CAGE); and massively parallel signature sequencing (MPSS)
3. High-throughput RNA-seq.

12.4.2 Transcriptomics in the Study of Nanosafety

The process of determining "phenotypic anchoring," a specific alteration in gene expression profiles and the toxicological phenotype of the organism for a particular exposure or dose, and at a particular time, can be defined by using transcriptome measurement. This approach of "cause and effect" can be used in conjunction with *in vivo* and *in vitro* study of ENMs and detection of their toxic mechanisms.

12.4.2.1 Toxicity Testing

Khan *et al.* [52] using a transcriptomics approach estimated the molecular effects of uptake of magnetite (Fe_3O_4) NPs. The transcriptional profiling revealed 69 genes to be differentially expressed upon Fe_3O_4 NPs treatment. Many of these genes are associated with TGF-beta signaling, including ID1, ID2, ID3, CASP9, SMAD6, and SMAD7, which are important negative regulators of signaling pathways involved in development and tumorigenesis. The further analysis showed the Fe_3O_4 NPs exposure can specifically interfere with TGF-beta signaling by inhibiting the expression of ID and SMAD genes. Similarly, the transcriptional profiling using whole-genome microarrays showed that the 18-nm AuNPs biological

safety, whereas in comparison, the 1.4-nm triphenylphosphinemonosulfonate capped Au NPs could trigger oxidative stress and mitochondrial damage [53, 54]. These reports confirm that the molecular effects of ENMs can vary according to their physiochemical properties. The utility of toxicogenomics approach helps to identify specific effects of NP upon cells and provides simultaneous clues about the biocompatibility and therapeutic potential of ENMs [52].

12.4.2.2 **Dosimetry Response**

Without a common method for measuring the amount of ENMs in contact with the target cells and organisms, it is commonly contradictory of the data between the *in vivo* and *in vitro* models of experimental toxicology, which will impede the accurate prediction or description of responses in *in vivo* systems and the deeper understanding of the root causes of nanotoxicity (Figure 12.7).

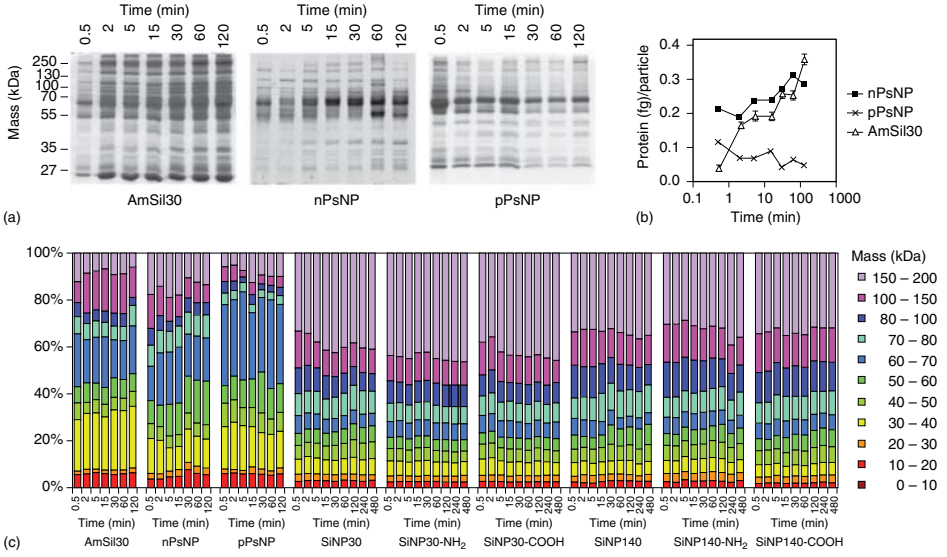

Figure 12.7 Protein coronas and their composition are established rapidly. (a) SDS-PAGE was used to visualize nanoparticle-bound plasma proteins. Molecular mass and time points are indicated. (b) Corona quantification (protein (fg) per particle at the indicated time points. Continuously increased protein binding was observed for AmSil30 and also, slightly, for nPsNPs, whereas pPsNPs showed decreased binding over time. Values are mean + s.d. from two independent experiments. (c,d) Classification of corona proteins identified on nine different nanoparticles by LC-MS according to their calculated molecular mass (c) or isoelectric point (d). Relative percentages are shown. (e) Plasma exposure time modulates protein abundance (averaged molecule number per nanoparticle) on the indicated silica nanoparticles. Compared with SiNP30, proteins bound to the larger SiNP140 in higher copy numbers. Relative numbers of proteins present at the indicated copy numbers per indicated nanoparticle are shown. (f) Dendrogram illustrating sample similarities between protein binding profiles, which shows that they are correctly kinetically classified and that significant changes in the corona composition occurred at early rather than at late exposure time periods. (Reprinted by permission from Macmillan Publisher Ltd: Nature Nanotechnology [55], copyright (2013).)

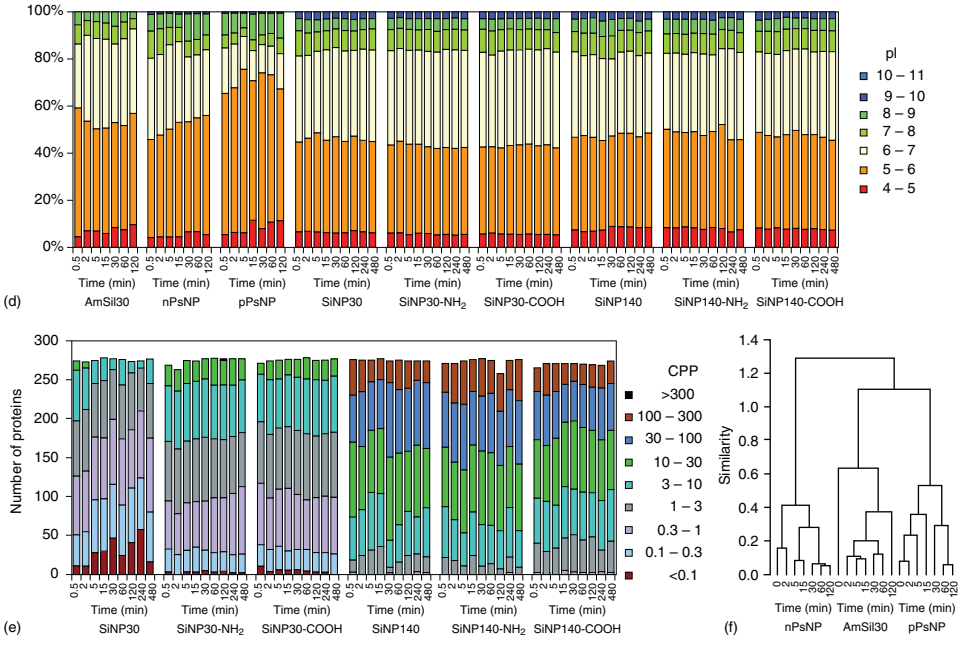

Figure 12.7 *Continued*

To directly test the comparability of *in vitro* and *in vitro* responses to ENMs, Teeguarden *et al.* [24] conducted coordinated *in vivo* and *in vitro* toxicity studies of superparamagnetic iron oxide nanoparticle (SPIONs, 12.8 nm) exposure, utilizing global transcriptome analysis to anchor genetic response to target cell dosimetry in the whole mouse lung (the Balb/c mouse, a common test animal) and in two pulmonary cell types resident in the alveolar region of lung (C10 lung epithelial cells and bone marrow derived macrophages). The genome microarray profiling identified 815 genes that were significantly changed in SPIONs exposed mice at the end of the 4 h exposure period compared to air-exposed controls. Hierarchical clustering of the genetic data demonstrated a strong transcriptional response that persists through 6 h postexposure and gradually declines over the next 7 days (Figure 12.8). Evaluation of the "up-" and "down-" regulated genes revealed that majority of the upregulated genes were involved in regulation of the immune response, chemotaxis, and leukocyte activation, consistent with the histopathology results showing infiltration of macrophage cells. The upregulated genes in the primary chemokines CCL3, CXCL5, CXCL1, CXCL1, CXCL3, CCL17, and CCL9 involved in macrophage recruitment were resolved to baseline levels when the macrophage levels were at their peak, indicating that these chemokines were likely being synthesized by lung epithelial cells as well as infiltrated immune cells. In contrast, many of the downregulated genes were persistently downregulated through the 7 day postexposure, indicating that the SPIONs exposed mice were not yet resolved to steady state while they continue to

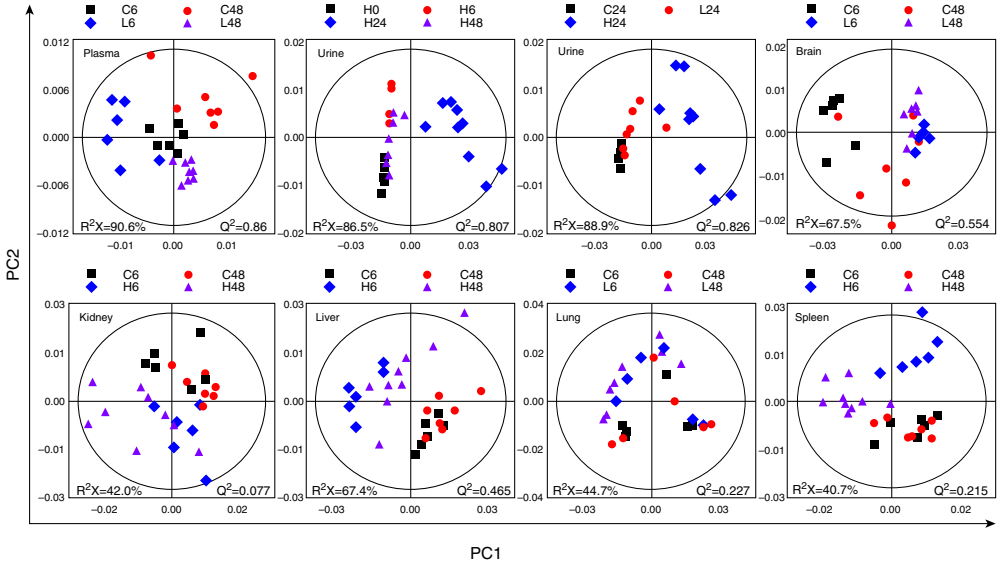

Figure 12.8 Representative PCA score plots (PC1 versus PC2) derived from the ^{1}H NMR data of body fluid samples (plasma and urine) and tissue samples (extracted from brain, kidney, liver, lung, and spleen) from the corresponding groups of rats: C, control group; L, low-dose group; H, high-dose group; 0, 0 h post-dose; 6, 6 h post-dose; 24, 24 h post-dose; 48, 48 h post-dose [29].

clear the particles from their tissues. The transcriptomics study demonstrates that there is a good correspondence between target cell doses triggering inflammatory processes *in vitro* and *in vivo* in the alveolar macrophage population, but not in the epithelial cells of the alveolar region [24].

12.4.2.3 Biological Endpoints

Much evidence has shown that the aspect ratio (morphology) is an important factor in the uptake and toxicity of ENMs [56]. For example, in studies of Ag NPs toxicity, silver oxidation and ionic silver (Ag^+) release were identified to be the mainly responsible for the toxicity of Ag NPs. However, it is unknown whether the molecular mechanisms of Ag^+, Ag NP, or silver nanowire (Ag NW) toxic pathways are the same [56]. The transcriptomic assays including pathway, gene ontology, and clustering analyses of gene expression response indicate that the biological effects of Ag NWs were distinct different from those of Ag^+ on *Daphnia magna* [56]. For the transcriptomic assays, the microarray data were deposited in NCBI's GEO and were accessible through GEO Series accession number GSE47064 (http://www.ncbi.nlm.nih.gov/geo/query/acc.cgi?acc=GSE47064). Totally 2801 genes were identified as differentially expressed gene candidates, but the gene expression response was not correlated to LC_{50} of the nanomaterials. Ag^+ caused the most robust response, followed by short polyvinyl pyrrolidone (PVP) modified Ag NWs (S-PVP-NW) and then SiO_2-coated Ag NWs (SiO_2-NW). The long PVP-modified Ag NWs (L-PVP-NW) resulted in more upregulated than downregulated genes. Only seven genes were common to all the nanomaterial-exposed conditions [56]. The results show that different Ag NWs elicit distinct gene expression profiles in *D. magna.* Each Ag NW displayed a distinct pattern of DGE with limited overlap among the different sizes and coatings of Ag NWs. The KEGG pathway analysis showed that Ag^+ exposure caused the most statistically significant pathway changes in oxidative phosphorylation and ribosomal pathways. The long SiO_2 NW affected the largest number of pathways, including peroxisome, lysosomal, and cytochrome P450 xenobiotic metabolism pathways (Table 12.1).

12.5 Proteomics Study for Nanosafety

12.5.1 Protein Corona

The interaction of ENMs with cells and living organisms is fundamentally different from those small molecules. ENM surface has a high free energy, which invites adherence of biomolecules (e.g., proteins, DNA, lipids, and sugars) when they enter living system, forming a so-called *corona* around the ENMs. ENMs opsonization by serum or membrane proteins is one of the key factors determining the fate and outcomes of ENMs interacting with biological systems. Proteins

Table 12.1 KEGG pathway analysis of gene expression data from *Daphnia magna* exposed to Ag NWs identified the enrichments of different biological pathways.[a]

Affected biological pathway	L-PVP	L-SiO_2	S-PVP	Silver
Oxidative phosphorylation	—	—	—	5.3×10^{-4}
Spliceosome	0.02	—	—	—
Peroxisome	—	0.02	—	—
Lysosome	—	0.04	—	—
Ribosome	0.01	—	0.01	1.8×10^{-4}
Progesterone-mediated oocyte maturation	—	0.01	—	—
Metabolism of xenobiotics by cytochrome P450	—	0.02	—	—
Drug metabolism-cytochrome P450	—	0.03	—	—
Retinol metabolism	—	0.05	—	—

[a] The *p* values 0.05 or less were considered significant. KEGG analysis on S-SiO_2-NW data found no statistically significant results.
Reprinted with permission from [56], Copyright (2013) American Chemical Society.

bind to ENMs via weak physical forces such as *van der Waals* and electrostatic interactions in thermodynamically favorable conditions. The chemical composition, size, shape, and surface characteristics of ENMs affect the protein binding and, in turn, influence the way in which ENM interact with cells and organisms. For instance, SWCNTs were found to be most absorbed with fibrinogen in plasma, which influenced their engulfment by cells and elimination by immune cells in the blood stream, thus effectively reducing their cytotoxicity but further decreasing their clearance and facility to delivery to the intended target sites [57]. The negatively charged poly(acrylic acid)-conjugated Au NPs were found to bind to and induce unfolding of fibrinogen, which promoted interaction with the integrin receptor, Mac-1, resulting in increase of NF-kB and thus inducing the release of inflammatory cytokines [58]. The selected absorption of pulmonary surfactant phospholipids, phosphatidylcholines and phosphatidylglycerols on the surface of SWCNTs in mouse lung, was found to markedly enhance the *in vitro* uptake of the nanomaterial by macrophages [59].

The adsorption of proteins on the surface of ENMs is governed by protein–ENM binding affinities and protein–protein interactions. Proteins that have high affinity for the particle surface form the "hard" coronas, which the tightly bound proteins do not readily desorb; in contrast, proteins that have low affinity form the "soft" coronas, which loosely bind on the surface [60] (Figure 12.5).

Soft and hard coronas can be defined based on their exchange times. Hard coronas usually show long exchange times in the order of several hours. The dynamic exchange of corona proteins can be measured by various techniques such as isothermal titration calorimetry (ITC), Langmuir absorption isotherms, surface plasmon resonance, quartz crystal microbalance (QCM), and differential centrifugal sedimentation (DCS). However, the identification and quantification of the complex proteins are difficult to assess. The proteomics approach can be applied to solve the problem.

Since protein solutions especially of plasma protein are complex mixtures that in a very wide dynamic range, spanning more than 10 orders of magnitude in terms of concentration, the most interesting proteins may be present only in minute concentrations. Therefore, appropriate steps for protein corona (PC) extraction from nanosurface and protein fraction separation are necessary. Generally, ultracentrifugation technique can be used for PC extraction. For protein fraction separation, the 1D and 2D gel electrophoresis and chromatography are usually used. After separations, the proteins and peptides can be performed in a tandem mass spectrometry for protein identification and quantification [13].

12.5.2 Protein Corona Isolation

ENMs are suspended in biological media, briefly sonicated in a bath sonicator, diluted with culture media, and incubated at 37 °C for various time. After that, the NP–biological mixture is centrifuged (e.g., 5 nm NPs at 50 000 × *g*; 10 nm NPs at 35 000 × *g*; 20 nm NPs at 20 000 × *g* [59]) for a few dozen minutes at 4 °C to remove the unbounded proteins. For CNT–protein mixtures, the centrifugation may be at approximately 20 000 × *g* [6]. Biological medium (e.g., plasma) without NPs is used as a control. Pellets are washed with washing buffers or PBS until the OD280 of the supernatant is less than 0.1. The bound proteins are eluted by heating the pellets to 70 °C for 10 min [61]. The protein concentration was determined using a protein assay solution.

12.5.3 Protein Separation

12.5.3.1 One-Dimensional (1D) and Two-Dimensional (2D) Gel Electrophoresis

1D electrophoresis (1DE) can resolve highly abundant and less abundant proteins in a wide molecular mass range of 10–300 kDa [62]. For 1DE, proteins are usually denatured with sodium dodecylsulfate (SDS) and heat treated. Then, a portion of protein sample is separated on a 12–15% sodium dodecylsulfate–polyacrylamide gel electrophoresis (SDS-PAGE) gel. The gel is run at a constant voltage of 200 V for 35 min and then stained.

In many proteomic experiments, the protein mixture is so complicated that protein separation only by size is not adequate. In 2D electrophoresis (2DE), proteins are first separated according to their isoelectric point (pI) in isoelectric focusing (IEF), then followed by SDS-PAGE separation according to molecular weight. For 2DE, after rehydration of immobilized pH gradient (IPG) strips over night at room temperature, protein was loaded onto each strip. IEF is performed by a program of progressively increasing voltage for a total of 30–45 kVh at 15 °C. The focused IPG strips are then equilibrated for 30 min with slow shaking in an equilibration buffer. Equilibrated IPG strips are transferred onto 8–15% SDS-PAGE and sealed with 1% agarose. The gels are run until the dye front migrated to the bottom of the gel. 2D gels are stained with silver or Coomassie blue according to published methods

[6, 58]. Gels are destained with distilled water overnight and then imaged. Proteins are identified by their pIs and mass using database (e.g., ExPASy).

12.5.3.2 Separation of Proteins by Chromatography

Generally, an appropriate portion of protein solution is reduced with dithiothreitol (DTT), diluted with 50 mM ammonium bicarbonate, pH 7.4, and digested with trypsin. Sequencing-grade trypsin is added at a substrate-to-enzyme ratio of 50 : 1 (mass:mass) and incubated at 37 °C for 15 h. Sample cleanup is achieved using a solid-phase extraction C18 column, and the samples are dried and stored at −20 °C until analyzed by liquid chromatography – mass spectroscopy (LC-MS).

Samples were prepared to an appropriate concentration using either 0.1% (v/v) formic acid for 1D LC-MS or 20 mM ammonium formate at pH 10 for 2D LC-MS. 1D nanoscale liquid chromatography (LC) separation of tryptic peptides is performed with a nano-LC system, equipped with C18 reversed-phase (RP) column. Samples are typically transferred with aqueous 0.1% (v/v) formic acid to the precolumn. After desalting and preconcentration, peptides are eluted from the precolumn to the analytical column and separated with a gradient elution. For 2D LC separation, cation/anion-exchange chromatography/RP or RP/RP chromatography can be implemented [63].

12.5.4 Mass Spectrometry and Protein Identification

Protein spots from 1D or 2D gels are excised and are enzymatically digested into peptides to facilitate protein identification. Digestion can be performed in-gel or in-solution using various enzymes. The most widely used enzyme is trypsin, which cleaves proteins at the C-terminal to residues Lys and Arg. The detailed process of the digestion with trypsin has been described in the previous work [64].

The extracted peptide mixtures are analyzed by high-resolution capillary or nano-LC-ESI-MS/MS. The masses of both the parent peptide and its daughter ions are detected by tandem mass spectrometry and used to search for protein candidates in protein sequence databases. The database searching for protein identification can be carried out using several search engines, for example, MASCOT, SEQUEST, OMSSA, and X!TANDEM.

Proteins of interest from 2DE can be digested with trypsin and subjected to MALDI-TOF/MS for protein identification [65].

12.5.5 Quantitative Proteomics

12.5.5.1 2D Electrophoresis-Based Quantification

2DE has been used to compare relative abundances of proteins in related samples, such as control and diseased/treated, allowing the comparison of relative differences of responses of proteins. To date, most comparative protein profiling studies have produced qualitative data, which accurately show a protein with an increase or decrease in expression. However, the accurate quantification from

traditional 2DE has some disadvantages. It has limited ($\sim 10^1$) dynamic range, and silver staining is incompatible with protein identification by MS, and additionally, the reproducibility of 2DE is poor [66].

The developed method of 2DE difference gel electrophoresis (DIGE) can overcome the aforementioned limitations of traditional 2DE and allows for more accurate and sensitive quantitative proteomics studies [11, 67]. The 2D-DIGE approach allows three different protein samples to be labeled with size-matched, charge-matched spectrally resolvable fluorescent dyes (e.g., Cy3, Cy5, Cy2) prior to 2DE. After the 2DE, the gel is scanned with the excitation wavelength of each dye [68]. In experiments comprising several gels, an internal standard is prepared by mixing several or all of the samples in the experiment. This allows the measurement of the abundance of a protein in each sample relative to the internal standard [66, 68].

12.5.5.2 **Mass-Spectrometry-Based Quantification**

12.5.5.2.1 **Stable Isotope Labeling Technique** Several MS-based techniques utilizing different stable isotope labeling strategies for proteomic quantification have been established [68–71]. Most of these techniques are through coding samples with reagent labeled with stable isotopes (^{13}C, ^{15}N, ^{2}H, and ^{18}O) and unlabeled reagent, following quantitative analysis by MS [71]. The introduction of the isotopic labels can be performed by metabolic, chemical, or enzymatic labeling [68–72]. The mainly relative quantitation methods utilizing stable isotope labeling include isotope-coded affinity tags (ICAT), stable isotope labeling with amino acids in cell culture (SILAC), isobaric tags for relative and absolute quantification (iTRAQ), tandem mass tags (TMT), terminal amine isotopic labeling of substrates (TAILS), isotope-coded protein labeling (ICPL) as well as several variants of these techniques [66, 72]. Here, quantitative changes of the proteome in ENM-treated samples compared with untreated ones can be determined by the comparison to an internal standard consisting of the isotope-labeled cells [11, 73, 74].

12.5.5.2.2 **Label-Free Quantification** Label-free quantification is a method in mass spectrometry that aims to determine the relative amount of proteins in two or more biological samples. It bases on precursor signal intensity or on spectral counting. The computational framework of label-free approach includes detecting peptides, matching the corresponding peptides across multiple LC-MS data, selecting discriminatory peptides [75]. The first step is termed *spectral counting*, that is, a counting comprises the number of fragment-ion spectra (MS/MS) acquired for peptides of a target protein. Since the number of tandem mass spectra of a peptide increases with an increasing amount of the corresponding protein, thus a relative quantification of proteins between different, thus a relative quantification of proteins between different samples is possible [75].

Generally, the particular peptide signals are detected at the MS1 level, and the patterns are then used to reconstruct a chromatographic elution profile of the monoisotopic peptide mass. The total ion current of the peptide signal is integrated and used as a quantitative measurement of the original peptide concentration.

12.5.6 Data Interpretation

To extract the biological relevance from the vast amount of proteomics data, deepening the functional annotation of the data and mapping the results into biological processes by biological information techniques are necessary. Furthermore, pathway analysis and construction of protein–protein interaction and PTM networks should be very useful for the mechanistic exploration. Especially, for clinical/toxic biomarker discovery studies, the integration of clinic/toxic–pathological data is crucial and can be used to explore whether the observed protein changes have been reported earlier in context of a particular disease/toxicity. To date, several databases and tools have been developed to extract biologically relevant information from large protein lists [76]. The widely used tools and resources have been summarized by Malik *et al.* [76].

12.5.7 Proteomics in the Study of Nanosafety

12.5.7.1 Protein-Corona Composition Analysis

In biological environments, ENMs forming a PC may alter the ENMs' pharmacokinetics and pharmacodynamics, thereby influencing their toxicity. Employing label-free LC-MS combined with 1D and 2D gel electrophoresis and immunoblotting methods may provide not only qualitative but also quantitative analysis of the composition of the PC [47, 55, 74, 77].

Using a label-free mass-spectrometry-based proteomics approach, the composition of the PC on the surface of a set of nanotubes including unmodified and carboxylated SWCNTs and MWCNTs, polyvinylpyrrolidone-coated multiwalled carbon nanotubes (MWCNT-PVP), and nanoclay was analyzed after 1 h incubation in cell culture. The results show that all CNTs are found to associate with a common subset of proteins including albumin, titin, and apolipoproteins. The modified CNTs bound a number of unique proteins, implying that hydrogen bonding and electrostatic interactions were involved in PC formation. The PC composition on the nanosurface was found to have no significant association with the pI, hydropathy, or aliphatic index of proteins, implying minimal roles of hydrophobic interaction and pi-stacking between ENMs and cell culture media [74].

It is hypothesized that chemical composition, size, and surface properties of NP play key roles in determining the composition of coronas, although the underlying physical mechanism is not yet fully understood. The label-free LC-MS quantitative analysis convincingly shows that the size of particle critically determines quantitatively but not qualitatively the binding of 37% of the identified corona proteins of SiO_2 NPs (20, 30, and 100 nm) [47]. Moreover, neither protein size nor charge significantly determined the protein fingerprints, suggesting that electrostatic effects do not act as the major driving force of the corona. The proteomics analysis revealed an enrichment of lipoproteins and proteins involved in coagulation and the complement pathway,

whereas immunoglobulin and acute-phase response proteins displayed lowers affinitie [47].

However, as biological systems are highly dynamic, it is important to understand the time-resolved knowledge of protein-corona formation, development, and biological relevancy. By using label-free snapshot proteomics method, the quantitative time-resolved profiles (from 0.5 to 120 min) of human plasma coronas formed on silica and polystyrene NPs of various sizes and surface functionalization were investigated (Figure 12.7) [55]. It is very interesting to find that the corona formation is time- and NP-specific. Approximately 300 different proteins in human plasma were found to form corona rapidly (<0.5 min), and the amounts of bound protein, not the composition, change significantly over time. Importantly, the rapid corona formation was found to kinetically impact on nanopathophysiology, including hemolysis, thrombocyte activation, NP uptake, and endothelial cell death at an early exposure time [55].

12.5.7.2 **Biomarker Identification**

Higashisaka *et al.* [12] identified biomarkers for predicting the exposure and toxicity of ENMs using proteomic technique. The approach was performed by analyzing the changes of protein expression in plasma after treatment with SiO_2 NPs. Their analyses identified haptoglobin, one of the acute-phase proteins, as a candidate biomarker. The results showed that the level of haptoglobin was significantly elevated in the plasma of mice exposed to SiO_2 NPs (70 nm) compared to normal and those exposed to large SiO_2-particle mice. The other acute-phase proteins, C-reactive protein (CRP) and serum amyloid A (SAA), were elevated in the plasma of SiO_2-NP treated mice either. The level of these acute-phase proteins was elevated in the plasma of mice after intranasal treatment with 30 nm SiO_2 NPs. The results suggest that haptoglobin, CRP, and SAA are highly sensitive biomarkers for assessing the risk of exposure to SiO_2 NPs.

12.5.7.3 **Inflammation Investigation**

The proinflammatory effects have been reported as the common toxicity induced by different ENMs. The current study focuses on the physiochemical properties of ENMs associated with inflammation production and the pathways for ENM to provoke the inflammation responses. Deng *et al.* [58] by using 2DE and mass spectroscopy confirmed that high-affinity of fibrinogen bounded on the negatively charged poly(acrylic acid)-coated gold nanoparticles (PAA-GNPs) in plasma. Importantly, they found that PAA-GNP could unfold fibrinogen, which promoted interaction with the integrin receptor, Mac-1. Further biochemical analysis showed that activation of Mac-1 increased the NF-kB signaling pathway, resulting in the release of inflammatory cytokines IL-8 and TNF-α. Intriguingly, the study showed not all NPs that bind to fibrinogen induced this effect [61]. The data show that though SiO_2 NPs (7 nm), TiO_2 NPs (21 nm), and ZnO NPs (30 nm) bound fibrinogen with approximately equal capacities, their ability to promote fibrinogen binding to THP-1 cells varied markedly. The research showed an alternative mechanism to the commonly described role of oxidative stress in the inflammatory response to ENMs.

The production of reactive oxygen species (ROS) has been demonstrated by the common mechanism of nanotoxicity. Leung *et al.* [63] investigated the toxicity of three different MgO NPs. They found the robust toxicity toward *E. coli* bacterial cells in the absence of ROS production for two MgO NPs. The further proteomics data clearly show the absence of oxidative stress and indicate that the primary mechanism of cell death is related to the cell membrane damage but not due to lipid peroxidation. During the experiments, TransOmics Informatics (Waters Corporation, Manchester, UK) was used to process all of the data acquired. Protein identifications were achieved by searching *E. coli* (strain K12) UniProt database. Importantly, MgO NPs have been demonstrated to exhibit an excellent antibacterial activity, but the mechanism is still unclear. In the study, when the identified proteins were classified according to Gene Ontology terms, the proteins were found to be involved in various biological processes, many cellular components and molecular functions, indicating that MgO NPs caused cell-wide disruption to the cellular structures and catalytic activity. Furthermore, when the identified proteins were mapped to the corresponding metabolic pathways, many key cellular pathways including amino acid metabolism, carbohydrate metabolism, energy metabolism, and nucleotide metabolism were found to be downregulated, indicating that metabolic activity decreased in the cells. The overall proteomic analysis highlights that MgO is a potent antimicrobial agent against bacteria [64].

PTM has emerged as a major contributor to variation, localization, and control of proteins. For nanosafety estimation study, PTM data set and investigation may provide underlying mechanisms of biological responses to ENM exposure. For instance, Sund *et al.* [11] revealed that the reversible protein acetylation was a major cellular regulation event occurring in ENM-exposed cells. In the first step, the cytoplasmic proteome changes in human monocyte-derived macrophages after exposure to different types of TiO_2 NPs were analyzed with the methods of 2D-DIGE and mass spectrometry. It was found that both the rutile TiO_2 NPs with or without silica coating evoked similar proteome alterations. The identified proteins were linked to metabolic homeostasis, cytoskeleton remodeling, and oxidative stress. The abundances of chloride intracellular channel protein 1 and cathepsin D changed only after exposure to TiO_2 NPs. More importantly, bioinformatics analysis revealed that 70% of the proteins with changed intensities contained acetylation sites, which indicated a significant induction of cytoplasmic protein acetylation after TiO_2 NP exposure. Collectively, it is demonstrated that lysine acetylation of cytoplasmic proteins in macrophages is a major cell regulation mechanism after TiO_2 NP exposure [11].

12.6 Metabolomics Study for Nanosafety

Transcriptomics and proteomics are the methods to indicate possible derangements of physiology, while metabolomics analyzes the shift in metabolites that indicates actual change in physiologic chemistry.

Metabolomics toxicity studies have been performed both *in vivo* and *in vitro.* The principal technologies for metabolomics studies are NMR spectroscopy and MS. NMR examines the proton spectrum of a sample, which represents a robust and quantitative measurement. Advantages of NMR are that it is noninvasive, requires no metabolite extraction procedure, and allows a relatively easy structural identification of metabolites. For MS, signals are characterized by mass and retention times. With developments in MS, it is now possible to rapidly measure thousands of metabolites simultaneously from a minimal amount of sample. To confirm the identities of metabolites, the mass and retention time of metabolites or NMR spectra can be compared to a database with annotated metabolites. Innovations in instrumentation, bioinformatic tools, and software enable the comprehensive analysis without bias [8].

Metabolomics applications in nanosafety study have been initiated only recently, but they are highly promising. As combination with transcriptomics and proteomics, in many instances, the metabolites can be spatially localized within biological specimens with imaging mass spectrometry and thus could provide insight into toxicity pathways.

12.6.1 Metabolomics Technology

Metabolomics is the global analysis of all or a large number of small-molecule metabolite profiles in a cell, tissue, organ, or organism. There are three major approaches used in metabolomics studies: (i) targeted analysis, (ii) metabolite profiling, and (iii) metabolic fingerprinting.

12.6.1.1 Metabolite Target Analysis

Target analysis is used to qualitatively and quantitatively measure a limited number of known metabolites that are related to a specific metabolic reaction precisely. Extensive sample preparation and separation from other metabolites are required. Generally, chromatographic separation is used, followed by sensitive MS detection.

12.6.1.2 Metabolic Fingerprinting

Metabolic fingerprinting considers a total profile, or fingerprint with high-throughput, rapid, global analysis in a particular cell line or tissue. It is usually performed with spectroscopic techniques such as NMR, MS, Fourier-transform infrared spectroscopy (FT-IR), and Fourier-transform ion cyclotron resonance–mass spectroscopy (FTICR-MS) with no prior separation. Metabolic fingerprinting is very useful in biomarker discovery and diagnostics.

12.6.1.3 Metabolite Profiling

Metabolite profiling is generally to identify and quantify selected metabolites, which is related to a specific metabolic pathway(s). For metabolite profiling, sample preparation is needed to isolate the metabolites from matrix before MS

detection. Metabolite profiling is widely used to study drug candidates, drug metabolic products, and the effects of therapeutic treatments.

12.6.2 Analytical Approach

12.6.2.1 Sample Preparation

There are multiple factors that may influence the composition of the metabolome, including the sampling time and the methods of sampling and storage. Both invasive (e.g., blood) and noninvasive (e.g., urine) sampling can be performed. Because metabolic processes are very rapid (<1 s), so samples should be processed rapidly by freezing in liquid nitrogen after harvesting and subsequent storage at 80 °C.

12.6.2.2 Analytical Techniques

There are multiple techniques that are generally used for metabolomics. The most often used techniques include NMR and MS. The combined separation techniques with MS include gas chromatography–mass spectrometry (GC-MS), LC-MS, and capillary electrophoresis–mass spectrometry (CE-MS).

12.6.3 Explore ENM Biological Effects Utilizing Metabolomics

Zanin *et al.* [26] used metabolomics to verify that small amounts of nanomaterial, that is, cellulose carbon nanoparticles (CCN), caused some cellular damage in NG97 cells. For the metabolomic assay, 10 and 100 μg/ml of CCN were added in the cells and incubated for 6 h. Then, the cells were coated with matrix α-cyano-4-hydroxycinnamic acid (10 mg/ml in 1 : 1 acetonitrile/methanol). Spectra were acquired using a MALDI LTQ-XL instrument (Thermo Scientific, USA). Data were proposed using the software ImageQuest v.1.0.1 (Thermo Scientific, USA). The ions were identified with MassFrontier software v.6.0 (Thermo Scientific, California, USA) and compared with a database and literature. The metabolomic assay showed the metabolites of 2-hydroxy-eicosanoic acid, 9*Z*,21*Z*-octacosadienoic acid, octadecanoic acid, and docosapentaenoic acid, which associate with the glioblastoma disease [26].

TiO_2 NPs have been shown to lead to toxic effects on human and environment. However, the mechanisms are still unclear. By GC/TOFMS-based metabolomics approach, the changes of amino acid levels in L929 cells after TiO_2 NP exposure were analyzed [28]. Spectral profiles were subjected to multivariate statistics, including Principal Component Analysis (PCA) and Orthogonal Projections to Latent Structures–Discriminant Analysis (OPLS-DA). Using the software of MetaboAnalyst 2.0, it was found that seven metabolic pathways (impact value >0.10) were significantly perturbed and 12 distinct amino acids were identified from these pathways, including L-α-alanine, β-alanine, glycine, L-aspartate, L-methionine, L-cysteine, glutamate, L-pyroglutamate, L-asparagine, L-glutamine, S-adenosylmethionine, and L-lysine. These results indicate that the disturbance

of amino acid metabolism plays an important role in the TiO_2-NP-induced cytotoxicity. Combined with earlier findings, the metabolomics approaches successfully demonstrate that TiO_2 NP caused toxicity via triggering cellular oxidative stress, induction energy damage, and inhibition of DNA and RNA synthesis [28].

The toxicological effects of SWCNTs were investigated using metabonomic analysis after intratracheal instillation of SWCNTs in Wistar rat for 15 days [78]. ^{1}H NMR spectra of the rat blood plasma and liver tissue extracts were obtained. ^{1}H NMR spectra and pattern recognition analyses showed remarkable differences in the excretion of lactate, trimethylamine oxide, bilineurin, phosphocholine, amylaceum, and glycogen. The increase of lactate and decrease of alanine in plasma were observed, indicating that the amino acid metabolism was impaired. The rise of choline and phosphocholine together with the decrease of lipids and lipoproteins in plasma and liver tissue extract indicates a disruption of membrane fluidity caused by lipid peroxidation. Moreover, energy, amino acid, and fat metabolism appeared to be affected by SWCNT exposure [78].

Mn NPs with favorable imaging capacity have been developed to improve the biocompatible profile of the existing Mn-based MRI contrast agent Mn-DPDP; thus, the biological effects and potential toxicity need to be understood. Li *et al.* [29] measured ^{1}H NMR-based metabolic profiling, integrated with traditional biochemical analysis and histopathological examinations to investigate the absorption, distribution, metabolism, excretion, and toxicity of MnO NPs. Their data showed that the metabolic responses in biofluids (plasma and urine) and tissues (liver, spleen, kidney, lung, and brain) from rats could be divided into four classes: Mn biodistribution-dependent, time-dependent, dose-dependent, and complicated metabolic variations (Figure 12.8). The variations of these metabolites were involved in lipid, energy, amino acid, and other nutrient metabolism, which disclosed the metabolic fate and biological effects of MnO NPs in rats. Furthermore, the changes of metabolic profile indicated that the impairment of biological functions induced by MnO NP treatments were correlated with the size and the surface chemistry of NPs [29].

Other biological effects and potential toxicology of ENMs, including SiO_2, ZrO_2, and $BaSO_4$ NPs [27, 30] in different animal species (rats and earthworms) [79] have been studied. Overall, the previous results show that the use of metabolomic technology provides a promising tool to understand the biological/toxic behavior of ENMs in biological systems.

12.7 Summary and Outlook

The size, crystal structure, and nanosurface characteristics of ENMs are relevant to their biological/toxicological effects in biological systems. The interactions of ENMs with biomolecules, such as proteins, DNA, RNA, carbohydrates, or lipids, are complicated and may influence their final biodistribution, circulation,

excretion, and toxicity. In addition to traditional methods in biochemical and molecular biology studies, and optical spectroscopic techniques to perform nanostructural studies, the generically called *omics* technologies including genomics, transcriptomics, proteomics, and metabolomics help to reveal the interactions with biomolecule that control cell function, communication, and adaptation to environmental changes and provide the promise to deeply understand biological/toxicological pathways of ENM exposure.

Further, currently, the toxicological study of ENMs transforms from descriptive to predictive approach. To examine one property parameter of ENMs at the time, it is able to draw correlations between the physiochemical characteristics of ENMS with specific biological responses. The data of multiparametric analysis can then be collected in populated databases to develop predictive models on how ENMs behave in one particularly biological system and predict the stability and potential toxicity of ENMs in biological systems. Such study could guide the design of the next generation of nanoscale devices that will be able to navigate in the body without significant side effects.

References

1. Valdes, A.M., Glass, D., and Spector, T.D. (2013) Omics technologies and the study of human ageing. *Nat. Rev. Genet.*, **14** (9), 601–607.
2. Tomescu, O.A., Mattanovich, D., and Thallinger, G.G. (2014) Integrative omics analysis. A study based on Plasmodium falciparum mRNA and protein data. *BMC Syst. Biol.*, **8** (Suppl. 2), S4.
3. Blankenburg, M., Haberland, L., Elvers, H.D., Tannert, C., and Jandrig, B. (2009) High-throughput omics technologies: potential tools for the investigation of influences of EMF on biological systems. *Curr. Genomics*, **10** (2), 86–92.
4. Buriani, A., Garcia-Bermejo, M.L., Bosisio, E. *et al.* (2012) Omic techniques in systems biology approaches to traditional Chinese medicine research: present and future. *J. Ethnopharmacol.*, **140** (3), 535–544.
5. Gioria, S., Chassaigne, H., Carpi, D. *et al.* (2014) A proteomic approach to investigate AuNPs effects in Balb/3T3 cells. *Toxicol. Lett.*, **228** (2), 111–126.
6. Haniu, H., Matsuda, Y., Takeuchi, K. *et al.* (2010) Proteomics-based safety evaluation of multi-walled carbon nanotubes. *Toxicol. Appl. Pharmacol.*, **242** (3), 256–262.
7. Gooderham, N.J. and Koufaris, C. (2014) Using microRNA profiles to predict and evaluate hepatic carcinogenic potential. *Toxicol. Lett.*, **228** (2), 127–132.
8. Patti, G.J., Yanes, O., and Siuzdak, G. (2012) Innovation: metabolomics: the apogee of the omics trilogy. *Nat. Rev. Mol. Cell Biol.*, **13** (4), 263–269.
9. Jain, M., Nilsson, R., Sharma, S. *et al.* (2012) Metabolite profiling identifies a key role for glycine in rapid cancer cell proliferation. *Science*, **336** (6084), 1040–1044.
10. Cai, X., Ramalingam, R., Wong, H.S. *et al.* (2013) Characterization of carbon nanotube protein corona by using quantitative proteomics. *Nanomed. Nanotechnol. Biol. Med.*, **9** (5), 583–593.
11. Sund, J., Palomaki, J., Ahonen, N. *et al.* (2014) Phagocytosis of nano-sized titanium dioxide triggers changes in protein acetylation. *J. Proteomics*, **108**, 469–483.
12. Higashisaka, K., Yoshioka, Y., Yamashita, K. *et al.* (2011) Acute phase proteins as biomarkers for predicting the exposure and toxicity of nanomaterials. *Biomaterials*, **32** (1), 3–9.
13. Sund, J., Alenius, H., Vippola, M. *et al.* (2011) Proteomic characterization of

engineered nanomaterial-protein interactions in relation to surface reactivity. *ACS Nano*, **5** (6), 4300–4309.
14. Ge, Y., Bruno, M., Wallace, K. *et al.* (2011) Proteome profiling reveals potential toxicity and detoxification pathways following exposure of BEAS-2B cells to engineered nanoparticle titanium dioxide. *Proteomics*, **11** (12), 2406–2422.
15. Shvedova, A.A., Pietroiusti, A., Fadeel, B. *et al.* (2012) Mechanisms of carbon nanotube-induced toxicity: focus on oxidative stress. *Toxicol. Appl. Pharmacol.*, **261** (2), 121–133.
16. Sabella, S., Maiorano, G., Rizzello, L. *et al*. (2012) Framing the nanobiointeractions by proteomics. Colloidal Nanocrystals for Biomedical Applications VII, 8232S.
17. Shannahan, J.H., Lai, X., Ke, P.C. *et al.* (2013) Silver nanoparticle protein corona composition in cell culture media. *PLoS One*, **8** (9), e74011.
18. Docter, D., Distler, U., Storck, W. *et al.* (2014) Quantitative profiling of the protein coronas that form around nanoparticles. *Nat. Protoc.*, **9** (9), 2030–2044.
19. Bergamaschi, E. (2012) Human biomonitoring of engineered nanoparticles: an appraisal of critical issues and potential biomarkers. *J. Nanomater.*, **2012**, 1–12, Article ID 564121.
20. Ma, J., Lue, X., and Huang, Y. (2011) Genomic analysis of cytotoxicity response to nanosilver in human dermal fibroblasts. *J. Biomed. Nanotechnol.*, **7** (2), 263–275.
21. Sos Poulsen, S., Jacobsen, N.R., Labib, S. *et al.* (2013) Transcriptomic analysis reveals novel mechanistic insight into murine biological responses to multiwalled carbon nanotubes in lungs and cultured lung epithelial cells. *PLoS One*, **8** (11), e80452.
22. Kim, H.G., Jo, S.-H., Yeon, S.-m. *et al.* (2013) Pluronic nanoparticles do not modulate immune responses mounted by macrophages. *Macromol. Res.*, **21** (12), 1355–1359.
23. Chatterjee, N., Eom, H.-J., and Choi, J. (2014) A systems toxicology approach to the surface functionality control of graphene-cell interactions. *Biomaterials*, **35** (4), 1109–1127.
24. Teeguarden, J.G., Mikheev, V.B., Minard, K.R. *et al.* (2014) Comparative iron oxide nanoparticle cellular dosimetry and response in mice by the inhalation and liquid cell culture exposure routes. *Part. Fibre Toxicol.*, **11** (46), 1–18.
25. Hancock, D.E., Indest, K.J., Gust, K.A. *et al.* (2012) Effects of C60 on the Salmonella typhimurium TA100 transcriptome expression: insights into C60-mediated growth inhibition and mutagenicity. *Environ. Toxicol. Chem.*, **31** (7), 1438–1444.
26. Zanin, H., Hollanda, L.M., Ceragioli, H.J. *et al.* (2014) Carbon nanoparticles for gene transfection in eukaryotic cell lines. *Mater. Sci. Eng. C Mater. Biol. Appl.*, **39**, 359–370.
27. Buesen, R., Landsiedel, R., Sauer, U.G. *et al.* (2014) Effects of SiO_2, ZrO_2, and $BaSO_4$ nanomaterials with or without surface functionalization upon 28-day oral exposure to rats. *Arch. Toxicol.*, **88** (10), 1881–1906.
28. Bo, Y., Jin, C., Liu, Y. *et al.* (2014) Metabolomic analysis on the toxicological effects of TiO_2 nanoparticles in mouse fibroblast cells: from the perspective of perturbations in amino acid metabolism. *Toxicol. Mech. Methods*, **24** (7), 461–469.
29. Li, J., Zhao, Z., Feng, J. *et al.* (2013) Understanding the metabolic fate and assessing the biosafety of MnO nanoparticles by metabonomic analysis. *Nanotechnology*, **24** (45), 455102.
30. Huang, S.M., Zuo, X., Li, J.J.E. *et al.* (2012) Metabolomics studies show dose-dependent toxicity induced by SiO_2 nanoparticles in MRC-5 human fetal lung fibroblasts. *Adv. Healthcare Mater.*, **1** (6), 779–784.
31. Pan, C., Kumar, C., Bohl, S. *et al.* (2009) Comparative proteomic phenotyping of cell lines and primary cells to assess preservation of cell type-specific functions. *Mol. Cell. Proteomics*, **8** (3), 443–450.
32. Pandey, U.B. and Nichols, C.D. (2011) Human disease models in *Drosophila melanogaster* and the role of the fly in

therapeutic drug discovery. *Pharmacol. Rev.*, **63** (2), 411–436.

33. Zhao, Y., Wu, Q., Li, Y. *et al.* (2014) In vivo translocation and toxicity of multi-walled carbon nanotubes are regulated by microRNAs. *Nanoscale*, **6** (8), 4275–4284.
34. Wu, Q., Zhao, Y., Zhao, G. *et al.* (2014) microRNAs control of in vivo toxicity from graphene oxide in *Caenorhabditis elegans*. *Nanomed. Nanotechnol. Biol. Med.*, **10** (7), 1401–1410.
35. Cromwell, W.A., Yang, J., Starr, J.L. *et al.* (2014) Nematicidal effects of silver nanoparticles on root-knot nematode in bermudagrass. *J. Nematol.*, **46** (3), 261–266.
36. Li, Y., Wu, Q., Zhao, Y. *et al.* (2014) Response of micrornas to in vitro treatment with graphene oxide. *ACS Nano*, **8** (3), 2100–2110.
37. Li, Y., Yu, S., Wu, Q. *et al.* (2013) Transmissions of serotonin, dopamine, and glutamate are required for the formation of neurotoxicity from Al_2O_3-NPs in nematode *Caenorhabditis elegans*. *Nanotoxicology*, **7** (5), 1004–1013.
38. Chen, P.H., Hsiao, K.M., and Chou, C.C. (2013) Molecular characterization of toxicity mechanism of single-walled carbon nanotubes. *Biomaterials*, **34** (22), 5661–5669.
39. Zhu, H., Zhang, J., Kim, M.T. *et al.* (2014) Big data in chemical toxicity research: the use of high-throughput screening assays to identify potential toxicants. *Chem. Res. Toxicol.*, **27** (10), 1643–1651.
40. Smyth, G.K. (2004) Linear models and empirical bayes methods for assessing differential expression in microarray experiments. *Stat. Appl. Genet. Mol. Biol.*, **3** (1), 1–26.
41. Cui, D., Tian, F., Ozkan, C.S. *et al.* (2005) Effect of single wall carbon nanotubes on human HEK293 cells. *Toxicol. Lett.*, **155** (1), 73–85.
42. Waters, K.M., Masiello, L.M., Zangar, R.C. *et al.* (2009) Macrophage responses to silica nanoparticles are highly conserved across particle sizes. *Toxicol. Sci.*, **107** (2), 553–569.
43. Lan, J., Gou, N., Gao, C. *et al.* (2014) Comparative and mechanistic genotoxicity assessment of nanomaterials via a quantitative toxicogenomics approach across multiple species. *Environ. Sci. Technol.*, **48** (21), 12937–12945.
44. Halder, T. (2013) Toxicogenomics – applications and future perspectives. *Int. J. Hum. Genet.*, **13** (1), 41–46.
45. http://en.wikipedia.org/wiki/Toxicogenomics (accessed 22 April 2016).
46. Walczyk, D., Bombelli, F.B., Monopoli, M.P. *et al.* (2010) What the cell "sees" in bionanoscience. *J. Am. Chem. Soc.*, **132** (16), 5761–5768.
47. Tenzer, S., Docter, D., Rosfa, S. *et al.* (2011) Nanoparticle size is a critical physicochemical determinant of the human blood plasma corona: a comprehensive quantitative proteomic analysis. *ACS Nano*, **5** (9), 7155–7167.
48. Szabo, D.T. (2014) in *Biomarkers in Toxicology* (ed. R.C. Gupta), Academic Press, Boston, MA, pp. 1033–1038.
49. Plessy, C., Desbois, L., Fujii, T. *et al.* (2013) Population transcriptomics with single-cell resolution: a new field made possible by microfluidics: a technology for high throughput transcript counting and data-driven definition of cell types. *Bioessays*, **35** (2), 131–140.
50. Garber, M., Grabherr, M.G., Guttman, M. *et al.* (2011) Computational methods for transcriptome annotation and quantification using RNA-seq. *Nat. Methods*, **8**, 469–477.
51. Zeng, W. and Mortazavi, A. (2012) Technical considerations for functional sequencing assays. *Nat. Immunol.*, **13** (9), 802–807.
52. Khan, J.A., Mandal, T.K., Das, T.K. *et al.* (2011) Magnetite (Fe_3O_4) nanocrystals affect the expression of genes involved in the TGF-beta signalling pathway. *Mol. Biosyst.*, **7** (5), 1481–1486.
53. Pan, Y., Leifert, A., Ruau, D. *et al.* (2009) Gold nanoparticles of diameter 1.4 nm trigger necrosis by oxidative stress and mitochondrial damage. *Small*, **5** (18), 2067–2076.
54. Khan, J.A., Pillai, B., Das, T.K. *et al.* (2007) Molecular effects of uptake

of gold nanoparticles in HeLa cells. *ChemBioChem*, **8** (11), 1237–1240.
55. Tenzer, S., Docter, D., Kuharev, J. *et al.* (2013) Rapid formation of plasma protein corona critically affects nanoparticle pathophysiology. *Nat. Nanotechnol.*, **8** (10), 772–781.
56. Scanlan, L.D., Reed, R.B., Loguinov, A.V. *et al.* (2013) Silver nanowire exposure results in internalization and toxicity to *Daphnia magna*. *ACS Nano*, **7** (12), 10681–10694.
57. Ge, C., Du, J., Zhao, L. *et al.* (2011) Binding of blood proteins to carbon nanotubes reduces cytotoxicity. *Proc. Natl. Acad. Sci. U.S.A.*, **108** (41), 16968–16973.
58. Deng, Z.J., Liang, M., Monteiro, M. *et al.* (2011) Nanoparticle-induced unfolding of fibrinogen promotes Mac-1 receptor activation and inflammation. *Nat. Nanotechnol.*, **6** (1), 39–44.
59. Kapralov, A.A., Feng, W.H., Amoscato, A.A. *et al.* (2012) Adsorption of surfactant lipids by single-walled carbon nanotubes in mouse lung upon pharyngeal aspiration. *ACS Nano*, **6** (5), 4147–4156.
60. Monopoli, M.P., Walczyk, D., Campbell, A. *et al.* (2011) Physical-chemical aspects of protein corona: relevance to in vitro and in vivo biological impacts of nanoparticles. *J. Am. Chem. Soc.*, **133** (8), 2525–2534.
61. Deng, Z.J., Mortimer, G., Schiller, T. *et al.* (2009) Differential plasma protein binding to metal oxide nanoparticles. *Nanotechnology*, **20** (45), 45510.
62. Graves, P.R. and Haystead, T.A.J. (2002) Molecular biologist's guide to proteomics. *Microbiol. Mol. Biol. Rev.*, **66** (1), 39–63.
63. Leung, Y.H., Ng, A.M.C., Xu, X. *et al.* (2014) Mechanisms of antibacterial activity of MgO: non-ROS mediated toxicity of MgO nanoparticles towards *Escherichia coli*. *Small*, **10** (6), 1171–1183.
64. Shevchenko, A., Tomas, H., Havlis, J. *et al.* (2007) In-gel digestion for mass spectrometric characterization of proteins and proteomes. *Nat. Protoc.*, **1** (6), 2856–2860.
65. Gomes, T., Chora, S., Pereira, C.G. *et al.* (2014) Proteomic response of mussels Mytilus galloprovincialis exposed to CuO NPs and Cu^{2+}: an exploratory biomarker discovery. *Aquat. Toxicol.*, **155**, 327–336.
66. Megger, D.A., Bracht, T., Meyer, H.E. *et al.* (2013) Label-free quantification in clinical proteomics. *Biochim. Biophys. Acta, Proteins Proteomics*, **1834** (8), 1581–1590.
67. Lilley, K.S. and Friedman, D.B. (2004) All about DIGE: quantification technology for differential-display 2D-gel proteomics. *Expert Rev. Proteomics*, **1** (4), 1–9.
68. Alban, A., David, S.O., Bjorkesten, L. *et al.* (2003) A novel experimental design for comparative two-dimensional gel analysis: two-dimensional difference gel electrophoresis incorporating a pooled internal standard. *Proteomics*, **3** (1), 36–44.
69. Ong, S.-E., Blagoev, B., Kratchmarova, I. *et al.* (2002) Stable isotope labeling by amino acids in cell culture, SILAC, as a simple and accurate approach to expression proteomics. *Mol. Cell Proteomics*, **1** (5), 376–386.
70. Ross, P.L., Huang, Y.N., Marchese, J.N. *et al.* (2004) Multiplexed protein quantitation in Saccharomyces cerevisiae using amine-reactive isobaric tagging reagents. *Mol. Cell Proteomics*, **3** (12), 1154–1169.
71. Gygi, S.P., Rist, B., Gerber, S.A. *et al.* (1999) Quantitative analysis of complex protein mixtures using isotope-coded affinity tags. *Nat. Biotechnol.*, **17** (10), 994–999.
72. Julka, S. and Regnier, F. (2004) Quantification in proteomics through stable isotope coding: a review. *J. Proteome Res.*, **3** (3), 350–363.
73. Zhang, H., Burnum, K.E., Luna, M.L. *et al.* (2011) Quantitative proteomics analysis of adsorbed plasma proteins classifies nanoparticles with different surface properties and size. *Proteomics*, **11** (23), 4569–4577.
74. Shannahan, J.H., Brown, J.M., Chen, R. *et al.* (2013) Comparison of nanotube-protein corona composition in cell culture media. *Small*, **9** (12), 2171–2181.

75. Asara, J.M., Christofk, H.R., Freimark, L.M. *et al.* (2008) A label-free quantification method by MS/MS TIC compared to SILAC and spectral counting in a proteomics screen. *Proteomics*, **8** (5), 994–999.

76. Malik, R., Dulla, K., Nigg, E.A. *et al.* (2010) From proteome lists to biological impact-tools and strategies for the analysis of large MS data sets. *Proteomics*, **10** (6), 1270–1283.

77. Capriotti, A., Caracciolo, G., Caruso, G. *et al.* (2013) Label-free quantitative analysis for studying the interactions between nanoparticles and plasma proteins. *Anal. Bioanal. Chem.*, **405** (2-3), 635–645.

78. Lin, B., Zhang, H., Lin, Z. *et al.* (2013) Studies of single-walled carbon nanotubes-induced hepatotoxicity by NMR-based metabonomics of rat blood plasma and liver extracts. *Nanoscale Res. Lett.*, **8** (1), 236.

79. Whitfield Aslund, M.L., McShane, H., Simpson, M.J. *et al.* (2012) Earthworm sublethal responses to titanium dioxide nanomaterial in soil detected by H NMR metabolomics. *Environ. Sci. Technol.*, **46** (2), 1111–1118.

13
Nanometallomics: New Approach on Analyzing Biological Effects of Metal-Related Nanomaterials[1)]

Yu-Feng Li, Jiating Zhao, Yuxi Gao, and Chunying Chen

13.1
Introduction

Metal-based and metal-containing nanomaterials are called *metal-related nanomaterials* in this chapter, which are frequently used as catalysts, sensors, or probes [1]. The metal-based nanomaterials include metal, metal crystals, metal nanoclusters, metal oxide, and other metal multi-component core/shell nanomaterials, intermetallic or alloyed nanomaterials, metal fluorescent nanoclusters, and metal nanoparticles-based hybrid nanomaterials. Quantum dots (QDs), which are semiconductor nanomaterials, with their cores consisting of a variety of metal complexes such as semiconductors, noble metals, and magnetic transition metals, can also be regarded as metal-based nanomaterials. Metallofullerenes (fullerenes encapsulated with metal atom(s)) are novel forms of fullerene-based materials having attractive applications in biomedicines [2], which can be regarded as metal-containing nanomaterials. Metal-decorated multi-wall carbon nanotubes (MWCNTs) [3] and metal-filled single-walled carbon nanotubes (SWCNTs) [4] can also be regarded as metal-containing nanomaterials.

Safety concerns on the potential risk of nanomaterials in biological systems are rising since nanomaterials are more and more widely used in different fields [5]. For example, it was found that nanoparticles can escape alveolar macrophage surveillance and enter the pulmonary interstitium with greater inflammatory effect than larger particles [6]. Animal studies showed that nanoparticles can move fast from pulmonary and gastrointestinal epithelium into the systemic circulation [7]. A new research field named as nanotoxicology was formed in recent years, which focuses on the study of the toxicological effects of nanomaterials [8].

In recent decades, great attention was paid to -omics studies, like genomics, proteomics, and metabolomics, aiming at the global characterization and quantification of pools of biological molecules that translate into the structure, function,

1) This chapter has been modified to feature as a review: Y.-F. Li, Y. Gao, Z. Chai, C. Chen, *Metallomics*, 2014, 6, 220-232.

Toxicology of Nanomaterials, First Edition. Edited by Yuliang Zhao, Zhiyong Zhang, and Weiyue Feng.

and dynamics of an organism [9]. Similarly, metallomics, the global understanding of the uptake, trafficking, role, and excretion of metal ions in biological systems, is attracting more attention [10]. It provides the systematic study of metallomes and the interactions and functional connections of metal ions and their species with genes, proteins, metabolites, and other biomolecules within organisms and ecosystems [11]. A series of meetings on metallomics have been held since 2007 and the journal named "metallomics" has been launched since 2009 [12]. Recently, the terminology "nanometallomics" was initiated as a branch of metallomics, and the application of advanced nuclear analytical techniques on the study of biological effects of metal-related nanomaterials was summarized [13]. Besides, a session for nanometallomics was organized at the fourth international symposium on metallomics in Spain in July 2013 [14]. The goals of nanometallomics include studies on (i) the quantification of metal-related nanomaterials in biological systems; (ii) distribution of studied metal-related nanomaterials in biological systems; (iii) the structural analysis of the metal-related nanomaterials in biological systems; (iv) the elucidation of reactions and related mechanisms of metal-related nanomaterials in biological systems; (v) metabolism of metal-related nanomaterials in biological systems; and (vi) the specific nano-scaled metal(loid)-assisted function biosciences in medicine, environment science, food science, agriculture, toxicology, biochemistry, and so on [13].

Different analytical techniques can be used to reach these goals. In this chapter, we will show the nanometallomics studies on absorption, distribution, metabolism, and excretion (ADME) behavior and their interactions with genes, proteins, and other biomolecules of metal-related nanomaterials in the biological system. Although a lot of related works have been published recently, only selective and representative works are cited here.

13.2 Integrated Approaches on the ADME of Metal-Related Nanomaterials in Biological Systems

Animals are exposed to metal-related nanomaterials through ingestion, inhalation, and dermal absorption. Integrated analytical approaches can be applied for the study of ADME of nanomaterials *in vivo* [15].

13.2.1 Studies on the Absorption and Excretion of Metal-Related Nanomaterials

Neutron activation analysis (NAA) can simultaneously measure more than 30 elements in a sample with detection limits of NAA ranging from 10^{-6} to 10^{-13} g/g [16]. One advantage of NAA is that it is nearly free of any matrix interference effects since the vast majority of samples are completely transparent to the neutron and the γ-rays. Besides, there is little, if any, opportunity for reagent or laboratory

contamination since NAA can most often be applied with no need for sample digestion or dissolution [17].

Sadauskas *et al.* [18] studied the fate of Au NPs (2, 40, and 100 nm) in female mice after intratracheal instillation using NAA. Results indicate that only a tiny fraction of the Au NPs was translocated into systemic circulation and the translocation of smaller particles is greater than that of the larger ones.

Inductively coupled plasma mass spectrometry (ICP-MS) can quantify elements rapidly and simultaneously in one run, which is extremely sensitive, due to the efficient ionization from plasma coupled with the sensitive detection of the mass spectrometer. At its best, the detection limits can be as low as parts per trillion. ICP-MS can detect most elements in biological systems, but sulfur, phosphorous, and halogens are not efficiently ionized by the inductively coupled plasma (ICP) owing to their high ionization energies. Meng *et al.* [19] studied the Cu content in mice after oral gavage of Cu NPs at the dose of 70 mg/kg body weight using ICP-MS. It was found that massive Cu enriches in renal tissue at 24 h. The Cu content in renal tissue decreases from 12.6 ± 2.2 to 6.5 ± 1.3 μg/g in Cu^{2+} group at 72 h, but high Cu content level maintains in kidney (11.5 ± 2.5 μg/g) in the Cu NP group. It implies that the rate of elimination of Cu NPs is very low in kidney.

The absorption and excretion behavior were different when exposed through inhalation. Kreyling *et al.* [20] studied the absorption and excretion of ^{192}Ir NPs (15 and 80 nm) after inhalation in young adult rats using radiotracer technique. Nanoparticles were predominantly cleared via airways into the gastrointestinal tract and feces during week 1 after inhalation. Additionally, less than 1% of the deposited particles were translocated into secondary organs such as liver, spleen, heart, and brain after systemic uptake from the lungs. The translocated fraction of the 80 nm particles was about an order of magnitude less than that of 15 nm particles.

The coating of nanomaterials could also influence their absorption and excretion behavior. Fischer *et al.* [21] found that QDs coated with mercaptoundecanoic acid and crosslinked with lysine were cleared from plasma with a clearance rate of 0.59 ± 0.16 ml/min/ kg. A higher clearance (1.23 ± 0.22 ml/min/kg) exists when the QDs are conjugated to bovine serum albumin ($p < 0.05$). QDs are not detected in feces or urine for up to 10 days after intravenous injection.

In general, vertebrate organisms tend to recognize nanoparticles as foreign objects, with elimination of the materials through the primary excretory organs/systems. It was found that the particles with sizes over 100 nm will be caught by the reticuloendothelial systems (RESs) while particles with sizes below 5 nm can be removed by the kidneys [22].

13.2.2
Studies on the Distribution of Metal-Related Nanomaterials in Biological Systems

Whole body quantification of exposed nanoparticles was generally achieved after sacrificing the animals. Liu *et al.* [23] evaluated the distribution of intranasal-instilled Cu NPs (23.5 nm) in mice using ICP-MS. After instillation of the particles

for 1 week, the Cu levels were significantly higher in liver, kidneys, olfactory bulb, and blood in high-dose group than the control, which is in agreement with the damages in liver, kidneys, and olfactory bulb seen in pathological examinations. Therefore, the nasal-inhaled Cu NPs at very high dosage can translocate to other organs and tissues and induce certain lesions.

The biodistribution of 20 and 120 nm ZnO at doses of 1, 2, 3, 4, 5 g/kg body weight on healthy adult mice after oral intake was studied by Wang *et al.* [24]. Significant increases of Zn concentrations were found in the kidney, pancreas, and bone ($p < 0.05$), and slight increases in the liver and heart in the 5 g/kg 20 nm ZnO–treated mice compared with the control. In contrast to the 120 nm ZnO–treated mice, the Zn contents in the liver, kidney, and pancreas of the 20 nm ZnO group mice showed a little bit higher, suggesting more Zn may excrete from the 20 nm ZnO–administrated mice than 120 nm ZnO mice. Bone was found to accumulate the highest Zn content, and the 120 nm ZnO mice retained significantly higher Zn in bone than the 20 nm ZnO mice. Therefore, the liver, spleen, heart, pancreas, and bone are the target organs for 20 and 120 nm ZnO after oral exposure. Studies on the distribution of many other metal-related nanomaterials like gold and silver NPs were also conducted, and liver and spleen were identified as target organs [25].

Noninvasive study of the biodistribution of nanomaterials was also achieved using specific tools. For example, the whole body distribution of Ag NPs labeled with ^{125}I after intravenous injection in Balb/c mice was studied using a computed tomography coregistered with single-photon emission computerized tomography (SPECT). It was found that predominant accumulation of the Ag NPs was in the spleen (41.5% ID/g) and liver (24.5% ID/g) at 24 h [26]. *In vivo* positron emission tomography (PET) imaging found that $^{64}Cu^{2+}$-labeled QDs (15.1 ± 7.6 nm) in mice was excreted via renal filtration shortly post-injection and accumulated in the liver [27].

Radioactive isotopic tracing techniques were used to study the biodistribution of $^{59}Fe_2O_3$ NPs. It was found that the $^{59}Fe_2O_3$ NPs could pass through the alveolar-capillary barrier into systemic circulation within 10 min after intratracheal instillation into the male SD rats [28]. The highest extrapulmonary ^{59}Fe levels were found in the liver, followed by spleen, heart, kidney, pancreas, testicle, and brain. The ^{59}Fe in the liver and heart showed time-response of accumulation from post-instilled day 1–21, and then decreased at day 50. These results indicate that $^{59}Fe_2O_3$ can easily pass through a number of tissue compartments and accumulate in the extrapulmonary organs.

All these studies indicate extensive wide distribution of metal-related nanomaterials in the RES, which deserves further investigation of the interaction of nanoparticles with hepatic and splenic tissues at the cellular level. This is critical for evaluation of the *in vivo* effects and potential toxicity of metal-related nanomaterials.

Dedicated tools are necessary to study the distribution of metal-related nanomaterials in a specific animal's organs or tissues, or in small-size animal models, even in cells. The accumulation of TiO_2 NPs (80 nm, rutile and 155 nm,

anatase; purity >99%) in murine brain was studied using synchrotron radiation X-ray fluorescence (SRXRF) after intranasally instilled with 500 μg of TiO_2 NPs suspension every other day for 30 days [29]. Titanium was found to accumulate mainly in the cerebral cortex, thalamus, and hippocampus, especially in the CA1 and CA3 regions of hippocampus at 30 days. The significantly increased Ti contents in the hippocampus lead to the obviously irregular arrangement and loss of neurons in the hippocampus. Intranasal instillation of either rutile or anatase TiO_2 NPs produced sustained accumulation in brain tissues, especially in the hippocampus, suggesting that the TiO_2 NPs can enter the brain via the olfactory bulb [29, 30].

SRXRF mapping was also applied to study the distribution of Cu nanoparticles in the whole body of *Caenorhabditis elegans* [31]. It was found that the exposure to Cu nanoparticles can lead to an obvious elevation of Cu and K levels, and a change of bio-distribution of Cu in nematodes. Cu accumulates in the head and at a location 1/3 of the way up the body from the tail compared to the control. A higher amount of Cu was detected in its excretory cells and intestine when exposed to Cu^{2+}. The nondestructive and multi-elemental SRXRF provides an important tool for mapping the elemental distribution in the whole body of a single tiny nematode at low levels.

The distribution of metal-related nanomaterials in cells can be studied by SRXRF with the nano-sized spatial resolution (nano-XRF (nano-X-ray fluorescence)). For example, Corezzi *et al.* [32] studied the distribution of a commercially available QD-secondary antibody conjugate in SKOV3 cancer cells. The intracellular distribution of S, Zn, Cd, and Se in the core shell of QDs was performed through pixel-by-pixel analysis of the elements. It was found that Zn and S were located mainly in the nuclear region, although a clear signal could also be detected in the cytoplasm. The relatively high concentration of these elements and their presence in both the test and control samples suggest that the main contribution to the detected signal comes from the elements naturally present in the cell. The Se signal is clearly detected only in the cytoplasm of the labeled sample and is not present in either the cytoplasm or the nucleus of the control sample while the Cd signal is almost undetectable.

The SRXRF technique has also been applied to study the distribution of carbon nanotubes (CNTs) in cells. Bussy and coworkers [33] investigated the distribution of unpurified and purified SWCNTs and MWCNTs in macrophages by monitoring the catalyst metals used in most synthesis technique of nanotubes. The SRXRF technique monitors the localization of CNTs at the single-cell level with simultaneous analysis of the biological response by observing the changes in cell elemental composition.

One of the limitations of synchrotron radiation-based bioimaging tools like SRXRF is the lack of sufficient beam time. Commercially available laser ablation inductively coupled plasma mass spectrometry (LA-ICP-MS) is a convenient alternative. LA-ICP-MS provides easy sample preparation, multielemental detection with high sensitivity, and high spatial resolution. The distribution of Au and Ag NPs in individual fibroblast cells was studied using LA-ICP-MS. Nanoparticles

were visualized with respect to cellular substructures and were found to accumulate in the perinuclear region with increasing incubation time [34].

13.2.3 Metabolism of Metal-Related Nanomaterials in Biological Systems

After entering the body, metal-related nanomaterials may be dissolved, decomposed, oxidized, or reduced, and this may lead to the electronic and/or ionic transfer either within the nanoparticles lattice or on release to culture medium. The dissolved, decomposed, oxidized, or reduced metal-related nanomaterials may behave like the metal ions in the body, while the remaining unchanged nanoparticles may still show their surface effect and quantum size effect.

Nanomaterials may dissolve in physiologically relevant media to form partially soluble metal ions or metal–ligand complex. Franklin *et al.* [35] compared the dissolution of both nano- and bulk ZnO in a freshwater system and found rapid dissolution of ZnO NPs with a saturation solubility in the milligram per liter range, similar to that of bulk ZnO. Further toxicity test confirmed that comparable toxicity to *Pseudokirchneriella subcapitata* for nanoparticulate ZnO, bulk ZnO, and $ZnCl_2$, suggesting that the toxicity aroused solely from the dissolved zinc. Further, an enhanced dissolution of iron oxide NPs in the acidic condition of lysosomes or in a microenvironment containing ligands with a strong affinity was also observed [36].

The toxicity of nanomaterials may occur due to their decomposition. Derfus *et al.* [37] observed the release of free Cd^{2+} from CdSe QDs and found that the cytotoxicity of CdSe QDs correlated with the free Cd^{2+} concentration in air-oxidized and UV-exposed samples. Besides, Qu *et al.* [38] found that CdSe@ZnS core/shell QDs were degraded in *C. elagans* and Se^{2-} in the CdSe core was oxidized to Se^{4+}. Both results confirmed that QDs could be decomposed in the body and lead to the nanotoxicity of QDs.

X-ray Absorption Spectroscopy (XAS) is a powerful tool to investigate the electronic and/or ionic transfers of metal-related nanomaterials in biological systems and can provide structural details of the metabolites. XAS was used to study the metabolism of gold nanorods in SD rat. It was found that long-term retention of gold nanorods in liver and spleen did not induce changes in the oxidation states of gold, suggesting gold nanorods are inert in the body [15]. For other elements, however, changed oxidation state was found in the body. For example, the metabolism of three Fe-based NPs in *Escherichia coli* was studied by Auffan *et al.* [39]. According to Fe K edge XAS spectra, three compounds, including γ-Fe_2O_3, Fe_3O_4, and γ-FeOOH, had different pre-edge intensity, position of pre-edge and absorption edge, and ramped absorption position. It was showed that Fe^{II} in Fe_3O_4 could be oxidated to Fe^{III} in contact with *E. coli* through the pre-edge. The Fe^0 atoms in zero-valent iron were highly active to oxygen atoms under the same condition and transformed into γ-FeOOH and Fe_3O_4 through XRD and XAS analysis. The process of Fe^0 and Fe^{II} oxidation resulted in ionic or electronic transfers on nanoparticle surface that might intervene with the metabolism of bacteria when

cell membrane and component contacted with them. Therefore, it was concluded that the toxicity of Fe-based NPs containing ferrous and zero-valent iron resulted from the generation of ROS or interference on electron/ion transport chains. This work showed that the toxicity of metal-related nanomaterials may be affected by their surface properties through ROS generation. Consequently, appropriate surface modification need to be considered in order to be more biocompatible and healthy.

The nanomaterials may induce other metabolic changes even if they are inert. The Au NRs-induced time-dependent metabolic changes in A549 and 16HBE cells were studied by ^{1}H NMR spectroscopy [40]. The dominant metabolites present in the cell extracts include a range of amino acids, organic acids (such as lactate, creatine, and citrate), membrane metabolites (including choline, phosphocholine, and glycerophosphocholine), and a number of nucleosides and nucleotides (such as inosine, adenosine, uracil, inosine-5′-monophosphate, and nicotinamide adenine dinucleotide). A significant reduction in the levels of lactate in both 16HBE and A549 cells suggests that protein-coated Au NRs exposure inhibits the intracellular anaerobic glycolysis process.

13.3 Interactions of Metal-Related Nanomaterials with Genes, Proteins, and Other Biomolecules

The metal-related nanomaterials and their metabolites can interact with genes, proteins, and other biomolecules in biological systems, and this may cause various biological effects. X-ray crystallography and solution structure determination by multi-dimensional nuclear magnetic resonance (NMR) can be applied for the study on the interactions of nanomaterials with genes, proteins, and other biomolecules. Other techniques include Mössbauer spectroscopy, XAS, electron paramagnetic resonance (EPR), and neutron scattering.

Nanomaterials are engineered to have various unique properties, which will affect their possible direct or indirect interactions with the DNA. The genotoxicity of TiO_2 and ZnO NPs in vitro (Ames' Salmonella gene mutation test and V79 micronucleus chromosome mutation test) or *in vivo* (mouse bone marrow micronucleus test and Comet DNA damage assay in lung cells from rats exposed by inhalation) were not observed [41]. However, it was found that Ag NPs in *Allium cepa* could penetrate plant system and impair stages of cell division causing chromatin bridge, stickiness, disturbed metaphase, multiple chromosomal breaks, and cell disintegration [42]. For most nanomaterials it is still less known whether they can directly interact with DNA or whether they can bring indirect effects such as inflammation-mediated oxidative stress, and this may infer a threshold for the genotoxicity of some nanomaterials [43].

QDs have been used as fluorescent markers in biological applications. However, it is essential to make sure that QDs themselves do not induce adverse effects when they are used in *in vivo* studies or DNA-based assays. Green and Howman [44]

observed the DNA damage occurred in plasmid nicking assays with water-soluble CdSe QDs by comparing the electrophoresis bands. Assays with DNA that had been incubated with QDs and exposed to UV light showed damage. Samples of DNA incubated with QDs in the dark also showed a damaged band not observed in assays using DNA stored alone in the dark. Up to 70% of the DNA coordinated to the dots non-specifically and was therefore unavailable for assay analysis. These results show that serious issues may exist concerning the use of such materials in DNA-based assays or in *in vivo* applications. This also highlights potential toxicological and environmental implications.

The interaction of DNA with nanomaterials is promising in medical applications. Hydroxylated C_{60} is a polyacid-like molecule, and each proton of the hydroxyl groups (C–OH) can dissociate in an aqueous solution, thus yielding a conjugated base C–O–. Fullerenols can encapsulate some Env plasmid DNA during the self-assembly by which the nanoadjuvant realizes dual functions as plasmid DNA carrier and activator of host immunity [45]. It was found that poly(diallyldimethylammonium chloride)- or polyethyleneimine-modified Au NRs could significantly promote cellular and humoral immunity as well as T cell proliferation by activating antigen-presenting cells if compared to naked HIV-1 Env plasmid DNA treatment *in vivo* [46]. Artificially synthesized CpG oligodeoxynucleotides (CpG ODNs) can imitate bacterial DNA and effectively stimulate the mammalian immune system [47]. Self-assembled polyvalent CpG-AuNP conjugates enhance the efficiency of cellular uptake and stimulate secretion of cytokines [48]. These findings have shed light on the intentional design of the interaction of low-toxic nanomaterials with biomolecules, which can be used as a versatile platform for drug and gene delivery systems and biomedical applications.

Studies find that nanoparticles can stimulate or suppress the immune responses. The study about the effect of $Gd@C_{82}(OH)_{22}$ nanoparticles on the release of Th1/Th2 cytokines found markedly enhanced immune responses and stimulated immune cells to release more cytokines, helping eliminate abnormal cells [49]. Exosomes are extracellularly secreted membrane vesicles for the dissemination and intercellular communication of natural nano-sized particles (like viruses). Maturation of dendritic cells and activation of splenic T cells were significantly induced by these exosomes when exposed to magnetic iron oxide NPs. Furthermore, the T-cell activation was more efficient toward sensitized T cells and in ovalbumin (OVA)-sensitized mice through exosome induction than in the unsensitized counterparts. The studies suggest that exosomes may act as conveyors for extrapulmonary signal transduction in nanoparticle-induced immune systemic responses [36].

Nanomaterials are foreign to the host; therefore, the penetration of nanomaterials into the organism by crossing the barriers like skin, lungs, gastrointestinal track, which are all patrolled and controlled by the immune system, will trigger the formation of a series of proteolytic enzymes and may cause the immunotoxicity [50]. For example, the viability study of dendritic cells incubating in Au NPs showed that these NPs were not cytotoxic even at high concentrations.

However, large amounts of Au NPs amassing in endocytic compartments were observed. Besides, the secretion of cytokines was significantly modified after such internalization. These results suggest that a potential perturbation of the immune response may occur [51].

When NPs enter a physiological environment, it can rapidly adsorb a layer of proteins to form the protein "corona" [52]. It was found that size, shape, and surface characteristics of NPs could affect protein adsorption and also the structure of the adsorbed proteins. This will affect the reactivity of NPs with cells and determine the route and efficiency of NP uptake. For example, NPs could accelerate the fibrillation of proteins and peptides, a process that is associated with several diseases like Alzheimer's disease [53]. The adsorbed proteins may also promote translocation of the NP across cellular barriers, and clearance or accumulation in vital organs. Useful insights into cytotoxic, inflammatory potential, and other key properties of these novel materials could be provided by understanding the dynamics of this complex interaction. This can be explored for developing safer and value-added nanomaterials for future applications. On the other hand, it was found that proteins in the corona were conserved and unique irrespective of the nanoparticle types. Moreover, both size and surface properties of nanomaterials played a very significant role in determining the nanoparticles' coronas on different nanoparticles composed of identical materials [54]. The protein "corona" may alter the size and interfacial composition of nanomaterials, thus inducing changes between their biological identity and their synthetic identity. For example, the melting point of Ag NPs with the adsorption of proteins was modified in a composition-and size-dependent manner [55]. Thorough understanding of NP–protein interactions might lead to strategic manipulation of NP surfaces to adsorb specific functional proteins or small drug molecules intended for delivery *in vivo*. Furthermore, this might be useful in predicting nanotoxicity-related safety concerns.

The study of the interactions of NPs with the biological process of cancer cells may help in designing drugs for cancer therapy. For example, metallofullerene NPs, formulated as $[Gd@C_{82}(OH)_{22}]_n$, was found to be able to penetrate plasma membrane of tumor cells and lead to the shrinkage of solid tumors. This decreases the activities of those enzymes responsible for catalyzing the production of reactive oxygen species *in vivo* [56]. Furthermore, pretreatment of the cisplatin-resistant human prostate cancer (CP-r) cells with $[Gd@C_{82}(OH)_{22}]_n$ was found to enhance the intracellular accumulation of cisplatin and formation of cisplatin-DNA adducts. This restored the defective endocytosis of the CP-r cancer cells. The results proved that $[Gd@C_{82}(OH)_{22}]_n$ could overcome tumor resistance to cisplatin by increasing its intracellular accumulation through the restoring defective endocytosis [57]. More importantly, it was found that $[Gd@C_{82}(OH)_{22}]_n$ could inhibit the metastasis of pancreatic tumor through the inhibition of matrix metalloproteinases (MMP-9) activity via an exocite interaction by interfering binding of the incoming ligands as remotely modulating the S1′ loop [58]. Through molecular-dynamics simulations, detailed inhibition dynamics, and molecular mechanism behind the $[Gd@C_{82}(OH)_{22}]_n$–MMP-9

interaction provided insights for de novo design of nanomedicine for fatal diseases such as pancreatic cancer.

13.4 Conclusions

Nanometallomics is the global study of the biological effects of metal-related nanomaterials. This includes the systematic study of the ADME of metal-related materials in biological systems. It also involves the study of the interactions and functional connections of metal-related nanomaterials with genes, proteins, metabolites, and other biomolecules within the organisms.

The ADME of metal-related nanomaterials in the biological systems are influenced by their physicochemical properties, the exposure route, and the bioenvironment of the deposition site. Nanomaterials may not only interact directly or indirectly with genes, proteins, and other molecules to bring genotoxicity, immunotoxicity, DNA damage, and cytotoxicity, but also may stimulate the immune responses, circumvent tumor resistance, and inhibit tumor metastasis.

Dedicated analytical tools are necessary to study the biological effects of metal-related nanomaterials [13, 59]. NAA, ICP-MS, XRF, and isotopic tracing are multielemental quantification techniques to study the ADME of metal-related nanomaterials. Since nanometallomics is such a young research field, publications on risk evaluation and biological behavior of these metal-related nanomaterials are sometimes contradictory. Therefore, standardized procedure for studying nanometallomics should be developed.

Acknowledgments

Y.-F. Li gratefully acknowledges the support of K. C. Wong Education Foundation, Hong Kong and the CAS Youth Innovation Association, Chinese Academy of Sciences (2011017). C. Chen gratefully acknowledges the support of Natural Science Foundation of China (11425520). This work was supported by Natural Science Foundation of China (11205168, 31070854 and 21277037) and the Ministry of Science and Technology of China (2011CB933401, 2012CB934003 and 2010CB934004).

References

1. Buzea, C., Pacheco, I.I., and Robbie, K. (2007) Nanomaterials and nanoparticles: sources and toxicity. *Biointerphases*, **2**, MR17–MR71.
2. Wilson, L.J., Cagle, D.W., Thrash, T.P., Kennel, S.J., Mirzadeh, S., Alford, J.M., and Ehrhardt, G.J. (1999) Metallofullerene drug design. *Coord. Chem. Rev.*, **190-192**, 199–207.
3. Espinosa, E.H., Ionescu, R., Bittencourt, C., Felten, A., Erni, R., Van Tendeloo, G., Pireaux, J.J., and Llobet, E. (2007) Metal-decorated multi-wall carbon nanotubes

for low temperature gas sensing. *Thin Solid Films*, **515**, 8322–8327.
4. Bendall, J.S., Ilie, A., Welland, M.E., Sloan, J., and Green, M.L.H. (2006) Thermal stability and reactivity of metal halide filled single-walled carbon nanotubes. *J. Phys. Chem. B*, **110**, 6569–6573.
5. Zhao, Y., Xing, G., and Chai, Z. (2008) Nanotoxicology: Are carbon nanotubes safe? *Nat. Nanotechnol.*, **3**, 191–192.
6. Oberdörster, G. (2000) Pulmonary effects of inhaled ultrafine particles. *Int. Arch. Occup. Environ. Health*, **74**, 1–8.
7. Nemmar, A., Hoylaerts, M.F., Hoet, P.H.M., Dinsdale, D., Smith, T., Xu, H., Vermylen, J., and Nemery, B. (2002) Ultrafine particles affect experimental thrombosis in an *in vivo* hamster model. *Am. J. Respir. Crit. Care Med.*, **166**, 998–1004.
8. Zhao, Y. and Nalwa, H.S. (2006) *Nanotoxicology – Interactions of Nanomaterials with Biological Systems*, American Scientific Publishers, California.
9. Seemungal, D. and Newton, G. (2001) in *Encyclopedia of Genetics* (eds B. Sydney and H.M. Jeffrey), Academic Press, New York, pp. 980–981.
10. Mounicou, S., Szpunar, J., and Lobinski, R. (2009) Metallomics: the concept and methodology. *Chem. Soc. Rev.*, **38**, 1119–1138.
11. Ge, R. and Sun, H. (2009) Metallomics: an integrated biometal science. *Sci. China, Ser. B Chem.*, **52**, 2055–2070.
12. http://pubs.rsc.org/en/journals/journalissues/mt#!recentarticles&all (accessed 23 April 2016).
13. Li, Y.-F., Wang, L., Zhang, L., and Chen, C. (2010) in *Nuclear Analytical Techniques for Metallomics and Metalloproteomics* (eds C. Chen, Z. Chai, and Y. Gao), RSC Publishing, Cambridge P342–P385.
14. http://blogs.rsc.org/mt/2012/11/14/metallomics-2013-8-11-july-oviedo-spain/.
15. Wang, L., Li, Y.-F., Zhou, L., Liu, Y., Meng, L., Zhang, K., Wu, X., Zhang, L., Li, B., and Chen, C. (2010) Characterization of gold nanorods *in vivo* by integrated analytical techniques: their uptake, retention, and chemical forms. *Anal. Bioanal. Chem.*, **396**, 1105–1114.
16. Chai, Z., Sun, J., and Ma, S. (1992) *Neutron Activation Analysis in Environmental Sciences, Biological and Geological Sciences*, Atomic Energy Press, Beijing.
17. Chai, Z. and Zhu, H. (eds) (1994) *Introduction to Trace Element Chemistry*, Atomic Energy Press, Beijing.
18. Sadauskas, E., Jacobsen, N.R., Danscher, G., Stoltenberg, M., Vogel, U., Larsen, A., Kreyling, W., and Wallin, H. (2009) Biodistribution of gold nanoparticles in mouse lung following intratracheal instillation. *Chem. Cent. J.*, **3**, 16.
19. Meng, H., Chen, Z., Xing, G., Yuan, H., Chen, C., Zhao, F., Zhang, C., and Zhao, Y. (2007) Ultrahigh reactivity provokes nanotoxicity: explanation of oral toxicity of nano-copper particles. *Toxicol. Lett.*, **175**, 102–110.
20. Kreyling, W.G., Semmler, M., Erbe, F., Mayer, P., Takenaka, S., Schulz, H., Oberdorster, G., and Ziesenis, A. (2002) Translocation of ultrafine insoluble iridium particles from lung epithelium to extrapulmonary organs is size dependent but very low. *J. Toxicol. Environ. Health A*, **65**, 1513–1530.
21. Fischer, H.C., Liu, L., Pang, K.S., and Chan, W.C.W. (2006) Pharmacokinetics of nanoscale quantum dots: *in vivo* distribution, sequestration, and clearance in the rat. *Adv. Funct. Mater.*, **16**, 1299–1305.
22. Li, Y.-F. and Chen, C. (2011) Fate and toxicity of metallic and metal-containing nanoparticles for biomedical applications. *Small*, **7**, 2965–2980.
23. Liu, Y., Gao, Y., Zhang, L., Wang, T., Wang, J., Jiao, F., Li, W., Liu, Y., Li, Y., Li, B., Chai, Z., Wu, G., and Chen, C. (2009) potential health impact on mice after nasal instillation of nano-sized copper particles and their translocation in mice. *J. Nanosci. Nanotechnol.*, **9**, 1–9.
24. Wang, B., Feng, W., Wang, M., Wang, T., Gu, Y., Zhu, M., Ouyang, H., Shi, J., Zhang, F., Zhao, Y., Chai, Z., Wang, H., and Wang, J. (2008) Acute toxicological impact of nano- and submicro-scaled zinc oxide powder on healthy adult mice. *J. Nanopart. Res.*, **10**, 263–276.

25. Lankveld, D.P.K., Oomen, A.G., Krystek, P., Neigh, A., Troost – de Jong, A., Noorlander, C.W., Van Eijkeren, J.C.H., Geertsma, R.E., and De Jong, W.H. (2010) The kinetics of the tissue distribution of silver nanoparticles of different sizes. *Biomaterials*, **31**, 8350–8361.
26. Chrastina, A. and Schnitzer, J.E. (2010) Iodine-125 radiolabeling of silver nanoparticles for *in vivo* SPECT imaging. *Int. J. Nanomed.*, **5**, 653–659.
27. Tu, C., Ma, X., House, A., Kauzlarich, S.M., and Louie, A.Y. (2011) PET imaging and biodistribution of silicon quantum dots in mice. *ACS Med. Chem. Lett.*, **2**, 285–288.
28. Zhu, M.-T., Feng, W.-Y., Wang, Y., Wang, B., Wang, M., Ouyang, H., Zhao, Y.-L., and Chai, Z.-F. (2009) Particokinetics and extrapulmonary translocation of intratracheally instilled ferric oxide nanoparticles in rats and the potential health risk assessment. *Toxicol. Sci.*, **107**, 342–351.
29. Wang, J., Chen, C., Liu, Y., Jiao, F., Li, W., Lao, F., Li, Y., Li, B., Ge, C., Zhou, G., Gao, Y., Zhao, Y., and Chai, Z. (2008) Potential neurological lesion after nasal instillation of TiO_2 nanoparticles in the anatase and rutile crystal phases. *Toxicol. Lett.*, **183**, 72–80.
30. Wang, J., Liu, Y., Jiao, F., Lao, F., Li, W., Gu, Y., Li, Y., Ge, C., Zhou, G., Li, B., Zhao, Y., Chai, Z., and Chen, C. (2008) Time-dependent translocation and potential impairment on central nervous system by intranasally instilled TiO_2 nanoparticles. *Toxicology*, **254**, 82–90.
31. Gao, Y., Liu, N., Chen, C., Luo, Y., Li, Y.-F., Zhang, Z., Zhao, Y., Zhao, Y., Iida, A., and Chai, Z. (2008) Mapping technique for biodistribution of elements in a model organism, *Caenorhabditis elegans*, after exposure to copper nanoparticles with microbeam synchrotron radiation X-ray fluorescence. *J. Anal. At. Spectrom.*, **23**, 1121–1124.
32. Corezzi, S., Urbanelli, L., Cloetens, P., Emiliani, C., Helfen, L., Bohic, S., Elisei, F., and Fioretto, D. (2009) Synchrotron-based X-ray fluorescence imaging of human cells labeled with CdSe quantum dots. *Anal. Biochem.*, **388**, 33–39.
33. Bussy, C., Cambedouzou, J., Lanone, S., Leccia, E., Heresanu, V., Pinault, M., Mayne-lhermite, M., Brun, N., Mory, C., Cotte, M., Doucet, J., Boczkowski, J., and Launois, P. (2008) Carbon nanotubes in macrophages: imaging and chemical analysis by X-ray fluorescence microscopy. *Nano Lett.*, **8**, 2659–2663.
34. Drescher, D., Giesen, C., Traub, H., Panne, U., Kneipp, J., and Jakubowski, N. (2012) Quantitative imaging of gold and silver nanoparticles in single eukaryotic cells by laser ablation ICP-MS. *Anal. Chem.*, **84**, 9684–9688.
35. Franklin, N.M., Rogers, N.J., Apte, S.C., Batley, G.E., Gadd, G.E., and Casey, P.S. (2007) Comparative toxicity of nanoparticulate ZnO, Bulk ZnO, and $ZnCl_2$ to a freshwater microalga (*Pseudokirchneriella subcapitata*): the importance of particle solubility. *Environ. Sci. Technol.*, **41**, 8484–8490.
36. Zhu, M., Li, Y., Shi, J., Feng, W., Nie, G., and Zhao, Y. (2012) Exosomes as extrapulmonary signaling conveyors for nanoparticle-induced systemic immune activation. *Small*, **8**, 404–412.
37. Derfus, A.M., Chan, W.C.W., and Bhatia, S.N. (2003) Probing the cytotoxicity of semiconductor quantum dots. *Nano Lett.*, **4**, 11–18.
38. Qu, Y., Li, W., Zhou, Y., Liu, X., Zhang, L., Wang, L., Li, Y.-f., Iida, A., Tang, Z., Zhao, Y., Chai, Z., and Chen, C. (2011) Full assessment of fate and physiological behavior of quantum dots utilizing *Caenorhabditis elegans* as a model organism. *Nano Lett.*, **11**, 3174–3183.
39. Auffan, M., Achouak, W., Rose, J., Roncato, M.-A., Chaneac, C., Waite, D.T., Masion, A., Woicik, J.C., Wiesner, M.R., and Bottero, J.-Y. (2008) Relation between the redox state of iron-based nanoparticles and their cytotoxicity toward *Escherichia coli*. *Environ. Sci. Technol.*, **42**, 6730–6735.
40. Zhang, L., Wang, L., Hu, Y., Liu, Z., Tian, Y., Wu, X., Zhao, Y., Tang, H., Chen, C., and Wang, Y. (2013) Selective metabolic effects of gold nanorods on normal and cancer cells and their application in anticancer drug screening. *Biomaterials*, **34**, 7117–7126.

41. Kumari, M., Mukherjee, A., and Chandrasekaran, N. (2009) Genotoxicity of silver nanoparticles in *Allium cepa*. *Sci. Total Environ.*, **407**, 5243–5246.
42. Ng, C.-T., Li, J.J., Bay, B.-H., and Yung, L.-Y.L. (2010) Current studies into the genotoxic effects of nanomaterials. *J. Nucl. Acids*, **2010**, 1–12.
43. Landsiedel, R., Kapp, M.D., Schulz, M., Wiench, K., and Oesch, F. (2009) Genotoxicity investigations on nanomaterials: methods, preparation and characterization of test material, potential artifacts and limitations—many questions, some answers. *Mutat. Res.*, **681**, 241–258.
44. Green, M. and Howman, E. (2005) Semiconductor quantum dots and free radical induced DNA nicking. *Chem. Commun.*, **122**, 121–123.
45. Xu, L., Liu, Y., Chen, Z., Li, W., Liu, Y., Wang, L., Ma, L., Shao, Y., Zhao, Y., and Chen, C. (2013) Morphologically virus-like fullerenol nanoparticles act as the dual-functional nanoadjuvant for HIV-1 vaccine. *Adv. Mater.*, **25**, 5928–5936.
46. Xu, L., Liu, Y., Chen, Z., Li, W., Liu, Y., Wang, L., Liu, Y., Wu, X., Ji, Y., Zhao, Y., Ma, L., Shao, Y., and Chen, C. (2012) Surface-engineered gold nanorods: promising DNA vaccine adjuvant for HIV-1 treatment. *Nano Lett.*, **12**, 2003–2012.
47. Wei, M., Chen, N., Li, J., Yin, M., Liang, L., He, Y., Song, H., Fan, C., and Huang, Q. (2012) Polyvalent immunostimulatory nanoagents with self-assembled CpG oligonucleotide-conjugated gold nanoparticles. *Angew. Chem. Int. Ed.*, **51**, 1202–1206.
48. Zhao, F., Zhao, Y., Liu, Y., Chang, X., Chen, C., and Zhao, Y. (2011) Cellular uptake, intracellular trafficking, and cytotoxicity of nanomaterials. *Small*, **7**, 1322–1337.
49. Liu, Y., Jiao, F., Qiu, Y., Li, W., Lao, F., Zhou, G., Zhao, Y., Sun, B., Xing, G., Dong, J., Chai, Z., and Chen, C. (2009) The effect of $Gd@C_{82}(OH)_{22}$ nanoparticles on the release of Th1/Th2 cytokines and induction of TNF-α mediated cellular immunity. *Biomaterials*, **30**, 3934–3945.
50. Dobrovolskaia, M.A. and McNeil, S.E. (2007) Immunological properties of engineered nanomaterials. *Nat. Nanotechnol.*, **2**, 469–478.
51. Villiers, C., Freitas, H., Couderc, R., Villiers, M.-B., and Marche, P. (2010) Analysis of the toxicity of gold nano particles on the immune system: effect on dendritic cell functions. *J. Nanopart. Res.*, **12**, 55–60.
52. Ge, C., Du, J., Zhao, L., Wang, L., Liu, Y., Li, D., Yang, Y., Zhou, R., Zhao, Y., Chai, Z., and Chen, C. (2011) Binding of blood proteins to carbon nanotubes reduces cytotoxicity. *Proc. Natl. Acad. Sci. U.S.A.*, **108**, 16968–16973.
53. Linse, S., Cabaleiro-Lago, C., Xue, W.-F., Lynch, I., Lindman, S., Thulin, E., Radford, S.E., and Dawson, K.A. (2007) Nucleation of protein fibrillation by nanoparticles. *Proc. Natl. Acad. Sci. U.S.A.*, **104**, 8691–8696.
54. Lundqvist, M., Stigler, J., Elia, G., Lynch, I., Cedervall, T., and Dawson, K.A. (2008) Nanoparticle size and surface properties determine the protein corona with possible implications for biological impacts. *Proc. Natl. Acad. Sci. U.S.A.*, **105**, 14265–14270.
55. Laera, S., Ceccone, G., Rossi, F., Gilliland, D., Hussain, R., Siligardi, G., and Calzolai, L. (2011) Measuring protein structure and stability of protein-nanoparticle systems with synchrotron radiation circular dichroism. *Nano Lett.*, **11**, 4480–4484.
56. Yin, J.-J., Lao, F., Fu, P.P., Wamer, W.G., Zhao, Y., Wang, P.C., Qiu, Y., Sun, B., Xing, G., Dong, J., Liang, X.-J., and Chen, C. (2009) The scavenging of reactive oxygen species and the potential for cell protection by functionalized fullerene materials. *Biomaterials*, **30**, 611–621.
57. Liang, X.-J., Huang, B., Meng, H., He, H., Meng, J., Wang, Y., Lu, J., Wang, P.C., Zhao, Y., Gao, X., Chen, C., Sun, B., Xing, G., Gottesman, M.M., Shen, D., and Jia, L. (2010) Metallofullerene nanoparticles overcome tumor resistance to cisplatin by reactivating endocytosis. *Proc. Natl. Acad. Sci. U.S.A.*, **107**, 7449–7454.

58. Kang, S.-G., Zhou, G., Yang, P., Liu, Y., Sun, B., Huynh, T., Meng, H., Zhao, L., Xing, G., Chen, C., Zhao, Y., and Zhou, R. (2012) Molecular mechanism of pancreatic tumor metastasis inhibition by $Gd@C_{82}(OH)_{22}$ and its implication for de novo design of nanomedicine. *Proc. Natl. Acad. Sci. U.S.A.*, **109**, 15431–15436.
59. Gao, Y., Chen, C.Y., and Chai, Z.F. (2007) Advanced nuclear analytical techniques for metalloproteomics. *J. Anal. At. Spectrom.*, **22**, 856–866.

14
Molecular Simulation Methods for Safety Analyses of Nanomaterials

Lina Zhao

14.1
Introduction

The sizes of nanomaterials are comparable to those of the important biounits, such as bacteria, virus, cell membrane, or even protein and nucleic acid molecules. Once these nanomaterials enter the organisms, they could influence the basic physiological function of whole biological systems by interacting with the important biomolecules and biounits directly, which could invoke the so-called biological effects and safety problems [1]. The studies on the safety analyses of nanomaterials have become a significant research area [2–5].

Experimental scientists investigate the interactions between nanomaterials and biological molecules, cells, organs, and living bodies by *in vitro* and *in vivo* testing techniques. However, when the samples we are interested in are at the molecular or atomic level, this studied size would be beyond the limit of experimental measurements. Besides, it is inevitable for the external experimental conditions and measurement techniques themselves to impact the test results at atomic and molecular scales. While, as we know, the molecular mechanism studies always focus on the atomic and molecular interaction relationship [6–9]. Fortunately, compared with experimental techniques, molecular simulations can directly build the interested complex and systems based on their molecular, atomic, or even electronic structures. It is natural to obtain the molecular interaction details along with the interaction process of nanomaterials and biosystems. In molecular simulations, the intrinsic mechanisms are able to be clarified and understood intuitively by excluding all the external confusing factors. Also, we can conveniently manipulate and adjust the external environmental conditions according to the study requirements. The multiscale simulations have sparked a revolution in material science, biological science, and also physicochemical science. The main contributors of molecular simulations, Karplus, Levitt, and Warshel, won the Nobel Prize of chemistry in 2013.

Toxicology of Nanomaterials, First Edition. Edited by Yuliang Zhao, Zhiyong Zhang, and Weiyue Feng.

Molecular simulations sprang up with the quick development of electronic computer since the 1950s [10]. The first molecular simulation may trace back to the equilibrium-state calculations of liquid models on MANIAC [11]. Nowadays, the applications of molecular simulations have extended into various research and industry fields. For different study purposes and scales, many methods have been developed for molecular simulations and modeling. In our scope for this chapter, we only adopt those most effective to the research of bioeffects of nanomaterials. Four molecular simulation methods named classical molecular dynamics (MD) , first-principles, quantum mechanics/molecular mechanics (QM/MM), and reactive MD are emphatically introduced. Based on the simulation scale from electron to atom and the modeling scale from "small" to "large," we briefly describe the algorithms and capabilities of these four methods in the 2D coordinate as Figure 14.1 shows. In the bioeffect studies, the biomolecules and biounits we considered are composed of millions of atoms and molecules. For the confirmation of the simulation of the large biosystems, classical MD at atomic scale is the most effective in accuracy and consumption. On the other side of simulation scale, the first-principles calculation is based on electronic scale, which is directly established from physical laws. The first-principles calculations can deal with the geometry optimization and electronic transition of nanosystems under hundreds of atoms normally. When the electronic transition of reactive site is focused in a large biological complex, we need the hybrid QM/MM method, which is combined with the advantages of speedy MM and precise QM. This method makes it possible to consider the chemical reactions in proteins, such as the chemical reaction between nanomaterials and the active center of an enzyme. In the event of broad distributed

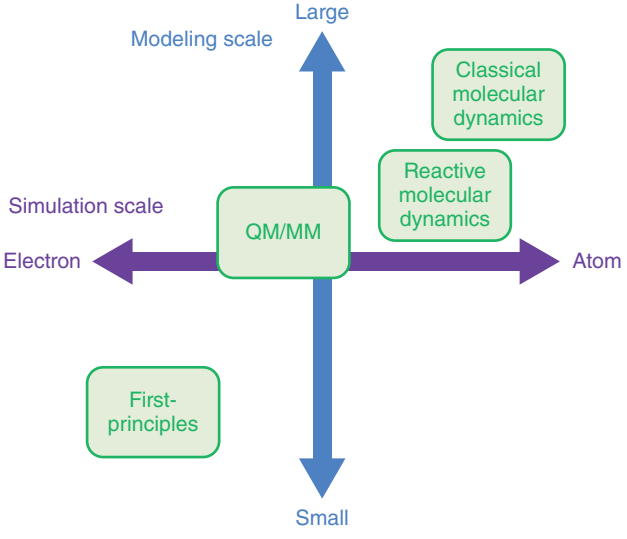

Figure 14.1 Four molecular simulation methods as classical molecular dynamics, first-principles, QM/MM, and reactive molecular dynamics in simulation scale–modeling scale coordinate.

chemical reactions other than concentrated ones in complex systems, we can turn to the reactive MD. This method stems from classical MD and introduces the additional bond order (BO) definition. In the following Section 14.2, we introduce the detailed theories and applicability of the four molecular simulations methods as classical MD, first-principles, QM/MM, and reactive MD, which are quite effective for the study of nanomaterials bioeffect mechanisms. In Section 14.3, we analyze and summarize the specific results of nanomaterial biological effects and molecular mechanism by the mentioned simulation methods. In Section 14.4, we forecast the research prospect of molecular simulation methods for the biological effects of nanomaterials.

14.2 The Molecular Simulation Methods for Nanomaterials and Biological Systems

In this section, we focus on four molecular simulation methods, which are effective for the studies of nanomaterial biological effects. Their principles and algorithms make them valid to simulate nanomaterials, biological systems, or the interaction between nanomaterials and biological systems. In Sections 14.2.1 – 14.2.4, we introduce the theories of classical MD, first-principles, QM/MM, and reactive MD, respectively.

14.2.1 Classical MD

Classical MD aims to observe the details of microstructures and the properties of macrostatistics. MD simulation builds the empirical interaction relationship between atoms or molecules, which is appropriate for describing the behavior of biological system. The empirical interaction relationship is based on the Newton equation, and it is called *molecular force field*.

14.2.1.1 Molecular Force Field

Molecular force field is one of the most important concepts in MD theory. There are several features in molecular force field. The classical interactions could introduce deviations into the results without considering quantum effects. Fortunately, it is acceptable for the biological systems. Under the Born – Oppenheimer approximation, the electrons are considered in the ground state without polarization and bond breaking or formation. In this case, the hydrogen bond cannot be displayed explicitly. Nowadays, there are four biological force fields used broadly as CHARMM (Chemistry HARvard Macromolecular Mechanics), AMBER (Assisted Model Building with Energy Refinement), GROMOS (GROningen Molecular Simulation), and OPLS-AA (Optimized Potential for Liquid Simulations – All Atom). They have the same function formation but different parameters.

Firstly, we take CHARMM force field as an example to discuss the function formation. The atomic interactional potential is divided into bonded interactional potential and nonbonded interactional potential.

$$U = U_{\text{bonded}} + U_{\text{non-bonded}} \tag{14.1}$$

The bonded part includes the bond stretching energy, angle bending energy, dihedral angle energy, and improper dihedral angle energy.

$$U_{\text{bonded}} = U_{\text{bonds}} + U_{\text{angles}} + U_{\text{dihedrals}} + U_{\text{impropers}} \tag{14.2}$$

where

$$U_{\text{bonds}} = \sum_{\text{bonds}} K_b(b - b_0)^2 \tag{14.3}$$

$$U_{\text{angles}} = \sum_{\text{angles}} k_\theta(\theta - \theta_0)^2 \tag{14.4}$$

$$U_{\text{dihedrals}} = \sum_{\text{dihedrals}} K_\varphi[1 + \cos(n\varphi - \delta)]^2 \tag{14.5}$$

$$U_{\text{impropers}} = \sum_{\text{impropers}} K_\omega(\omega - \omega_0)^2 \tag{14.6}$$

Among the functions, b_0, θ_0, δ, and ω_0 are the equilibrium bond length, equilibrium angle, equilibrium dihedral angle, and equilibrium deviation angle from the plane. Their values compose the systematical parameters of force field, together with the values of K_b, k_θ, K_{UB}, K_φ, and K_ω.

To correct the angle bending term, CHARMM force field introduces additional Urey–Bradley 1–3 energy considering the energy of the two nonadjacent atoms as $U_{\text{Urey-Brayley}} = \sum_{\text{Urey-Brayley}} K_{\text{UB}}(\theta^{1-3} - \theta_0^{1-3})^2$ Moreover, the cross-term map (CMAP) based on quantum mechanical results is adopted to correct the behavior of protein backbone [12].

The nonbonded part includes the van der Waals interaction potential and Coulomb interaction potential.

$$U_{\text{non-bonded}} = U_{vdW} + U_{\text{Coulomb}} \tag{14.7}$$

The van der Waals interaction is in the formation of Lennard-Jones potential as

$$U_{vdW} = \sum_{\text{nonb.pairs}} \varepsilon_{ij} \left[\left(\frac{R_{\min_{ij}}}{r_{ij}} \right)^{12} - 2 \left(\frac{R_{\min_{ij}}}{r_{ij}} \right)^{6} \right] \tag{14.8}$$

where ε_{ij} is the depth of Lennard-Jones potential well and $R_{\min_{ij}}$ is the location of the potential well. In the practical MD simulation, the van der Waals interaction could be cut off directly for its fast decay of long-range potential. The Coulomb interaction is

$$U_{\text{Coulomb}} = \sum_{\text{nonb.pairs}} \frac{q_i q_j}{\varepsilon r_{ij}} \tag{14.9}$$

where ε is the effective dielectric coefficient, q_i q_j are the local charges on atoms, and r_{ij} is the distance between these atoms. It is not appropriate to cut off the Coulomb interaction directly because its long-range part cannot be ignored. Generally, we use Ewald summation to simplify the Coulomb interaction calculation. The basic idea is based on Gaussian distributed shielding charge to divide the long-range force of point charge into two short-range parts of real space and Fourier space, which could be cut off directly, respectively. Furthermore, we utilize particle mesh Ewald (PME) method to reduce the computational complexity [13, 14].

As for the systematical parameters for force field, the parameter-determined principle is to reconstruct the important properties of materials. Normally, the parameter-determined processes try to fit the results from quantum chemistry calculations and experimental data set and use the fitted results into the test set for adjusted parameters. CHARMM, AMBER, GROMOS, and OPLS-AA choose different subsets for fitting, so the parameters in different force fields should not be substituted for each other.

14.2.1.2 Newton Equation Solution

The force field describes the interactional potentials of atoms and molecules under which the classical behaviors of atoms and molecules obey the Newton equation. The equations of MD motion are

$$m_i \frac{d^2 r_i}{dt^2} = F_i = -\frac{\partial U}{\partial r_i} \tag{14.10}$$

where

$$v_i = \frac{dr_i}{dt}, \quad a_i = \frac{d^2 r_i}{dt^2} \tag{14.11}$$

We can obtain the location and velocity information $(r_i(t),\ v_i(t))$ of each atom in modeling system by solving the equation group. As a result, the motion trajectory of the whole system can be achieved in this manner.

Verlet algorithm was proposed by Verlet [15]. It is the most widely used algorithm for motion equation solution in MD simulations. Firstly, $r(t)$ is converted into Taylor expansion, and its small high-order terms are omitted as

$$r(t + \delta t) = r(t) + v(t)\delta t + \frac{1}{2}a(t)(\delta t)^2 + \mathcal{O}(\delta t)^3 \tag{14.12}$$

$$r(t - \delta t) = r(t) - v(t)\delta t + \frac{1}{2}a(t)(\delta t)^2 + \mathcal{O}(\delta t)^3 \tag{14.13}$$

By addition and subduction, the aforementioned equations can be converted as

$$r(t + \delta t) = 2r(t) - r(t - \delta t) + a(t)(\delta t)^2 \tag{14.14}$$

$$v(t) = \frac{r(t + \delta t) - r(t - \delta t)}{2\delta t} \tag{14.15}$$

Then we can obtain the location and velocity $(r_i(t), v_i(t))$ of each atom at each moment by iteration.

As an improvement, velocity-Verlet algorithm was proposed by Swope *et al.* [16]. In the velocity-Verlet algorithm, $r(t+\delta t)$ $v(t+\delta t)$ $F(t+\delta t)$ can be obtained from $r(t)$, $v(t)$, and $F(t)$. That is, from

$$a(t) = \frac{F(t)}{m} \tag{14.16}$$

We obtain

$$v\left(t+\frac{1}{2}\delta t\right) = v(t) + \frac{F(t)}{m}\cdot\frac{1}{2}\delta t \tag{14.17}$$

$$r(t+\delta t) = r(t) + v\left(t+\frac{1}{2}\delta t\right)\cdot\delta t \tag{14.18}$$

$$F(t+\delta t) = -\frac{\partial U}{\partial r(t+\delta t)} \tag{14.19}$$

$$v(t+\delta t) = v\left(t+\frac{1}{2}\delta t\right) + \frac{F(t+\delta t)}{m}\cdot\frac{1}{2}\delta t \tag{14.20}$$

To summarize, the location and velocity of each atom at each moment can be gained from the initial location and velocity of each atom.

14.2.1.3 Boundary Condition

The Newton equation is solved following a certain aforementioned algorithm, at the same time, it also should be solved under some boundary condition. Normally, the boundary conditions include periodic boundary condition, free boundary condition, and rigid boundary condition. The periodic boundary condition is often adopted in MD simulations, especially in the biological molecules and nanomaterials including MD simulations. In the simulation box with periodic boundary condition, the particle moving out from one edge can enter into the simulation box at the same moment from the other edge. In this case, the particles in simulation box are able to interact with infinite image particles in periodic simulation boxes. Therefore, the modeling system could reach up to 10^{23} particles, which is appropriate to be analyzed by the basic concepts of equilibrium statistical physics under the thermodynamic limit assumptions.

14.2.1.4 Ensembles

All results of MD simulations are meaningful only in the specific ensemble. Here, we refer to various ensembles as microcanonical ensemble, canonical ensemble and isothermal isobaric ensemble. The microcanonical ensemble is called *NVE ensemble*, which contains definite particle number N, volume V, and energy E. To maintain the constant of energy E is the key point to achieve the microcanonical ensemble. The canonical ensemble is called NVT ensemble, which contains definite particle number N, volume V, and temperature T. Several methods have been developed to maintain T invariant, such as IsoKinetics thermostat, Berendsen thermostat, and Nośe–Hoover thermostat. Besides temperature T, the pressure P is also maintained as a constant in the isothermal isobaric ensemble (NPT ensemble). Berendsen barostat and Hoover barostat are the barostats used normally. Generally, the simulated biophysical properties from NPT ensemble could directly compare with the results from experiments.

14.2.2 First-Principles Approach

First-principles approach is a theoretical method based on QM to calculate the systemic physicochemical properties. There are two branches in the first-principles method development: one is the self-consistent field method based on the Hartree–Fock equation and the other is the density function theory (DFT) method based on the local electron-density distribution. These theoretical methods have made many important contributions to quantum chemistry and quantum computation [17]. The founders of self-consistent field method and DFT method, John Pople and Walter Kohn, shared the Nobel Prize in chemistry in 1998 because of their outstanding works. John Pople completed quantum chemical methodology systematically and developed Gaussian quantum chemical calculation software. Walter Kohn established DFT method and decreased the calculation cost largely. DFT method takes the electron density as the unique variable, which can be directly observed in the experiments. This method has been applied in many important nano/bio complex systems. In the following, we introduce the basic theory of first-principles and emphatically introduce the DFT method for its effectiveness and universality.

14.2.2.1 Schrödinger Equation

In the traditional quantum chemical theory, the quantum system is described by the wave functions of all electrons in their Schrödinger equation [18]. The basic idea of first-principles is to solve the Schrödinger equation independent of the time variable.

$$\hat{H}\psi(r,R) = E\psi(r,R) \tag{14.21}$$

When ignoring the relativistic effects, Hamiltonian $\hat{H}$ is

$$\begin{aligned}\hat{H}(r,R) &= \hat{H^e} + \hat{H^V} + \hat{H^{eV}} \\ &= -\sum_i \frac{\hbar^2}{2m_e}\nabla^2_{r_i} + \frac{1}{2}\sum_{i,i'}\frac{e^2}{|r_i - r_{i'}|} - \sum_j \frac{\hbar^2}{2M}\nabla^2_{R_j} \\ &\quad + \frac{1}{2}\sum_{jj'}\frac{Z^2e^2}{|R_j - R_{j'}|} - \sum_{i,j}\frac{{Z_e}^2}{|r_i - R_j|}\end{aligned} \tag{14.22}$$

where r and R are the coordinates of electron and the nucleus, m_e and M_j are the masses of the electron and the nucleus. The first item is the kinetic energy of electrons, the second one is the Coulomb interaction energy between electrons, the third one is the kinetic energy of nucleuses, the fourth one is the Coulomb interaction energy between nucleuses, and the last one is the interaction energy of electrons and nucleuses.

14.2.2.2 Born–Oppenheimer Approximation

It is impossible to accurately solve the Schrödinger equation except a few simple systems, such as hydrogen atomic system and hydrogen-like ionic system. Some

approximations have to be considered to solve the Schrödinger equation. The most important approximation is the Born–Oppenheimer approximation, also known as adiabatic approximation [19].

The basic idea of Born–Oppenheimer approximation is to decouple the movements of electrons and nuclei. The electron could instantaneously adjust its location when the nucleus moves because the mass of nucleus is much larger than that of electron (up to 1836 times even in the lightest nucleus as one proton). For Equation 14.22, we can divide the movements of electrons and nuclei by Born–Oppenheimer approximation as

$$\hat{H}(r,R) = -\sum_i \frac{\hbar^2}{2m_e}\nabla_{r_i}^2 + \frac{1}{2}\sum_{i',j}\frac{e^2}{|r_i - r_{i'}|} - \sum_{i,j}\frac{Ze^2}{|r_i - R_j|} \tag{14.23}$$

Under the Born–Oppenheimer approximation, we are only concerned about the movement of electrons, and the nucleus is considered as fixed. In other words, we solve the Schrödinger equation of electrons to learn their movements in the electrical field of nucleus.

14.2.2.3 Hartree–Fock Equation

Multielectron wave function can be decomposed into the product of each single-electron wave function by orbital approximation as

$$\psi(r) = \psi_1(r_1)\psi_2(r_2), \ldots, \psi_n(r_n) \tag{14.24}$$

In Equation 14.24, the single-electron wave functions satisfy the Hartree equation:

$$\hat{H}_i\psi_i(r_i) = E_i\psi_i(r_i) \tag{14.25}$$

$$\hat{H}_i = -\frac{\hbar^2}{2m_e}\nabla^2 + V(r_i) + \sum_{i'(i'\neq i)}\int dr_i \frac{|\psi_{i'}(r_{i'})|^2}{|r_{i'} - r_i|} \tag{14.26}$$

where $V(r_i)$ is the interaction potential of this electron from the nucleus and $\sum_{i'(i'\neq i)}\int dr_i \frac{|\psi_{i'}(r_{i'})|^2}{|r_{i'} - r_i|}$ describes the average interaction potential of all other electrons. Considering the antisymmetry of electronic exchange, Fork transformed the wave function in product of orbitals into Slater determinant wave function fitting the Pauli principles. Thus, the single-electron wave functions satisfy the Hartree–Fork equation as

$$\left[-\frac{\hbar^2}{2m_e}\nabla^2 + V\left(r_i\right)\right]\psi_i(r_i) + \sum_{i'(i'\neq i)}\int dr_{i'}\frac{|\psi_{i'}(r_{i'})|^2}{|r_{i'} - r_i|}\psi_i(r_i)$$
$$-\sum_{i'(i'\neq i)}\int dr_{i'}\frac{\psi_{i'}^*(r_{i'})\psi_i(r_{i'})}{|r_{i'} - r_i|}\psi_{i'}(r_i) = \sum_{i'}\lambda_{ii'}\psi_i(r_i) \tag{14.27}$$

Compared with the Hartree equation, the Hartree–Fock equation consists of one additional term, which is known as the *exchange interaction term*. It includes the exchange interaction between electrons, but excludes the relativistic effects and electric correlation effects [20].

14.2.2.4 Hohenberg–Kohn Theory

Hohenberg and Kohn proposed the inhomogeneous electron gas theory in 1964 [21]. The Hohenberg–Kohn theorem could successfully solve the problems in building accurate density functional theory.

The first theorem of Hohenberg–Kohn theory: the external potential $V_{\text{ext}}(\vec{r})$ of N particle system is determined by the electron density $\rho(\vec{r})$ or plus one additional insignificant constant. The second theorem of Hohenberg–Kohn theory: in the condition of $\tilde{\rho}(\vec{r}) \geq 0$ and $\int \rho(\vec{r})d\vec{r} = N$ for any test density function $\tilde{\rho}(\vec{r})$, $E_0 \leq E_v[\tilde{\rho}]$. E_0 is the ground state energy, $E_v[\tilde{\rho}]$ is the functional form of the energy expressed by the particle density.

Through the aforementioned two theorems, we define the total energy function relating to the external potential as follows:

$$E_v[\rho] = T[\rho] + V_{\text{ne}}[\rho] + V_{ee}[\rho] \tag{14.28}$$

where the first term is the kinetic energy function, the second one is the attraction energy function of nucleus, and the third one is the interaction function of electrons. There is one part having nothing to do with the external potential in the total energy function, which is

$$F_{\text{HK}}[\rho] = V_{\text{ne}}[\rho] + V_{ee}[\rho] \tag{14.29}$$

This function is a universal form. Moreover, electron density should satisfy the wave functions in the following equation:

$$\hat{H}\psi = \left(\sum_{i=1}^{N}\left(-\frac{1}{2}\tilde{N}_i^2\right) + \sum_{i=1}^{N} V(\vec{r}_i) + \sum_{i<j}^{N}\frac{e^2}{r_{ij}}\right)\psi = E\psi \tag{14.30}$$

For a fully antisymmetric wave function of N electrons, we could obtain the following using the energy variational principle:

$$\langle\psi_\rho|\hat{H}|\psi_\rho\rangle = \langle\psi_0|\hat{H}|\psi_0\rangle = E_0 \tag{14.31}$$

We search the wave function of minimum energy within some functional subspace with the fixed density. Then, we keep on searching by changing the density of functional subspace until we find the wave function of the ground state. The process can be represented as

$$E_0 = \min_{\rho}\{\min_{\psi\to\rho}[\langle\psi|\hat{H}|\psi\rangle]\} \tag{14.32}$$

Therefore, we can change the definition of the universal function as

$$F[\rho] = \min_{\rho}[\langle\psi|\hat{T} + \hat{V}_{\text{ee}}|\psi\rangle] \tag{14.33}$$

14.2.2.5 Kohn–Sham Equation

In the practical calculation by DFT, we have to obtain the expression of the energy function. But it is very difficult to obtain the expression by calculating electronic system. To meet this challenge, Kohn and Sham introduced an imaginary

multi-electron system without any interaction in 1965 [22]. The Hamiltonian is

$$\hat{H}_s = \sum_i^N \left(-\frac{1}{2}\nabla_i^2\right) + \sum_i^N V_s(\vec{r}) \tag{14.34}$$

Kohn and Sham supposed the aforementioned particle density of the ground state ρ is the same as that of a practical system with normal interactions. So we can define the universal function as

$$F[\rho] = T_s[\rho] + J[\rho] + E_{\text{xc}}[\rho] \tag{14.35}$$

The density of system ρ and the kinetic energy function $T_s[\rho]$ could be represented as

$$\rho = \sum_{i=1}^N \varphi_i(\vec{r})\varphi_i^*(\vec{r}) \tag{14.36}$$

$$T_s[\rho] = \sum_{i=1}^N \left\langle \varphi_i \left| \frac{1}{2}\nabla_i^2 \right| \varphi_i \right\rangle \tag{14.37}$$

The exchange correlation energy function $E_{\text{xc}}[\rho]$ is

$$E_{\text{xc}}[\rho] = T[\rho] - T_s[\rho] + V_{\text{ee}}[\rho] - J[\rho] \tag{14.38}$$

The total energy is

$$E[\rho] = \int \rho(\vec{r})V(\vec{r})d\vec{r} + T_s[\rho] + J[\rho] + V_{\text{xc}}[\rho] \tag{14.39}$$

The Kohn–Sham equation can be achieved by substituting T_s and ρ into Equation 14.39 and making variation on the single-electron orbital

$$(\hat{T}_s + \hat{V}_{\text{eff}})|\varphi_i\rangle = \varepsilon_i|\varphi_i\rangle \tag{14.40}$$

where

$$V_{\text{eff}}(\vec{r}) = V_{\text{ne}}(\vec{r}) + \int \frac{\rho(\vec{r}')d\vec{r}'}{|\vec{r}' - \vec{r}'|} + \frac{\delta E_{\text{xc}}}{\delta\rho(\vec{r})} \tag{14.41}$$

The first term on the right-hand side is the core attraction potential, the second one is the Coulomb potential between electrons, and the third one is the exchange correlation potential. The Kohn–Sham equation appears to be similar to the Hartree–Fork equation. Actually, it is quite different for the effective potential. The effective potential of the Kohn–Sham equation is local, while that of the Hartree–Fork equation contains the nonlocal exchange term. The local effective potential in the Kohn–Sham equation provides a lot of convenience for calculations.

14.2.2.6 Exchange Correlation Energy Function

Based on the Kohn–Sham equation, the multielectron problem could be transited into the effective single-electron problem. The key point is to find the accurate and convenient expression of the exchange correlation function E_{xc}. There are some important exchange correlation energy approximation methods.

The first one is the local spin density approximation (LSDA) method. Under this approximation, the exchange correlation energy function is only the function of the electron density ρ. Then, the exchange correlation energy function can be expressed as

$$E_{\mathrm{xc}}^{\mathrm{SDA}}[\rho] = \int \rho(r)\varepsilon_{\mathrm{xc}}^{\mathrm{hom}}[\rho(r)]dr \tag{14.42}$$

$$E_{\mathrm{xc}}^{\mathrm{LSDA}}[\rho_\alpha + \rho_\beta] = \int \rho(\overrightarrow{r})\varepsilon_{\mathrm{xc}}^{\mathrm{hom}}[\overrightarrow{\rho}_\alpha, \overrightarrow{\rho}_\beta]dr \tag{14.43}$$

$\varepsilon_{\mathrm{xc}}^{\mathrm{hom}}$ is the exchange correlation energy of electrons.

The second one is the generalized gradient approximation (GGA) method. In order to correct the errors of LSDA due to the nonuniform distribution of electron density, GGA method introduces the nonuniform electron density into the basic expression of the exchange correlation energy. The exchange correlation energy function is

$$\begin{aligned} E_{\mathrm{XC}}^{\mathrm{LSDA}}[\rho_\alpha + \rho_\beta] &= \int \rho(\overrightarrow{r})\varepsilon_{\mathrm{xc}}^{\mathrm{hom}}[\overrightarrow{\rho}_\alpha, \overrightarrow{\rho}_\beta, |\nabla\rho_\alpha|, |\nabla\rho_\beta|, \ldots]d\overrightarrow{r} \\ &= \int \rho(\overrightarrow{r})\varepsilon_x^{\mathrm{hom}}F_{\mathrm{xc}}[\overrightarrow{\rho}_\alpha, \overrightarrow{\rho}_\beta, |\nabla\rho_\alpha|, |\nabla\rho_\beta|, \ldots]d\overrightarrow{r} \end{aligned} \tag{14.44}$$

F_{xc} is an infinite dimensional function and $\varepsilon_{\mathrm{xc}}^{\mathrm{hom}}$ is the exchange energy of nonpolarized electrons. Additionally, there are more higher-level approximation methods, including Meta-GGA, Hyper-GGA, and Double-Hyper-GGA.

14.2.3 QM/MM Method

It is still a huge challenge to simulate a chemical reaction in biological molecule by traditional QM or MM. Fortunately, the hybrid QM/MM method can solve the problem by dealing with the electric transition with high precision of QM and the biological complex with high speed of MM.

14.2.3.1 Basic Concept of QM/MM Method

The hybrid QM/MM concept was proposed by Warshel and Levitt in 1976. The basic idea is to divide the whole system into QM region and MM region. These two regions are coupled with QM part handled by QM and MM part handled by MM. Based on the basic concept of QM/MM method, many QM/MM combination calculation strategies to especially solve the biology-related problems have been developed [23].

Essentially, the potential energy of system is the driving force for its dynamic evolution whether in first-principles method or in classical MD method. The QM/MM method is no exception, so the key point of the whole method is to construct the potential energy function of system with division strategy. Currently, there are two kinds of widely used energy expressions in QM/MM method, which are additive schemes and subtractive schemes. In the additive

schemes, the energy expression is

$$E_{\mathrm{QM/MM}}(S) = E_{\mathrm{MM}}(O) + E_{\mathrm{QM}}(I+B) + E_{\mathrm{QM-MM}}(I,O) \tag{14.45}$$

where E_{QM} and E_{MM} are the energies of independent QM and MM regions respectively. $E_{\mathrm{QM-MM}}$ is the coupling term between QM and MM regions. Generally, DFT or semiempirical method is used to deal with the calculation of QM region. The additive scheme strategy is widely adopted in the hybrid QM/MM calculation, especially for the studies of biological macromolecules. As for the subtractive scheme strategy, it refers to calculate the whole system with the classic MM simulation and combine the results to the QM calculation, then subtract the repeated MM calculation from QM region. The expression is

$$E_{\mathrm{QM/MM}}(S) = E_{\mathrm{MM}}(S) + E_{\mathrm{QM}}(I+B) - E_{\mathrm{MM}}(I+B) \tag{14.46}$$

The subtractive scheme strategy is less precise than the additive scheme one because it ignores the polarity changes from the coupling term.

We could describe the system of composite potential field by using the effective Hamiltonian operator H_{eff} referring to the quantum chemistry simulation method. Additionally, we could obtain the total energy of molecular structure E_{total} by solving the following Schrödinger equation:

$$\hat{H_{\mathrm{eff}}}\psi(r_i, R_\alpha, R_{\mathrm{M}}) = E_{\mathrm{total}}(R_\alpha, R_{\mathrm{M}})\psi(r_i, R_\alpha, R_{\mathrm{M}}) \tag{14.47}$$

where r_i and R_α, respectively, represent the coefficients of the electron and the nucleus in the QM region. R_{M} represents the coefficient of the atom in the MM region. So we also could construct the Hamiltonian calculated by the additive schemes:

$$\hat{H}_{\mathrm{eff}} = \hat{H}_{\mathrm{QM}}(I+B) + \hat{H}_{\mathrm{MM}}(O) + \hat{H}_{\mathrm{QM/MM}}(I,O) \tag{14.48}$$

The third item $E_{\mathrm{QM/MM}}$ is the unique part of the QM/MM method.

14.2.3.2 The Coupling Potential Energy

In general, the coupling potential energy can be divided into three parts:

$$E_{\mathrm{QM/MM}} = E_{vdW} + E_{\mathrm{electrostatic}} + E_{\mathrm{MM\text{-}bonded}} \tag{14.49}$$

The aforementioned three items represent the van der Waals interaction, electrostatic interaction, and boundary bonding term, respectively [17].

Firstly, the van der Waals interaction is often calculated with Leonard-Jones empirical potential field:

$$E_{vdW} = \sum_{A,B} \varepsilon_{AB} \left[\left(\frac{\sigma_{AB}}{r_{AB}} \right)^{12} - \left(\frac{\sigma_{AB}}{r_{AB}} \right)^{6} \right] \tag{14.50}$$

Secondly, to deal with the mixed electrostatic interaction between the charge density of QM region and charge model of MM region, we can utilize different computation levels with various polarization ranges between the QM region and MM region. There are three kinds of embedding approaches to handle the electrostatic potential interaction as mechanical embedding, electrostatic embedding,

and polarized embedding. In the mechanical embedding, the calculation of QM region is considered as the gas phase lacking the mixed interaction with the environment. The electrostatic potential interaction between QM and MM regions is omitted or is calculated in the MM region. In order to overcome the defects of the mechanical embedding, we introduce the electrostatic embedding approach with high accuracy. In this approach, the polarization of QM region generated by the charge distribution of MM region can be considered as part of the electric structure calculation of QM region. In the calculation, $E_{\text{electrostatic}}$ and E_{QM} can be obtained through an equivalent Hamiltonian:

$$E_{\text{electrostatic}} + E_{\text{QM}} = \langle \psi | \hat{H_{\text{eff}}} | \psi \rangle \tag{14.51}$$

The equivalent Hamiltonian can be written as follows:

$$\hat{H_{\text{eff}}} = -\frac{1}{2}\sum_{i}^{N_{\text{eff}}} \nabla_i^2 + \sum_{i \neq j}^{N_{\text{eff}}} \frac{1}{r_{ij}} - \sum_{i}^{N_{\text{eff}}} \sum_{\alpha \in \text{QM}} \frac{Z_\alpha}{r_{\alpha i}} + \sum_{\alpha 1 \neq \alpha 2 \in \text{QM}} \frac{Z_{\alpha 1} Z_{\alpha 2}}{r_{\alpha 1 \alpha 2}} - \sum_{i}^{N_{\text{eff}}} \sum_{\beta \in \text{MM}} \frac{q_\beta}{r_{i\beta}} + \sum_{\alpha \in \text{QM}, \beta \in \text{MM}} \frac{Z_\alpha q_\beta}{r_{\alpha\beta}} \tag{14.52}$$

The inner electronic structure can adapt to the change of environment (MM) charge and be polarized by environment because the electrostatic effect caused by MM region is adopted into the QM calculation. Nowadays, the electrostatic embedding approach is utilized very broadly in biomolecule simulations. Based on the electrostatic embedding approach, the polarized embedding approach includes the polarization effect in MM region generated by the charge distribution of QM region. However, there is no suitable polarized force field established for biological macromolecules. Thus, the polarized embedding approach is still applied in a very limited range although it is the most accurate approach. To summarize, the electrostatic embedding approach is the most practical one in the nano/bio complex simulations.

Thirdly, when the boundary bonded term involved with crossing the chemical bonds, there will be inconsistent calculation methods about the two ends of the bond. Many ways to deal with this problem, such as link atom method, localized orbital method, and boundary atom method, have been developed. The link atom method is the most direct way to deal with the boundary problem between QM and MM regions. This method simply introduces a virtual atom, usually a hydrogen atom, as a "cap" to the broken free radical in the QM region. The virtual atoms are set to satisfy the electron density of the severed parts. Thus, the link atoms together with other atoms in QM region form the closed shell system for the QM calculation, while the link atoms have no interaction with the atoms in MM region. We always consider the direct link atom method as not an ideal way for changing the original configuration. The localized orbital is another method to deal with QM/MM boundary bonding problem. This method uses localized bonding orbital to saturate the free radicals from the broken covalent bonds between QM and MM regions. Theoretically, the localized orbital method is more physically reasonable than the link atom method because this method could support

the QM description of the charge distribution at QM/MM boundary. Based on the localized orbital method, many orbital methods, including the hybrid orbital method, the local self-consistent field (LSCF) method, and the generalized hybrid orbital (GHO) method have been developed. Another important method to handle boundary bonding problem is the boundary atom method. In this method, it uses the parameterized atom to imitate the MM boundary atom, which has been cut off. The parameterized atom possesses the Janus nature, and it could be involved in both the QM and MM calculations at the same time. The expect properties can be obtained by the parameterization. The frequently used methods include the adjusted connection atoms method, the pseudobond method, and the effective group potential (EGP) method. The boundary atom method does not introduce any additional atom as does the link atom method, and it is much easier than the localized orbital method. As a result, it could provide the smooth connection for the QM/MM boundary.

14.2.3.3 Dynamics Calculation

The essence of QM/MM calculation is to find the real-time energy value E_{total} of the entire system [24]. Whether in the Hamiltonian description of QM method or in the Newtonian description of MM method, the instant energy change eventually dominates the molecular movement and change in the next moment. Once we obtain the total energy of the entire system, the force between atoms could be calculated by energy gradient conveniently:

$$F_{\alpha} = -\frac{\partial E_{\text{total}}}{\partial R_{\alpha}} \tag{14.53}$$

$$F_{\text{M}} = -\frac{\partial E_{\text{total}}}{\partial R_{\text{M}}} \tag{14.54}$$

Then, we could use the classical MM method to perform the following geometry optimization, MD, or Monte Carlo computation. The following strategy is identical for the QM/MM method and the traditional MD simulation.

14.2.4 Reactive MD

The reactive MD simulation method is based on the reaction force field as the bridge between the quantum chemistry method and classical MD method. This method makes it possible to study the chemical reaction process in large-scale condensed matter. In the reaction force field, the chemical bonds could break or connect freely rather than being fixed with the connections. Thus, compared to the classical MD method, the reaction force field is able to handle the chemical reaction process. On the other hand, compared to the quantum chemistry method, the reaction force field has the advantages of high calculation efficiency and large simulation system for the chemical reaction computation. The reaction force field has a great application prospect in the reaction dynamics between nanomaterials and biomolecules.

14.2.4.1 The Potential Function of ReaxFF

Nowadays, the most widely used reaction force field is ReaxFF developed by Duin and Goddard III [25]. It has also been successfully utilized in the biological systems [26, 27]. ReaxFF is built up based on the BO concept. Through calculating the BO between any two atoms, the ReaxFF simulations consider the energy of single atom or entire system under the influences of bond breaking or connecting. In this way, we could learn about the instant bond connectivity between atoms and its evolution along with time. In ReaxFF, the atomic connection list is updated constantly along with the breaking and connecting of bonds. Therefore, the core of ReaxFF is around the BO expression. Based on the BO conception, the interaction between atoms is defined as the function of BO, which is divided into terms such as bond, angle, dihedral angle, conjugate, Coulomb, van der Waals, and adjustments. Each part of the intramolecular energy is expressed by BO, except the nonbonding interactions:

$$\begin{aligned} E_{\text{system}} =& E_{\text{bond}} + E_{\text{lp}} + E_{\text{over}} + E_{\text{under}} + E_{\text{val}} + E_{\text{pen}} + E_{\text{coa}} + E_{C2} + E_{\text{triple}} \\ &+ E_{\text{tors}} + E_{\text{conj}} + E_{\text{H-bond}} + E_{\text{vd Waals}} + E_{\text{Coulomb}} \end{aligned} \tag{14.55}$$

The basic assumption of BO definition is the certain function relation between BO and the distance between atoms. In other words, the BO between any two atoms could be directly determined by distance calculation of these two atoms. In ReaxFF, BO_{ij} is defined as the function of the distance r_{ij} between atoms. We can divide BO into three parts with chemical meaning contributed by single bond BO_{ij}^{σ}, double bond BO_{ij}^{π}, and triple bond $\text{BO}_{ij}^{\pi\pi}$:

$$\begin{aligned} \text{BO}'_{ij} &= \text{BO}_{ij}^{\sigma} + \text{BO}_{ij}^{\pi} + \text{BO}_{ij}^{\pi\pi} \\ &= \exp\left[p_{bo1}\left(\frac{r_{ij}}{r_O^{\sigma}}\right)^{p_{bo2}}\right] + \exp\left[p_{bo3}\left(\frac{r_{ij}}{r_O^{\pi}}\right)^{p_{bo4}}\right] + \exp\left[p_{bo5}\left(\frac{r_{ij}}{r_O^{\pi\pi}}\right)^{p_{bo6}}\right] \end{aligned} \tag{14.56}$$

The new BO_{ij} and the excessive coordination Δ are obtained by using a series of correction functions:

$$\Delta_i = -\text{Val}_i + \sum_{j=1}^{neighbors(i)} \text{BO}_{ij} \tag{14.57}$$

Therefore, we could obtain the bond energy E_{bond} of any two atoms based on BO:

$$E_{\text{bond}} = -D_c^{\sigma}\cdot\text{BO}_{ij}^{\sigma}\cdot\exp[p_{bc1}(1-(\text{BO}_{ij}^{\sigma})^{p_{bc2}})] - D_c^{\pi}\cdot\text{BO}_{ij}^{\pi} - D_c^{\pi\pi}\cdot\text{BO}_{ij}^{\pi\pi} \tag{14.58}$$

There are two specific functions Δ_i^e and $n_{\text{lp},i}$ introduced to represent the contribution of lone pair electrons to the system energy in ReaxFF.

$$\Delta_i^e = -\text{Val}_i^e + \sum_{j=1}^{neighbors(i)} \text{BO}_{ij} \tag{14.59}$$

$$n_{\text{lp},i} = \text{int}\left(\frac{\Delta_i^e}{2}\right) + \exp\left[-p_{\text{lp1}}\left(2 + \Delta_i^e - 2\,\text{int}\left(\frac{\Delta_i^e}{2}\right)\right)^2\right] \tag{14.60}$$

When chemical reaction occurs, E_{lp} can be calculated:

$$E_{\mathrm{lp}} = \frac{p_{\mathrm{lp2}} \cdot \Delta_i^{\mathrm{lp}}}{1 + \exp(-75 \cdot \Delta_i^{\mathrm{lp}})} \tag{14.61}$$

In the ReaxFF calculation, the coordination number is changed continuously. When $\Delta_i > 0$, it means the number of other atoms connected to the atom has exceeded the bonding ability of the atom. Thus, it is required to correct the system energy as following two functions:

$$E_{\mathrm{over}} = \frac{\sum_{j=1}^{n\,\mathrm{bond}} p_{\mathrm{ovun1}} \cdot D_c^{\sigma} \cdot \mathrm{BO}_{ij}}{\Delta_i^{\mathrm{lpcorr}} + \mathrm{Val}_i} \cdot \Delta_i^{\mathrm{lpcorr}} \cdot \left[\frac{1}{1 + \exp\left(p_{\mathrm{ovun2}} \cdot \Delta_i^{\mathrm{lpcorr}}\right)} \right] \tag{14.62}$$

$$\Delta_i^{\mathrm{lpcorr}} = \Delta_i - \frac{\Delta_i^{\mathrm{lp}}}{1 + p_{\mathrm{ovun3}} \cdot \exp\left(p_{\mathrm{ovun4}} \cdot \left\{ \sum_{j=1}^{\mathrm{neighbors}(i)} \left(\Delta_j - \Delta_j^{\mathrm{lp}}\right) \cdot \left(O_{ij}^{\pi} + \mathrm{BO}_{ij}^{\pi\pi}\right) \right\}\right)} \tag{14.63}$$

When $\Delta_i < 0$, it indicates that the atom is in the deficient coordination state. So it also needs to correct the system energy with the existence of π bond.

$$E_{\mathrm{under}} = -p_{\mathrm{ovun5}} \cdot \frac{1 - \exp(p_{\mathrm{ovun6}} \cdot \Delta_i^{\mathrm{lpcor}})}{1 + \exp(-p_{\mathrm{ovun2}} \cdot \Delta_i^{\mathrm{lpcor}})} \cdot \frac{1}{1 + p_{\mathrm{ovun7}} \cdot \exp\left[p_{\mathrm{ovun8}} \cdot \left[\sum_{j=1}^{\mathrm{neighbors}(i)} \left(\Delta_j - \Delta_j^{\mathrm{lp}}\right) \cdot \left(\mathrm{BO}_{ij}^{\pi} + \mathrm{BO}_{ij}^{\pi\pi}\right)\right]\right]} \tag{14.64}$$

The energy of valence angel is expressed as BO function, which is similar to the valence bond. The equilibrium bond angle θ_0 depends on the sum of π-bonded BO (SBO) function. We could achieve the hybridization state of the atom at the center of the bond angle.

$$E_{\mathrm{val}} = f_7(\mathrm{BO}_{ij}) \cdot f_7(\mathrm{BO}_{jk}) \cdot f_8(\Delta_j) \cdot \{p_{\mathrm{val1}} - p_{\mathrm{val1}} \cdot \exp[-p_{\mathrm{val12}} \cdot (\theta_0(\mathrm{BO}) - \theta_{ijk})^2]\} \tag{14.65}$$

$$f_7(\mathrm{BO}_{ij}) = 1 - \exp(-p_{\mathrm{val3}} \cdot \mathrm{BO}_{ij}^{p_{\mathrm{val4}}}) \tag{14.66}$$

$$f_8(\Delta_j) = p_{\mathrm{val5}} - (p_{\mathrm{val5}} - 1) \cdot \frac{2 + \exp(p_{\mathrm{val6}} \cdot \Delta_j^{\mathrm{angle}})}{1 + \exp(p_{\mathrm{val6}} \cdot \Delta_j^{\mathrm{angle}}) + \exp(-p_{\mathrm{val7}} \cdot \Delta_j^{\mathrm{angle}})} \tag{14.67}$$

$$\mathrm{SBO} = \sum_{n=1}^{\mathrm{neighbors}(j)} (\mathrm{BO}_{jn}^{\pi} + \mathrm{BO}_{jn}^{\pi\pi}) + \left[1 - \prod_{n=1}^{\mathrm{neighbors}(j)} \exp(-\mathrm{BO}_{jn}^{8})\right] \cdot (-\Delta_j^{\mathrm{angle}} - p_{\mathrm{val8}} n_{\mathrm{lp},j}) \tag{14.68}$$

$$\Delta_i^{\mathrm{angle}} = -\mathrm{Val}_i^{\mathrm{angle}} + \sum_{n=1}^{\mathrm{neighbors}(j)} \mathrm{BO}_{jn} \tag{14.69}$$

$$\mathrm{SBO2} = 0 \quad \text{if } \mathrm{SBO} \le 0 \tag{14.70}$$

$$\mathrm{SBO2} = \mathrm{SBO}^{p_{\mathrm{val9}}} \quad \text{if } 0 < \mathrm{SBO} < 1 \tag{14.71}$$

$$\mathrm{SBO2} = 2 - (2 - \mathrm{SBO})^{P_{\mathrm{val9}}} \quad \text{if } 1 < \mathrm{SBO} < 2 \tag{14.72}$$

$$\mathrm{SBO2} = 2 \quad \text{if } \mathrm{SBO} > 2 \tag{14.73}$$

$$\theta_0(\mathrm{BO}) = \pi - \theta_{0.0} \cdot \{1 - \exp[-p_{\mathrm{val10}} \cdot (2 - \mathrm{SBO2})]\} \tag{14.74}$$

When two double bonds connect to both sides of an atom at the center of the bond angle, ReaxFF introduces a penalty term to correct the bond angle energy:

$$E_{\mathrm{pen}} = p_{\mathrm{pen1}} \cdot f_9(\Delta_j) \cdot \exp[-p_{\mathrm{pen2}} \cdot (\mathrm{BO}_{ij} - 2)^2] \cdot \exp[-p_{\mathrm{pen2}} \cdot (\mathrm{BO}_{ij} - 2)^2] \tag{14.75}$$

$$f_9(\Delta_j) = \frac{2 + \exp(-p_{\mathrm{pen3}} \cdot \Delta_j)}{1 + \exp(-p_{\mathrm{pen3}} \cdot \Delta_j) + \exp(p_{\mathrm{pen1}} \cdot \Delta_j)} \tag{14.76}$$

In the conjugate system, the triploid conjugation is introduced:

$$\begin{aligned} E_{\mathrm{con}} = {} & p_{\mathrm{con1}} \cdot \frac{1}{1 + \exp(p_{\mathrm{con2}} \cdot \Delta_j^{\mathrm{val}})} \cdot \exp\left[-p_{\mathrm{con3}} \cdot \left(-\mathrm{BO}_{ij} + \sum_{n=1}^{\mathrm{neighbors}(i)} \mathrm{BO}_{\mathrm{in}}\right)^2\right] \\ & \cdot \exp\left[-p_{\mathrm{con3}} \cdot \left(-\mathrm{BO}_{jk} + \sum_{n=1}^{\mathrm{neighbors}(i)} \mathrm{BO}_{kn}\right)^2\right] \\ & \cdot \exp[-p_{\mathrm{con4}} \cdot (\mathrm{BO}_{ij} - 1.5)^2] \cdot \exp[-p_{\mathrm{con4}} \cdot (\mathrm{BO}_{jk} - 1.5)^2] \end{aligned} \tag{14.77}$$

Similarly to the bond angle, the dihedral angle energy requires the determination of the BO connecting to four atoms as

$$\begin{aligned} E_{\mathrm{tors}} = {} & f_{10}(\mathrm{BO}_{ij}, \mathrm{BO}_{jk}, \mathrm{BO}_{kl}) \cdot \sin(\theta_{ijk}) \cdot \sin(\theta_{jkl}) \\ & \cdot \left[\frac{1}{2} \cdot V_1 \cdot \left(1 + \cos\omega_{ijkl}\right) + \frac{1}{2} \cdot V_2 \cdot \exp\{p_{\mathrm{tor1}} \cdot (\mathrm{BO}_{jk}^{\pi} - 1 + f_{11}(\Delta_j, \Delta_k)^2)\}\right. \\ & \left. \times \left(1 + \cos\omega_{ijkl}\right) + \frac{1}{2} \cdot V_3 \cdot (1 + \cos 3\omega_{ijkl})\right] \end{aligned} \tag{14.78}$$

$$f_{10}\left(\mathrm{BO}_{ij},\mathrm{BO}_{jk},\mathrm{BO}_{kl}\right) = \left[1-\exp\left(-p_{\mathrm{tor2}}\cdot\mathrm{BO}_{ij}\right)\right]\cdot\left[1-\exp\left(-p_{\mathrm{tor2}}\cdot\mathrm{BO}_{jk}\right)\right]\cdot\left[1-\exp\left(-p_{\mathrm{tor2}}\cdot\mathrm{BO}_{kl}\right)\right] \tag{14.79}$$

$$f_{11}\left(\Delta_j,\Delta_k\right) = \frac{2+\exp\left[-p_{\mathrm{tor3}}\cdot\left(\Delta_j^{\mathrm{angle}}+\Delta_k^{\mathrm{angle}}\right)\right]}{1+\exp\left[-p_{\mathrm{tor3}}\cdot\left(\Delta_j^{\mathrm{angle}}+\Delta_k^{\mathrm{angle}}\right)\right]+\exp\left[p_{\mathrm{tor4}}\cdot\left(\Delta_j^{\mathrm{angle}}+\Delta_k^{\mathrm{angle}}\right)\right]} \tag{14.80}$$

The tetraploid conjugation is

$$E_{\mathrm{conj}} = f_{12}(\mathrm{BO}_{ij},\mathrm{BO}_{jk},\mathrm{BO}_{kl})\cdot p_{\mathrm{cot}1}\cdot[1+(\cos\omega_{ijkl}^2-1)\cdot\sin\theta_{ijk}\cdot\sin\theta_{jkl}] \tag{14.81}$$

$$f_{12}(\mathrm{BO}_{ij},\mathrm{BO}_{jk},\mathrm{BO}_{kl}) = \exp\left[-p_{\mathrm{cot}2}\cdot\left(\mathrm{BO}_{ij}-\frac{3}{2}\right)^2\right] \cdot\exp\left[-p_{\mathrm{cot}2}\cdot\left(\mathrm{BO}_{jk}-\frac{3}{2}\right)^2\right]\cdot\exp\left[-p_{\mathrm{cot}2}\cdot\left(\mathrm{BO}_{kl}-\frac{3}{2}\right)^2\right] \tag{14.82}$$

The hydrogen bond energy term is

$$E_{\mathrm{H\,bond}} = p_{\mathrm{hb1}}\cdot[1-\exp(p_{\mathrm{hb2}}\cdot\mathrm{BO}_{\mathrm{XH}})]\cdot\exp\left[p_{\mathrm{hb3}}\left(\frac{r_{\mathrm{hb}}^o}{r_{\mathrm{HZ}}}+\frac{r_{\mathrm{HZ}}}{r_{\mathrm{hb}}^o}-2\right)\right]\cdot\sin\left(\frac{\theta_{\mathrm{XHZ}}}{2}\right)^8 \tag{14.83}$$

In ReaxFF, there is a very strong triple bond supported to the molecule of two C atoms (C2), whose energy is much higher than that of the C═C double bond. However, the triple bond could be greatly weakened by the free radicals at the end of the molecule, which makes the energy of the triple bond to be lower than that of the double bond. The new energy correction E_{C2} is introduced for correction.

$$E_{c2} = k_{c2}(\mathrm{BO}_{ij}-\Delta_i-0.04\cdot\Delta_i^4-3)^2 \quad \text{if } \mathrm{BO}_{ij}-\Delta_i-0.04\cdot\Delta_i^4>3 \tag{14.84}$$

$$E_{c2} = 0 \quad \text{if } \mathrm{BO}_{ij}-\Delta_i-0.04\cdot\Delta_i^4\le 3 \tag{14.85}$$

The triple bond correction:

$$E_{\mathrm{trip}} = p_{\mathrm{tripl}}\cdot\exp[-p_{\mathrm{trip2}}\cdot(\mathrm{BO}_{ij}-2.5)^2] \cdot\frac{\exp\left[-p_{\mathrm{trip4}}\cdot\left(\sum_{k=1}^{\mathrm{neighbors}}\mathrm{BO}_{ik}-\mathrm{BO}_{ij}\right)\right]+\exp\left[-p_{\mathrm{trip4}}\cdot\left(\sum_{k=1}^{\mathrm{neighbors}}\mathrm{BO}_{jk}-\mathrm{BO}_{ij}\right)\right]}{1+25\exp[p_{\mathrm{trip3}}\cdot(\Delta_i+\Delta_j)]} \tag{14.86}$$

The nonbonding interaction need not be expressed in BO function because it should describe all atoms in the entire system. The Morse function is utilized in the description of the van der Waals interaction.

$$E_{vdw\ \mathrm{aals}} = \mathrm{Tap}\cdot D_{ij}\cdot\left\{\exp\left[a_{ij}\cdot\left(1-\frac{f_{13}\left(r_{ij}\right)}{r_{vdw}}\right)\right]-2\cdot\exp\left[\frac{1}{2}\cdot a_{ij}\cdot\left(1-\frac{f_{13}\left(r_{ij}\right)}{r_{vdw}}\right)\right]\right\} \tag{14.87}$$

At the same time, the short-range repulsion is introduced to avoid the high repulsion between the two bonding atoms and the two interval atoms.

$$f_{13}(r_{ij}) = \left[r_{ij}^{p_{vdW1}} + \left(\frac{1}{\gamma_\omega} \right)^{p_{vdW1}} \right]^{\frac{1}{p_{vdW1}}} \tag{14.88}$$

The expression of Coulomb interaction is shown as

$$E_{\text{coulomb}} = \text{Tap} \cdot C \cdot \frac{q_i \cdot q_j}{[r_{ij}^3 + (1/\gamma)^3]^{1/3}} \tag{14.89}$$

To sum up, there is no definition of atom type in ReaxFF different from the traditional molecular force field. ReaxFF is a reactive force field based on the elements. There is no need to fix the connectivity of atoms in the input file preparation. ReaxFF is relatively easy to apply. However, the functions in ReaxFF are more complicated than those in traditional force field, so it is much difficult to develop the force field parameters for ReaxFF.

14.2.4.2 Dynamic Calculation Method and Charge Balance Method

To complete the expression of force field function (energy function) of the reaction system means to disclose all governing information for the dynamics of each atom. Therefore, we could calculate the movement of each atom by the basic principles and methods in classical MD. The coordination and the velocity of each atom can be obtained through solving the Newton mechanics equation in the Hamiltonian version.

$$\begin{aligned} H(p_i, r_i) &= \sum_{i=1}^{N} \frac{P_i^2}{2m_i} + U(r_i) \\ \dot{p}_i &= -\frac{\partial H}{\partial r_i} = f_i \\ \dot{r}_i &= \frac{\partial H}{\partial p_i} = \frac{p_i}{m_i} \end{aligned} \tag{14.90}$$

The potential $U(r_i)$ is E_{system} in ReaxFF.

Another important issue is the charge balance because the chemical reaction is involved in the ReaxFF calculation. In the practical chemical reaction process, the atomic charges especially ionic charges could change along with the bonding or breaking of bonds between atoms. Meanwhile, ReaxFF needs to describe the Coulomb force between atoms, which also requires the information of atomic charge change with the atomic movement. In ReaxFF, the charge balance is described independent of the force field function. From the algoristic point of view, the ReaxFF calculation requires the charge changes to be synchronous with the atomic movement. Therefore, the charge distribution on atoms should be updated for each step in the calculation of atomic dynamics. In the practical applications, the Q Equilibration (QEq) method and Electron Equilibration (EE) method are widely utilized in the numerical calculation of real-time atomic charge distribution. Taking the QEq method as an example, the aim is to solve

the following equation and find the optimal solution.

$$\text{Minimize} \quad E(q_1, \ldots, q_N) = \sum_i \left(E_{io} + \chi_i^0 q_i + \frac{1}{2} J_{ii}^0 q_i^2 \right) + \sum_{i<j} (J_{ij} q_i q_j)$$

$$\text{subject to} \quad q_{\text{net}} = \sum_{i=1}^{N} q_i \tag{14.91}$$

In the QEq method, the charge distribution is calculated to achieve the minimum electrostatic energy of the entire system for each step in the dynamics process based on the systemic constant net charge.

ReaxFF is a molecular simulation method based on the classical molecular simulation method but qualified to describe the chemical processes. By introducing BO and its functions, the connectivity of atoms could be determined by the distance between the atoms. It has been proved that ReaxFF could be applied conveniently in biological systems.

14.3 The Scientific Problems in Biological Effects of Nanomaterials Studied by Molecular Simulations

In the research of nanomaterial biological effects, most of the critical scientific problems are around the molecular mechanism of the microeffects of nanomaterials to the biological systems. On the molecular and atomic level, multiscale molecular simulation methods could compensate the detection limit of experimental measurements to support the detailed molecular interactions and intrinsic mechanisms without the disturbances from external experimental conditions and measurement techniques themselves. The key characteristics of interaction between nanomaterials and biological systems have been successfully investigated by the multiscale molecular simulation methods mentioned earlier. We focus on some of the key scientific problems as interaction process, interaction mode, binding stability, conformation change, and electric transition in the following subsections.

14.3.1 Interaction Process

Interaction process is the basic information of the interaction between nanomaterials and biological systems. Based on the binding/adsorption interaction processes, many important applications can be developed, including Nanomaterials synthesis regulation, Encapsulation, Nanomaterials modification, and Manipulation. Molecular simulation theoretical methods build up simulation system on atomic and molecular level, which are widely used to deal with the molecular details in the interaction process between nanomaterials and biomolecules.

Classical MD simulation is able to record the dynamic interaction process of nanomaterials and biomolecules along with the time evolution. In our previous

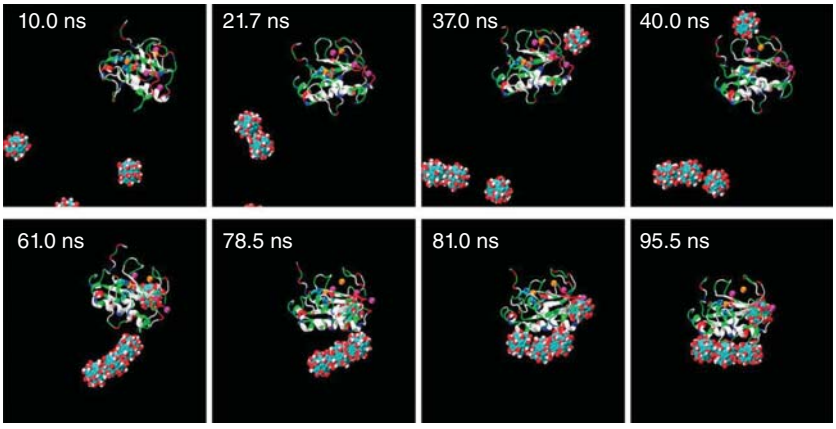

Figure 14.2 Characteristic snapshots of the simulation interaction process of $Gd@C_{82}(OH)_{22}$ binding to MMP-9 [28].

work (Figure 14.2), it is a clear interaction process of four $Gd@C_{82}(OH)_{22}$ NPs binding to matrix metalloproteinases-9 (MMP-9) step by step [28]. The interaction details are reserved in trajectory results, which can be rebuilt and analyzed for all spatial information. The carbon-based NPs could also interact with nucleotide strongly. In the binding process of C_{60} to double-strand DNA (dsDNA), C_{60} NPs show great preference for the hydrophobic ends and the minor groove of the nucleotide [29]. More detailed binding preferences can be achieved by classical MD analysis for the interaction between C_{60} and dsDNA as well as RNA [30].

Besides the particle nanomaterials binding to biomolecule, the process of protein adsorption on nanomaterial surface can also be simulated by the classical MD method [31]. By learning the adsorption behaviors of antibody on the silicon nanosurfaces with different modifications, the mechanism revealed that the different water pockets formed near the nanosurfaces directly influence the antibody adsorption degree. Moreover, the antibody would lose its activity when the adsorption increases. As a result, on the ultrananocrystalline diamond surface, the antibody can maintain the activity because of the reduced adsorption interaction.

14.3.1.1 Nanomaterial Synthesis Regulation

Based on the mechanism of protein adsorption on nanosurfaces, one can develop the biomolecule-assisted synthesis of nanomaterials with programmable shape, structure, and properties [32]. In this process, classical MD simulations support the molecular details of the peptide adsorption on platinum surface, Pt (100) and Pt (111) surfaces, and find that the peptides tend to adopt a predictable conformation on the platinum surface and demonstrated the peptide recognition behavior.

14.3.1.2 Encapsulation

Similarly to the protein adsorption to the exterior surface of nanomaterials, the interactions between protein and inner surface of nanomaterials are studied by the

classical MD method for encapsulation application. The collagen-like peptide [33] and globular protein [34] can encapsulate into carbon nanotubes (CNTs) spontaneously. The diameters and chiral of CNTs could affect the globular protein [35] and alpha-helical peptide [36] encapsulation processes.

14.3.1.3 Nanomaterials Modification

On the contrary of protein encapsulation into nanomaterials, nanomaterials could enter the large biological system, such as cell membrane, to cause the biotoxicity. The uptake process of CNTs into lipid bilayer cell membrane could be adjusted by polyethyleneglycol (PEG)-functionalized nanomaterial modification [37]. It shows that the penetration depth and speed could be controlled by PEG-modified CNTs. At the same time, the PEGs could greatly decrease the adhesion energy between CNTs and the lipid membrane.

14.3.1.4 Manipulation

The interaction processes mentioned earlier are all spontaneous, while the steered dynamics process is another important application for manipulation of nanomaterial. CNTs can be built as a probe to manipulate ubiquitin on the graphene surface [38]. The prior condition and pulling strategy could be studied by classical MD and steered MD simulation methods for protein manipulation by CNT tips.

14.3.2 Interaction Modes

Interaction modes could be analyzed from the specific binding sites between nanomaterials and biomolecules, which are extremely important for the design of nanomedicine delivery and targeting detection.

Nowadays, there are two kinds of nanomaterials interested in biological effects research. One is the carbon-based nanomaterials, and the other is the noble metallic nanomaterials. Firstly, the carbon-based nanomaterials, such as fullerene, CNT, graphene, and their derivatives, have attracted many efforts to study their toxicity and biocompatibility. The molecular simulation methods have been verified to be effective in the interaction modes and interaction mechanisms of fullerenes and CNTs on the ion channel proteins [39, 40]. When CNTs enter the blood circulation system, they can be adsorbed by different serum proteins, which reduce their cytotoxicity [41]. Figure 14.3 indicates the competitive adsorption details of different serum proteins onto CNT surface. From classical MD quantitative analysis, the $\pi-\pi$ stacking interaction mode is critical for determining the protein adsorption capacity. At the same time, the protein/CNT adsorption is size-dependent. In the same hydrophobic core site of Ca^{2+}-bound calmodulin (CaM) protein, CNTs (4,4), (5,5), (6,6), and (7,7) could bind but with different binding stabilities [42]. When CNTs are delivered into the cells, it is necessary to learn the interaction mode between CNTs and phospholipids of the cell membrane [43]. The phospholipids absorb on CNTs with their hydrophobic chains. While their polar groups still stay in the aqueous

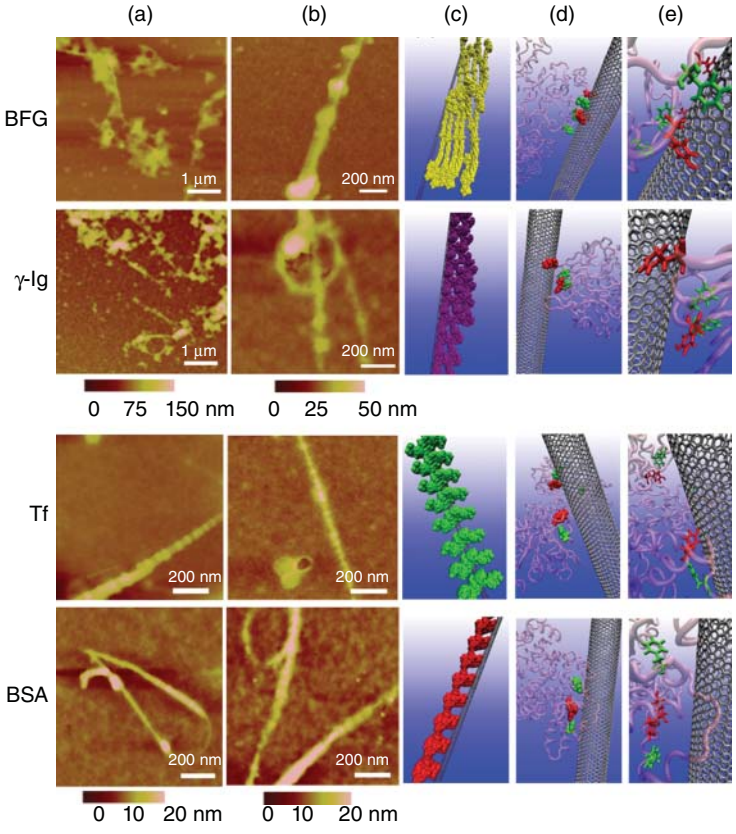

Figure 14.3 Interactions between BFG, Ig, Tf, BSA, and SWCNTs. (a,b) AFM images of proteins after incubation with SWCNTs for 10 min and 5 h. (c) Molecular modeling illustrations for proteins binding to SWCNTs after incubation d,e Locations and the interaction details of the most preferred binding sites on proteins for SWCNTs [41].

solution. A similar interaction mode can be found between phospholipids and graphene and graphene oxide [44]. In the encapsulation of peptide inside CNT as mentioned in the previous subsection, the van der Waals interaction contributes to the inserting process, while the major resistance comes from the repelling of water molecules and the hydrogen-bond breaking among the water network around the peptide [33]. Generally, the interactions between carbon nanomaterials and biomolecules are mainly driven by hydrophobic interaction [45–47], pi–pi interaction [48, 49], and so on. For some derivatives of carbon-based nanomaterials, the electrical interaction and hydrogen bond [50] also contribute to the bio–nano interaction mode. It is promising to develop the novel nanomedicine delivery system based on the typical interaction modes between carbon nanomaterials and biomolecules.

Secondly, the noble metallic nanomaterials, such as Au and Ag, have been widely studied in the biological effects for their fluorescent stability and precise quantitation. The interaction modes can be different when peptides adsorb on Au and Ag surfaces [51]. The adsorption conformations of peptides on Au surface are flat, while the conformations are 3D and in great variety on Ag surface. Taking a close look at the molecular details, there are direct interactions between peptide and Au surface, while there are solvent-mediated interactions between peptide and Ag surface. By using replica exchange with solvent tempering (REST) MD simulations, recognition principles of peptides on Au surface can be learned as enthalpically driven or entropically driven [52]. In this way, the anchored residues of the peptides could be predicted. The adsorption of protein onto Au surface is more complicated than that of peptide. For BSA absorbed on the surface of Au NPs, the interaction mode is specified as Au–S bond chemical adsorption by combination of steered MD simulations and experiments [53]. For the two kinds of Au NPs, the citrate stabilized spherical Au NPs and the CTAB-stabilized spherical Au NPs, BSA binds on the Au NP surface with different interaction modes and totally different binding orientations by molecular docking method analysis [54]. So, it is clear to know that modified Au NP surfaces can invoke different interaction modes and different adsorption behaviors of protein. The hydrophobic, hydrophilic, or amphipathic residues in cytochrome C play different roles in the adsorption on to modified Au NP surfaces [55]. The specific interaction modes between noble metals and biomolecules inspire us to develop the targeting detection system.

Furthermore, some interaction modes relate to the electric transitions beyond the aforementioned intermolecular interaction modes. In combination with classical MD simulation, the first-principle calculation methods, such as DFT, play an important role in investigating the electronic properties during the interactions between nanomaterials and biomolecules. When amino acids adsorb on CNTs, they could adjust the electric structure and electric transport of CNTs through DFT and nonequilibrium Green's function (NEGF) calculations [56]. The chemical adsorption could also be studied by DFT calculation method. When proline interacts with the Au NP surface, there is charge transition [57], which means the interaction mode is partially covalent. Because nucleic acid bases are full of charges, the electric transition is concerned when they interact with nanomaterials, such as the interaction between guanine and fullerenes [58]. Also, different nucleic acid bases exhibit various abilities to adsorb onto CNTs. The guanine could form the strongest interaction with CNT [59]. Besides the guanine, the thymine monomer is focused for its electric transition with CNT, which serves as one of the fundamental studies about DNA/CNT interaction mode [60]. Additionally, the DNA/CNT arrays are studied on the electric transition and its transition mechanism by classical MD combined quantum mechanical simulations [61].

14.3.2.1 Nanomedicine Delivery

Based on the typical interaction modes between nanomaterials and biomolecules, some nanomedicine designs have been proposed to provide defense against critical diseases. The fullerenes derivatives could specifically bind to the HIV-1

protease [62]. Because the fullerene derivatives bind to the original active site of HIV-1, they are predicted to inhibit the activity of HIV-1 protease. Later, several optimal fullerene derivatives have been designed as potential effective inhibitors of HIV by using molecular docking simulations in combination with classical MD simulations [63–67]. Similarly to fullerenes derivatives, CNTs were also investigated as an inhibitor of HIV protease by molecular simulation methods [68, 69].

Tumor is another lethal disease, and MMP is considered as one of the anticancer pathways. In the classical MD simulation of the interaction between $Gd@C_{82}(OH)_{22}$ and MMP-9, $Gd@C_{82}(OH)_{22}$ could specifically bind near the ligand-specificity loop of MMP-9 and inhibit the activity of protein. Therefore, $Gd@C_{82}(OH)_{22}$ NPs work as a potential anticancer medicine [28]. Additionally, it is found that $Gd@C_{82}(OH)_{22}$ also could distract the original binding ligand from SH3 domain [70]. $Gd@C_{82}(OH)_{22}$ NP inhibitor has high specific binding ability to the active part of SH3 domain. Alzheimer's disease is related with the abnormal aggregation of the Aβ peptide. The conformations of Aβ (16–22) octamers are simulated in the absence and presence of CNT by performing extensive replica-exchange molecular dynamics (REMD) method. The results show that CNTs inhibit the β-sheet formation and disturb the prefibrillar β-sheet stability. This brings a light on the cure of Alzheimer's disease by the evidence of CNT inhibiting Aβ fibrillation [71].

Beyond the carbon-based NP nanomedicine, the noble metal–peptide complex is promising to be developed as novel molecular metallic medicine. Au_{25} cluster–tridecapeptide complex induces the tumor cell apoptosis by targeting and suppressing the TrxR1 activity in cytoplasm [72]. At the same time, the Au-based nanomedicine can be traced as a fluorescent nanoprobe.

14.3.2.2 **Targeting Detection**

From the earlier discussion, Au cluster–peptide complex possesses dual function as both targeting nanomedicine and targeting detector. Au cluster–peptide complex is qualified to targeting detection because of their fluorescent stability and precise quantitation. The sensitivity of Au cluster–peptide complex makes it possible to apply the targeting complex in early diagnosis of lethal diseases. Integrin is an ideal molecular biomarker for tumor and thrombosis. The optimized Au cluster–peptide complex can be designed as the nanoprobe to specifically detect $\alpha_{IIb}\beta_3$ integrin by DFT and classical MD simulation methods [73]. Combined with experimental verification, it is prospective to develop the molecular simulation design of nanoprobes to various targeting proteins as a methodology. This study direction is promising to develop for its scientific importance.

14.3.3
Binding Stability

Once nanomaterials contact biomolecules and bind together, the binding stability is another concerned basic scientific problem. Especially, in the

nanomedicine delivery and targeting detection applications, the binding stabilities of nanomedicine and nanoprobe are both the most important factors for the efficiencies of cure and diagnosis. There are some technical parameters that help in understanding the binding stability of nanomaterials/biomolecules complex systems, including minimum distance, contact atom number/contact surface area, and free-energy analysis. These biophysical features can be achieved by molecular simulation approaches.

14.3.3.1 Minimum Distance between Nanomaterials and Biomolecules

The relative locations of nanomaterials and biomolecules can be reflected by the minimum distance between nanomaterials and biomolecules during their diffusion process [48]. When the minimum distance reaches a stable value and maintains the value in a long period, the nanomaterials contact the surface of biomolecules and bind together with a high binding stability.

14.3.3.2 Contact Atom Number/Contact Surface Area

The contact atom number and contact surface area could also indicate the binding stability of nanomaterials and biomolecules quantitatively [48, 53]. The stable large contact atom number or contact surface area is the guarantee for the stable binding behavior in the nano/bio interface. It is necessary to note that the increase in the contact surface area could reflect not only the binding process but also the deformation of biomolecules [49].

14.3.3.3 Free-Energy Landscape

Generally, the binding stability can be represented by measuring the system energy before and after the binding process. The free energy can be calculated by investigating the potential of mean force (PMF) [34]. In the process of pulling proteins out of the CNT, the increasing PMF indicates that the encapsulation conformation is prior in energy. In CNT/DNA complex system, the free-energy landscape can specify the typical binding conformations and their binding abilities by REMD simulations [74]. The binding energies of C_{60} to DNA have been calculated to contrast different binding sites of C60 on DNA [29]. In the regulation of fullerenols on actin polymerization, the binding modes and binding stability of two kinds of fullerenols can be compared through analyzing the binding free-energy landscapes [75].

14.3.4 Conformation Change

The conformation of biomolecule directly decides its function. In the nanomedicine inhibition mechanisms, one pathway is to block the active site of biomolecule, the other one is to change the conformation of biomolecule, which makes the biomolecule lose its normal physiological function. Thus, the conformation change of biomolecule is one of the most important scientific

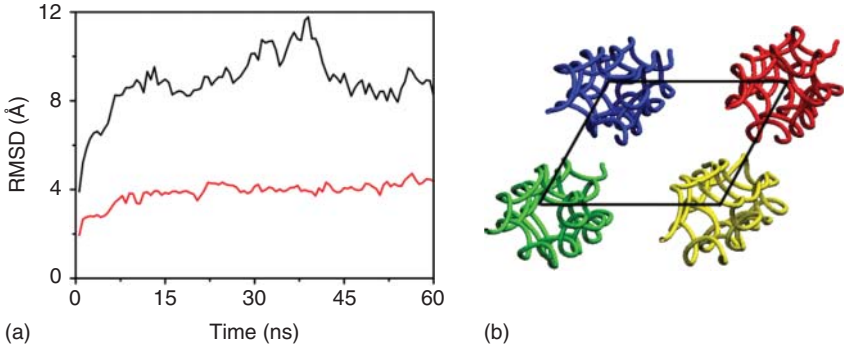

Figure 14.4 (a) RMSD of the backbone of the whole four-triplex bundle with reference to the initial conformation in Tetramer-0 (black), and Tetramer-Gd (red) systems. (b) Initial conformation of the four collagen triplexes [50].

problems in biological effects of nanomaterials. The conformation change of biomolecule can be conveniently observed by molecular simulations in molecular details. The technical parameters, root mean square deviation (RMSD) and root mean square fluctuation (RMSF), could present the conformation change of biomolecules directly.

By RMSD and RMSF analysis, the impacts on collagen molecules have been analyzed under the interactions of two kinds of fullerene derivatives: $C_{60}(OH)_{24}$ and $Gd@C_{82}(OH)_{22}$ [50, 76]. Both nanoparticles can facilitate the collagen triplexes assembly as the "fullerenol-mediated bridge" (Figure 14.4). Additionally, from the conformation change results of collagen molecules, $Gd@C_{82}(OH)_{22}$ behaved more effectively than $C_{60}(OH)_{24}$ because of its negative charge and evenly distributed hydroxyl groups.

The abnormal aggregation of Aβ peptide is critical for Alzheimer's disease. The conformation change (aggregation) of Aβ (16–22) peptide can be inhibited by fullerenes through the REMD simulations [77]. From the deformation analysis, the C_{60} fullerenes can greatly inhibited the beta-sheet formation at high concentration, and C_{180} fullerenes have unexpected stronger inhibitions. While in the nucleotide system, the structure of biomolecule is disrupted under C_{60} interaction [30]. For single-strand DNA, the structure could be deformed by the binding of C60. As for A-form double-strand DNA, C_{60} could penetrate into the double helix and occupy the damaged sites stably [29].

The noble metallic nanomaterials also could deform the biomolecules. When BSA adsorbed on AuNP, the protein would change its conformation badly. The conformational change occurred not only in the Au–S bond formation process, but also continually to form an extended contact surface area. In the simulations, α-helices have been observed into unfolding secondary structures, which supported the corresponding experiment data strongly [53]. In the AuNP uptake into DMPC bilayer process, the local membrane configuration and fluidity would be affected by AuNP [78]. The lipids near AuNP are impacted to disorder

and decreased thickness with a high degree. These nearby lipids tend to form a complex with AuNP, and they move with AuNP slowly.

14.3.5 Chemical Reaction

The scientific problems mentioned earlier almost concern the unbond interactions. However, nanomaterials have large specific surface area and their surficial molecules and atoms are quite active. The electric transitions possibly occur on the nano/bio interface when nanomaterials interact with biomolecules. QM/MM method is proposed to deal with the local chemical reaction in the biological system. Nowadays, this hybrid method is successfully applied in reaction dynamics of the active center in enzymes. During the reaction process, both the electronic transitions and the protein structure changes could be effectively learned. The results help us to better understand the properties and functions of enzymes [79, 80]. QM/MM method is powerful in the reaction mechanism study with the protein structure prediction and the free-energy calculation [81]. Based on the results of docking and classical MD simulations, QM/MM is used to explore the catalyzing process, and the intermediates and transition states in dinuclear Zn-containing enzyme [82]. When nanomaterials invoke electronic transitions in active sites of enzymes or other proteins, QM/MM method is able to solve the reaction mechanism with its advantages in considering the electronic transitions, protein structure changes, and the environmental effects together. Therefore, it is a promising method for reaction mechanism study on nanomaterials/biomolecules interface.

When the chemical reactions extend to much broader distribution other than being localized in the active center of an enzyme, the reactive MD method is a suitable approach to meet the challenge. ReaxFF is a force field for large-scale reactive systems, which has successfully solved the damage mechanism of free radicals to biomolecules. The electric transitions could be specified in detail (Figure 14.5) [83]. The randomly distributed clusters of diatomic OH radicals could damage DNA by attacking the sugar rings. The holes in sugar moiety grow up between the bases and backbone of DNA, which could cause DNA single- and double-strand break [26]. In the interaction of O and OH radicals with lipids, the O and OH radicals most typically abstract a H atom from the fatty acids and change the general lipid composition of the skin [84]. By ReaxFF simulations, the radicals of OH, O, O_3, and H_2O_2 can break structurally important bonds of peptidoglycan, which could support the destruction mechanism of the bacterial cell wall [85, 86]. Many nanomaterials have been confirmed could generate free radicals after they enter the biological environment. In the biological system, the OH, HO_2, and H_2O_2 travel deeply into the liquid layer [87]. The phenomenon guarantees that the free radicals invoked by nanomaterials could reach the biomolecules and induce additional damage. This brings a new insight into the study of nanomaterial cytotoxicity (biological effect) by ReaxFF method. The fundamental knowledge is promising to be revealed in this molecular simulation strategy.

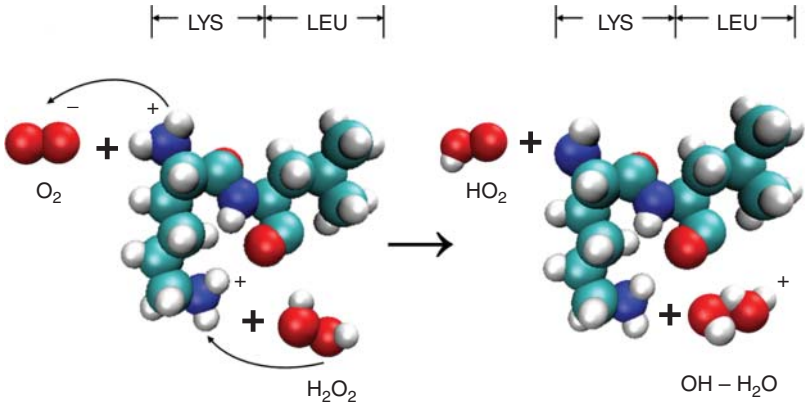

Figure 14.5 The electric details during the transitions [83].

14.4 Summary and Outlook

In the nanomaterial biological effect investigation, molecular simulation methods build the interaction system consisting of nanomaterials and biomolecules on atomic or electrical level without the microscale limits of experimental techniques. Moreover, molecular simulation methods change key variables of the complex system conveniently, which is easy to optimize interaction conditions for bioeffective applications. By controlling the environmental conditions of nano/bio complex system, molecular simulation methods could disclose the atomic or electrical interaction mechanism and provide the fundamental biophysical knowledge. We focus on four molecular simulation methods that are effective for the study of nanomaterial biological effects, as classical MD, DFT, QM/MM, and ReaxFF methods. These multiscale theoretical methods are competent to deal with the scientific problems concerned with the nanomaterial biological effect study, interaction process, interaction mode, binding stability, conformation change, and chemical reaction, together with the auxiliary molecular techniques, such as molecular docking. Among the nanomaterial biological effect applications, targeting nanomedicine delivery and nanoprobe detection are the most significant for the effective cure and early diagnosis of lethal diseases. Molecular simulation methods are very promising in the nano targeting complex design and targeting insight interpretation difficult to obtain otherwise. With the increasing computation speed, more complicated interaction systems and more accuracy interaction details are expected reasonably in the future.

Acknowledgments

This work was financially supported by the National Key Basic Research Program of China (Grants 2013CB932703, 2013CB933704) and the National Natural Science Foundation of China (Grants 11404333, 31571026).

References

1. Nel, A.E., Maedler, L., Velegol, D. *et al.* (2009) Understanding biophysicochemical interactions at the nano-bio interface. *Nat. Mater.*, **8** (7), 543.
2. Chowdhury, E.H. and Akaike, T. (2005) Bio-functional inorganic materials: an attractive branch of gene-based nanomedicine delivery for 21st century. *Curr. Gene Ther.*, **5** (6), 669.
3. Baca, H.K., Carnes, E., Singh, S. *et al.* (2007) Cell-directed assembly of bio/nano interfaces – a new scheme for cell immobilization. *Acc. Chem. Res.*, **40** (9), 836.
4. Pelaz, B., Charron, G., Pfeiffer, C. *et al.* (2013) Interfacing engineered nanoparticles with biological systems: anticipating adverse nanobio interactions. *Small*, **9** (9-10), 1573.
5. Zhao, Y.L., Xing, G.M., and Chai, Z.F. (2008) Nanotoxicology: are carbon nanotubes safe? *Nat. Nanotechnol.*, **3**, 191.
6. Chiti, F. and Dobson, C.M. (2006) Protein misfolding, functional amyloid, and human disease. *Annu. Rev. Biochem.*, **75**, 333.
7. MacKerell, A.D., Bashford, D., Bellott, M. *et al.* (1998) All-atom empirical potential for molecular modeling and dynamics studies of proteins. *J. Phys. Chem. B*, **102** (18), 3586.
8. Karplus, M. and McCammon, J.A. (2002) Molecular dynamics simulations of biomolecules. *Nat. Struct. Biol.*, **9** (9), 646.
9. Brooks, B.R., Brooks, C.L. III,, Mackerell, A.D. Jr., *et al.* (2009) Charmm: the biomolecular simulation program. *J. Comput. Chem.*, **30** (10), 1545.
10. Wood, W.W. (1985) Early History of Computer Simulations in Statistical Mechanics. Los Alamos National Lab., NM(USA), Carroll College, Helena, MT.
11. Metropolis, N., Rosenbluth, A.W., Rosenbluth, M.N. *et al.* (1953) Equation of state calculations by fast computing machines. *J. Chem. Phys.*, **21** (6), 1087.
12. MacKerell, A.D., Feig, M., and Brooks, C.L. (2004) Improved treatment of the protein backbone in empirical force fields. *J. Am. Chem. Soc.*, **126** (3), 698.
13. York, D.M., Wlodawer, A., Pedersen, L.G., and Darden, T.A. (1994) Atomic-level accuracy in simulations of large protein crystals. *Proc. Natl. Acad. Sci. U.S.A.*, **91** (18), 8715.
14. Zhou, R.H., Harder, E., Xu, H.F., and Berne, B.J. (2001) Efficient multiple time step method for use with Ewald and particle mesh Ewald for large biomolecular systems. *J. Chem. Phys.*, **115** (5), 2348.
15. Verlet, L. (1967) Computer experiments on classical fluids. I. Thermodynamical properties of Lennard-Jones molecules. *Phys. Rev.*, **159** (1), 98.
16. Swope, W.C., Andersen, H.C., Berens, P.H., and Wilson, K.R. (1982) A computer-simulation method for the calculation of equilibrium-constants for the formation of physical clusters of molecules – application to small water clusters. *J. Chem. Phys.*, **76** (1), 637.
17. Leach, A.R. (2001) *Molecular Modelling Principles and Applications*, 2nd edn, Prentice Hall, Dorchester, Dorset.
18. SCHRÖDINGER, E. (1926) An undulatory theory of the mechanics of atoms and molecules. *Phys. Rev.*, **28**, 1049.
19. Born, M. and Huang, K. (1954) *Dynamical Theory of Crystal Lattices*, Oxford University Press, New York.
20. Lowdin, P.O. (1959) Correlation problem in many-electron quantum mechanics. 1. Review of different approaches and discussion of some current ideas. *Adv. Chem. Phys.*, **2**, 207.
21. Hohenberg, P. and Kohn, W. (1964) Inhomogeneous electron gas. *Phys. Rev. B*, **136** (3B), B864.
22. Kohn, W. and Sham, L.J. (1965) Self-consistent equations including exchange and correlation effects. *Phys. Rev.*, **140** (4A), A1133.
23. Kang, J., Hagiwara, Y., and Tateno, M. (2012) Biological applications of hybrid quantum mechanics/molecular mechanics calculation. *J. Biomed. Biotechnol.*, **2012**, 236157.
24. Lin, H. and Truhlar, D.G. (2007) Qm/mm: what have we learned, where are we, and where do we go from here? *Theor. Chem. Acc.*, **117** (2), 185.

25. van Duin, A.C.T., Dasgupta, S., Lorant, F., and Goddard, W.A. III, (2001) Reaxff: a reactive force field for hydrocarbons. *J. Phys. Chem. A*, **105** (41), 9396.
26. Abolfath, R.M., van Duin, A.C.T., and Brabec, T. (2011) Reactive molecular dynamics study on the first steps of DNA damage by free hydroxyl radicals. *J. Phys. Chem. A*, **115** (40), 11045.
27. Zhu, R., Janetzko, F., Zhang, Y. *et al.* (2008) Characterization of the active site of yeast rna polymerase ii by dft and reaxff calculations. *Theor. Chem. Acc.*, **120** (4-6), 479.
28. Kang, S.G., Zhou, G.Q., Yang, P. *et al.* (2012) Molecular mechanism of pancreatic tumor metastasis inhibition by $gd@c_{82}(oh)_{22}$ and its implication for de novo design of nanomedicine. *Proc. Natl. Acad. Sci. U.S.A.*, **109** (38), 15431.
29. Zhao, X.C., Striolo, A., and Cummings, P.T. (2005) C-60 binds to and deforms nucleotides. *Biophys. J.*, **89** (6), 3856.
30. Xu, X., Wang, X., Li, Y. *et al.* (2012) A large-scale association study for nanoparticle c60 uncovers mechanisms of nanotoxicity disrupting the native conformations of DNA/RNA. *Nucleic Acids Res.*, **40** (16), 7622.
31. Radadia, A.D., Stavis, C.J., Carr, R. *et al.* (2011) Control of nanoscale environment to improve stability of immobilized proteins on diamond surfaces. *Adv. Funct. Mater.*, **21** (6), 1040.
32. Ramakrishnan, S.K., Martin, M., Cloitre, T. *et al.* (2013) Insights on the facet specific adsorption of amino acids and peptides toward platinum. *J. Chem. Inf. Model.*, **53** (12), 3273.
33. Yu, K., Qi, W., Ying-Chun, L. *et al.* (2008) Dynamic mechanism of collagen-like peptide encapsulated into carbon nanotubes. *J. Phys. Chem. B*, **112** (15), 4801.
34. Kang, Y., Liu, Y.-C., Wang, Q. *et al.* (2009) On the spontaneous encapsulation of proteins in carbon nanotubes. *Biomaterials*, **30** (14), 2807.
35. Yu, K., Qi, W., Ying-Chun, L. *et al.* (2010) Diameter selectivity of protein encapsulation in carbon nanotubes. *J. Phys. Chem. B*, **114** (8), 2869.
36. Zhang, Z.-S., Kang, Y., Liang, L.-J. *et al.* (2014) Peptide encapsulation regulated by the geometry of carbon nanotubes. *Biomaterials*, **35** (5), 1771.
37. Skandani, A.A. and Al-Haik, M. (2013) Reciprocal effects of the chirality and the surface functionalization on the drug delivery permissibility of carbon nanotubes. *Soft Matter*, **9** (48), 11645.
38. Firouzi, M.A.M., Pishkenari, H.N., Mahboobi, H., and Meghdari, A. (2014) Manipulation of biomolecules: a molecular dynamics study. *Curr. Appl Phys.*, **14** (9), 1216.
39. Kraszewski, S., Tarek, M., Treptow, W., and Ramseyer, C. (2010) Affinity of c-60 neat fullerenes with membrane proteins: a computational study on potassium channels. *ACS Nano*, **4** (7), 4158.
40. Park, K.H., Chhowalla, M., Iqbal, Z., and Sesti, F. (2003) Single-walled carbon nanotubes are a new class of ion channel blockers. *J. Biol. Chem.*, **278** (50), 50212.
41. Ge, C.C., Du, J.F., Zhao, L.N. *et al.* (2011) Binding of blood proteins to carbon nanotubes reduces cytotoxicity. *Proc. Natl. Acad. Sci. U.S.A.*, **108** (41), 16968.
42. Gao, J., Wang, L.M., Kang, S.G. *et al.* (2014) Size-dependent impact of cnts on dynamic properties of calmodulin. *Nanoscale*, **6** (21), 12828.
43. Kapralov, A.A., Feng, W.H., Amoscato, A.A. *et al.* (2012) Adsorption of surfactant lipids by single-walled carbon nanotubes in mouse lung upon pharyngeal aspiration. *ACS Nano*, **6** (5), 4147.
44. Tu, Y., Lv, M., Xiu, P. *et al.* (2013) Destructive extraction of phospholipids from escherichia coli membranes by graphene nanosheets. *Nat. Nanotechnol.*, **8** (8), 594.
45. Zuo, G.H., Huang, Q., Wei, G.H. *et al.* (2010) Plugging into proteins: poisoning protein function by a hydrophobic nanoparticle. *ACS Nano*, **4** (12), 7508.
46. De Leo, F., Sgrignani, J., Bonifazi, D., and Magistrato, A. (2013) Structural and dynamic properties of monoclonal antibodies immobilized on cnts: a computational study. *Chem. Eur. J.*, **19** (37), 12281.
47. Zuo, G.H., Kang, S.-G., Xiu, P. *et al.* (2013) Interactions between proteins

and carbon-based nanoparticles: exploring the origin of nanotoxicity at the molecular level. *Small*, **9** (9-10), 1546.

48. Shi, B.Y., Zuo, G.H., Xiu, P., and Zhou, R.H. (2013) Binding preference of carbon nanotube over pro line-rich motif ligand on sh3-domain: a comparison with different force fields. *J. Phys. Chem. B*, **117** (13), 3541.
49. Zuo, G.H., Zhou, X., Huang, Q. *et al.* (2011) Adsorption of villin headpiece onto graphene, carbon nanotube, and c60: effect of contacting surface curvatures on binding affinity. *J. Phys. Chem. C*, **115** (47), 23323.
50. Yin, X., Zhao, L., Kang, S.G. *et al.* (2013) Impacts of fullerene derivatives on regulating the structure and assembly of collagen molecules. *Nanoscale*, **5** (16), 7341.
51. Palafox-Hernandez, J.P., Tang, Z., Hughes, Z.E. *et al.* (2014) Comparative study of materials-binding peptide interactions with gold and silver surfaces and nanostructures: a thermodynamic basis for biological selectivity of inorganic materials. *Chem. Mater.*, **26** (17), 4960.
52. Tang, Z., Palafox-Hernandez, J.P., Law, W.-C. *et al.* (2013) Biomolecular recognition principles for bionanocombinatorics: an integrated approach to elucidate enthalpic and entropic factors. *ACS Nano*, **7** (11), 9632.
53. Wang, L.M., Li, J.Y., Pan, J. *et al.* (2013) Revealing the binding structure of the protein corona on gold nanorods using synchrotron radiation-based techniques: understanding the reduced damage in cell membranes. *J. Am. Chem. Soc.*, **135** (46), 17359.
54. Chaudhary, A., Gupta, A., Khan, S., and Nandi, C.K. (2014) Morphological effect of gold nanoparticles on the adsorption of bovine serum albumin. *Phys. Chem. Chem. Phys.*, **16** (38), 20471.
55. Hung, A., Mwenifumbo, S., Mager, M. *et al.* (2011) Ordering surfaces on the nanoscale: implications for protein adsorption. *J. Am. Chem. Soc.*, **133** (5), 1438.
56. Abadir, G.B., Walus, K., Turner, R., and Pulfrey, D.L. (2008) Effect of single-biomolecule adsorption on the electrical properties of short carbon nanotubes. 2008 8th IEEE Conference on Nanotechnology.
57. Rai, S. and Singh, H. (2013) Electronic structure theory based study of proline interacting with gold nano clusters. *J. Mol. Model.*, **19** (10), 4099.
58. Shukla, M.K. and Leszczynski, J. (2009) Fullerene (c-60) forms stable complex with nucleic acid base guanine. *Chem. Phys. Lett.*, **469** (1-3), 207.
59. Shukla, M.K., Dubey, M., Zakar, E. *et al.* (2009) Interaction of nucleic acid bases with single-walled carbon nanotube. *Chem. Phys. Lett.*, **480** (4-6), 269.
60. Rajarajeswari, M., Iyakutti, K., and Kawazoe, Y. (2011) Adsorption mechanism of single guanine and thymine on single-walled carbon nanotubes. *J. Mol. Model.*, **17** (11), 2773.
61. Lu, G., Maragakis, P., and Kaxiras, E. (2005) Carbon nanotube interaction with DNA. *Nano Lett.*, **5** (5), 897.
62. Friedman, S.H., Decamp, D.L., Sijbesma, R.P. *et al.* (1993) Inhibition of the hiv-1 protease by fullerene derivatives – model-building studies and experimental-verification. *J. Am. Chem. Soc.*, **115** (15), 6506.
63. Zhu, Z.W., Schuster, D.I., and Tuckerman, M.E. (2003) Molecular dynamics study of the connection between flap closing and binding of fullerene-based inhibitors of the hiv-1 protease. *Biochemistry*, **42** (5), 1326.
64. Lee, V.S., Nimmanpipug, P., Aruksakunwong, O. *et al.* (2007) Structural analysis of lead fullerene-based inhibitor bound to human immunodeficiency virus type 1 protease in solution from molecular dynamics simulations. *J. Mol. Graphics Modell.*, **26** (2), 558.
65. Durdagi, S., Mavromoustakos, T., Chronakis, N., and Papadopoulos, M.G. (2008) Computational design of novel fullerene analogues as potential hiv-1 pr inhibitors: analysis of the binding interactions between fullerene inhibitors and hiv-1 pr residues using 3d qsar, molecular docking and molecular dynamics simulations. *Bioorg. Med. Chem.*, **16** (23), 9957.
66. Durdagi, S., Mavromoustakos, T., and Papadopoulos, M.G. (2008) 3d qsar comfa/comsia, molecular docking and

molecular dynamics studies of fullerene-based hiv-1 pr inhibitors. *Bioorg. Med. Chem. Lett.*, **18** (23), 6283.

67. Tzoupis, H., Leonis, G., Durdagi, S. *et al.* (2011) Binding of novel fullerene inhibitors to hiv-1 protease: insight through molecular dynamics and molecular mechanics Poisson-Boltzmann surface area calculations. *J. Comput.-Aided Mol. Des.*, **25** (10), 959.
68. Cheng, Y., Li, D.C., Ji, B.H. *et al.* (2010) Structure-based design of carbon nanotubes as hiv-1 protease inhibitors: atomistic and coarse-grained simulations. *J. Mol. Graphics Modell.*, **29** (2), 171.
69. Meher, B.R. and Wang, Y. (2012) Binding of single walled carbon nanotube to wt and mutant hiv-1 proteases: analysis of flap dynamics and binding mechanism. *J. Mol. Graphics Modell.*, **38**, 430.
70. Kang, S.-g., Tien, H., and Zhou, R. (2013) Metallofullerenol gd@c-82(oh)(22) distracts the proline-rich-motif from putative binding on the sh3 domain. *Nanoscale*, **5** (7), 2703.
71. Li, H., Luo, Y., Derreumaux, P., and Wei, G. (2011) Carbon nanotube inhibits the formation of beta-sheet-rich oligomers of the Alzheimer's amyloid-beta(16-22) peptide. *Biophys. J.*, **101** (9), 2267.
72. Liu, R., Wang, Y., Yuan, Q. *et al.* (2014) The au clusters induce tumor cell apoptosis via specifically targeting thioredoxin reductase 1 (trxr1) and suppressing its activity. *Chem. Commun.*, **50** (73), 10687.
73. Zhao L.N., Zhai J., Zhang X.J. *et al.* (2016) Computational design of peptide-Au cluster probe for sensitive detection of $\alpha_{IIb}\beta_3$ integrin. *Nanoscale.* **8**, 4203.
74. Johnson, R.R., Kohlmeyer, A., Johnson, A.T.C., and Klein, M.L. (2009) Free energy landscape of a DNA-carbon nanotube hybrid using replica exchange molecular dynamics. *Nano Lett.*, **9** (2), 537.
75. Dong Y., Pan H., Xing G.M., Zhao L.N. Fullerenol molecules inhibit the self-assembling of actin by dual mechanism. *unpublished*.
76. Song, Y., Zhang, M.Y., Zhao, L.N. *et al.* (2014) Regulation on mechanical properties of collagen: enhanced bioactivities of metallofullerol. *Nanomedicine*, **10** (4), 783.
77. Xie, L.G., Luo, Y., Lin, D.D. *et al.* (2014) The molecular mechanism of fullerene-inhibited aggregation of Alzheimer's beta-amyloid peptide fragment. *Nanoscale*, **6** (16), 9752.
78. Zheng, F.X., Pan, J., Yin, X.H. *et al.* (2013) Simulation study on gold nanoparticle-cellular membrane complex in endocytosis process. *J. Nanosci. Nanotechnol.*, **13** (6), 3990.
79. Greco, C., Bruschi, M., De Gioia, L., and Ryde, U. (2007) A qm/mm investigation of the activation and catalytic mechanism of fe-only hydrogenases. *Inorg. Chem.*, **46** (15), 5911.
80. Lyne, P.D., Mulholland, A.J., and Richards, W.G. (1995) Insights into chorismate mutase catalysis from a combined qm/mm simulation of the enzyme reaction. *J. Am. Chem. Soc.*, **117** (45), 11345.
81. Ryde, U. (2003) Combined quantum and molecular mechanics calculations on metalloproteins. *Curr. Opin. Chem. Biol.*, **7** (1), 136.
82. Dutta, D. and Mishra, S. (2014) The structural and energetic aspects of substrate binding and the mechanism of action of the dape-encoded n-succinyl-l,l-diaminopimelic acid desuccinylase (dape) investigated using a hybrid qm/mm method. *Phys. Chem. Chem. Phys.*, **16** (47), 26348.
83. Chen C., Liu Y.F., Liu D.X., Zhao L.N., Kong M.G. Reactive molecular dynamics simulation on the mechanism of chemical reactions between plasma ross and Aβ peptides and the synergistic effect of ross. *unpublished*.
84. Jonas Van der, P., Stefaan, A., Adri, C.T.v.D. *et al.* (2013) Interaction of o and oh radicals with a simple model system for lipids in the skin barrier: a reactive molecular dynamics investigation for plasma medicine. *J. Phys. D: Appl. Phys.*, **46** (39), 395201.
85. Yusupov, M., Bogaerts, A., Huygh, S. *et al.* (2013) Plasma-induced destruction

of bacterial cell wall components: a reactive molecular dynamics simulation. *J. Phys. Chem. B*, **117** (11), 5993.

86. Yusupov, M., Neyts, E.C., Khalilov, U. *et al.* (2012) Atomic-scale simulations of reactive oxygen plasma species interacting with bacterial cell walls. *New J. Phys.*, **14** (9), 093043.

87. Yusupov, M., Neyts, E.C., Simon, P. *et al.* (2014) Reactive molecular dynamics simulations of oxygen species in a liquid water layer of interest for plasma medicine. *J. Phys. D: Appl. Phys.*, **47** (2), 025205.

15
Ecotoxicity Analyses of Nanomaterials

Peng Zhang

15.1
Introduction

Nanomaterials existing in the environment include natural nanomaterials and engineered nanomaterials (ENMs). Naturally occurring nanomaterials (e.g., clays and minerals) that are generated in the geological and biological process have been in the environment since the history of the earth, while the investigation of ENMs started only several decades ago. Increasing body of literature has reported the potential adverse effects of ENMs to the environment and human health. ENMs are inevitably released into the environment through different pathways including air, soil, and water during their production, transportation, application, and disposal. Several case studies indicate that TiO_2 and Ag NPs in paints on buildings were emitted and released into the environment as urban runoff [1, 2]. Washing of textiles can also make the Ag NPs fall off and release into domestic wastewater [3, 4]. In addition to their potential effects to a certain living organism, ENMs may transport for a long distance in the environment and potentially bring negative impacts on the whole ecosystem.

One of the important issues researchers are concerned about is the prediction of the concentration of ENMs that have been accumulated and will be discharged into the environment and link the concentration to its possible ecotoxicological effects [5]. However, to quantify the concentration of ENMs is difficult, mainly because it is related to various factors including production, application and release volume, physicochemical properties, background concentration, translocation, and transformation of ENMs. ENMs can directly enter into the terrestrial environment as fertilizer additives [6], crop protection products [7], or biosolids [8]. They may also enter into the aquatic environment through industrial discharge, wastewater effluents, or surface runoff from soils. ENMs may also enter into air with the discharge of exhaust gas from automobiles and factories. These processes make the prediction of ENM concentrations very complicated. On the other hand, it is almost impossible for ENMs to retain their pristine physicochemical properties in the environment, but undergo a

Toxicology of Nanomaterials, First Edition. Edited by Yuliang Zhao, Zhiyong Zhang, and Weiyue Feng.

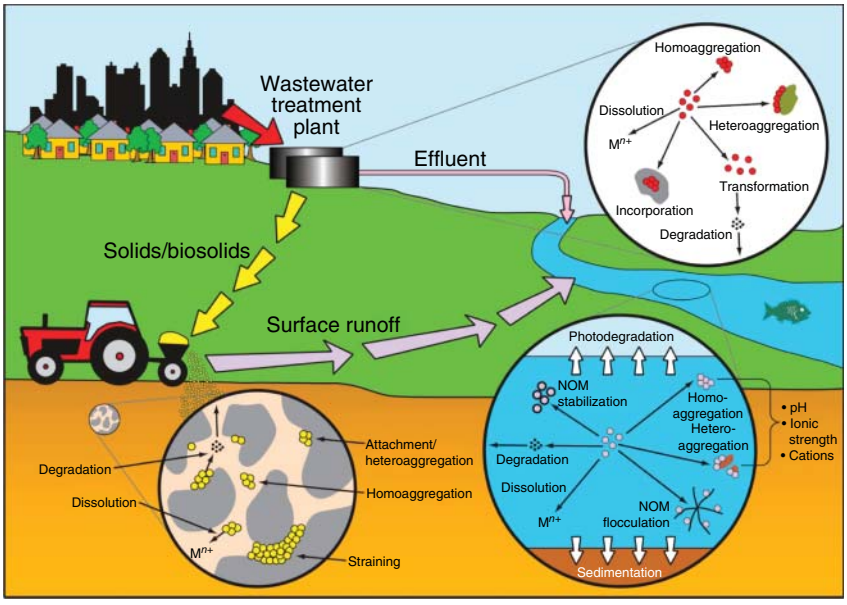

Figure 15.1 Pathway and transformation of nanomaterials in the environment. (Reprinted with permission from [11].)

number of potential transformations instead, such as dissolution, agglomeration, aggregation, oxidation, reduction, and surface modification [9]. ENMs with different physicochemical properties may transform to different forms and extents, which make its behavior and fate more complicated. Most importantly, these transformation processes may affect and determine the toxicity of ENMs to living organisms. Typical release pathway and transformation of ENMs in the environment are illustrated in Figure 15.1 [11] and discussed therein after.

15.2 Transformation of ENMs in the Environment

The current research predominantly focuses on the behavior and toxicity of "as-manufactured" ENMs. Unfortunately, it is almost impossible that ENMs can retain their original form and physicochemical properties after production and introduction into dynamic environmental systems. Even in a stock solution, the properties of ENMs may be changed due to the ready release of metallic ions, consequently resulting in the alteration of its toxicity [12]. High surface area and reactivity of ENMs make it more dynamic in the environment than traditional contaminants. Once entering into the environment, various physical, chemical, and biological transformations of ENMs could occur, depending on

the intrinsic properties of ENMs and the ambient environment. Several reports have proved that the toxic effects of ENMs (e.g., CeO_2 and Ag NPs) are related to the transformation and modulated by the transformation processes [13–16]. In some cases, toxicity of ENMs may be enhanced by these transformations, but in other cases, toxicity may be reduced [17]. Therefore, comprehensive investigation of the transformation process of ENMs is essential to assess and understand the mechanism of the effects of ENMs on environmental organisms.

Aggregation is a typical physical transformation process for all the ENMs in natural environment. Physical interaction of ENMs with inorganic ions, natural organic matters (NOMs), biomolecules, soil particles, and natural colloids may induce both heteroaggregation and homoaggregation. Homoaggregation is caused by the direct interactions between nanoparticles, which are triggered by the compression of the double electric layers on the particle surfaces. This aggregation makes the nanoparticles grow into large particles and clusters. Heteroaggregation between nanoparticles and natural components such as soil particles makes the nanoparticles a part of and also behave as soil particles. Both forms of aggregation will decrease the mobility of ENMs and make it more persistent in the environment. Aggregation also decreases the bioavailability of NPs in living organisms and consequently affects the toxicity. For example, the diameter of the pores in the cell walls of living plant cells is only 3.5–6 nm, which is a natural barrier to limit the entering of external substance with large size into plant cells [18]. Physical interactions of ENMs with environmental components such as NOMs may prevent aggregation and increase the mobility by modifying the properties of a particle surface [19, 20]. This process may increase the bioavailability and toxicity of nanoparticles in living organisms [21].

Dissolution is the most concerned chemical transformation when investigating the toxic mechanism of metal-based ENMs (e.g., Ag, Zn, Cu, and rare earth elements). One possible and widely accepted origin of the toxicity of metal-based ENMs is the release of toxic metal ions. Dissolution is always accompanied by other chemical processes including redox reaction, sulfidation, phosphorylation and complexation [10, 14, 22, 23]. Copper NPs may be oxidized under environmental conditions and a layer of oxide coating formed on the surface can reduce further oxidation and dissolution [24]. Oxidation is also required for the release of Ag^+ ions from Ag NPs [25]. CNTs can be oxidized and carboxylated by hydroxyl radicals, which are produced by horseradish peroxidase [26]. On the contrary, interactions with plant root exudates, which contain large amount of organic acids and reducing substances (e.g., phenols), can induce the reduction of CeO_2 NPs and the release of Ce^{3+} ions [10]. Graphene oxides were reduced when incubating with bacteria via the respiration activities of bacteria [27]. Bacteria can even digest and use the polymer coatings on the nanoparticle surface as carbon resources [28]. All of these transformation processes may readily occur in the environment and biological systems; consequently, the physicochemical properties, behavior, and effects of ENMs will be greatly affected and even determined by these processes.

15.3 Toxicity of ENMs in Terrestrial Ecosystem

15.3.1 Microorganisms

Microorganisms are ubiquitous in the earth and living organisms and account for half of the earth's biomass, playing a critical role in material cycle, energy flow, and ecological balance. They are positioned at the base of the food web, where they drive most biogeochemical cycles and the so-called ecosystem services. Recently, many novel ENMs with antibacterial properties have been designed intentionally [29–32]. However, these novel ENMs are also double-edged swords and may affect the growth and community of microorganism in the environment despite of its beneficial applications. The high ecological importance and ease of culture have made bacteria the foci of nanoecotoxicity studies. A recent review outlined five reasons to use bacteria as a subject when assessing the environmental hazards and fates of ENMs [33], which are as follows: ENMs may reduce the diversity of bacterial community; ENMs can alter bacterial physiology and thus nutrient cycling; bacteria affect ENM physical characteristics and partitioning; bacteria may degrade ENMs; bacteria can initiate ENM trophic transfer to higher level organisms. Various bacteria models have been used in nanotoxicity studies including *Escherichia coli*, *Staphylococcus aureu*, *Bacillus subtilis*, *Enterococcus faecalis*, *Pseudomonas aeruginosa*, *Shewanella oneidensis*, and *Nitrosomonas europaea* [34]. Fungi such as *Saccharomyces cerevisiae*, *Antrodia serialis*, and *Phellinus viticola* were also used to assess the ecotoxicity of ENMs [35]. *E. coli* is the most commonly used bacteria model in nanotoxicity studies because its backgrounds of basic biology and molecular genetics have been well understood. Effect of ENMs on bacteria can be assessed by measuring the different endpoints of bacterial growth and population [36]. These endpoints include direct measurement of cell number in a liquid medium or solid mass (e.g., turbidity, microscopic counting) or indirect measurement of the endpoints, which are proportional to live or dead cell membranes (e.g., MTT assay, live/dead cell staining). Molecular biological techniques such as DGGE (denaturing gradient gel electrophoresis), T-RFLP (terminal restriction fragment length polymorphism), and ARDRA (amplified ribosomal DNA restriction analysis) are always used to assess the alteration of bacterial community. Generally, culture of bacteria in nanotoxicity studies can be divided into two groups: monoculture of single bacterial string and culture of natural bacterial isolates. The latter would be more close to the natural conditions where the ENMs interact with bacteria; however, the drawback is such a model system lacks the ability to explore the toxic mechanism.

Although the microorganism species and model vary a lot, there are some general mechanisms that can be used to explain the toxicity of ENMs to bacteria. NP-induced reactive oxygen species (ROS) production is one of the most important reasons involved in the toxicity of ENMs [37]. Nakamura and Mashino [38] reported that C_{60}-bis(*N*, *N*-dimethylpyrrolidinium iodide), a C_{60} derivative,

exhibited excellent antimicrobial effect by producing ROS, which could inhibit the respiratory chain. Under UV light exposure, some ENMs can produce ROS and increase its antibacterial properties. Wiesner and coworkers compared the photoactivity and antibacterial properties of C_{60} fullerenes and TiO_2 NPs [39]. The toxicity of TiO_2 NPs to *E. coli* was primarily attributed to its photochemical properties (mainly by producing superoxide). However, in contrast, toxicity of C_{60} was not solely due to the ROS production, since the toxicity of C_{60} showed no correlation with light exposure. THF/nC_{60} showed a strong toxicity regardless of light while no significant amount of ROS was detected [40]. Fullerol produced ROS, but the quantity was not sufficient to induce a significant toxic effect to bacteria [41]. Li *et al.* [42] studied the ROS generation kinetics of seven metal oxide NPs under UV radiation. TiO_2 NPs and ZnO NPs showed the strongest ability to generate ROS including superoxide radical, hydroxyl radical, and singlet oxygen. Subsequent toxicity tests suggested that there was linear correlation between the survival rates of *E. coli* cells, which were exposed to NP suspension under UV irradiation and the average concentration of generated ROS ($R^2 = 0.84$).

Dissolution and the release of toxic metal ions are an important factor that results in the toxicity of metal-based ENMs. A most studied and commercially used ENMs is Ag NPs due to its unique antibacterial properties. The association of release of Ag^+ from Ag NPs and its toxicity to bacteria have been evidenced by many studies. Xiu *et al.* [43] demonstrated that the toxicity of Ag NPs to *E. coli* directly correlated with the released Ag^+ concentration under both aerobic and anaerobic conditions, no matter what size and surface coating of the Ag NPs were. Reinsch *et al.* [44] provided an indirect evidence for the ion-related toxicity of Ag NPs. They sulfurized the as-prepared Ag NPs to varying degrees by exposing the Ag NPs to Na_2S solution with different Ag/S ratios. Monodispersed Ag NPs were fully transformed to Ag_2S with time. A higher Ag_2S/Ag^0 ratio in the sulfurized nanoparticles reduced the release of Ag^+ ions and consequently reduced the toxicity of Ag NPs to *E. coli.* Such ion-related toxicity is also involved in the interaction of bacteria with ZnO, CuO, quantum dots, and rare earth oxide (REO) NPs [45–48]. As described earlier, it is certain that ion release is related to the toxicity of ENMs. Therefore, quantitative analysis of the released ions during the NP–cell interaction is crucial to elucidate the relationship between the ions and toxicity. A widely adopted method for this is first to separate the released ions from NPs in the culture solutions with or without cells by centrifugation or filtration and then to analyze the ion concentrations by ICP-MS [49]. However, this method overlooks the fact that part of the released ions may absorb on the particles or cells and cannot be easily separated. He *et al.* [48] evaluated the dissolution of REO NPs (La_2O_3, Gd_2O_3, and Yb_2O_3) after incubation with *E. coli* using two different methods, ICP-MS and XAS. For ICP-MS, the mixtures were centrifuged and the ion concentrations in the supernatant were determined. As for XAS, the samples were prepared only by freeze-drying the whole cultures without separation. Compared with the ICP-MS measurements, XAS analyses reported much more dissolution of REO NPs. This can be explained by two reasons: first, RE ions have high affinity with phosphates and carboxyl groups in bacterial cell wall,

and most of the dissolved RE^{3+} were bound to the cell wall components. Second, part of the dissolved ions were adsorbed on the surface of particles and removed together with particles during the centrifugation process. The authors suggested that XAS could be a unique technique to determine the real extent of dissolution of metal-based ENMs in organisms and cell cultures and thus advance the mechanic understanding of ENMs toxicity.

ENMs may also present its toxicity by inducing physical damage to bacterial membrane. For example, highly purified SWCNTs exhibited strong antibacterial activity (~80% were dead after incubation with 5 mg/l SWCNTs) by inducing a direct cell membrane damage. Cell membrane damages also induced a significant leakage of plasmid DNA and RNA [32]. Graphene and graphene oxide nanosheets also exhibited toxicity to *E. coli* by directly disrupting the cell membrane [50].

In the natural environment, the toxicity of ENMs greatly depends on the ambient environment. High ionic strength may increase the aggregation and sedimentation of NPs and reduce the toxicity [51]. NOMs may absorb on the surface of NPs, decrease the interactions of NPs with bacterial cells, and thus decrease the toxicity [52]. Types and strength of ions in culture solutions also affect the toxicity of ENMs to bacteria. He *et al.* [53] found that CeO_2 NPs showed different toxicities to *E. coil* in normal saline (NS) and phosphate-buffered saline (PBS). In NS, CeO_2 NP were positively charged due to the adsorption of Na^+ on the particle surface and, therefore, easily contacted with the positively charged membrane by electrostatic attraction (Figure 15.2a). The direct contact induced destabilization of the outer membrane, ROS increase, and loss of viability. In contrast, CeO_2 NPs were repulsed away from the bacterial membrane in PBS since the particle surfaces were negatively charged due to the adsorption of large amount of PO_4^{3-} (Figure 15.2b). Lin *et al.* [45] indicated that toxicity of ZnO NPs to *E. coli* in five different culture media decreased as follows: ultrapure water > 0.8% NaCl > Minimal Davis (MD) > Luria Bertani (LB) > PBS. Formation of precipitates $Zn_3(PO_4)_2$ in PBS and complexes (zinc with citrates and amino acids) in MD and LB significantly decreased Zn^{2+} concentration, resulting in the lower toxicity. Based on these research studies, the ambient exposure environment should be taken into account and more attention is paid when assessing the toxicity of ENMs.

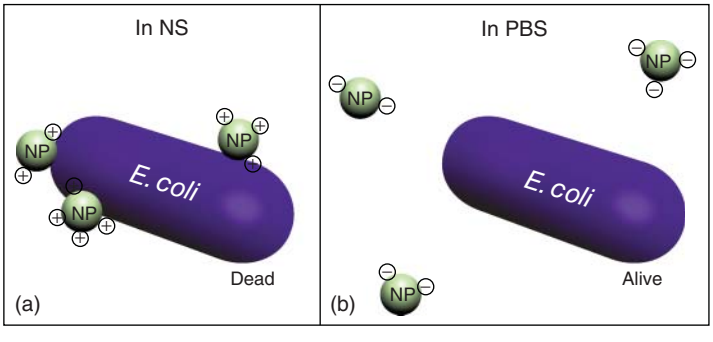

Figure 15.2 Interactions between *E. coli* and CeO_2 NPs: in NS (a) and in PBS (b).

Soil microbial communities are sensitive indicators of soil quality and perturbations under external stress and contaminations [54].The responses of soil communities can be monitored by microbial activities (e.g., β-glucosidase, urease, dehydrogenase, and nitrogen cycle), abundance, and diversity, and so on [55–57]. Compared with research studies on single bacterial strains, studies on soil bacterial community are relatively limited. Most of the current studies pertaining to ENMs–bacterial community are on the metal-based NPs and few of them are on carbon nanomaterials [58]. Generally, metal-based NPs seem to induce higher toxicity than organic NPs to soil microbial community. It was reported that metal-based NPs modified the enzymatic activities even at very low concentrations [59, 60]. For example, Ag NPs at 0.0032–0.32 mg/kg reduced net nitrogen mineralization and increased the metabolic quotient, indicating a reduction in substrate use efficiency by the bacterial community [60]. In another case, Ag NPs (0.14 mg/kg) were found to reduce enzymatic activity and respiration after 50 days [59]. In contrast, carbon nanomaterials showed low toxic potential [61–64]. C_{60} had no significant effects on soil enzymatic activities after 180 days [61]. MWCNTs and SWCNTs showed reduction of enzyme activities only at high concentrations (300–5000 mg/kg·soil), which is far beyond realistic concentration for now [62, 63].

Microbial biomass and abundance are also sensitive indicators to the assessment of the soil contamination and have been applied in nanoecotoxicology studies. The soil microbial biomass can be quantified by several methodologies such as fumigation incubation, fumigation extraction, and substrate-induced respiration [65]. In addition to quantification of the total biomass, abundance of specific bacteria groups can be quantified by quantitative PCR using 16S or 18S rRNA as target genes. Ag NPs at an extremely low concentration (0.0032 mg/kg·soil) induced reduction of soil microbial biomass [60]. However, magnetic iron NPs (Fe_2O_3 and Fe_3O_4) at 10 and 100 mg/kg·soil showed no effect on the biomass [66, 67]. TiO_2 and ZnO NPs both reduced microbial biomass, but the effect of ZnO was stronger than that of TiO_2 [68]. Discrepancy of the toxicity may be highly related to their different behavior, for example, the dissolution of Ag and ZnO is much easier in the environment, and the release of toxic metal ions may be part of the reason.

Soil microbial diversity, namely soil community structure, is considered to be the best and sensitive indicator to the assessment of the soil nutrient, quality, and contamination [69]. It includes the genetic diversity among species and abundance and functional group diversity in community. Methodologies including PCR-DGGE, PLFA profiles, and T-RFLP have been applied to assess the effect of ENMs on microbial diversity. By using RFLP and PCR-DGGE, Ag and Fe_3O_4 NPs were found to change the soil bacterial community structure after a short-term exposure [59, 70]. Taxa with specific function for soil were also changed after exposure with Fe_3O_4, TiO_2, and ZnO NPs [70]. Groups of *Actinobacteria*, *Duganella*, *Streptomycetaceae*, and *Nocardioides*, which can facilitate the decomposition of organic matter in soil, were stimulated after exposure with Fe_3O_4 NPs observed from DGGE sequencing. While functional groups involved in nitrogen fixation such as *Rhizobiales*, *Bradyrhizobiaceae*, and

Bradyrhizobium and methane oxidation (*Methylobacteriaceae*) were inhibited after exposure with TiO_2 and ZnO NPs [68, 71]. For carbon nanomaterials, effects can only be found at high concentrations [72, 73].

Study on the whole community structure can provide environmental relevancy; however, the complexity in a real soil environment limits the ability of such research studies to elucidate the toxic mechanism. Studies in laboratory and environmental conditions should be combined together in the future and linked with the behavior and fate of ENMs in soil environment to address the toxic mechanism.

15.3.2 Toxicity of ENMs to Higher Plants

Plants are an essential component in the environment, playing a crucial role in preserving the ecological equilibrium as well as providing food sources for animals and human beings. It exposes huge interfaces into the air and soil environment, making it possible that NPs enter into plants through the air and root pathways and pose a threat to plant growth. Intentional application of ENMs in agriculture for the antidisease purpose is also a pathway of ENMs contacting with plants [7]. Persistent introduction of ENMs in plants may cause accumulation and transfer of ENMs among different species via food chains, giving rise to a risk in the whole ecosystem. Unfortunately, research studies pertaining to the phytotoxicity of ENMs are still at the early stage compared with that on animals and cells. Plants that have been tested are mainly for human consumption, including crops (e.g., wheat, rice, corn, and soybean), fruit and vegetable plants (e.g., cucumber, tomato, carrot, lettuce, spinach, radish, and pumpkin), and herbages (e.g., alfalfa and ryegrass) [74]. Phytotoxicity of ENMs is always assessed based on the following endpoints: (i) morphology and anatomy, including germination rate, root length, biomass, seedling length, root numbers; (ii) physiology, including chlorophyll, photosynthetic intensity, transpiration, enzymatic activity, ROS content, and membrane integrity; and (iii) genetic changes.

The ENMs that have been examined for their phytotoxicity include zero-valence metal NPs (e.g., Fe, Cu, Zn, Al, Ag, Au, and Pd), metal oxide NPs (TiO_2, Al_2O_3, CuO, ZnO, Fe_3O_4, La_2O_3, Yb_2O_3, and CeO_2), and carbon nanomaterials (e.g., CNTs, graphene, and fullerene) as well as quantum dots [75, 76]. Both positive and negative effects of ENMs on plants are reported. TiO_2 at a concentration of 40 g/kg promoted the growth of spinach by stimulating the photosynthesis of leaves and nitrogen fixation ability of roots [77]. SiO_2 NPs at 500 mg/l enhanced the growth of *Pinus sylvestris* [78]. Al_2O_3 showed no toxic effects to the root growth of *Arabidopsis* even up to 4000 mg/l [79]. However, in general, most research studies indicated that ENMs may show toxic effects to plants at certain concentrations [76].

15.3.2.1 Factors Affecting the Phytotoxicity of ENMs

Various factors may affect the phytotoxicity of ENMs such as plant species, seed size, growth stage, exposure medium, and physicochemical properties of ENMs

[76]. Different plant species may response differently to the same ENMs. SWCNTs inhibited the root elongation of carrot, tomato, cabbage, and lettuce after 24–48 h exposure, but promoted the growth of onion and cucumber [80]. CeO_2 NPs inhibited the root growth of lettuce, but showed no effect to other six species (radish, rape, tomato, wheat, cabbage, and cucumber), indicating the phytotoxicity related to plant species [81]. It is assumed that the different toxicity among the plant species may be related to the discrepancy in the seed size or xylem structure of monocot and dicot plants [82, 83]. However, there is no direct evidence.

Plants at different growth stages may exhibit different sensitivity to external stresses. Stampoulis *et al.* [84] reported that MWCNTs, Cu, and Ag NPs had no effects on the germination of pumpkin, but significantly reduced the biomass of seedlings after 15 days. Yb_2O_3 NPs inhibited the root growth of cucumber at high concentrations (200 and 2000 mg/l) after germination for 5 days. However, Yb_2O_3 NPs significantly reduced the biomass production starting from a very low concentration (0.32 mg/l) [85]. These results indicate that biomass at growth stage maybe a more sensitive indicator and long-term examination is necessary.

NPs with a small size generally show higher toxicity than that with larger size. EL-Temsah and Joner [86] found that 0.6–2 nm Ag colloids exhibited higher toxicity than 5 and 20 nm ones to flax, barley, and ryegrass. CeO_2 NPs with a size of 7 nm showed more inhibition to root growth of *Lactuca* plants than that of 25 nm size [13]. Surface chemistry is also an important factor affecting the toxicity. Cañas *et al.* [80] compared the effects of nonfunctional and functional CNTs on the root elongation of six plant species and found that functionalization significantly decreased the toxicity of CNTs. The toxicity of Al_2O_3 to five crop species was also relived after a surface modification with phenanthrene [87]. Since most commercial ENMs are surface coated or modified with stabilizer, surface chemistry of ENMs should be taken into account when evaluating the toxicity. Barrena *et al.* [88] found that three commercial ENMs (Au, Ag, and Fe_3O_4) were not toxic to lettuce and cucumber, which is partially due to the presence of stabilizer on the particle surface.

Another factor that may affect the toxicity of ENMs is culture medium. Nutrient solution, agar medium, silica sand, vermiculite, and soil have been used in phytotoxicity studies of ENMs. Hydroponic solution is the mostly used culture medium for plants, since it is a simple system that allows exploration of the toxic mechanism. NPs are easier to transfer and contact with plant roots in nutrient solutions compared with those in a real soil medium where NPs can be adsorbed by soil particles and colloids. This is the main reason that ENMs always show low toxicity in soil medium because of the interaction between ENMs and soil particle and other components [89]. In addition to the root exposure, there are some studies exposing plant leaves to ENMs [90–93]. The uptake and toxicity of ENMs are generally limited in a foliar exposure. Hong *et al.* [93] recently reported that foliar-exposed CeO_2 NPs were taken up and translocated to other parts of cucumber plants, and some of the enzymatic activities in the roots (catalase) and shoots (ascorbate peroxidease) were modulated, indicating that the atmospheric NPs also pose threat to the environment [93].

15.3.2.2 Possible Mechanism Involved in Phytotoxicity of ENMs

The exact mechanism of ENM phytotoxicity is not fully understood yet. ENMs may act on plants through different mechanisms both physically and chemically [94]. Physical toxicity can be induced by a direct contact of NPs and plants. NPs may impede the absorption of water and nutrient elements by blocking the water transportation channel. For example, many reports indicate that NPs located in the intercellular spaces thus may clog the water flow in the apoplastic pathway, which is a very important transport route of water and solutes across plant tissues. Small-size NPs may also stick in the plasmodesmata and influence the symplastic pathway through which the water, small molecules, and ions can flow between cells. Asli and Neumann [95] found that TiO_2 treatment decreased the root hydraulic conductivity and leaf transpiration and growth of *Zea mays*, probably due to the blocking of water transport route. This was further evidenced by the decrease of pore size of the root cell walls from 6.6 to 3 nm. A physical interaction may also be positive for plant growth. For instance, CNTs could penetrate the seed coat of tomato and act as a channel for water transport, resulting in stimulation of seed germination and growth [96].

Metal-based NPs may release toxic ions after interaction with plants. One possible ending of these toxic ions is combining with –SH and –COOH in proteins, inducing the dysfunction of proteins [97]. Due to their large surface area and high reactivity, NPs can adsorb on the cell membrane or coated by proteins, forming the so-called protein corona, altering the normal function of the cell membrane and proteins [98]. Moreover, some NPs (Ag and Au) can irreversibly combine with residual amino acids such as cysteine by covalent bond [99, 100]. The high reactive surface of NPs may also serve as a catalytic center for certain chemical reactions (e.g., redox reaction) in plants [101]. NPs may also induce oxidative damage by creating or increasing the production of ROS [102].

Various mechanisms may be simultaneously involved in the phytotoxicity of ENMs. This should be taken into consideration when interpreting the effect of ENMs in plants. In addition to exploring the toxic mechanism from the interactions between plants and "as-manufactured" NPs, the role of modification of NPs within the plants should also be considered [103]. As described earlier, ENMs may undergo various transformations after interaction with culture medium and diverse components in plant tissues, including aggregation, dissolution, reduction, oxidation, sulfidation, phosphorylation, and surface modification. These processes will alter the physicochemical properties and determine the ultimate fate and toxicity of ENMs in plants. Typical cases are the research studies on the phytotoxicity of REO NPs, which indicate that REO NPs released RE^{3+} ions and further transformed to RE phosphates and carboxylates and resulted in the toxicity [13, 15, 85, 104]. ENMs may also be inactivated by forming an oxidation layer, which may inhibit the release of toxic ions and final toxic effects [24]. Therefore, evaluating the transformation and fate of ENMs in plants is another research focus when assessing and interpreting the phytotoxicity of ENMs.

15.3.2.3 Uptake, Translocation, and Transformation of ENMs in Plants

Phytotoxicity of ENMs correlates with its accumulation in plant tissues. It is easy to understand that high accumulation of ENMs in plants leads to higher toxicity. Cellular penetration is the most accepted mode by which the plant cells internalize the ENMs [5]. Studies on the isolated plant cells indicated that ENMs may be absorbed by cells via endocytosis pathway, which has been well recognized in animal cells [105, 106]. For example, *Nicotiana tabacum* protoplast can take up the Au NPs by both clathrin-dependent and clathrin-independent mechanisms [107]. Clathrin invaginations formed when a clathrin-dependent endocytosis occurs, leading to the budding of clathrin-coated vesicles. While a clathrin-independent endocytosis is not well understood, probably via lipid-raft-mediated phagocytosis or fluid-phase endocytosis pathway.

For a real plant, NPs contact with plants through different pathways. NPs may enter into plants through leaf epidermis, stoma, and pollen stigma and further transfer to other tissues via apoplastic pathway [94]. Root is the most important entry point where NPs enter into plants. NPs can enter into plants at the meristematic zone, epidermis, lateral roots, and wound regions of roots. The entered NPs can translocate to other parts in the xylem and phloem [23]. Uptake and translocation of NPs in plants vary among different plant species and culture media and depend on the physicochemical properties of NPs [103]. Different plant species always show different uptake abilities of NPs, probably due to the discrepancy in the xylem and phloem structure, transpiration efficiency, and so on. Uptake of NPs in hydroponic condition is always higher than that in agar, sand, and soil media, mainly because NPs can easily move and contact with plant roots in a hydroponic condition, while they are immobilized by components in those complex media. Components in culture media such as inorganic ions and organic matters have a great impact on the mobility and uptake of NPs in plants [104, 108]. CeO_2 NPs more readily accumulate in the roots of plants cultured in NOM-rich soil, while they are difficult to translocate to the aerial part [109]. Humic acids, the major components of NOMs, contain a large number of carboxyl and hydroxyl groups and can be binding sites for NPs. This will immobilize NPs in soil and limit the translocation from soil to the aerial parts. Phosphate, which widely exists in natural environment and living organisms, was proved to be an important factor modulating the uptake and translocation of CeO_2 in cucumber plants [104]. The cucumber plants were exposed to CeO_2 NPs (~25 nm) with (+P) and without (−P) phosphates in the nutrient solution. Translocation ability of Ce in −P group was much higher than that in +P group. Large quantities of needle-like $CePO_4$ were found outside the epidermis in the +P group. While in the −P group, $CePO_4$ were only found in the intercellular regions and vacuole of root cells. The involved mechanism was uncovered by the synchrotron-radiation-based X-ray absorption near-edge structure spectra (XANES) studies. Ce presented as CeO_2 and cerium carboxylates in the shoots. The content of Ce carboxylates in the shoots of −P group (418 mg/kg, 67.5%) was much higher than those in the +P group (30.1 mg/kg, 21%). This study indicates that phosphate might firstly influence the transformation process of

CeO_2 NPs in plant roots and subsequently their translocation and ultimate fate. Physicochemical properties undoubtedly affect the behavior of NPs in plants. NPs with a small size are always easier to translocate than that with a large size. Using a radiotracer technique, Zhang *et al.* [110] found that cucumber seedlings treated with 7 nm CeO_2 NPs showed significantly higher Ce contents in both roots and shoots than those exposed to 25 nm ceria particles at all test concentrations (2, 20, and 200 mg/l). Ce concentrations in cucumber leaves decreased with the distance from the roots, that is, in the order of old leaf > young leaf > apical meristem. Surface chemical properties including surface charge and modification also affect the behavior of NPs. Zhu *et al.* [111] compared the uptake and translocation of four Au NPs with well-defined surface charges. Positively charged Au NPs tended to accumulate in roots, while negatively charged Au NPs were easier to translocate to aerial parts. The root exudates, which contain a lot of mucilage with negative charges, can easily bind with Au NPs that are positively charged by electrostatic interactions. However, Au NPs with negative charges can be taken up and translocated with the water flow rather than be adsorbed by the roots.

Phytotoxicity of ENMs are increasingly being studied; however, transformation of ENMs and its role involved in the toxicity are not fully understood yet. A typical transformation for metal-based ENMs is dissolution, and its role in the toxicity of ENMs has been in controversy since the beginning of nanotoxicity studies. Recently, many authors have proved that the toxicity induced by the release of metal ions cannot be ignored and even plays the most important role in the toxicity of metal-based ENMs [13, 43, 44]. For instance, Xiu *et al.* [43] indicated that the particle effect in the antibacterial activity of Ag NPs is negligible, by operating all the synthesis and antibacterial test under strictly anaerobic conditions that preclude Ag (0) oxidation and Ag^+ release. Similarly, release of toxic ions is also an important factor involved in the phytotoxicity of other ENMs. Metal-based ENMs such as ZnO, CuO, and Ag NPs, which are easily dissolved in biological and environmental media, show significant toxicity to plants [112–114]. Plant roots can secrete large number of exudates including ions, small molecular substances (e.g., phenols, aldehydes, amino acids, and organic acids), and high molecular pectin (e.g., polysaccharide and fatty acids), forming a microenvironment around the root called *rhizosphere* [10]. In most cases, ENMs directly contact with plant root and the root exudates will accelerate the release of ions and subsequent transformation of ENMs. Biotransformation of ZnO NPs has been investigated by several studies, and the results showed that no pristine ZnO NPs were internalized in plants evidenced by XANES, but present as transformed Zn(II) species such as Zn-citrate, Zn-phosphate, and Zn-phytate [113, 115, 116]. A systematical investigation on the transformation and toxic mechanism of REO NPs (La_2O_3, Yb_2O_3, and CeO_2) in higher plants was performed by our group [10, 13, 14, 85, 117, 118]. Dissolution and transformation of these NPs with the assistance of plant exudates were highlighted in the phytotoxicity. Promotion of dissolution by the root exudates was proved by a higher concentration of ions in the rhizosphere solution than that in the exposure solution [85]. The released RE^{3+} ions are easily combined with small organic acids and phosphates, which can be further translocated

or immobilized in plants [10, 85]. These processes determined the uptake, translocation, and final fate of the REO NPs in plants. CeO_2 NPs are among the most studied ENMs in nanotoxicity due to their promising application as fuel additives, cosmetic additives and antioxidants [119]. We demonstrated for the first time that CeO_2 NPs, which were considered to be highly stable, could undergo transformation in higher plants [10]. Linear combination fitting analyses on the bulk XANES spectra of Ce show that Ce presented as different chemical species in the plant roots (66% CeO_2 and 34% $CePO_4$), leaves (78.5% CeO_2 and 21.5% cerium carboxylates), and stems (86.4% CeO_2 and 13.6% cerium carboxylates). Evidence of transformation was further provided at nanoscale by TEM- and SR-based scanning transmission X-ray microscopy (STXM)/XANES. A large number of needle-like clusters were observed in the intercellular regions and on the epidermis of the roots by TEM. These clusters were proved to be $CePO_4$ by STXM/XANES technique (Figure 15.3). The mechanism involved in the transformation and translocation was speculated as follows: CeO_2 NPs were first absorbed on the root surfaces and partially dissolved with the assistance of the organic acids and reducing substances excreted by the roots. The released Ce^{3+} ions were partially precipitated on the root surfaces and in the intercellular spaces with phosphate, which widely existed in plants and nutrient solutions or formed complexes with carboxyl compounds during translocation in xylems. Although it is a fact that transformation of CeO_2 really occurred, compared with La_2O_3 NPs, CeO_2 NPs are always less transformed in plants [14]. This explains the origin of the different toxicities of CeO_2 (no toxicity) and La_2O_3 NPs (strong toxicity) to cucumber plants. Transformation of CeO_2 NPs was also found in *Lactuca* plants and associated with its species-specific toxicity [13]. CeO_2 NPs released a small number of Ce^{3+} ions (less than 6.2% of total Ce in roots) and transformed to Ce carboxylates in the roots of *Lactuca* plants. Although similar transformations were also found in other plant species such as wheat and cucumber, *Lactuca* plants were highly sensitive to Ce^{3+} ions (toxicity started from 0.5 mg/l), resulting in the species-specific toxicity to CeO_2 exposure. More interestingly, in another study, asparagus lettuce – a subspecies of *Lactuca* plants – showed much higher sensitivity to the toxicity of Ce^{3+} ions in agar media (toxicity started from 5 μg/l) than that in aqueous media [15]. Such high sensitivity resulted in a higher toxicity of CeO_2 NPs in agar media (toxicity started from 500 mg/l) than in the aqueous media (toxicity started from 2000 mg/l). These studies provide direct evidences that transformation of NPs really matters and in some cases dominates the toxicity of ENMs.

15.4 Other Terrestrial Organisms

15.4.1 Earthworm

Earthworms play a critical role in soil macrofauna biomass and soil formation, by consuming and fragmenting organic matter and mixing it with soil particles to

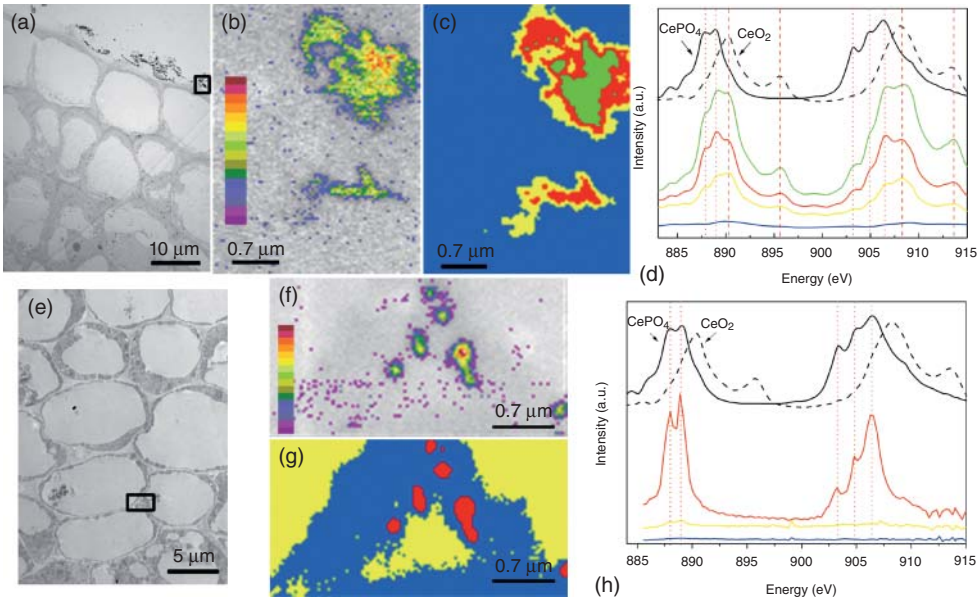

Figure 15.3 (a,e) TEM images of root cells and (b,f) Ce maps of rectangle area in (a) and (e) obtained by a ratio of 886 and 888 eV images. Color bar values are estimated from Ce absorption coefficients and X-ray absorption measurements (in g/cm^2). The calculated surface densities are respectively between 1.1×10^{-5} to 6.4×10^{-5} and 2.4×10^{-6} to 2.8×10^{-5} g/cm^2; (c,g) color-coded maps of Ce components in (b) and (f) derived from an STXM Ce M edge stack analysis. The order of Ce contents is as follows: green > red > yellow; blue color represents the non-Ce regions; panels (d) and (h) are respectively the XAFS spectra extracted from the image sequences of (c) and (g). The black line spectra above belong to the standard compounds and the colored spectra below belong to the root samples. The vertical red dotted lines indicate the characteristic peaks of $CePO_4$ and the dash lines indicate the characteristic peaks of CeO_2 NPs. (Reprinted with permission from [10]. Copyright (2012) American Chemical Society.)

form water-stable aggregates [120]. Since earthworms locate in the bottom of the terrestrial food chains, most pollutants can be enriched by them, causing toxic effects to earthworms and organisms in high trophic level through food chains. Furthermore, earthworms always show higher sensitivity to toxicant than many other soil animals. Therefore, earthworm is one of the priority indicator species of terrestrial ecotoxicology, for characterization of hazardous chemicals pollution levels in soils. Acute and subacute toxicity tests using earthworm have become an international standard method for ecotoxicology research [121].

Most of the current researches pertaining to earthworm and ENMs use metal-based NPs as of choice, for example, TiO_2, ZnO, Al_2O_3, Cu, Ag, and Au [122–127]. In these studies, mortality, reproductive ability, ROS generation, and gene expression were assessed. Hu *et al.* [128] compared the acute toxicity of TiO_2 and ZnO NPs on *Eisenia fetida* using filter paper method and solution method. After exposure for 48 h, both TiO_2 and ZnO NPs caused no death to

earthworm at concentrations ranging from 0 to 3.0 mg/cm^2 when exposed to filter papers. When exposed to 0–100 mg/l TiO_2 or ZnO NPs in solution, MDA and antioxidant enzyme activities (CAT and GPX) were not altered; however, significant DNA damages were observed. This indicated that DNA damage can be used as a more sensitive indicator for nano pollutants. Effects of NPs on earthworm varied among different types or sizes of NPs, soil properties, and even seasons. Schlich *et al.* [129] found that uncoated TiO_2 NPs stimulated earthworm reproduction in a concentration-dependent manner in winter, increasing the number of offspring by up to 50% with comparison to control. While in summer, there was no stimulation. Coated TiO_2 NPs did not influence the earthworm production. Uptake of ENMs by earthworm was evidenced in these studies, but most of these cases indicated that uptake and toxicity of ENMs were less than those of the ionic counterparts. For Cu and Ag NPs, oxidation of NPs was found in worms [124, 130]. A study on Au NPs showed that earthworms accumulated both 22 and 55 nm Au NPs primarily in the gut but also in the whole body [126]. Generally, mechanisms of how earthworm responds to NPs and how the NPs behave in the earthworm body are not fully understood. More studies on the whole effect of ENMs on earthworm growth and behavior and the ecological significance of these effects are needed in the future.

15.4.2 *Caenorhabditis elegans*

Caenorhabditis elegans is a free-living nematode in temperate soil environment. Since it has a short growth period and transparent body, and is easy for culture, it has been a model organism in environmental and ecological toxicology studies [131]. The general method for exposure of *C. elegans* to ENMs is incorporating NPs into agar plates, or adding the NPs to a suspension of *E. coli* and then coating on agar plates. Endpoints such as body length, breeding, behavior, and metabolism are always used for testing the toxicity of ENMs to *C. elegans.* Negative effects of ENMs to *C. elegans* (especially the reproductive ability) have been reported in many studies [16, 131–133]. A sensitive indicator of *C. elegans* is oxidative stress, which is one of the important mechanisms involved in the toxicity of NMs [134]. A typical case is the toxicity of CeO_2 NPs to the *C. elegans* at an environmental relevant concentration. Zhang *et al.* [131] found that CeO_2 NPs significantly increased the ROS levels in *C. elegans* and finally led to a decreased lifespan even at an extremely low concentration (1 nmol/l). Henceforward, negative effects at environmental relevant concentrations of many other NPs (e.g., TiO_2, Al_2O_3, Fe_2O_3, and SiO_2) on *C. elegans* were reported [135–138]. Another unique feature of *C. elegans* is the transparent body, which makes it easy to monitor the distribution of NPs in the body. Qu *et al.* [139] performed a full assessment of the fate and physiological behavior of three types of quantum dots in *C. elegans* using SR-based μ-XRF technique in combination with XANES. Mapping of different elements of the QDs in *C. elegans* body at microscale can be achieved. Variations of chemical

species of Se in different body regions were observed *in situ*, indicating the degradation of QDs in the alimentary system.

15.5 Aquatic Organisms

The aquatic environment is the major sink of ENMs after their release into the environment. The chemistry of naturally occurring colloids and NPs have been extensively studied in aqueous phase [140]. Similar studies on ENMs were also carried out recently and obtain knowledge from the previous studies on natural colloids. However, since ENMs are always designed with various sizes, surface chemistries, and morphologies, behavior and effect of ENMs in aquatic system will be far more complicated [141]. Diverse organisms in aquatic system could be the target of ENMs. ENMs may not only affect the growth of these organisms but also affect the whole ecological balance in the aquatic system. Herein, studies on some important vertebrate and invertebrate species including fish and *Daphnia*, and also the hydrophyte will be briefly introduced.

15.5.1 Fish

Fish is a common aquatic vertebrate, serving an important ecological role in aquatic systems. It is also an important food source for humans. Study on the toxicity and behavior of ENMs in fish directly related to human safety.

Zebrafish is a model animal that is recognized by the International Standardization Organization for (ISO) for toxicity testing [142]. The advantages of using zebrafish include short growth period, high survival rate, and high similarity of early embryo development with higher animals. Hatching rate, survival rate, body length, morphology distortion, and antioxidant enzyme activities are commonly used indicators in zebrafish embryo assays. Bai *et al.* [143] studied the impact of ZnO NPs on the development of zebrafish embryos and found that 50 – 100 mg/l exposure killed the embryos; 1 – 50 mg/l exposure suppressed embryo hatching, resulting in shorter length and tail distortion. Asharani *et al.* [144] found that exposure to 5 μg/ml Ag NPs (5 – 20 nm) increased the mortality of zebrafish embryos in a dose-dependent manner, with morphological and physiological abnormalities such as curvature of the spine, slowing down of blood flow, pericardial edema, and cardiac arrhythmias. Ag NP treatment induced significant oxidative and genetic damage to liver tissues. Surface chemistry might affect the toxicity of NPs to the embryo development. Xia *et al.* [145] compared the toxicity of ZnO NPs with and without Fe doping. Due to the stable dopants present in the ZnO lattice, the dissolution of the doped particles was reduced compared to that of undoped particles. Results indicated that similarly to the effect of metal chelators, Fe doping was capable of interfering in the inhibitory effects of $ZnCl_2$ and ZnO NPs.

Another study showed that surface-modified C_{60} derivatives exhibited much lower toxicity to the development of zebrafish embryo than pristine C_{60} [146]. These studies suggest that the toxicity of ENMs to zebrafish is highly related to the surface chemistry of ENMs. Toxicity of ENMs to other fish species has also been reported. For example, Japanese medaka has been widely used as a model organism for testing the wastewater during printing and dyeing. Chae *et al.* [147] found that Ag NPs showed higher oxidative damage and genotoxicity to medaka than Ag^+ at the same dose, indicating that the "particle effect" exists. Smith *et al.* [148] treated rainbow trout with SWCNTs and found that a series of pathological symptoms including gill edema, hyperplasia, brain aneurysms, and liver cells atrophy occurred. MDA content and activities of antioxidant enzymes in gills, liver, and brain increased, indicating severe oxidative damage. Fish can take up ENMs through pathways of diet and gill respiration or direct contact with skin [149]. Similarly, ENMs may be excreted from the body by the same pathway or through the liver metabolism.

15.5.2 *Daphnia*

Daphnia are a freshwater zooplankton found in ponds and lakes all over the world. They are excellent organisms to be used in bioassays because they are sensitive to changes in water chemistry and are simple and inexpensive to raise in an aquarium. They mature in just a few days, so it does not take long to grow a culture of test organisms. *Daphnia* are filter feeders, which have combs of setae on their limbs in the trunk. These combs serve as a mesh by which water is filtered and particles caught. *Daphnia magna* can filter and feed on particles in the size ranging from 0.4 to 40 μm (e.g., algal cells, bacteria, and other organic or inorganic particles) [150, 151]. Thus, it is inevitable that NPs may enter into the body of *D. magna* as food. Indeed, uptake of NPs has been found in many reports. Ingestion of C_{60} and TiO_2 NPs was obvious as indicated by the presence of NPs in the digestive track after exposure for 48 h [152]. Adhesion of TiO_2 NP aggregates to the exoskeleton and antennae of *D. magna* was also found, which might cause physical effects and loss of mobility [150]. Lovern *et al.* [153] observed significant changes in *D. magna* behavior including swimming in circles at water surface, hop number, and heart rate changes after exposure to C_{60} and its derivative. The reason was not clear, perhaps related to the adhesion or other factors. Zhu *et al.* [154] investigated the acute toxicity of a host of NPs (Al_2O_3, TiO_2, ZnO, SWCNTs, and MWCNTs) to *D. magna.* The EC_{50} of these NPs ranged from 0.662 (ZnO) to 114.357 mg/l (Al_2O_3), and ZnO NPs exhibited the highest toxicity. Diamond NPs killed all the *D. magna* at a concentration of 12.5 mg/l and induces reproductive toxicity at a low concentration of 1.3 mg/l [155]. Genetic toxicity was found after exposure to 1 mg/l CeO_2 NPs as indicated by the DNA breakage, and the extent of DNA damage directly correlated with the mortality [156]. TiO_2 (21 nm) showed no effect to *D. magna* after exposure for 48 h; however, significant toxicity was observed after 72 h, and severe growth retardation and death were found after 21 days, indicating

the toxicity related to the exposure time [157]. TiO_2 NPs were difficult to eliminate from *D. magna* and accumulated in the body with time, probably resulting in the toxicity after exposure for a long time.

15.6 Challenges and Perspective

Although studies on the environmental risks and safety of ENMs are continuing to increase, gaps still exist in the understanding of the toxic mechanisms of ENMs. The first challenge is the assessment of the risks of ENMs in a complex system rather than a simple system and a single species. Currently, effects of ENMs on an intact ecosystem are poorly studied. Indeed, to perform such a study on a complex ecosystem (terrestrial and aquatic) and interpret the relation among the components in the system is difficult. Studies using microcosm, mesocosm, and field experiments to simulate the real environment are critical to understand the behavior and effects of ENMs in ecosystems [59, 158–160]. The second challenge is the characterization of ENMs in the complex environment. Various separation methods including asymmetric-flow field flow fractionation (AF_4), ultrafiltration, membrane filtration, size-exclusion chromatography, and cloud point extraction have been applied to extract NPs from complex matrix for further characterization [161]. However, these methods are tricky when facing complex environmental media. More efforts from analysts are needed for characterization of ENMs in the environment. Recently, SR-based techniques have emerged as important tools for determining the ENMs and their transformation products in biological and environmental samples [162]. Detailed description of these techniques and their applications can be found in Chapter 5 of this book. The third challenge is the quantification of ENMs. ICP-MS is an excellent technique for most of the elements in the periodic table, of which the detection limit can be part per trillion. However, it will be difficult using ICP-MS when the samples contain a high background of the target element, for example, Fe, Si, and even Ti. One powerful technique for quantifying the ENMs in a complex matrix is isotopic tracer techniques including radiotracers and stable isotopic tracers, although they are not always applicable [110, 158]. More practical and elegant techniques need to be developed for accurate quantification of the ENM in the environment.

References

1. Kaegi, R., Sinnet, B., Zuleeg, S. *et al*. (2010) Release of silver nanoparticles from outdoor facades. *Environ. Pollut.*, **158** (9), 2900–2905.
2. Kägi, R., Ulrich, A., Sinnet, B. *et al*. (2008) Synthetic TiO_2 nanoparticle emission from exterior facades into the aquatic environment. *Environ. Pollut.*, **156** (2), 233–239.
3. Benn, T., Cavanagh, B., Hristovski, K. *et al*. (2010) The release of nanosilver from consumer products used in the home. *J. Environ. Qual.*, **39** (6), 1875–1882.
4. Windler, L., Lorenz, C., Von Goetz, N. *et al*. (2012) Release of titanium dioxide from textiles during washing. *Environ. Sci. Technol.*, **46** (15), 8181–8188.

5. Maurer-Jones, M.A., Gunsolus, I.L., Murphy, C.J. *et al*. (2013) Toxicity of engineered nanoparticles in the environment. *Anal. Chem.*, **85** (6), 3036–3049.
6. Mastronardi, E., Tsae, P., Zhang, X. *et al*. (2015) *Nanotechnologies in Food and Agriculture* (eds M. Rai, C. Ribeiro, L. Mattoso, and N. Duran), Springer, pp. 25–67.
7. Khot, L.R., Sankaran, S., Maja, J.M. *et al*. (2012) Applications of nanomaterials in agricultural production and crop protection: a review. *Crop Prot.*, **35**, 64–70.
8. Westerhoff, P.K., Kiser, M.A., and Hristovski, K. (2013) Nanomaterial removal and transformation during biological wastewater treatment. *Environ. Eng. Sci.*, **30** (3), 109–117.
9. Lowry, G.V., Gregory, K.B., Apte, S.C. *et al*. (2012) Transformations of nanomaterials in the environment. *Environ. Sci. Technol.*, **46** (13), 6893–6899.
10. Zhang, P., Ma, Y., Zhang, Z. *et al*. (2012) Biotransformation of ceria nanoparticles in cucumber plants. *ACS Nano*, **6** (11), 9943–9950.
11. Batley, G.E., Kirby, J.K., and McLaughlin, M.J. (2012) Fate and risks of nanomaterials in aquatic and terrestrial environments. *Acc. Chem. Res.*, **46** (3), 854–862.
12. Kittler, S., Greulich, C., Diendorf, J. *et al*. (2010) Toxicity of silver nanoparticles increases during storage because of slow dissolution under release of silver ions. *Chem. Mater.*, **22** (16), 4548–4554.
13. Zhang, P., Ma, Y., Zhang, Z. *et al*. (2013) Species-specific toxicity of ceria nanoparticles to *Lactuca plants*. *Nanotoxicology*, **9** (1), 1–8.
14. Ma, Y., Zhang, P., Zhang, Z. *et al*. (2015) Origin of the different phytotoxicity and biotransformation of cerium and lanthanum oxide nanoparticles in cucumber. *Nanotoxicology*, **9** (2), 262–270.
15. Cui, D., Zhang, P., Ma, Y. *et al*. (2014) Effect of cerium oxide nanoparticles on asparagus lettuce cultured in an agar medium. *Environ. Sci. Nano*, **1** (5), 459–465.
16. Yang, X., Gondikas, A.P., Marinakos, S.M. *et al*. (2011) Mechanism of silver nanoparticle toxicity is dependent on dissolved silver and surface coating in *Caenorhabditis elegans*. *Environ. Sci. Technol.*, **46** (2), 1119–1127.
17. Levard, C., Mitra, S., Yang, T. *et al*. (2013) Effect of chloride on the dissolution rate of silver nanoparticles and toxicity to E. coli. *Environ. Sci. Technol.*, **47** (11), 5738–5745.
18. Lin, S., Reppert, J., Hu, Q. *et al*. (2009) Uptake, translocation, and transmission of carbon nanomaterials in rice plants. *Small*, **5** (10), 1128–1132.
19. Hyung, H., Fortner, J.D., Hughes, J.B. *et al*. (2007) Natural organic matter stabilizes carbon nanotubes in the aqueous phase. *Environ. Sci. Technol.*, **41** (1), 179–184.
20. Pelley, A.J. and Tufenkji, N. (2008) Effect of particle size and natural organic matter on the migration of nano-and microscale latex particles in saturated porous media. *J. Colloid Interface Sci.*, **321** (1), 74–83.
21. Chen, J., Xiu, Z., Lowry, G.V. *et al*. (2011) Effect of natural organic matter on toxicity and reactivity of nano-scale zero-valent iron. *Water Res.*, **45** (5), 1995–2001.
22. Levard, C., Reinsch, B.C., Michel, F.M. *et al*. (2011) Sulfidation processes of PVP-coated silver nanoparticles in aqueous solution: impact on dissolution rate. *Environ. Sci. Technol.*, **45** (12), 5260–5266.
23. Wang, Z., Xie, X., Zhao, J. *et al*. (2012) Xylem-and phloem-based transport of CuO nanoparticles in maize (*Zea mays* L.) *Environ. Sci. Technol.*, **46** (8), 4434–4441.
24. Mudunkotuwa, I.A., Pettibone, J.M., and Grassian, V.H. (2012) Environmental implications of nanoparticle aging in the processing and fate of copper-based nanomaterials. *Environ. Sci. Technol.*, **46** (13), 7001–7010.
25. Levard, C., Hotze, E.M., Lowry, G.V. *et al*. (2012) Environmental transformations of silver nanoparticles: impact on stability and toxicity. *Environ. Sci. Technol.*, **46** (13), 6900–6914.

26. Allen, B.L., Kichambare, P.D., Gou, P. *et al*. (2008) Biodegradation of single-walled carbon nanotubes through enzymatic catalysis. *Nano Lett.*, **8** (11), 3899–3903.
27. Akhavan, O. and Ghaderi, E. (2012) *Escherichia coli* bacteria reduce graphene oxide to bactericidal graphene in a self-limiting manner. *Carbon*, **50** (5), 1853–1860.
28. Kirschling, T.L., Golas, P.L., Unrine, J.M. *et al*. (2011) Microbial bioavailability of covalently bound polymer coatings on model engineered nanomaterials. *Environ. Sci. Technol.*, **45** (12), 5253–5259.
29. Kim, J.S., Kuk, E., Yu, K.N. *et al*. (2007) Antimicrobial effects of silver nanoparticles. *Nanomed. Nanotechnol. Biol. Med.*, **3** (1), 95–101.
30. Ren, G., Hu, D., Cheng, E.W.C. *et al*. (2009) Characterisation of copper oxide nanoparticles for antimicrobial applications. *Int. J. Antimicrob. Agents*, **33** (6), 587–590.
31. Petkova, P., Francesko, A., Fernandes, M.M. *et al*. (2014) Sonochemical coating of textiles with hybrid ZnO/chitosan antimicrobial nanoparticles. *ACS Appl. Mater. Interfaces*, **6** (2), 1164–1172.
32. Kang, S., Pinault, M., Pfefferle, L.D. *et al*. (2007) Single-walled carbon nanotubes exhibit strong antimicrobial activity. *Langmuir*, **23** (17), 8670–8673.
33. Holden, P.A., Schimel, J.P., and Godwin, H.A. (2014) Five reasons to use bacteria when assessing manufactured nanomaterial environmental hazards and fates. *Curr. Opin. Biotechnol.*, **27**, 73–78.
34. Niazi, J.H. and Gu, M.B. (2009) *Atmospheric and Biological Environmental Monitoring* (eds Y.J. Kim, U. Platt, M.B. Gu, and H. Iwahashi), Springer, pp. 193–206.
35. Navarro, E., Baun, A., Behra, R. *et al*. (2008) Environmental behavior and ecotoxicity of engineered nanoparticles to algae, plants, and fungi. *Ecotoxicology*, **17** (5), 372–386.
36. Mitchell, R. and Gu, J.-D. (2010) *Environmental Microbiology*, John Wiley & Sons, Inc.
37. Hajipour, M.J., Fromm, K.M., Ashkarran, A.A. *et al*. (2012) Antibacterial properties of nanoparticles. *Trends Biotechnol.*, **30** (10), 499–511.
38. Nakamura, S. and Mashino, T. (2009) Biological activities of water-soluble fullerene derivatives. *J. Phys. Conf. Ser.*, **159**, 012003.
39. Chae, S.-R., Therezien, M., Budarz, J.F. *et al*. (2011) Comparison of the photosensitivity and bacterial toxicity of spherical and tubular fullerenes of variable aggregate size. *J. Nanopart. Res.*, **13** (10), 5121–5127.
40. Lyon, D.Y., Brunet, L., Hinkal, G.W. *et al*. (2008) Antibacterial activity of fullerene water suspensions (nC60) is not due to ROS-mediated damage. *Nano Lett.*, **8** (5), 1539–1543.
41. Brunet, L., Lyon, D.Y., Hotze, E.M. *et al*. (2009) Comparative photoactivity and antibacterial properties of C60 fullerenes and titanium dioxide nanoparticles. *Environ. Sci. Technol.*, **43** (12), 4355–4360.
42. Li, Y., Zhang, W., Niu, J. *et al*. (2012) Mechanism of photogenerated reactive oxygen species and correlation with the antibacterial properties of engineered metal-oxide nanoparticles. *ACS Nano*, **6** (6), 5164–5173.
43. Xiu, Z.M., Zhang, Q.B., Puppala, H.L. *et al*. (2012) Negligible particle-specific antibacterial activity of silver nanoparticles. *Nano Lett.*, **12** (8), 4271–4275.
44. Reinsch, B.C., Levard, C., Li, Z. *et al*. (2012) Sulfidation of silver nanoparticles decreases *Escherichia coli* growth inhibition. *Environ. Sci. Technol.*, **46** (13), 6992–7000.
45. Li, M., Zhu, L., and Lin, D. (2011) Toxicity of ZnO nanoparticles to *Escherichia coli*: mechanism and the influence of medium components. *Environ. Sci. Technol.*, **45** (5), 1977–1983.
46. Yang, Y., Mathieu, J.M., Chattopadhyay, S. *et al*. (2012) Defense mechanisms of *Pseudomonas aeruginosa* PAO1 against quantum dots and their released heavy metals. *ACS Nano*, **6** (7), 6091–6098.
47. Yang, Y., Wang, J., Zhu, H. *et al*. (2012) Relative susceptibility and transcriptional response of nitrogen cycling

bacteria to quantum dots. *Environ. Sci. Technol.*, **46** (6), 3433–3441.
48. He, X., Pan, Y., Zhang, J. *et al*. (2015) Quantifying the total ionic release from nanoparticles after particle-cell contact. *Environ. Pollut.*, **196**, 194–200.
49. Zhang, J., He, X., Zhang, P. *et al*. (2015) Quantifying the dissolution of nanomaterials at the nano-bio interface. *Sci. China Chem.*, **58**, 761–767.
50. Liu, S., Zeng, T.H., Hofmann, M. *et al*. (2011) Antibacterial activity of graphite, graphite oxide, graphene oxide, and reduced graphene oxide: membrane and oxidative stress. *ACS Nano*, **5** (9), 6971–6980.
51. French, R.A., Jacobson, A.R., Kim, B. *et al*. (2009) Influence of ionic strength, pH, and cation valence on aggregation kinetics of titanium dioxide nanoparticles. *Environ. Sci. Technol.*, **43** (5), 1354–1359.
52. Li, Z., Greden, K., Alvarez, P.J.J. *et al*. (2010) Adsorbed polymer and NOM limits adhesion and toxicity of nano scale zerovalent iron to E. coli. *Environ. Sci. Technol.*, **44** (9), 3462–3467.
53. He, X., Kuang, Y., Li, Y. *et al*. (2012) Changing exposure media can reverse the cytotoxicity of ceria nanoparticles for *Escherichia coli*. *Nanotoxicology*, **6** (3), 233–240.
54. Giller, K.E., Witter, E., and Mcgrath, S.P. (1998) Toxicity of heavy metals to microorganisms and microbial processes in agricultural soils: a review. *Soil Biol. Biochem.*, **30** (10), 1389–1414.
55. Brookes, P.C. (1995) The use of microbial parameters in monitoring soil pollution by heavy metals. *Biol. Fertil. Soils*, **19** (4), 269–279.
56. Griffiths, B.S. and Philippot, L. (2013) Insights into the resistance and resilience of the soil microbial community. *FEMS Microbiol. Rev.*, **37** (2), 112–129.
57. Schloter, M., Dilly, O., and Munch, J.C. (2003) Indicators for evaluating soil quality. *Agric. Ecosyst. Environ.*, **98** (1), 255–262.
58. Simonin, M. and Richaume, A. (2015) Impact of engineered nanoparticles on the activity, abundance, and diversity of soil microbial communities: a review. *Environ. Sci. Pollut. Res. Int.*, **22**, 1–14.
59. Colman, B.P., Arnaout, C.L., Anciaux, S. *et al*. (2013) Low concentrations of silver nanoparticles in biosolids cause adverse ecosystem responses under realistic field scenario. *PLoS One*, **8** (2), e57189.
60. Hänsch, M. and Emmerling, C. (2010) Effects of silver nanoparticles on the microbiota and enzyme activity in soil. *J. Plant Nutr. Soil Sci.*, **173** (4), 554–558.
61. Tong, Z., Bischoff, M., Nies, L. *et al*. (2007) Impact of fullerene (C60) on a soil microbial community. *Environ. Sci. Technol.*, **41** (8), 2985–2991.
62. Chung, H., Son, Y., Yoon, T.K. *et al*. (2011) The effect of multi-walled carbon nanotubes on soil microbial activity. *Ecotoxicol. Environ. Saf.*, **74** (4), 569–575.
63. Jin, L., Son, Y., Yoon, T.K. *et al*. (2013) High concentrations of single-walled carbon nanotubes lower soil enzyme activity and microbial biomass. *Ecotoxicol. Environ. Saf.*, **88**, 9–15.
64. Shrestha, B., Acosta-Martinez, V., Cox, S.B. *et al*. (2013) An evaluation of the impact of multiwalled carbon nanotubes on soil microbial community structure and functioning. *J. Hazard. Mater.*, **261**, 188–197.
65. Schinner, F., Öhlinger, R., Kandeler, E. *et al*. (2012) *Methods in Soil Biology*, Springer Science & Business Media.
66. Antisari, L.V., Carbone, S., Gatti, A. *et al*. (2013) Toxicity of metal oxide (CeO_2, Fe_3O_4, SnO_2) engineered nanoparticles on soil microbial biomass and their distribution in soil. *Soil Biol. Biochem.*, **60**, 87–94.
67. He, S., Feng, Y., Ren, H. *et al*. (2011) The impact of iron oxide magnetic nanoparticles on the soil bacterial community. *J. Soils Sediments*, **11** (8), 1408–1417.
68. Ge, Y., Schimel, J.P., and Holden, P.A. (2011) Evidence for negative effects of TiO_2 and ZnO nanoparticles on soil bacterial communities. *Environ. Sci. Technol.*, **45** (4), 1659–1664.

69. Torsvik, V. and Øvreås, L. (2002) Microbial diversity and function in soil: from genes to ecosystems. *Curr. Opin. Microbiol.*, **5** (3), 240–245.
70. Ben-Moshe, T., Frenk, S., Dror, I. *et al.* (2013) Effects of metal oxide nanoparticles on soil properties. *Chemosphere*, **90** (2), 640–646.
71. Ge, Y., Schimel, J.P., and Holden, P.A. (2012) Identification of soil bacteria susceptible to TiO_2 and ZnO nanoparticles. *Appl. Environ. Microbiol.*, **78** (18), 6749–6758.
72. Johansen, A., Pedersen, A.L., Jensen, K.A. *et al.* (2008) Effects of C60 fullerene nanoparticles on soil bacteria and protozoans. *Environ. Toxicol. Chem.*, **27** (9), 1895–1903.
73. Rodrigues, D.F., Jaisi, D.P., and Elimelech, M. (2012) Toxicity of functionalized single-walled carbon nanotubes on soil microbial communities: implications for nutrient cycling in soil. *Environ. Sci. Technol.*, **47** (1), 625–633.
74. Miralles, P., Church, T.L., and Harris, A.T. (2012) Toxicity, uptake, and translocation of engineered nanomaterials in vascular plants. *Environ. Sci. Technol.*, **46** (17), 9224–9239.
75. Ma, X., Geiser-Lee, J., Deng, Y. *et al.* (2010) Interactions between engineered nanoparticles (ENPs) and plants: phytotoxicity, uptake and accumulation. *Sci. Total Environ.*, **408** (16), 3053–3061.
76. Rico, C.M., Majumdar, S., Duarte-Gardea, M. *et al.* (2011) Interaction of nanoparticles with edible plants and their possible implications in the food chain. *J. Agric. Food Chem.*, **59** (8), 3485–3498.
77. Yang, F., Liu, C., Gao, F. *et al.* (2007) The improvement of spinach growth by nano-anatase TiO_2 treatment is related to nitrogen photoreduction. *Biol. Trace Elem. Res.*, **119** (1), 77–88.
78. Bao-shan, L., Chun-hui, L., Li-jun, F. *et al.* (2004) Effect of TMS (nanostructured silicon dioxide) on growth of Changbai larch seedlings. *J. For. Res.*, **15** (2), 138–140.
79. Lee, C.W., Mahendra, S., Zodrow, K. *et al.* (2010) Developmental phytotoxicity of metal oxide nanoparticles to *Arabidopsis thaliana*. *Environ. Toxicol. Chem.*, **29** (3), 669–675.
80. Cañas, J.E., Long, M., Nations, S. *et al.* (2008) Effects of functionalized and nonfunctionalized single-walled carbon nanotubes on root elongation of select crop species. *Environ. Toxicol. Chem.*, **27** (9), 1922–1931.
81. Ma, Y., Kuang, L., He, X. *et al.* (2010) Effects of rare earth oxide nanoparticles on root elongation of plants. *Chemosphere*, **78** (3), 273–279.
82. Judy, J.D., Unrine, J.M., Rao, W. *et al.* (2012) Bioavailability of gold nanomaterials to plants: importance of particle size and surface coating. *Environ. Sci. Technol.*, **46** (15), 8467–8474.
83. Lee, W.-M., An, Y.-J., Yoon, H. *et al.* (2008) Toxicity and bioavailability of copper nanoparticles to the terrestrial plants mung bean (*Phaseolus radiatus*) and wheat (*Triticum aestivum*): plant agar test for water-insoluble nanoparticles. *Environ. Toxicol. Chem.*, **27** (9), 1915–1921.
84. Stampoulis, D., Sinha, S.K., and White, J.C. (2009) Assay-dependent phytotoxicity of nanoparticles to plants. *Environ. Sci. Technol.*, **43** (24), 9473–9479.
85. Zhang, P., Ma, Y., Zhang, Z. *et al.* (2012) Comparative toxicity of nanoparticulate/bulk Yb2O3 and YbCl3 to cucumber (*Cucumis sativus*). *Environ. Sci. Technol.*, **46** (3), 1834–1841.
86. El-Temsah, Y.S. and Joner, E.J. (2012) Impact of Fe and Ag nanoparticles on seed germination and differences in bioavailability during exposure in aqueous suspension and soil. *Environ. Toxicol.*, **27** (1), 42–49.
87. Yang, L. and Watts, D.J. (2005) Particle surface characteristics may play an important role in phytotoxicity of alumina nanoparticles. *Toxicol. Lett.*, **158** (2), 122–132.
88. Barrena, R., Casals, E., Colón, J. *et al.* (2009) Evaluation of the ecotoxicity of model nanoparticles. *Chemosphere*, **75** (7), 850–857.
89. Boxall, A.B.A., Tiede, K., and Chaudhry, Q. (2007) Engineered nanomaterials in soils and water: how do they behave and could they pose a risk

to human health? *Nanomedicine*, **2** (6), 919–927.

90. Birbaum, K., Brogioli, R., Schellenberg, M. *et al*. (2010) No evidence for cerium dioxide nanoparticle translocation in maize plants. *Environ. Sci. Technol.*, **44** (22), 8718–8723.
91. Larue, C., Castillo-Michel, H., Sobanska, S. *et al*. (2014) Foliar exposure of the crop *Lactuca sativa* to silver nanoparticles: evidence for internalization and changes in Ag speciation. *J. Hazard. Mater.*, **264**, 98–106.
92. Wang, W.-N., Tarafdar, J.C., and Biswas, P. (2013) Nanoparticle synthesis and delivery by an aerosol route for watermelon plant foliar uptake. *J. Nanopart. Res.*, **15** (1), 1–13.
93. Hong, J., Peralta-Videa, J.R., Rico, C. *et al*. (2014) Evidence of translocation and physiological impacts of foliar applied CeO2 nanoparticles on cucumber (*Cucumis sativus*) plants. *Environ. Sci. Technol.*, **48** (8), 4376–4385.
94. Dietz, K.-J. and Herth, S. (2011) Plant nanotoxicology. *Trends Plant Sci.*, **16** (11), 582–589.
95. Asli, S. and Neumann, P.M. (2009) Colloidal suspensions of clay or titanium dioxide nanoparticles can inhibit leaf growth and transpiration via physical effects on root water transport. *Plant Cell Environ.*, **32** (5), 577–584.
96. Khodakovskaya, M., Dervishi, E., Mahmood, M. *et al*. (2009) Carbon nanotubes are able to penetrate plant seed coat and dramatically affect seed germination and plant growth. *ACS Nano*, **3** (10), 3221–3227.
97. Walkey, C.D. and Chan, W.C.W. (2012) Understanding and controlling the interaction of nanomaterials with proteins in a physiological environment. *Chem. Soc. Rev.*, **41** (7), 2780–2799.
98. Lundqvist, M., Stigler, J., Elia, G. *et al*. (2008) Nanoparticle size and surface properties determine the protein corona with possible implications for biological impacts. *Proc. Natl. Acad. Sci. U.S.A.*, **105** (38), 14265–14270.
99. Sudeep, P.K., Joseph, S.T.S., and Thomas, K.G. (2005) Selective detection of cysteine and glutathione using gold nanorods. *J. Am. Chem. Soc.*, **127** (18), 6516–6517.
100. Shang, L. and Dong, S. (2009) Sensitive detection of cysteine based on fluorescent silver clusters. *Biosens. Bioelectron.*, **24** (6), 1569–1573.
101. Meng, H., Chen, Z., Xing, G. *et al*. (2007) Ultrahigh reactivity provokes nanotoxicity: explanation of oral toxicity of nano-copper particles. *Toxicol. Lett.*, **175** (1), 102–110.
102. Begum, P., Ikhtiari, R., and Fugetsu, B. (2011) Graphene phytotoxicity in the seedling stage of cabbage, tomato, red spinach, and lettuce. *Carbon*, **49** (12), 3907–3919.
103. Zhang, P., Ma, Y., and Zhang, Z. (2015) *Nanotechnology and Plant Sciences* (eds M.H. Siddiqui, M.H. Al-Whaibi, and F. Mohammad), Springer, pp. 77–99.
104. Rui, Y., Zhang, P., Zhang, Y. *et al*. (2015) Transformation of ceria nanoparticles in cucumber plants is influenced by phosphate. *Environ. Pollut.*, **198**, 8–14.
105. Liu, Q., Chen, B., Wang, Q. *et al*. (2009) Carbon nanotubes as molecular transporters for walled plant cells. *Nano Lett.*, **9** (3), 1007–1010.
106. Kurepa, J., Paunesku, T., Vogt, S. *et al*. (2010) Uptake and distribution of ultrasmall anatase TiO_2 Alizarin red S nanoconjugates in *Arabidopsis thaliana*. *Nano Lett.*, **10** (7), 2296–2302.
107. Onelli, E., Prescianotto-Baschong, C., Caccianiga, M. *et al*. (2008) Clathrin-dependent and independent endocytic pathways in tobacco protoplasts revealed by labelling with charged nanogold. *J. Exp. Bot.*, **59** (11), 3051–3068.
108. Trujillo-Reyes, J., Vilchis-Nestor, A.R., Majumdar, S. *et al*. (2013) Citric acid modifies surface properties of commercial CeO $_2$ nanoparticles reducing their toxicity and cerium uptake in radish (*Raphanus sativus*) seedlings. *J. Hazard. Mater.*, **263**, 677–684.
109. Zhao, L., Peralta-Videa, J.R., Varela-Ramirez, A. *et al*. (2012) Effect of surface coating and organic matter on the uptake of CeO 2 NPs by corn plants grown in soil: insight into the

uptake mechanism. *J. Hazard. Mater.*, **225**, 131–138.

110. Zhang, Z., He, X., Zhang, H. *et al.* (2011) Uptake and distribution of ceria nanoparticles in cucumber plants. *Metallomics*, **3** (8), 816–822.

111. Zhu, Z.-J., Wang, H., Yan, B. *et al.* (2012) Effect of surface charge on the uptake and distribution of gold nanoparticles in four plant species. *Environ. Sci. Technol.*, **46** (22), 12391–12398.

112. Lin, D. and Xing, B. (2008) Root uptake and phytotoxicity of ZnO nanoparticles. *Environ. Sci. Technol.*, **42** (15), 5580–5585.

113. Dimkpa, C.O., McLean, J.E., Latta, D.E. *et al.* (2012) CuO and ZnO nanoparticles: phytotoxicity, metal speciation, and induction of oxidative stress in sand-grown wheat. *J. Nanopart. Res.*, **14** (9), 1–15.

114. Gubbins, E.J., Batty, L.C., and Lead, J.R. (2011) Phytotoxicity of silver nanoparticles to *Lemna minor* L. *Environ. Pollut.*, **159** (6), 1551–1559.

115. López-Moreno, M.L., de la Rosa, G., Hernández-Viezcas, J.Á. *et al.* (2010) Evidence of the differential biotransformation and genotoxicity of ZnO and CeO_2 nanoparticles on soybean (*Glycine max*) plants. *Environ. Sci. Technol.*, **44** (19), 7315–7320.

116. La Rosa, D., Guadalupe, L.-M., Martha Laura, H.-V., Jose, A. *et al.* (2011) Toxicity and biotransformation of ZnO nanoparticles in the desert plants *Prosopis juliflora*-velutina, *Salsola tragus* and *Parkinsonia florida*. *Int. J. Nanotechnol.*, **8** (6-7), 492–506.

117. Ma, Y., Zhang, P., Zhang, Z. *et al.* (2015) Where does the transformation of precipitated ceria nanoparticles in hydroponic plants take place? *Environ. Sci. Technol.*, **49** (17), 10667–10674.

118. Ma, Y., He, X., Zhang, P. *et al.* (2011) Phytotoxicity and biotransformation of La2O3 nanoparticles in a terrestrial plant cucumber (*Cucumis sativus*). *Nanotoxicology*, **5** (4), 743–753.

119. Cassee, F.R., van Balen, E.C., Singh, C. *et al.* (2011) Exposure, health and ecological effects review of engineered nanoscale cerium and cerium oxide associated with its use as a fuel additive. *Crit. Rev. Toxicol.*, **41** (3), 213–229.

120. Curry, J.P. (2004) *Earthworm Ecology* (ed. C.A. Edwards), CRC Press, pp. 3–11.

121. OECD (1994) *OECD Guidelines for the Testing of Chemicals*, OECD.

122. Bigorgne, E., Foucaud, L., Lapied, E. *et al.* (2011) Ecotoxicological assessment of TiO_2 byproducts on the earthworm *Eisenia fetida*. *Environ. Pollut.*, **159** (10), 2698–2705.

123. Cañas, J.E., Qi, B., Li, S. *et al.* (2011) Acute and reproductive toxicity of nano-sized metal oxides (ZnO and TiO_2) to earthworms (*Eisenia fetida*). *J. Environ. Monit.*, **13** (12), 3351–3357.

124. Unrine, J.M., Tsyusko, O.V., Hunyadi, S.E. *et al.* (2010) Effects of particle size on chemical speciation and bioavailability of copper to earthworms (*Eisenia fetida*) exposed to copper nanoparticles. *J. Environ. Qual.*, **39** (6), 1942–1953.

125. Coleman, J.G., Johnson, D.R., Stanley, J.K. *et al.* (2010) Assessing the fate and effects of nano aluminum oxide in the terrestrial earthworm, *Eisenia fetida*. *Environ. Toxicol. Chem.*, **29** (7), 1575–1580.

126. Unrine, J.M., Hunyadi, S.E., Tsyusko, O.V. *et al.* (2010) Evidence for bioavailability of Au nanoparticles from soil and biodistribution within earthworms (*Eisenia fetida*). *Environ. Sci. Technol.*, **44** (21), 8308–8313.

127. Shoults-Wilson, W.A., Reinsch, B.C., Tsyusko, O.V. *et al.* (2011) Effect of silver nanoparticle surface coating on bioaccumulation and reproductive toxicity in earthworms (*Eisenia fetida*). *Nanotoxicology*, **5** (3), 432–444.

128. Hu, C.W., Li, M., Cui, Y.B. *et al.* (2010) Toxicological effects of TiO 2 and ZnO nanoparticles in soil on earthworm *Eisenia fetida*. *Soil Biol. Biochem.*, **42** (4), 586–591.

129. Schlich, K., Terytze, K., and Hund-Rinke, K. (2012) Effect of TiO_2 nanoparticles in the earthworm reproduction test. *Environ. Sci. Eur.*, **24**, 5.

130. Shoults-Wilson, W.A., Reinsch, B.C., Tsyusko, O.V. *et al*. (2011) Role of particle size and soil type in toxicity of silver nanoparticles to earthworms. *Soil Sci. Soc. Am. J.*, **75** (2), 365–377.
131. Zhang, H., He, X., Zhang, Z. *et al*. (2011) Nano-CeO2 exhibits adverse effects at environmental relevant concentrations. *Environ. Sci. Technol.*, **45** (8), 3725–3730.
132. Ma, H., Kabengi, N.J., Bertsch, P.M. *et al*. (2011) Comparative phototoxicity of nanoparticulate and bulk ZnO to a free-living nematode *Caenorhabditis elegans*: the importance of illumination mode and primary particle size. *Environ. Pollut.*, **159** (6), 1473–1480.
133. Kim, J., Takahashi, M., Shimizu, T. *et al*. (2008) Effects of a potent antioxidant, platinum nanoparticle, on the lifespan of *Caenorhabditis elegans*. *Mech. Ageing Dev.*, **129** (6), 322–331.
134. Nel, A., Xia, T., Mädler, L. *et al*. (2006) Toxic potential of materials at the nanolevel. *Science*, **311** (5761), 622–627.
135. Li, Y., Wang, W., Wu, Q. *et al*. (2012) Molecular control of TiO_2-NPs toxicity formation at predicted environmental relevant concentrations by Mn-SODs proteins. *PLoS One*, **7** (9), e44688.
136. Li, Y., Yu, S., Wu, Q. *et al*. (2013) Transmissions of serotonin, dopamine, and glutamate are required for the formation of neurotoxicity from Al_2O_3-NPs in nematode *Caenorhabditis elegans*. *Nanotoxicology*, **7** (5), 1004–1013.
137. Wu, Q.L., Li, Y.P., Tang, M. *et al*. (2012) Evaluation of environmental safety concentrations of DMSA coated Fe2O3-NPs using different assay systems in nematode *Caenorhabditis elegans*. *PLoS One*, **7** (8), e43729.
138. Zhao, Y., Wu, Q., Li, Y. *et al*. (2013) Translocation, transfer, and in vivo safety evaluation of engineered nanomaterials in the non-mammalian alternative toxicity assay model of nematode *Caenorhabditis elegans*. *RSC Adv.*, **3** (17), 5741–5757.
139. Qu, Y., Li, W., Zhou, Y. *et al*. (2011) Full assessment of fate and physiological behavior of quantum dots utilizing *Caenorhabditis elegans* as a model organism. *Nano Lett.*, **11** (8), 3174–3183.
140. Wigginton, N.S., Haus, K.L., and Hochella, M.F. Jr., (2007) Aquatic environmental nanoparticles. *J. Environ. Monit.*, **9** (12), 1306–1316.
141. Pérez, S., la Farré, M., and Barceló, D. (2009) Analysis, behavior and ecotoxicity of carbon-based nanomaterials in the aquatic environment. *TrAC, Trends Anal. Chem.*, **28** (6), 820–832.
142. Fako, V.E. and Furgeson, D.Y. (2009) Zebrafish as a correlative and predictive model for assessing biomaterial nanotoxicity. *Adv. Drug Delivery Rev.*, **61** (6), 478–486.
143. Bai, W., Zhang, Z., Tian, W. *et al*. (2010) Toxicity of zinc oxide nanoparticles to zebrafish embryo: a physicochemical study of toxicity mechanism. *J. Nanopart. Res.*, **12** (5), 1645–1654.
144. Asharani, P.V., Wu, Y.L., Gong, Z. *et al*. (2008) Toxicity of silver nanoparticles in zebrafish models. *Nanotechnology*, **19** (25), 255102.
145. Xia, T., Zhao, Y., Sager, T. *et al*. (2011) Decreased dissolution of ZnO by iron doping yields nanoparticles with reduced toxicity in the rodent lung and zebrafish embryos. *ACS Nano*, **5** (2), 1223–1235.
146. Usenko, C.Y., Harper, S.L., and Tanguay, R.L. (2007) In vivo evaluation of carbon fullerene toxicity using embryonic zebrafish. *Carbon*, **45** (9), 1891–1898.
147. Chae, Y.J., Pham, C.H., Lee, J. *et al*. (2009) Evaluation of the toxic impact of silver nanoparticles on *Japanese medaka* (*Oryzias latipes*). *Aquat. Toxicol.*, **94** (4), 320–327.
148. Smith, C.J., Shaw, B.J., and Handy, R.D. (2007) Toxicity of single walled carbon nanotubes to rainbow trout, (*Oncorhynchus mykiss*): respiratory toxicity, organ pathologies, and other physiological effects. *Aquat. Toxicol.*, **82** (2), 94–109.
149. Handy, R.D., Henry, T.B., Scown, T.M. *et al*. (2008) Manufactured nanoparticles: their uptake and effects on fish—a mechanistic analysis. *Ecotoxicology*, **17** (5), 396–409.

150. Baun, A., Hartmann, N.B., Grieger, K. *et al*. (2008) Ecotoxicity of engineered nanoparticles to aquatic invertebrates: a brief review and recommendations for future toxicity testing. *Ecotoxicology*, **17** (5), 387–395.

151. Filella, M., Rellstab, C., Chanudet, V. *et al*. (2008) Effect of the filter feeder Daphnia on the particle size distribution of inorganic colloids in freshwaters. *Water Res.*, **42** (8), 1919–1924.

152. Baun, A., Sørensen, S.N., Rasmussen, R.F. *et al*. (2008) Toxicity and bioaccumulation of xenobiotic organic compounds in the presence of aqueous suspensions of aggregates of nano-C_{60}. *Aquat. Toxicol.*, **86** (3), 379–387.

153. Lovern, S.B., Strickler, J.R., and Klaper, R. (2007) Behavioral and physiological changes in *Daphnia magna* when exposed to nanoparticle suspensions (titanium dioxide, nano-C60, and C60HxC70Hx). *Environ. Sci. Technol.*, **41** (12), 4465–4470.

154. Zhu, X., Zhu, L., Chen, Y. *et al*. (2009) Acute toxicities of six manufactured nanomaterial suspensions to *Daphnia magna*. *J. Nanopart. Res.*, **11** (1), 67–75.

155. Mendonça, E., Diniz, M., Silva, L. *et al*. (2011) Effects of diamond nanoparticle exposure on the internal structure and reproduction of *Daphnia magna*. *J. Hazard. Mater.*, **186** (1), 265–271.

156. Lee, S.-W., Kim, S.-M., and Choi, J. (2009) Genotoxicity and ecotoxicity assays using the freshwater crustacean *Daphnia magna* and the larva of the aquatic midge *Chironomus riparius* to screen the ecological risks of nanoparticle exposure. *Environ. Toxicol. Pharmacol.*, **28** (1), 86–91.

157. Zhu, X., Chang, Y., and Chen, Y. (2010) Toxicity and bioaccumulation of TiO_2 nanoparticle aggregates in *Daphnia magna*. *Chemosphere*, **78** (3), 209–215.

158. Zhang, P., He, X., Ma, Y. *et al*. (2012) Distribution and bioavailability of ceria nanoparticles in an aquatic ecosystem model. *Chemosphere*, **89** (5), 530–535.

159. Ferry, J.L., Craig, P., Hexel, C. *et al*. (2009) Transfer of gold nanoparticles from the water column to the estuarine food web. *Nat. Nanotechnol.*, **4** (7), 441–444.

160. Buffet, P.-E., Richard, M., Caupos, F. *et al*. (2013) A mesocosm study of fate and effects of CuO nanoparticles on endobenthic species (*Scrobicularia plana*, *Hediste diversicolor*). *Environ. Sci. Technol.*, **47** (3), 1620–1628.

161. Tiede, K., Boxall, A.B.A., Tear, S.P. *et al*. (2008) Detection and characterization of engineered nanoparticles in food and the environment. *Food Addit. Contam.*, **25** (7), 795–821.

162. Chen, C., Li, Y.-F., Qu, Y. *et al*. (2013) Advanced nuclear analytical and related techniques for the growing challenges in nanotoxicology. *Chem. Soc. Rev.*, **42** (21), 8266–8303.

Index

Toxicology of Nanomaterials, First Edition. Edited by Yuliang Zhao, Zhiyong Zhang, and Weiyue Feng.